

Development of CRISPR gene therapy for retinal degenerations

Thesis submitted for the degree of Doctor of Philosophy

Lewis E Fry

Hertford College & Merton College
Nuffield Department of Clinical Neurosciences
University of Oxford

Supervisors:
Professor Robert E MacLaren
Dr Michelle E McClements

Michaelmas Term 2021













Abstract

Inherited retinal degenerations (IRDs) are a leading cause of blindness, caused by mutations in genes leading to dysfunction and death of cells in the outer retina. Gene-supplementation therapies using adeno-associated viral (AAV) vectors have been developed, however, they are limited to the treatment of recessive IRDs and genes with small coding sequences. The engineering of the clustered regularly interspaced short palindromic repeats (CRISPR)-CRISPR-associated (Cas) nuclease system has enabled facile gene editing of human cells. Herein, I explore CRISPR-Cas mediated gene editing of both DNA and RNA, to develop therapeutic strategies to alter or correct genes implicated in IRD pathogenesis.

This thesis firstly investigated aspects of AAV-mediated delivery of CRISPR-Cas for retinal gene inactivation. The orientation of the guide RNA (gRNA) relative to *Staphylococcus aureus*-derived SaCas9 within an all-in-one AAV-CRISPR vector was compared. I demonstrated *in vitro* that forward orientation of the gRNA improved expression and editing rates relative to reverse orientated gRNAs. Secondly, CasX—a novel, engineered, minimal Cas nuclease—was delivered within an all-in-one AAV vector via subretinal injection. Using *in vivo* imaging and functional studies, I showed CasX potently inactivated *EGFP* in rod photoreceptors and established safe and toxic doses in *nrl-EGFP*$^{+/-}$ mice.

This thesis secondly investigated aspects of base editing for the correction of point mutations in IRD genes. Large datasets were used to explore the landscape of IRD mutations amenable to base editing in large genes not treatable with AAV gene supplementation. Identifying the common *USH2A* (c.11864G>A; p.W3955X) mutation, I then developed and evaluated CRISPR-Cas13b-mediated RNA adenosine base editing approaches to correct p.W3955X and the homologous *Ush2a* (p.W3947X) mouse mutation *in vitro*. Subsequently, an *Ush2a*-W3947X mouse model of the syndromic IRD Usher syndrome was developed and

characterised. I finally used subretinal, AAV-delivered RNA base editors to successfully correct the molecular phenotype of the homozygous *Ush2a*-W3947X mouse.

Acknowledgements

I am sincerely grateful to my supervisor Prof Robert MacLaren for his encouragement and vision throughout my DPhil and beyond. Thank you for challenging me and supporting me to thrive. I am grateful to Dr Michelle McClements for guiding my journey in the lab. With kindness and skill from my start as a molecular biology novice. I would also like to acknowledge the input of Dr Alun Barnard to the early stages of my project.

The lab has been a fantastic place to grow *E. Coli*, ideas, and friendships, at the bench and over questionable lab dinner desserts. I thank all those who contributed their time and effort to teaching me so much. Of particular note: Dr Maria Patrício generously helped me start my lab work with her on choroideremia projects, Dr Cristina Martinez-Fernandez de la Camara gave me scientific and moral support built on a bedrock of coffee and Spanglish, Dr Ahmed Salman was magnanimous with his time and spirit, and I am ever grateful to Dr Lucy McDermott the Western Blot Whisperer. Dr Imran Yusuf and Dr Harry Orlans not only climbed Hawaiian mountains with me but were also excellent subretinal surgery tutors. Dr Caroline Peddle's gene editing expertise and sticker charts were crucial contributions with Marta Stevanovic to Team CRISPR. Thank you to Dr Laurel Chandler for your great company at Merton and at our 5pm statistics conundrums, and to Dr Mark Hassall for introducing me to Oxford.

The extended lab family has supported me throughout and I also thank Prof Peter Charbel-Issa, Prof Susan Downes, Dr Arantxa Bolinches Amorós, Federica Staurenghi, Elena Piotter, Dr Jasleen Jolly, Dr Tom Buckley, Ariel Kantor, Dr Connie Han, Dr Sophia Bellingrath, Amandeep Josan, Laura Taylor, and Joel Quinn, as well as Solomon Merepa and Dr Ricardo Parolin Schnekenberg. A special thanks to Dr Britt Hanson, a brilliant friend to navigate through New York and the genome engineering world.

I have benefitted from many collaborations and discussions in this work. Particularly I would like to acknowledge Dr Brett Staahl, Dr Cecilé Fortuny and Dr Maroof Adil at Scribe

Therapeutics; Michelle Stewart and the team at the Mary Lyon Centre, MRC Harwell; Prof Andrew King, Dr Chris Breen and Dr Philip Hublitz at the University of Oxford; and Prof Vasiliki Kalatzis and Dr Carla Sanjurjo-Soriano at Institut des Neurosciences de Montpellier. Thank you also to Prof Feng Zhang and Soumya Kannan at the Broad Institute; Dr Jonathan Gootenberg and Dr Omar Abudayyeh at the Massachusetts Institute of Technology; Prof Jun Yang at the University of Utah and Prof Luk Vandenberghe of Harvard Medical School; who all provided valuable materials for this work.

To the staff of the John Radcliffe BMS, thank you for the dedicated care for our animals.

I am sincerely grateful to The Rhodes Trust. The Moussouris-Rhodes Scholarship enabled me to come to Oxford and provided me not only with financial support, but a strong community and life-long friends. I am also grateful for the support of The North Harbour Club and The Amar-Franses and Foster-Jenkins Trust. Merton College and the NDCN have supported my travel for conferences to present my work, while the Alain Locke Studentship from Hertford College allowed me to finish this work after disruption by COVID-19. All have been critical to the completion of this DPhil.

Finally, thank you to my family and friends for their unconditional support. To my parents: my love of learning was nurtured by you, thank you for your love, inspiration, and guidance. To Amelia: this thesis would not be possible without your patience, joy and enthusiasm for touchdowns and knockdowns. You are my rock.

Declaration

The work presented in this thesis was undertaken in Professor Robert MacLaren's laboratory at the Nuffield Department of Clinical Neurosciences, University of Oxford, between 2017 and 2021.

I, Lewis Fry, hereby declare that all work presented is my own unless otherwise indicated. Contributions are indicated in the figure legend for the relevant data. Experimental data from Dr Caroline Peddle and Dr Marta Stefanovic contributed to Chapter 3. AAV vectors used in Chapter 4 were designed and produced by Scribe Therapeutics (Alameda, CA, USA). Experimental data from Cecilé Fortuny (Scribe Therapeutics) contributed to Chapter 4. Michelle McClements assisted with animal procedures that contributed data in Chapter 4. The experimental design and generation of the *Ush2a*-W3947X mouse described in Chapter 6 was performed by the Mary Lyon Centre, MRC Harwell (Harwell, UK) in collaboration with myself as part of the Genome Editing Mice for Medicine Programme. DNA sequencing was commercially outsourced to Source Bioscience (Nottingham, UK), Genewiz (South Plainfield, NJ, USA), Eurofins Genomics (Ebersberg, Germany). Sources for all material from commercial manufacturers or provided as kind gifts from other researchers are acknowledged throughout, and fully summarised in the Appendix.

All figures are original unless otherwise stated. Schematic diagrams were produced with Biorender.com. This thesis includes content (data, figures and text) produced by me during this thesis that has been published. Where chapters contain published content, this is clearly stated and details of relevant re-use permissions are listed in the appendix. The word count (excluding table of contents, lists of figures and tables, figure legends and references) is 49,980 words.

No material presented here has been previously submitted to the University of Oxford, or to any other academic institution, for another degree or qualification.

--- Lewis Fry 2021

Contents

Abstract ..... **ii**

Acknowledgements ..... **iv**

Declaration ..... **vi**

Contents ..... **vii**

Table of Figures ..... **xvi**

Table of Tables ..... **xix**

List of Abbreviations ..... **xx**

1 Introduction **1**

1.1 The Retina and Inherited Retinal Disease 1

1.1.1 The Retina 1

1.1.1.1 Cellular structure 2

1.1.1.2 Photoreceptor cells 5

1.1.1.3 Comparative anatomy of the retina in *Mus musculus* 6

1.1.2 Inherited retinal degeneration 7

1.1.3 Treatments for inherited retinal degeneration 10

1.1.3.1 Gene supplementation with AAV vectors 11

1.1.3.2 Gene modulation approaches 16

1.1.4 Unmet needs in inherited retinal disease treatment 17

1.2 *USH2A*-related retinal degeneration 18

1.2.1 Clinical Manifestations 19

1.2.2 Molecular genetics of *USH2A* 22

1.2.2.1 Isoforms of *USH2A* 22

1.2.2.2 Usherin protein structure 22

1.2.2.3 Usherin localisation, function and interactions 24

1.2.3 Common variants and genotype-phenotype correlations 26

1.2.4 *USH2A* Models 27
1.2.4.1 Cellular models 27
1.2.4.2 Animal models 28
1.2.5 Treatment of *USH2A*-related disease 30
1.3 Genome Editing in Inherited Retinal Disease 32
1.3.1 Development of CRISPR-Cas Systems 32
1.3.1.1 Early gene editing systems 32
1.3.1.2 Development of CRISPR-Cas for gene editing 32
1.3.1.3 The growing CRISPR family 33
1.3.2 DNA Editing with CRISPR-Cas in the Retina 34
1.3.2.1 Active Cas Nucleases 34
1.3.2.2 Transcriptional regulation 39
1.3.2.3 Base and Prime Editing 39
1.3.3 RNA Targeting with CRISPR in the Retina 48
1.3.3.1 Retinal RNA therapeutics 48
1.3.3.2 Cas13 for RNA targeting 48
1.3.3.3 RNA base editing with CRISPR-Cas13 49
1.3.4 Translational considerations of retinal genome editing 57
1.3.4.1 Genotoxicity 57
1.3.4.2 Immunogenicity 59
1.3.4.3 Disease targets 59
1.4 Thesis outline 60
1.4.1 Knowledge gaps 60
1.4.2 Thesis aims 61

2 Materials and Methods 63
2.1 Molecular Biology 63
2.1.1 *In Silico* Design and Analysis 63
2.1.2 Polymerase Chain Reaction 63
2.1.3 Restriction Digestion 65
2.1.4 Agarose Gel Electrophoresis and Gel Extraction 66
2.1.5 Nucleic acid quantification 66
2.1.6 Plasmid Cloning Techniques 66
2.1.6.1 Oligonucleotide annealing and phosphorylation 66
2.1.6.2 Ligation of single fragments 67

2.1.6.3 Multi-fragment DNA Assembly 67
2.1.7 Transformation 67
2.1.8 Colony selection and plasmid amplification 68
2.1.9 Genomic DNA Extraction 69
2.1.10 RNA Extraction 69
2.1.11 cDNA Synthesis 69
2.1.12 Reverse Transcription quantitative-PCR 70
2.1.13 Protein Extraction and Quantification 71
2.1.14 Western Blot 72
2.1.15 Sanger Sequencing 73
2.2 Cell Culture 73
2.2.1 Cell Lines & Maintenance 73
2.2.2 *In Vitro* Plasmid transfection 74
2.2.3 *In Vitro* Viral transduction 75
2.2.4 Cell Harvesting 75
2.3 AAV Production 76
2.3.1 Plasmids for AAV production 76
2.3.2 Transfection of HEK293T cells 76
2.3.3 Harvesting and Lysis 77
2.3.4 Isolation of AAV particles 78
2.3.5 Purification and concentration of AAV 79
2.3.6 AAV Capsid Analysis with SDS-PAGE 80
2.3.7 AAV Titration 80
2.3.8 Endotoxin Testing 81
2.4 *In Vivo* Procedures 81
2.4.1 Anaesthesia and Mydriatics 81
2.4.2 Subretinal Injections 82
2.4.3 Retinal imaging 83
2.4.3.1 Confocal Laser Scanning Ophthalmoscopy 84
2.4.3.2 Optical Coherence Tomography 85
2.4.4 Electroretinography 86
2.5 Cell and Tissue Analysis 89
2.5.1 Retinal Tissue Collection 89
2.5.2 Immunohistochemistry 89

2.5.3 Immunocytochemistry 90
2.5.4 Microscopy 91
2.5.4.1 Confocal Microscopy 91
2.5.4.2 EVOS LED Microscopy 91
2.6 Statistical Analysis 92

3 Promoter Orientation Within An AAV-CRISPR Vector Affects Cas9 Expression and Gene Editing Efficiency 93
3.1 Introduction 93
3.1.1 Chapter Aims 95
3.2 Methods 95
3.2.1 Plasmid Cloning 95
3.2.2 Cell Culture 95
3.2.3 Analysis of editing efficiency 96
3.2.4 RNA analysis 97
3.2.5 Protein Analysis 98
3.2.5.1 Western blot 98
3.2.5.2 Protein fluorescence assay 98
3.2.6 Statistical analysis 99
3.3 Results 100
3.3.1 Plasmid Design 100
3.3.2 Pilot experiment targeting EGFP 101
3.3.2.1 On-target editing of EGFP 101
3.3.2.2 Expression of SaCas9 and gRNA following transfection 103
3.3.3 Effect of U6-reversal using gRNAs targeting retinal loci 103
3.3.3.1 Qualitative and Quantitative Analysis of AAV Vectors 104
3.3.3.2 Plasmid and AAV dose and effect on editing rates 106
3.3.3.3 Effect of reverse orientation of the U6-gRNA on editing rates 107
3.3.3.4 Effect of reverse orientation of the U6-gRNA on *SaCas9* and gRNA expression 108
3.3.3.5 Effect of reverse orientation of the U6-gRNA on SaCas9 protein expression 110
3.4 Discussion 111
3.4.1 Conclusion 115

4 *In Vivo* Editing with CasX, a Novel Class 2 CRISPR System....116
4.1 Introduction 116
4.1.1 Chapter Aims 119
4.2 Methods 120
4.2.1 Animal models and procedures 120
4.2.2 Retinal imaging and quantification 120
4.2.3 Construct cloning and AAV production 121
4.2.4 Western Blot 122
4.2.5 Immunohistochemistry 124
4.2.6 Next generation sequencing 124
4.2.7 Statistical analysis 125
4.3 Results 126
4.3.1 Assessment of EGFP knockdown with CSLO autofluorescence imaging 126
4.3.2 SD-OCT assessment of retinal structure following treatment 129
4.3.3 Molecular analysis of EGFP editing 132
4.3.4 Immunohistochemistry and microscopy of treated retinas 136
4.3.5 Electroretinogram assessment of retinal function following treatment 140
4.4 Discussion 143
4.4.1 Conclusion 147

5 Analysis of Pathogenic Variants Correctable With CRISPR Base Editing Among Patients With Recessive Inherited Retinal Degeneration 148
5.1 Introduction 148
5.1.1 Chapter Aims 150
5.2 Methods 152
5.2.1 Leiden Open Variation Database Search and Variant Coding 152
5.2.2 Analysis of variants by individual 153
5.2.3 Statistics and analysis 154
5.3 Results 155
5.3.1 Prevalence of Editable Variants in LOVD 155
5.3.2 Patients with Editable Variants 161
5.4 Discussion 167
5.4.1 Conclusion 171

6 Development of a Cas13-Mediated RNA Editing Approach to Correct Nonsense Mutations in *USH2A* 172

6.1 Introduction 172

6.1.1 Chapter Aims 174

6.2 Materials and Methods 175

6.2.1 Dual Luciferase Assay 175

6.2.1.1 Dual Luciferase assay design and cloning 175

6.2.1.2 Cell culture and transfection for dual luciferase assay 177

6.2.1.3 Dual-Glo luciferase assay 177

6.2.1.4 Editing efficiency calculation 177

6.2.2 Cloning of Cas13-ADAR editing plasmids 178

6.2.2.1 Cas13b-ADAR2$_{DD}$ and gRNA plasmids 178

6.2.2.2 Bulk guide RNA cloning 180

6.2.2.3 Cloning of short promoters & polyA sequences 181

6.2.2.4 Cloning of AAV RNA editor plasmids 182

6.2.3 Detection of RNA editing with RT-PCR Sequencing 185

6.2.4 Western blot 185

6.2.5 Immunocytochemistry 186

6.3 Results 187

6.3.1 Development of a Luciferase assay to report RNA editing 187

6.3.1.1 Validation of luciferase reporter plasmids 187

6.3.1.2 Pilot of RNA editing detection with luciferase assay 190

6.3.2 Testing and optimisation of RNA editing constructs 192

6.3.2.1 Guide RNA screening 192

6.3.2.2 Dose optimisation of dPspCas13b-ADAR2$_{DD}$ and gRNA constructs 194

6.3.2.3 Comparison of RNA editing constructs 196

6.3.2.4 Evaluation of minimal Cas13bt orthologues 198

6.3.3 Comparison of luciferase assay with Sanger sequencing 199

6.3.4 Local off-target effects detected by Sanger sequencing 202

6.3.5 Evaluation of minimal regulatory elements to enable AAV packaging 207

6.3.5.1 Minimal RNA Pol II promoters 207

6.3.5.2 Minimal polyA sequence 208

6.3.5.3 tRNA Promoter to drive gRNA expression 208

6.3.6 Cloning and testing of AAV-Cas13-ADAR2$_{DD}$ Constructs 210

6.3.6.1 Testing of EFS driven RNA editing constructs 210
6.3.6.2 Generation of RK Driven constructs 215
6.4 Discussion 217
6.4.1 Luciferase assay development 217
6.4.2 Use of the luciferase assay for quantifying RNA editing 218
6.4.3 Insights from gRNA screening 219
6.4.4 Comparison of RNA editing constructs 220
6.4.5 Off-target editing 221
6.4.6 Optimisation of RNA editing constructs for AAV packaging 222
6.4.7 Conclusion 223

7 Development and Correction of a Mouse Model of Usher Syndrome 224
7.1 Introduction 224
7.1.1 Aims 226
7.2 Methods 228
7.2.1 Animal models and procedures 228
7.2.1.1 Genotyping 228
7.2.1.2 ddPCR copy counting assay 229
7.2.1.3 Auditory brainstem responses 229
7.2.2 Western blot 231
7.2.3 Immunohistochemistry 232
7.2.3.1 Retinal Sections 232
7.2.3.2 Cochlea wholemounts 233
7.2.4 Editing efficiency quantification 233
7.2.4.1 Target amplification 233
7.2.4.2 Sanger sequencing 234
7.2.4.3 Targeted Deep Sequencing 234
7.3 Results 235
7.3.1 Comparison of *USH2A* species homology 235
7.3.2 Characterisation of the *Ush2a*-W3947X mouse 237
7.3.2.1 Design, generation & genotyping 237
7.3.2.2 Molecular analysis of *Ush2a*-W3947X retinas 239
7.3.2.3 Natural history of the retinal phenotype of the *Ush2a*-W3947X mouse 242
7.3.2.4 Characterisation of the cochlea phenotype 246
7.3.3 Pilot study of EFS-driven AAV vectors for *Ush2a*-W3947X repair 248

7.3.3.1 AAV Vector production 248
7.3.3.2 On-target m*Ush2a* editing with dual vector EFS-dPspCas13b-del-ADAR(E488Q) strategy 250
7.3.3.3 Analysis of expression from EFS-driven vectors 253
7.3.3.4 Analysis of retinal structure in EFS-dual vector strategy pilot 256
7.3.4 Pilot study of RK-driven AAV vectors for *Ush2a*-W3947X repair 258
7.3.4.1 AAV Production 258
7.3.4.2 RK-dPspCas13b-del-ADAR(E488Q) dual vector strategy 260
7.3.4.3 All-in-one AAV-RK-Cas13bt3-ADAR(E488Q)-U6-gRNA pilot 266
7.3.5 Local off-target editing *in vivo* 269
7.4 Discussion 272
7.4.1 *Ush2a*-W3947X mouse 272
7.4.1.1 Molecular Characterisation 272
7.4.1.2 Natural History 274
7.4.2 AAV-dCas13-ADAR2$_{DD}$ RNA editors for repair of *Ush2a* 275
7.4.2.1 RNA editors are capable of *in vivo* repair in photoreceptors 275
7.4.2.2 Off-target effects and toxicity 276
7.4.2.3 AAV-mediated expression of dCas13b-ADAR 278
7.4.3 Translational considerations 279
7.4.4 Conclusions 280

8 General Discussion 281
8.1 Summary of thesis aims and outcomes 281
8.2 Delivery of CRISPR-Cas with AAV Vectors for inherited retinal disease 284
8.2.1 Alternative perspectives on AAV delivery 285
8.3 Next generation gene editing therapeutics for inherited retinal disease 286
8.3.1 Protein discovery and engineering 286
8.3.2 DNA editing without double stranded breaks 287
8.3.3 RNA Base editing 288
8.4 Models and therapeutics for Usher syndrome 290
8.5 Progress in genetic therapeutics for inherited retinal disease 290
8.6 Societal considerations of gene editing 292
8.7 Conclusions 293

References 294

Appendix **342**

A. Nucleotide sequences **342**

B. Key Resources List **353**

C. Code and Macros **363**

D. Publications, Presentations, Reviews, Grants, Awards & Prizes **367**

Table of Figures

Figure 1-1 Normal retinal anatomy 4
Figure 1-2 Photoreceptor structure 6
Figure 1-3 Frequently implicated IRD genes and site of expression 9
Figure 1-4 Wildtype AAV genome and generation of recombinant AAV 13
Figure 1-5 Frequency and modes of inheritance of common genes implicated in inherited retinal disease in UK Families 18
Figure 1-6 Retinal features of *USH2A*-related retinal degeneration 21
Figure 1-7 Usherin isoforms, localisation and interacting proteins 23
Figure 1-8 Overview of DNA Editing Approaches 38
Figure 1-9 Mechanism of adenosine to inosine deamination 51
Figure 1-10 Schematic overview of RNA editing approaches 55
Figure 2-1 Iodixanol gradient formation 79
Figure 2-2 Operative images of subretinal injection 83
Figure 2-3 Retinal imaging of animals with cSLO and OCT 85
Figure 2-4 Measurement of ERG responses 87
Figure 3-1 Example output of TIDE Analysis 97
Figure 3-2 Cloning of the reverse U6-gRNA transgene 100
Figure 3-3 Effect of U6-gRNA orientation in plasmids targeting EGFP following transfection 102
Figure 3-4 Experimental outline of reverse U6 experiment targeting retinal genes 104
Figure 3-5 SDS-PAGE analysis of AAV vectors 105
Figure 3-6 AAV Dose Response Experiments 107
Figure 3-7 Comparison of effect of U6-reversal between plasmid transfection and AAV transduction 109
Figure 3-8 Western blot of SaCas9 expression levels 110
Figure 3-9 Model of promotor proximity in an AAV vector 115
Figure 4-1 Schematic of CasX gRNA target 117
Figure 4-2 Mean Grey Value Measurement of Blue Autofluorescence cSLO Fundus Images 121
Figure 4-3 Vector and target map 122
Figure 4-4 *In vivo* imaging of *Nrl.EGFP*$^{+/-}$ mice following subretinal injection 127
Figure 4-5 Fundus BAF mean grey value 4 weeks post injection 128

Figure 4-6 Fundus BAF mean grey value 12 weeks post injection 129
Figure 4-7 Photoreceptor layer thickness 4-weeks post-injection 130
Figure 4-8 Photoreceptor layer thickness 12-weeks post-injection 132
Figure 4-9 On-target editing efficiency following AAV.CasX injection 133
Figure 4-10 Analysis of protein expression in AAV.CasX injected retinas 136
Figure 4-11 Immunofluorescence analysis of retinas following AAV.CasX treatment 138
Figure 4-12 Confocal imaging across the bleb border in AAV.CasX injected eyes 139
Figure 4-13 Retinal function assessed with dark adapted ERG 141
Figure 4-14 Tests of cone function with flicker and light-adapted ERG 142
Figure 5-1 Flow diagram outlining method of LOVD analysis 153
Figure 5-2 Distribution of alleles in the Leiden Open Variation Database 156
Figure 5-3 Common editable alleles and mutation type breakdown in the LOVD 159
Figure 5-4 Analysis of editable variants within patients in the Oxford and Stone et al. data sets 164
Figure 6-1 Dual luciferase reporter assay for RNA editing 176
Figure 6-2 Representative full plasmid maps of Cas13b and cRNA plasmids 179
Figure 6-3 *In Vivo* Assembly of tRNA(GLN) gRNA promoter construct 182
Figure 6-4 Cloning of AAV RNA editor plasmids 183
Figure 6-5 Dose response of luciferase plasmids in HEK293T cells 189
Figure 6-6 Calculation of RNA editing efficiency from luciferase assay 191
Figure 6-7 Initial guide RNA screening for *hUSH2A*-W3955X and *mUsh2a*-W3947X repair 193
Figure 6-8 Extended gRNA screen for *hUSH2A*-W3955X and *mUsh2a*-W3947X repair 194
Figure 6-9 Dose response testing of dPspCas13b-ADAR2$_{DD}$ constructs 195
Figure 6-10 Comparison of dPspCas13b-ADAR2$_{DD}$ editing constructs 197
Figure 6-11 Guide screening and comparison of Cas13bt orthologues 199
Figure 6-12 Editing efficiency from RNA sanger sequencing and decomposition 201
Figure 6-13 Correlation between RNA editing with dPspCas13b-ADAR2$_{DD}$ measured by luciferase assay and sanger sequencing 202
Figure 6-14 Local off-target analysis by sanger sequence decomposition 204
Figure 6-15 RNA structures of *USH2A* targets 206
Figure 6-16 Minimal promoters and polyA signals for RNA editing 209
Figure 6-17 RNA editing activity of EFS-driven AAV plasmid constructs 213

Figure 6-18 Protein expression from EFS-driven AAV plasmid constructs in HEK293T cells 214
Figure 6-19 Vector maps of RK-driven AAV RNA editor constructs 216
Figure 7-1 Auditory Brainstem Response Recording Setup 231
Figure 7-2 Comparison of human and murine usherin coding and protein sequences 236
Figure 7-3 Generation and genotyping of *Ush2a*-W3947X mouse 238
Figure 7-4 Usherin expression in retina of *Ush2a*-W3947X mouse 240
Figure 7-5 *Ush2a* mRNA expression in retina of *Ush2a*-W3947X mouse 241
Figure 7-6 USH2A antibody testing 241
Figure 7-7 Natural history of CSLO retinal imaging of *Ush2a*-W3947X mouse 243
Figure 7-8 Natural history of OCT imaging of *Ush2a*-W3947X mouse 244
Figure 7-9 Natural history of ERG function of *Ush2a*-W3947X mouse 245
Figure 7-10 Cochlea phenotype of *Ush2a*-W3947X mouse 247
Figure 7-11 Analysis of EFS-driven AAV Vectors 249
Figure 7-12 EFS-driven dPspCas13b-del-ADAR(E488Q) on-target editing 251
Figure 7-13 Analysis of EFS-driven transgene expression 253
Figure 7-14 Expression GFP under an EFS promoter following subretinal injection 255
Figure 7-15 Retinal structure following subretinal injection of EFS-driven AAVs 257
Figure 7-16 Analysis of RK-driven AAV Vectors 259
Figure 7-17 RK-driven dPspCas13b-del-ADAR(E488Q) on-target editing of *Ush2a*-W3947X 261
Figure 7-18 Usherin expression following RK-dPspCas13bdel-ADAR(E488Q) repair of *Ush2a*-W3947X mutation 262
Figure 7-19 Analysis of RK-driven dPspCas13b-del-ADAR(E488Q) expression 264
Figure 7-20 Retinal structure following subretinal injection of RK-dPspCas13bdel-ADAR(E488Q) AAV vectors 265
Figure 7-21 *Ush2a* RNA editing with all-in-one Cas13bt3 vectors 268
Figure 7-22 Retinal structure following subretinal injection of all-in-one dCas13bt3-ADAR(E488Q)-U6-gRNA AAV vectors 269
Figure 7-23 Local off-target editing with RK-dPspCas13b-del-ADAR(E488Q) 271
Figure 7-24 Potential alternative *Ush2a* polyA site 274

Table of Tables

Table 1-1 Overview of *in vivo* gene engineering studies targeting retinal cells implicated in retinal disease 47
Table 1-2 Comparison of RNA editing tools 57
Table 2-1 General criteria for design of PCR primers 64
Table 2-2 General PCR Cycle Conditions for KOD Hotstart Mastermix 65
Table 2-3 General PCR Cycle conditions Phusion Polymerase 65
Table 2-4 qPCR Cycling Conditions 71
Table 2-5 Cell Seeding Density for Plasmid Transfection 75
Table 2-6 Calculation table for plasmid transfection for rAAV production 77
Table 2-7 Preparation of Iodixanol Gradients 78
Table 2-8 ERG recording protocol 88
Table 3-1 FIPA Buffer Recipe 99
Table 3-2 AAV titre determined by qPCR 105
Table 4-1 Table of antibodies 124
Table 5-1 Prevalence of the most common six large recessive genes among patients with a molecular diagnosis of inherited retinal disease 151
Table 5-2 Spectrum of pathogenic alleles in the LOVD 158
Table 5-3 Most common editable mutations in the LOVD 161
Table 5-4 Common Editable Alleles in the Oxford Dataset 164
Table 5-5 Common Editable Alleles in the Stone et al. Dataset 166
Table 6-1 dCas13b-ADAR2$_{DD}$ and gRNA plasmids 180
Table 6-2 Cloning of AAV plasmids with multi-fragment assembly 184
Table 6-3 Luciferase assay characteristics with triple transfection 188
Table 6-4 Characteristics of Cas13b orthologues used 198
Table 6-5 Codon changes due to off-target editing 205
Table 7-1 Current mouse models of IRD with G>A transitions 227
Table 7-2 Allelic Discrimination Assay Mastermix 229
Table 7-3 Towbin Buffer (10✕) 232
Table 7-4 Primary antibodies used for western blot and immunohistochemistry 232

List of Abbreviations

AAV	Adeno-Associated Virus
ABCA4	ATP-binding cassette, subfamily A, member 4
ABE	Adenine base editors
ABR	Auditory brainstem response
AD	Autosomal dominant
$ADAR_{DD}$	Adenosine deaminase acting on RNA deaminase domain
AMD	Age-related macular degeneration
ANOVA	Analysis of variance
AR	Autosomal recessive
ART	Automated real time
ASO	Antisense oligonucleotides
ATP	Adenosine Triphosphate
BAF	Blue autofluorescence
bGH	Bovine growth hormone polyA
BSA	Bovine serum albumin
Cas	CRISPR-associated proteins
CBE	Cytosine base editor
cDNA	Complementary DNA
CDS	Coding sequence
CEP290	Centrosomal protein, 290-KD
CMV-IE	Cytomegalovirus Intermediate Early Enhancer
CNV	Copy number variation
CORD	Cone rod dystrophy
CRISPR	Clustered regularly interspaced short palindromic repeats
CRISPRa/i	CRISPR activation/interference
crRNA	CRISPR RNA
cSLO	Confocal laser scanning ophthalmoscope
CSNB	Congenital stationary night blindness
dCas	Dead (inactivated) Cas
ddPCR	Digital droplet PCR
DMEM	Dulbecco's Modified Eagle Medium

DNA	Deoxyribonucleic Acid
DPOAE	Distortion product otoacoustic emission
DR	Direct repeat
DSB	Double stranded break
dsRNA/DNA	Double stranded RNA/DNA
EFS	elongation factor-1α core / short promoter
EGFP	Enhanced Green Fluorescent Protein
EIAV	Equine infectious anaemia virus
ELM	External limiting membrane
ERG	Electroretinogram
EYS	Eyes shut homologue
GAF	Green autofluorescence
GCL	Ganglion cell layer
GFAP	Glial fibrillary acidic protein
GFP	Green fluorescent protein
gRNA	Guide RNA
HDR	Homology directed repair
HEK293T	Human Embryonic Kidney 293 Cells Expressing Mutant SV40 T Antigen
HEPN	Higher eukaryotes and prokaryotes nucleotide-binding domain
HI-FBS	Heat Inactivated FBS
HITI	Homology-independent targeted insertion
ICGA	indocyanine green angiography
ILM	Inner limiting membrane
INL	Inner nuclear layer
IPL	Inner plexiform layer
iPSC	Induced pluripotent stem cells
IRD	Inherited retinal degeneration
IS	Inner segment
ITR	Inverted terminal repeat
LCA	Leber's congenital amaurosis
LEAPER	Leveraging Endogenous ADAR for Programmable Editing of RNA
LED	Light emitting diode
LOVD	Leiden Open Variation Database
MCP	MS2 bacteriophage coat protein

mGV	Mean grey value
MMEJ	Microhomology-mediated end joining
MOI	Multiplicity of infection
NGS	Normal goat serum
NGS	Next generation sequencing
NHEJ	Non-homologous end joining
NHP	Non-human primate
NIR	Near infrared reflectance
Nrl	Neural leucine zipper
OCT	Optical coherence tomography
OCT	Optimal cutting temperature compound
OKR	Optokinetic response
ONL	Outer nuclear layer
OPL	Outer plexiform layer
ORF	Open reading frame
OS	Outer segment
OTC	Ornithine transcarbamylase
PAGE	Polyacrylamide Gel Electrophoresis
PAM	Protospacer adjacent motif
PBS	Phosphate Buffered Saline
PCR	Polymerase Chain Reaction
PEI	Polyethylenimine
PFA	Paraformaldehyde
PFS	Protospacer flanking site
PMC	Periciliary membrane complex
PNK	Polynucleotide Kinase
PR	Photoreceptor
PRL	Photoreceptor layer
PTC	Premature termination codon
PVDF	Polyvinylidene difluoride
rAAV	Recombinant Adeno-Associated Virus
RCS	Royal College of Surgeons rat
REPAIR	RNA Editing for Programmable A to I Replacement
RESCUE	RNA Editing for Specific C to U Exchange

RESTORE	Recruiting Endogenous ADAR to Specific Transcripts for Oligonucleotide-mediated RNA Editing
RFP	Red fluorescent protein
RGC	Retinal ganglion cell
RK	Rhodopsin kinase
RNA	Ribonucleic Acid
RNP	Ribonuclear protein
RP	Retinitis pigmentosa
RPE	Retinal pigment epithelium
RT-qPCR	Reverse Transcription quantitative-PCR
SCP1	Super core promoter 1
SD	Standard deviation
SDS	Sodium-Dodecyl-Sulfate
SEM	Standard error of the mean
siRNA	small interfering RNA
sNRP1	Soluble neuropilin-1 polyA
ssRNA/DNA	Single stranded RNA/DNA
SV40	Simian virus-40
TadA	tRNA-specific adenosine deaminase
TAE	Tris/Acetate/Ethylenediaminetetraacetic Acid
TBS	Tris-Buffered Saline
TBS-T	Tris-Buffered Saline with 0.01% Tween-20
USH	Usher syndrome
USH2A	Usher syndrome, type 2A
VEGF	Vascular endothelial growth factor
VEP	Visual evoked potential
VP (1,2,3)	Virion Protein (1,2,3)
WT	Wildtype
XL	X-linked
ZFN	Zinc finger nucleases

1 INTRODUCTION

1.1 The Retina and Inherited Retinal Disease

1.1.1 The Retina

The retina is the thin, multi-layered structure in the posterior segment of the eye responsible for the conversion of light energy into electric potentials. Light enters the eye through the cornea and lens and is focused on the retina, where it is converted to an electrical signal to be transmitted via the optic nerve and thalamus to the striated region (V1 or Brodmann area 17) of the visual cortex of the brain (Figure 1-1). At a macroscopic level, the human retina has a nasally displaced optic nerve head from which vascular arcades extend superiorly and inferior around the macula, a central region responsible for the central visual field. Light is focused on the central macula at the fovea, a specialised region for high acuity vision. Inner retinal neurons are displaced away from the fovea to form a pit consisting entirely of cone photoreceptors in order to maximise light detection.[1] Cone density is maximal at the fovea and decreases with eccentricity, while rod photoreceptor density is maximal in the perifoveal region before decreasing with further eccentricity.

Text, figures, and tables in this chapter have been published as: Fry LE, Peddle CF, Barnard AR, et al. RNA editing as a therapeutic approach for retinal gene therapy requiring long coding sequences. Int J Mol Sci. 2020;21. DOI: 10.3390/ijms21030777.

1.1.1.1 Cellular structure

Derived from neuroectoderm, the retina develops to contain seven major neuronal cell types organised in three layers of cell bodies (nuclear layers) separated by two synaptic layers (plexiform layers) (Figure 1-1).[1]

The outer nuclear layer (ONL) contains the cell bodies of light sensitive photoreceptors cells. Rod photoreceptors express the highly sensitive opsin rhodopsin, and mediate vision in low-light conditions. Cone photoreceptors express photopsin proteins, and mediate high acuity vision in bright conditions and enable the perception of colour. Photoreceptors form synaptic connections in the outer plexiform layer (OPL) with cells of the inner nuclear layer (INL), the bipolar, horizontal and amacrine cells. Cells in the INL are responsible for the transmission and horizontal processing of visual signals, and these cells form synaptic connections in the inner plexiform layer (IPL) with retinal ganglion cells (RGCs) lying in the innermost nuclear layer.

RGC axons extend through the retinal nerve fibre layer to the optic nerve head, where they form the optic nerve and project to the brain. The INL also contains the cell bodies of Müller glia, which project throughout the layers of the retina and provide structural and homeostatic support. The inner footplates of the Müller glia form the inner limiting membrane (ILM) overlying the nerve fibre layer, while the outer footplates form the external limiting membrane (ELM) of the outer retina.

The retina overlies the retinal pigment epithelium (RPE). The RPE is a specialised pigmented monolayer that forms the outer blood-retinal barrier and provides critical homeostatic support functions for the overlying photoreceptor layer. While also of neuroectodermal origin, invagination of the optic cup during development separates progenitor cells that form the RPE and the neural retina, resulting in a potential anatomical space between the retina and RPE.

Light passes through the transparent retina to the photoreceptor layer, where photons are absorbed by photopigment molecules. Light-induced conformational change to the opsins

bound to photopigment molecules initiates the phototransduction cascade, a complex second messenger system that results in closing of cyclic nucleotide-gated ion channels, hyperpolarisation of the photoreceptor and a reduction in glutamate release at the photoreceptor synapse, triggering an electrical signal at second order neurons in the INL.[2] The visual cycle is completed by a series of molecular events to terminate phototransduction and recycle the photopigments for further phototransduction.

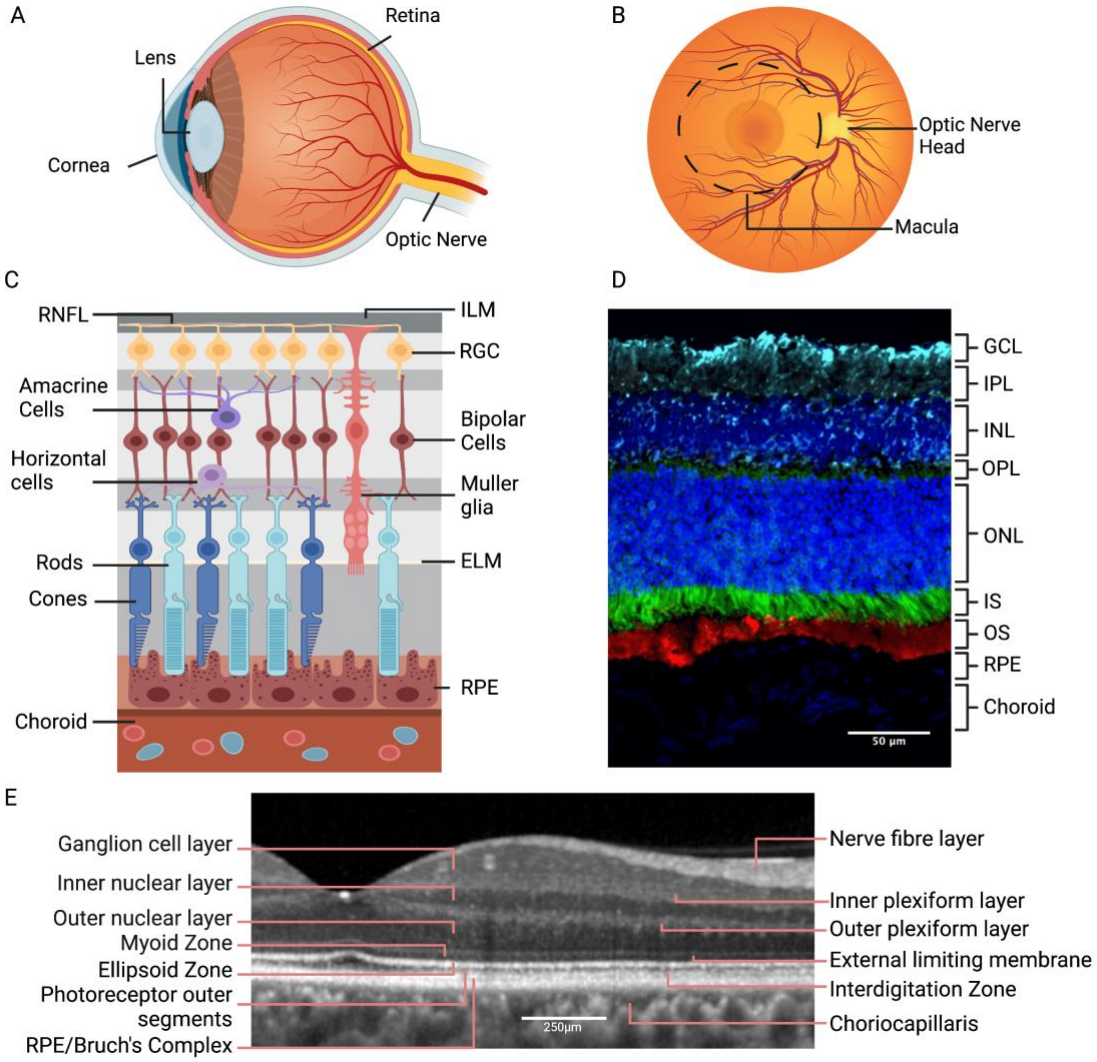


Figure 1-1 Normal retinal anatomy

A. Cross section of the human eye **B.** Diagram of human fundus demonstrating macula and optic nerve head. **C**. Schematic representation of retinal cells and their connections within the retinal layers. **D.** Histological section of a mouse retina demonstrating the corresponding histological retinal layers. Image courtesy of M. McClements. **E.** Spectral domain optical coherence tomography (OCT) cross section of the normal human retina at the macula. Labelled according to the international nomenclature for OCT.[3] RNFL = retinal nerve fibre layer. ILM = inner limiting membrane. GCL = Ganglion cell layer. IPL = inner plexiform layer. INL = inner nuclear layer. OPL = outer plexiform layer. ONL = outer nuclear layer. ELM = external limiting membrane. IS = photoreceptor inner segment. OS = photoreceptor outer segment. RPE = retinal pigment epithelium. Created with BioRender.com. OCT Image courtesy of Dr Thomas Buckley, Oxford Eye Hospital.

1.1.1.2 Photoreceptor cells

Photoreceptors have a polarised structure consisting of four compartments: an axonal/synaptic compartment, the cell body, the inner segment (IS) and the outer segment (OS) (Figure 1-2). The synaptic terminal forms connections in the INL, while the cell body contains the cell nucleus. Protein synthesis and metabolism occurs in the IS, and proteins must be trafficked across the connecting cilium to the OS.

The connecting cilium (CC) is a narrow bridge linking the IS and OS.[1] It is cylindrical with a narrow internal ciliary lumen and an outer ring formed of axonal microtubules surrounded by ciliary membrane, to which it is linked by fibrous Y-link structures.[4,5] The axonemal microtubules extend from the basal body in the distal IS, through the transition zone in the connecting cilium and into the outer segment. At the transition zone, the microtubules are anchored tightly by transition fibres at the base of the cilium. The structures of the connecting cilium are proposed to act as a diffusion barrier to divide the specialised functions of the IS and OS.[4,6] The ciliary rootlet, formed primarily from the protein rootletin,[7] is a large cytoskeleton-like structure which extends from the basal body to the axon terminal.[6]

Phototransduction occurs in the OS, a modified non-motile cilium that contains stacks of membranous discs organised to enable a high density of opsin proteins.[1] During the visual cycle, discs are generated in the proximal OS and move distally as old OS discs are phagocytosed at the RPE apical membrane, which approximates the OS base. The OS structure differs between cones and rods. Rods contain individual discs separated from the enveloping plasma membrane, while the discs of cones are contiguous with the cone plasma membrane. Rods have a long thin OS morphology, and phototransduction is initiated by the photopigment rhodopsin. Cones derive their name from the more conical appearance of the OS. The human retina has three subtypes of cones, each containing a different photopigment molecule sensitive to a different wavelength of light to permit colour vision i.e. S-cones (short wavelength), M-cones (medium wavelength) and L-cones (long wavelength).

As the primary site of pathology in many inherited retinal degenerations, the structure, function, and distribution of photoreceptors have important implications for retinal function, disease and treatment strategies. The developed human retina contains approximately 92 million rods and 4.6 million cones.[8] These cells are post-mitotic and do not divide or regenerate following injury.

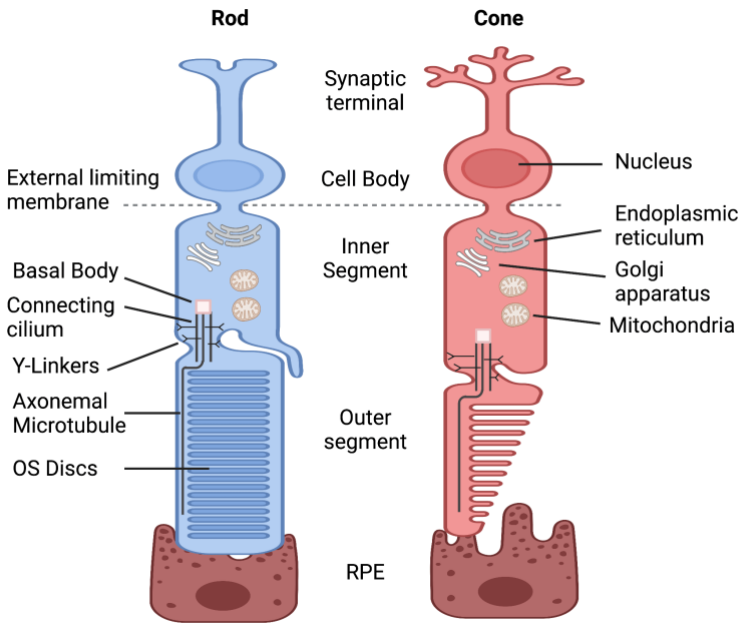


Figure 1-2 Photoreceptor structure
Schematic diagram of rod and cone photoreceptors. Synaptic connections are made in the outer plexiform layer via ribbon synapses. Organelles for protein and energy production are enriched in the inner segment. Protein trafficking to the outer segment occurs via the basal body and the connecting cilium. Y-linker structures anchoring the connecting cilium to the plasma membrane are shown. The outer segment contains horizontally arranged membrane discs rich in visual pigments embedded in the disc membrane. In rod photoreceptors the discs are separate from the plasma membrane in the rod-shaped outer segment. Cone photoreceptors have a conical outer segment with discs continuous with the plasma membrane. The apical photoreceptor outer segment is adjacent to the RPE where discs are shed, and rhodopsin is transferred in the classical visual cycle. Created with BioRender.com.

1.1.1.3 Comparative anatomy of the retina in *Mus musculus*

The stratified cell layers of the retina are shared among mammalian species, including between *Homo sapiens* and the house mouse (*Mus musculus)*. Mice are commonly used to model retinal degeneration and investigate pre-clinical therapeutics, however a number of key

differences exist between the human and mouse retina.[9] The mouse has a central optic nerve with vascular arcades extending radially across the retina. As a nocturnal animal, mice do not have a macula and possess a much higher rod density than humans, with fewer cones.[10,11] Cone photoreceptors are distributed throughout the retina, with no clearly defined region for high acuity vision. Mice are dichromats with L/M-cones sensitive to long wavelength light distributed mostly in the superior retina, and S-cones distributed in the inferior retina, with some cones expressing both opsins.[12]

1.1.2 Inherited retinal degeneration

Inherited retinal degenerations (IRDs) are a diverse family of disorders caused by genetic mutations that lead to dysfunction and death of cells in the outer retina.[13] IRDs affect an estimated 1:2000-7000 people[14,15] and are a major cause of vision loss and disability as the leading cause of blindness in people of working age in high-income countries.[16–18]

Clinically, IRDs can be broadly divided into subtypes based on age of onset, rate of progression and clinical features.[14] Leber congenital amaurosis (LCA) is the most severe form, in which rods and cones are non-functional at birth or are lost within the first few years of life, causing blindness in childhood. Retinitis pigmentosa (RP), also known as rod-cone dystrophy, is the most common IRD and is characterised by the progressive and bilateral degeneration of rod photoreceptors, with cone photoreceptor degeneration eventually following rod death by a secondary mechanism.[19] Patients typically present in young adulthood with difficulties with dark adaptation and night vision due to rod dysfunction, followed by progressive concentric peripheral visual field loss with age. The central retina remains relatively preserved until the end stages of degeneration, meaning visual acuity can remain close to normal until the later stages of disease, however patients are often legally blind by 40 due severe visual field deficits.[20] Cone and cone-rod dystrophies primarily present in early adulthood with a loss of central vision, photophobia and loss of colour vision due to the involvement of cone photoreceptors.[21] Cone-

rod dystrophies can be distinguished from cone dystrophies by the presence of early nyctalopia due to the involvement of rods.[21] Some subtypes of IRD primarily affect the macula, termed macular dystrophies. These are characterised by bilateral, relatively symmetrical macular abnormalities that cause central visual loss. These clinical subtypes are often eponymously named and linked to a limited number of genes, including Stargardt disease (*ABCA4)*, Best Disease (*BEST1*), Doyne Honeycomb Retinal Dystrophy (*EFEMP1*) or Sorsby Fundus Dystrophy (*TIMP3*). Others include X-linked retinoschisis (*RS1*) and pattern dystrophy (*PRPH2*). Other single gene disorders include choroideremia (*CHM*), which causes degeneration of photoreceptors, the RPE and choroid leading to a characteristic atrophic fundus appearance.

Although IRDs commonly manifest only in the retina (termed non-syndromic IRD), over 80 syndromes include both IRD and extra-ocular systemic features have been described (termed syndromic IRD). Usher syndrome and Bardet-Biedl syndrome are the most common forms.[22,23] Usher syndrome is characterised by retinitis pigmentosa with sensorineural hearing loss, while Bardet-Biedl syndrome is associated with retinitis pigmentosa, obesity, cognitive impairment, polydactyly, hypogonadism and renal disease.[20]

Finally, IRDs also include non-degenerative forms termed stationary diseases. Common stationary subtypes include congenital stationary night blindness and achromatopsia (rod monochromatism). Although typically considered non-progressive, some stationary diseases such as achromatopsia have subsets of patients where limited progression has been observed.[24]

IRDs can be inherited in autosomal recessive (AR), autosomal dominant (AD) and X-linked (XL) patterns, and mitochondrial and digenic inheritance has also been described.[20] Many genes are associated with a single mode of inheritance, however others may have multiple modes of inheritance, such as *BEST1*, which is associated with both AD and AR inheritance.[25]

Over 270 genes have now been identified to be mutated in one or more of these IRD subtypes affecting a range of retinal cells and cellular processes (Figure 1-3).[22] IRDs are clinically

and genetically heterogenous, which can present a challenge to establishing a clinical and molecular diagnosis. Patient presentations can sit on a spectrum within these clinically defined subtypes. Further, IRD subtypes can be associated with more than one causative genes, and similarly some genes are associated with several different presentations. For example, mutations in *USH2A* are often associated with Usher syndrome but can also cause non-syndromic RP,[26] while rod-cone dystrophies are associated with over 70 different genes.[20] Nevertheless, the development of molecular diagnostic techniques combined with specialist clinics and ongoing efforts in gene discovery have greatly enhanced clinical and molecular diagnosis for IRD patients, with typical diagnostic yields of 50-60%.[13,27–30] Despite advances in diagnosis, many IRDs still lack viable treatment options. A primary theme of this thesis considers the development of pre-clinical therapeutic strategies and pathways to translate these for the treatment of patients.

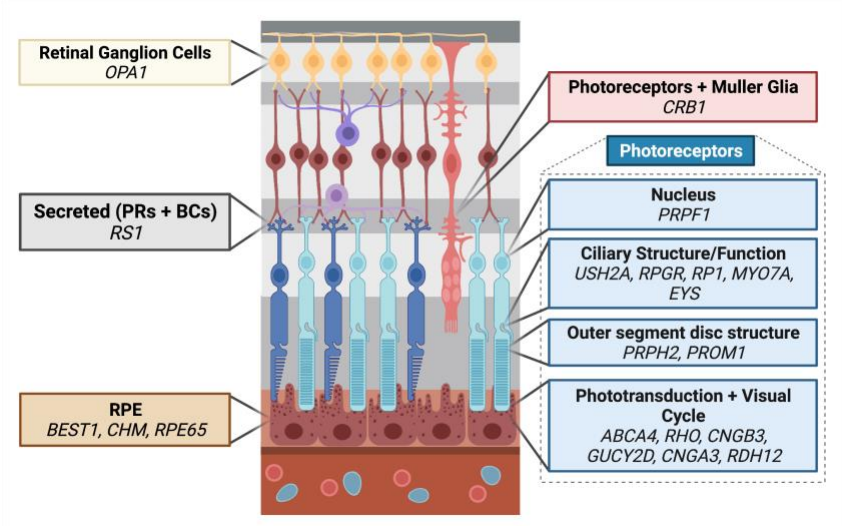


Figure 1-3 Frequently implicated IRD genes and site of expression
Diagram to illustrate the 20 genes most frequently implicated in the pathogenesis of inherited retinal disease in a large cohort of patients in the United Kingdom (also see Figure 1-5). Genes are organised by location of expression within the retina. Over 270 genes have been implicated in inherited retinal disease. Figure adapted from Pontikos et al.[31] RPE = retinal pigment epithelium, PR = photoreceptor, BC = bipolar cell. Created with BioRender.com.

1.1.3 Treatments for inherited retinal degeneration

Historically, care for patients has focused on ensuring patients are linked with appropriate support services and addressing reversible causes of visual impairment such as refractive error, cataract and macular oedema.[14] Beyond limited evidence that dietary supplements and control of light exposure could improve outcomes in subtypes of retinitis pigmentosa,[14,32] investigation of neuroprotective strategies to prevent photoreceptor degeneration and disease progression have largely failed to demonstrate efficacy in IRDs.[14,33] Cellular therapies and electronic implants have offered hope to those at the end stage of disease. Transplantation of RPE, photoreceptors and photoreceptor precursor cells derived from pluripotent-stem cell populations[34] aim to achieve cellular integration and retinal regeneration, and several trials are underway to evaluate these.[35] Electronic retinal prostheses, implanted either epi- or sub-retinally can convert external light signals to electrical impulses to stimulate the neural retina and mediate visual function.[36] For patients with end-stage RP, the Argus II (Second Sight Medical Products) has FDA approval, and the Alphas IMS (Retinal Implant AG) is in multi-centre trials, both reporting restoration of some functional vision.[36]

The understanding of the genetic basis of IRDs, however, has created an opportunity to create molecular therapeutics that treat the underlying genetic cause of the disease at a stage in the disease process to prevent or slow the progression of retinal degeneration.

Genetic therapies aim to introduce nucleic acids to cells in order to replace, supplement or repair genes and express protein products for a therapeutic or prophylactic effect.[37] The eye is highly suited for genetic therapies as: (1) the blood-retinal barrier provides relative immune privilege, (2) it is surgically accessible, (3) the enclosed and small structure requires low doses of vector for delivery, and (4) the target retinal cells such as the RPE and photoreceptors are post-mitotic meaning any permanent genetic intervention is likely to persist for the life of that cell.[37]

1.1.3.1 Gene supplementation with AAV vectors

Gene supplementation therapy introduces a functional copy of a gene to replace a missing or dysfunctional copy in the genome of patients or deliver gene products that improve disease phenotypes. To express a protein in the retina, a transgene containing the protein coding sequence together with required regulatory elements for protein expression must be delivered to target cells. There are now over 50 ocular gene therapy clinical trials for at least 17 indications.[38] These predominantly investigate the treatment of monogenic recessive disorders using adeno-associated viral vectors (AAV) to deliver the transgene.[39] The AAV-based therapy voretigene neparvovec (Luxturna)[40] has been approved for the treatment of *RPE65*-associated LCA by regulatory authorities in the United States and the United Kingdom, and has underscored both the safety and potential of AAV-delivered gene supplementation therapy for IRDs. Clinical trials using AAV-gene therapy are currently underway for choroideremia (*CHM*),[41,42] X-linked retinitis pigmentosa (*RPGR*),[43–46] autosomal recessive retinitis pigmentosa (*MERTK,*[47] *PDE6A,*[48] *PDE6B*[49]*, RLBP1*[50]), X-linked retinoschisis (*RS1*),[51,52] Bietti's crystalline dystrophy (*CYP4V2*)[53] and achromatopsia (*CNGA3,*[54,55] *CNGAB3*[56,57]).

1.1.3.1.1 AAV Biology

AAVs are single-stranded DNA parvoviruses with a small non-enveloped icosahedral capsid that are non-replication competent in the absence of a helper virus or cellular stress.[58] The AAV genome consists of two inverted terminal repeat (ITR) sequences flanking a *rep* gene required for AAV genome replication and virion assembly, and a *cap* gene encoding for the three capsid proteins Virion Protein 1 (VP1), VP2 and VP3 (Figure 1-4A).[58] For recombinant AAV (rAAV) vectors used in gene therapy, the *rep* and *cap* genes are replaced with a transgene flanked by AAV ITRs (Figure 1-4B). The required *rep*/*cap* genes, together with adenovirus helper genes needed for AAV replication, are provided *in trans* during rAAV production in HEK293 cells to create rAAVs that carry the transgene of interest but are devoid of elements

required for further viral replication. AAV ITRs are 145-nt hairpin structures critical for directing AAV Rep and host cell proteins to replicate and encapsidate the viral genome, and are essential for viral production.[59] ITRs derived from the AAV2 serotype are commonly used for transgene cloning, and can be packaged within any AAV capsid serotype.[59] At least 12 naturally occurring serotypes of AAV have been described, and many further capsid mutants have been engineered or identified, each with differing cellular tropism and binding receptors.[58] In animal models and in retinal gene therapy trials, AAV2 has been used for its tropism for RPE and to a lesser extent photoreceptors, while AAV5 and AAV8 capsids show excellent transduction of photoreceptors.[60,61] Many other serotypes are in pre-clinical and clinical development.[58]

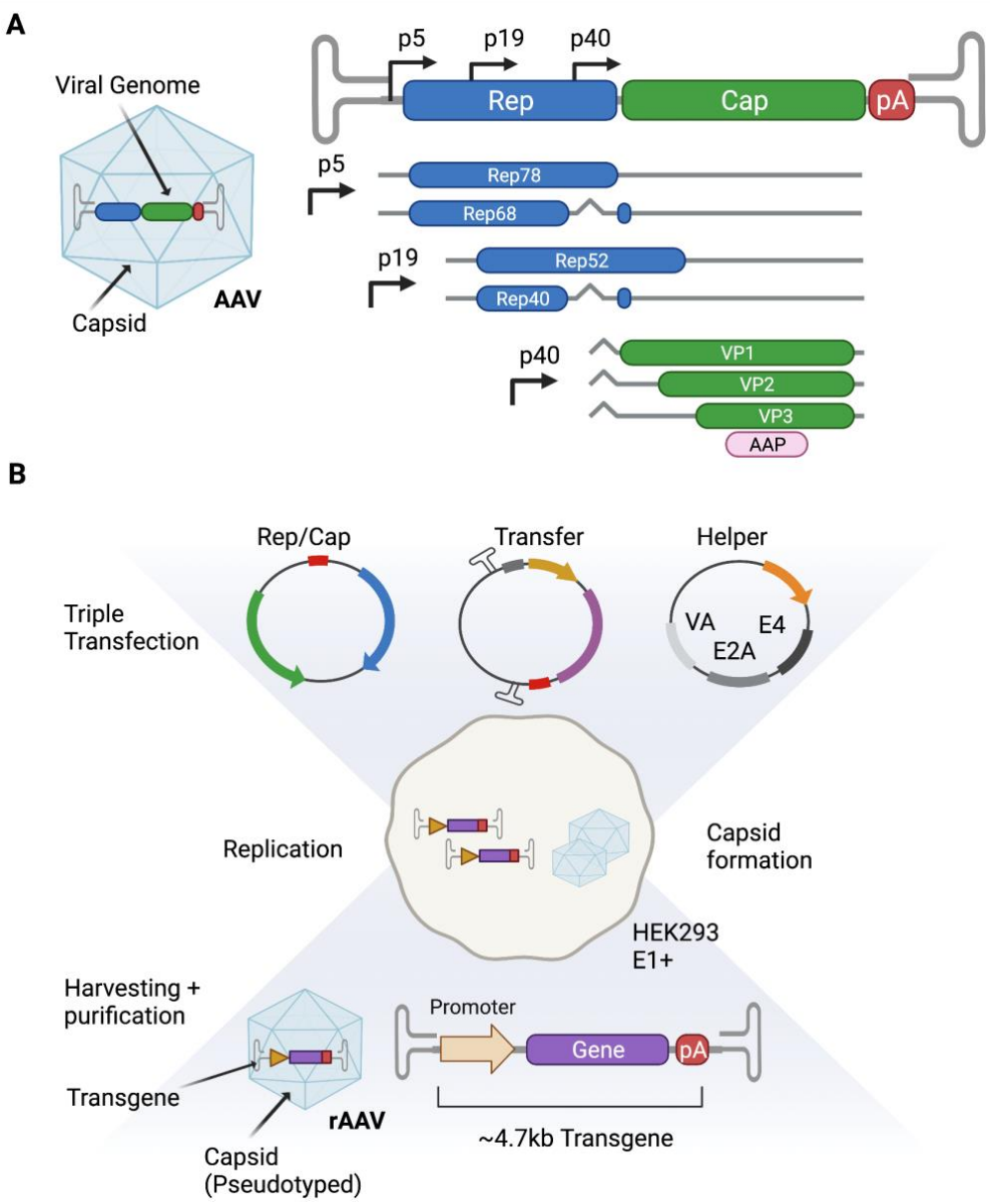


Figure 1-4 Wildtype AAV genome and generation of recombinant AAV
A. The 4.7kb ssDNA wildtype AAV genome is flanked by inverted terminal repeats (ITRs) and packaged within an icosahedral protein capsid. The Rep open reading frame (ORF) encodes four regulatory proteins important for replication and encapsidation of the viral genome (Rep78, Rep68, Rep52 and Rep40) driven by the P5 and P19 promoters. The Cap ORF encodes the capsid proteins VP1, VP2 and VP3 expressed in a 1:1:10 ratio, and the assembly-activating protein (AAP) required for capsid construction,[62] all driven by the P40 promoter. **B.** Production of recombinant AAV (rAAV) via triple transfection in HEK293 cells. The transfer plasmid contains the viral transgene for packaging within ITRs. Genes for rep/cap are provided *in trans*, allowing for alternative capsid genes to be provided for AAV pseudotyping. A helper plasmid encoding the adenovirus genes E4, E2A and VA, in addition to E1 expressed in HEK293 cells, are provided to mediate AAV replication. Infectious AAV particles are produced in HEK293 cells, and subsequently recovered.

1.1.3.1.2 Clinical considerations of AAV gene therapy

AAVs are the favoured vectors for IRD gene therapy due to the efficient transduction of retinal cells, the demonstrated efficacy of gene supplementation approaches to improve the retinal phenotype of dozens of animal models, and the now well-established safety profile of ocular AAV gene therapy in human clinical trials.[60,63] After transduction the viral genome forms stable episomal circular concatamers by recombination at the ITRs. This enables long-term persistent expression following a single administration, which is an advantage in the majority of cases but may be a drawback where cessation of therapy may be required.[64] In the absence of the *rep* and *cap* genes the recombinant virus is non-replicating, and is practically non-integrating with an estimated integration rate of fewer than 0.1% of AAV genomes.[65,66]

Relative to other viral vectors, the non-enveloped AAV is less immunogenic[67–69] and has been tolerated across multiple clinical trials including in those using systemic delivery outside the relative immune-privilege of the eye.[65] Dose-dependent localised ocular inflammation has been observed in patients and animal models mediated by both innate and adaptive immune responses following subretinal AAV delivery, although these are generally well controlled by short corticosteroid-based immunosuppressive regimens.[70,71] Wildtype AAV infection in humans is broadly considered non-pathogenic, however prior infection can result in pre-existing cellular and humoral immunity to gene therapy AAV capsids that may induce inflammatory responses and antibody-mediated neutralisation of AAV particles.[72] Research continues to investigate the drivers of the host response to AAV gene therapy (e.g. the relative contributions of the capsid, transgene or the transgene product) and methods of reducing and controlling inflammation.[71,73]

The principal limitation of AAV vectors is the small packaging capacity of the approximately 4.7kb AAV genome. As a therapeutic transgene requires ITRs, promoter sequences to drive RNA transcription, polyA signals to terminate and polyadenylate the transcript and other regulatory elements to enhance expression and stability, it is challenging to

deliver genes with coding sequences larger than 4kb. The upper limit of AAV packaging capacity can be extended to 5.2kb with optimal single-stranded DNA folding,[74,75] however this can result in lower viral yields due to inefficient packaging, and AAVs packaged with truncated genomes. The single stranded genome is packaged into pre-formed AAV capsids in the nucleoplasm in a 3'-5' direction, and packaging of larger genomes may stall when the capsid is full, with the unpackaged 5' end degraded by cellular nucleases.[76,77] Strategies that use dual vector systems to deliver larger transgenes split over two vectors have been tested preclinically.[78,79] These approaches require successful co-transduction of a cell with two vectors and accurate, efficient reconstitution of a full length gene product, which has limited their efficacy and risks the creation of unwanted gene products.[79]

1.1.3.1.3 Lentiviruses and non-viral delivery methods

In addition to AAV, lentiviruses have also been used for viral transgene delivery. Lentiviruses are enveloped, integrating, single stranded RNA retroviruses that efficiently transduce non-dividing cells.[80] Current clinical ocular gene therapy vectors are based on the equine infectious anaemia virus (EIAV) due to the inability of EIAV to replicate in human cells.[80] Lentiviruses have the advantage of a large genome of approximately 8-10kb, which allows the packaging of longer gene coding sequences. To this end, two clinical trials with EIAV vectors have been performed with genes with coding sequences too large for AAV, those implicated in Stargardt disease (*ABCA4*)[81] and Usher Syndrome 1B (*MYO7A*).[82] While these did not demonstrate safety concerns,[83] both trials were terminated early without demonstration of efficacy. The lack of clinical efficacy data from ocular lentiviral gene therapy trials, the limited ability to of lentiviruses to transduce mature photoreceptors,[84] and concerns over lentiviral envelope immunogenicity[68] and cytotoxicity[85,86] have raised barriers to the successful translation of lentiviral approaches to clinical trial.

In addition to viral vector delivery, a wide variety of non-viral vector systems are known, with examples including physical methods such as DNA electroporation and chemical-based methods such as virus-like particles, metallic nanoparticles, cationic lipids or cell penetrating peptides.[87] For retinal gene therapy however, to date few non-viral methods have achieved efficient, non-toxic, tissue specific and persistent gene expression required for gene supplementation.[88]

1.1.3.2 Gene modulation approaches

Gene modulation strategies aim to alter the expression of a gene and include splicing, post-transcriptional silencing and transcriptional readthrough therapies.

1.1.3.2.1 Antisense oligonucleotide therapy

Antisense oligonucleotides (ASO) are synthetic, modified nucleic acid molecules which can target complementary transcripts through base pairing.[89] These may be used to modify splicing or induce post-transcriptional silencing. One splice-modifying single stranded ASO currently undergoing clinical trials for LCA10 is designed to hybridise to nascent pre-mRNA and mask a deep intronic cryptic splice site in CEP290 (c.2991 + 1655A>G) to rescue aberrant splicing.[90] Encouraging results in Phase I/II clinical trials that showed sustained visual recovery following a single treatment in select patients and demonstrate the potential for targeted genetic therapeutics to rescue cell function.[91]

ASOs can also induce transcript silencing through binding to mature mRNAs to create RNA-DNA duplexes targeted for degradation by RNase H.[89] This can be used in diseases caused by toxic gain of function mutations in dominantly inherited diseases. One example of this is currently in clinical trial is an ASO designed to induce allele-specific knockdown of the mutant transcript in patients with autosomal dominant RP caused by heterozygous P23H/+ *RHO* mutations.[92] Other approaches to mediate transcript knockdown have been developed

pre-clinically but not in clinical trial for IRD include small interfering RNA (siRNA) and ribozyme therapeutics (reviewed in[93]).

1.1.3.2.2 Translational readthrough

Translational readthrough therapies utilise small molecule drugs to bypass premature termination codons (PTC), inserting an alternative amino acid and allowing the translation of a full-length protein.[94] An example of this includes the drug PTC124 (ataluren), which has been applied pre-clinically for the readthrough of PTCs in choroideremia and RP.[94] Although an attractive strategy due to the prevalence and pathogenicity of PTCs, current challenges to successful translation of these drugs include obtaining therapeutic concentrations of the drugs in retinal tissue and overcoming highly variable readthrough rates which appear to vary based on factors such as the stop codon identity and upstream and downstream mRNA sequences.[94]

1.1.4 Unmet needs in inherited retinal disease treatment

Despite the encouraging progress made in genetic therapies for IRDs with AAV gene supplementation, a clear unmet need exists for patients with autosomal recessive IRDs that are caused by mutations in large genes that are not deliverable with AAV. As demonstrated in Figure 1-5, genes such as *USH2A* and *ABCA4* are the most commonly implicated genes in IRDs, but their coding sequences greatly exceed 4.7kb.

Additionally, there are no current treatments for dominantly inherited diseases that require silencing of the mutant allele, such as RP caused by dominant *RHO* mutations.

As discussed in the following sections, recently developed gene editing technologies may offer potential therapeutic approaches to these problems.

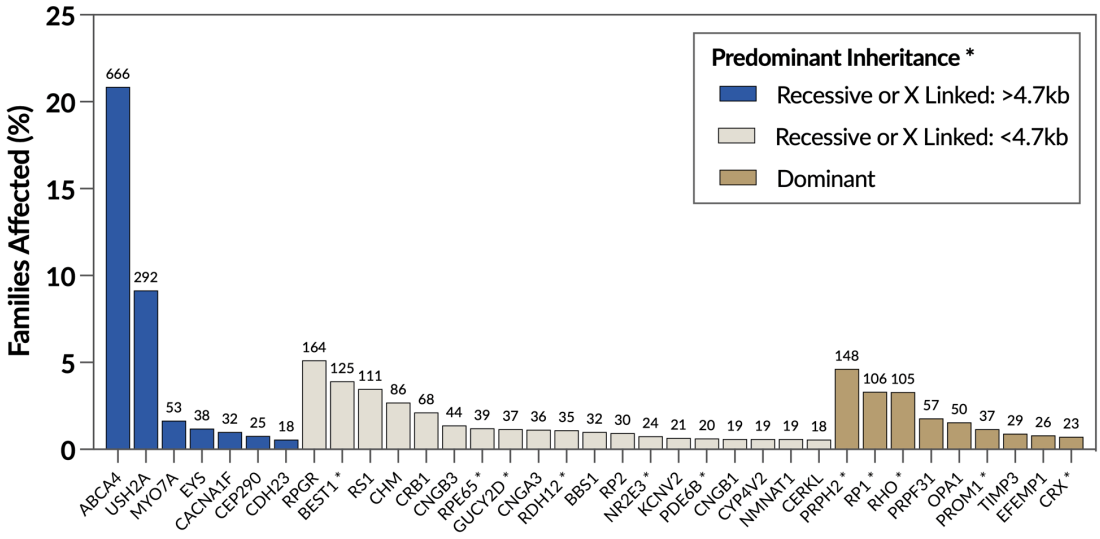


Figure 1-5 Frequency and modes of inheritance of common genes implicated in inherited retinal disease in UK Families

The most common 35 genes implicated in inherited retinal disease in UK families. Recessively inherited genes are grouped by whether their coding sequences exceed (blue) or fall within (grey) the total packaging capacity of an AAV vector (4.7kb). Dominantly inherited diseases likely not amenable to gene supplementation approaches are grouped to the right (brown). Annotated figures are the number of families affected (total cohort 3195 families). Data adapted from Pontikos et al. (2020), Full Cohort, Supp. Data Table 1.[31] *Genes that may also be inherited in other patterns, mutation dependent

1.2 *USH2A*-related retinal degeneration

Mutations in the gene *USH2A* are a common cause of IRD. In large cohorts of IRD patients, *USH2A* is frequently the second most common implicated gene after *ABCA4* and accounts for approximately 9% of all families with an IRD in the UK.[31,95,96]

While the first half of this thesis considers molecular therapies broadly applicable to a range of IRDs, the second half focuses on the development and treatment of a mouse model with a mutation in *Ush2a*. As such, *USH2A*-related retinal degeneration is reviewed in greater detail here.

1.2.1 Clinical Manifestations

Mutations in *USH2A* are associated with autosomal recessive retinitis pigmentosa. This can occur in isolation as non-syndromic RP, and is estimated to be implicated in 12-25% of non-syndromic RP.[97] *USH2A* mutations are also associated with syndromic RP, causing Usher syndrome.

Usher syndrome was first described by Albrecht Von Graefe in 1858,[98] and subsequently as an inherited disorder by Charles Usher in 1914.[99] Patients with Usher syndrome have RP combined with bilateral congenital sensorineural hearing loss, with or without vestibular dysfunction. Usher syndrome has an estimated prevalence of 3-6 per 100,000 people worldwide.[100,101]

Usher syndrome can be categorised into three subtypes (I-III), with mutations in *USH2A* associated with Usher syndrome type II (USH2). USH2 is the most common form of usher syndrome (approximately 50% of Usher syndrome patients) and is predominantly caused by mutations in *USH2A*, accounting for approximately 80% of USH2 patients.[102] It is associated with mild to moderate low frequency and severe high frequency sensorineural hearing loss, with normal vestibular function.[103] Hearing loss is typically diagnosed during childhood (median age approximately 5-9 years)[104,105] or during new-born screening and is generally considered non-progressive.[104,106] This is in contrast to Usher syndrome type I, which is the most severe and associated with profound congenital sensorineural hearing loss often associated with non-progressive vestibular areflexia.[103] Usher syndrome type III (USH3) is rare (2-4% of Usher Syndrome patients)[102] and more clinically variable. Progressive hearing loss presents typically in the first decade of life, with vestibular abnormalities affecting approximately half of patients.[103] Due to founder effects, USH3 is more common in Finnish[107] and Ashkenazi Jewish[108] populations. Across the three syndromes, 14 associated loci or genes have been identified, with mutations in *USH2A* the most common cause.[109]

The retinal features of patients with *USH2A* mutations are consistent with other causes of rod-cone dystrophies as described in section 1.1.2, and are demonstrated in Figure 1-6. Visual acuity is relatively preserved with one to two lines of vision loss at 30, and a median age of legal blindness at 58 years of age.[110,111] Perimetry typically reveals a mid-peripheral scotoma in areas of degeneration with foveal sparing until late in the disease.[112] These can be visualised with OCT imaging demonstrating a loss of outer retinal structures with time, including thinning of the ellipsoid zone, external limiting membrane and ONL. Macula oedema is also a common finding in *USH2A* patients and a cause of central vision loss.[112] Autofluorescence imaging shows a central region of relatively greater autofluorescence intensity surrounded by a darker zone, with areas of hypo-autofluorescence in areas of RPE degeneration.[112] Additionally, a hyperautofluorescent ring in the macula is seen at transition border between degenerative and normal retina in most patients, which reduces in area over time.[113,114] Full-field electroretinogram (ERG) responses demonstrates a predominant pattern of rod impairment: dark-adapted ERG responses are highly diminished and while light-adapted responses are also reduced with delayed implicit times, they are relatively preserved compared to the dark-adapted response.

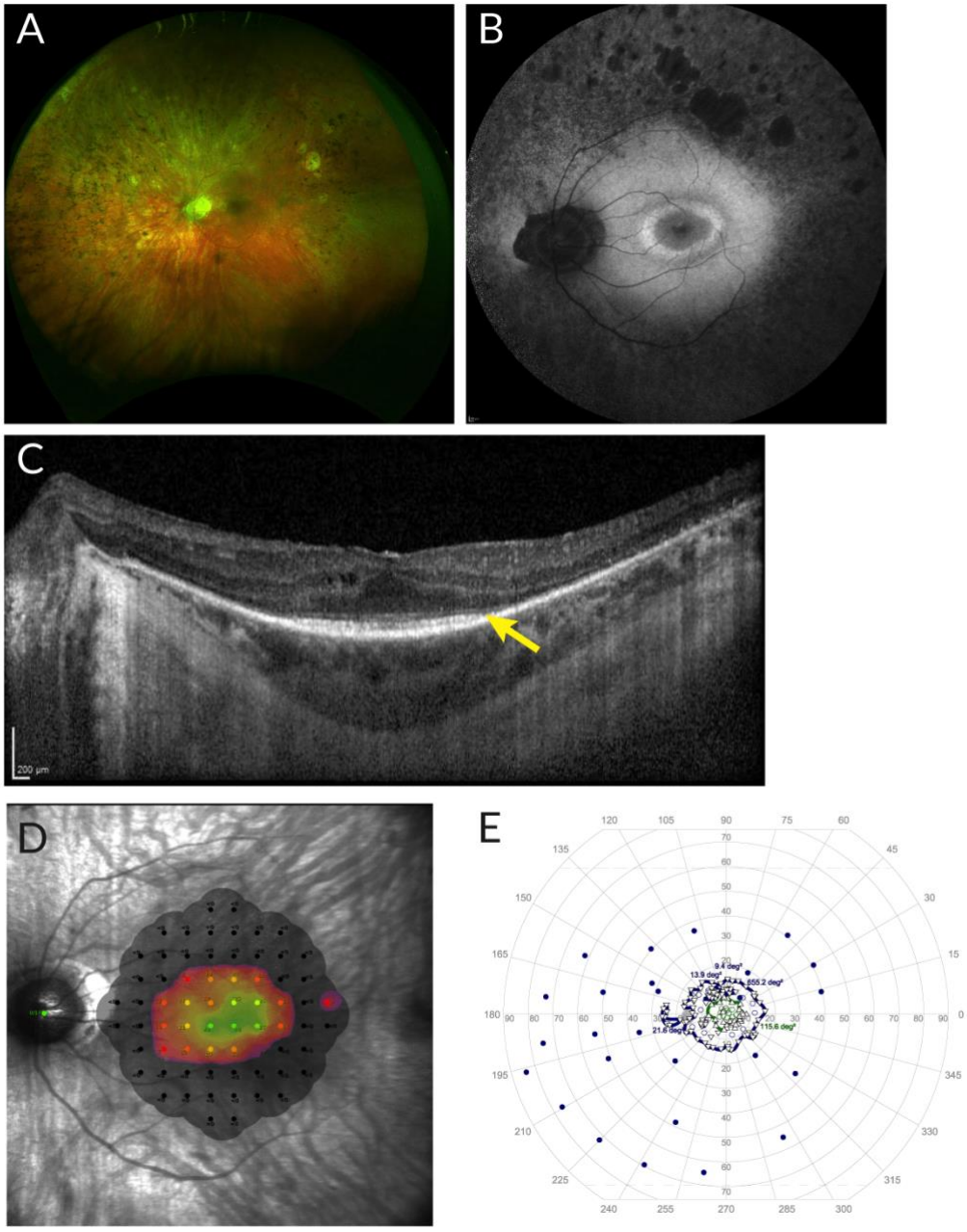


Figure 1-6 Retinal features of *USH2A*-related retinal degeneration
Clinical features of patient with a compound for c.2299delG / c.2276G>T *USH2A* mutations. Best corrected visual acuity was OD 62 letters (6/24), OS 76 letters (6/9.5). **A.** Optos widefield colour fundus photo demonstrating peripheral pigmentary retinopathy, retinal thinning and vascular attenuation. **B.** Short wave fundus autofluorescence demonstrating peripheral hypo-autofluorescence and patches of RPE atrophy. A hyper-autofluorescent ring at the macula is present. **C.** Macula OCT scan showing outer retinal thinning and loss of ellipsoid zone. Arrow demonstrates edge of remaining viable retina at the fovea. **D.** Microperimetry sensitivity map demonstrating loss of macula sensitivity with central sparing at the fovea. **E.** Octopus kinetic perimetry showing peripheral field loss. Images courtesy of Laura Wood, Oxford Eye Hospital.

1.2.2 Molecular genetics of *USH2A*

1.2.2.1 Isoforms of *USH2A*

The usherin protein is encoded by the gene *USH2A* located on the long arm of chromosome 1 (Chr 1q41)[115,116]. *USH2A* produces two alternatively spliced protein coding sequences (Figure 1-7).[117] Initial studies characterised the short isoform (isoform A, 4,627bp, 21 exons, 5146aa, 170kDa), encoding a secreted protein[115,116] lacking a transmembrane domain detected in the basement membrane of a variety of tissues including the testis, intestine and pancreas.[117–120] A long isoform (isoform B, 15,609bp, 72 exons, 5,202aa, ~590kDa) was subsequently identified as the predominant transcript expressed in the retina and cochlea containing 51 further 53' exons encoding a transmembrane protein with a very short intracellular domain and a long extracellular domain.[117]

1.2.2.2 Usherin protein structure

The N-terminus of usherin common to both the long and short isoform consists of an extracellular domain containing laminin globular-like, laminin N-terminal, and 10 laminin epidermal growth factor domains (Figure 1-7).

A β-sandwich conformation with folding of the laminin epidermal growth factor domain repeats is maintained by disulphide bonds.[121] *In silico* modelling suggests that pathogenic missense variants commonly occur in residues that disrupt disulphide bonds and affect the correct conformation of these β-sandwich domains.[121] *In vitro,* the laminin epidermal growth factor domains interact with collagen[120] and fibronectin,[122] consistent with the proposed role of the short isoform as an extracellular matrix protein.[123]

The long isoform additionally contains 2 laminin globular domains, 34 fibronectin domains, an α-helix transmembrane domain and a looped intracellular domain.[121] The cytosolic C-terminal has a PDZ1-binding motif that interacts with Usherin interactome complex proteins in photoreceptors and hair cells described below.[124]

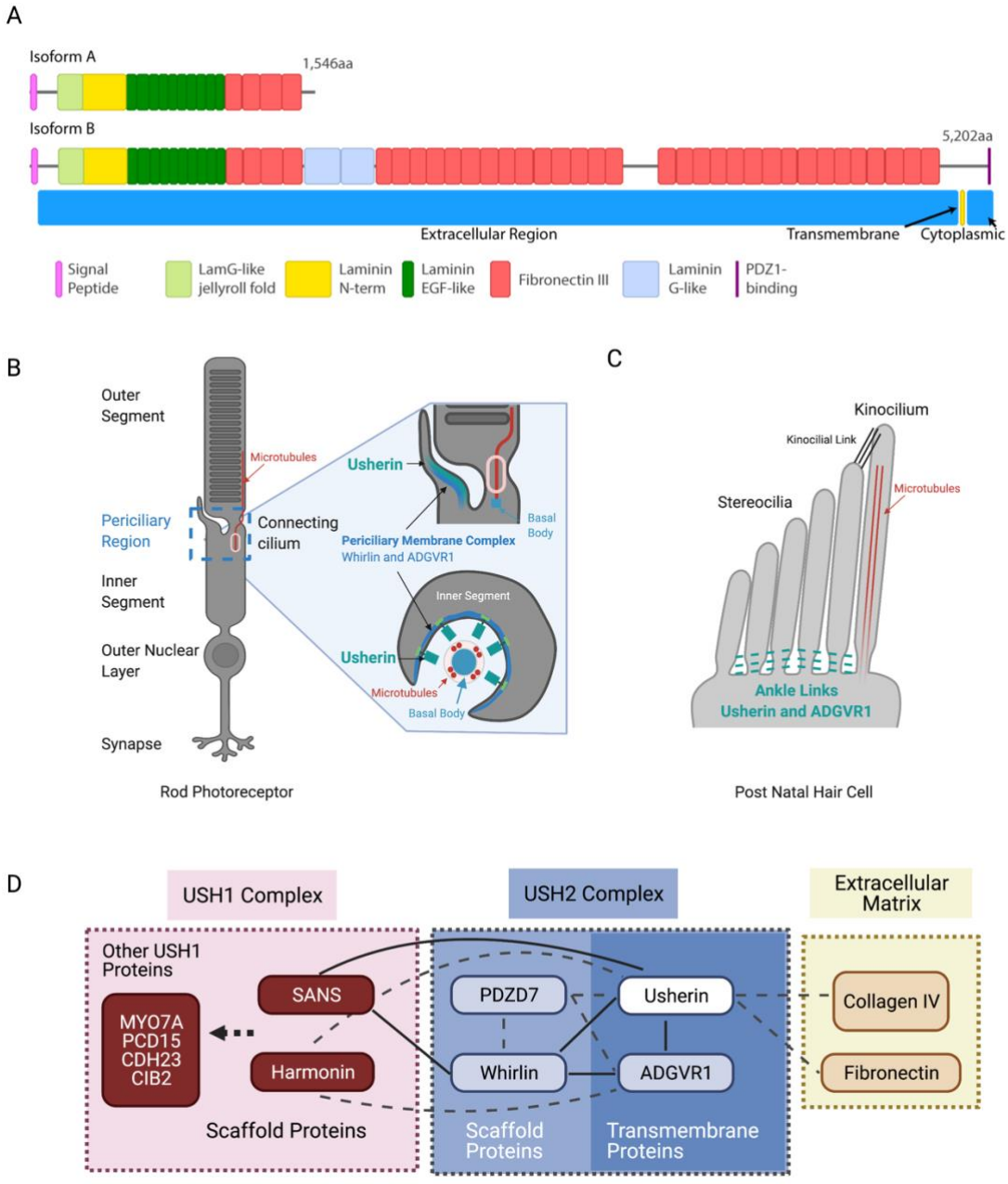


Figure 1-7 Usherin isoforms, localisation and interacting proteins

A. Schematic depicting the domain structure of the two isoforms of *USH2A* **B.** Usherin is expressed at the periciliary membrane complex in the periciliary region of the apical inner segment of rod and cone photoreceptors. This region sits adjacent to and around the connecting cilium. The short transmembrane region of usherin lies in the inner segment membrane. **C**. Stereocilia at the apical portion of the post-natal hair cell. Usherin is expressed with ADGVR1 at the ankle links that tether the basal stereocilia. With development the kinocilium regresses and the ankle links disappear. **D.** Interaction of Usherin in the USH2 complex in photoreceptors. Solid lines represent *in vivo* validated interactions in photoreceptors. Dotted lines are interactions validated biochemically or in other tissues. Multiple interactions occur between the USH1 complex proteins, not detailed here. Diagrams adapted from Toualbi et al.[125]

1.2.2.3 Usherin localisation, function and interactions

The exact role of usherin remains to be elucidated but is generally considered to have an important structural function at the photoreceptor periciliary region and a developmental function in the sensory hair cells of the cochlea. Usherin is a component of the 'Usher interactome', a network of proteins identified through their involvement with Usher Syndrome Type 1 (USH1) and Type 2 (USH2).[124] The Usher interactome contains a diverse set of proteins that form a dynamic network with functions of cell structure and adhesion, intracellular transport, cellular signalling and protein scaffold assembly.[109]

In the retina, *USH2A* expression is restricted to rod and cone photoreceptors.[126,127] It remains unknown why rods degenerate first in *USH2A*-retinopathy, but it is hypothesised that usherin may be more critical in the long-term maintenance of rods or that cones may be able to compensate for deficiencies in usherin function.[125] Usherin co-localises with two other USH2-related proteins at the periciliary membrane, to form the periciliary membrane complex (PMC) with interacting proteins adhesion G protein-coupled receptor V1 (ADGVR1, USH2C) and whirlin (USH2D) (Figure 1-7).[117,128,129] Whirlin anchors the complex by interaction between the whirlin PDZ (PSD95/Dlg1/ZO-1) motif and the PDZ1-binding motifs on the cytoplasmic terminals of the transmembrane proteins Usherin and ADGVR1.[130–134] It is thought that the long extracellular domains of this complex contribute to fibres that span between the inner segment membrane and the connecting cilium in a structural role.[132,135] In addition, the PMC is thought to be involved in the docking and fusion of vesicles for transport across the connecting cilium towards the OS.[109, 124,135] The interactions of Usherin with the USH1 scaffold proteins Harmonin (USH1C) and SANS (USH1G),[135,136] thought to be involved in the transport of cargo vesicles towards the OS[132,137,138] support this purported role.

In the cochlea, an USH2 complex of Usherin, ADGVR1, whirlin and PDZD7 form a transient fibrous structure called ankle links at the base of stereocilia in developing hair cells

(Figure 1-7).[139–141] The expression of the USH2 complex is necessary for the formation of these links, and are essential for the regulation of stereocilia growth and development.[109,142]

Usherin does not appear to have a role in mature hair cells, with USH2A expression restricted to between post-natal day (P)0-15 in mice,[140] corresponding to the presence of ankle links between P0-12.[142]

Beyond the retina and cochlea, transcripts of the short isoform of *USH2A* have been detected in a variety of tissues including the testis, pancreas, small and large intestines, spleen and ovary, and USH2A protein detected via N-terminal antibody staining in the basement membrane of histological sections from these tissues.[118,119] Weak expression of transcripts of the long isoform have additionally been detected in the heart and kidney.[117] Most recently, the long isoform of Usherin has been detected in Meissner's corpuscles in the skin, where it was demonstrated to play a role in vibration sensation in both humans and mice.[143] *Ush2a*-null mice displayed an absence of Usherin expression in Meissner's corpuscles and reduced afferent responses to vibration stimuli without apparent morphological changes to the end-organ. *USH2A* may play a role in mechanosensation without causing degeneration of Meissner's corpuscles or associated afferent neurons.

Due to the association of Usherin with the cilium, investigations into ciliary function in USH2 patients have been undertaken. Conflicting findings have reported variable structural and functional changes to sperm cells, however patients do not report fertility impairments.[144,145] Studies have investigated olfactory dysfunction in Usher syndrome, however there is no clear association of patients with *USH2A* mutations and olfactory abnormalities.[146,147]

1.2.3 Common variants and genotype-phenotype correlations

Over 1800 unique variants have been described in *USH2A*, with 970 of these classed as likely pathogenic or pathogenic (LOVD Database, accessed May 6 2021),[148,149] with variants located throughout the length of the gene and across domains.[149]

Although most variants in *USH2A* are private and infrequent, a small number of variants are more prevalent. For unknown reasons, the two most common pathogenic variants occur in in exon 13. The c.2299delG (p.Glu767Serfs*21) variant produces a predicted premature termination codon, and accounts for 15-31% of cases.[149] It is likely to have arisen from a common European ancestor,[150,151] although cases are now observed throughout populations around the world.[149] The second common exon 13 variant, c.2276G>T (p.Cys759Phe), accounts for approximately 8% of cases.[125] This produces a missense change in a highly conserved EGF laminin domain, predicted to affect the interaction of Usherin with the extracellular matrix and destabilise the protein through disruption of disulphide bonds and protein misfolding.[152] Finally, the third most common pathogenic variant reported is c.11864G>A (p. Trp3955*) mutation in exon 61. Although only accounting for 3-5% of cases worldwide,[149] it is particularly common in European populations where it was the most frequent pathogenic variant in two cohorts[153,154] and in 84% of cases in Slovenia.[155]

Some correlation between genotype and phenotype has been established. USH2 syndromic patients demonstrate earlier onset and more severe visual loss compared to non-syndromic patients.[110,156] Patients with two protein truncating mutations are associated with a more severe auditory phenotype than those with just one or no truncating mutations.[104,157] Lenassi et al. have proposed an allele hierarchy whereby they define a group of 'retinal-disease specific' variants that are more commonly associated with non-syndromic RP rather than Usher syndrome. They propose that these variants may partially function in the cochlea to allow normal inner hair cell development, but still be pathogenic for the retina.[158] An example of this is the common p.Cys759Phe mutation. Patients homozygous for p.Cys759Phe are more commonly associated

with non-syndromic RP.[152] Patients that inherit p.Cys759Phe in complex heterozygosity with a truncating variant are more commonly associated with an USH2 phenotype and more severe visual loss.[105,152] Despite this, there is significant heterogeneity amongst patients, indicative of other epigenetic or environmental disease modifiers. This is best demonstrated by a case report of two siblings with the same genotype; one was diagnosed with USH2 while the other had preserved visual function and was the first reported case of non-syndromic deafness associated with *USH2A* variants.[159]

1.2.4 *USH2A* Models

1.2.4.1 Cellular models

In vitro models that endogenously express *USH2A* are useful for investigating aspects of *USH2A* expression, pathophysiology and therapeutics. Due to the cell specificity of *USH2A*^{isoB} expression, few immortal cell lines express *USH2A* transcripts or protein. Two retinoblastoma derived cell lines WERI-Rb-1[160] and Y79[161] are known to weakly express *USH2A (*ref[117] and unpublished data), but are difficult to both transfect and transduce in culture. Recently, preliminary data have shown that the immortalised OC-k1 cell line[162] derived from mouse cells isolated from the organ of Corti expresses USH2A at the base of a primary cilia, and an OC-k1-*Ush2a* knockout line has been generated.[163]

Human retinal tissue explants can be cultured *in vitro*[164] however the availability of tissue from appropriate donors is limited. Other primary human tissues have been used in the study of *USH2A*. Nasal epithelial biopsies have been used to study splicing of *USH2A* transcripts, but not cultured for the evaluation of therapeutics.[165] *USH2A* RNA is expressed at very low levels in cultured patient-derived fibroblasts and used in the testing of antisense oligonucleotide therapies.[166] Similarly, low levels are observed in induced pluripotent stem cells (iPSCs) derived from fibroblasts and have been used to study *in vitro* genome editing approaches to *USH2A* mutations.[167]

Retinal organoids differentiated from human-iPSCs form 3D self-organising optic cup-like structures with a laminated cellular architecture and transcriptional profile similar to the human retina.[126,168] Organoids have been used to identify previously unknown pathogenic splicing variants in *USH2A* and early studies have shown these may be useful for understanding role of Usherin in the mature and developing photoreceptor.[169,170] Organoids appear to be useful for the study of genes associated with ciliopathies; organoids with mutations affecting cilia-associated genes CEP290,[171] RPGR[172] and RP2[173] appear to replicate the degenerative phenotype of the human condition, and abnormal photoreceptor cilia morphology and function were correctable *in vitro* with antisense oligonucleotide[171] and gene editing[172] therapies. Organoids are therefore an exciting prospect for the study of *USH2A* pathogenesis and therapy.

1.2.4.2 Animal models

A number of animal models have been generated for the investigation of the pathogenesis and treatment of *USH2A*-related disease *in vivo*. An *Ush2a*-null mouse was generated by Liu et al. through the removal of exon 5, demonstrating knockout of *Ush2a* in both the retina and inner ear.[128] Homozygous *Ush2a*$^{-/-}$ mice displayed a slow and late-onset retinal degeneration and non-progressive hearing loss without vestibular dysfunction. At 10 months shortening of the inner and outer segments and loss of photoreceptor layer thickness was observed, which progressed to a loss of 50% of photoreceptor layer thickness by 20 months. This was accompanied by losses in amplitudes of the ERG a- and b-waves which were reduced by 60% at 20-months. Earlier changes have been noted. Histologically, at 2 months upregulation of retinal glial fibrillary acidic protein (GFAP) was observed, a non-specific indicator of photoreceptor stress.[128] At 3 months, mis-localisation of red-green cone opsin has been observed, perhaps indicating alterations in intracellular trafficking, however the mechanism for these observations has not been confirmed.[174] Additionally, mild losses in contrast sensitivity and visual acuity measured by optomotor testing are seen from approximately 12 months of

age.[174] In the mutant cochlea, distortion and disorganisation of developing hair cell bundles is associated with non-progressive impaired hearing function detected early as 1 month as measured by auditory brainstem response (ABR) and distortion product otoacoustic emission (DPOAE) testing.[128,142] Although *Ush2a* is not expressed in the brain, emerging evidence suggests that both heterozygous and homozygous *Ush2a* mutant mice demonstrate higher-order auditory processing deficits and neuroanatomical abnormalities in the central auditory processing centres of the medial geniculate nucleus and superior olivary complex.[175,176] This may play a role in the finding that *USH2A* variants are associated with an increased risk of developmental language disorders in humans.[175]

Recently, Pendse et al. have also described an *Ush2a*-ΔEx12 mouse model generated using CRISPR-Cas9 to excise exon 12 and portions of the flanking introns.[177] Exon 12 of *Ush2a* is homologous to exon 13 of *USH2A*, where approximately 30% of *USH2A* mutations occur. Deletion of exon 12 (and similarly exon 13 in humans) results in an in-frame deletion, and excision of the coding sequence for four of the ten repetitive laminin EGF-like domains. Exon skipping therapies are therefore a potential strategy for mutations occurring in exon 13. Pre-print data demonstrates that the *Ush2a*-ΔEx12 mouse produces a truncated but functional Usherin protein that restores inner hair cell function and reduces cone opsin mislocalisation in the retina compared to the $Ush2a^{-/-}$ mouse.[163]

Additionally, zebrafish *USH2A* models have been developed. Zebrafish possess a retina that is structurally similar to humans but is predominantly cone-dominated.[178] Rods are not fully developed until 20 days post-fertilisation, and rod-specific degeneration is typically less pronounced in zebrafish models.[178] Four different *ush2a*-null zebrafish lines ($ush2a^{rmc1}$, $ush2a^{b1245}$, $ush2a^{hzu6}$ and $ush2a^{n507}$) show late onset retinal thinning detectable between 6 and 12 months post-fertilisation.[114, 127,179] Similar to the mouse, opsin mis-localisation has also been identified from 6 months post fertilisation.[114] Despite an apparently structurally normal retina, earlier deficits in the ERG have been noted by post-fertilisation day 5-7 in *ush2a* mutant zebrafish at

an age when rods do not contribute to the ERG.[127,179] This may suggest an element of early cone dysfunction in these models, consistent with observations of reduced rod and cone function in adolescent *USH2A* patients.[180] Finally, a humanised *ush2a*-knockin zebrafish model containing the deep intronic mutation c.7595-2144A>G was generated.[181] Although this did not display a phenotype, it was used to demonstrate the use of antisense morpholino treatment to restore the aberrantly spliced transcript generated by this mutation to the wildtype transcript.

Overall, the phenotype of the animal models together with the temporal expression, structure, localisation, and interactions of Usherin support a role for Usherin in the development of hair cells, and primarily in the maintenance rather than the development of photoreceptors. These features broadly recapitulate the human disease, however like other mouse models of Usher syndrome such as the Whirlin-null and ADGVR1-null,[133] mouse models display a milder retinal degeneration phenotype relative to humans. Differences in the structure of the mouse and human periciliary region[182] or differences in retinal anatomy such as a relative enrichment of rod photoreceptors may account for this, however the reasons for the milder phenotype remain unknown.

1.2.5 Treatment of *USH2A*-related disease

There are currently no approved treatments for *USH2A*-related retinal degeneration. Clinical trials have been initiated for ASO candidate QR-421a developed by ProQR therapeutics (Leiden, Netherlands).[183] This approach uses an ASO to bind and mask canonical splice sites to induce in-frame exon skipping of skipping of exon 13, a pathogenic hotspot containing the common c.2299delG (p.Glu767Serfs*21) and c.2276G>T (p.Cys759Phe) mutations. Pre-clinical studies demonstrated ASO exon-skipping restored *Usherin* expression in the zebrafish *ush2a*^{rmc1} model containing a frameshift mutation in exon 13, prolonged uptake and expression in mouse photoreceptors following intravitreal delivery, and dose dependent exon-skipping of up to 63% of transcripts in iPSC-derived photoreceptor progenitor cells.[90] Initial

data from phase I/II trials[183] in patients with exon 13 *USH2A* mutations found patients tolerated intravitreal injection without significant safety concerns, and improvements to best corrected visual acuity (BCVA) in patients with advanced disease.[184] Phase II/III trials are now planned.

ASOs have also been studied pre-clinically for the *USH2A* deep intronic mutation c.7595-2144A>G that causes the insertion of a pseudoexon. Results showed the correction of aberrant splicing in both patient-derived fibroblasts and in minigene assays.[166]

Finally, PTC124 (Ataluren) has been used to substantially increase *USH2A* expression in HEK293 cells transiently transfected with an *USH2A* cDNA fragment containing the c.11864G > A p.(Trp3955*) premature termination variant.[185]

While these therapeutic options are encouraging, key roadblocks to the developing further treatments for *USH2A* mutations include the lack of effective vector options to deliver the large transgene to photoreceptors, and a lack of appropriate models for testing the efficacy of mutation-specific strategies developed *in vitro*.

1.3 Genome Editing in Inherited Retinal Disease

1.3.1 Development of CRISPR-Cas Systems

1.3.1.1 Early gene editing systems

Over the last thirty years, our growing understanding of the genetic basis of disease has been accompanied by a desire to manipulate the genome to understand gene function and to repair genetic errors. Broadly, programmable gene editing of nucleic acids requires a molecular machine that contains two main parts: 1) a nucleic acid-binding domain capable of sequence specific recognition and 2) an effector domain capable of nucleic acid cleavage (such as a nuclease domain) or alteration (such as a deaminase domain). Genome editing with protein-based DNA-recognition domains has been possible since the early 1990s with development of engineered megaucleases,[186] zinc finger nucleases (ZFNs)[187] and Transcription Activator-Like Effector Nucleases (TALENs)[188,189] (for review, see Urnov[190]). These systems require engineering of new enzymes for each new DNA target, and widespread adoption of these gene editing technologies for clinical applications was hampered by the relative complexity of their design and difficulties in delivery for *in vivo* editing.[191]

1.3.1.2 Development of CRISPR-Cas for gene editing

Work on the adaptive immune system of prokaryotes lead to the identification of a family of nucleases that protect against invading nucleic acids.[192] Unusual repeat sequences found in bacterial genomes,[193] termed clustered regularly interspaced short palindromic repeats (CRISPR) arrays, were found to consist of repeated sequences interleaved by spacer sequences acquired from foreign genetic elements (protospacers). These spacers form templates for CRISPR RNAs (crRNAs) that guide a CRISPR-associated (Cas) nuclease to cleave complementary nucleic acid sequences. In most systems, cleavage will only occur if a short sequence motif (~2-7bp) is located adjacent to the protospacer (termed the protospacer adjacent motif, PAM) in the target sequence, which prevents self-targeting of the CRISPR array.

The power and simplicity of using an RNA-guided nuclease for use in genome editing was recognised, and in 2012 the CRISPR-Cas9 system was adapted to be directed to the target by an engineered guide RNA (gRNA) and used to edit the genome of eukaryotic cells.[194–196] Naturally occurring CRISPR systems are guided to target sequences by a two-part hybrid RNA consisting of a spacer sequence complementary to the target and a trans-activating CRISPR RNA (tracrRNA) recognised by the Cas9 protein. gRNAs in engineered CRISPR systems are generally composed of a single RNA encoding a short (~20nt) spacer sequence complementary to the target and a hairpin scaffold sequence that allows binding to the Cas enzyme. This made a simple two-component gRNA and Cas system that was easily programmable to almost any target in the genome, simply through designing a gRNA sequence complementary to a target with an appropriate PAM sequence. CRISPR revolutionised the genome editing field and generated novel therapeutic approaches to treat human disease.

1.3.1.3 The growing CRISPR family

While the description and classification of diverse CRISPR systems is constantly evolving, there are broadly two classes each containing multiple CRISPR types.[197] Class 1 contains type I, type III and type IV systems, while Class 2 contains type II, V and VI systems. Class 1 systems contain multiple Cas proteins that combine to form multi-unit effector complexes, while Class 2 systems encompass systems with a single, multi-domain protein capable of both crRNA binding and nuclease activity. The simpler class 2 systems have been most widely adopted for genome engineering applications for both DNA and RNA. The effector nuclease of both type II (Cas9) and type V (Cas12) systems predominantly targets DNA, while the effector of type VI (Cas13) exclusively targets RNA.[197] Extensive mining of genomic and metagenomic data from prokaryotes has revealed a wide array of Cas9, Cas12 and Cas13 orthologues that differ in properties such as their size, nuclease activity, and canonical PAM recognition sites (for review see[197]). Of these, the nuclease derived from *Streptococcus Pyogenes* (SpCas9) has been the most

widely used, due to its efficiency and simple 5'-NGG-3' PAM. The challenges of delivering the long coding sequence of SpCas9 (4.2kb) has led to the identification and *in vivo* use of other Type II Cas9 orthologues from *Staphylococcus aureus* (SaCas9, 3.2kb),[198] *Campylobacter jejuni* (CjCas9, 2.9kb)[199], *Neisseria meningiditis* (NmeCas9, ~3.2kb)[200], and Type V Cas12 orthologues from *Acidaminococcus* (AsCas12a, ~3.9kb)[201] or from *Lachnospiraceae* (LbCas12a, (~3.7kb).[202] The smaller size of these and other recently identified minimal proteins[203–207] offer the opportunity to deliver both the Cas and the gRNA in a single AAV vector. Additionally, both these natural orthologues and many engineered variants[208] have provided a wider range of PAM requirements to expand the targeting scope of these nucleases to almost any site in the genome. Nucleases of all types of Class 2 systems derived from different organisms are used for genome and transcriptome editing in this thesis.

1.3.2 DNA Editing with CRISPR-Cas in the Retina

Following the first proof-of-principle demonstrations of *in vivo* editing of retinal cells including photoreceptors, RGCs and RPE with CRISPR-Cas9 in 2016,[209,210] a wide range of strategies have been developed for retinal genome editing that harness the nucleic acid binding and nuclease functions of Cas enzymes (Figure 1-8). The results of these studies are summarised in Table 1-1, and the respective strategies are described herein.

1.3.2.1 Active Cas Nucleases

Genome editing using active Cas enzymes uses the Cas nuclease to generate double-stranded breaks (DSBs) in DNA. In the case of Cas9, this is mediated by two catalytic domains that cleave each strand (the HNH and RuvC-like domains), while Cas12 nucleases contain only a RuvC-like domain that cleaves both strands.[197] When delivered to a cell with a gRNA, the Cas-gRNA complex interrogates DNA, searching for an appropriate PAM sequence for that nuclease.[211] Upon PAM recognition, the Cas unwinds the DNA, allowing the associated gRNA to hybridise with the exposed protospacer target. If the DNA sequence is complementary to

the gRNA sequence, the Cas undergoes a conformational change allowing DNA cleavage.[211] The initial 10-12 nucleotides of the gRNA sequence proximal to the PAM are known as the seed region, and mismatches in this region lead to the reduction or abrogation of editing.[211]

1.3.2.1.1 Non-homologous end joining repair

Generation of a DSB itself does not edit DNA; how the cell repairs the lesion determines the sequence alteration. In eukaryotic cells, the predominant method of DSB repair is non-homologous end joining (NHEJ), which can occur throughout the cell cycle, including in post-mitotic cells.[212] Error-prone, NHEJ repair results in random insertions and deletions (indels), which in most cases results in frameshift mutations and disruption of the target sequence.[212] Most simply, this has been used for gene knockdown, for example the targeted deletion of the *Vegfa* or *Hif1a* genes in RPE cells, where upregulation of these genes is implicated in the pathogenesis of angiogenesis in wet age-related macular degeneration.[199, 202,213–217] In the case of autosomal dominant RP caused by mutations in *RHO*, NHEJ-mediated knockdown has been used to reduce the expression of a mutant allele in disease models. Strategies have employed a mutation-independent block and replace strategy, by knockout of all *Rho* alleles and subsequent *Rho* supplementation.[218] Alternatively, other approaches use the sequence specificity of the gRNA seed region or PAM sequence to selectively knockdown the mutant allele leaving the wildtype allele intact.[209,219–222] These approaches have demonstrated encouraging functional and structural preservation of rod photoreceptors following treatment in models that lead to rapid retinal degeneration. Another approach has been to stimulate cellular reprogramming by targeting knockdown of transcription factors. CRISPR ablation of the transcription factor *Nrl*, which controls photoreceptor fate, induced a more cone-like phenotype in edited cells and rescued rod-specific degeneration in mouse models with mutations in rhodopsin (*Rho*$^{-/-}$, *RHO*^{P347S} transgenic) and *Pde6b* (*Rd10*).[223]

One approach using active Cas9 has been translated to clinical trials by Editas Medicine as previously discussed.[224] Using *SaCas9* and two gRNAs expressed from a subretinally delivered AAV5 vector, two cut sites are made in intronic regions flanking the c.2991 + 1655A>G *CEP290* cryptic splice site mutation. Studies in humanised mice and non-human primates demonstrated encouraging editing rates of up to 60% and 28% respectively without significant off-target events or significant inflammatory reactions in the primate studies.[225]

1.3.2.1.2 Homology directed-repair and other template-repair mechanisms

The second major repair pathway of DSBs is homology-directed repair (HDR), which uses DNA templates for relatively error-free repair, ideal for the correction of mutations. As HDR is active in the late S/G2 phases,[212] it is less suited to *in vivo* editing as it is inefficient in post-mitotic retinal neurons and requires the delivery of donor sequences with long homology arms. Studies using HDR in photoreceptors have predominantly reported very low repair rates with an excess of indel formation due to the predominance of NHEJ.[226–230] HDR repair remains a viable strategy for the *ex vivo* repair of patient-derived cells for autologous transplantation, with successful use of HDR repair of patient-derived cells in a variety of retinal genes[231–234] including *USH2A*.[167,235,236]

Alternative repair mechanisms to integrate donor sequences *in vivo* have also been evaluated. In microhomology-mediated end-joining (MMEJ) repair, repair is directed by re-annealing of regions of microhomology in strands exposed by 5′ resection of DSB ends. MMEJ has been harnessed for donor template knock-in by providing a template *in trans* with complementary gRNA binding regions that cleave adjacent to short microhomology arms (5-25bp).[237] This has enabled knock-in of donor sequences without HDR repair, and up to 10% knock-in efficiency has been observed in photoreceptors with this method *in vivo*.[238,239] Another method, homology-independent targeted insertion (HITI), is designed to knock-in donor sequences using NHEJ.[238] In HITI, a donor sequence is cleaved at flanking gRNA binding sites

identical to the target loci in genomic DNA. Repair of the genomic DSB can then integrate the linearised donor via NHEJ, enabling targeted knock-in while avoiding the HDR pathway which is not active in non-dividing cells. This was used to knock-in a 1.9kb sequence to repair *Mertk* in the Royal College of Surgeons (RCS) rat, partially restoring visual function.[238]

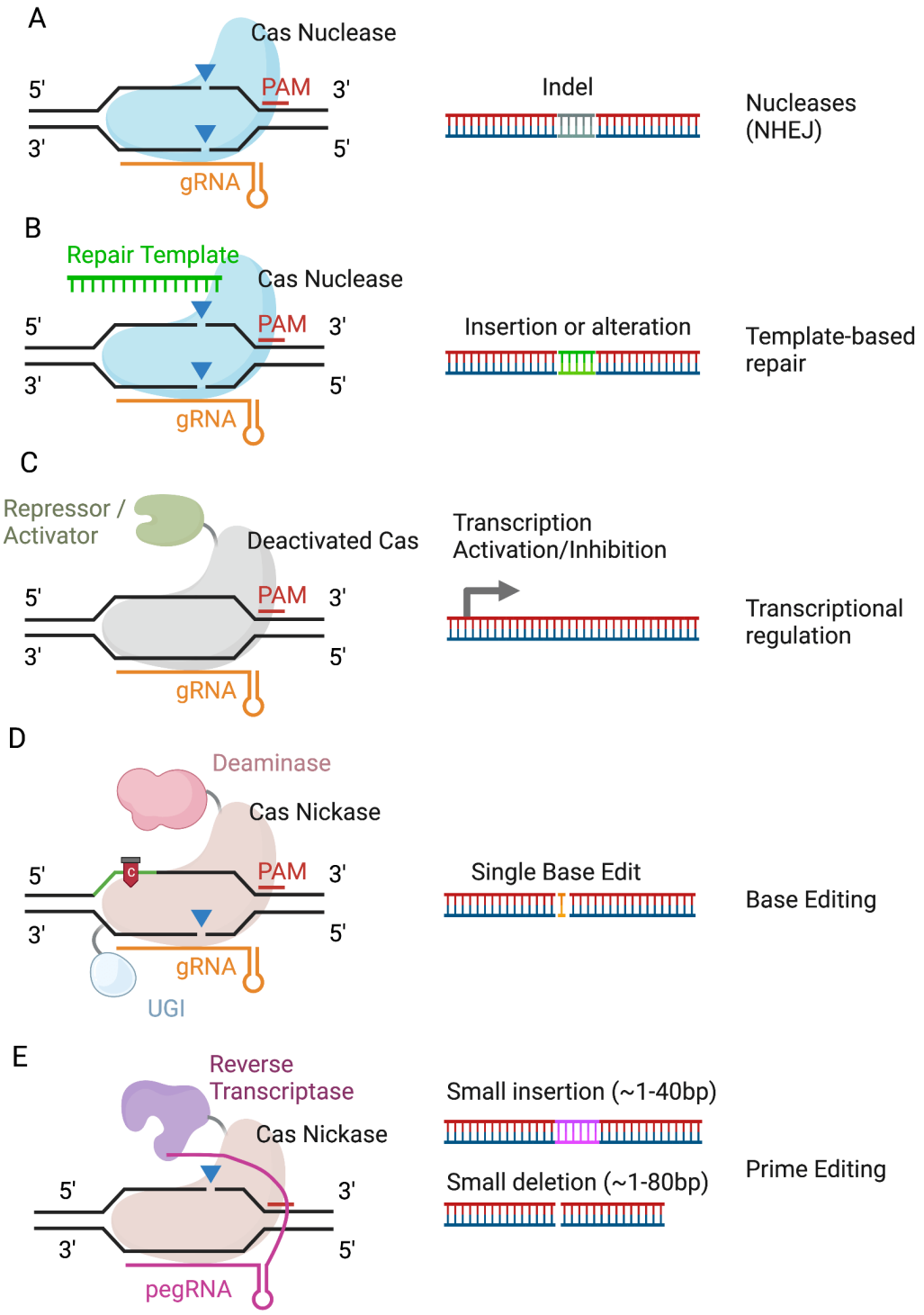


Figure 1-8 Overview of DNA Editing Approaches

Five approaches for genome editing including (**A**) active nucleases to introduce indels or deletions via non-homologous end joining (NHEJ), (**B**) using template-based repair mechanisms for precision insertion of sequences (**C**) transcriptional regulation via repression or activation (**D**) precision single base editing using fused deaminase constructs or (**E**) insertion or deletion of short sequences with prime editing. PAM = protospacer adjacent motif. pegRNA = prime editing guide RNA.

1.3.2.2 Transcriptional regulation

Transcriptional regulation can be used to modulate gene expression using CRISPR interference (CRISPRi) and activtation (CRISPRa) to up- and down-regulate transcription of a target gene respectively.[240] These approaches utilise a catalytically inactive ('dead') Cas enzyme (dCas) with preserved gRNA-directed DNA binding functions. dCas alone can cause repression through steric hindrance of RNA polymerase progression or interference with transcription factor binding sites to a promoter region. The fusion of dCas to gene-regulatory repressor (for example a Krüppel associated box (KRAB) domain) or activator protein domains enhance the potency of gene regulation.[240] In the retina this has been used to induce repression of *Nrl* in to reprogram rods to a cone-phenotype in a rod-degeneration model.[241] Additionally a transcriptional activator system has been used to upregulate expression of m-opsin in a heterozygous *Rho* knockout model and achieve relative preservation of ERG amplitudes.[242]

While active nuclease strategies typically achieve a higher knockdown efficiency, transcriptional regulation offers several advantages including not causing permanent genomic changes, and thus far CRISPRi appears highly specific, with a low tolerance to mismatches and few off-target effects detectable on RNA-seq.[243]

1.3.2.3 Base and Prime Editing

To enable precision correction of mutations without the limitations associated with HDR repair, DNA base- and prime-editing have been developed. Base-editing systems generate precise point mutations without generating DSBs. DNA base editors comprise two key components: a catalytically impaired Cas nuclease, and a fused enzymatic domain that acts on ssDNA to install the base change.[244] The gRNA-Cas complex localises and unwinds a small segment of DNA at the target loci, allowing the enzymatic domain to access and modify the target nucleotide. A Cas9 'nickase' is often used to create a single strand cut in the non-edited strand to promote repair of the non-edited strand using the edited strand as a template.[244] The

commonly used systems are cytosine (CBE) and adenine (ABE) base editors, which use deaminase enzymes to mediate C>T and A>G base pair changes in the target strand respectively. As the complementary strand can also be edited, collectively these enable the correction of all four transition mutations (C>T, T>C, A>G, G>A) representing about 30% of currently annotated pathogenic human variants.[245]

The first generation of CBEs used the rat-derived cytidine deaminase APOBEC1, which facilitates the conversion of cytosine to uridine.[246] Subsequently, the first generation of ABEs were developed, using a *Escherichia Coli*-derived TadA adenosine deaminase to convert adenosine to inosine.[247] These uracil and inosine intermediates are subsequently repaired to thymine and guanosine respectively following DNA repair to install the desired edit. In both of these systems, the target base must lie within an 'editing window', located a short distance from the PAM sequence. Multiple iterations of these systems have been developed since they were first described in 2016 and 2017, using different Cas and deaminases as well as protein engineering approaches to improve efficiency, specificity and targeting range (this constantly developing field is recently reviewed in[248]). Recently, four groups have described cytosine to guanine (CGBE) editors that mediate C>G edits to expand targetable mutations to include C>G and G>C transversions, albeit with lower efficiency than current generations of ABEs and CBEs.[249,250] Cytosine base editing of mitochondrial DNA was also recently described using TALE-deaminase fusions to overcome the difficulty of delivering the gRNA used in CRISPR-based systems into mitochondria.[251] Although yet to enter clinical trials, impressive studies showing the *ex vivo* correction of donor haemopoetic stem cells[252] and *in vivo* results such as the AAV-mediated delivery of an ABE to correct and profoundly prolong the lifespan of mouse models of Hutchinson–Gilford progeria syndrome[253] demonstrate the therapeutic potential of the suite of base editing tools.

The delivery of the large base-editing fusion constructs remains a challenge as the coding sequences typically exceed the capacity of a single AAV. A dual AAV approach, which splits

the transgene across two constructs and uses trans-splicing inteins to reconstitute the N- and C-terminal halves of the base editor following translation, has proved successful with therapeutically relevant editing rates *in vivo* in a range of tissues including the retina.[253,254] For retinal disease, a lentiviral delivered ABE construct demonstrated the correction of a nonsense mutation in *Rpe65* in an LCA mouse model, with up to 29% on target correction, minimal off-target mutations and restoration of protein expression and function, as well as improvements in measures of visual function.[255] Engineering of minimal constructs has also yielded base editors deliverable within a single AAV, which have been used for editing in retinal organoids and correction of the Usher syndrome-associated gene *PCDH15* in HEK293 cells.[256]

The mutations correctable with base editors are currently limited to point mutations editable by the functional enzymatic domains. Prime editors are a recently developed class that utilise a Cas9 nickase fused to a reverse-transcriptase domain to install short insertions or deletions specified by a prime editing gRNA (pegRNA).[257] This offers the possibility of correction of all single base changes in addition to indel mutations. Furthermore, the PAM requirements and concerns with editing of bystander nucleotides that restrict some base editing approaches are minimised with prime editing. Prime editing has now been demonstrated across a range of human cell types including iPSCs.[257,258] In addition to prime editing, Cas-fused transposases have been used to insert large genomic cargos in bacterial genomes but have yet to be used in human cells.[259]

Strategy	Disease & Gene target	Model and age at treatment	Orthologue and Delivery method	Main Outcomes *in vivo*	Reference
NHEJ					
Allele-specific knockdown	adRP *Rho*	*Rho-S334ter* (rat). P0 mice	SpCas9, Plasmid electroporation	Allele specific editing (~33% of mutant allele) Relative ONL preservation	Bakondi[209]
Knockdown of human allele	adRP *RHO*	*RHO*$^{P23H\ Tg}$:*Rho*$^{-/-}$ Mouse, P0 mice	SpCas9, Plasmid electroporation	~18% on-target editing, 63.5% RHO protein reduction	Latella[260]
Allele-specific knockdown	adRP *Rho*	*Rho*$^{P23H/+}$ P0 mice	SpCas9(VQR), Plasmid electroporation	Allele specific editing (~45% of mutant allele), 38% reduction in mutant mRNA Relative ONL preservation	Li[219]
Allele-specific knockdown	adRP *Rho*	*Rho*$^{P23H/+}$ P0 mice	SpCas9(VQR), Plasmid electroporation Intravitreal AAV9.PHP-B	Allele specific editing (~50-70% of mutant allele in FACS selected cells) Relative preservation of ONL thickness, scotopic ERG a-wave and b-wave	Gianelli[220]
Allele-specific knockdown	adRP *Rho*	*RHO*$^{P23H\ Tg}$ (pig) 7wks old	SaCas9, subretinal single AAV5	Allele specific editing (3.8% of mutant allele) 3wks post injection	Burnight[231]
Allele-specific knockdown	adRP *Rho*	*RHO*$^{P347S\ (Tg)}$ P7 mice	SpCas9 or SpCas9(VQR-HF1). Subretinal dual AAV8	9-12% on target editing with allele specific editing shown *in vitro*. Improved RHO trafficking and scotopic B wave amplitude	Patrizi[221]
Block and replace	adRP *Rho*	*Rho*$^{P23H/+}$, *Rho*$^{P23H/P23H}$, *Rho*$^{D190N/+}$ (P1-3)	SpCas9, Subretinal dual AAV8-Y733F with *Rho* supplementation	91% on-target *Rho* editing Relative preservation of ONL thickness, scotopic ERG a-wave and b-wave	Tsai[218]
Rod reprogramming	RP (ad/ar) *Nrl*	*Nrl-EGFP, WT,* *Rho*$^{P23H/+}$, *Rd10, Rho*$^{-/-}$. P14 mice	SpCas9, subretinal dual AAV8	~90% on-target editing of *nrl* in FACS sorted cells. Partial ERG rescue of ERG in range of models, rods adopting cone-like phenotype	Yu[223]
Rod reprogramming	RP (ad/ar) *Nrl, Nr2e3*	*Rd10, FVB/N* P7 mice	SpCas9, subretinal dual AAV8	Increase in cone-like cells by histology and qPCR, partial rescue of ONL thickness and ERG amplitudes in both models	Zhu[261]

Strategy	Disease & Gene target	Model and age at treatment	Orthologue and Delivery method	Main Outcomes *in vivo*	Reference
Intronic deletion	LCA10 *CEP290*	*WT* 8-10wks old	SpCas9, Dual AAV5	~20% on-target editing to remove IVS26 intron in WT mice	Ruan[262]
Mutation excision	LCA10 *CEP290*	c.2991 + 1665 A>G IVS26 CEP290 knockin mouse, NHPs	SaCas9, subretinal single AAV5	60% editing in huIVS26 mice 28% editing at 1×10^{11} vg/eye in NHPs Safety and tolerability in NHPs	Maeder[225]
Proof of principle editing of WT locus	CORD *GUCY2D/ Gucy2e*	*WT* NHP, $GC1^{+/-}$:$GC2^{-/-}$ mice	SaCas9, subretinal dual AAV5	Up to 81% editing in sorted mouse PRs. 10-20% editing in NHP. T-cell responses in NHPs to SaCas9, editing unaffected by previous SaCas9 exposure.	McCullough[263]
Proof of principle editing of WT locus	ACHM *CNGB3*	*WT* NHP	SpCas9, subretinal dual AAV9	12-14% on-target editing in bleb area. mfERG reduction in edited eye. SpCas9 transcripts not detected in other organs at 1yr post injection	Lin[264]
Proof of principle editing, self-targeting construct	No retinal disease *YFP*	*Thy1-YFP*. 12-16wks old	SpCas9, Dual AAV2, intravitreal + self-targeting construct	20-30% on-target editing with ~84% reduction in YFP in transduced RGCs. ~50% reduction in SpCas9 expression with self-targeting without loss of on-target editing.	Hung[210] Li[265]
Proof of principle, orthologue comparison	No retinal disease *YFP*	*CMV-Cre:Rosa26-YFP*. 8-12wks old	SpCas9, SaCas9, CjCas9 dual and single AAV7m8, intravitreal	Efficiency greater with SpCas and Cas12a than SaCas9 and CjCas9. No difference in single or dual vector systems	Li[201]
Signalling pathway knockdown	Wet AMD *Vegfa, Hif1a*	*WT,* laser induced CNV. 8wks old	CjCas9, intravitreal single AAV9	RPE on-target: 22% *Vegfa* and 31% *Hif1a* Reduced CNV by 20% and 24% respectively Maintained expression without toxicity of off-target effects at 14mo post injection	Kim[199] Jo[266]
Signalling pathway knockdown	Wet AMD *Vegfa, Hif1a*	*WT,* laser induced CNV. 8wks old	LbCas12a, intravitreal single AAV9	On target efficiency: 57-59% in PRs, 6-17% in RPE. Minimal off-targets. 34-42% CNV reduction, no toxicity on ERG.	Koo[202]

Strategy	Disease & Gene target	Model and age at treatment	Orthologue and Delivery method	Main Outcomes *in vivo*	Reference
Signalling pathway knockdown	Wet AMD *Vegfa*	*WT,* laser induced CNV. 6-8wks old	SpCas9 dual AAV8 and SaCas9 single AAV8, subretinal	SpCas9 (22%) greater on-target efficacy than SaCas9 (2%). SpCas9 22% reduction in CNV area	Chung[216]
Signalling pathway knockdown	Wet AMD *Vegfa*	*WT*. 8-9wks old	SpCas9, subretinal lentiviral	36-85% on-target editing of sorted RPE cells	Holmgaard[214]
Signalling pathway knockdown	Wet AMD *Vegfa*	*WT*. 8-9wks old	SpCas9, subretinal RNP Lipofectamine 3000. Modified guides	2-5% on-target editing at high doses with inflammatory/toxic RPE response.	Holmgaard[215]
Signalling pathway knockdown	Wet AMD *Vegfa*	*WT,* laser induced CNV. 6-8wks old	SpCas9, subretinal RNP, Lipofectamine 2000	25% on-target editing in dissected cells. 58% reduction in CNV area, 30% reduction in Vegf protein. No detected off-targets	Kim[213]
Signalling pathway knockdown	Wet AMD *Vegfa*	*WT,* laser induced CNV. 8wks old	SpCas9, subretinal chimeric lentiviral mRNA delivery system	44% on-target RPE editing with minimal PR transduction, time limited expression, innate and adaptive immune response minimal. 35% Vegfa reduction, 63% CNV reduction	Ling[217]
Signalling pathway knockdown	Optic nerve degeneration *Sarm1, Ddit3*	*WT*, Optic nerve crush 3-8wks old	SpCas9, dual AAV2 triple mutant (Y444, 500, 730F)	11% (*Ddit3)* and 95% (*Sarm1)* on-target editing of sorted cells. Relative preservation of RGC soma and axons following crush injury.	Wang[267]
<u>Template-Based Repair</u>					
HDR repair	LCA2 *Rpe65*	*Rd12* 3wk old	SpCas9, dual subretinal AAV9	Low HDR efficiency (~1%) in RPE with no HDR in PRs, and ~20% indel rate. Partial recovery of ERG a- and b- wave amplitude maintained to 7mo. ONL thickness increased.	Jo[226]
HDR Repair	arRP *Pde6b*	*Rd10* P3-P8	SpCas9 + ssDNA donor Plasmid electroporation	Low HDR efficiency (~0.2%) in PRs. Partial preservation of optomotor and VEP response	Vagni[228]

Strategy	Disease & Gene target	Model and age at treatment	Orthologue and Delivery method	Main Outcomes *in vivo*	Reference
HDR Repair	X-linked RP *Rpgr*	*Rpgr*$^{/y}$:*SpCas9*$^{+/WT}$ 6mo old mice	SpCas9 (endogenous), subretinal dual AAV8 with gRNA and donors	86% HDR efficiency reported, no indel assessment. Rescue of ONL thickness.	Hu[229]
HDR repair enhanced with RecA	arRP *Pde6b*	*Rd1*. Neonatal	SpCas9 + RecA-MS2 / sgRNA-MCP recruitment system + ssDNA template. Plasmid Electroporation	Low levels of HDR mediated repair (unquantified) with some restoration of Pde6b protein. Partial rescue of pupillary light response.	Cai[230]
HDR-mediated protein tagging	No disease. *Rho, Arr, Glul, PSD-95*	*WT. Neonatal.*	SpCas9 + ssDNA donor. Plasmid electroporation	C-terminal knock-in of fluorescent reporters to PRs and muller glia. ~10% efficiency	Matsuda[227]
HITI-mediated exon insertion	arRP *Mertk*	RCS Rat (*Mertk* exon 2 deletion). 3wks old.	SpCas9, dual subretinal AAV8	Successful insertion of *Mertk* exon 2 Partial rescue of scotopic ERG b-wave and cone flicker responses	Suzuki[238]
MMEJ-mediated repair	CSNB *Gnat1*	Gnat1$^{IRD2/IRD2}$: Pde6c$^{cpfl1/cpfl1}$	SaCas9, single subretinal AAV8	~10% successful insertion of donor sequence, Partial rescue of flicker ERG, VEP and OKR	Nishiguchi[239]
MMEJ-mediated knock-in/-out	Glaucoma *CAT*	*WT*. 5wks old	SaCas9, single intravitreal AAV2	Knock-in of iLOV (mini-GFP) to replace *CAT* locus of RGCs. RGC survival reduced.	Katayama[268]
<u>Transcriptional regulation</u>					
CRISPRi: rod reprogramming	RP (ad/ar) *Nrl*	*Nrl-EGFP, Rd10* Neonatal	Split-intein dual dSpCas9±KRAB, AAV2-Y444F, tail vein and subretinal injection	*Nrl-GFP*: Evidence of rod-cone reprogramming *Rd10*: Relative preservation of ONL, photopic B-wave, OKR	Moreno[241]
CRIPSRi: Proof of principle	No disease *NHE8*	*WT*. 4wks old	dNmCas9-KRAB, subretinal dual AAV9-2YF	Reduction in *NHE8* transcripts, local ONL loss	Xia[269]
CRISPRa: opsin transactivation	*Opn1mw*	*Rho*$^{+/-}$	Split-intein dual dSpCas9-VPR	Increased M-opsin expression, improved scotopic B-wave, relative ONL preservation	Böhm[242]

Strategy	Disease & Gene target	Model and age at treatment	Orthologue and Delivery method	Main Outcomes *in vivo*	Reference
DNA Base Editing					
CBE and ABE: proof of principle	No retinal disease target *Dnmt1*	*Rho-iCre:Ai9* 2wks old	Split-intein AAV.PHP-B-SaCas9-CBE and AAV.Anc80-SaCas9-ABE, Subretinal injection	CBE: 48% editing in FACS sorted cells (19% total retina). Indels up to 34% ABE: 37% editing in FACS sorted cells. (26% total retina). Few indels	Levy[254]
ABE mutation correction	LCA2 *Rpe65*	*Rd12* 4wk old	SpCas9 ABE, single subretinal lentivirus	~16% editing of unsorted RPE without significant off-targets or indels, Rpe65 protein expression. 65% restoration of scotopic B-wave, restoration of optomotor response	Suh[255]
Prime Editing					
Proof of principle	No retinal disease *Atb7b*	*WT*	SpCas9-PE2 Trans-splicing AAV8 triple vector. Intravitreal	1.8% on-target editing in PRs and RPE. No detected off-targets	Jang[270]
Mutation correction	LCA2 *Rpe65*	*Rd12* 3wk old	SpCas9-PE2 Trans-splicing AAV8 triple vector. Subretinal	6.4% on-target editing in RPE, no detected off-targets. Rescue of scotopic ERG and optomotor testing.	Jang[270]
Proof of principle	No retinal disease. *Dnmt1*	*WT CD1* 6wks olds	SpCas9-PE2. Split-intein AAV8 dual vector. Subretinal.	1.7% on-target with 0.17% indels.	Zhi[271]
RNA cleavage					
Glial reprogramming	Retinal degeneration *Ptbp1*	*WT, Ai9*. NMDA induced degeneration. 4-8wks old	CasRx (Cas13d), AAV-PHPB. Subretinal and intravitreal.	~81% *Ptb1* knockdown *in vitro*.. *In vivo* conversion of muller glia to RGCs (~20 cells per 1mm × 10μm field. Restoration of ~21% of RGCs following NMDA induced injury. Restoration of VEP in injured retina to close to uninjured levels.	Zhou[272]

Signalling pathway knockdown	Wet AMD *Vegfa*	*WT,* laser induced CNV. 6-8wks old	CasRx (Cas13d), AAV-PHPB. Intravitreal.	Significant reduction in *Vegfa* mRNA and protein, reduction in CNV area	Zhou[273]

Table 1-1 Overview of *in vivo* gene engineering studies targeting retinal cells implicated in retinal disease

Summary of currently published (to August 2021) studies investigating CRISPR-mediated gene engineering *in vivo* in the retina. Where dual AAV vectors are specified, one vector typically expresses the Cas nuclease with the second vector the gRNA. Models refer to mice unless otherwise specified. ABE = adenosine base editor, arRP = Autosomal recessive retinitis pigmentosa, adRP = Autosomal dominant retinitis pigmentosa, CBE = cytosine base editor, CORD = cone rod dystrophy, CSNB = congenital stationary night blindness, CRISPRi = CRISPR interference, CRISPRa = CRISPR activation, ERG = electroretinogram, FACS = fluorescent activated cell sorting, HDR = homology directed repair, HITI = homology independent targeted integration, LCA = Leber's congenital amaurosis, MMEJ = microhomology-mediated end joining, NHEJ = non-homologous end-joining, NHP = non-human primate, OKR = optokinetic response, ONL = outer nuclear layer, PR = photoreceptor, RGCs = retinal ganglion cells, RNP = ribonuclear protein, RPE = retinal pigment epithelium, ssDNA = single stranded DNA, VEP = visual evoked potential, WT = wildtype.

1.3.3 RNA Targeting with CRISPR in the Retina

1.3.3.1 Retinal RNA therapeutics

As mentioned in section 1.1.3.2.1, therapies to target RNA have a long history of development for ocular disease, dating back to the first clinically approved AON therapy, fomivirsen, for cytomegalovirus-associated retinitis.[274] This section considers emerging RNA editing therapeutics based on CRISPR and RNA base editing technologies, with other modalities such as AON and RNA interference more thoroughly reviewed elsewhere.[89,275]

1.3.3.2 Cas13 for RNA targeting

RNA targeting with CRISPR-Cas was first demonstrated with the engineering of SpCas9 systems by introducing a PAM-presenting oligonucleotide (PAMmer) to stimulate single-stranded RNA cleavage.[276] It has now also been demonstrated that SpCas9 can be used to repress translation of certain mRNAs in the absence of a PAMmer.[277,278]

These repurposed DNA targeting enzymes demonstrated the potential of targeting RNA, however the identification of the type VI Cas13 endonucleases represented a significant advance. Following the first identified orthologue C2c2,[279,280] later renamed to Cas13a, orthologues in subtypes Cas13a, Cas13b,[281] Cas13c,[282] Cas13d,[283] Cas13X[284] and Cas13Y[284] have been identified, and used for RNA-guided RNA cleavage.[197] RNase activity is mediated by higher eukaryotes and prokaryotes nucleotide-binding (HEPN) domains, that exclusively cleave ssRNA.[283] Although in bacterial cells Cas13 orthologues demonstrate preferences for protospacer flanking site (PFS) sequences, these preferences are broadly not observed for many orthologues in mammalian cells, giving a much greater targeting range than Cas9 orthologues constrained by PAM sites.[285,286] One drawback, is that these enzymes exhibit varying levels of collateral non-specific RNA cleavage activity upon target binding,[286] however this effect is markedly reduced or not detectable in mammalian compared to bacterial cells.[285]

Of all of these effectors, the Cas13d effector from *Ruminococcus flavefaciens* (named CasRx) has demonstrated the most widespread use and best efficiency for RNA knockdown, and has been used for ophthalmology applications. Delivered via AAV, Cas13Rx was used to target the polypyrimidine tract-binding protein 1 (*Ptbp1*) *in vivo* in mice to not only facilitate the conversion of Müller glia to RGCs, but also replenish RGC populations and visual function in models of RGC injury.[272] CasRx has also been used for the targeting of *VEGF* in angiogenesis models with significant reductions in mRNA and protein levels.[273]

1.3.3.3 RNA base editing with CRISPR-Cas13

RNA base editing targets the transcriptome for specific conversion of bases in RNA. To date, RNA base editing has not been used for targeting retinal genes. Retinal RNA editing using Cas13 is a significant theme of this thesis and review of the field is described herein.

1.3.3.3.1 Harnessing ADAR for RNA editing

Most RNA base editing approaches exploit the family of Adenosine Deaminase Acting on RNA (ADAR) enzymes. These were first proposed to be used for targeted editing over 25 years ago,[287] and have since been employed using a variety of RNA targeting systems (Figure 1-10 and Table 1-2).[288] These systems all broadly use two components: (1) a gRNA and binding effector that can hybridize to the target RNA, and (2) a recruited or fused ADAR deaminase domain ($ADAR_{DD}$). ADARs are endogenously expressed in human tissues, converting adenosine to inosine (A-I) in regions of double stranded RNA (dsRNA) >15-20nt of length[289] such as found in introns[290] or *Alu* repeats.[291] Inosine is similar to guanosine and is read as guanosine in cellular processes such as translation and splicing, and therefore can be used to install A>G edits and correct G>A mutations (Figure 1-9).[292]

For targeted RNA base editing, a complementary gRNA hybridises to the target sequence to create the local dsRNA sequence necessary for the $ADAR_{DD}$ to catalyse hydrolytic deamination. A base-flipping mechanism rotates the target adenine base from the RNA helix

into the enzyme catalytic pocket to allow the enzyme to attack the target C6 carbon.[293] As ADAR editing preferentially occurs at adenosines that are mismatched with a cytidine opposite the target adenosine,[294] an A-C mismatch is commonly encoded in the gRNA at the target adenosine to improve editing efficiency and specificity.

Two catalytically active isoforms of ADAR edit RNA in human cells using similar mechanisms.[292] ADAR1 is expressed ubiquitously from two promoters: one directs constitutive expression of the truncated ADAR-p110 isoform in the nucleus while the second directs inducible expression of the full-length ADAR-p150 isoform in the nucleus and cytoplasm in response to type I and II interferon.[295,296] ADAR2 is more selectively expressed, predominantly in the brain with nuclear localisation.[296,297]

Engineering of the ADAR deaminase domain has produced mutants that alter editing efficiency and specificity. The $ADAR2_{DD}$-E488Q mutation markedly increases editing activity (up to 12-fold relative to wildtype) through increasing base flipping stability and deamination rates,[293,298,299] however the E488Q mutation is also known to increase off-target editing throughout the transcriptome.[300,301] An $ADAR2_{DD}$-E488Q/T375G double mutant has demonstrated promise for much greater specificity although with some loss of on-target efficiency.[300] The $ADAR1_{DD}$-E1008Q variant demonstrates similar hyperactivity like that seen for ADAR2-E488Q.[302] Recently, mutagenesis studies have been used to introduce 16 mutations to $ADAR2_{DD}$ to create a system capable of C-U editing in addition to A-I editing.[303]

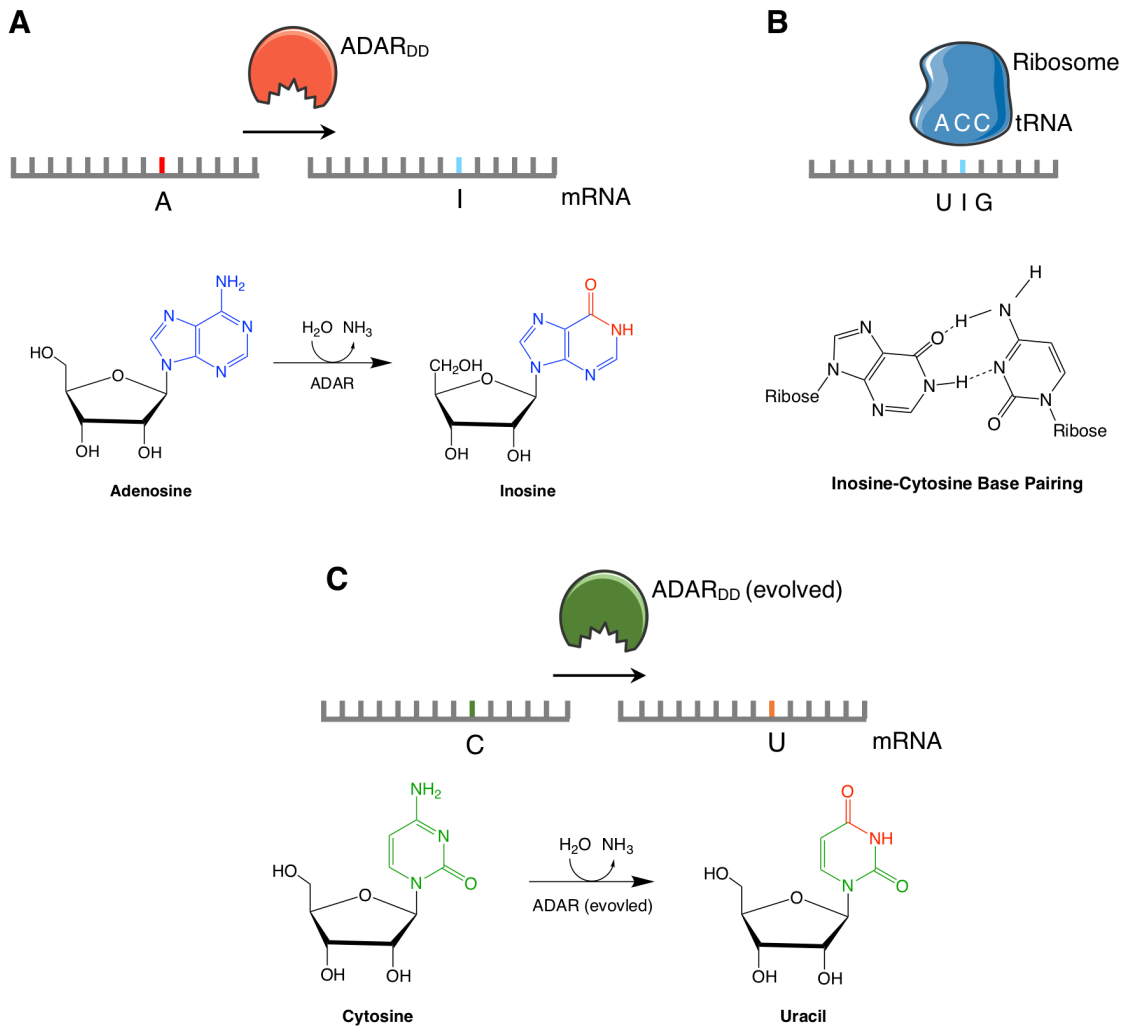


Figure 1-9 Mechanism of adenosine to inosine deamination
A. Demonstrates the hydrolytic deamination of adenosine to inosine. **B.** Base pairing between inosine and cytosine allow inosine to be read as a guanosine during translation by the ribosome, effectively an A-G edit. **C.** Evolved mutants of human ADAR allow for deamination of cytosine to uracil for C-U editing. ADAR = adenosine deaminase acting on RNA, DD = deaminase domain

1.3.3.3.2 CRISPR-Cas13-ADAR$_{DD}$

CRISPR-based RNA editors use the RNA binding capabilities of Cas13, but with deactivated HEPN domains to prevent RNA cleavage. Fused to ADAR$_{DD}$ these can be used for programmable RNA editing. Following screening of a range of Cas13 orthologues, Cox et al. first developed the REPAIR system (RNA Editing for Programmable A to I Replacement) using dPspCas13b derived from *Prevotella Sp.*[300] REPAIRv1 used the ADAR2$_{DD}$(E488Q) to demonstrate editing efficiencies of 15-40% against endogenous targets, but also widespread off-

target editing. REPAIRv2, paired with the more specific $ADAR2_{DD}$(E488Q/T375G) mutant, produced a 900-fold reduction in off-target editing but also a 2-fold reduction in on-target efficiency.[300]

A drawback of dPspCas13b is that its coding sequence size makes it challenging for delivery with a fused $ADAR2_{DD}$ (total construct size 4.47kb). Cox et al. also described a C-terminally truncated dPspCas13b protein (Δ984-1090) that is relatively uncharacterised, but purported to retain the RNA editing activity with a construct size packageable in AAV (4.15kb). Since this description, a number of recent papers have now identified and used smaller Cas13 orthologues for RNA editing including Cas13bt,[282] Cas13Rx[304] and Cas13X.[284]

Editing systems to allow C-U editing have now also been developed. The RESCUE system (RNA Editing for Specific C to U Exchange) used an engineered ADAR mutant fused to dRanCas13b derived from *Riemerella anatipestifer* to allow both C-U and A-I editing *in vitro.*[305]A more specific variant with a S375A mutation (RESCUE-S) was also developed to reduce the A-I off-targets and, to a lesser extent the C-U off-targets, that occur with RESCUE. This yielded an approximately 12-fold reduction in A-I off-targets and ~1.8-fold reduction in C-U off-targets while maintaining specificity.[305] More recently, a system using the APOBEC3A cytidine deaminase in place of ADAR was used with both dPspCas13b and dCas13Rx for on-target C-U editing only.[306]

An important observation for Cas-guided RNA editing systems, was that REPAIR was active against in a broad range of sequence contexts and without PFS preferences. Wildtype ADARs have a native preference for editing adenosines a nearest neighbour 5'-A or -U and a 3'-G,[293] and other approaches including those using the E488Q mutant have demonstrated reductions in efficiencies against adenosines located within a GAN triplet motif.[299] Luciferase reporter studies of the REPAIR system demonstrated it could edit all 16 possible NAN codons, potentially due to its high binding affinity to the target.[300]

1.3.3.3.3 Other exogenous ADAR RNA editing strategies

Cas13-ADAR editing systems can be defined as exogenous ADAR systems—the $ADAR_{DD}$ is overexpressed by exogenous delivery, rather than relying on harnessing endogenously expressed ADAR in cells. The Cas13-ADAR systems all build on other described RNA editing systems (for a detailed review see Fry et al.[288]).

One of the first described RNA editing systems used the bacteriophage-derived λN peptide fused to $ADAR2_{DD}$, which binds short stem-loop RNA structures called BoxBs.[307–309] Although likely less efficient than dPspCas13b-ADAR2(E488Q),[300] this minimal system is able to be delivered with AAV, and has been used to edit *Mecp2* in primary murine neurons.[310,311] Off-target events seem to be particularly prevalent with the BoxB-λN-ADAR system, although localizing expression to the nucleus may improve these.[301]

The MS2 bacteriophage coat protein (MCP) editing system fuses $ADAR_{DD}$ to MCP. MCP binds MS2 RNA stem-loop structures attached to gRNAs for site-directed editing.[312–314] Notably, MCP-$ADAR1_{DD}$(E1008Q) and MCP-$ADAR2_{DD}$(E488Q) constructs have been delivered by AAV *in vivo*. An AAV8-MCP-$ADAR1_{DD}$(E1008Q) construct delivered with an MS2 gRNA demonstrated 2% on-target efficiency and partial restoration of dystrophin expression in an *mdx* mouse model of muscular dystrophy.[312]

The GluR2 system uses the Q/R motif in the *GRIA2* transcript, a natural target for the binding of the dsRBD domains of full-length ADAR2. Attaching an optimised Q/R hairpin motif to gRNA sequences recruits full-length ADAR2.[312,315] Katrekar et al. delivered the 2.1kb ADAR2 and ADAR2(E488Q) sequences with GluR2-gRNAs via AAV8 intramuscularly to the *mdx* mouse and systemically to the sparse fur ash (*spf^{ash}*) mouse model of ornithine transcarbamylase (OTC) deficiency.[312] This resulted in the low-level correction of a stop codon and splice defect in each model respectively, with resultant rescue of protein expression.

The SNAP-ADAR system uses SNAP-tags, enzymes that form covalent linkages with a O6-benzyl-guanine (BG) substrate.[316] SNAP-tags fused to $ADAR_{DD}$ can bind to gRNAs

conjugated with BG that then bind an RNA target.[299,316,317] Although these demonstrate high efficiency and specificity *in vitro*, the gRNAs must be chemically modified for the attachment of the BG and for nuclease-protection and this limits their potential clinical utility.

Finally, the synthetic CRISPR-Cas Inspired RNA targeting system (CIRTS) was developed, which synthetically combines protein domains derived entirely humans to overcome concerns over the potential immunogenicity of bacterial derived effectors,. These domains were designed to mimick Cas13 ssRNA recognition, binding and gRNA targeting functions and fused to $ADAR_{DD}$(E488Q), achieving editing rates of up to 50% *in vitro* on luciferase reporter targets.[318]

1.3.3.3.4 Endogenous ADAR RNA editing

In contrast to exogenous strategies, endogenous strategies try to recruit and provide the substrate for ADAR expressed in human cells, typically using antisense methods.

The LEAPER (Leveraging Endogenous ADAR for Programmable Editing of RNA) system uses long gRNAs (71-191 nts) to create long dsRNA regions for the binding of naturally expressed ADAR1.[319] These have achieved high editing rates in the 5'UTR of endogenous genes, and at lower efficiencies in coding regions, with improved editing with chemical modification of the guides.

The RESTORE editing system (Recruiting Endogenous ADAR to Specific Transcripts for Oligonucleotide-mediated RNA Editing) used shorter (20-40 nt) chemically modified oligonucleotides with the GluR2 R/G domain to recruit ADAR1.[320] Notably, editing rates are markedly improved by the interferon mediated induction of ADAR1p150 expression.[320] Katrekar et al. also found that short 20 nt guides with a single GluR2 domain delivered alone via AAV8 to the mouse model of ornithine transcarbamylase (OTC) deficiency were able to mediate very low (0.6%) editing rates.[312]

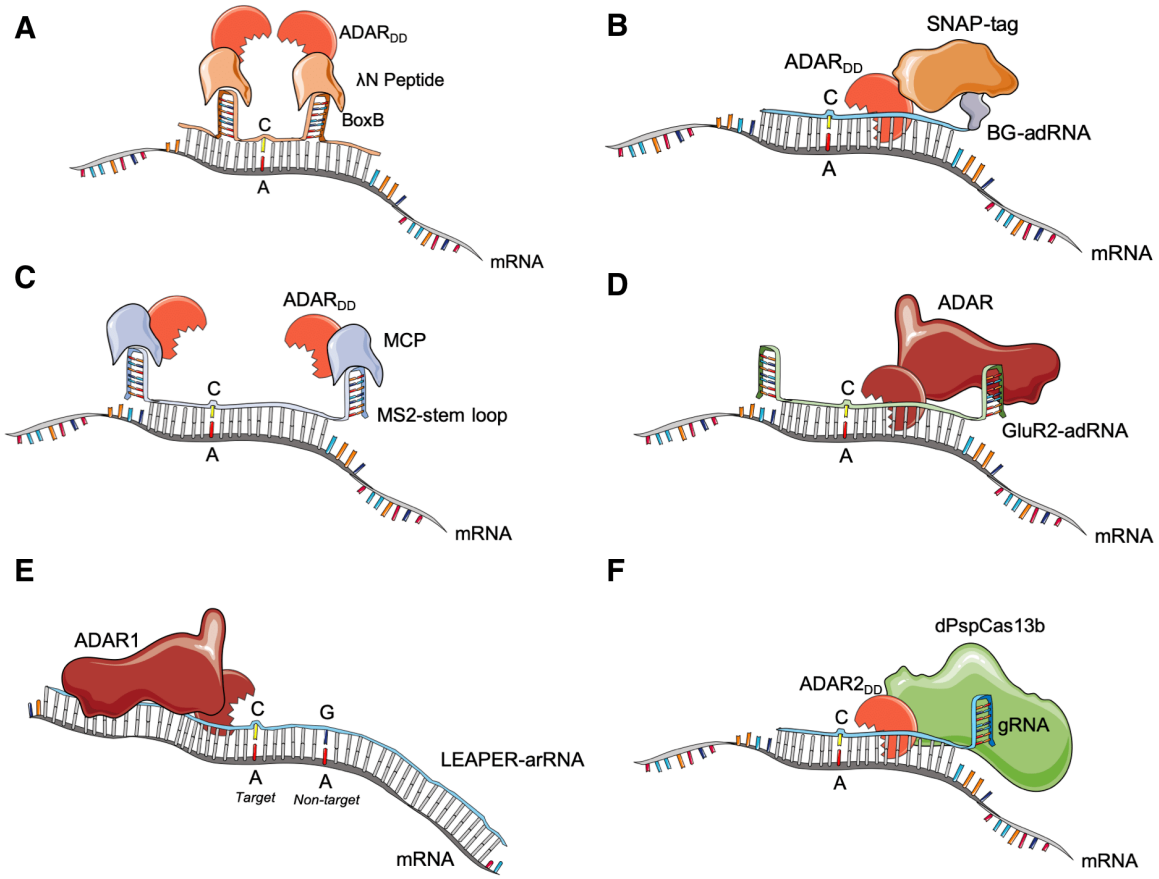


Figure 1-10 Schematic overview of RNA editing approaches

A. BoxB-λN-ADAR with a dual BoxB design to recruit the λN peptide. **B.** SNAP-tag-ADAR fusion with a O6-benzyl-guanine (BG) conjugated gRNA. **C.** Glu-adRNA approach where the GluR2 R/G hairpin recruits exogenous or endogenous full-length ADAR. **D.** MS2-MCP-ADAR stem-loop approach with dual MS2 stem-loop hairpins recognized by the MCP binding protein. **E.** An example of endogenous ADAR recruitment using long LEAPER antisense gRNAs and G-A mismatches within the guide region to reduce off-target editing. **F.** The REPAIR system with dPspCas13b-ADAR fusions recruited by a guide RNA with a direct repeat. Note the A-C mismatch at the target adenosine in each strategy to promote editing at the target site.

System		Immortalised cells	Primary cells	*In Vivo*	Ref
Exogenous ADAR					
BoxB-λN-ADAR	**Gene**	*Mecp2*	*Mecp2*	Not tested	301, 308,310
	Model	N2A	Murine neuron		
	Efficiency	25-50%	72%		
	Delivery	Plasmid transfection	AAV		
SNAP-ADAR	**Gene**	Many targets	Not tested	Not tested	299
	Model	HEK293			
	Efficiency	Up to 90%			
	Delivery	Guide transfection			
MS2-MCP-ADAR	**Gene**	Many targets	Not tested	*Dmd*	312,313
	Model	HEK293T		*mdx* mouse	
	Efficiency	10-80%		AAV	
	Delivery	Plasmid transfection		2%	
GluR2-ADAR	**Gene**	*PINK1*		*Dmd, Otc*	312,315
	Model	HELA HEK293T	Not tested	*mdx* mouse model *spf*^{ash} mouse model	
	Efficiency	10-40%		0.8% (*mdx*) 4.6-8.2% (*spf*^{ash})	
	Delivery	Plasmid transfection		AAV	
REPAIR: CRISPR-Cas13b-ADAR (A-I)	**Gene**	*KRAS, PPIB*	Not tested	Not tested	300
	Model	HEK293FT			
	Efficiency	28%			
	Delivery	Plasmid			
RESCUE: CRISPR-Cas13b-ADAR (C-T)	**Gene**	Multiple	*CTNNB1*	Not tested	303
	Model	HEK293FT	HUVEC cells		
	Efficiency	3-42% in 5% when multiplexed	Not reported		
	Delivery	Plasmid transfection	Plasmid transfection		
Endogenous ADAR					
LEAPER (long gRNA)	**Gene**	Many targets	Many targets	Not tested	319
	Model	Multiple lines	Multiple lines		
	Efficiency	Up to 50%. 6% (lenti)	30-80%		

	Delivery	Plasmid Lentivirus	Plasmid electroporation		
RESTORE (ASO, chemical modification)	**Gene**	Many targets	*GAPDH, STAT1, SERPINA1*	Not tested	[320]
	Model	Many cell types	Multiple lines		
	Efficiency	3-34%	Up to 27%		
	Delivery	ASO Transfection	ASO Transfection		
GluR2	**Gene**	RAB7A, KRAS, CKB	Not tested	*Otc*	[312]
	Model	HEK293T		*spf*^{ash} mouse model	
	Efficiency	10-18%		0.6%	
	Delivery	Plasmid transfection		AAV	

Table 1-2 Comparison of RNA editing tools
Comparison of each RNA editing tools and their on-target efficiencies for endogenous transcripts. Over-expressed or reporter transcript efficiencies are not reported here.

1.3.4 Translational considerations of retinal genome editing

In considering how genome or transcriptome editing might be applied for the treatment of IRDs, the growing array of tools provides numerous strategies, each with unique advantages. In addition to the challenges with delivering large genetic payloads as already discussed, a broad set of translational considerations are relevant for any CRISPR-based gene editing strategy.

1.3.4.1 Genotoxicity

The likelihood and location of unintended edits is driven by Cas-dependent and Cas-independent effects.[321] Cas-dependent off-targets occur predominantly in regions of complementarity to the gRNA sequence and are affected by the fidelity of the endonuclease.[322] *In silico* and *in vitro* tools for prediction and screening of Cas-dependent off-target events allow for the survey of potential sites where editing occurs at sequences similar to the target loci. This allows for focused interrogation in the disease-relevant tissue. The generation of a range of high-fidelity orthologues has enabled the substantial reduction of Cas- and gRNA-dependent

off-target edits.[321] For nucleases that create DSBs, cases of large chromosomal rearrangements[323] and insertion of AAV genomes[324] have been widely documented, increasing the appeal of strategies that don't require the generation of DSBs such as base editing.

For DNA and RNA base editors using effector domains, Cas-independent off-targets can also occur. One example of these are local 'bystander' edits that occur within the editing window or hybridisation region of the gRNA, for instance the deamination of nearby adenosines aside from the target base.[244] These might be limited with a narrower editing window for a DNA base editor,[245] or in RNA editing, placing mismatched guanines in the gRNA opposite non-target adenosines.[319] Genome- and transcriptome-wide off-target deamination is also observed with both DNA and RNA base editors.[325] Protein engineering to improve the fidelity of these tools has reduced the frequency of DNA and RNA off-targets,[326] such as the discussed E488Q/T375G $ADAR_{DD}$ mutation.[300]

Detection of these editing events remains a technical challenge.[327] A wide variety of protocols now exist for the unbiased detection of off-target events at a genome wide level with both biochemical and cell-based assays.[321] Transcriptome wide RNA sequencing protocols have also been developed for detecting off-target RNA events.[325] Limitations of these methods include the need for high-cost sequencing methods, applicability to the cell type of interest and low detection sensitivity, among others.[321]

Encouragingly, strategies that have now entered clinical trial have been well characterised and optimised to minimise off-target effects to become near undetectable.[225,328,329] For example, the *CEP290* editing strategy developed by Editas Medicine identified potential off-target sites for their gRNAs using *in silico* and in unbiased *in vitro* screens, and then used targeted deep sequencing of potential off-target sites in retinal explants and ARPE-19 cells transduced with the AAV-CRISPR constructs.[225] No off-target editing sites were detected above the 0.1% detection limit. It is possible the Cas-nuclease in itself may be toxic to cells, however long-term studies in mice with AAV-CjCas9,[330] and the generation of a transgenic SpCas9 mouse[331] have

so far not demonstrated concerning cellular toxicity or oncogenicity. One benefit of delivery to the eye is that small, localised doses minimise the exposure of other tissues to the nuclease, and minimal evidence of systemic distribution of these has been produced to date.

1.3.4.2 Immunogenicity

The bacterial origin of CRISPR-Cas components raises concerns for immune or inflammatory reactions in response to transgene expression, especially considering the detection of pre-existing antibodies to SaCas9 and SpCas9 in humans and NHPs.[332] Nevertheless, only minimal to mild inflammation was detected in NHPs following delivery of AAV5-SaCas9 constructs in two different studies, and systemic immunosuppression was not required.[225,263] Interestingly in both studies high pre-existing anti-SaCas9 T-Cells correlated with greater editing efficiency, although the explanation for this finding remains unknown. The relative immune privilege of the subretinal space may be advantageous for limiting the exposure of the immune system to the transgene. For instance, one study delivering Cas9 mRNA in a lentiviral vector noted that injection to the murine footpad induced a robust anti-Cas9 IgG response, but this was not observed following a similar dose delivered subretinally.[217] The use of Cas enzymes derived from bacterial species that humans are not commonly exposed to may reduce the chance of pre-existing immunity and strength of immune response.[332]

1.3.4.3 Disease targets

Selection of appropriate disease targets is an important consideration for gene editing. The record of safety and efficacy of AAV-gene therapy suggests that this remains the foremost approach for the treatment of recessive IRDs caused by genes with small coding sequences and a loss-of-function mechanism. Gene editing is most likely to be useful for disease where there is a need to silence a dominant-negative or gain-of-function allele, or for the precision correction of mutations to restore expression. For the most part, these strategies require a mutation-specific approach. A thorough understanding is therefore required of the

epidemiology of not only the genes that cause IRD, but also the frequency of the different variants within these genes and their pathogenic mechanisms.

1.4 Thesis outline

Inherited retinal diseases are a significant cause of irreversible vision loss and substantially impact the lives of affected patients and their families.[333] While currently few treatments exist for a narrow spectrum of these conditions, huge strides in the genetic understanding of these diseases and advances in genetic therapeutics hold promise for future therapies. One such therapeutic approach is to use recently developed gene editing tools to correct the cause of the disease.

1.4.1 Knowledge gaps

Clear knowledge gaps exist that require further research for the successful translation of gene editing therapeutics.

Firstly, adeno-associated viral vectors are clinically established for gene therapy in the retina and excellent candidates for the delivery of gene editing systems. Ideally, it would be possible to deliver these in a single AAV vector. While several studies have delivered CRISPR constructs to the retina, few of these have involved an all-in-one delivery system including the gRNA and the Cas9, and there has been little published on how these might be optimised. Potential optimisation strategies include development of new Cas orthologues, minimisation and characterisation of vector regulatory elements, and evaluation of the organisation of elements in a vector, to achieve effective gene editing.

Secondly, while IRDs are well-placed as targets for clinical gene editing, choosing a target can be challenging. This is especially the case for mutation specific approaches such as base editing where there is a plethora of potentially targetable mutations. It would seem prudent to develop strategies that would benefit the most patients, for genes for which gene supplementation approaches are unlikely to be successful and data is required to guide this.

Thirdly, one approach to avoid the risk of creating permanent off-target edits in the genome with DNA editors is to target the transcriptome with RNA editors. RNA editors have not been used in inherited retinal disease and little is known about the function of RNA editors in photoreceptors. Cas13-based RNA editors are an emerging therapeutic tool but require further characterisation.

1.4.2 Thesis aims

Based on these knowledge gaps, the following aims were explored, described by chapter:

1. ***To investigate the effect of promoter orientation within an AAV-CRISPR vector***

In an all-in-one vector, the Cas and gRNA expression cassettes are tightly arranged. Hypothesising that the orientation of the promoters may affect editing rates due to a transcriptional interference mechanism, the effect of reversing the U6-gRNA expression cassette relative to a CMV-SaCas9 cassette in an AAV vector targeting retinal genes was investigated.

2. ***To characterise a novel class II Cas nuclease for in vivo editing of photoreceptors***

A new CRISPR orthologue, CasX, has recently been identified and subsequently highly engineered to enhance editing efficiency and specificity. Highly compact, CasX is easily packageable in an AAV vector, however has not yet been tested for activity in retinal cells. To explore the hypothesis that an all-in-one AAV-CasX vector could produce robust editing of mature photoreceptors, AAV-CasX vectors targeting GFP were delivered to transgenic mice expressing GFP selectively in rods. In collaboration with Scribe Therapeutics (Alameda, CA, USA), this aimed to characterise a dose range, editing efficiency and toxicity to lay the groundwork for future studies in a therapeutically relevant model

3. To analyse 'base-editable' pathogenic variants causing IRD

Rapid developments in DNA and RNA base editors have made this technology a promising therapeutic prospect. To guide the development of these strategies, data sets were analysed to determine which are the most common recessive genes that are not suited for gene supplementation and are good candidates for base editing, and what are the most common base-editable mutations that occur within these genes.

4. To develop a CRISPR-based RNA editing approach to correct a common mutation in USH2A

Based on the analysis in aim 3, a common mutation in *USH2A* was identified that was amenable to correction with base editing (c.11864G>A, W3955X). I hypothesised that recently described dCas13-ADAR editing systems might be used to efficiently correct this, and that this may be more suited to an AAV-delivery approach, as long-term expression of the editing system is desired (unlike in DNA editing). In this chapter I develop an RNA editing system targeting mutations in *USH2A* and the mouse orthologue *Us2ha,* and an *in vitro* assay to test this.

5. To develop a novel mouse model of USH2A amenable to base editing and test AAV-delivered RNA editing systems in this model

Limited animal models of IRDs with single base mutation amenable to base editing exist for the testing of base editing therapeutics. Given *USH2A* is a large gene for which base editing is a promising approach, a mouse model bearing a base editable mutation in a homologous location to the human sequence (c. 11840G>A, W3947X) was generated in collaboration with The Mary Lyon Institute (Medical Research Council (MRC) Harwell Institute, UK). Hypothesising that the homozygous mouse would be an *Ush2a*-null, the molecular and functional phenotype of this new model was investigated. Furthermore, a range of strategies to deliver AAV-Cas13 RNA editors to attempt to correct this mutation were undertaken.

2

MATERIALS AND METHODS

Experiments were performed in laboratory conditions using calibrated instruments. Details of nucleotide sequences, software versions, kits, product codes and suppliers for the general methods and all chapter methods are listed in the Appendix. Dilutions are performed in molecular biology grade water (Ambion Nuclease Free Water, Thermo Fisher Scientific, Waltham, MA, USA) unless otherwise stated.

2.1 Molecular Biology

2.1.1 *In Silico* Design and Analysis

Geneious software was used for the design of cloning experiments, primer design and interpretation of sequencing chromatograms. Cloning experiments using NEBuilder HiFi DNA Assembly (New England Biolabs (NEB), Ipswich, MA, USA) were designed with the NEBuilder Assembly Tool.

2.1.2 Polymerase Chain Reaction

Polymerase chain reaction (PCR) was performed using a SimpliAmp themocycler (Thermo Fisher Scientific). Primers were designed according to the general criteria listed in Table 2-1 and commercially synthesised (Sigma-Aldrich, St. Louis, MO, USA; Integrated DNA Technologies (IDT), Coralville, IA, USA).

Property	Criteria
Length	18-25 nucleotides
Melting temperature (T_m)	50-65°C
T_M difference between primer pairs	Maximum 5°C
GC Content	40-60%
GC Clamp	Minimum 1 GC nucleotide within two bases of the 3' end of the primer
5' cloning overhang	Addition of restriction site + six random nucleotides to facilitate cleavage
Predicted hairpin	Nil
Predicted self-dimerisation	Nil

Table 2-1 General criteria for design of PCR primers

PCR was performed with either KOD Hotstart Mastermix (Sigma-Aldrich) or Phusion High Fidelity DNA Polymerase (NEB) according to the manufacturer's instructions. Typical reactions contained a template of either 1-20 ng of plasmid DNA, 100 ng of genomic DNA or 2-3 μL of a reverse transcription reaction. KOD Mastermix reactions were performed with the cycle conditions listed in Table 2-2 using forward and reverse primers at a final concentration of 0.3 μM each. Phusion reactions were performed with cycle conditions listed in Table 2-3 in 20 μL reactions with final concentrations Phusion polymerase (0.4units/reaction), HiFi reaction buffer (1×), dNTPs (200 μM), and forward and reverse primers (0.5 μM).

Where required, gradient PCR was performed by running simultaneous identical reactions at different annealing temperature to determine the optimal annealing temperature for a primer pair and minimise non-specific amplification.

Step	Target Size			
	<500 bp	500-1000 bp	1000-3000 bp	>3000 bp
Polymerase Activation	95°C 2 min	95°C 2 min	95°C 2 min	95°C 2 min
Denature	95°C 20 sec	95°C 20 sec	95°C 20 sec	95°C 20 sec
Annealing	Lowest primer T_M for 10 sec			
Extension	70°C 10 sec/kbp	70°C 15 sec/kbp	70°C 20 sec/kbp	70°C 25 sec/kbp

Table 2-2 General PCR Cycle Conditions for KOD Hotstart Mastermix
General conditions used with KOD Hotstart Mastermix for PCR amplification for cloning and sequencing. In general, a cycle number of 25-35 cycles was used.

Step	Temp	Time	Cycles
Initial Denaturation	98 °C	30 seconds	1
Denaturation	98 °C	10 seconds	25-35
Annealing	Variable	20-30 seconds	
Extension	72 °C	30 seconds/kb	
Final Extension	72 °C	5 minutes	1

Table 2-3 General PCR Cycle conditions Phusion Polymerase
Cycle conditions for Phusion polymerase reactions. Annealing temperature was calculated using the primer sequences input to the NEB Tm Calculator (https://tmcalculator.neb.com/)

2.1.3 Restriction Digestion

Unless otherwise specified, restriction enzymes were obtained from NEB, and restriction digestion performed according to the supplier's instructions. Reactions (volume 20-50μL) containing restriction enzyme at a ratio of 1 unit to 1 μg of substrate DNA and 1× buffer solution were incubated at 37 °C for 30-60 minutes. Single- and no-enzyme reactions were run in parallel as control reactions to confirm enzyme activity. Where required, plasmid backbones were dephosphorylated with calf intestinal alkaline phosphatase (NEB).

2.1.4 Agarose Gel Electrophoresis and Gel Extraction

Agarose gels were created using agarose (Sigma-Aldrich) diluted at 1-2% in Tris/Acetate/EDTA (TAE) buffer (Thermo Fisher Scientific) and 0.5 μg/mL ethidium bromide (Thermo Fisher Scientific). Following electrophoresis, gels were visualised using an ultraviolet (UV) transilluminator (U:Genious, Syngene, Cambridge, UK). DNA was extracted from the excised gel bands using a QIAquick gel extraction kit (Qiagen, Hilden, Germany).

2.1.5 Nucleic acid quantification

Nucleic acid concentrations were determined by spectrophotometry using a NanoDrop spectrophotometer (Thermo Fisher Scientific). The ratio of absorbance at 280 nm/260nm was examined, with a ratio of 1.7 to 1.9 indicating acceptable purity for DNA and ~2.0 for RNA. The ratio of absorbance at 230 nm/260nm assessed for sample contamination, with an acceptable ratio ranging from 2.0-2.2.

Amplicon samples submitted for next generation sequencing (NGS) were also assessed with fluorometric quantification using the QuBit dsDNA HS Assay Kit (Thermo Fisher Scientific).

2.1.6 Plasmid Cloning Techniques

2.1.6.1 Oligonucleotide annealing and phosphorylation

Complementary oligonucleotide pairs were designed to form a double stranded fragment with 5' and 3' ends complementary to the desired restriction site. A 20 μL combined annealing and phosphorylation reaction was created containing a final concentration of the forward and reverse oligonucleotide (1.25 μM), 1 μL T4 polynucleotide kinase (PNK) (Thermo Fisher Scientific), reaction buffer A for T4 PNK (1×) and adenosine triphosphate (ATP, 1mM). Phosphorylation was performed at 37°C for 20 mins, and then oligonucleotides annealed by incubating at 95°C for four minutes before slowly cooling to room temperature over one hour.

2.1.6.2 Ligation of single fragments

Plasmid ligations were performed in a 10 μL reaction with 1 μL of T4 DNA ligase (NEB), 1uL of T4 DNA ligase buffer and 30 ng of plasmid backbone. For ligation of annealed oligonucleotides, 1 μL of a 1:25 dilution of the annealing reaction was added to the ligation mix. For larger single dsDNA fragments, a mass of insert was used that corresponded to a 3:1 to 10:1 molar ratio of the backbone mass, depending on the ligation reaction. Reactions were typically incubated for 2hrs at room temperature, but incubation times varied from 1-48 hours. Control reactions were run to assess for degree of background backbone re-ligation and levels of uncut backbone. Completed reactions were heat inactivated at 65°C for ten minutes.

2.1.6.3 Multi-fragment DNA Assembly

NEBuilder Hifi DNA Assembly (NEB) was used for the assembly of three or more fragments according to the manufacturer's instructions. Assembly reactions of 20 μL were prepared to contain 10 μL of NEBuilder HiFi DNA Assembly Mastermix, 50 ng of vector backbone and inserts at a 2:1 molar ratio of insert:backbone. Samples were incubated at 50°C for 60 minutes and then stored on ice prior to transformation.

2.1.7 Transformation

A range of *E. Coli* cells were used for different cloning applications. 5-Alpha competent cells (NEB) were used for simple plasmids ligated with annealed oligos such. Stable Competent cells (NEB) were used for plasmids assembled with NEBuilder HiFi assembly, XL10-Gold Ultracompetent *E. Coli* Cells (Agilent Technologies, Santa Clara, CA, USA) pretreated with 1 μL of 1.43 M β-mercaptoethanol per 30 μL of cells for ten minutes were used for transformation of plasmids containing AAV inverted terminal repeats.

A general transformation protocol was used for all types. 2-5 μL of ligation products were added to 30-50 μL of cell suspension and incubated for 30 minutes on ice. Cells were heat

shocked at 42°C for 30 seconds, incubated for 2 minutes on ice and then added to 450 μL super optimal broth with catabolite repression (SOC) outgrowth medium (Thermo Fisher Scientific) or Stable Outgrowth Medium (NEB). and placed into an incubator-shaker at 37°C for 225rpm for 60 minutes. 100-200 μL of outgrowth medium was added to Luria Broth (LB)-Agar plates prepared with 100 μg/mL ampicillin (Sigma-Aldrich) and incubated at 37°C overnight.

2.1.8 Colony selection and plasmid amplification

Individual colonies were selected and cultured in 4 mL of LB with ampicillin (100 μg/mL) in an incubator-shaker at 37°C at 225 rpm overnight. Glycerol stocks were created by mixing 500 μL culture broth with 500 μL of 50% glycerol for storage at -80°C. The remaining culture broth was then centrifuged at 5,000 *g* (Megafuge, Thermo Fisher Scientific) to obtain bacterial cell pellets, and plasmids isolated from the lysed cells using a plasmid miniprep kit according to the manufacturers protocol (GenElute Plasmid Miniprep Kit, Sigma-Aldrich; Zyppy Plasmid Miniprep Kit, Zymo Research, Irvine, CA, USA). Plasmid minipreps were screened for correct ligation products using a restriction digest assay, and subsequently confirmed by commercial Sanger sequencing.

For plasmid preparations created for use in mammalian cell culture, endotoxin-free preparations were created as per the manufacturers protocol using a PureLink HiPure Plasmid Midiprep Kit (Thermo Fisher Scientific) or an EndoFree Plasmid Maxi Kit (Qiagen). Starter cultures were created by inoculating LB-ampicillin broth with bacteria from glycerol stocks or from individual colonies and placed in an incubator-shaker for eight hours. Larger overnight culture for midipreps were created by adding 100 μL of starter culture to 50 mL of LB broth, or for maxipreps by adding 500uL of starter culture to 250 mL of LB broth. Cell cultures were pelleted down in 500 mL Nalgene flasks in a Megafuge at 5,000 *g* for 20 minutes at 4 °C

2.1.9 Genomic DNA Extraction

For extraction from cell pellets, pellets were defrosted and resuspended in PBS and proteinase K. DNA extraction was performed with a QIAamp DNA mini kit (Qiagen) following the manufacturer's instructions and eluted in molecular grade water.

2.1.10 RNA Extraction

Before RNA extraction, environmental RNAses were removed from surfaces and instruments with RNaseZAP wipes (Thermo Fisher Scientific). All samples were stored at -80°C and thawed on ice prior to RNA extraction.

For RNA extraction from cells to obtain mRNA, the RNeasy Plus Mini kit (Qiagen) was used. Cells were lysed using the RLT Plus buffer supplemented with 10 µl b-mercaptoethanol per mL and homogenised by vortexing. Lysates were run through supplied DNA eliminator columns. Additional DNA removal was performed by on-column DNAse digestion (Qiagen) according to the manufacturer's protocol. RNA was then isolated in accordance with manufacturer's instructions and yields determined by spectrophotometry.

For samples where short RNA species such as guide RNAs were required to be isolated, or for RNA extraction from neural retinal tissue, the phenol-chloroform based (TRIzol) miRNeasy Mini kit (Qiagen) was used for RNA extraction. In the first step of this process, samples were thawed on ice, combined with TRIzol and homogenised and disrupted with vortexing (cells) or using a handheld homogeniser and pestle (retinal tissue). RNA was then isolated in accordance with manufacturer's instructions and was eluted RNAse-free water.

2.1.11 cDNA Synthesis

RNA was reverse transcribed to complementary DNA (cDNA) using the Superscript III first strand synthesis system (Thermo Fisher Scientific). A. standardised input (500 ng or 1000 ng) of RNA was combined with a nucleoside triphosphate solution, reverse transcription

primers and H_2O and incubated at 65°C for 5 minutes. Superscript III reverse transcription enzyme was added to a mixture of buffer, reducing agent (DTT), magnesium ($MgCl_2$), and RNase inhibitor, and added to the RNA solution. The reaction was incubated at 50°C for 50 minutes before the reaction was terminated. RNase H solution was added to the solution to digest remaining RNA. The cDNA was subsequently purified with a PCR Purification Kit (Qiagen). Negative controls were run in parallel where no reverse transcriptase was added to the reaction.

2.1.12 Reverse Transcription quantitative-PCR

Reverse Transcription quantitative-PCR (RT-qPCR) was used to measure levels of gene expression in cDNA samples. Reactions were all performed in triplicate in opaque 96 well plates (Bio-Rad Laboratories, Hercules, CA, USA) using a real time PCR machine (CFX Connect Optics Module, Bio-Rad Laboratories). Two different qPCR chemistries were used, with cycle conditions listed in Table 2-4.

Dye-based SYBR green (Bio-Rad Laboratories) assays were performed in a total reaction volume of 10 µl containing 1 µl of cDNA template, 1 µl each of 2 µM forward and reverse primers, 2 µl molecular biology grade water, and 5 µl SYBR Green PCR Mastermix (Bio-Rad Laboratories). Melt curve analysis was performed after the cycling protocol, consisting of 60-95 °C with 0.5 °C increments (each held for five seconds) to assess for a single peak indicating a single amplification product.

Probe-based TaqMan chemistry assays were performed using custom or predesigned TaqMan Assays (Thermo Fisher Scientific). A total reaction volume of 20 µL containing 2 µL of cDNA diluted 1 in 10, 10 µL of TaqMan Fast Universal Mastermix and 1 µL of assay solution was used. Reactions were performed using the following settings: 95°C for 20s, then 40 cycles of denaturation for 3 seconds at 95°C and annealing and extension for 30 seconds at 60°C.

All assays and primer pairs were validated prior to use in test plates using five log_{10} dilution series of the linear target DNA to ensure reaction efficiency of 90-105%. No template control samples were included in every plate to assess for contamination during reaction setup. No-reverse-transcription controls were run to assess for carryover genomic DNA contamination.

Measurement of housekeeper genes expressed stably across experimental conditions[334,335] were measured in parallel to allow normalisation and between sample comparison. Gene expression was measured via the Livak method ($2^{-\Delta\Delta CT}$).[336] Threshold cycle (C_T; or quantification cycle, C_q) values were determined using regression mode in CFX Maestro Software (Bio-Rad Laboratories). Statistical comparisons between groups were performed on raw ΔCT data.

Step	SYBR		TaqMan		Cycles
	Temp (°C)	Time (s)	Temp (°C)	Time (s)	
Initial Denaturation	95	180	95	20	1
Denaturation	95	10	95	3	40
Annealing + Extension	60	30	60	30	

Table 2-4 qPCR Cycling Conditions
Cycling conditions used for both SYBR Green and TaqMan Assay based qPCR protocols

2.1.13 Protein Extraction and Quantification

Radio-immunoprecipitation assay (RIPA) buffer (Sigma-Aldrich) (150 mM NaCl, 1.0% IGEPAL CA-630, 0.5% sodium deoxycholate, 0.1% SDS, 50 mM Tris, pH 8.0) was mixed with cOmplete mini protease inhibitor (Sigma-Aldrich) and used to resuspend and lyse the cell pellet or retinal tissue. Cells were disrupted with a handheld rotor, left on ice for 30 minutes and then centrifuged for 10 minutes at 10,000 *g* at 4°C. The supernatant was transferred for a new tube for downstream use.

Lysate total protein was quantified using a colorimetric method with the Pierce Pierce bicinchoninic acid (BCA) protein assay kit (Thermo Fisher Scientific) in accordance with the manufacturer's instructions. Samples were diluted 1 in 10 and incubated with the assay reagents at 37°C for 30mins, before absorbance readings were measured at 562nm with a plate reader

(iMark, Bio-Rad Laboratories). Protein concentration was determined using a standard curve derived from diluted bovine serum albumin (BSA) standards (25-2000μg/mL.).

2.1.14 Western Blot

Protein lysates were prepared to contain an equal mass of protein made up to equal volumes with RIPA buffer, and combined with 5X reducing sample buffer (National Diagnostics, USA) and at room temperature for 15 minutes. Samples were loaded to wells adjacent to 5 μL protein size ladder (BLUeye, GeneFlow) in pre-cast Tris-Glycine gels (Criterion TGX, Bio-Rad Laboratories) submerged in Tris-Glycine Sodium-Dodecyl-Sulfate PAGE(SDS-PAGE) running buffer (National Diagnostics, USA) and subject to electrophoresis.

Low fluorescence polyvinylidene difluoride (PVDF) membranes (Bio-Rad Laboratories) were activated with methanol and prepared in transfer stacks soaked in 1× Transblot Turbo transfer buffer (Bio-Rad Laboratories). Gels were gently opposed to the prepared PVDF membranes and proteins were transferred using the semi-dry Trans-Blot Turbo transfer system (Bio-Rad Laboratories) set to the 'Mixed Weight' (2.5A/25V, 7 minutes) or 'High MW' (2.5A/25V, 10 minutes) programmes. Following protein transfer, PVDF membranes were washed once in Tris-Buffered Saline (TBS) (Bio-Rad Laboratories) and then placed in blocking solution of either Odyssey TBS Blocking Buffer (LI-COR Biosciences, Lincoln, NE, USA) or a dilute (5-10%) skim milk in TBS solution for 1 hour. Membranes were incubated in primary antibody solution for two hours at room temperature or overnight at 4 °C. Following washing in TBS with 0.01% Tween-20 (Sigma-Aldrich) (TBS-T), membranes were incubated in secondary antibody solution containing appropriate fluorescent labelled antibodies (IRDye, LI-COR Biosciences) for 1 hour at room temperature protected from light. Membranes were washed in TBS-T before imaging. All incubation steps were performed with gentle agitation, and washes were performed three times for ten minutes unless specified.

Membranes were imaged using the Odyssey Fc imaging system (LI-COR Biosciences) using 700 nm and 800 nm detection channels with an exposure time of 2 or 10 minutes. Image Studio Lite software (v5.2.5, LI-COR Biosciences) was used for band densitometry for quantification of protein expression. Bands of interest were outlined using a border selection tool. Band signal was calculated as the greyscale pixel intensity of each band following local background subtraction. Local background was calculated using the following settings: median background, all borders, border size = 3. Expression of the protein of interest for each sample was normalised to a stably expressed loading control, and mean expression in the experimental condition calculated as a relative fold change to the mean of control condition.

2.1.15 Sanger Sequencing

Sanger sequencing was performed commercially (Source Bioscience, Nottingham, UK; Genewiz, South Plainfield, NJ, USA; Eurofins Genomics, Ebersberg, Germany) using custom designed sequencing primers.

2.2 Cell Culture

2.2.1 Cell Lines & Maintenance

Cell culture was performed in a designated tissue culture laboratory within class II biological safety cabinets with vertical laminar flow. Regular testing for mycoplasma was not undertaken. Media solutions are described with the final concentrations of any additives in brackets.

Human embryonic kidney 293 cells expressing mutant simian virus-40 (SV40) T antigen (HEK293T) were cultured in complete high glucose (25 mM) Dulbecco's Modified Eagle Medium (DMEM) containing phenol red, L-glutamine (4 mM) and sodium pyruvate (1 mM) supplemented with 10% heat-inactivated fetal bovine serum (HI-FBS) and 1% penicillin-streptomycin (100units/mL-0.1mg/mL). Cells were cultured at 37°C in a 5% CO_2 humidified

incubator in adherent T75 flasks. Cells were passaged every 3-5 days prior to reaching confluency. During subculture, media was removed, the culture washed with warmed PBS and cells dissociated with 1 mL of TrypLE Express dissociation reagent (Thermo Fisher Scientific). Cells were then resuspended in medium and 10% of the solution was seeded into a new T75 flask.

Human embryonic kidney 293 cells that stably express enhanced green fluorescent protein (EGFP) (HEK293-EGFP cells, #SC001, GenTarget Inc, San Diego, CA, USA) under a CMV promoter were cultured in complete high glucose (25 mM) DMEM containing phenol red, L-glutamine (4 mM) and sodium pyruvate (1 mM) supplemented with 10% HI-FBS, 1% penicillin-streptomycin (100units/mL-0.1mg/mL), and 1% non-essential amino acids (1×). HEK293-EGFP cells were maintained as described for HEK293T cells.

2.2.2 *In Vitro* Plasmid transfection

HEK293T or HEK293-EGFP cells approaching confluence in a T75 Flask (Sarstedt, Hildesheim, Germany) were dissociated as described in section 2.2.1, resuspended in 5 mL of DMEM and centrifuged for 5 minutes at 300 *g*, and then resuspended in 10 mL of fresh DMEM. 100 μL of diluted cell suspension was mixed with 100 μL of undiluted 0.4% Trypan Blue Solution to assess for cell viability, and cells were counted with a TC20 automated cell counter (Bio-Rad Laboratories). The cell suspension was diluted to the required concentration in DMEM and seeded into adherent tissue culture plates at seeding densities optimised for each well plate outlined in Table 2-5.

Cells were transfected at 24 hours following seeding when cells had reached approximately 80% confluence. TransIT-LT1 transfection reagent (Mirus Bio, Cambridge, UK) was mixed with OptiMEM reduced serum media (Thermo Fisher Scientific) and endotoxin-free plasmid at a ratio of 3 μL per 1 μg of plasmid DNA. DNA complexes were allowed to form for 20

minutes at room temperature, and the solution added to the plates. Unless otherwise stated, cells were harvested for further analysis at 48 hours post transfection.

Plate	Well size (cm^2)	Seeding Density (cells/well)	
		HEK293T	HEK293-EGFP
6 well	8.87	-	8.0×10^5
12 well	3.65	4.0×10^5	4.0×10^5
24 well	1.82	2.0×10^5	2.0×10^5
96 well*	0.32	4.5×10^4	-

Table 2-5 Cell Seeding Density for Plasmid Transfection
Seeding density (cells per well) in Sarstedt adherent tissue culture plates. *Optimised for Corning White Polystyrene Microplate (Sigma-Aldrich)

2.2.3 *In Vitro* Viral transduction

HEK293T or HEK293-EGFP cells approaching confluence were diluted in DMEM and seeded into 12 or 24 well tissue culture plates (Sarstedt) at a density of 5.5×10^5 cells/well and 2.5×10^5 cells/well respectively. Cells were transduced at 24 hours following seeding when cells had reached approximately 95% confluence. To calculate the viral dose required for a given multiplicity of infection (MOI), cells were counted prior to transduction in a nominated counting well as described in section 2.2.2. AAV diluted to the appropriate concentration and volume in PBS and added dropwise to cells. The plate was gently rocked to mix and then returned to the incubator. For transduction with AAV8 serotypes, cells were pre-treated by addition of doxorubicin (final concentration 400nM) to the cell culture media 4 hours prior to transduction.

2.2.4 Cell Harvesting

For cell harvesting, cells were dissociated and resuspended with ice cold PBS. Cell suspensions were transferred to microcentrifuge tubes, and centrifuged at 300 *g* for 5 minutes. Supernatant was then carefully removed, and the pellet resuspended in ice cold PBS to wash and centrifuged again. PBS was then aspirated and the cells re-suspended in ice cold PBS as a

final wash. The PBS cell resuspension was then split across microcentrifuge tubes as required to enable downstream analysis with different techniques from the same sample. Following a final centrifuge step, PBS was aspirated and cells were snap frozen on dry ice before being transferred to a -80°C freezer.

2.3 AAV Production

2.3.1 Plasmids for AAV production

Recombinant AAV gene transfer vectors were produced by transient transfection of HEK293T cells with plasmids encoding the necessary elements for AAV formation.[337] A transgene plasmid (pTransgene) contained the intended AAV genome flanked by ITRs. Sequences encoding AAV *rep* and *cap* genes and adenovirus helper genes VA, E2A, and E4 genes of adenovirus 5 were provided *in trans* on separate plasmids.

For AAV2 production, a single plasmid encoding both the *rep/cap* and helper genes (pDG plasmid, PlasmidFactory, Bielefield, Germany)[338] was used together with pTransgene in a dual plasmid transfection. For tyrosine mutant AAV8 production, a triple transfection method using pTransgene together with separate plasmids encoding the helper genes (pAdΔF6, a gift from M McClements) and the rep2/cap8-Y733F genes (pAAV2/8-Y733F, a gift from M McClements) was used.

2.3.2 Transfection of HEK293T cells

HEK293T cells were seeded into two CellBIND Surface HYPERflasks (Corning, New York, NY, USA) per vector to be made and incubated at 37 °C 5% CO2 for 72 hours until 80% confluent. Hyperflasks were transfected using the cationic polymer polyethylenimine (PEI) protocol.[337] Each hyperflask was transfected with a total of 500 μg of plasmid DNA, where the mass of each plasmid transfected was calculated to adjust for plasmid size so that each construct was delivered at an equimolar ratio, as shown in Table 2-6.

AAV2			AAV8-Y733F		
Plasmid	**Size (kb)**	**Mass (μg)**	**Plasmid**	**Size(kb)**	**Mass (μg)**
pTransgene	T	T × R	**pTransgene**	T	T × R
pDG	21.9	21.9 × R	**pRep/Cap**	7.3	7.3 × R
			pAdΔF6	15.4	15.4 × R
Total	K	500 μg	**Total**	K	500 μg
Ratio (R) mass/kb	500/K		**Ratio (R) mass/kb**	500/K	

Table 2-6 Calculation table for plasmid transfection for rAAV production
For the production of an rAAV containing a transgene of a given size (T), the mass of each plasmid to transfect was calculated so that the ratio (R) of transgene to helper and rep/cap plasmids was equimolar for a total (K) of 500 μg of plasmid DNA transfected. The ratio R is multiplied by the respective plasmid size to yield the amount of plasmid needed for one transfection.

The plasmids were mixed in solution made up to 10 mL with 150 mM NaCl. Separately, 1.125 mL of 1 mg/mL PEI was mixed with 8.875 mL of 150 mM NaCl. The PEI mixture was added dropwise to the plasmid mixture and incubated for 20 minutes at room temperature to allow polyplex formation. The plasmid-PEI mixture was then added to 500 mL of transfection media prepared with complete high glucose (25 mM) DMEM containing phenol red, L-glutamine (4 mM) and sodium pyruvate (1 mM) supplemented with 2% HI-FBS and 1% penicillin-streptomycin. The hyperflask culture media was then drained, and the transfection media containing the complexed DNA added to fill the hyperflask. Bubbles were carefully removed and the hyperflasks were incubated at 37 °C 5% CO2 for a further 72 hours.

2.3.3 Harvesting and Lysis

To dissociate the cells, 200 mL of media was drained from the hyperflask, and then the hyperflask was shaken vigorously until cells were observed to be resuspended by light microscopy. The cells were then pelleted by centrifugation at 1,200 *g* for 10 minutes at room temperature in 500 mL flasks before the supernatant was aspirated.

For lysis, 15 mL of autoclaved lysis buffer conating 1M tris(hydroxymethyl)aminomethane (VWR, Radnor, PA, USA) with 150 mM NaCl (Sigma-Aldrich) was added to each pellet and

mixed with a serological pipette. A protease inhibitor solution containing 1 tablet of cOmplete mini protease inhibitor (Sigma-Aldrich) in 1 mL of lysis buffer was prepared, and 500 μL added to the cell lysate and mixed.

Each lysate was then subjected to three freeze-thaw cycles. The cell lysate was frozen at -80°C for one hour, before being incubated in a water bath at 37°C for 15 minutes and shaken vigorously halfway through this incubation. This was repeated once more before being stored at -80°C until the AAV isolation step, where the final thaw was performed.

2.3.4 Isolation of AAV particles

Frozen lysate was thawed at 37°C and then unpackaged DNA was digested by incubation with benzonase (final concentration 50 units/mL) (Merck Millipore, Burlington, MA, USA) at 37°C for a further 45 minutes with vigorous shaking every 15 minutes. The lysate was then centrifuged at 3,700 *g* for 20 minutes at room temperature.

AAV was isolated using iodixanol gradients.[339] Each fraction was prepared according to Table 2-7.

Fraction	Iodixanol	5M NaCl	5× PBS-MK	H_2O	Phenol Red
15%	4 mL	3.2 mL	3.2 mL	5.6 mL	-
25%	5 mL	-	2.4 mL	4.6 mL	20 μl
40%	6.7 mL	-	2 mL	1.3 mL	-
60%	10 mL	-	-	-	20 μl

Table 2-7 Preparation of Iodixanol Gradients
Volumes of constituent parts required to prepare two iodixanol gradients. OptiPrep density gradient medium (Sigma-Aldrich); 5× PBS-MK: PBS with 5 mM $MgCl_2$ plus 12.5 mM KCl; H_2O: sterile molecular biology grade water (Sigma-Aldrich); Phenol Red: 0.5% solution (Sigma-Aldrich).

Gradients beginning with 7.2 mL of the 15% fraction, 4.8 mL of the 25% fraction, 4 mL of the 40% fraction, and finally 4 mL of the 60% fraction were successively underlaid into an OptiSeal ultracentrifuge tube (Beckman Coulter, Brea, CA, USA) using long-necked pipettes (Figure 2-1). The supernatant from the centrifuged lysates was then carefully overlaid on the

gradients and then any remaining volume was filled with lysis buffer. Tubes were then sealed with caps and centrifuged at 59,000 rpm in a 70 Ti rotor in a Optima XE-90 ultracentrifuge (Beckman Coulter) for 90 minutes at 20 °C.

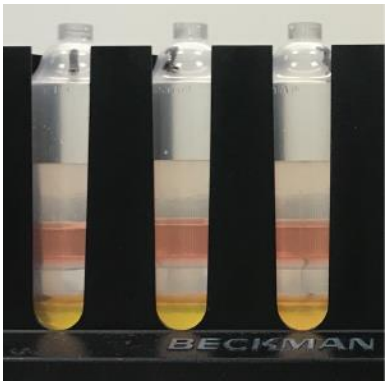


Figure 2-1 Iodixanol gradient formation
Iodixanol gradients layered within OptiSeal tubes. Layers from top to bottom: 15% iodixanol fraction (colourless), 25% iodixanol fraction (pink), 40% iodixanol fraction (colourless), 60% iodixanol fraction (yellow). Lysate is added above the 15% fraction before centrifugation.

AAV particles were isolated by aspirating 1.5-2 mL of the colourless 40% fraction where AAV is concentrated following centrifugation. An 18G needle was attached facing bevel up to a 5 mL syringe and used to pierce each OptiSeal tube at the interface of the 60-40% phase, angling up into the 40% fraction and taking care not to aspirate the proteinaceous material at the 40-25% interface. The collected fraction was stored overnight at 4 °C.

2.3.5 Purification and concentration of AAV

The collected iodixanol fraction was made up to a volume of 15 mL with sterile PBS and the solution mixed well by pipetting. The total volume was then transferred into a pre-wet Amicon Ultra 100K filter (Merck Millipore) centrifuged at 3000 xg at 20 °C to concentrate the volume to less than 500 µL over 60-90 minutes. The flow through was discarded. The filter was washed three times by adding 15 mL of PBS and then centrifuging until concentrated to <500 µL. On the final wash step, volume was concentrated to <250 µL. and then divided into 10 µL

aliquots for storage at -80 °C. Finally, a 'wash' suspension was created by adding 500 μL of PBS to rinse the empty filter and collect any remaining AAV particles.

2.3.6 AAV Capsid Analysis with SDS-PAGE

SDS-PAGE analysis of AAV preparations was undertaken to evaluate for capsid yield and purity.[340] Samples of pure AAV (10 μL) and AAV wash (24 μL) were denatured by adding 5× reducing sample buffer (National Diagnostics, USA) and heating to 95°C for 10 minutes. Samples were loaded adjacent to 5 μL of protein size ladder (BLUeye, GeneFlow, UK) in pre-cast Criterion TGX gels submerged in Tris-Glycine SDS-PAGE running buffer (National Diagnostics, USA). Following electrophoresis, gels were washed three times for five minutes in distilled water under agitation. To stain for protein, gels were submerged in EZBlue Gel Staining Reagent (Sigma-Aldrich) for 90 minutes with gentle agitation. Gels were then further washed three times, and then imaged using the Odyssey Fc imaging system.

2.3.7 AAV Titration

The concentration of DNase-resistant viral genomes in each purified rAAV preparation was determined using qPCR.[341] A total volume of 10 μL was prepared containing 1 μL of concentrated or wash AAV sample, 1 μL of DNase I (NEB), 1 μL of DNase 10× buffer, and 7 μL of molecular biology grade water. Samples were incubated at 37 °C for 30 minutes and subsequently denatured and heat-inactivated at 95°C for 10 minutes.

qPCR was performed as described in section 2.1.12 using transgene specific primers. The DNase digested AAV samples were diluted 1:10 and 1:100. A five-fold $\log_{10}$ dilution series of linearised plasmid containing the transgene used to generate the vector was created to generate a standard curve. Viral genome copy number was determined by interpolation from the standard curve.

The qPCR titre reports the number of genome copies present in each sample but does not quantify the number of viral particles present to allow calculation of the ratio of full to empty capsids. Examination of the viral preparations with scanning electron microscopy (SEM) can be used to identify empty capsids within a sample and is used when preparing vectors in good manufacturing standard protocols for clinical trials, however the use of SEM was beyond the scope of this work.

2.3.8 Endotoxin Testing

AAV preparations were tested for levels of bacterial endotoxin using the Pierce *Limulus* Amebocyte Lysate (LAL) Chromogenic Endotoxin Quantitiation Kit (Thermo Fisher Scientific) according to the manufacturer's instructions using a 1 in 10 dilution of pure AAV preparation.

2.4 *In Vivo* Procedures

All animal work was performed in accordance with the Animals (Scientific Procedures) Act 1986, UK, with the Association for Research in Vision & Ophthalmology (ARVO) statements on the care and use of animals in ophthalmic research, and with the University of Oxford policy on the use of animals in scientific research. Animal procedures were conducted under UK Home Office Personal License ID0CCFCED and Project Licenses 30/3363 (Expiry Dec 2020) and PP3038118 (Expiry Dec 2025). Mice were housed in individually ventilated cages at the Biomedical Sciences Division, University of Oxford with a 12-hour light/dark cycle and food and water available *ad libitum*.

2.4.1 Anaesthesia and Mydriatics

Mice were anesthetised by intraperitoneal injection of a cocktail of ketamine (Narketan, Vetoquinol, Magny-Vernois, France, final concentration 8mg/mL) and xylazine (Rompun, Bayer, Leverkusen, Germany, final concentration 1mg/mL) in 0.9% normal saline at a dose of

0.1mL/10g bodyweight. Anaesthesia was reversed with intraperitoneal injection of atipamezole (Antisedan, Zoetis, NJ, USA, final concentration 0.2mg/mL) in 0.9% normal saline at a dose of 0.1mL/10g bodyweight. During recovery, mice were placed in a temperature-controlled chamber set to 35°C and Viscotears Liquid Gel was applied to prevent corneal desiccation until the blink reflex was re-established. Pupils were dilated using tropicamide 1% and phenylephrine hydrochloride 2.5% topical eye drops applied sequentially (Bausch + Lomb, Laval, Canada).

2.4.2 Subretinal Injections

Mice were anaesthetised, pupils dilated and topical proxymetacaine (Bausch + Lomb) was applied for corneal anaesthesia. Mice were positioned on a foam mat to stabilise the head and a Leica operating microscope (Leica Biosystems, Wetzlar, Germany) was used for appropriate visualisation (Figure 2-2A-B).

A paracentesis was performed with a 33G needle (TSK laboratory, Netherlands) in the mid-peripheral cornea to lower the intraocular pressure to minimise trans-scleral reflux of the subretinal injection. The small gauge of the needle allows the incision to self-seal, preventing further aqueous leak and allows the intraocular pressure to stabilise following surgery.

The eye was covered with Viscotears Liquid Gel (0.2 mg/g polyacrylic acid) and a 6 mm round cover slip was placed on the eye for direct view of the fundus. Injections were performed with a 35G bevelled NanoFil needle mounted on a Nanofil 10 µl syringe (both World Precision Instruments, Sarasota, FL, USA). Gripping the superior rectus muscle with notched forceps to stabilise the eye, the needle was carefully introduced through the sclera adjacent to the superior rectus and into the subretinal space under direct visualisation until the needle bevel was visible beneath the retina. Successful subretinal injection could be visualised by the creation of a bullous superior hemi-retinal detachment (Figure 2-2C). The needle was then carefully withdrawn, the glass cover slip removed, and 0.5% chloramphenicol topical drops were applied.

Any complications such as haemorrhage extraocular reflux of injected substance, or inadvertent retinotomy were recorded at the time of surgery and excluded from analysis.

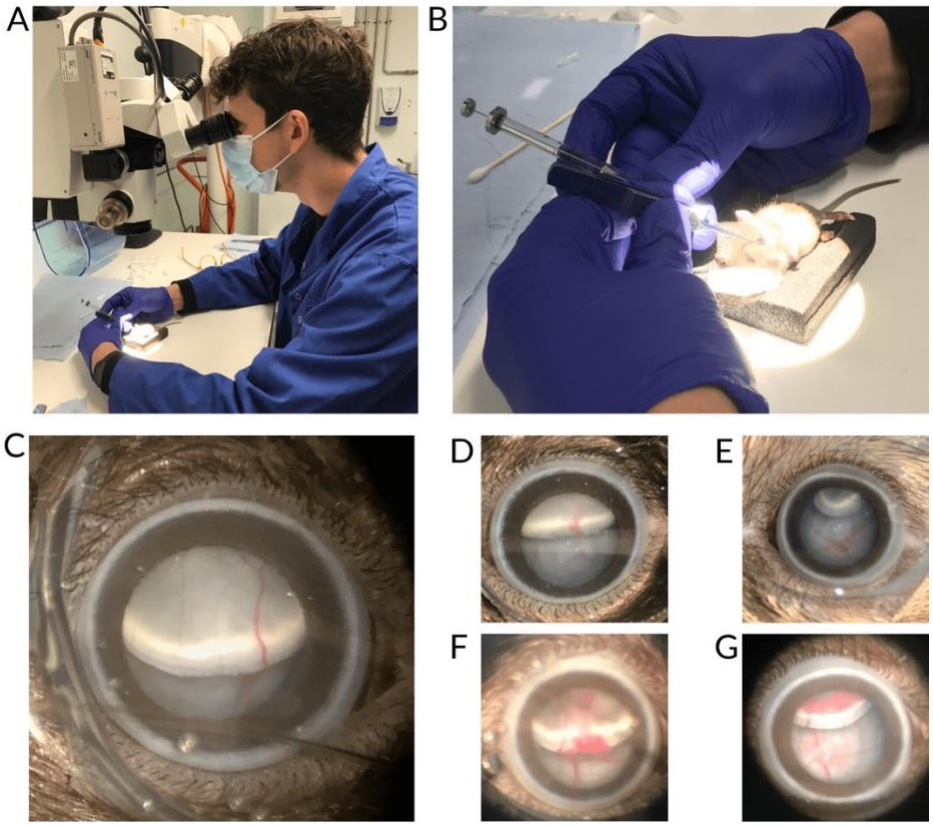


Figure 2-2 Operative images of subretinal injection
A-B. Set up and positioning for subretinal injection. **C.** View down the operating microscope following successful subretinal injection with creation of a superior large hemi-retinal bleb that extends below the horizontal meridian without complications achieved for most injections. Note the optic nerve head is not seen. **D.** Hemi-retinal bleb with small epiretinal bleed. Similar small and limited epiretinal bleeds from a single vessel were not excluded. **E.** Uncomplicated, but small subretinal bleb with optic nerve head still visible, indicating less than total hemi-retinal detachment. Excluded due to likely suboptimal delivery of full vector dose. **F.** Significant epiretinal/intravitreal bleed – excluded. **G**. Subretinal bleed – excluded.

2.4.3 Retinal imaging

Retinal imaging was performed using a Spectralis (Heidelberg Engineering, Heidelberg, Germany) device fitted with a 55° lens. Mice were anaesthetised and pupils dilated. Coupling fluid (Hypromellose 0.3%; Blumont Healthcare Ltd., Grantham, UK) was applied to the cornea, and then a custom made contact lens (polymethyl methacrolate mouse lens, back optic

zone radius of 1.7 mm, total diameter of 3.2 mm, centre thickness of 0.4 mm, straight sides; Cantor and Nissel, Brackley, UK)[342] was applied and carefully positioned in the centre of the cornea. Mice were placed on a platform mounted on the chin rest of the Spectralis so that its eyes were positioned at the height marking for a human patients' eye position (Figure 2-3).

2.4.3.1 Confocal Laser Scanning Ophthalmoscopy

Confocal laser scanning ophthalmoscopy (cSLO) generates high resolution *en face* retinal images using a narrow wave-length laser swept across the retina to excite fluorescent signal at each point scanned.[343] Passage of light through a confocal pinhole eliminates out-of-plane and scattered light to enable optical sectioning.[343] CSLO images were recorded with a standard technique[342] in 'High Resolution' mode (8 bits/pixel and 1536 × 1536 pixel resolution) with automatic real-time (ART) averaging set to 20 images with normalisation turned off. ART mode creates an average of sequential image frames to create a higher resolution composite image to compensate for movement artefact from respiration.

Careful image alignment was required for optimal imaging. In near infrared reflectance (NIR) mode, the optic disc was centred in the image. The dioptric focus was used to locate the plane of highest paracentral NIR reflectivity with the greatest number of saturated pixels when using a detector sensitivity with slight overexposure. As the highest bands of reflectivity on optical coherence tomography (OCT) approximate the RPE and use a similar excitation wavelength, this plane likely represents the outer retina.[342] Uniform illumination of the posterior pole was achieved by ensuring balanced exposure in the superior, temporal, nasal, and temporal quadrants. Images were acquired in NIR, infrared autofluorescence and blue autofluorescence (BAF) modes without barrier filters. For acquisition of images for *in vivo* EGFP quantification, BAF mode was used with a 488nm laser and a 500-700nm bandpass filter to eliminate autofluorescence outside the EGFP emission spectrum.[344] Images were collected at sensitivities in descending steps from 100 to 50%.

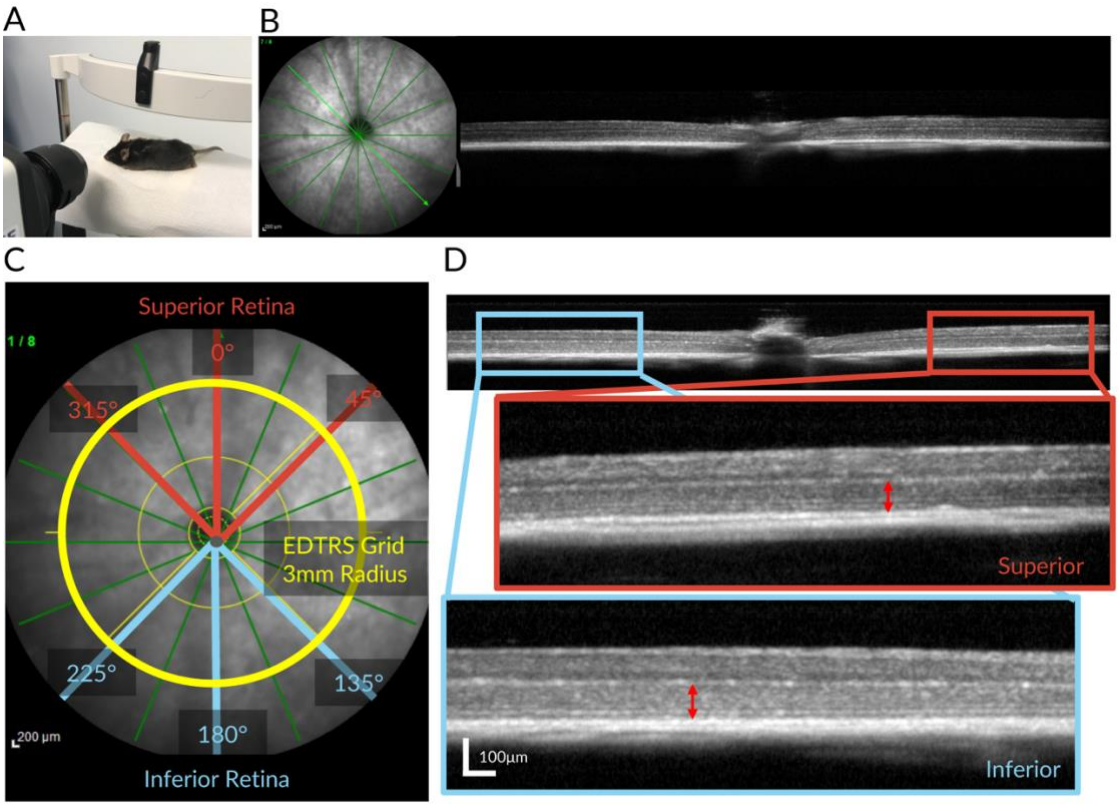


Figure 2-3 Retinal imaging of animals with cSLO and OCT
A. The mouse is positioned on the platform on the Heidelberg Spectralis with the head perpendicular to the camera and at the level of the notch indicating positioning eye. **B.** *En face* infrared cSLO image demonstrating the location of eight radial scans centred on the optic nerve with representative example of an OCT from a wildtype mouse demonstrating the cross-sectional image of the retina. **C.** For retinal thickness measurements, an Early Treatment of Diabetic Retinopathy (EDTRS) grid was overlaid on the *en face* image, and all thickness measurements performed at a 3 mm radius from the optic disc. **D.** The mean superior photoreceptor layer thickness was calculated from the superior line scans at 315°, 0° and 45°. The mean inferior photoreceptor layer thickness was calculated from the inferior line scans at 135°, 180° and 225°. The photoreceptor layer thickness (red arrows) was measured between the hyper-reflective outer plexiform and RPE bands.

2.4.3.2 Optical Coherence Tomography

Spectral domain optical coherence tomography (SD-OCT) images were captured with the Spectralis OCT module using a superluminescence diode laser (weighted average wavelength of 870 nm) to produce a cross-sectional B scan of the retina. SD-OCT images. SD-OCT images were captured with the 55° lens following cSLO imaging with the animal in the same position with the contact lens in place. To adjust for the axial length of the mouse eye, the reference arm

of the OCT was manually adjusted in the software.[345] The positioning of the camera was adjusted to ensure a flat section oriented horizontally in the image. A standard OCT protocol was used to capture eight line scans oriented radially extending from the optic nerve head (Figure 2-3). Images were captured using ART averaging of 25 images. Photoreceptor layer (PRL) thickness was measured at a fixed 3000 μm distance from the optic disc defined by an overlaid Early Treatment of Diabetic Retinopathy Treatment Study (EDTRS) grid centred on the optic disc in the HEYEX software. PRL thickness was measured using software callipers between the inferior aspect of the hyper-reflective outer plexiform band to the superior aspect of the hyper-reflective RPE band.

2.4.4 Electroretinography

Active contact lens electrodes were created by attaching silver-coated nylon thread Dawson, Trick & Litzkow (DTL) Plus electrodes (Diagnosys Ltd., Cambridge, UK) to custom contact lenses created from achromatic Aclar (Honeywell International, USA) as described by Sagdullaev et al.[346] Mice were dark-adapted overnight for a minimum of 12 hours in a light-proof cabinet. Procedures were performed in a light-proof dark room with dim-red illumination. Mice were anaesthetised and eyes dilated as described in section 2.4.1. Ground and reference electrodes were placed subcutaneously oriented cranially in the midline, in the flank at the tail base and between the eyes respectively. Topical hypromellose 1% (Alcon, Geneva, Switzerland) coupling solution was applied bilaterally and an active contact lens electrode placed centrally on each cornea. Active electrode impedence was maintained between 5-10kΩ. Animals were positioned on a heated platform set to 35 °C inside a light-tight Faraday cage dark containing a Ganzfield stimulator dome (Colordome Electroretinography Machine, Diagnosys) and monitored via a video feed. Following a brief acclimatisation period, a custom stimulus protocol controlled by Espion v6 software (Diagnosys) was commenced (Table 2-8). Electroretinogram (ERG) a- and b-wave amplitudes were measured manually using Espion v6

software as demonstrated in Figure 2-4.[347]. The a-wave was defined as the first negative deflection and is mainly reflective of the physiological response of photoreceptors. The b-wave was defined as the peak of the subsequent larger positive deflection, reflecting the response of the more inner retina, predominantly bipolar and Müller cells. Flicker stimuli amplitudes were measured from the peak to the trough at approximately 200ms post-stimuli onset. For all recordings, a 0-500Hz bandpass filter was used with line filtering, an amplifier gain of 8, a 4000Hz sampling frequency and 600ms sweep length.

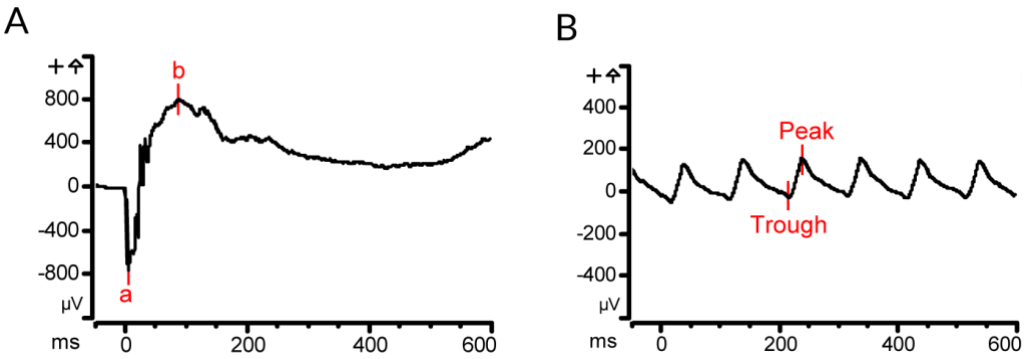


Figure 2-4 Measurement of ERG responses
A. Analysis of ERG waveform recorded in response to a 25 cd.s/m^2 0.5Hz flash in a dark-adapted mouse. The a- and b-waves are manually annotated, with the a-wave amplitude calculated from the pre-stimulus baseline to the first negative trough. The b-wave amplitude is calculated as the difference between the trough to the major positive peak. **B.** Analysis of the ERG waveform in response to a 3 cd.s/m^2 10Hz continuous flicker stimuli. Flicker amplitude was defined from the trough to the peak of a single waveform recorded at approximately 200ms into the sweep recording.

Step	Description	Photopic Log cd.s/m²	Background (cd/m²)	Sweeps (n)	Intersweep Delay (ms)	Pulse Frequency (Hz)	Pre-step Adaption Time (s)
1	Single 0.5Hz 1×10^{-6} cd.s/m²	1e-6	0	16	2000	0.5	0
2	Single 0.5Hz 1×10^{-5} cd.s/m²	1e-5	0	16	2000	0.5	5
3	Single 0.5Hz 1×10^{-4} cd.s/m²	1e-4	0	9	5000	0.5	10
4	Single 0.5Hz 1×10^{-3} cd.s/m²	1e-3	0	9	5000	0.5	30
5	Single 0.5Hz 1×10^{-2} cd.s/m²	1e-2	0	9	5000	0.5	30
6	Single 0.5Hz 1×10^{-1} cd.s/m²	1e-1	0	4	20000	0.5	30
7	Single 0.5Hz 1.0 cd.s/m²	0	0	4	20000	0.5	45
8	Single 0.5Hz 1×10^{1} cd.s/m²	1	0	2	40000	0.5	90
9	Single 0.5Hz 25 cd.s/m²	1.4	0	1	0	0.5	180
10	Continuous 10Hz 3.0 cd.s/m²	0.5	0	20	0	10	60
11	Continuous 20Hz 3.0 cd.s/m²	0.5	0	20	0	20	10
12	Continuous 30Hz 3.0 cd.s/m²	0.5	0	20	0	30	10
	Light adaption						600
13	Single 0.5Hz 1.0 cd.s/m²	0.5	30	10	1000	0.5	5
14	Continuous 20hz 3.0 cd.s/m²	0.5	30	20	0	20	5
15	Single 0.5Hz 10 cd.s/m²	1	30	5	1000	0.5	5

Table 2-8 ERG recording protocol

Standard ERG recording protocol used for the assessment of photopic and scotopic retinal function of mice, programmed with Espion software (Diagnosys).

2.5 Cell and Tissue Analysis

2.5.1 Retinal Tissue Collection

Eyes were enucleated shortly after confirmation of death and transferred to cold sterile PBS and visualised under a dissecting microscope. After removal of connective tissue and musculature, the cornea was punctured with a 23G needle and then excised with Vannas scissors peripherally just anterior to the limbus. The iris and zonules were bluntly dissected and then the lens gently extracted with forceps to avoid retinal traction.

For immunohistochemistry the resulting eye cup was fixed in cold 4% paraformaldehyde (PFA) on ice for 30 minutes and then washed briefly in PBS. The eyecup was cryoprotected using a sucrose gradient, incubating in 10% and 20% sucrose solutions for at least 60 minutes or until the eyecup has sunk to the bottom of the solution. The eyecup was finally incubated overnight in 30% sucrose at 4°C. Eyecups were embedded in optimal cutting temperature (OCT) compound in foil moulds with the optic nerve oriented up. Specimens were frozen in cooled isopentane on dry ice and stored at -80 °C until sectioning.

For extraction of the neural retina, the optic nerve was trimmed at the base and then the sclera removed with a combination of blunt and sharp dissection to leave the intact neural retina. Retinas were snap frozen on dry ice and stored at -80 °C until further processing.

2.5.2 Immunohistochemistry

Frozen sections 16-18 μm thickness were cut on a cryostat (Leica Biosystems) pre-chilled to -20°C, mounted onto Superfrost Plus slides (VWR) and allowed to dry at room temperature overnight. A hydrophobic barrier pen was used to create an encircling border around the sections. Slides were stored at -20°C and thawed at room temperature for subsequent use.

For immunohistochemistry, slides were washed with a standard wash step by immersion in 0.01M PBS three times for five minutes per wash. Sections were blocked and permeabilised

in 400 μL 0.01M PBS with 5-10% serum (Normal Goat Serum, NGS; or Normal Donkey Serum, NDS), 1% bovine serum albumin (BSA) and 0.2% Triton X for 20 minutes at room temperature followed by a wash step. Primary antibody diluted in 250 μL 0.01M PBS with 1% serum, 1% BSA and 0.1% Triton X-100 was then added to the main section of slides. A smaller secondary-only control area of each slide was covered in diluent only. Slides were incubated overnight at 4 °C and then washed. Secondary antibody diluted in 250 μL 0.01M PBS with 1% serum, 1% BSA and 0.1% Triton X-100 was then added. Slides were incubated in the dark at room temperature for two hours and then washed. Sections were stained with 250 μL Hoechst 33342 diluted 1:1000 in 0.01M PBS for 15 minutes at room temperature and then washed. Slides were mounted in ProLong Dimaond Antifade mounting medium (Thermo Fisher Scientific), left to cure overnight and then were stored at 4°C until imaging. Primary antibodies used are indicated in the relevant chapter. Secondary antibodies used were AlexaFluor antibodies (Thermo Fisher Scientific) raised in the appropriate species for the blocking agent (goat or donkey) against the appropriate species for the primary antibody (see Appendix).

2.5.3 Immunocytochemistry

For cell culture, 13 mm No.1 circular coverslips were UV-sterilised and then incubated in poly-D-lysine (0.5μg/mL in PBS) at room temperature for 30 minutes. Treated coverslips were briefly washed then allowed to air-dry for two hours. HEK293T cells were cultured on treated coverslips in 24 well plates. This allowed culture, transfection and staining of the cells in the same well. For immunocytochemistry, media was removed, and cells were washed gently with a standard wash step with 200 μL of 0.01M PBS for 5 minutes. The cell monolayer was then fixed with 200 μL of ice cold 4% PFA in 0.01M PBS at room temperature for 15 minutes before being washed twice. Cells were permeabilised by incubation in 200 μl 0.2% Triton X-100 in 0.01M PBS for ten minutes and then washed once. Cells were then blocked in 200 μl 10% serum (donkey or goat), 10% BSA and 0.1% Triton X-100 in 0.01M PBS for 1 hr at room

temperature and then washed once. Primary antibody diluted in 100 μL in 0.01M PBS with antibody solution of 1% serum, 1% BSA and 0.1% Triton X-100 was applied for two hours at room temperature and then washed three times. Secondary antibody diluted in 100 μL of antibody solution, applied for 1 hour at room temperature and then washed three times. Cells were stained with Hoechst 33342 diluted 1:1000 in 0.01M PBS for 10 minutes at room temperature and then washed. Coverslips were then removed from the wells and mounted onto slides in ProLong Diamond Antifade mounting medium. Slides were left to cure overnight and then were stored at 4°C until imaging.

2.5.4 Microscopy

2.5.4.1 Confocal Microscopy

Confocal microscopy was performed using a LSM-710 inverted confocal microscope using Zen software (Zeiss, Oberkochen, Germany). Areas of interest were imaged on oil-immersion objectives (40×, 63×). Image exposure was optimised with adjustments to laser power, gain and offset. Images were acquired with an XY resolution of 1024 × 1024 pixels. Z-stack images were acquired at the optimal thickness determined by the software for the objective and laser configuration. For comparison between experimental samples, identical settings were saved and re-used. For analysis image files were exported from the Zen software in *.lsm* file format and opened in FIJI ImageJ (National Institutes of Health, USA). Z-stack images were merged as maximum intensity projections.

2.5.4.2 EVOS LED Microscopy

The EVOS FL Auto 2 Cell Imaging systems (Thermo Fisher Scientific) is a fixed wavelength light emitting diode (LED) based imaging system with a motorised stage that allows for fast automated imaging with stitching of adjacent images to visualise large areas of a well plate and entire retinal sections. Incident light was reduced using a neutral density filter cover provided with the microscope. LED light intensity and gain were adjusted to avoid saturation

of images. For quantitative analysis of fluorescent protein expression between samples, the light intensity and gain for each channel was kept constant across experiments.

2.6 Statistical Analysis

Statistical analysis was performed using Prism (v9.2.0, GraphPad, San Diego CA, USA), or with the Base R programming language (v4.0.0) where indicated using the RStudio (v1.2.5024, Boston, MA, USA) graphical interface. Data is presented as mean ± SEM unless otherwise stated. Statistical tests are described associated with each data, and in more detail for specific methods such as off-target discovery. Broadly, data was assessed for normality by frequency distributions, QQ plots and the Shapiro-Wilk test when data set size was large enough. Direct comparisons were performed with unpaired or paired t-tests for unpaired and paired data respectively, or a Mann-Whitney test for non-parametric data. For three or more independent groups, a one-way ANOVA or Kruskal-Wallis test was used for parametric or non-parametric data respectively, with *post hoc* testing for multiple comparisons. To examine for the effects of multiple factors within two groups, two-way analysis of variance (ANOVA) tests were used. *Post hoc* tests to adjust for multiple comparisons were performed in the case of a significant main effect. *Post hoc* testing is described for each data analysed. Unless otherwise stated, a p value of less than 0.05 was considered significant.

3

PROMOTER ORIENTATION WITHIN AN AAV-CRISPR VECTOR AFFECTS CAS9 EXPRESSION AND GENE EDITING EFFICIENCY

3.1 Introduction

CRISPR-mediated gene editing requires the expression of both the Cas nuclease and the gRNA in the target cell. AAV vector delivery of CRISPR-Cas9 is a promising approach for gene editing of somatic tissues *in vivo*, including to the retina.[225] Lessons from clinical gene therapy development have demonstrated that maximising the potency of a vector is important to achieve sufficient transgene expression for a therapeutic effect and to minimise the dose of AAV vector required in order to reduce toxicity or immunogenicity.[348] For these reasons, an all-in-one vector design is preferred for clinical translation whereby both the Cas9 and gRNA components are packaged together with their respective promoters within the limited capacity of a single AAV (~4.7 kb).[349] Although dual-vector strategies have been explored in the retina, all-in-one vectors avoid concerns of dual-vector approaches such as low co-transduction efficiency of both vectors to a single cell and the need for a higher total dose of viral genomes to express both transgenes.[79,350]

Data and figures from this chapter has been published as: Fry LE, Peddle CF, Stevanovic M, et al. Promoter Orientation within an AAV-CRISPR Vector Affects Cas9 Expression and Gene Editing Efficiency. CRISPR J. 2020;3:276–83. DOI: 10.1089/crispr.2020.0021.

The development of Cas orthologues[198–200, 207,351] with shorter coding sequences have enabled the generation of all-in-one CRISPR vectors. The *Staphylococcus aureus*-derived SaCas9 (3.2kb) is the most well characterised orthologue used for AAV delivery,[198, 225, 262,352–357] and is used in the first and only currently registered clinical trial to investigate the use AAV-CRISPR gene therapy is currently underway in patients with Leber's Congenital Amaurosis Type 10 (ClinicalTrials.gov NCT03872479)[224].

An unexplored area of transgene design in the generation of all-in-one vectors is how to arrange the Cas9 and gRNA expression cassettes with respect to each other within the vector genome. There is evidence that the arrangement of expression cassettes within a bi-cistronic construct can affect expression of one or both of the transgenes.[358–362] Authors have noted that alterations to the position of the U6-gRNA transcriptional unit within a vector can affect the efficiency of gene editing,[198, 254,353] however there is little data to quantify the magnitude of this effect. Furthermore, as AAV generation is both time and resource intensive, transgenes are often tested and optimised in plasmid transfection experiments prior to creating AAV vectors with the best candidates. There is no published data that explores whether transcription from the expression cassettes in the vector may be affected by the method of transgene delivery, and whether findings from optimisation of transgenes in plasmids translates when this transgene is packaged within AAV.

I hypothesised that transcription of either the Cas9 or gRNA expression cassettes may be affected by their respective orientations. This in turn could affect the potency of transgene expression and gene editing efficiency.

3.1.1 Chapter Aims

This chapter sought to investigate two simple questions to inform vector design.

1. Does the orientation of the gRNA transcriptional unit relative to the Cas9 transcriptional unit affect transcription of the Cas9 or gRNA, or editing rates of the vector?
2. Are there differences in the effect of gRNA orientation between transgenes delivered to cells *in vitro* via plasmid transfection and AAV transduction?

The results of this chapter address these questions in two parts. Firstly, an exploratory pilot study is described, from where the first question arose while attempting to optimise editing rates to target the fluorescent protein EGFP. Secondly, a more thorough study was undertaken to answer these questions targeting genes involved in the pathogenesis of the eye diseases age-related macular degeneration (Vascular Endothelial Growth Factor, *VEGF*) and retinitis pigmentosa (Rhodopsin, *RHO*).

3.2 Methods

3.2.1 Plasmid Cloning

The pX601-AAV-CMV-SaCas9-U6-sgRNA plasmid was a gift from Feng Zhang (plasmid #61591, Addgene, Watertown, MA, USA).[198] The reverse-oriented U6-gRNA plasmid was generated by PCR amplification and subcloning with NotI and KpnI (primer sequences listed in Appendix A) of the U6-gRNA complex. gRNAs were subcloned with BsaI (NEB). gRNAs targeted vascular endothelial growth factor (*VEGF*)[363] and Rhodopsin (*RHO*) (gRNA sequences listed in Appendix A).

3.2.2 Cell Culture

All transfection and transduction experiments were performed in HEK293-EGFP cells maintained as described in the general methods. For experiments targeting EGFP, cells were

seeded in 6-well plates and transfected with 1μg of plasmid. For experiments targeting *RHO* and *VEGF*, cells were seeded in 24-well plates and transfected with 500 ng of plasmid. Cells were harvested 48 hours post-transfection. For AAV transduction experiments, cells were seeded in 12-well plates, transduced at 24 hours post-seeding when approaching confluency at a multiplicity of infection (MOI) of 300 viral genomes/cell, and harvested at 72 hours post-transduction. Harvested cells were divided, and frozen in aliquots to allow for analysis of DNA, RNA and protein on the same sample. A ubiquitous dsRed plasmid (gift from Dr Michelle McClements) was used as a positive control for transfection experiments.

3.2.3 Analysis of editing efficiency

Locus PCR of the relevant target was performed with a high-fidelity polymerase (KOD Hotstart Mastermix, Merck-Millipore, USA) to generate ~700 bp amplicons (primer sequences listed in Appendix A) from genomic DNA. Products were analysed on an agarose gel to confirm a single clean band, and subjected to Sanger sequencing. DNA editing efficiency was calculated by uploading chromatograms (.abi files) to the Tracking of Indels by Decomposition (TIDE)[364] online software (Figure 3-1), shown to give comparable results to next generation sequencing for on-target editing.[364] Chromatograms from non-transfected cells were used as a control. Decomposition windows and left boundaries were optimized to obtain the highest alignment possible. Indel sizes were kept constant at 10. The significance cutoff was maintained at $p<0.001$.

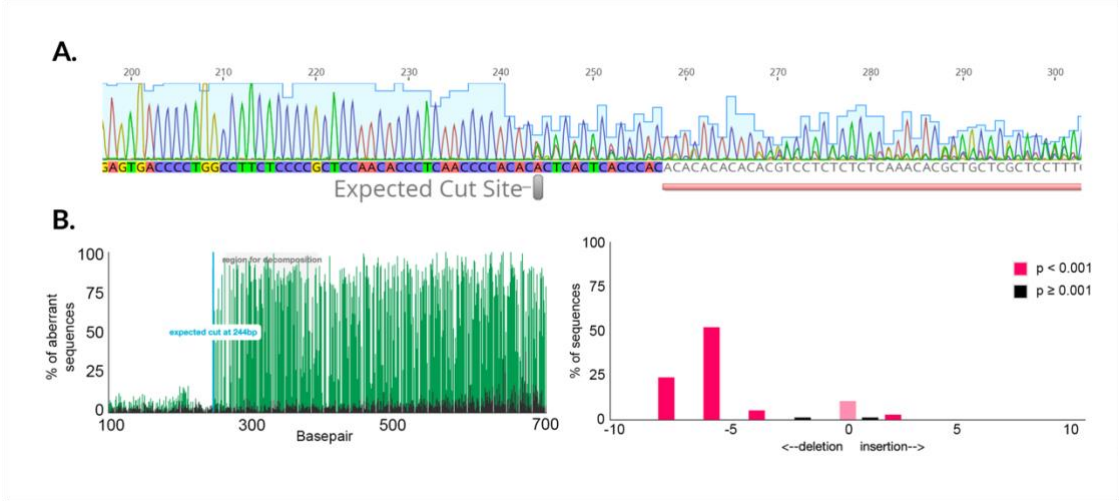


Figure 3-1 Example output of TIDE Analysis
A. An example of a Sanger sequencing chromatogram of an amplicon from an edited cell line. Non-homologous end joining repair of the dsDNA break occurs after the expected cut site, resulting imperfect repair and indels at the target loci. These heterologous repair outcomes are seen as a mixed chromatogram trace after the expected cut site. **B.** Output from the TIDE software characterising the spectrum an frequency of indels following trace decomposition, which also estimates on-target editing efficiency.

3.2.4 RNA analysis

RNA extraction, reverse transcription and qPCR were performed as described in the general methods. RNA was extracted using the miRNAeasy mini kit (Qiagen) to ensure capture of the small gRNA fragments. Each reverse transcription reaction used 1µg of RNA primed with oligo dT primers and with gene specific primers to the direct repeat region of the SaCas9-gRNA. Gene expression levels were determined with qPCR using TaqMan assays (Thermo Fisher Scientific) targeting *EGFP, SaCas9* and *SaCas9-gRNA* normalised to the expression of the *GAPDH* and *ACTB*. The *SaCas9-gRNA* assay primers targeted the direct repeat region, common to all gRNAs. For these reactions, betaine 1× (Sigma-Aldrich) was added to the amplification reaction to reduce secondary structure formation of the target.

3.2.5 Protein Analysis

3.2.5.1 Western blot

Protein extraction, quantification and western blotting were performed as described in the general methods. Protein samples (50μg) were run in 10% Tris-Glycine extended gels (Criterion TGX Precast Gel, Bio-Rad Laboratories) and transferred to a polyvinylidene difluoride membrane using a TransBlotTurbo (Bio-Rad Laboratories). Membranes were blocked in Odyssey blocking buffer in PBS (LI-COR Biosciences) for one hour, incubated in primary antibody solution with rabbit anti-SaCas9 (1:10,000, ab203933, Abcam, Cambridge, UK) and mouse anti-alpha-Tubulin (1:5000, ab7291, Abcam) for two hours, and incubated in IRDye fluorescent secondary antibody solution (Donkey anti-rabbit 800W, donkey anti-mouse 680RD, both 1:10,000, LI-COR Biosciences) for one hour. Semi-quantitative analysis of SaCas9 expression levels were assessed using band densitometry normalized to Alpha-tubulin levels and presented as relative to expression from the forward-oriented U6.gRNA constructs.

3.2.5.2 Protein fluorescence assay

Cell pellets were lysed with sonication for 10s at 20% power in radio-immunoprecipitation assay buffer modified for fluorescence measurement (FIPA buffer) (Table 3-1) mixed with protease inhibitor. Following centrifugation at 4°C for 10mins at 10,000g, the supernatant was transferred to a new tube and protein quantified using a BCA assay. Fluorescence emission from the protein lysate was measured in technical duplicates using a VICTOR3 plate reader (PerkinElmer, Waltham, MA, USA) at 485nm.

Component	Final Concentration
NaCl	150 mM
Tris Base	50 mM
EDTA	2 mM
Triton-X 100	1%

Table 3-1 FIPA Buffer Recipe
Components of radio-immunoprecipitation assay buffer modified for fluorescence measurement (FIPA buffer). Make up to 500 mL in de-ionised water, adjust to pH 7.4 and sterile filter. EDTA = Ethylenediaminetetraacetic acid

3.2.6 Statistical analysis

Statistics are presented as mean [95% confidence interval]. Statistical analysis was performed using a two-way ANOVA with main and interaction effects reported with the F ratio (numerator degrees of freedom (DF), denominator DF). For all experiments comparing different gRNA sequences oriented in different directions, the gRNA identity and direction were entered as independent factors, and all levels were tested for main effects and interaction. Interactions between factors are reported when significant ($p<0.05$). *Post hoc* comparison testing was performed with Sidak's post-test.

3.3 Results

3.3.1 Plasmid Design

Two AAV-CRISPR vectors were designed using the short SaCas9 orthologue. The cytomegalovirus intermediate-early enhancer and promoter (CMV-IE) was used to drive SaCas9 expression, and the gRNA was expressed under the human U6 (hU6) promoter. Both these promoters are short and have strong ubiquitous expression, making them popular choices for all-in-one vectors. In the first vector the U6-gRNA is downstream and orientated in the forward direction, while in the second vector the U6-gRNA is downstream but orientated in the reverse direction. The plasmids were cloned with restriction enzyme subcloning (Figure 3-2) to leave all other elements within the plasmid identical.

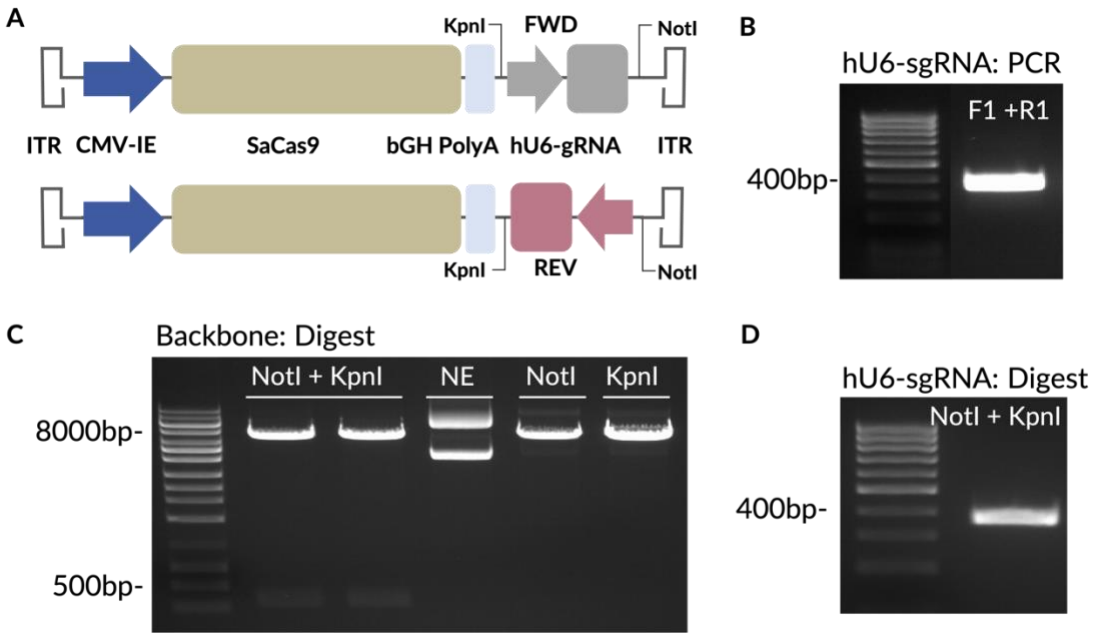


Figure 3-2 Cloning of the reverse U6-gRNA transgene
A. Vector diagram demonstrating the forward and reverse oriented plasmids flanked by AAV2 ITR sequences. **B.** The hU6-gRNA segment of the forward plasmid was PCR amplified to include the KpnI and NotI restriction sites. **C.** Digestion of the vector backbone for restriction cloning. **D**. Digestion of the PCR fragment from (B) for subcloning to the backbone in (C).

3.3.2 Pilot experiment targeting EGFP

The question of whether the orientation of the U6 promoter-gRNA complex might affect on-target editing rates arose during experiments within the laboratory to optimise the editing efficiency of a construct targeting EGFP in a transgenic HEK293-EGFP cell line. Two gRNAs (EGFP-13 and EGFP-15) were previously identified to have the highest on target editing efficiency in a screen of gRNAs targeting EGFP (C Peddle, personal communication), however these guides still edited at a relatively low efficiency of 10-15%. It was hypothesised that the transcription of one or both of the SaCas9 or gRNA transcriptional units might be affected by their orientation with respect to each other and this could affect downstream editing rates.

3.3.2.1 On-target editing of EGFP

In HEK293-EGFP cells transiently transfected with plasmids containing EGFP-13 or EGFP-15, no difference in editing rates assessed by TIDE analysis were observed between constructs with guides oriented in the forward or reverse direction (Figure 3-3). This was further supported by no difference being observed between rates of *EGFP* transcript knockdown or EGFP fluorescence detected in cell protein lysates (Figure 3-3).

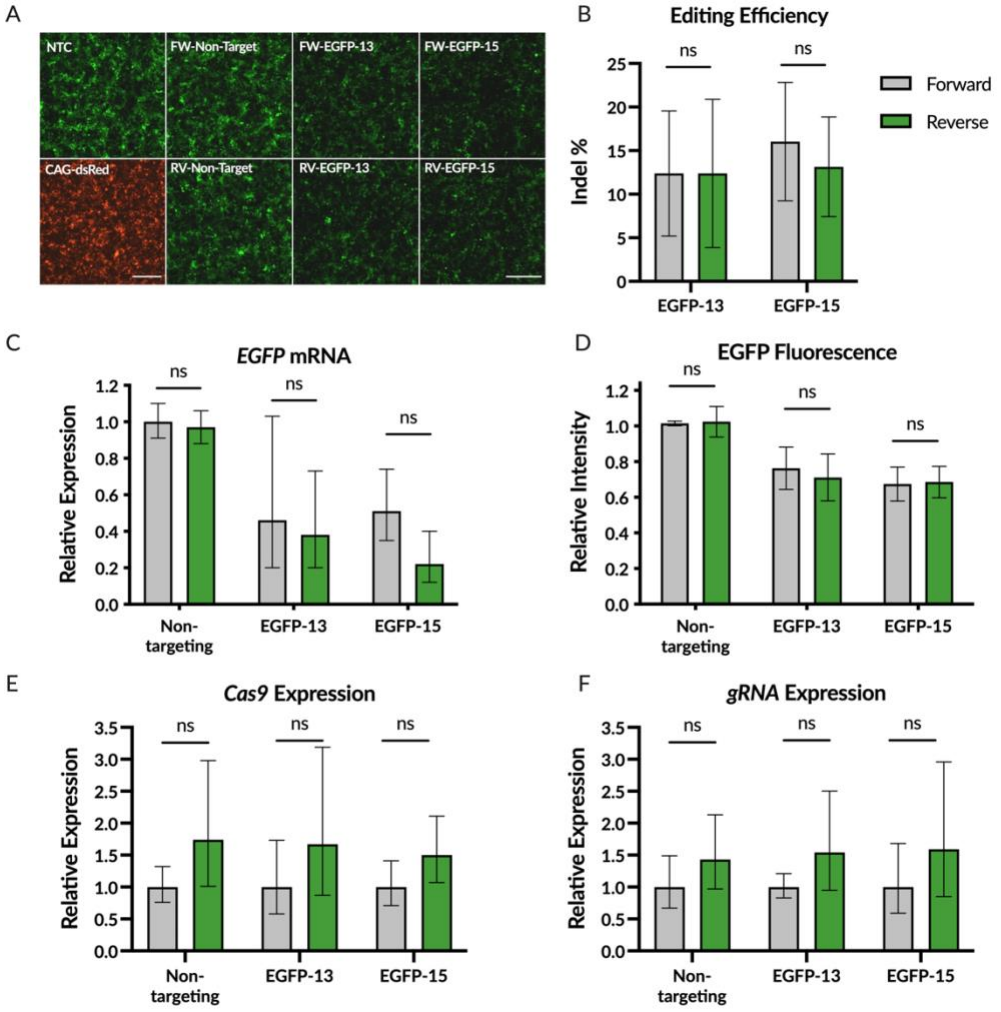


Figure 3-3 Effect of U6-gRNA orientation in plasmids targeting EGFP following transfection

A. Representative fluorescence microscopy images taken 48 hours following transfection. NTC = non-transfected control. CAG-dsRed was used as a positive transfection control. Scale = 500 μm. **B.** Editing efficiency of the two targeting guides assessed via TIDE analysis ($F(1, 16) = 0.32$, $p = 0.58$ for effect of orientation, $n = 5$). **C.** Relative expression of *EGFP* mRNA assessed via RT-qPCR normalised to *EGFP* expression in samples transfected with a forward-oriented non-targeting guide ($F(2, 18) = 2.08$, $p = 0.16$ for effect of orientation, $n = 4$). **D.** EGFP expression normalised to samples transfected with a forward-oriented non-targeting guide detected in protein lysates assessed via a protein fluorescence assay ($F(2, 17) = 0.12$, $p = 0.73$ for effect of orientation, $n = 4$). **E.** Relative expression of *SaCas9* mRNA assessed via RT-qPCR from samples transfected with forward or reverse orientated U6-gRNA elements ($F(1, 23) = 5.99$ for effect of orientation, $p = 0.022$, $n = 5$, all $p > 0.05$ on *post hoc* testing). **F.** Relative expression of gRNA from samples transfected with forward or reverse orientated U6-gRNA elements. ($F(1, 23) = 5.08$ for effect of orientation, $p = 0.034$, $n = 5$; all $p > 0.05$ on *post hoc* testing). B-F assessed by ordinary two-way ANOVA with gRNA and orientation as factors, with Sidak's test for multiple comparisons. Data presented as mean [95% CI]. *SaCas9* and gRNA expression calculated as fold change relative to the forward oriented gRNA.

3.3.2.2 Expression of SaCas9 and gRNA following transfection

To further investigate the hypothesised mechanism that orientation may affect transcription, the level of expression of *SaCas9* mRNA and gRNA was assessed with RT-qPCR. Main effects analysis using two-way ANOVA indicated the reverse orientation significantly increased the expression of *SaCas9* ($F(1, 23)=5.99$ for effect of orientation, $p=0.022$) and gRNA ($F(1, 23)=5.08$ for effect of orientation, $p=0.034$), with no significant interactions between the gRNA identity and orientation (Figure 3-3). *Post hoc* testing did not reveal a significant difference for any individual guide (all $p>0.05$, Sidak's multiple comparison testing). It is noted however that there is high inter-replicate variability between these samples, with increased variability amongst the reverse orientated samples.

3.3.3 Effect of U6-reversal using gRNAs targeting retinal loci

Although results from the pilot experiment targeting EGFP suggested that an effect of U6 promoter orientation is possible, the confidence in these results was tempered by significant variability. Furthermore, the low editing rate of the guides (range 12.4-16.0%) did not give a large dynamic range required to allow easy detection of a meaningful difference in editing rate the orientation of the promoter might produce. Due to these limitations, further experiments were designed with the aim to investigate these findings with greater precision and with gRNAs targeting loci that were more relevant to retinal disease.

Guides targeting retinitis pigmentosa-related (*RHO*) and age-related macular degeneration (*VEGFA*) genes were chosen. Both guides were previously validated and known to have high *in vitro* editing efficiencies of approximately 50% (C Peddle, personal communication), improving the dynamic range of detection of changes to editing efficiency. Additionally, as AAV would be the ultimate delivery vehicle for CRISPR-Cas constructs for therapeutic applications, plasmids cloned for transient plasmid transfection experiments were packaged into AAV

vectors to investigate a more meaningful question: does the orientation of the guide influence expression of the vector components from an AAV vector? The AAV2 capsid was chosen as it effectively transduces HEK293 cells[365] and is used in retinal gene therapy for targeting of photoreceptors and RPE.[41] The experimental plan comparing the effect of U6 orientation in plasmid transfection and AAV transduction is outlined in Figure 3-4.

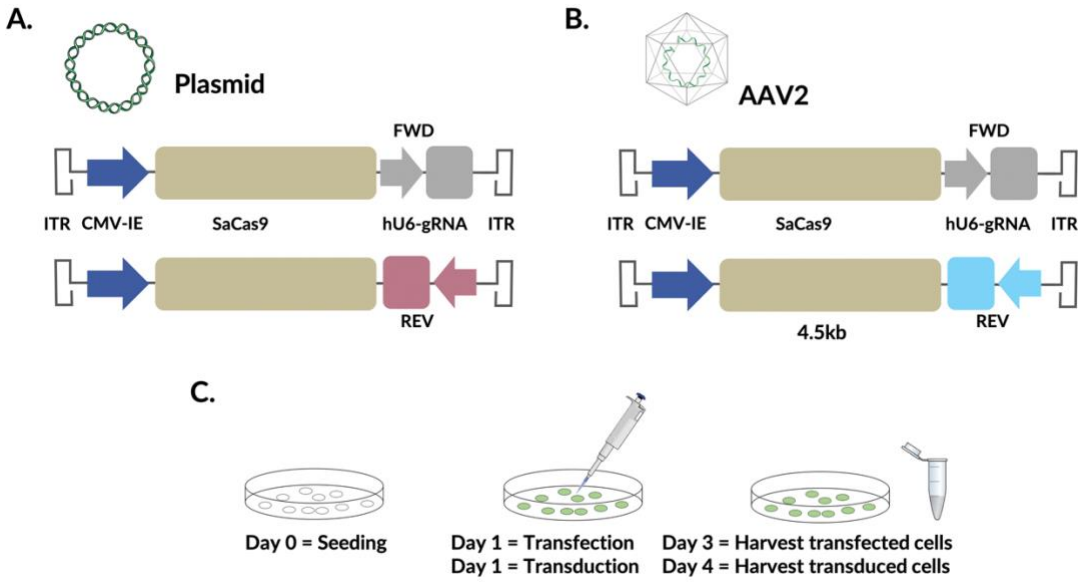


Figure 3-4 Experimental outline of reverse U6 experiment targeting retinal genes
A. Vector diagram of the forward and reverse oriented U6-gRNA promoter plasmids used for transient transfection. **B.** Vector diagram of the forward- and reverse-oriented U6-gRNA promoter AAV vectors used for transduction. **C**. Outline of transfection and transduction protocols.

3.3.3.1 Qualitative and Quantitative Analysis of AAV Vectors

Four recombinant AAV2/2 vectors were produced, to contain either the *VEGF* or *RHO* targeting gRNA downstream of the U6 promoter in the forward or reverse orientation. The titre of each batch of AAV was determined using qPCR detailed in Table 3-2. Denatured concentrated AAV samples were analysed by SDS-PAGE electrophoresis and total protein staining, which demonstrated three distinct bands representing the AAV capsid subunits (Figure 3-5). No additional bands were detected, indicating pure AAV preparations, and the strength of the protein staining correlated with the titres determined by qPCR.

	Concentrate Titre (gc/mL)	Wash Titre (gc/mL)
VEGF-Fwd	1.34e+11	1.62e+8
VEGF-Rev	4.74e+11	1.88e+8
RHO-Fwd	1.88e+11	1.02e+9
RHO-Rev	1.96e+11	2.33e+8

Table 3-2 AAV titre determined by qPCR
AAV2/2 titres were determined by qPCR interpolated from a standard curve constructed using a linearised vector plasmid standard. Reaction efficiency determined from standard curve serial dilutions were 98-100% in all reactions. gc/mL = genome copies per mL

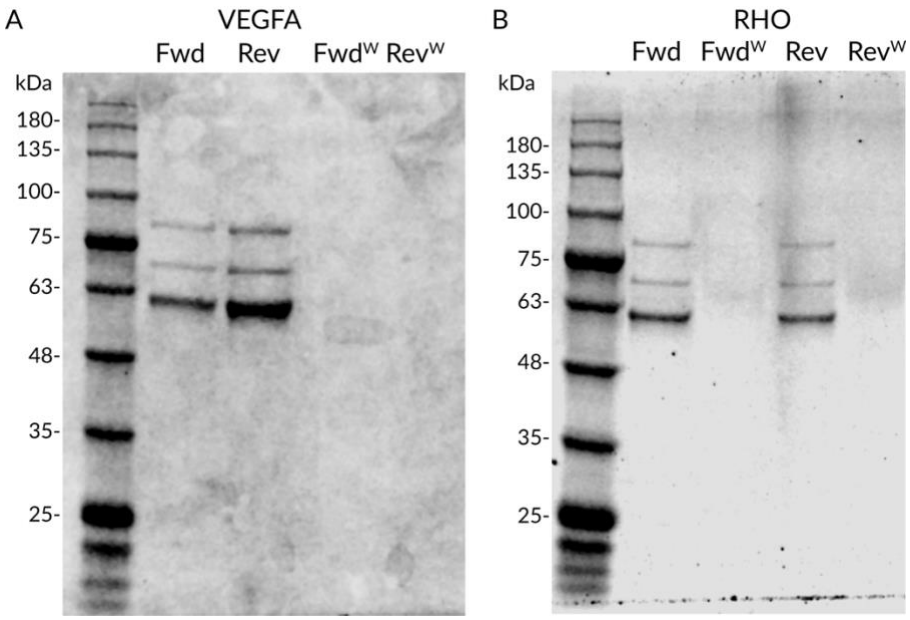


Figure 3-5 SDS-PAGE analysis of AAV vectors
Sodium dodecyl sulphate polyacrylamide gel electrophoresis (SDS-PAGE) of samples of AAV vectors containing the *VEGF* (A) and *RHO* (B) gRNAs in the forward (Fwd) and reverse (Rev) direction for both the concentrated and the wash (Fwd^W, Rev^W) samples. The gel was subject to total protein staining to detect capsid proteins VP1 (87kDa), VP2 (72kDa), and VP3 (62kDa) at the predicted ratio of VP1:VP2:VP3 of 1:1:10.

3.3.3.2 Plasmid and AAV dose and effect on editing rates

Dose response experiments of both plasmid and AAV were conducted in HEK293 cells to identify the dynamic range of editing rates possible with plasmid and AAV delivery. Delivered via plasmid transfection, editing rates approached saturation of 56-58% at doses of 750 ng in a 24-well plate, before dose-limiting toxicity and cell death were observed (Figure 3-6). Similar toxicity was also observed with control plasmids, suggesting the toxicity may be attributable either to the total dose of plasmid or to the transfection reagent, rather than the expression of the SaCas9 or gRNA from the transgene. Delivered via AAV transduction, a sigmoidal dose-response curve with a steep slope was observed, without significant toxicity. Western blotting confirmed SaCas9 expression in both transfected and transduced cells (Figure 3-6). At an MOI of 100 or less, low editing efficiencies were observed and SaCas9 expression was below the limit of detection by western blot. For further experiments, a total plasmid mass of 500 ng and an AAV MOI of 300 were chosen as doses that produced sub-maximal editing rates that would allow for any effect of changes to the U6-promoter orientation to be detected.

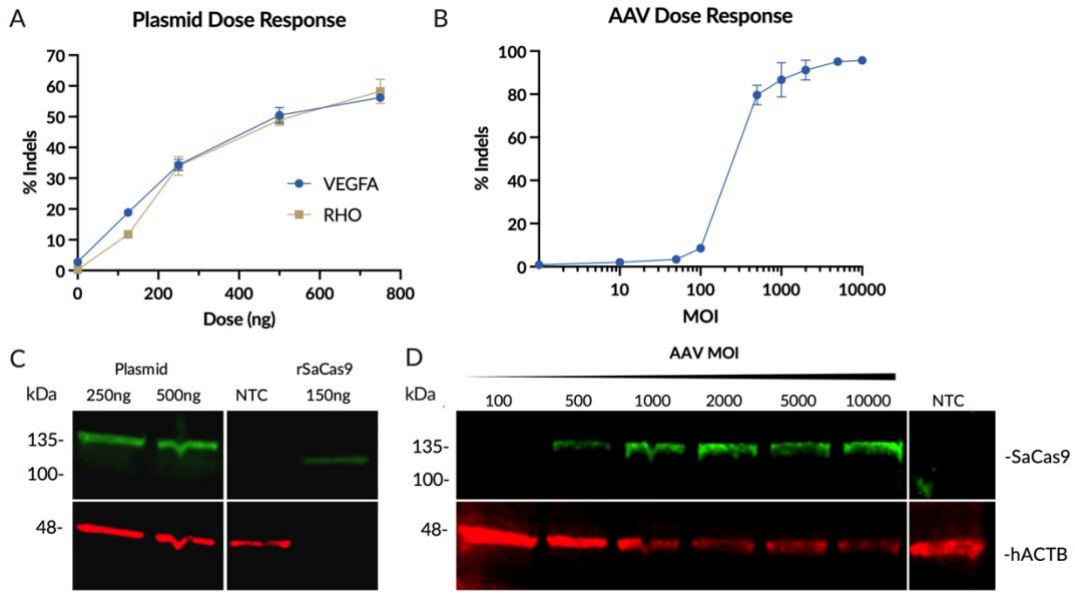


Figure 3-6 AAV Dose Response Experiments

A. Editing efficiency at 48 hours post-transfection determined by TIDE analysis at different doses of pSaCas9-gRNA plasmid in HEK293 cells in 24-well plates (n = 3). Data for panel A courtesy of C Peddle. **B**. Editing efficiency at 72 hours post-transduction determined by TIDE analysis at different doses of AAV2-SaCas9-gRNA(*VEGF*) in HEK293 cells in 12-well plates (n = 2). **C.** Western blot of protein lysates (30μg) from HEK293 cells transfected with plasmid. Recombinant SaCas9 protein (rSaCas9) is used as a positive antibody control. **D.** Western blot of protein lysates (50μg) to assess SaCas9 expression at a range of AAV2-SaCas9-gRNA(*VEGF*) doses. MOI = multiplicity of infection, NTC = non-transduced control, hACTB = human beta-actin. Data = mean ± SEM

3.3.3.3 Effect of reverse orientation of the U6-gRNA on editing rates

Consistent with data from the EGFP pilot study, cells transiently transfected with plasmids demonstrated no difference in editing rate between constructs with guides oriented in the forward or reverse direction with either the *VEGF* or *RHO* guides (Figure 3-7). In cells transduced with AAV however, U6-gRNA orientation significantly affected editing rates ($F(1,20)=15.01$, $p=0.0009$ for effect of orientation) (Figure 3-6). On multiple comparison testing, a relative reduction in editing rate of 28.7% (95% CI [12,45], $p=0.0009$) was seen for the *VEGF* guide oriented in the reverse compared to the forward direction. A 16.3% relative difference between the forward and reverse *RHO* guide was not statistically significant (95% CI [-15,48], $p=0.39$).

3.3.3.4 Effect of reverse orientation of the U6-gRNA on *SaCas9* and gRNA expression

To investigate if the reduction in editing correlated with *SaCas9* or gRNA transcript levels, RT-qPCR was performed on RNA extracted from the same samples. In cells transfected with the plasmid constructs no significant effect on *SaCas9* or gRNA transcripts was observed across either gRNA, expressed in either the forward or reverse orientation (Figure 3-7).

When delivered via AAV, the reverse-oriented U6 construct resulted in a significant reduction in *SaCas9* transcripts ($F(1,16)=26.81$ for effect of orientation, $p<0.0001$) (Figure 3-7). This was observed independent of the guide sequence used, with a 54% relative reduction ($p=0.0005$) in *SaCas9* mRNA observed in the *VEGF* targeting constructs and a 44% relative reduction ($p=0.023$) was observed in *RHO* targeting construct. A similar, significant reduction in gRNA expression was also observed ($F(1,16)=24.53$ for effect of orientation, $p=0.0001$). The reduction in gRNA expression was also independent of the gRNA sequence, with a significant reduction of 44% ($p=0.01$) and 37% ($p=0.02$) of gRNA expression for the *VEGF* and *RHO* guides respectively when expressed in the reverse relative to the forward direction.

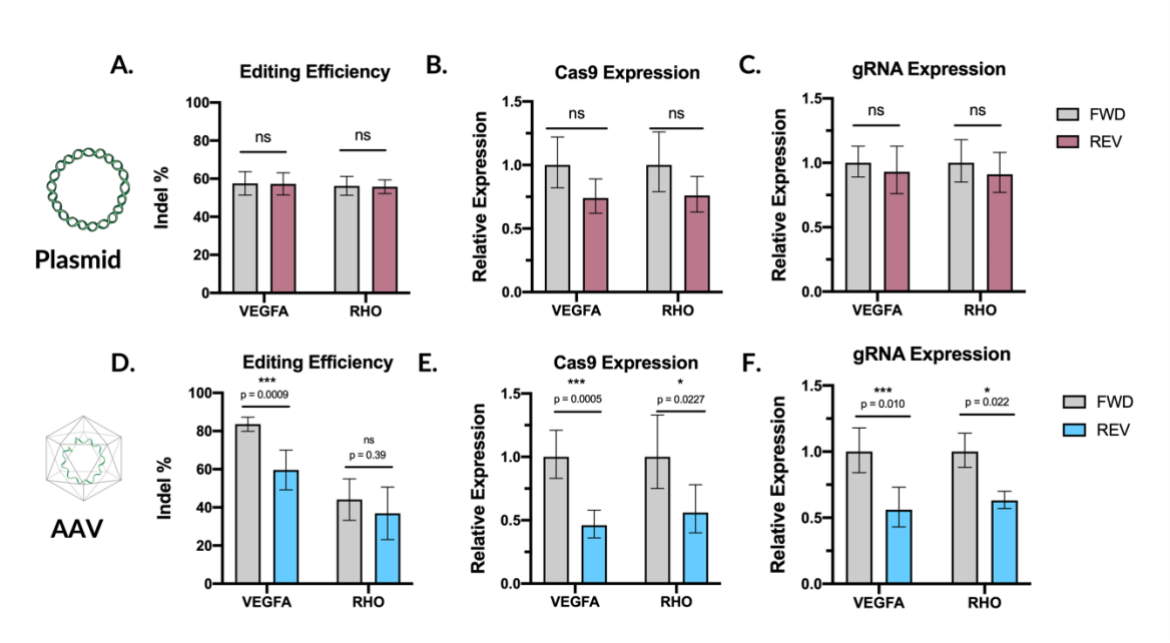


Figure 3-7 Comparison of effect of U6-reversal between plasmid transfection and AAV transduction

A. On-target editing efficiency in plasmid-transfected samples for guides targeting *VEGF* and *RHO* ($F(1,20) = 0.032$, $p = 0.86$ for effect of orientation, n = 6) **B.** *SaCas9* mRNA expression from plasmid transfected samples demonstrated a significant main effect of gRNA orientation on Cas9 expression ($F(1,18) = 7.80$, $p = 0.012$) but no significant differences were observed for individual guides on *post hoc* testing (*VEGF* $p = 0.13$, n = 5; *RHO* $p = 0.12$, n = 6). **C.** No significant difference in gRNA expression from plasmid transfected samples was observed due to gRNA orientation ($F(1,18) = 0.98$, $p = 0.34$; *VEGF* n = 5; *RHO* n = 6). **D**. On-target editing efficiency in AAV transduced cells was significantly reduced by the reverse orientation of the gRNA ($F(1,20) = 15.01$, $p = 0.0009$ for effect of orientation) with a significant reduction in editing at the *VEGF* locus ($p = 0.0009$, n = 6) but no significant reduction at the *RHO* locus ($p = 0.39$, n = 6). **E**. *SaCas9* expression in AAV transduced cells was significantly reduced by reverse gRNA orientation ($F(1,16) = 26.81$ for effect of orientation, $p < 0.0001$). The effect was independent of the gRNA sequence (*VEGF* $p = 0.0005$, n = 6; *RHO* $p = 0.023$, n = 4). **F.** *gRNA* expression in AAV transduced cells was significantly reduced by reverse gRNA orientation ($F(1,16) = 24.53$ for effect of orientation, $p = 0.0001$). The effect was independent of the gRNA sequence (*VEGF* $p = 0.01$, n = 6; *RHO* $p = 0.02$, n = 4). Data presented as mean [95% CI], ordinary two-way ANOVA with Sidak's *post hoc* testing. *SaCas9* and gRNA expression calculated as fold change relative to the forward oriented gRNA. Experiments for panel A performed by C Peddle, experiments for panels B-C performed by C Peddle and M Stevanovic.

3.3.3.5 Effect of reverse orientation of the U6-gRNA on SaCas9 protein expression

To correlate reduced *SaCas9* mRNA levels with SaCas9 protein expression, AAV-transduced samples were analysed by western blot. For both the *VEGF* and *RHO* guides, SaCas9 protein expression appeared reduced in constructs with the gRNA in the reverse direction (Figure 3-8). Using band densitometry for semi-quantitative analysis, a significant reduction in SaCas9 protein was seen when the U6-gRNA cassette was in the reverse compared to forward orientation ($F(1,16)=46.08$ for effect of orientation, $p<0.0001$), with a significant reduction in SaCas9 expression from vectors with guides in the reverse direction targeting either *VEGF* (62% reduction, 95%CI [33,91], $p=0.0001$) or *RHO* (30% reduction, 95%CI [13,47] $p=0.001$). The greater reduction in expression we observed in the reverse-oriented *VEGF*-targeting construct compared to the *RHO*-targeting construct is consistent with the greater loss of editing efficiency in the *VEGF* reverse construct and with the extent of differences in SaCas9 mRNA levels from FWD and REV treated samples.

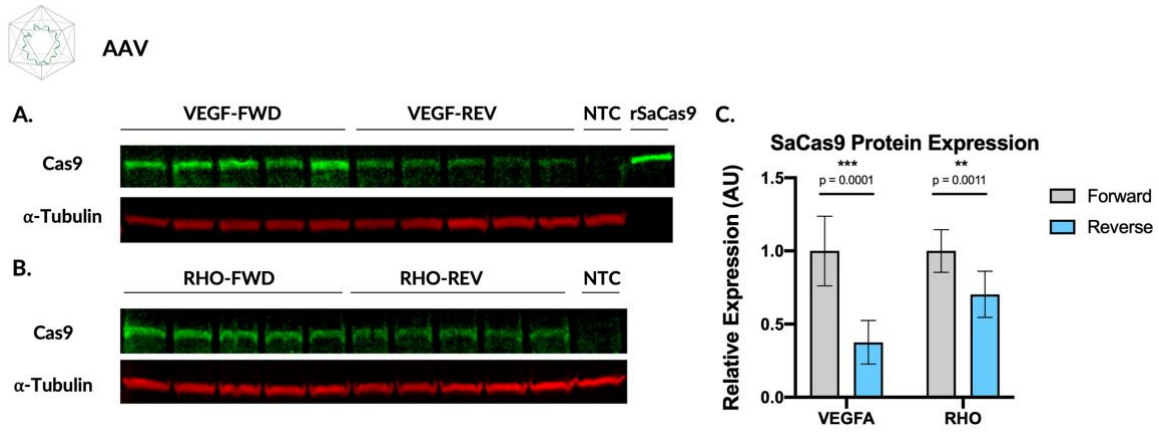


Figure 3-8 Western blot of SaCas9 expression levels
A. Western blot of AAV transduced samples targeting *VEGF*. **B**. Western blot of AAV-transduced samples targeting *RHO*. **C**. Quantitative analysis of band densities normalised to alpha-Tubulin, relative to the expression of SaCas9 with U6 in the forward orientation. A significant reduction in SaCas9 expression is observed ($F(1,16) = 46.08$ for effect of orientation, $p < 0.0001$), for both the *VEGF* ($p = 0.0001$, $n = 5$) and *RHO* ($p = 0.001$, $n = 5$) constructs. Data presented as mean ± 95% CI, ordinary two-way ANOVA with Sidak's multiple comparison testing. NTC = non transfected control, rSaCas9 = 100 ng recombinant Cas9 protein.

3.4 Discussion

In the years following the demonstration of the potential of AAV vectors for gene therapy by the laboratories of Samulski[366] and Byrne,[367] numerous incremental developments have been made to improve the efficacy of gene therapy vectors.[368] These include small changes to the transgene that have been shown to improve potency, durability or viral packaging.[348,369,370] Examples of these include the addition of post-transcriptional regulatory elements,[371] inclusion of intron-exon splice sequences in the 5' UTR,[372] or elimination of hairpin structures that mimic ITR sequences.[373]

As gene editing using AAV delivered CRISPR-Cas9 moves towards the clinic,[225] optimisation of AAV-CRISPR transgene design is important to maximise therapeutic efficacy. This chapter demonstrates that a simple change to the design of a bi-cistronic AAV-CRISPR vector, reversing the direction of the U6 promoter and gRNA cistron, has a marked impact on Cas9 and gRNA expression and subsequent editing rates in a vector with SaCas9 driven by the CMV-IE promoter. This effect was seen most clearly when the transgene was packaged and delivered via AAV, rather than through plasmid transfection. These results indicate that data from experiments using plasmid transfection do not necessarily correlate with those found following AAV transduction. The high variability amongst the pilot data targeting EGFP by transfection precludes drawing strong conclusions from this dataset. Repeat EGFP experiments may have clarified the results, but it was considered more valuable to repeat these with gRNAs targeting retinal genes.

This work adds direct comparative evidence to observations in the literature that the orientation of the U6 promoter within an AAV-CRISPR vector can affect editing rates. In the initial characterisation of SaCas9, Friedland et al. packaged two U6-gRNA complexes with D10A SaCas9 nickase in the forward and reverse direction into AAV constructs.[353] Friedland showed reduced Cas9 expression and editing efficiencies when the U6-gRNA complexes were oriented in the reverse direction. The U6-gRNA cassette in Friedland et al. was located upstream

of the Cas9, compared to the downstream location in the present study. Ran et al. evaluated both the *in vitro* and *in vivo* gene editing activity of SaCas9 using a vector expressing SaCas9 and gRNA.[198] The plasmid used in the *in vitro* characterisation (pX601, available from Addgene) has been widely used, including in this chapter, and contains the U6-gRNA in the forward direction.[198] When Ran et al. developed an AAV for the *in vivo* characterisation of SaCas9, however, the AAV transgene contained the U6-gRNA in the reverse direction. No data were presented to compare the activity of the forward and reverse constructs or validate why the U6-gRNA complex was reversed in the AAV vector.[198] Most recently, Levy et al. engineered a dual-AAV split-intein SaCas9 base editor and found that moving the U6-gRNA complex from upstream of the SaCas9 in the forward orientation to downstream in the reverse orientation substantially improved editing rates.[254]

This data builds on work in other systems that have demonstrated that the arrangement of expression cassettes in a bi-cistronic design can affect transgene expression. When a second promoter is added, the activity of both the upstream and downstream promoter was shown to be affected in eukaryotes with lentiviral[358] and transient transfection systems,[359] and in prokaryotes with transient transfection systems.[374] Although each of these studies examined two polymerase II promoters, in the two studies that compared placement of the downstream promoter in reverse compared to a forward direction, the reverse direction enhanced expression of both promoters.[359,374]

How bi-cistronic constructs are affected also appears to depend on the promoter used, in addition to how they are arranged. For example, an interphotoreceptor retinoid binding protein promoter suppressed the activity of a rhodopsin kinase promoter, but only when located in the downstream but not the upstream position.[360] Variable results have been found when the U6 promoter is used in combination with other promoters. Placed divergent to a ubiquitin C (UbiC) promoter, U6 promoter activity was inhibited compared to a tandem orientation in a retroviral system.[361] Conversely, when the U6 promoter was paired with a phosphoglycerate kinase (PGK)

promoter[361] or another U6 promoter[362] in any orientation, the activity of the U6 promoter was not affected. A lack of agreement between published studies prevents the extrapolation of general rules about the optimal arrangement of promoters for other vectors.

The results of this study contain several limitations. Firstly, these experiments only investigate the combination of the CMV-IE and the hU6 promoter in a single cell type. For clinical gene therapy vectors it is likely that at least the Cas9 would be expressed under a tissue specific promoter. Secondly, this head-head comparison only investigated the hU6 located 3' to the Cas9, and it is not known what effect locating the hU6-gRNA complex in different orientations 5' to the Cas9 would have. Thirdly, this effect was not explored at multiple doses. The dose response experiments in Figure 3-6 suggest the plasmid transfection dose was close to saturated expression, which may limit the ability to detect a difference from transfected plasmids. It would be of interest to explore this effect across a range of transfected and transduced doses. Finally, these results were not tested *in vivo* to confirm the *in vitro* findings. Within the limitations of this data and together with the literature discussed, it is reasonable to suggest that it is necessary to assess each system and set of promoters in the process of optimising a transgene such as an all-in-one AAV-CRISPR vector, and ideally to do so packaged as an AAV.

The underlying mechanisms of these findings remain unknown, however this data generates hypotheses that can be used to guide future investigations. In the current study, I observed that the reversal of the RNA-pol III U6 promoter impairs expression from the U6 promoter itself and also an RNA-Pol II CMV-IE promoter upstream in the same construct, but only when expressed in an AAV system. Torsional effects from the unwinding of DNA during active transcription within the AAV episome may be implicated.[375] Transcription from the U6 promoter in the forward direction would result in relaxed negatively supercoiled DNA upstream of the promoter. In contrast, orientation of the downstream U6 promoter in the reverse direction could result in an accumulation of tightly wound positively supercoiled DNA

between the cistrons, downstream of both the CMV-IE and U6 promoter; this may stall transcription of both promoters.[374,376]

Transcriptional interference arising from one transcribing RNA polymerase directly impeding another transcribing RNA polymerase[377] may also play a role. Following AAV transduction, AAV genomes form double-stranded episomal circular monomers and concatemers, where viral transgenes form linked circles connected by ITRs.[378,379] Within the circular episome, the transgenes can be linked to one another in any direction, 5'-3' or 3'-5'. For a given transgene, there are three possible arrangements (Figure 3-9). In the vectors containing the U6-gRNA in the forward orientation relative to the Cas9, only one of these combinations places two promoters directly adjacent to one another, separated by ITRs. In the vectors containing the U6-gRNA in the reverse orientation relative to the Cas9 however, in all possible arrangements, the promoters are directly adjacent to one another. This is the case whether the U6-gRNA is located upstream[353] or downstream of the Cas9 cassette. The closer physical proximity of both the polymerase II and III promoters in the concatemers when the gRNA is in the reverse direction may increase the susceptibility of expression from these promoters being affected by transcriptional interference and local torsional effects of transcription. ITRs are known to possess promoter activity,[380] and the reverse orientation also places both promoters immediately adjacent to the ITRs in the concatemer. In plasmid transfection, the plasmid backbone is maintained and separates the ends of the transgene and formation of transgene monomers and concatemers does not occur. This model may explain the observed differences in expression between plasmid transfection and AAV transduction.

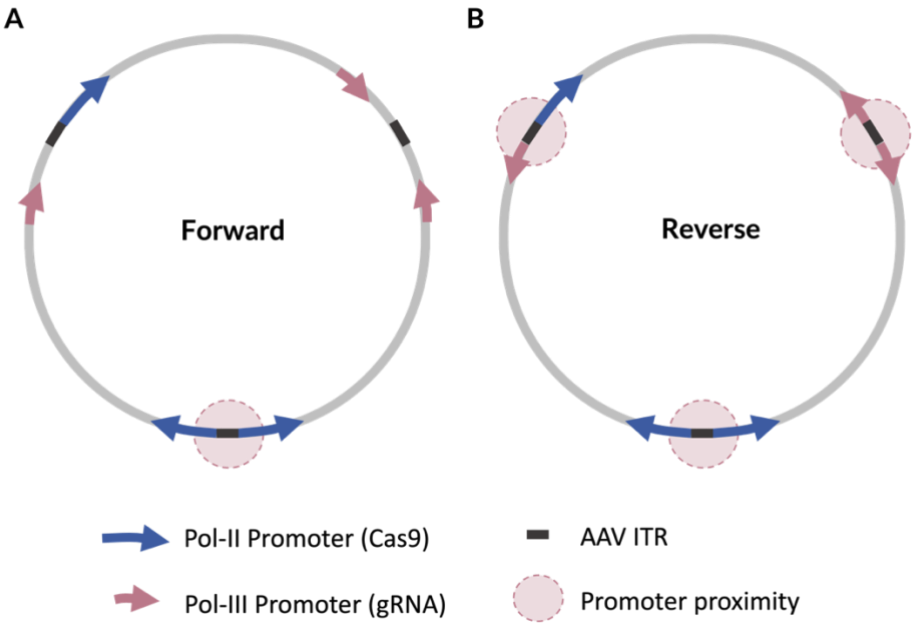


Figure 3-9 Model of promotor proximity in an AAV vector
The diagram shows the three possible arrangements of a dual-transgene containing Cas9 driven by a Pol-II promoter and a gRNA driven by a Pol-III promoter in a circular episomal concatemer. (A) With the gRNA and its promoter oriented in the forward direction, only one conformation of transgene concatemer results in promoter proximity. (B) In concatemers with the gRNA and its promoter oriented in the reverse direction, all conformations of the transgene concatemer result in proximity between the promoters.

3.4.1 Conclusion

The results of this chapter highlight two key points. Firstly, for the design of all-in-one AAV-CRISPR vectors, it is important to consider the orientation of promoters within the transgene when optimising transgene expression. This effect has been seen using the CMV-IE and hU6 promoter *in vitro*. Expression is likely to be promoter dependent, and further work is needed to test different vector designs across different tissue types, including *in vivo*. This includes further evaluation of other promoters like a cell-specific promoter for each specific application. Secondly, this study suggests that some steps of testing and optimisation should ideally be performed with AAV vectors, as results found from plasmid transfection may not translate to those found with AAV vectors.

4

IN VIVO EDITING WITH CASX, A NOVEL CLASS 2 CRISPR SYSTEM

4.1 Introduction

Following the development of *Streptococcus Pyogenes* (SpCas9) for programmable genome editing,[194–196] a range of further Cas orthologues have been identified, with ongoing efforts to identify ideal Cas nucleases for therapeutic use.[197] The properties of an ideal Cas orthologue include robust target cleavage activity at human body temperature, a small protein size for delivery, a simple PAM sequence with minimal constraints to permit wide targeting throughout the genome, and high target specificity to prevent off-site targeting and genotoxicity. Class 2 CRISPR systems have proven ideal for biotechnology applications due to their simplicity, requiring only a single multi-functional endonuclease and engineered gRNA. The most used nucleases are the Type II Cas9 and Type V Cas12a (also known as Cpf1) effector families. Some small orthologues, such as SaCas9[198,225] used in the previous chapter (~3.2kb, PAM: NGRRT), and CjCas9[199] (~2.9kb, PAM: NNNRYAC), are packageable within a single AAV for *in vivo* editing. Use of these and other smaller orthologues have been limited by factors such as complex PAM requirements and, in the case of CjCas9, variable reports of *in vivo* efficacy.[201] Protein engineering of mainly Cas9 and Cas12a orthologues using rational design and directed evolution techniques to iteratively select for protein function have yielded a broad family of

engineered nucleases with some of these desired properties.[381] Additionally, screening of genomic and metagenomic databases has now rapidly expanded the repertoire of known CRISPR endonucleases as candidates for use in human genome editing.[197]

One such candidate family of orthologues is CasX (also known as Cas12e), a recently described Class 2, Type V CRISPR system.[207] A compact nuclease with a coding sequence of ~2.9kb, CasX is easily packageable within AAV for therapeutic delivery. Identified from metagenomic analysis of microbial DNA recovered from groundwater samples, the CasX subtype is distinct within an ever-growing phylogenetic tree that now encompasses 10 identified type V subtypes.[197,382] Unlike the archetypal Type II (Cas9) effectors that contain two nuclease domains (RuvC-like and HnH), each responsible for the cleavage of one strand of dsDNA, Type V effectors contain only one RuvC-like domain for cleavage of both strands. CasX-mediated cleavage generates a staggered dsDNA break directed by a 20nt programmable gRNA. The target strand and non-target strands are cleaved 12-14 nucleotides and 22-25 nucleotides after the PAM site which is located 5' to the target sequence, in contrast to the 3' PAM in Cas9 systems (Figure 4-1). Unlike Cas12a, which exhibits non-specific collateral cleavage activity of ssDNA following target binding,[383,384] the *trans*-cleavage activity of CasX was found to be minimal.[207]

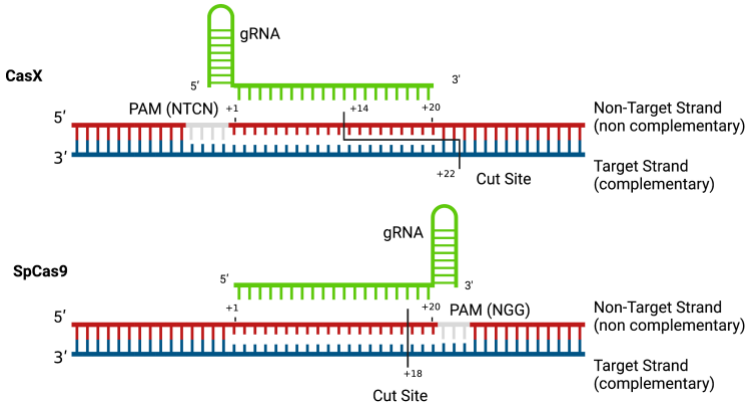


Figure 4-1 Schematic of CasX gRNA target
Schematic comparing the gRNA target site of CasX to SpCas9, showing relative locations of the PAM site and gRNA scaffold, and differing cleavage sites.

In the initial description of CasX, two wildtype orthologues derived from Deltaprotobacteria (DpbCasX) and Planctomycetes (PlmCasX) were evaluated with PlmCasX found to edit target sequences with a TTCN PAM and exhibit approximately 30% that of the editing activity of wildtype SpCas9 against a GFP target in HEK293 cells.[207] Building on these findings, Scribe Therapeutics have made extensive modifications to both the wildtype gRNA scaffold and the CasX protein sequence via codon optimisation, directed evolution, domain swapping and rational design.[385] This generated a modified chimeric CasX protein based on the wildtype PlmCasX sequence, whereby the non-target strand binding (NTSB) domain and helical I domain were swapped for those derived from the DpbCasX, and additional substitutions and deletions were introduced in the helical II and RuvC domains. These changes were also found to allow cleavage of sequences with a more permissible NTCN PAM. Furthermore, extensive modifications were introduced to the gRNA scaffold, with deletions, substitutions and swapping of the stem-loop structure found to improve editing efficiency. Collectively these changes were found to improve on-target editing up to 24-fold relative to wildtype CasX at a given spacer, with an on-target EGFP editing rate of greater than 70% in HEK293T-GFP reporter cells.[385] Altogether, this process has generated a highly engineered compact Cas nuclease, herein referred to simply as 'CasX', capable of high *in vitro* editing rates in human cells with a minimal PAM.

Initial proof-of-concept experiments using AAV-mediated delivery of CasX to the retina have been performed at Scribe Therapeutics. However, the dose range, toxicity and efficacy has yet to be established. In collaboration with Scribe Therapeutics, in this chapter I sought to further characterise the use of subretinally injected AAV.CasX vectors for *in vivo* genome editing of post-mitotic rod photoreceptors.

4.1.1 Chapter Aims

1. Assess *in vivo* on target editing efficiency of CasX delivered via AAV in mature rod photoreceptors, through subretinal injection of one of two doses 1×10^9 gc/eye (1E+9) or 1×10^{10} gc/eye (1E+10) of an AAV8.hRHO.CasX.bGH.U6-gRNA (AAV.CasX) vector designed to knockdown EGFP in an *Nrl.EGFP* mouse model that expresses *EGFP* specifically in rods. Editing efficiency will be monitored with *in vivo* cSLO imaging, DNA deep sequencing, protein western blot and immunofluorescence.
2. Assess *in vivo* toxicity by way of structural and functional changes at two doses of subretinal AAV.CasX using OCT imaging and ERG in the *Nrl.EGFP* mouse model relative to a buffer injected control eye.

4.2 Methods

4.2.1 Animal models and procedures

Heterozygous *Nrl.EGFP* mice (*Nrl.EGFP*$^{+/-}$) were generated by crossing B6.Cg-Tg(*Nrl-EGFP*)1Asw/J homozygotes (gift from Anand Swaroop, National Eye Institute, Bethesda, MD, USA) with C57BL/6J (Charles River, Harlow, UK). Each allele of the *Nrl.EGFP* transgenic strain contains three copies of a transgene containing the mouse neural leucine zipper (*Nrl*) promoter driving the expression of *EGFP* specifically in rod photoreceptors.[386] Animal maintenance was performed as described in general methods.

Subretinal injections were performed as described in the general methods on equal numbers of male and female six-week-old animals. A single 1.5 μL injection of either AAV or buffer solution was delivered to the superior retina, with successful injections observed by the creation of a superior hemi-retinal bleb without complications of bleeding or retinotomy. AAV doses of 1E+9 gc/eye or 1E+9 gc/eye were used. An initial cohort (1E+9 n = 16, 1E+10 n = 18) were injected but only a portion of this cohort (1E+9 n = 7, 1 E+10 n = 7) received bilateral injections without complications and were included in the imaging cohort. Mice receiving a unilateral uncomplicated injection were included for molecular analysis. A second cohort received bilateral injections without complications (1E+9 n = 7, 1E+10 n = 3).

Electroretinography was performed to assess retinal function at ten weeks post-injection as described in general methods.

4.2.2 Retinal imaging and quantification

CSLO and OCT imaging was performed using a Spectralis device (Heidelberg Engineering) fitted with a 55° lens as described in general methods.

For BAF image analysis, a detector sensitivity of 75% was used to maximise the signal dynamic range without signal saturation. Images were exported in .tiff format and using FIJI (Version 2.10, National Institutes of Health, USA). Prior work in the lab established a 'band'

mean grey value (mGV) protocol, which measured the mean grey value of the total retina via a circumferential band area surrounding the optic nerve. Extending this, a FIJI macro was written to quantify mGV of the superior, inferior, and whole retinal areas (Figure 4-2) to allow batch processing of collected images (see Appendix for code).

Measurement of the photoreceptor (PRL) layer thickness was performed as described in the general methods.

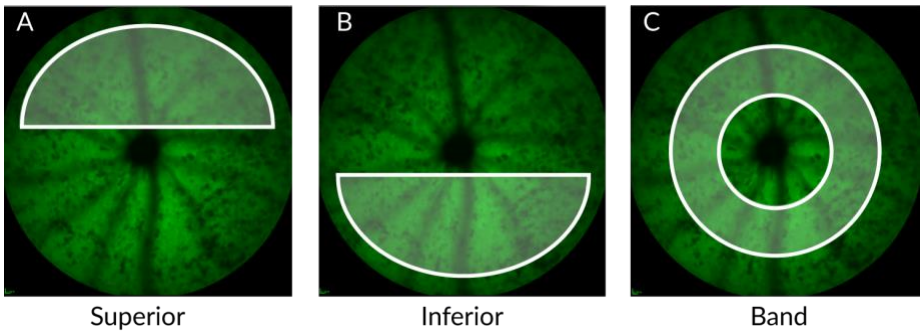


Figure 4-2 Mean Grey Value Measurement of Blue Autofluorescence cSLO Fundus Images
Images were centred on the optic disc and uniform illumination of the posterior pole achieved. Custom FIJI macros were used to create sampling areas superior **(A)**, inferior **(B)** and circumferential **(C)** to the optic disc. The mean grey value quantifies the average pixel intensity within the sampling area. Greyscale images presented with a green lookup table.

4.2.3 Construct cloning and AAV production

Molecular cloning of the constructs was performed using standard molecular cloning techniques described in the general methods by Scribe Therapeutics according to the vector map in Figure 4-3. A previously validated 20nt EGFP targeting gRNA was cloned 3' of the gRNA scaffold, designed to target just downstream of the EGFP chromophore region (Figure 4-3). Recombinant AAV2/8 vectors were produced by the University of North Carolina (UNC) Vector Core (USA) by triple transfection in HEK293 cells and purified by caesium chloride (CsCl) gradient density ultracentrifugation. The final vector name was 'AAV.CasX.Stx.Issac', herein referred to as AAV.CasX. Concentrated virus titre was determined by qPCR as 2.4×10^{13}

gc/mL. AAV aliquots were frozen in storage buffer containing PBS supplemented with 250mM NaCl and 5% sorbitol. For subretinal injection, AAV was diluted in PBS with 0.002% Pluoronic-F68 non-ionic surfactant to reduce adherence and retention of AAV capsids within the injection device.

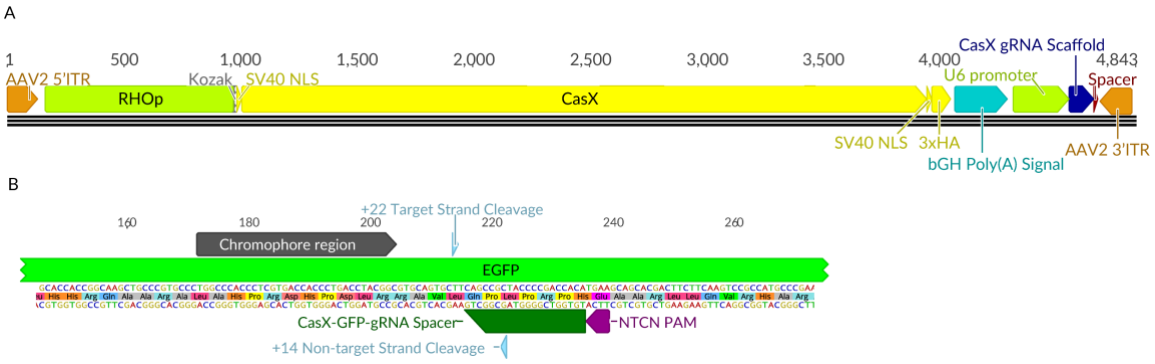


Figure 4-3 Vector and target map
A. Vector map of the AAV transgene packaged into recombinant AAV2/8 vectors. The transgene consists of a modified CasX protein fused to SV40 nuclear localisation sequences under the expression of the 806bp human rhodopsin promoter with a bovine growth hormone (bGH) polyA sequence. The modified gRNA scaffold and spacer sequence was cloned downstream of the U6 promoter. **B.** Map of the spacer targeting region in EGFP 3' of the chromophore region. Predicted staggered cleavage sites are annotated. The 5' NTCN PAM is labelled. Construct cloning and gRNA validation performed by Scribe Therapeutics.

4.2.4 Western Blot

Animals were sacrificed and eyes were freshly enucleated, dissected in ice-cold PBS to isolate the neural retina, and snap-frozen in dry ice. Western blot was performed by Cécile Fortuny (Scribe Therapeutics). Protein was extracted from individual freshly thawed retinas in RIPA buffer freshly supplemented with protease inhibitors (Sigma-Aldrich) (5mg/mL final concentration), Dithiothreitol and phenylmethylsulfonyl fluoride (final concentration 1 mM respectively). Retinal tissue was homogenised using RNA-free disposable pellet pestles (Fisher scientific, #12-141-364) and incubated on ice for 30 minutes. Samples were then centrifuged at 4 °C at full speed for 20 minutes to pellet gDNA. Protein extracts and gDNA cell pellets were

then separated. For protein extracts, supernatants were collected, and concentration measured with a Pierce 660nm assay as per the manufacturer's instructions (Thermo Fisher Scientific).

15µg of whole cell lysate was loaded into each well of a TGX Stain-Free gel (Bio-Rad Laboratories) and subject to SDS-PAGE. Total protein was visualised by UV photoactivation of the gel and imaged on a ChemiDoc-MP (Bio-Rad Laboratories). Protein transfer was performed as described in general methods. Membranes were blocked with 5% milk in PBS-T for 1 hour at room temperature and incubated overnight at 4 °C with the primary antibodies against GFP and GAPDH (Table 4-1). Membranes were washed three times with TBS-T, then incubated with horseradish peroxidase-conjugated secondary antibody for 1 h at room temperature. After washing three times, the membranes were developed with 1 mL of Clarity Western ECL Substrate (Bio-Rad Laboratories) and imaged on a ChemiDoc-MP. Following imaging, the HRP signal was quenched by incubating the blot in 30% hydrogen peroxide for 15 minutes at room temperature. The membrane was rinsed once and washed three times for 5 minutes each time with PBS-T before blocked with 5% milk in PBST. The membrane was then blotted overnight at 4 °C with anti-HA primary antibody, then processed for secondary antibody labelling and imaging as described. Band intensities and total protein signal were quantified with Image Studio Lite software (v5.2.5, LI-COR Biosciences), and band intensity normalised to total protein staining. Knockdown in treated samples was quantified relative to the mean of buffer injected controls.

Antibody	Source	Working dilution
Western Blot Primaries		
Mouse anti-GAPDH	Sigma (G8795)	1:1000
Rabbit anti-GFP (N-term)	Sigma (G1544)	1:1000
Rabbit anti-HA	Sigma (H9658)	1:1000
Western Blot Secondaries		
Goat anti-rabbit IgG, HRP-conjugate	Sigma (12-34812	1:5000
Goat anti-mouse IgG (Fab Specific)-peroxidase conjugate	Sigma (A9917)	1:5000
IHC Primaries		
Mouse anti-HA	Abcam (ab18181)	1:500
IHC Secondaries		
AlexaFluor goat anti-mouse 568	Thermo Fisher (A-11004)	1:500

Table 4-1 Table of antibodies
List of antibodies used in this chapter for western blot and immunohistochemistry

4.2.5 Immunohistochemistry

Immunohistochemistry and microscopy were performed as described in general methods. Sections were incubated in blocking solution (2% BSA, 2% NGS, 0.2% Triton X-100 in PBS) for one hour at room temperature, before overnight incubation at 4 °C with primary antibody diluted in blocking solution (Table 4-1). Secondary antibody diluted in blocking solution was incubated for two hours at room temperature.

4.2.6 Next generation sequencing

Next generation sequencing (NGS) was conducted at Scribe Therapeutics. gDNA was isolated from retinas as described in section 4.2.4 and processed with the DNeasy Blood & Tissue Kit (Qiagen) according to the manufacturer's instructions. Amplicons of the target region were generated from gDNA, bead-purified (Agencourt Ampure XP, Beckman Coulter USA) and then re-amplified to add 5' Illumina adapter sequences as well as a 16nt random unique molecular identifier (UMI) sequence. Quality and quantification of the amplicon was assessed using a Fragment Analyser DNA kit (Agilent, dsDNA 35-1500bp). Amplicons were

sequenced on a MiSeq platform (Illumina, San Diego, CA, USA) according to the manufacturer's instructions. Raw fastq files from sequencing were processed as follows: (1) the sequences were trimmed for quality and for adapter sequences using the program cutadapt (v. 2.1); (2) the sequences from read 1 and read 2 were merged into a single insert sequence using the program flash2 (v2.2.00); and (3) the consensus insert sequences were run through the program CRISPResso2 (v 2.0.29).[387] The editing efficiency of the CasX molecule was quantified as the total percent of reads that contain insertions and/or deletions (indels) anywhere within a 30 bp window centred at –3 bp from 3' end of spacer.

4.2.7 Statistical analysis

Treatment was assigned at random to each eye within a subject. For analysis of paired eye *in vivo* data, a two-way ANOVA was used treating the eyes as randomised blocks,[388] with multiple comparison testing using the Sidak method. For analysis of unpaired data, a one-way ANOVA comparing to the mean of the buffer control group was used, with Dunnett's *post hoc* testing. Correlations were assessed with Pearson's correlation coefficient. Graphed data are presented as means ± SEM.

4.3 Results

4.3.1 Assessment of EGFP knockdown with CSLO autofluorescence imaging

To investigate the potential of CasX for targeted gene disruption in mature postmitotic rod photoreceptors, all-in-one AAV8 vectors were generated to express CasX together and a EGFP targeting gRNA with extensive *in vitro* validation performed by Scribe Therapeutics (unpublished data). The natural tropism of AAV8 for photoreceptors, together with the rod-specific expression of the hRHO promoter was designed to restrict CasX expression to rods.[389] Six-week-old *Nrl.EGFP*$^{+/-}$ mice that expressed EGFP in rod photoreceptors received a subretinal injection to create a superior hemi-retinal bleb with one of two vector doses, 1E+9 or 1E+10 gc/eye, with the contralateral eye receiving a matched buffer control injection to control for the effect of surgical trauma or buffer-related toxicity.

EGFP expression was monitored *in vivo* at 4- and 12-weeks post injection using blue autofluorescence (BAF) CSLO imaging and quantified by measurement of image mean grey value (mGV) (Figure 4-4). As the lateral spread of AAV8 vectors is limited and transduction is mostly confined to the bleb area created in the superior hemi-retina, EGFP knockdown was expected to localise superior to the optic nerve. mGV was therefore quantified in the superior and inferior hemi-retina. Measurement of the mGV of the untransduced inferior retina provides a natural internal control of superior retinal BAF measurement, and the calculation of a ratio of signal from the superior to inferior retina. This ratio controls for variables that lead to inter-session and inter-eye variability in *in vivo* BAF measurement such as contact lens placement, pupillary dilation, corneal hydration and coupling fluid volume as observed in prior studies.[342,344] Additionally, mGV was measured with a circumferential band surrounding the optic nerve ('whole retina mGV') as described previously.[344]

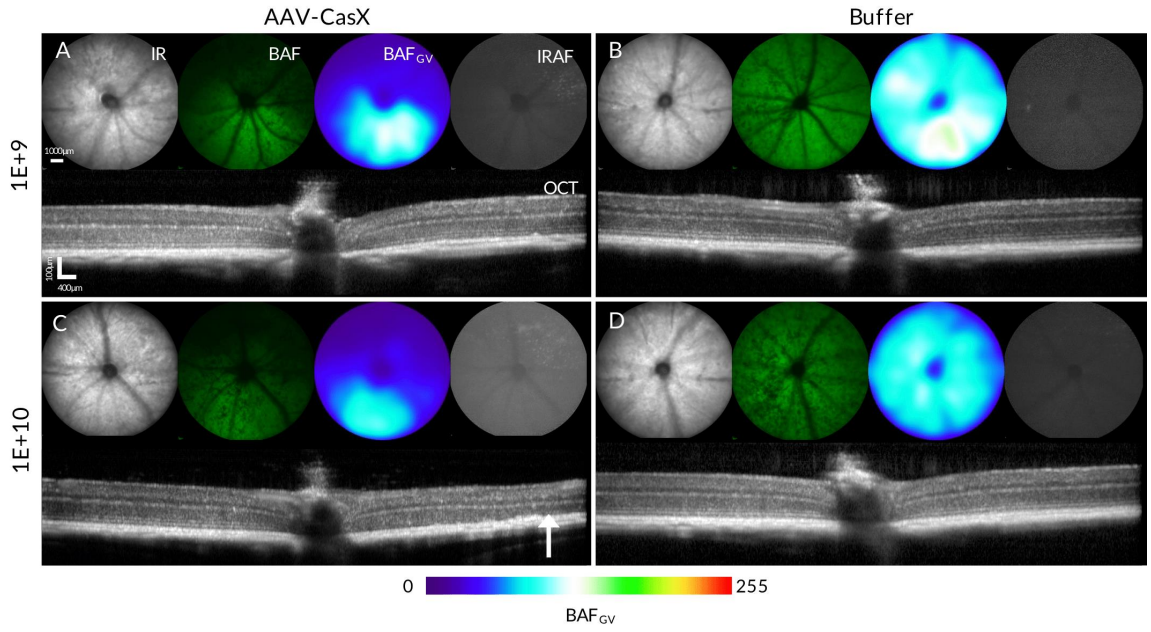


Figure 4-4 *In vivo* imaging of *Nrl.EGFP*$^{+/-}$ mice following subretinal injection
Retinal imaging of paired eyes from mice 4-weeks following subretinal injection with AAV.CasX or buffer at a 1E+9 (**A, B**) or 1E+10 (**C, D**) dose. For each panel, the top row shows CSLO fundus imaging using infrared reflectance (IR), blue autofluorescence (BAF), the grey value of blue autofluorescence quantified on a heat map scale (BAF_{GV}) with scale inset, and infrared autofluorescence. The bottom row shows an OCT B-scan from inferior (left) to superior (right). AAV.CasX treated retinas show superior hemi-retinal reduction in BAF. A punctate hyper-autofluorescent pattern in the IRAF channel is observed in the treated eyes, consistent with subretinal macrophage activity. This pattern was seen across both buffer and AAV treated eyes, although more commonly in the AAV treated eyes. OCT images demonstrate preservation of the normal retinal structure following injection. In the 1E+10 group, retinal thinning with loss of the hyper-reflective lines representing the ellipsoid zone and the external limiting membrane is seen superiorly (arrow).

At four weeks post-injection, superior retinal mGV in eyes injected with AAV-CasX were reduced compared to buffer injected paired control eyes ($F(1,22)=8.07$, $p=0.0095$ for effect of treatment) (Figure 4-5). On multiple comparison testing, a 44% reduction ($p=0.015$, 95% CI [8,80]) was seen in the 1E+10 group. No significant reduction was observed in the inferior retina, or the retina as whole. The superior:inferior mGV ratio demonstrated a significant reduction in superior EGFP expression due to AAV-CasX treatment ($F(1,22)=27.85$, $p<0.0001$ for effect of treatment), with a 24% ($p=0.01$, 95% CI [5, 43]) and 41% ($p=0.0006$, 95% CI [18, 63]) reduction in the 1E+9 and 1E+10 groups respectively.

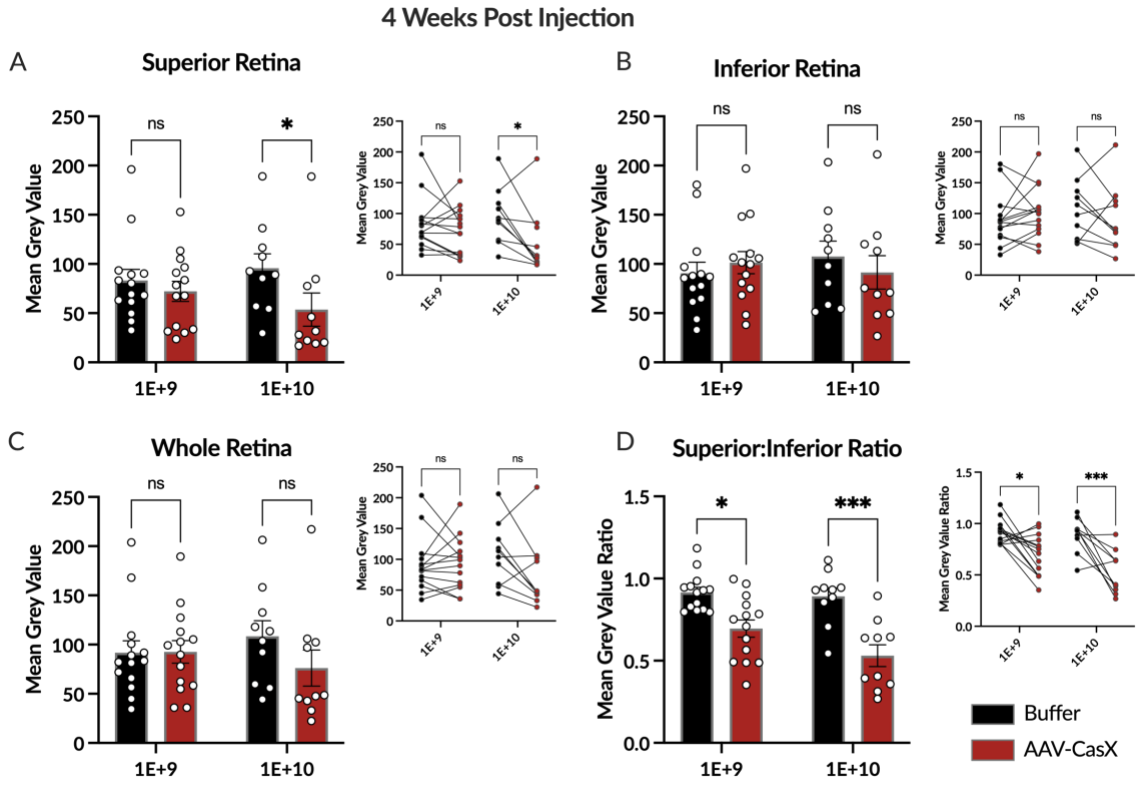


Figure 4-5 Fundus BAF mean grey value 4 weeks post injection
Quantification of mean grey value of BAF CSLO fundus imaging grouped by AAV dose in the superior (**A**) and inferior (**B**) hemi-retina, and the whole retina by a 360° sampling band (**C**). The superior:inferior ratio is calculated from the ratio of the mean grey value from the transduced superior to untransduced inferior retina (**D**). Analysis includes injection cohort 1 and 2 (1E+9 n = 14, 1e+10 n = 10). Bars demonstrate mean ± SEM, with dot plots showing difference between paired eyes. Two-way ANOVA with Sidak's multiple comparison testing. * $p < 0.05$, *** $p < 0.001$.

At 12 weeks post-injection, superior retinal mGV in eyes injected with AAV-CasX were reduced compared to buffer injected paired control eyes ($F(1,22)=16.83$, $p=0.0005$ for effect of treatment). This was reduced by 37% ($p=0.00284$, 95% CI [13,61]) in the 1E+9 group. While no significant difference was observed in the superior mGV in the 1E+10 group, a significant reduction in the superior:inferior ratio ($F(1,22)=22.64$, $p<0.0001$ for effect of treatment) was observed, with a 29% ($p=0.0047$, 95% CI [9,50]) reduction in the 1E+9 group and a 31% ($p=0.0062$, 95% CI [8,53]) reduction in the 1E+10 group.

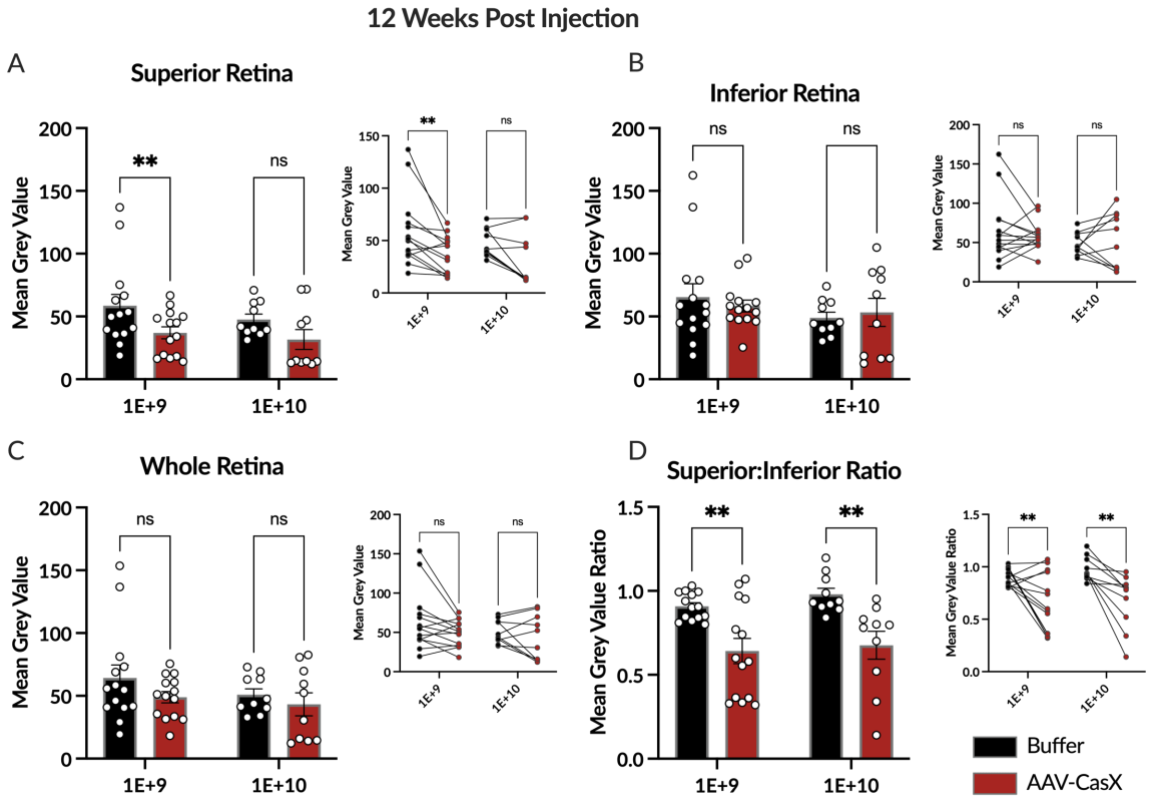


Figure 4-6 Fundus BAF mean grey value 12 weeks post injection
Quantification of mean grey value of BAF CSLO fundus imaging grouped by AAV dose in the superior (**A**) and inferior (**B**) hemi-retina, and the whole retina by a 360° sampling band (**C**). The superior:inferior ratio is calculated from the ratio of the mean grey value from the transduced superior to untransduced inferior retina (**D**). Bars demonstrate mean ± SEM, with dot plots showing difference between paired eyes. Two-way ANOVA with Sidak's multiple comparison testing. * $p < 0.05$, ** $p < 0.01$.

4.3.2 SD-OCT assessment of retinal structure following treatment

To assess retinal structure, SD-OCT was performed, and photoreceptor layer (PRL) thickness was measured. This is a sensitive measure of photoreceptor degeneration due to the effect of the surgery, or toxicity related to the AAV capsid or transgene. Given EGFP is expressed in rods, loss of rods in the PRL could account for reduction in GFP expression rather than due to CasX-mediated GFP inactivation.

Consistent with the BAF imaging, there was minimal surgery-related damage. The mean ratio of PRL thickness between the superior and inferior retina across all buffer injected groups

was 0.95 (95% CI [0.93, 0.96]) with no significant differences amongst the groups (F(3, 34)=0.5739, p=0.64, One-way ANOVA), indicating an approximate 5% loss of PRL thickness due to surgical trauma.

In the 1E+9 group, no PRL structural changes were observed at 4- or 12- weeks (Figure 4-7, Figure 4-8). Importantly, no focal thickness loss was observed in the superior retina at either timepoint in the 1E+9 dose, indicating a lack of toxicity specifically in the transduced area relative to the inferior retina.

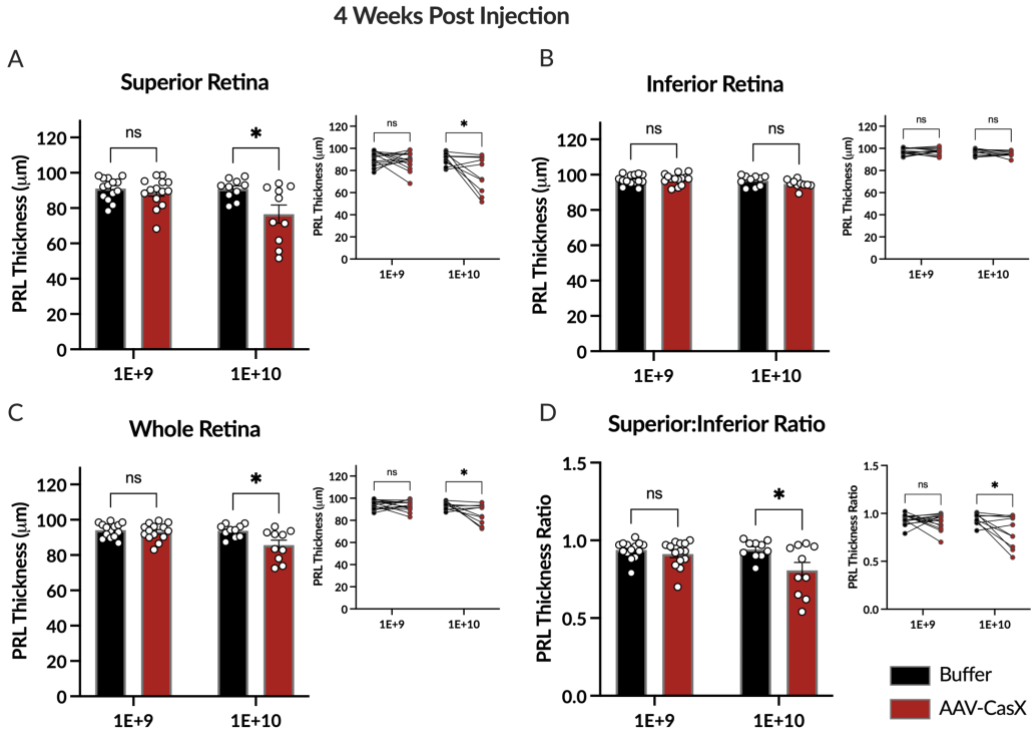


Figure 4-7 Photoreceptor layer thickness 4-weeks post-injection
Photoreceptor layer thickness was measured on SD-OCT images in the superior (**A**) and inferior (**B**) retina, and the whole retina (**C**, mean of superior and inferior retina). The ratio of superior to inferior thickness (**D**) quantified the superior thickness loss due to transduction. Analysis includes injection cohort 1 and 2 (1E+9 n = 14, 1e+10 n = 10). Bars demonstrate mean ± SEM, with dot plots showing difference between paired eyes. Two-way ANOVA with Sidak's multiple comparison testing. * $p < 0.05$.

Dose-related losses of superior PRL thickness were observed at both 4-weeks ($F(1, 22)=5.960$, $p=0.0231$) (Figure 4-7) and 12-weeks ($F(1,22)=11.84$, $p=0.0023$) (Figure 4-8), attributable to the high dose group. For mice injected with the 1E+10 dose, at 4-weeks post-injection superior retinal thickness was reduced in AAV relative to buffer injected eyes by 9% ($p=0.01$, 95% CI [2,15]), but relatively preserved in the inferior retina (Figure 4-7). By 12-weeks post injection a 32% ($p=0.0001$, 95% CI [16,47)]) reduction in superior PRL thickness was observed, with a small 7% ($p=0.007$, 95% CI [2,12]) loss in the inferior PRL. This effect was consistent with toxicity in the transduced superior retina due to AAV-CasX injection at the high 1E+10 dose, and can be clearly appreciated in the superior:inferior ratio of thickness, where the inferior retina acts as an internal control.

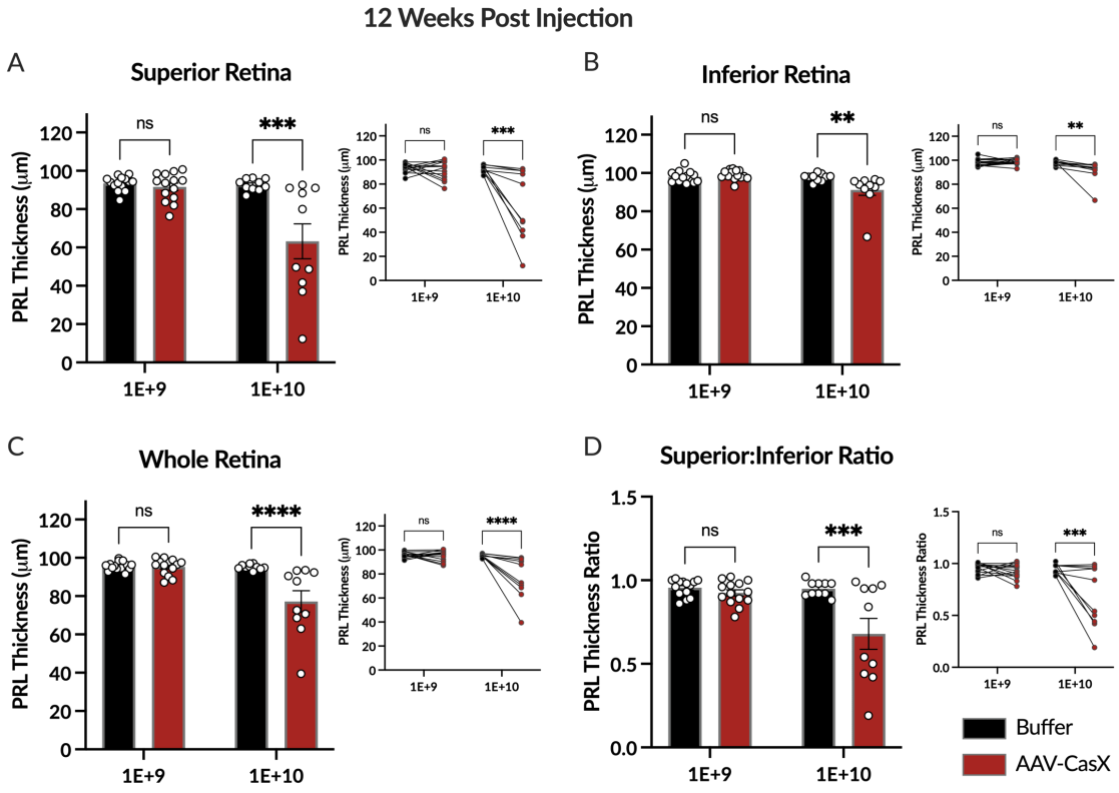


Figure 4-8 Photoreceptor layer thickness 12-weeks post-injection
Photoreceptor layer thickness was measured on SD-OCT images in the superior (**A**) and inferior (**B**) retina, and the whole retina (**C**, mean of superior and inferior retina). The ratio of superior to inferior thickness (**D**) quantified the superior thickness loss due to transduction. Bars demonstrate mean ± SEM, with dot plots showing difference between paired eyes. Two-way ANOVA with Sidak's multiple comparison testing. ** p <0.01 *** p < 0.001 **** p < 0.0001.

4.3.3 Molecular analysis of EGFP editing

To quantify on-target editing efficiency, DNA and protein were extracted from whole retinas with a small cohort of eyes from mice with unpaired injections culled at 4-weeks post-injection, and paired eyes from the imaging cohort culled at 12-weeks post-injection. Deep sequencing of the EGFP target site demonstrated editing activity in AAV.CasX treated eyes (Figure 4-9), with no editing detected in buffer injected eyes ($F(4,31)=6.811$, $p=0.0005$, one-way ANOVA). In the 1E+9 group, mean editing efficiencies of 6.7% (range 0-23%) and 4.5% (range 0-18%) were observed at 4- and 12-weeks respectively, however 2-3 retinas in each of these groups had undetectable editing. In the 1E+10 group, mean editing efficiencies of 14%

(range 0-36%, p=0.04) and 22% (range 1.5-46%, p<0.0001) were observed at 4- and 12-weeks respectively at rates significantly greater than the buffer injected eyes. In retinas where editing was undetectable, these samples were correlated with operative notes where a smaller bleb was noted. It is likely that a proportion of the variation in editing rates seen within groups can be attributed to variations in surgical success and bleb size.

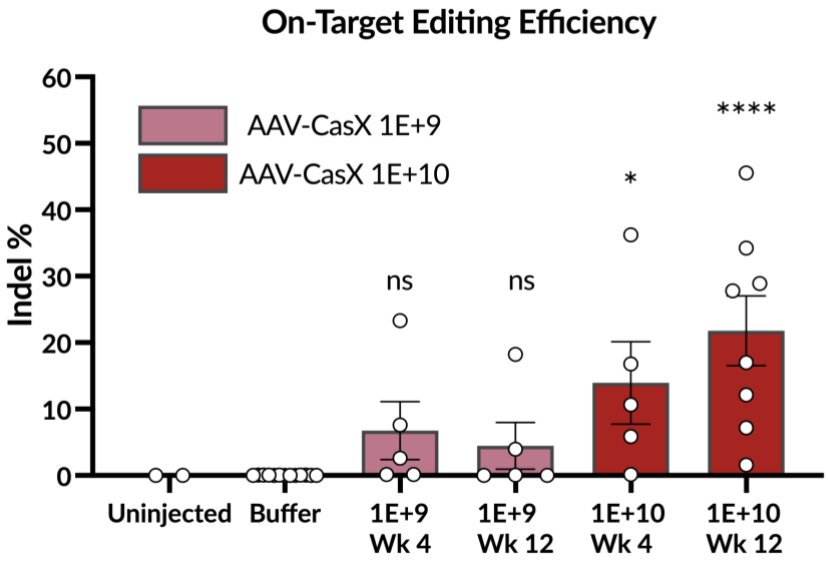


Figure 4-9 On-target editing efficiency following AAV.CasX injection
On-target editing efficiency was quantified by indel rates detected by deep sequencing at 4- and 12-weeks post-injection. Relative to buffer injected retinas, significant editing was detected at both time points with the 10E+10 dose. Mean ± SEM, one-way ANOVA relative to buffer control, Dunnet's *post hoc* test. * $p < 0.05$, **** $p < 0.0001$. Next generation sequencing performed by Cécile Fortuny, Scribe Therapeutics.

Western blot was performed on retinas from the 12-week post-injection cohort for which protein was also extracted, and EGFP knockdown was semi-quantitatively analysed by band densitometry. While in the 1E+9 group a significant difference in EGFP expression was not seen, a 25% (p=0.016, 95%CI [5,45]) reduction in EGFP expression was observed in the 1E+10 group relative to the buffer injected eyes, consistent with the 22% indel rate (Figure 4-10). NGS editing rates were significantly negatively correlated with the level of EGFP knockdown

measured by western blot (r=-0.82, p=0.0005) and also by the superior-inferior mean grey value ratio from *in vivo* BAF imaging (r=-0.90, p=0.0002).

Levels of CasX expression in each sample were then assessed using an antibody to the c-terminal HA tag on the CasX protein. Overall, higher transgene expression was observed in samples treated with the 1E+10 dose than the 1E+9 dose. A positive relationship between CasX expression and editing was observed, with samples with greater CasX expression also demonstrating higher editing rates and lower EGFP expression.

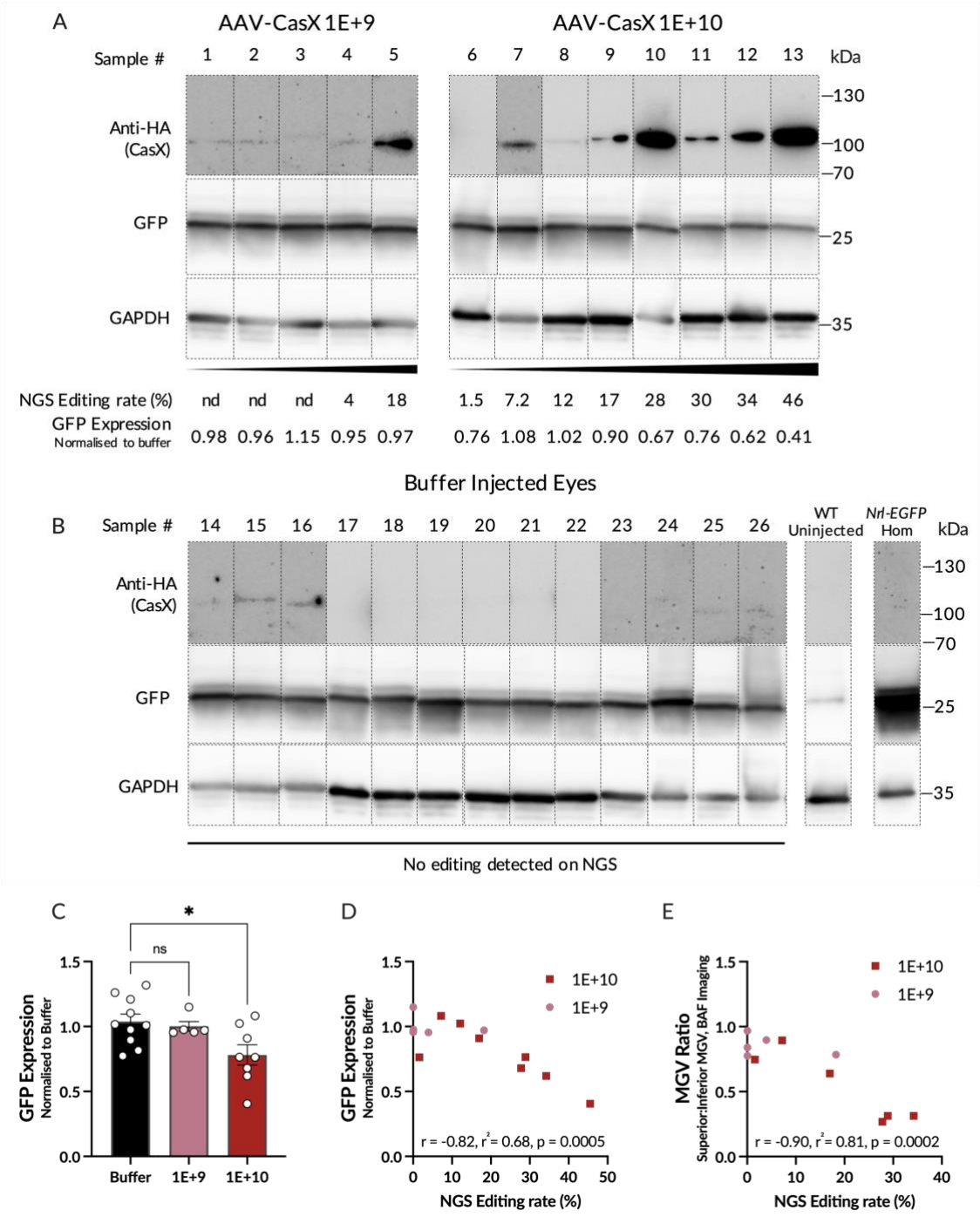

A
AAV-CasX 1E+9
AAV-CasX 1E+10
Sample # 1 2 3 4 5 6 7 8 9 10 11 12 13 kDa
Anti-HA (CasX)
GFP
GAPDH
130
100
70
25
35
NGS Editing rate (%) nd nd nd 4 18 1.5 7.2 12 17 28 30 34 46
GFP Expression Normalised to buffer 0.98 0.96 1.15 0.95 0.97 0.76 1.08 1.02 0.90 0.67 0.76 0.62 0.41
Buffer Injected Eyes
B
Sample # 14 15 16 17 18 19 20 21 22 23 24 25 26 WT Uninjected Nrl-EGFP Hom kDa
Anti-HA (CasX)
GFP
GAPDH
130
100
70
25
35
No editing detected on NGS
C
GFP Expression Normalised to Buffer
ns
*
Buffer
1E+9
1E+10
D
GFP Expression Normalised to Buffer
1E+10
1E+9
r = -0.82, r² = 0.68, p = 0.0005
NGS Editing rate (%)
E
MGV Ratio Superior:Inferior MGV, BAF Imaging
1E+10
1E+9
r = -0.90, r² = 0.81, p = 0.0002
NGS Editing rate (%)

Figure 4-10 Analysis of protein expression in AAV.CasX injected retinas
A. Western blot of transduced retinas at 1E+9 and 1E+10 doses, with samples ordered from left to right by escalating editing rate determined by NGS. A positive relationship between CasX expression and editing is seen. Higher editing rates and lower EGFP expression is seen in samples with higher levels of CasX expression detected with an anti-HA antibody. **B.** Western blot of retinas injected with buffer control. No CasX expression is observed in buffer injected eyes although faint bands are seen in samples 15 and 16. **C.** Band densitometry of EGFP expression relative to the mean of EGFP expression in buffer injected eyes. Mean ± SEM, one-way ANOVA. * $p < 0.05$. **D.** A negative correlation is observed between NGS editing rate and EGFP expression measured by band densitometry. **E.** A negative correlation is observed between NGS editing rate and EGFP expression measured by the superior:inferior mean grey value ratio on CSLO BAF imaging. Correlation of ungrouped data calculated with Pearson's R. Western blot performed by Cécile Fortuny, Scribe Therapeutics.

4.3.4 Immunohistochemistry and microscopy of treated retinas

In addition to analysis by western blot, retinas from two mice from each dose were processed for immunohistochemistry. Tiled overview scans using LED microscopy demonstrated EGFP knockdown throughout the superior retina in the AAV.CasX treated eyes. Retinal structure was broadly preserved in treated eyes, with some retinal thinning in the 1E+10 dose commensurate with the PRL thinning observed with OCT (Figure 4-11). Confocal microscopy revealed dropout of EGFP positive inner segments and nuclei in the ONL, with near complete loss of EGFP in the superior retina at the 1E+10 dose. Staining for CasX expression using an anti-HA antibody demonstrated reactivity throughout the ONL, IS and OS. Tiled confocal imaging across the bleb border revealed a gradient loss of EGFP signal and increase in CasX expression, demonstrating EGFP knockdown only in areas of AAV transduction (Figure 4-12).

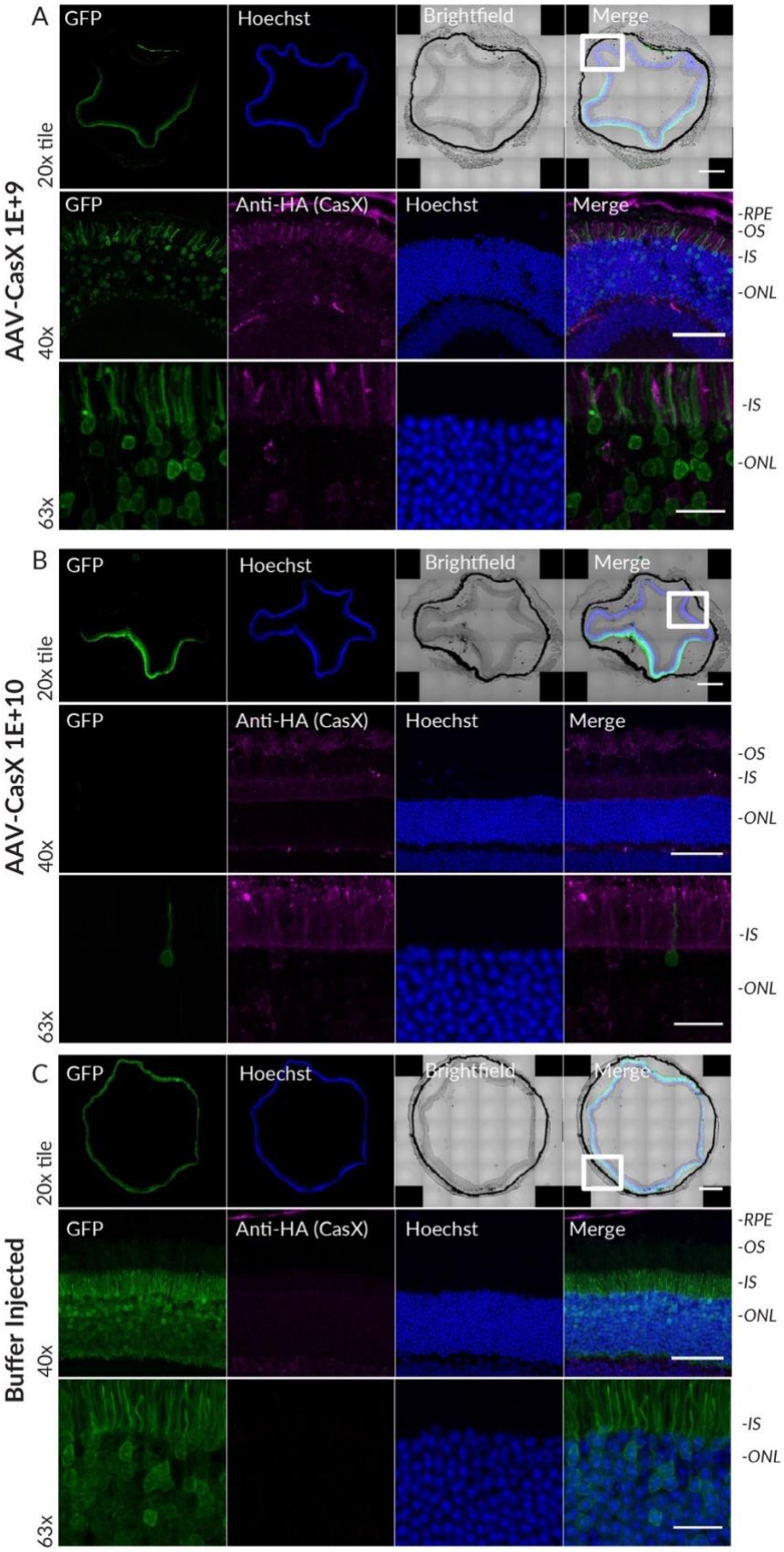

A
GFP
Hoechst
Brightfield
Merge
20x tile
AAV-CasX 1E+9
GFP
Anti-HA (CasX)
Hoechst
Merge
-RPE
-OS
-IS
-ONL
40x
-IS
-ONL
63x
B
GFP
Hoechst
Brightfield
Merge
20x tile
AAV-CasX 1E+10
GFP
Anti-HA (CasX)
Hoechst
Merge
-OS
-IS
-ONL
40x
-IS
-ONL
63x
C
GFP
Hoechst
Brightfield
Merge
20x tile
Buffer Injected
GFP
Anti-HA (CasX)
Hoechst
Merge
-RPE
-OS
-IS
-ONL
40x
-IS
-ONL
63x

Figure 4-11 Immunofluorescence analysis of retinas following AAV.CasX treatment
Retinal sections with endogenous EGFP fluorescence from *Nrl.EGFP* mice treated with AAV.CasX, stained with an anti-HA antibody. Overview 20× LED microscopy tile scans (top row) were taken to demonstrate knockdown pattern, with the superior retina at the top of the image. Confocal images were taken at 40× and 63× magnification. **A.** At the 1E+9 dose, partial EGFP knockdown in the superior retina is seen in the overview scan. At higher magnification, dropout of EGFP positive nuclei and outer segments is observed. CasX staining is seen in the photoreceptor nuclei and inner segments. **B.** 1E+10 dose, with almost complete loss of EGFP expression in the injected superior retina. One EGFP positive rod can be seen in the 63× image. **C.** Strong EGFP expression is seen throughout the retina in the buffer injected control. Signal in the RPE in the mouse anti-HA (CasX) channel is seen in the buffer injected controls, due to mouse-on-mouse non-specific primary binding. Scale bars: 20× = 500 μm, 40× = 50 μm, 63× = 15 μm. RPE = retinal pigment epithelium, OS = outer segment, IS = inner segment, ONL = outer nuclear layer

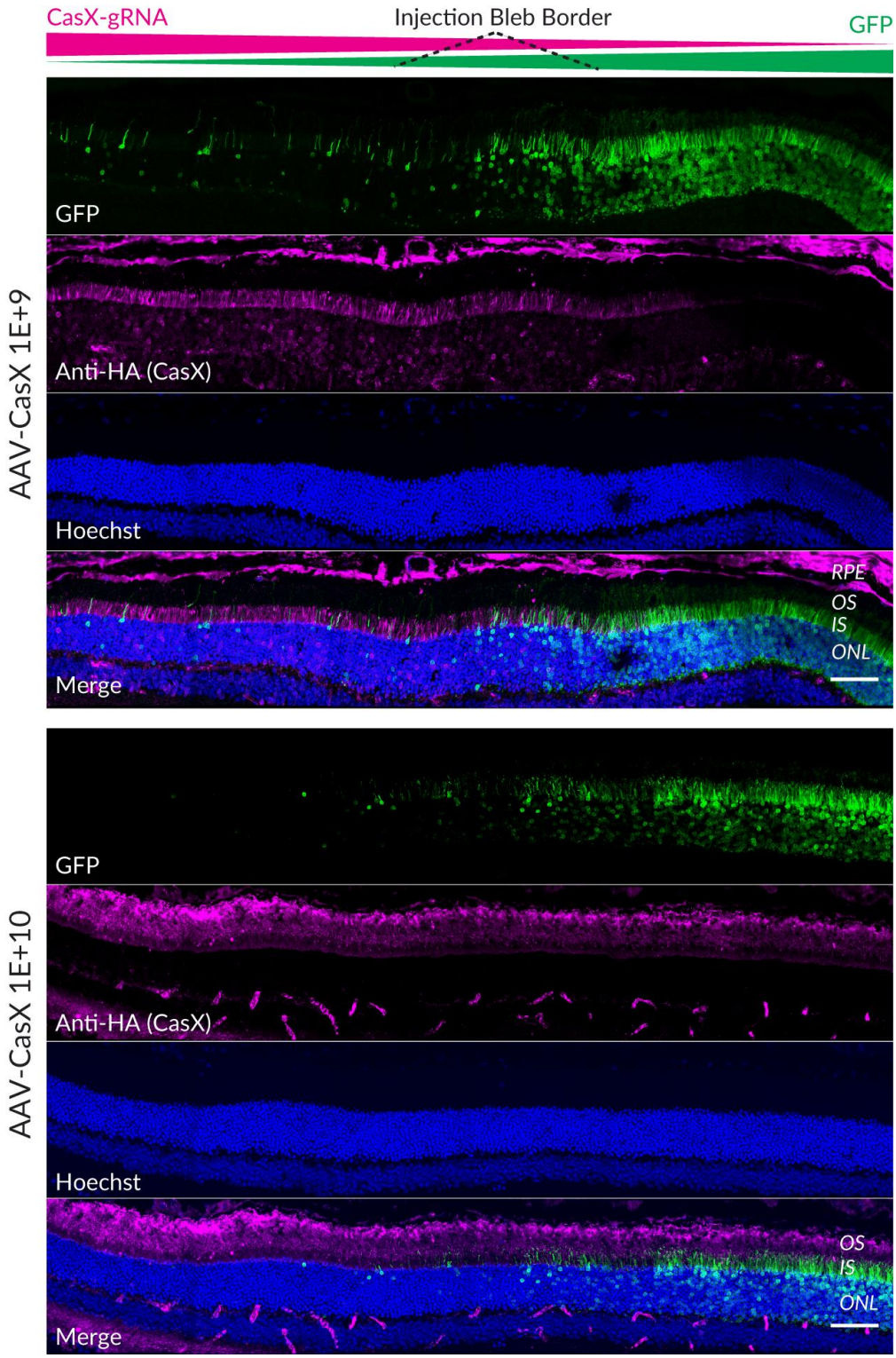


Figure 4-12 Confocal imaging across the bleb border in AAV.CasX injected eyes
Tiled confocal microscopy imaging across the transduced bleb border demonstrating EGFP knockdown in areas of CasX (anti-HA) expression, and EGFP preservation outside the transduced area in both 1E+9 and 1E+10 doses. Mouse-on-mouse background signal is observed to stain the RPE and retinal vasculature. Scale = 50 μm. RPE = retinal pigment epithelium, OS = outer segment, IS = inner segment, ONL = outer nuclear layer

4.3.5 Electroretinogram assessment of retinal function following treatment

Finally, at week 10 post-injection ERG was performed to assess retinal function. Full-field dark-adapted ERG demonstrated no difference in a-wave ($F(1,30)=0.66$, $p=0.42$, two-way ANOVA for effect of treatment) or b-wave ($F(1,62)=0.028$, $p=0.87$) responses in the 1E+9 group relative to paired buffer injected eyes. In the 1E+10 group, a significant reduction in dark-adapted b-wave amplitudes is seen between the AAV and buffer injected eyes ($F(1,71)=66.53$, $p<0.0001$), but no difference was observed in a-wave amplitudes ($F(1,35)=2.53$, $p=0.12$). The dark adapted weak 0.1 cd.s/m^2 flash characterises rod photoreceptor responses in the a-wave, with the b-wave characterising rod-initiated bipolar on-pathways. At this flash strength no change was seen in the a-wave at either the 1E+9 dose or 1E+10 dose. A 22% reduction ($p=0.0029$, 95% CI [8, 36]) in the b-wave amplitude was seen in the 1E+10 group, a change of similar magnitude to the PRL thinning seen on OCT.

To isolate cone function, a dark- and light-adapted flicker stimulus series was used to provide flashes at a frequency greater than rod integration and recovery periods. Across both doses, no differences in flicker response amplitudes were seen between buffer and AAV injected eyes. In a light-adapted single flash protocol, a 19% reduction ($p=0.0064$, 95% CI [6,32]) in b-wave amplitude was seen in response to a bright 10 cd.s/m^2 light-adapted flash in the 1E+10 group, reflecting a reduction in on- and off-bipolar cell responses.

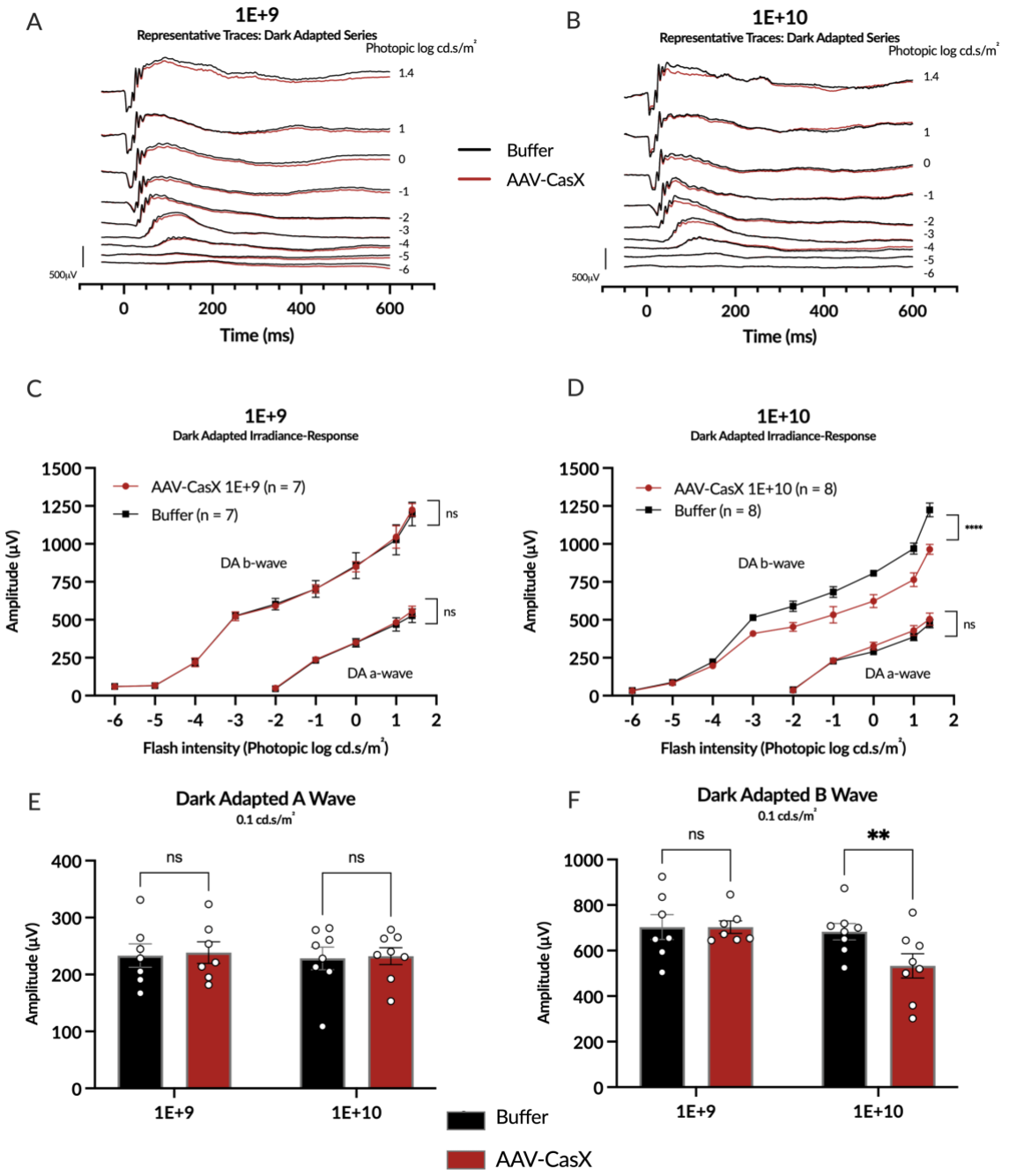


Figure 4-13 Retinal function assessed with dark adapted ERG

Full-field dark-adapted ERG irradiance-response curves in mice with paired buffer and AAV-CasX injections at 10-weeks post-injection. (**A & B**) Representative traces are shown from animals in the 1E+9 and 1E+10 dose groups. (**C & D**) For each dose a- and b-wave amplitudes are plotted. Two-way ANOVA for effect of treatment ****$p<0.00001$. **E.** Dark adapted a-wave amplitudes compared at 0 photopic log cd.s/m^2. **F.** Dark adapted b-wave amplitudes compared at 0.1 cd.s/m^2. Two-way ANOVA for effect of treatment, Sidak multiple comparisons. **$p<0.01$. Mean ± SEM.

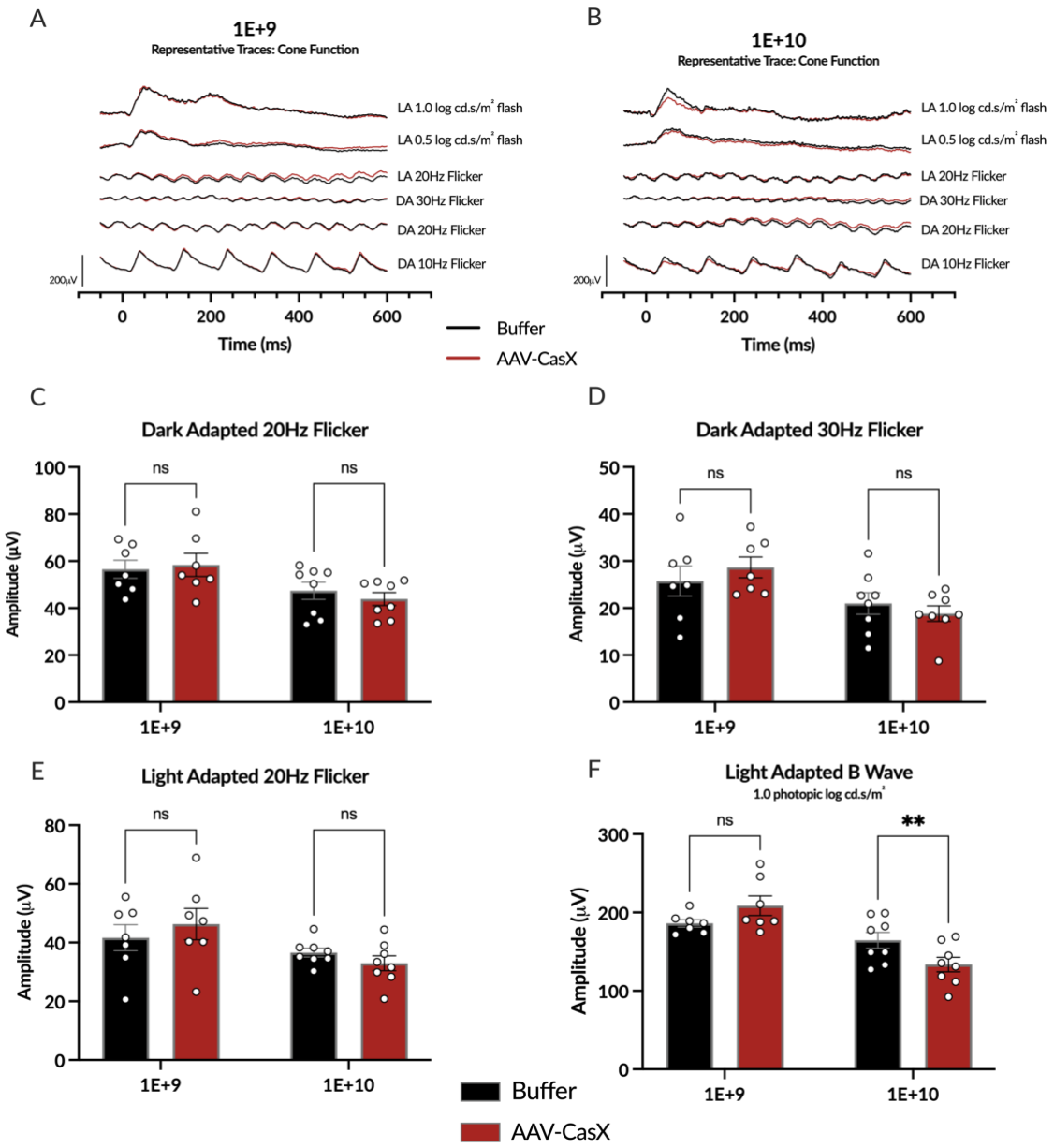


Figure 4-14 Tests of cone function with flicker and light-adapted ERG

To test for cone dysfunction, a flicker series was performed at a range of frequencies following both dark and light adaption, in addition to full-field light-adapted single flash series in mice with paired buffer and AAV-CasX injections at 10-weeks post-injection. (**A & B**) Representative traces are shown from animals in the 1E+9 and 1E+10 dose groups. (**C-E**) Flicker response amplitudes in both dark adapted and light adapted flicker. No differences were observed at any flicker frequency. **F.** Light adapted b-wave amplitudes compared at 1.0 photopic log cd.s/m². All tested with two-way ANOVA for effect of treatment, Sidak multiple comparisons. **p<0.01. Mean ± SEM.

4.4 Discussion

Gene editing strategies that use CRISPR-Cas to introduce indels and produce a permanent knockout of gene function hold great potential for human therapeutic use. In the retina, these strategies may be especially useful for conditions where a reduction in the expression of a toxic gene product is required, such as autosomal dominant RP caused by rhodopsin mutations. Successful approaches will critically depend on optimised and tissue specific delivery of a highly active molecule at a therapeutic dose, as elegantly demonstrated in recent clinical trials for the treatment of transthyretin amyloidosis using CRISPR-induced knockout in the liver.[329]

In this chapter, therefore, we sought to characterise the *in vivo* efficacy of CasX, a promising, novel, engineered Cas nuclease and gRNA delivered to the retina using a single AAV vector using two different doses. Building upon *in vitro* data (unpublished, Scribe Therapeutics) suggesting this was a highly active system, we sought to understand the on-target editing efficiency in post-mitotic rod photoreceptors by targeting endogenous *EGFP* expressed specifically in rods. Further, we sought to investigate dose-related efficacy and toxicity to provide an indication of the optimal dose for future studies.

On-target editing efficiency was evaluated using *in vivo* CSLO retinal imaging, deep sequencing, western blot, and histology. At the 1E+9 dose a mean on-target editing efficiency of 4.5-6.7% with rates of up to 18% was observed. This correlated with a 24% and 29% EGFP reduction detected on CSLO imaging at 4- and 12-weeks respectively. Significant EGFP knockdown on western blot was not appreciated in the 12-week group retinas analysed. At the 1E+10 dose, on-target editing was observed at 14% at 4-weeks rising to 22% at 12-weeks post-injection, with rates of up to 46%. This correlated with a 41% and 33% reduction in EGFP knockdown detected on CSLO at 4- and 12-week respectively, and a 25% reduction in EGFP on western blot. Notably, editing efficiency and measures of EGFP knockdown were correlated amongst individual samples, confirming the validity of *in vivo* imaging. Editing rates obtained by whole-retina NGS likely substantially under-estimate the true editing rate in transduced cells.

Firstly, the EGFP locus is present in all retinal cells, but the construct is only being expressed in photoreceptors. Secondly only approximately 30-50% of rods will be transduced by a reasonable-sized subretinal bleb. Similar studies[225] have used a correction factor of 3.3 to obtain an estimate of a 'productive editing rate', which in this case would be a mean of 16% at the 1E+9 dose and 73% at the 1E+10 dose at 12-weeks post-injection. In the example of the retina that achieved a 46% editing rate, it is likely that at least 50% of the retina was transduced, and this would result in a productive editing rate of upwards of 90%. This productive editing rate would be consistent with the effect of knockdown observed on retinal imaging and in the significant knockout observed on immunofluorescence of retinal sections.

These data support that CasX-mediated editing is causally linked to EGFP knockdown. Assessment of CasX expression using western blot clearly demonstrated a positive relationship between editing rate and level of transgene expression. Assessment of CasX expression with histology demonstrated that EGFP reduction occurred specifically in transduced cells. Furthermore, they show the *Rho* promoter drives CasX expression in photoreceptors where EGFP is expressed, concordant with studies that have demonstrated the *Rho* promoter to be rod-specific.[390] While it is not possible to quantify the effect that PRL thinning observed in the 1E+10 dose had on EGFP expression, these data suggest it is unlikely that this solely underpinned the EGFP knockdown observed in this group.

Assessment of the effect of AAV.CasX on retinal structure and function were undertaken with OCT and ERG respectively. These modalities successfully demonstrated the safety of the 1E+9 dose and established a dose limiting toxicity at 1E+10, with the higher dose causing a 32% reduction in PRL thickness and ~20% reductions in dark- and light-adapted b-wave amplitudes. These functional changes could not be directly attributed to rod- or cone-photoreceptor function quantified through changes to amplitudes of the dark-adapted a-wave or flicker responses respectively. It is not possible from this data to attribute these to reaction to the AAV capsid or to levels of transgene expression and high doses of AAV in the range of

1E+10 are known to causes toxic effects in the mouse retina.[391,392] This has established a therapeutic dose range for future studies. Further studies should investigate other safety aspects, including genotoxicity, immune responses, and systemic vector distribution. While limited histological analysis demonstrated no gross abnormalities in the retinas examined, further studies to investigate retinal immune responses will be warranted at chosen doses in future studies.

This is the first physiological and histological evaluation of CasX for *in vivo* retinal editing. As described in detail in the general introduction, studies have delivered other Cas orthologues to the retina using a variety of approaches. Many of these however, have delivered transgenes to neonatal (P0-P7) retinas[209, 218–221, 223,260,261] where photoreceptors are immature, rods have not yet exited the cell cycle and the outer limiting membrane remains poorly developed. These factors are known to affect both AAV transduction and CRISPR editing.[393,394] This study was designed to assess a more clinically relevant time point with delivery to post-mitotic rods, and assess editing rate without selecting for transduced cells. To date, only one group has sub-retinally injected an all-in-one AAV-CRISPR construct to mice, using SaCas9 to achieve a corrected 'productive editing rate' (± SD) of 44% ± 20 at 1E+9 gc/eye, 60% ± 30 at 3E+9 gc/eye and 25% ± 13.5 at 1E+10 gc/eye.[225] Similar to the rates achieved here, they also suggest a dose range of 1-3E+9 appears to achieve optimal editing without toxicity.

This data has two key limitations. Firstly, due to technical difficulties with subretinal injections, a smaller sample size with bilateral uncomplicated injections was achieved than initially planned. These technical factors also likely contributed to greater variability in bleb sizes and subsequent data variability. To address this, a second cohort was injected under identical conditions with improved surgical success. This cohort contributed to the greater number of eyes available for *in vivo* analysis, with further molecular analysis after the 12-week time point being completed by Scribe Therapeutics at time of writing.

A second limiting factor was the use of only a buffer injected control in the paired eye. This was chosen to control for the effects of surgical trauma, buffer-related toxicity and to assess efficacy and toxicity attributable to AAV.CasX on GFP knockdown and retinal function and structure. The addition of further groups comparing an AAV.CasX vector with a non-targeting gRNA to a buffer control, and directly comparing AAV.CasX with targeting and non-targeting constructs in paired eyes was considered, however not undertaken in this pilot study due to constraints on time and animal numbers required by testing two doses. These controls would have allowed further analysis of gRNA independent effects of AAV.CasX treatment. Furthermore, as off-target analysis was not a primary outcome specified in this study, a non-targeting control was not required for this. Non-targeting controls have now been incorporated into ongoing studies in disease models to obtain these data.

This study developed an automated method of quantifying EGFP knockdown *in vivo* using a FIJI macro to measure the mean grey value of CSLO images in the superior and inferior retina. Previous studies have not used this to quantify EGFP expression specifically at the bleb site, and this provided a more sensitive measure of knockdown. Inter-eye and inter-session variability are significant issues in rodent BAF imaging, and this provides an internal control with the inferior retina normalising the measured mean grey value for that imaging session. One drawback of this approach is that if parts of the inferior retina are transduced, this may result in a reduction in BAF in the inferior retina. While this was not commonly seen in any of the imaging in this study, at worst this leads to a slight under-estimation of superior BAF knockdown. It was found in this study that obtaining well-balanced and exposed images is critical to accurate quantification, and that this does increase the time required to obtain useful images. It was noted that the brightness of EGFP decreased with age in buffer injected eyes, which is presently unexplained but may be a result of increasing eye size with a fixed number of post-mitotic rods distributed over a greater retinal area with age.

4.4.1 Conclusion

Taken together these results support that CasX can be safely and effectively delivered within an AAV vector via subretinal injection to edit the genome of post-mitotic rods. This will enable further studies that will aim to use an AAV.CasX construct to ameliorate the phenotype of relevant disease models, where further studies of safety and efficacy can be undertaken.

5

ANALYSIS OF PATHOGENIC VARIANTS CORRECTABLE WITH CRISPR BASE EDITING AMONG PATIENTS WITH RECESSIVE INHERITED RETINAL DEGENERATION

5.1 Introduction

AAV vectors are a popular delivery method for retinal gene therapy however a key limitation is that many genes implicated in recessively inherited IRDs have coding sequences that exceed the ~4.7kb capacity of a single AAV vector. These large genes are therefore not easily treatable with AAV-gene therapy, notwithstanding advances made to deliver large genes with strategies such as dual-AAV gene therapy.[79]

A potential therapeutic alternative for these large genes is to use gene editing to correct the endogenous genetic sequence. Tools such as the CRISPR-Cas system enable the precise and efficient alteration of nucleic acids.[194] As described in the general introduction, base editors are a class of gene editing tool that can directly create point mutations at specified loci in DNA or RNA.[244]

Text, figures and tables from this chapter have been published as: Fry LE, McClements ME, MacLaren RE. Analysis of Pathogenic Variants Correctable With CRISPR Base Editing Among Patients With Recessive Inherited Retinal Degeneration. JAMA Ophthalmol. 2021;139:319. DOI: 10.1001/jamaophthalmol.2020.6418.

DNA base editors are capable of repairing all four transition variants (C>T, G>A, T>C, A>G) through hydrolytic deamination.[244] Cytosine base editors convert a C-G into a T-A base pair, while adenine base editors convert an A-T to a G-C base pair. Unlike other gene correction methods, base editing does not require the generation of double stranded breaks in DNA[218,225] or require a donor template of DNA for repair.[230,238]

RNA base editors predominantly can mediate adenosine to inosine (A>I) transitions in targeted RNA loci through the action of ADAR deaminase. Inosine is read as guanosine by cellular machinery, effectively mediating an A>G change in messenger RNA.[288] Additionally, alternative deaminase enzymes have been engineered to also mediate cytosine to uracil conversions.[303,306] Together these allow the directed correction of G>A and T>C genomic variants in RNA. One potential benefit of RNA editors, is that edits to transient RNA molecules are not permanent, theoretically reducing the impact of off-target editing relative to the permanent changes introduced by DNA base editors.[288]

Over 270 genes have been implicated in the pathogenesis of IRD.[395] Base editing strategies must necessarily be focused on individual single nucleotide variants within those genes. It is therefore important to know which genes, and which pathogenic variants within those genes, should be prioritised for the development of a base editing therapeutic.

To focus the scope of this analysis, the six most commonly occurring large recessive genes in patients with a molecular diagnosis identified from four recent, large and geographically diverse cohorts of 6986 patients with an IRD (Table 5-1).[31, 95,96,396] Each of these genes has a coding sequence that exceeds the packaging capacity of a single AAV vector. These genes included ATP-binding cassette, subfamily A, member 4 (*ABCA4*; mean [SD] prevalence, 20.0% [2.4%]); Usher syndrome, type 2A (*USH2A*; 8.0% [2.0%]); myosin 7A (*MYO7A*; 1.6% [0.4%]); eyes shut homologue (*EYS*; 2.5% [1.8%]); centrosomal protein, 290-KD (*CEP290*; 2.3% [2.3%]); and Usher syndrome, type 1D (*CDH23;* 0.5% [0.1%]). These genes cumulatively accounted for 35% of all individuals with IRD in these studies.

It is currently unknown how many pathogenic variants in these genes might be editable (i.e., how many are transition variants that could potentially be corrected with a base editor) and what the most commonly occurring editable alleles are for each gene. It is also unknown how many patients might have editable alleles.

5.1.1 Chapter Aims

This chapter seeks to establish a roadmap to guide the direction of the development of base editing strategies towards pathogenic variants that affect the greatest number of patients that are currently not easily treatable with AAV gene supplementation strategies. Using large data sets from the Leiden Open Variation Database (LOVD) and from IRD patients diagnosed in tertiary referral hospital genetics services in the United Kingdom (UK) and from previously published data from Stone et al[95] from the United States of America (USA), it aims to:

1. Identify the most common pathogenic transition variants that are potentially correctable with currently available base editing tools among the most common six large genes that cause recessively inherited retinal degeneration.
2. Identify amongst a cohort of patients with IRD, the proportion of patients with one of these common genes that have a pathogenic variant potentially correctable with base editing.

Gene	Range of phenotypes	CDS (kb)	Prevalence, number of individuals (%)				Mean % (SD)
			UK[31] (n = 4236)	USA[95] (n = 760)	Brazil[396] (n = 400)	Israel[96] (n = 1590)†	
ABCA4	Stargardt macular dystrophy, cone-rod dystrophy	6.8	789 (18.6)	173 (22.8)	84 (21.0)	278 (17.5)	20.0 (2.4)
USH2A	RP, Type 2 Usher syndrome	15.6	342 (8.1)	76 (10.0)	21 (5.3)	133 (8.4)	8.0 (2.0)
MYO7A	Type 1 Usher syndrome	6.6	58 (1.4)	8 (1.1)	8 (2.0)	29 (1.8)	1.6 (0.4)
EYS	RP	9.4	43 (1.0)	6 (0.8)	16 (4.0)	64 (4.0)	2.5 (1.8)
CEP290	LCA, Joubert syndrome, ciliopathies	7.4	35 (0.8)	18 (2.4)	22 (5.5)	6 (0.4)	2.3 (2.3)
CDH23	Type 1 Usher syndrome	10.1	20 (0.5)	4 (0.5)	0	1 (0.1)	0.5 (0.1)
All Genes	*NA*		1287 (30.4)	285 (37.5)	151 (37.8)	511 (32.1)	34.6 (3.7)

Table 5-1 Prevalence of the most common six large recessive genes among patients with a molecular diagnosis of inherited retinal disease
Prevalence of the large recessive genes with a coding sequence greater than the AAV packaging capacity of 4.7kb analysed in this study in recent large, published cohorts of individuals with a molecular diagnosis of an inherited retinal disease. †n = families, rather than individuals. RP = retinitis pigmentosa LCA = Leber's congenital amaurosis CDS = Coding sequence length UK = United Kingdom, USA = United States of America

5.2 Methods

5.2.1 Leiden Open Variation Database Search and Variant Coding

Variants in the Leiden Open Variation v3.0 Inherited Retinal Disease gene variant database[148] (https://databases.lovd.nl/shared/genes/) were downloaded on September 6th 2019 for the following genes: *ABCA4* (OMIM 601691; NM_000350.2), *CEP290* (OMIM 610142; NM_025114.3), *CDH23* (OMIM 601067; NM_022124.5), *EYS* (OMIM 612424; NM_001142800.1), *MYO7A* (OMIM 276903; NM_000260.30), *USH2A* (OMIM 276901; NM_206933.2). The *CEP290* LOVD contains records derived from the Gent *CEP290* database (https://cep290base.cmgg.be/).[397] The Gent database was filtered for pathogenic variants only and downloaded. Records in the Gent and LOVD *CEP290* databases were combined, and duplicate entries were excluded to yield a single dataset.

LOVD records were processed according to the flow diagram in Figure 5-1. Records were cleaned and coded for pathogenicity and mutational consequence. Where variant pathogenicity was not annotated, variants were cross-referenced with the pathogenicity comprehensively labelled in Messchaert et al.[398] (for *EYS)*, Cornelis et al.[399] (for *ABCA4)* and the Gent database (for *CEP290)*. The *USH2A*, *MYO7A* and *CDH23* datasets were complete in annotations for pathogenicity. Where variant pathogenicity uncertainty remained, this was checked using ClinVar,[400] literature sources, or excluded from analysis if it could not be determined. Benign, likely benign and variants of unknown significance were excluded to yield a final dataset of 'likely pathogenic' or 'pathogenic' variants. Each variant was categorized by expected mutation consequence as 'Termination', 'Missense', 'Synonymous', 'Untranslated region', 'Intronic', 'Splice', 'Insertion/Duplication/Deletion', 'Unknown'. 'Termination' was defined as an SNV generating a stop codon, 'Splice' as disrupting a canonical splice donor (+1, +2 position relative to the exon/intron boundary) or acceptor (-2, -1) site, and 'Intronic' variants as occurring

between the intronic +3 to -3 positions. Complex alleles harboring more than one pathogenic variant were classified as un-editable alleles.

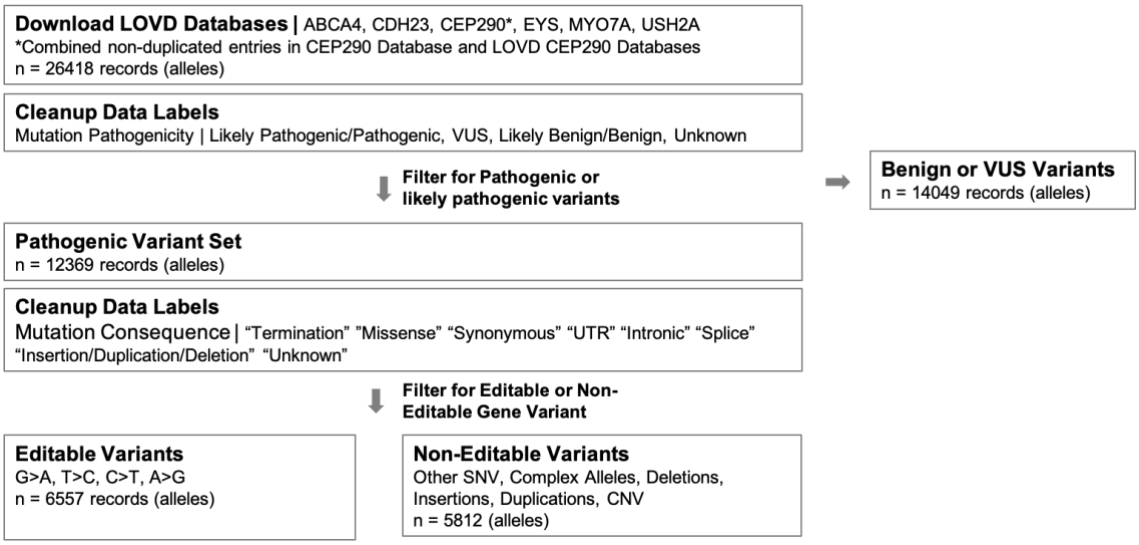


Figure 5-1 Flow diagram outlining method of LOVD analysis
Data downloaded from LOVD were processed to yield a final data set of pathogenic variants for analysis

5.2.2 Analysis of variants by individual

Analysis was conducted on a list of previously collected non-identifiable variants identified retrospectively by the Oxford University Hospitals (OUH) Medical Genetics Laboratories for patients referred for a suspected IRD between July 2013-November 2019.

Details of the pipeline for genetic diagnosis at the Oxford Medical Genetics Laboratory are described in detail by Shah et al.[29] As data analysed in this chapter was already generated as part of another study,[29] these methods did not form part of the work in this thesis. Briefly, patients are referred for genetic diagnosis using one of 11 next generation sequencing (NGS) panels as indicated by the clinical phenotype. Pooled, multiplexed NGS sequencing was undertaken on an MiSeq instrument (Illumina) using a MiSeq v3 kit as per the manufacturer's instructions. Custom bioinformatics pipelines developed by the Oxford Medical Genetics Laboratory were used by Laboratory staff to analyse the NGS data, which used Burrows-

Wheeler Alignment algorithms to align reads[401] and Platypus software to call variants.[402] Copy number variation (CNV) calling was performed on NGS data using the custom application Dosage Quotients for Massively Parallel Sequencing.[29] Suspected CNVs were confirmed using Multiplex Ligation-dependent Probe Amplification techniques.[29] Assignment of pathogenicity was based on the American College of Medical Genetics guidelines.[403] Variants were classified as either highly likely to be pathogenic (class 5), likely to be pathogenic (class 4) or a variant of uncertain significance (class 3).

Records were filtered to yield only patients with biallelic class 5 or class 4 variants in *ABCA4*, *CEP290*, *CDH23*, *EYS*, *MYO7A*, *USH2A*. The mutation consequence of each variant was labelled as described for the LOVD analysis. CNVs or complex alleles harboring more than one variant were classified as un-editable.

Further validation analysis using the same methods was conducted on previously published data by Stone et al.[95]

5.2.3 Statistics and analysis

Data were analysed using Prism 8 (GraphPad Software, USA) and Excel (Microsoft, USA). Data were presented as descriptive statistics and means were reported with standard deviation (SD) where appropriate. This study followed the Strengthening the Reporting of Observational Studies in Epidemiology (STROBE) reporting guideline for cross-sectional studies.

5.3 Results

5.3.1 Prevalence of Editable Variants in LOVD

To assess the prevalence of alleles with editable pathogenic variants in the 6 most common large recessive genes, we analysed data from the LOVD, which contains curated repositories of sequenced variants in the alleles of patients with IRD. For the genes examined (*ABCA4*, *CEP290*, *CDH23*, *EYS*, *MYO7A*, and *USH2A*), the LOVD contained a total of 26,418 alleles. Because base editing strategies focus on pathogenic variants, benign variants and variants of uncertain significance were excluded, which left a data set of 12,369 pathogenic or likely pathogenic alleles for further analysis.

Editable transition variants represented 53.0% of all pathogenic variants in all genes, with the remainder comprising noneditable variants, such as transversion SNVs, complex alleles, insertions, duplications, or deletions (Figure 5-2; Table 5-2). Variants G>A (23.1%) and C>T (18.1%) were the most prevalent types, with fewer T>C (7.0%) and A>G (4.8%) variants.

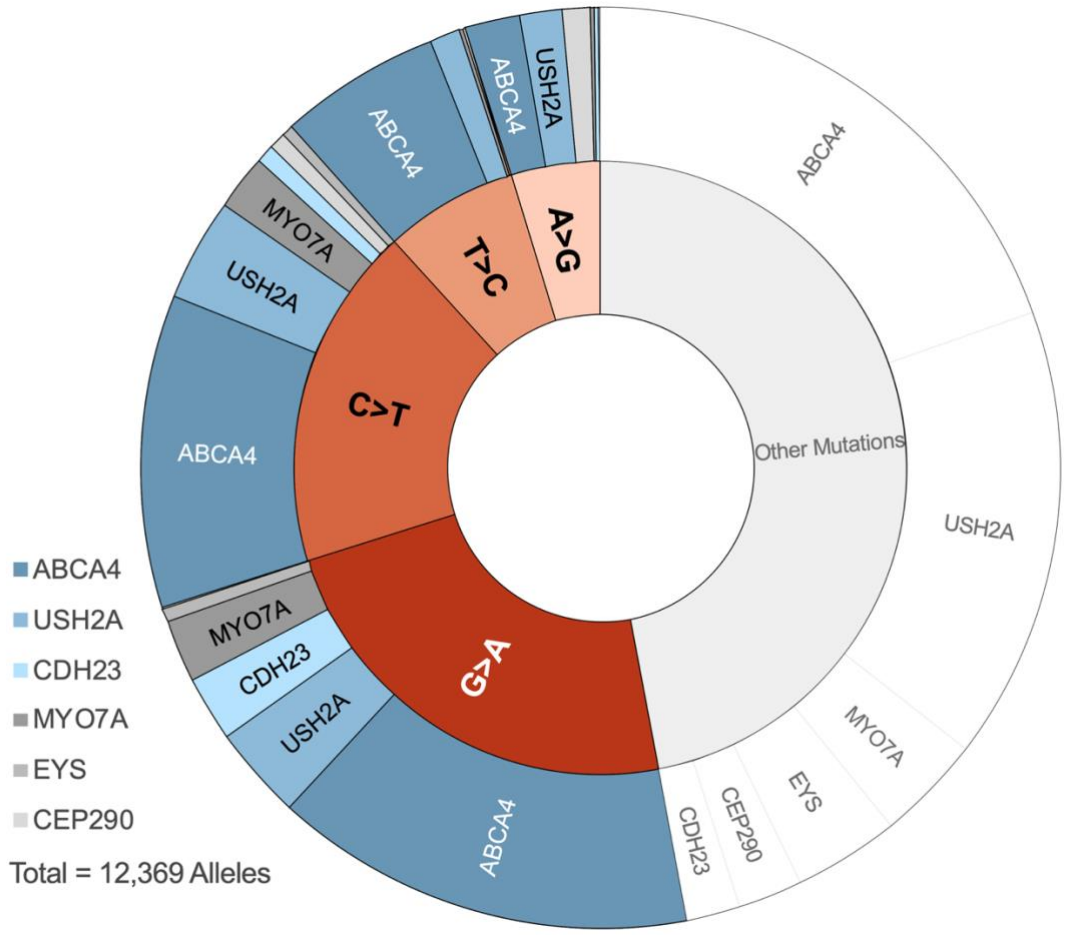


Figure 5-2 Distribution of alleles in the Leiden Open Variation Database
Analysis of 12,369 individual pathogenic or likely pathogenic alleles in the Leiden Open Variation Database (LOVD) across the six most common large recessive genes implicated in inherited retinal degeneration. Alleles with transition mutations targetable with base editing (G>A, C>T, T>C, A>G) are common across all genes. Other mutations are not targetable with base editing, including transversion mutations, insertions, duplications, deletions, and complex alleles. Further breakdown per gene is provided in Table 5-2.

Gene	Mutation	Alleles (n)	Proportion of alleles per gene (%)	Total Alleles (n)
ABCA4	G>A	1832	28.0%	
	T>C	704	10.8%	
	C>T	1358	20.8%	
	A>G	236	3.6%	
	Other Mutations	2410	36.9%	
	Subtotal			6540
CEP290	G>A	10	2.1%	
	T>C	1	0.2%	
	C>T	70	14.5%	
	A>G	120	24.8%	
	Other Mutations	282	58.4%	
	Subtotal			483
CDH23	G>A	286	47.0%	
	T>C	2	0.3%	
	C>T	79	13.0%	
	A>G	15	2.5%	
	Other Mutations	227	37.3%	
	Subtotal			609
EYS	G>A	62	10.5%	
	T>C	9	1.5%	
	C>T	51	8.7%	
	A>G	9	1.5%	
	Other Mutations	458	77.8%	
	Subtotal			589
MYO7A	G>A	268	26.7%	
	T>C	13	1.3%	
	C>T	240	23.9%	
	A>G	20	2.0%	
	Other Mutations	464	46.2%	
	Subtotal			1005
USH2A	G>A	405	12.9%	
	T>C	134	4.3%	
	C>T	444	14.1%	
	A>G	189	6.0%	
	Other Mutations	1971	62.7%	
	Subtotal			3143
Total				12369

Table 5-2 Spectrum of pathogenic alleles in the LOVD
Pathogenic alleles from the LOVD broken down by gene and mutation type. As analysed in Figure 5-2.

Within each gene, the proportion of editable mutations varied. Most of the alleles in *ABCA4* (63.1%), *CDH23* (62.7%), and *MYO7A* (53.8%) were editable transition variants, while a lower proportion of variants were editable in genes *CEP290* (41.6%), *USH2A* (37.3%), and *EYS* (22.2%) (Figure 5-3A).

The five editable pathogenic variants that occurred most frequently in each gene were identified (Figure 5-3; Table 5-3), accounting for a mean (SD) of 19.1% (9.5%) of all pathogenic alleles within each gene. In *ABCA4* (21.1%), *CEP290* (29.4%), *CDH23* (28.9%), and *MYO7A* (19.1%), the five most common editable variants accounted for a substantial proportion of all alleles (Figure 5-3A).

Variants associated with nonsense-mediated decay of the transcript, such as premature termination variants and variants that disrupt splicing, are expected to be particularly amenable to treatment, as correction is likely to rescue a null allele. Editable termination variants (defined as SNVs that are associated with in-frame codons being altered to stop codons) accounted for a mean (SD) of 12.6% (4.7%) of variants across all genes (Figure 5-3B). Common termination variants were found in *USH2A, MYO7A*, and *EYS* (Table 5-3). Editable variants in the canonical donor or acceptor splice sites (defined as splice variants in this study) accounted for a mean (SD) of 5.9% (4.2%) in each gene and were comparatively more prevalent in *CDH23, USH2A* and *MYO7A*. Intronic variants such as deep intronic splice variants and non-canonical splice site variants accounted for a mean (SD) of 8.3% (9.6) in each gene and were notably predominant in *CEP290* (24%). Deep intronic variants were most common in both *CEP290* and *CHD23*. Missense variants were the predominant editable variants observed in gene *ABCA4* (45.5%), and these variants were also common in *CDH23* and *MYO7A* (Figure 5-3B).

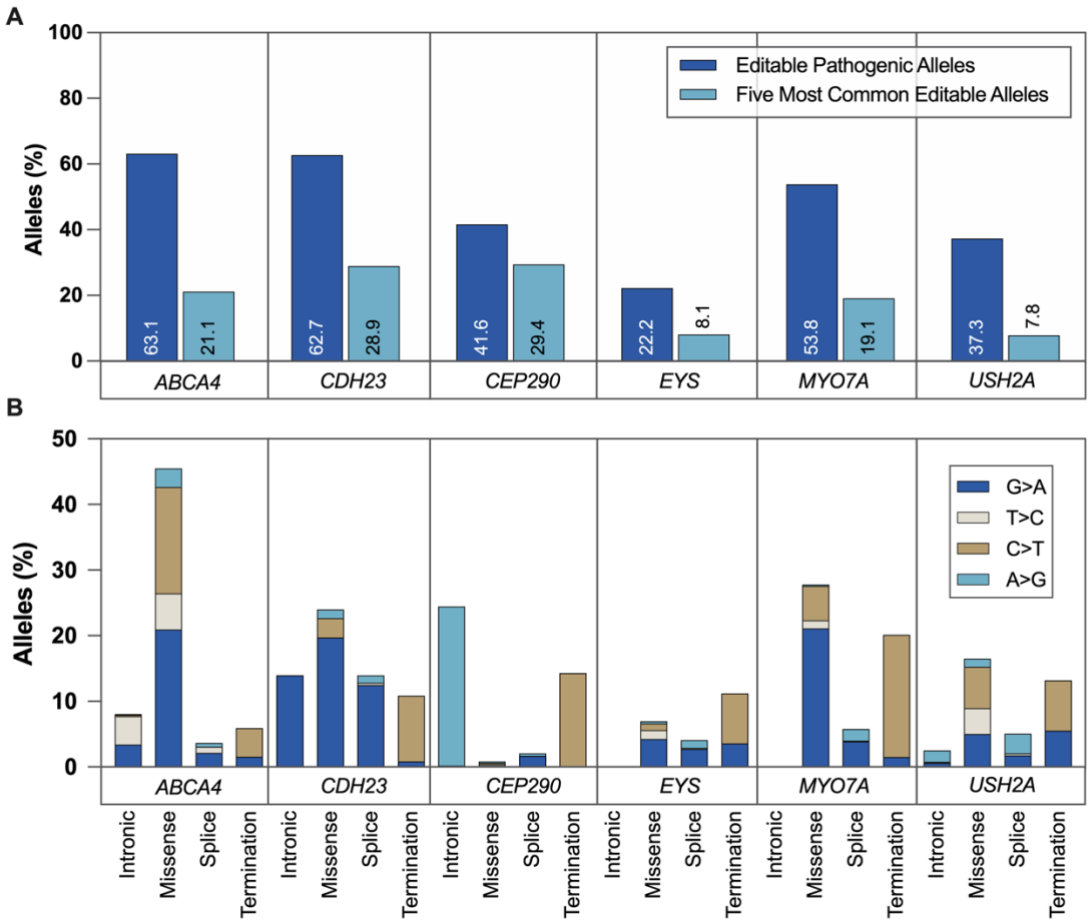


Figure 5-3 Common editable alleles and mutation type breakdown in the LOVD
A. The overall proportion of all pathogenic alleles that are editable in each gene is expressed as a percentage (left bar, dark). The proportion of pathogenic alleles formed from the five most common alleles occurring in each gene are shown as a percentage (right bar, light). The five most common editable alleles for each gene (see Table 5-3) comprise a mean (SD) of 19.1% (9.5%) of all pathogenic mutations. **B.** Mutations are summarised by consequence, expressed as a percentage of pathogenic alleles analysed for each gene: *ABCA4* (6540 alleles), *CDH23* (609 alleles), *CEP290* (483 alleles), *EYS* (589 alleles), *MYO7A* (1005 alleles), *USH2A* (3142 alleles). Termination mutations are defined as a SNV that causes an in-frame codon to be mutated to a stop codon. Splicing mutations are defined as affecting the canonical (+1,+2,-1,-2) positions of the donor or acceptor splice sites. Intronic mutations are defined as occurring in intronic regions beyond the canonical sites.

Gene	cDNA Change	Protein Change	Alleles (n)	Proportion of alleles (%)
ABCA4	c.5882G>A	p.(Gly1961Glu)	630	9.6%
	c.5461-10T>C	p.(Thr1821Aspfs*6)	268	4.1%
	c.6079C>T	p.(Leu2027Phe)	165	2.5%
	c.4469G>A	p.(Cys1490Tyr)	159	2.4%
	c.5714+5G>A	p.?	157	2.4%
	Total		**1379**	**21.1%**
CEP290	c.2991+1655A>G	p.(Cys998*)	117	24.2%
	c.4393C>T	p.(Arg1465*)	10	2.1%
	c.3811C>T	p.(Arg1271*)	6	1.2%
	c.4882C>T	p.(Gln1628*)	5	1.0%
	c.5824C>T	p(Gln1942*)	4	0.8%
	Total		**142**	**29.4%**
CDH23	c.6050-9G>A	p.[(=, Val2018Alafs*10)]	82	13.5%
	c.2968G>A	p.(Asp990Asn)	26	4.3%
	c.5237G>A	p.(Arg1746Gln)	25	4.1%
	c.2289+1G>A	p.?	22	3.6%
	c.336+1G>A	p.(?)	21	3.4%
	Total		**176**	**28.9%**
EYS	c.6557G>A	p.(Gly2186Glu)	17	2.9%
	c.7919G>A	p.(Trp2640*)	14	2.4%
	c.6632C>T	p.(Ser2211Leu)	6	1.0%
	c.2380C>T	p.(Arg794*)	6	1.0%
	c.5928-2A>G	p.?	5	0.8%
	Total		**48**	**8.1%**
MYO7A	c.1797G>A	p.(Met599Ile)	50	5.0%
	c.3719G>A	p.(Arg1240Gln)	49	4.9%
	c.5581C>T	p.(Arg1861*)	47	4.7%
	c.3508G>A	p.(Glu1170Lys)	26	2.6%
	c.640G>A	p.(Gly214Arg)	20	2.0%
	Total		**192**	**19.1%**
USH2A	c.11864G>A	p.(Trp3955*)	106	3.4%
	c.7595-2144A>G	p.(Lys2532Thrfs*56)	39	1.2%
	c.1876C>T	p.(Arg626*)	35	1.1%
	c.10712C>T	p.(Thr3571Met)	34	1.1%
	c.9799T>C	p.(Cys3267Arg)	31	1.0%
	Total		**245**	**7.8%**

Table 5-3 Most common editable mutations in the LOVD

The five most common editable mutations present in the LOVD for each gene are listed with their protein consequence, number of alleles present (n) and as a percentage of all pathogenic mutations (%). Totals refer to the total number of alleles accounted for by the five most common mutations.

5.3.2 Patients with Editable Variants

Many patients with IRD have compound heterozygous pathogenic variants, and correction of only one of these alleles should theoretically be sufficient to ameliorate the condition in many cases. To ascertain the number of potentially treatable patients within a typical large ophthalmology genetic service data set, we analysed a data set of patients who received genetic screening for a suspected IRD at the Oxford University Hospitals Medical Genetics Laboratories. Unlike the LOVD, which only provides data of the frequency of variants, this data set contained information of the variants *in trans* on each allele within an individual. The records were filtered to include only patients with biallelic pathogenic variants in the 6 most common recessive genes, yielding a data set of 179 patients with 358 alleles. The distribution of alleles within the Oxford data set was comparable to that of the LOVD data set (Figure 5-4A). Similar to alleles in the LOVD data set, 204 of 358 alleles (57.0%) were editable, with G>A (83 of 358 alleles [23.2%]) and C>T (84 of 358 alleles [23.5%]) variants the most common.

Patients were classified as having editable variants if they had at least 1 editable allele. Among 179 total patients in the Oxford data set, 137 individuals (76.5%) had editable variants, and 42 individuals (23.5%) did not have editable variants (Figure 5-4C). Individuals with pathogenic variants in *ABCA4* (59.8%) and *USH2A* (31.3%) represented the majority of patients in the Oxford data set, and so further analysis was performed on these genes. Among 107 patients with pathogenic variants in *ABCA4*, 95 individuals (88.8%) had an allele with an editable transition variant; among 56 patients with pathogenic variants in *USH2A*, 32 individuals (57.1%) had an editable allele (Figure 5-4E).

As base editing would require an individual guide RNA for each variant, the most commonly occurring editable alleles were identified. The 5 most frequent editable alleles collectively accounted for 32.2% of *ABCA4* alleles and 17.0% of *USH2A* alleles (Table 5-4). Because most patients are heterozygous, 53 of 107 patients (49.5%) with pathogenic variants in gene *ABCA4* and 16 of 56 patients (28.6%) with pathogenic variants in gene *USH2A* had at least one of these common variants (Figure 5-4, Table 5-4), suggesting that 5 guide RNAs (one for each pathogenic variant) could be used to treat a substantial proportion of patients.

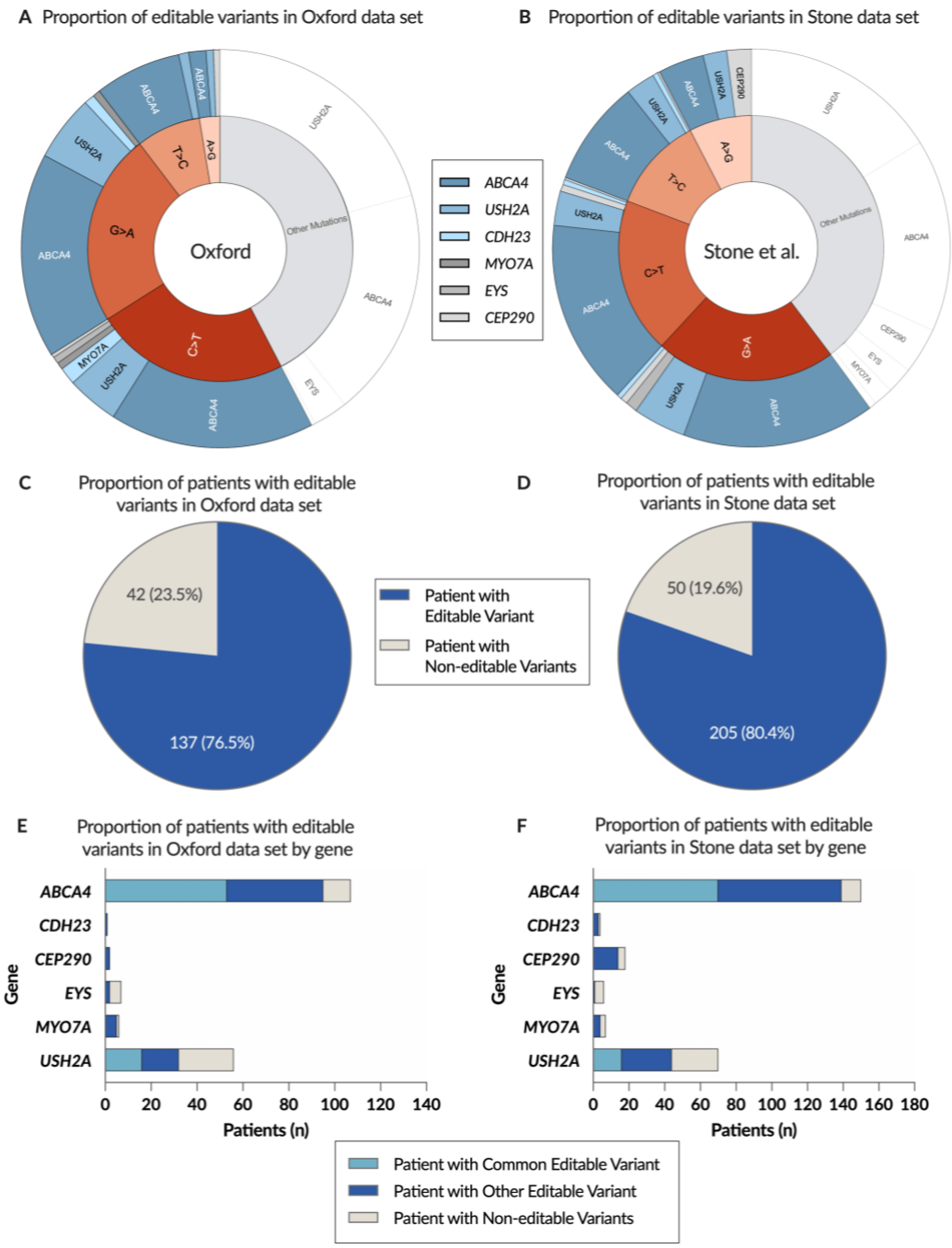

A Proportion of editable variants in Oxford data set
B Proportion of editable variants in Stone data set
Oxford
Stone et al.
ABCA4
USH2A
CDH23
MYO7A
EYS
CEP290
C Proportion of patients with editable variants in Oxford data set
D Proportion of patients with editable variants in Stone data set
42 (23.5%)
137 (76.5%)
50 (19.6%)
205 (80.4%)
Patient with Editable Variant
Patient with Non-editable Variants
E Proportion of patients with editable variants in Oxford data set by gene
F Proportion of patients with editable variants in Stone data set by gene
Gene
Patients (n)
Patient with Common Editable Variant
Patient with Other Editable Variant
Patient with Non-editable Variants

Figure 5-4 Analysis of editable variants within patients in the Oxford and Stone et al. data sets

A. Proportion of editable variants from Oxford data set classified by nucleotide change in 358 alleles from 179 patients with 2 confirmed pathogenic or likely pathogenic variants (American College of Medical Genetics class 4 or 5) in the 6 most common recessive genes. B. Proportion of editable variants from Stone et al.[95] data set classified by nucleotide change in 510 alleles from 255 patients with in the 6 most common recessive genes. C. Proportion of the 179 patients in the Oxford data set with at least one (of two) alleles classified as editable. **D.** Proportion of the 255 patients in the Stone et al.[95] data set with at least one (of two) alleles classified as editable. **E**. Patients in Oxford data set by implicated gene. For *ABCA4* and *USH2A*, patients were classified as having a common editable variant if they had 1 of the 5 most common variants (see Table 5-4) **F**. Patients in Stone et al.[95] data set by implicated gene. For genes *ABCA4* and *USH2A*, patients were classified as having a common editable variant if they had 1 of the 5 most common variants (see Table 5-5).

Gene	cDNA Change	Protein Change	Alleles, n (%)	Unique patients with at least one common editable variant, n (%)
ABCA4	c.5882G>A	p.(Gly1961Glu)	20 (9.3)	
	c.5461-10T>C	p.(Thr1821Aspfs*6)	14 (6.5)	
	c.6079C>T	p.(Leu2027Phe)	14 (6.5)	
	c.4139C>T	p.(Pro1380Leu)	11 (5.1)	
	c.5714+5G>A	p.?	10 (4.7)	
Sub-Total			**69 (32.2)**	**53 (49.5)**
USH2A	c.10073G>A	p.(Cys3358Tyr)	7 (6.3)	
	c.10342G>A	p.(Glu3448Lys)	4 (3.6)	
	c.12574C>T	p.(Arg4192Cys)	3 (2.7)	
	c.3407G>A	p.(Ser1136Asn)	3 (2.7)	
	c.8740C>T	p.(Arg2914*)	2 (1.8)	
Sub-Total			**17.0%**	**16 (29)**

Table 5-4 Common Editable Alleles in the Oxford Dataset

Summary of the most common five alleles for *ABCA4* and *USH2A* in the Oxford dataset. The number of unique patients that harbour at least one of these alleles is summarised. Homozygous patients or patients compound heterozygous for two of the common alleles are counted as a single patient. Protein changes are not listed for the non-canonical splicing variant in *ABCA4*.

To validate this finding, an identical analysis of data from a similar genetic service in the United States of America was performed, which was previously published by Stone et al.[95] (Figure 5-4). Among 255 patients with 510 alleles in the 6 most common recessive genes, 205 individuals (80.4%) had editable variants, and 50 individuals (19.6%) did not have editable variants. Among those with pathogenic variants in genes *ABCA4*, 139 of 150 patients (92.7%) had an allele with an editable transition variant, while 44 of 70 patients (62.9%) with pathogenic variants in gene *USH2A* had an allele with an editable transition variant. In the Stone et al.[95] data set, the 5 most frequent common variants in *ABCA4* accounted for 26.3% of alleles and at least one of these alleles were present in 71 of 150 patients (47.3%). In *USH2A* the 5 most common variants comprised 12.9% of alleles and at least one was present in 16 of 70 patients (22.9%). These data from a geographically separate population are consistent with the findings from the UK-based data set.

Comparing the most frequent 5 variants in genes across these 3 data sets, in *ABCA4* 3 variants (c.5882G>A, c.5461-10T>C, and c.5714 + 5G>A) were present in each data set. In *USH2A*, no single variant was present in the 5 most frequent variants of all data sets. Three variants (c.11864G>A, c.7595-2144A>G, and c.10073G>A) occurred in 2 of the 3 data sets.

Gene	cDNA Change	Protein Change	Alleles, n (%)	Unique patients with at least one common editable variant, n (%)
ABCA4	c.5461-10T>C	p.(Thr1821Aspfs*6)	24 (8.0)	
	c.5882G>A	p.(Gly1961Glu)	20 (6.7)	
	c.4139C>T	p.(Pro1380Leu)	12 (4.0)	
	c.3113C>T	p.(Ala1038Val)	12 (4.0)	
	c.5714+5G>A	p.?	11 (3.7)	
Sub-Total			**79 (26.3)**	**71 (47.3)**
USH2A	c.11864G>A	p.(Trp3955*)	7 (5.0)	
	c.1606T>C	p.(Cys536Arg)	3 (2.1)	
	c.10073G>A	p.(Cys3358Tyr)	3 (2.1)	
	c.7595-2144A>G	p.?	3 (2.1)	
	c.12575G>A	p.(Arg4192His)	2 (1.4)	
Sub-Total			**18 (12.9%)**	**16 (22.9)**

Table 5-5 Common Editable Alleles in the Stone et al. Dataset

Summary of the most common five alleles for *ABCA4* and *USH2A* in the Stone et al.[95] dataset. The number of unique patients that harbour at least one of these alleles is summarised. Homozygous patients or patients compound heterozygous for two of the common alleles are counted as a single patient. Protein changes are not listed for the non-canonical splicing variants.

5.4 Discussion

This chapter sought to create a roadmap for base editing for inherited retinal disease, identifying key potential target pathogenic variants in recessive genes that are common, and not readily treatable with currently used gene therapy technologies. Using available population data, six common recessive genes that are implicated in IRD and are too large for delivery within a single AAV were chosen and the spectrum of potential base editing targets assessed. Recessive diseases are ideal targets, as it is likely that a base editing strategy to correct only 1 of 2 alleles is required in many cases. Over half of the pathogenic variants in the genes *ABCA4*, *CEP290*, *CDH23*, *EYS*, *MYO7A*, *USH2A* are caused by transition SNVs that are editable with the current classes of base editors. This was consistent across the global LOVD dataset, and two large ophthalmic genetic services in the United Kingdom and United States of America. Although transitions account for only four of the possible twelve SNVs, they are more prevalent than transversions throughout the human genome.[404] GC-AT base pair transitions are particularly common due to spontaneous deamination secondary to oxidative DNA damage,[405,406] and, consistent with this, 41.3% of pathogenic variants in the LOVD were G>A and C>T transitions in the studied genes. Due to the frequency of transition variants, we find that in two separate cohorts, 76-80% of patients with disease caused by biallelic pathogenic variants in the six genes analysed had at least one editable allele.

Base editors were first described by Liu and colleagues in 2016 as a new method to introduce specific single nucleotide changes without the generation of double stranded breaks in DNA.[246] This was a significant advance in the gene editing field, as gene editing was no longer reliant of technologies that rely on the cleavage of the nucleic acid backbone and subsequent cellular repair mechanisms to install nucleic acid edits. Nucleases that cause double stranded breaks in DNA risk the generation of translocations and rearrangements,[407,408] and installation of specific edits require the delivery of donor templates and the use of inefficient homology directed repair mechanisms.[409] Since the publication of the initial DNA cytosine base editor

(termed base editor 1, BE1), rapid iterative development has yielded numerous generations and types of base editors[244,410] now capable of cytosine and adenosine editing in both DNA and RNA with greater specificity[252, 299–301,326] and efficiency.[247, 252,410,411]

Recent data has demonstrated the therapeutic potential of base editors for inherited retinal disease. Firstly, base editors have shown *in vivo* activity in photoreceptors[254] and in retinal pigment epithelium.[255] Secondly, although efficacious delivery remains a perennial challenge in gene therapy, efforts to enable the delivery of DNA base editors using single or dual-AAV vector approaches,[254,412,413] lentiviral vectors,[255] or non-viral delivery[414–417] continue. Many RNA editors are deliverable within a single AAV[309, 311,312,320] and have shown promise *in vivo*.[312] Thirdly, the targeting range of base editors has expanded rapidly. For RNA base editing with Cas13 or antisense methods, there are few known targeting restrictions, although some modalities have local nucleotide preferences.[288, 300, 312,319] For DNA base editing, Cas enzymes with flexible or alternative PAM sequences have enabled targeting of almost any sequence in the genome.[208,418,419] Therefore in this chapter, all pathogenic transition variants were considered potential targets irrespective of their local sequence context.

A limitation of base editing strategies is that they are mutation dependent; that is, a guide RNA is required for each individual variant. Although many heterogenous private variants occur in each gene, analysis of the LOVD demonstrates that targeting the most common five editable variants allows for approximately one-fifth of pathogenic variants in each gene to be targeted respectively.

Pathogenic variants in *ABCA4* are commonly associated with Stargardt disease. The most common variant is the c.5882G>A; p.(Gly1961Glu), which emerged from Eastern Africa and spread throughout the global population.[420] Phenotypically, patients with a c.5882G>A mutation have later onset disease typically in the mid-twenties, often associated with a bulls eye maculopathy and central visual loss.[420,421] Homozygous c.5882G>A mutations are found uncommonly in Stargardt patients, but are commonly disease-causing in compound

heterozygosity with a second mutation, especially truncating variants.[399] In a large survey, c.5882G>A mutations were present in hetero- or homozygosity 339/3928 (8.6%) of *ABCA4* cases.[399] The c.5461-10T>C; p.([Thr1821Valfs, Thr1821Aspfs]) is a common non-canonical splice variant present predominantly in European populations.[422] As this variant results in frame-shifting due to exon skipping, correction of this allele would likely restore expression from a null background. While most variants in *ABCA4* are SNVs, a substantial proportion (approximately 10%)[420] are complex alleles, which contain two variants.[399] The presence of more than one variant would be challenging to correct with a base editing approach; thus, complex alleles were not considered editable variants in this study.

Pathogenic variants in *USH2A* can present as non-syndromic RP or as Usher syndrome type II, associated with RP and hearing loss. A minority of pathogenic variants in *USH2A* were identified as editable (7.8%), and the two most common variants (c.2299delG; p.(Glu767fs), c.2276G>T; p.(Cys759Phe)) in exon 13 accounted for approximately 35% of cases.[149,150,152] Though neither variant is amenable to base editing, inducing exon-skipping using antisense oligonucleotides,[166,183] using base editing to alter splice acceptor sites[423] or CRISPR-Cas13 mediated splice site repression[285] are alternative approaches. For direct base editing, the c.11864G>A; p.(Trp3955*) was the most common target, and appears to be prevalent in European populations.[153, 155,424] Data from translation read-through strategies suggest that even partial correction of nonsense targets may be sufficient to rescue the phenotype.[185]

Although *CEP290, MYO7A* and *CDH23* represent less frequent causes of IRD, we identified prevalent editable variants in these genes. The common deep intronic variant in *CEP290,* c.2991+1655A>G; p.(Cys998*)[425] is an editable variant associated with Leber's congenital amaurosis that creates a new intronic splice donor site. Approaches to correct this variant are currently in clinical trial.[225,91,426]

Loss of function *MYO7A* variants cause Usher syndrome type 1[427] and more than 50% of *MYO7A* alleles in the LOVD data set were editable, with almost 15% of alleles accounted for

by three pathogenic variants. *CDH23* variants are also associated with USH1[428–430] with protein truncating mutations typically associated with Usher syndrome type 1D and missense mutations with non-syndromic deafness (DFNB12).[428–430]. A high proportion (62.7%) of the *CDH23* alleles were editable, with 38.7% due to variants expected to be protein truncating (splice, intronic or termination). The non-canonical splice site variant c.6050-9G>A was a prevalent editable variant (13.5%). This induces aberrant splicing with a frameshift, causing nonsense-mediated decay of the transcript.[431]

Pathogenic variants in *EYS* underlie 5-10% of non-syndromic RP, however a minority are editable in the alleles in LOVD to date. The dataset contains an array of private variants, with a high proportion of insertions, duplications and deletions, comprising 51.6% of all variants. This may be because the vast majority of missense mutations in *EYS* are currently still classed as variants of unknown significance and thus excluded from this analysis. Further work is required to ascribe their pathogenicity.[398] Neither of the most common mutations (c.4957dup; p.(Ser1653Lysfs*2), 13.9% and c.8805C>A; p.(Tyr2935*), 6.8%) are editable.

A limitation of this study is that as the datasets were not reliably coded with ethnicity or demographic information, this analysis does not take into account sampling biases and differences in population prevalence of certain variants or genes. A further limitation is that the local nucleotide context of each mutation was not considered, and whether the potential for bystander deamination of off-target nucleotides would affect the suitability of a mutation for a base editing approach. As the bystander deamination profile of each type of base editor will differ, this should be considered in the development of a targeting strategy for each mutation. Additionally, as it sought to identify targets that are known to cause disease, it only considers definitively pathogenic variants and not variants of unknown significance. For variants not amenable to base editing, other molecular engineering strategies such as AON therapy, prime editing and strategies such as microhomology-mediated end joining may be applicable.[432]

5.4.1 Conclusion

Base editing tools are one tool in a rapidly expanding array of molecular therapies.[433] Here, a rationale and approach for potential base editing targets in the retina from 3 data sets is presented. The study's findings support the conclusion that base editing is a promising approach with many potential therapeutic targets in IRD, particularly for patients with variants in large genes that are not readily treatable with AAV gene supplementation.

6

DEVELOPMENT OF A CAS13-MEDIATED RNA EDITING APPROACH TO CORRECT NONSENSE MUTATIONS IN *USH2A*

6.1 Introduction

The previous chapter established a range of clinically relevant single nucleotide mutations amenable to correction with a base editing approach. One such approach is site directed RNA editing, using an ADAR deaminase to correct G>A mutations in mRNA.[288]

This chapter investigates the use of a CRISPR-Cas13-ADAR RNA editing approach. As described in the general introduction, deactivated Cas13 (dCas13) orthologues fused to the deaminase domain of ADAR2 ($ADAR2_{DD}$) can be directed to a mutation of interest by a gRNA.[300] Binding of the Cas13-ADAR-gRNA complex creates a region of double stranded RNA at the gRNA binding site, allowing the $ADAR2_{DD}$ to mediate A-I base conversion.[300] The targeted A base is specified by an A-C mismatch encoded within the gRNA sequence. As inosine is interpreted as a guanosine by the translation and splicing machinery of the cell, this effectively installs an A>G transition in RNA and can be used for the correction of G>A mutations (see Figure 6-1B).[292] The dCas13b-$ADAR2_{DD}$ system was first described by Cox et al. in 2017, using the *Prevotella Sp.* orthologue (PspCas13b) fused to $ADAR2_{DD}$ with an E488Q hyperactive mutation that introduced high rates of editing with higher rates of off-target

deamination.[300] An more specific E488Q/T375G ADAR2$_{DD}$ mutant encouragingly abrogated almost all off-target editing while retaining reasonable on-target efficiency. More recently, a range of minimal Cas13-ADAR effectors have been described,[282, 284,304] including dCas13bt-ADAR,[282] with smaller coding sequences to allow easier packaging within AAV. To date, CRISPR-based RNA editing constructs have not been used *in vivo,* and RNA editing of IRD-related genes or in photoreceptors has yet to be demonstrated.

An ideal candidate mutation to investigate the use of RNA editing for inherited retinal disease is c.11864G>A (W3955X) in *USH2A*, identified from the previous chapter. This results in a premature termination (X) codon (TAG) rather than a tryptophan (W) codon (TGG) encoded in exon 61. It is the third most common *USH2A* pathogenic mutation reported in the LOVD-Usher dataset comprising 3.6% of all reported mutations.[148] In a large European *USH2A* cohort, this mutation was detected in 23% (54/236) of patients[153] and its pathogenicity confirmed in multiple cohorts.[117, 153–155,424] Developing an RNA editing therapy to target restoration of the c.11864G>A mutation offers an opportunity to treat a significant number of patients. To demonstrate a proof of principle for *in vivo* AAV-delivered RNA editing for *USH2A* mutations, an appropriate animal model is required. The homologous region of the mouse *Ush2a* gene is exon 60, where an equivalent tryptophan is encoded at amino acid 3947. An *Ush2a* mouse model with a W3947X mutation developed for the testing of base editing therapeutics is described in further detail in the following chapter. Although homologous, *Ush2a* exon 60 and *USH2A* exon 61 display a 77% nucleotide sequence identity, meaning different gRNAs are required to target each mutation.

A key challenge for developing *USH2A* RNA editing strategies is that *USH2A*^{isoB} expression is restricted to photoreceptors and inner hair cells,[126,127] and it is poorly expressed in widely available cell lines (see section 1.2.4.1). For the optimisation of editing constructs and screening of many potential gRNAs, a low-cost and relatively high-throughput *in vitro* method

in easily cultured cells is required. The gold-standard of sequencing RNA extracted from edited cells is time and resource intensive, and not suited for screening applications.

6.1.1 Chapter Aims

The overall aim of this chapter is to develop a dCas13-ADAR2$_{DD}$ based RNA editing approach for the correction of the human *USH2A* (*hUSH2A*) W3955X mutation and to the mouse *Ush2a* (*mUsh2a*) W3947X mutation, which can be packaged within an AAV vector. To achieve this, the following aims will be explored:

1. Develop a luciferase-based *in vitro* assay for the facile screening of RNA editing constructs and gRNAs
2. Identify efficient gRNAs targeting the *hUSH2A*-W3955X and *mUsh2a*-W3947X mutations *in vitro*
3. Compare the on-target activity of different Cas13 orthologues including dPspCas13b and dCas13bt
4. Explore the on-target and local off-target profiles of ADAR2$_{DD}$ mutants *in vitro* at the human and mouse USH2A locus
5. Screen and identify small regulatory elements including promoters and polyA sequences that drive RNA editing and permit minimisation of the construct size
6. Create and test RNA editing plasmids with transgenes designed for packaging within an AAV vector

6.2 Materials and Methods

6.2.1 Dual Luciferase Assay

6.2.1.1 Dual Luciferase assay design and cloning

Dual luciferase constructs for RNA editing reporting were cloned using the pSGDlucV3.0 plasmid (gift from John Atkins, Addgene plasmid #119760).[434,435] A single SV40 promoter drives the production of a transcript encoding Renilla as a normalisation control, a 'target cassette' containing the mutation of interest with flanking F2A sequences, Firefly as a reporter of editing activity and a SV40 PolyA site from 5' to 3' (Figure 6-1). The two F2A sequences enables co-translational excision of the target cassette peptide, encoding Renilla and Firefly proteins independent of the identity of the intervening target cassette sequence. Although the F2A sequence leaves a 32aa sequence on the C-terminal of Renilla, this does not affect Renilla luminescence.[435] At baseline, Firefly is turned off as the presence of the termination codon stalls translation after the production of Renilla but before the production of Firefly. Repair of the premature stop codon to a non-stop amino acid codon allows translation to proceed and Firefly is turned on (see section 6.2.1.4 for editing efficiency calculations)

Target cassettes were cloned into the 5' PspXi and 3' BglII flanking restriction sites as per the general methods. Target sequences containing the G>A mutation of interest and the 200 bp region surrounding the *hUSH2A*-W3955X and *mUsh2a*-W3947X mutations were synthesised as double stranded DNA fragments (Thermo Fisher Scientific) To generate the in-frame positive control vector, complementary oligonucleotides were generated with 5' and 3' restriction overhangs (Sigma-Aldrich) and annealed and phosphorylated.

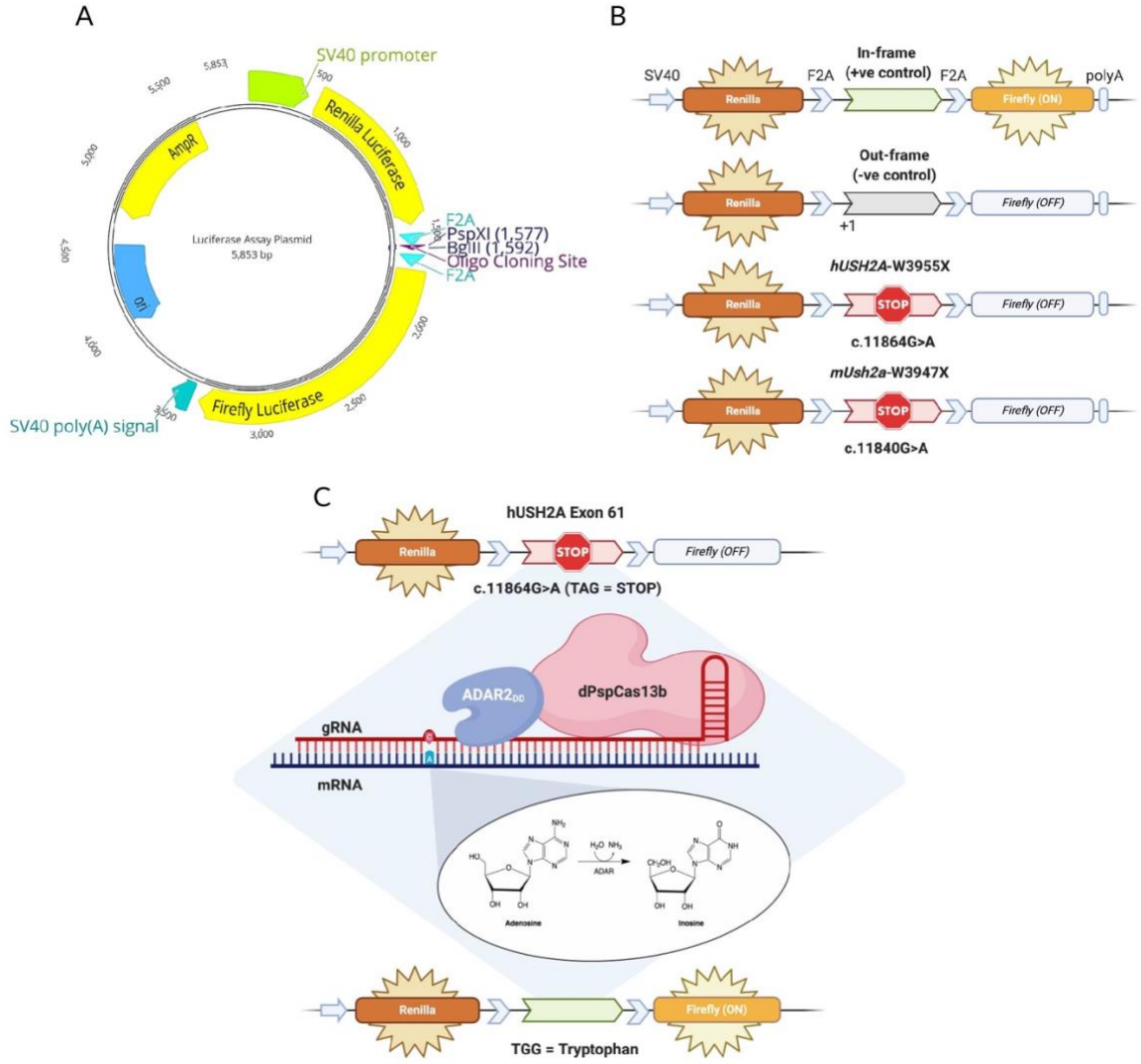


Figure 6-1 Dual luciferase reporter assay for RNA editing

A. Map of the dual luciferase plasmid. A cloning site flanked by restriction enzymes (PspXI and BglII) allows the insertion of the target sequence of interest between the F2A sequences. **B.** Linear maps of control and experimental dual luciferase constructs. Renilla is constitutively expressed as a normalisation control. When a stop codon precedes the firefly, firefly is not expressed. The positive control plasmid places firefly in-frame with no intervening stop codon, while the negative control plasmid places firefly out-of-frame with a preceding termination codon. F2A sequences (also known as StopGo sequences or 2A self-cleaving peptides) are short sequences that cause a conformational change within the ribosome, disrupting the peptide linkage between C-terminal proline and glycine residues.[436] Downstream translation continues in-frame beyond the 2A sequence, generating equimolar amounts of two separate amino acid sequences from the same transcript, 'cleaved' at the C-terminus of the 2A sequence.[436] **B.** Diagram demonstrating repair of a TAG stop codon in a target sequence to a TGG tryptophan codon by RNA editing with dPspCas13b-ADAR$_{DD}$ with a targeting guide RNA. The A-C mismatch specifying the nucleotide to be edited is demonstrated. Successful RNA editing of adenosine to inosine (read as guanosine by the ribosome) repairs the stop codon and turns on firefly expression, with the ratio of renilla and firefly expression used to calculate editing efficiency.

6.2.1.2 Cell culture and transfection for dual luciferase assay

For the luciferase assay, 100uL of HEK293T cells at a density of 4.5×10^4cells/well were seeded in Corning white-walled 96 well adherent plates (Sigma-Aldrich) in phenol-red-free Dulbecco's Modified Eagle Medium (DMEM) (Thermo Fisher Scientific), supplemented with L-glutamine (2 mM) (Sigma-Aldrich), sodium pyruvate (1 mM) (Thermo Fisher Scientific), 10% heat-inactivated fetal bovine serum (HI-FBS) (Thermo Fisher Scientific) and 1% penicillin-streptomycin (Sigma-Aldrich). Cells were transfected with Transit-LT1 (Mirus Bio) at 24 hours post-seeding with 50 ng of dual luciferase reporter, 75 ng of RNA editing effector and 150 ng of gRNA construct unless otherwise stated. Positive and negative control wells were included on all plates, transfected with identical quantities of luciferase plasmid, RNA editing effector and non-targeting gRNA plasmids as in the experimental plates. All transfected plasmid preparations were made with endotoxin-free mini- (Zymo Research) or maxi-prep kits (Qiagen).

6.2.1.3 Dual-Glo luciferase assay

The Dual-Glo luciferase assay kit (Promega, Madison, WI, USA) was used to detect luciferase expression according to the manufacturer's instructions. Briefly, plates were allowed to come to room temperature, and 50 μL of media was removed. For cell lysis and detection of firefly activity, 60 μL of Dual-Glo luciferase reagent containing firefly luciferase substrate was added to each well and left to incubate at room temperature for 15 minutes. Luminescence was recorded using a FLUOstar Omega microplate reader (BMG Labtech, Ortenberg, Germany). For renilla detection, 60 μL of Stop & Glo reagent was added to quench firefly activity and provide renilla luciferase substrate, left to incubate for 15 minutes and luminescence recorded.

6.2.1.4 Editing efficiency calculation

Mean background firefly and renilla luminescence was calculated from transfection-reagent-only wells and subtracted from all raw values. The editing efficiency is calculated from a ratio of firefly to renilla luciferase activity, determined for each well. All assays were performed

in technical duplicates, and the experimental sample ratio is the mean of the duplicates for that condition. To obtain an editing percentage, this ratio is normalised between the positive control and negative control ratios where the positive control represents 100% editing and the negative control represents 0% editing. Editing efficiency can then be calculated using the firefly:renilla ratios of each condition:

$$Editing\ efficiency\ (\%) = \frac{(Experimental\ sample\ ratio) - (negative\ control\ ratio)}{(Positive\ control\ ratio) - (negative\ control\ ratio)}$$

6.2.2 Cloning of Cas13-ADAR editing plasmids

6.2.2.1 Cas13b-ADAR2$_{DD}$ and gRNA plasmids

Plasmids encoding variants of deactivated Cas13b derived from *Prevotella Sp.*(dPspCas13b) with an HIV nuclear export signal (NES_{HIV}) fused via a linker to the human ADAR2 deaminase domain ($hADAR2_{DD}$) and two associated guide RNA constructs were obtained from Addgene (Table 6-1).[300] These deactivated variants contains the H133A and H1058A mutations which inactivate the HEPN RNase domains of Cas13b.[300] A representative plasmid map is shown in Figure 6-2 with comparative schematics in Figure 6-10. Plasmids encoding the minimal deactivated Cas13bt orthologues derived from metagenomic screens with equivalent deactivating HEPN mutations were a gift from Feng Zhang and Soumya Kannan (Table 6-4).[282] Plasmid identity was confirmed with Sanger sequencing.

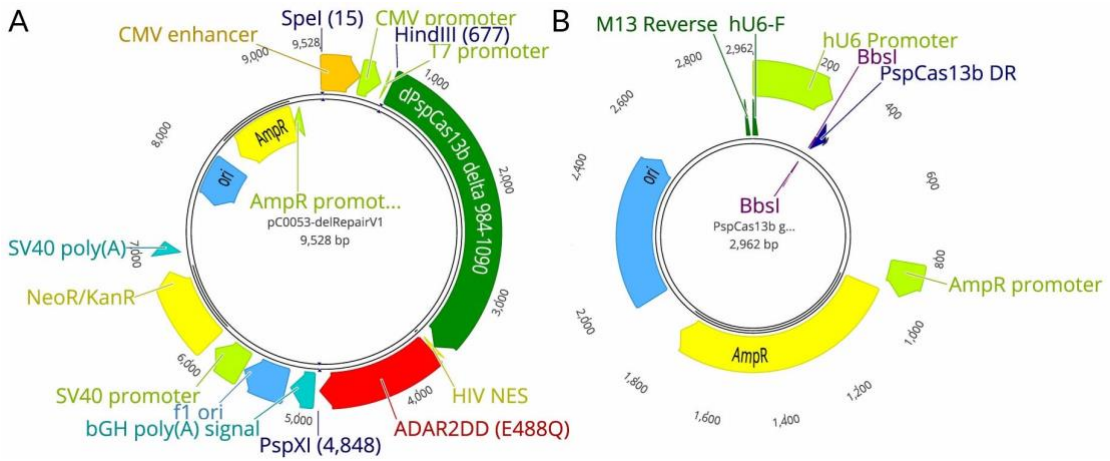


Figure 6-2 Representative full plasmid maps of Cas13b and cRNA plasmids
A. Plasmid map of pC0053-CMV-IE-dPspCas13b-GS-ADAR2DD(E488Q)-delta-984-1090. This is representative of the initial Cas13b constructs. The dCas13b-ADAR2$_{DD}$ construct is driven by the CMV-IE promoter with a C-terminal NES$_{HIV}$ on the dCas13b and a 3' bGH polyA signal. SpeI and HindIII sites allow for the excision of the CMV-IE promoter, and SpeI and PspXI sites allow for excision of the Cas13-ADAR construct. **B.** Plasmid map of the empty gRNA cloning vector (pC0043-U6-PspCas13b crRNA). Guide RNA expression is driven by the hU6 promoter. A polyT sequence terminates transcription after the direct repeat. A BbsI cloning sites allows insertion of guide sequences. The M13_reverse and hU6-fwd primer sites allow for easy sequencing to confirm gRNA insertion.

Full Construct Name	Source
pC0048-CMV-IE-dPspCas13b-longlinker-ADAR2DD(E488Q)	103864
pC0053-CMV-IE-dPspCas13b-GS-ADAR2DD(E488Q)-delta-984-1090	103869
pC0054-CMV-IE-dPspCas13b-longlinker-ADAR2DD(E488Q/T375G)	103870
pC0055-CMV-IE-dPspCas13b-GS-ADAR2DD(E488Q/T375G)-delta-984-1090	103871
pC0043-U6-PspCas13b crRNA backbone	103854
pC0052-REPAIR non-targeting guide clone into pC0043	103868
CMV-IE-HIVNES-dCas13bt1-ADAR2DD(E488Q)-bGH	F. Zhang
CMV-IE-HIVNES-dCas13bt3-ADAR2DD(E488Q)-bGH	F. Zhang
CMV-IE-HIVNES-dCas13bt5-ADAR2DD(E488Q)-bGH	F. Zhang
Bt1-cRNA	F. Zhang
Bt3-cRNA	F. Zhang
Bt5-cRNA	F. Zhang

Table 6-1 dCas13b-ADAR2$_{DD}$ and gRNA plasmids
List and origin of Cas13b effector and cRNA plasmids used. dPspCas13b plasmids were obtained via Addgene (reference numbers listed), Cas13bt plasmids were obtained directly from Feng Zhang. Delta-984-1090 plasmids contain a C-terminal truncation of the Cas13b. ADAR2$_{DD}$ variants contain either the hyperactive E488Q mutation or the more specific E488Q/T375G double mutation. The crRNA backbones contain golden gate cloning sites to insert spacer sequences to form a single gRNA driven by a U6 promoter.

6.2.2.2 Bulk guide RNA cloning

For screening of gRNAs, 20-40 gRNA constructs were cloned in parallel. Standard cloning protocols for annealed oligos as described in the general methods were performed in PCR strip tubes with minimised volumes of reagents. 1 μL of diluted (1 in 25) duplexed gRNA solution was added strip tubes using multichannel pipettes. To this, 9 μL of prepared mastermix of ligation mix was added, consisting of 6 μL of MG-H_2O. 1 μL of T4 DNA ligase, 1 μL of T4 DNA ligase buffer and 1 μL of 30 ng/μL digested plasmid backbone. Ligation mixes were incubated at room temperature for 1 hour. 5 μL of ligation mix was transformed into to 25 μL of 5-alpha cells (NEB), and then briefly incubated in 200 μL of SOC medium in an incubator-shaker at 37°C for 225rpm for 20 minutes before plating and overnight culture. A single colony per guide was cultured for miniprep and screened for successful with Sanger sequencing using

a common sequencing primer (M13_Rev or U6_Fwd) upstream of the gRNA promoter stored at the sequencing service (Eurofins Genomics). The typical yield of successfully inserted guides from screening was ~90% from a single colony and 100% from three colonies.

6.2.2.3 Cloning of short promoters & polyA sequences

The CMV-IE promoter was excised from the dPspCas13bdel-ADAR2$_{DD}$(E488Q) vector at the SpeI and HindIII sites (Figure 6-2). The SCP1 and EFS promoters were synthesised as double-stranded DNA fragments (IDT) and cloned into the linearised backbone.

For cloning the sNRP1 polyA sequence, a double-stranded fragment (IDT) encoding a dual sNRP1 was cloned into a pU6 vector backbone (pU6-Cj-sgRNA, Addgene #89753) digested with SalI and XbaI to form a pU6-sNRP1 vector. CMV-IE-dPspCas13b-delta984-1090-ADAR$_{DD}$(E488Q) was then excised at the SpeI and PspXi sites and cloned upstream of the sNRP1 polyA in the pU6-sNRP1 vector.

The tRNA(GLN) promoter was cloned into the pC0043-pspCas13 empty gRNA cloning backbone to replace the U6 promoter via *in vivo* assembly (Figure 6-3).[437] PAGE purified forward and reverse primers were designed with 3' annealing regions to bind 5' to the hU6 promoter and 5' to the direct repeat region respectively, and 5' overlapping homology regions to encode the tRNA(GLN) promoter and BbsI restriction site. Following amplification of the plasmid template with Phusion polymerase (NEB) over 18 cycles, 1 µL of FastDigest DpnI (Thermo Fisher Scientific) restriction enzyme was added and the reaction was incubated at 37°C for 15 minutes to digest residual plasmid template prior to transformation.

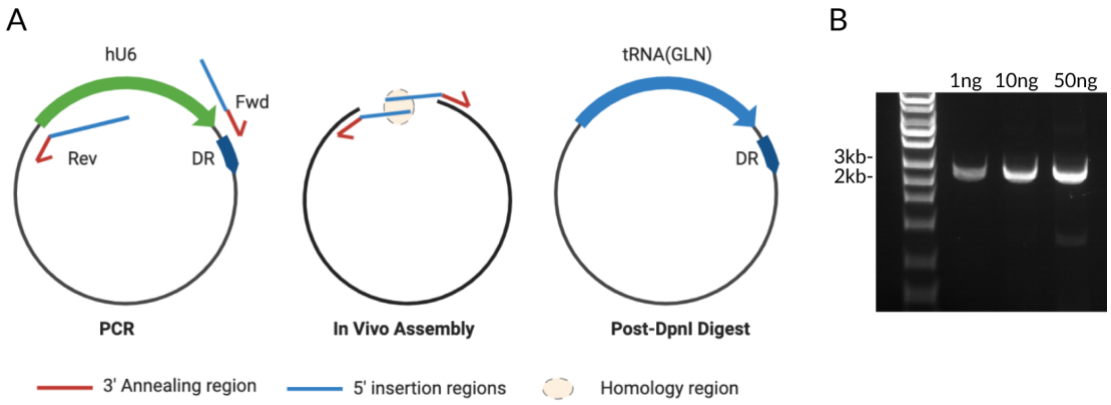


Figure 6-3 *In Vivo* Assembly of tRNA(GLN) gRNA promoter construct
A. Diagram demonstrating the *in vivo* assembly cloning protocol for the generation of the tRNA(GLN) guide RNA construct. The vector backbone was amplified with high fidelity polymerase, to generate a linear fragment with long overhang primers encoding the tRNA(GLN) insert with regions of central homology. DpnI digest prior to transformation eliminates the template plasmid. Transformation of XL-10 Gold cells with the linear fragments products allows recA-independent homologous recombination and generation of the new plasmid, replacing the hU6 promoter with the tRNA(GLN) promoter. **B.** Electrophoresis of PCR products following DpnI digest with a range of starting template concentrations. All show formation of an appropriately sized linear fragment prior to transformation.

6.2.2.4 Cloning of AAV RNA editor plasmids

For multi-fragment assembly, NEBuilder HiFi DNA assembly (NEB) was used as described in the general methods (Figure 6-4). For all assemblies the AAV plasmid backbone was produced by digestion of the pX601 vector with NotI and XbaI restriction enzymes to excise the CMV-SaCas9-gRNA transgene, leaving flanking ITRs. Each AAV plasmid and cloning details are listed in Table 6-2. Primers for multi-fragment assembly are listed in the appendix.

Final plasmid maps of all vectors are shown in Figure 6-1 and Figure 6-19. Cloning of gRNAs following assembly was performed with golden gate cloning as described in the general methods. All assemblies were screened with restriction enzyme digests, including with XmaI to confirm the presence of the ITRs, and then transgene identity confirmed with Sanger sequencing. Sequences of all relevant primers and synthetic fragments are listed in the appendix.

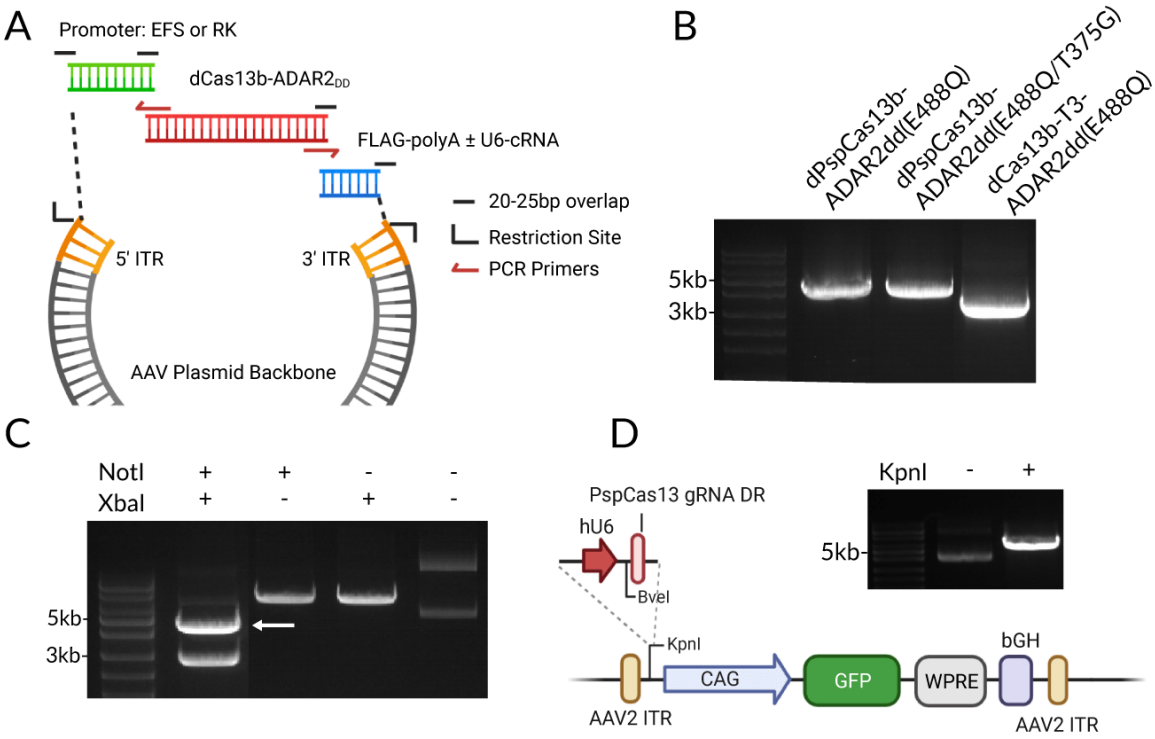


Figure 6-4 Cloning of AAV RNA editor plasmids

A. Schematic of multi-fragment DNA assembly using NEBuilder HiFi DNA Assembly to construct the AAV plasmids containing dCas13b-ADAR2$_{DD}$ constructs. Fragments were generated to contain complementary 20-25bp overlaps for assembly. To generate the backbone, a plasmid with AAV ITRs was digested to remove the transgene, as shown in (C). To introduce dCas13b-ADAR2$_{DD}$ constructs, primers were designed to amplify the appropriate region from the original plasmid as shown in (D). To introduce promoters, FLAG tags, polyA signals and U6-gRNA elements, synthetic fragments were generated to contain appropriate overlaps on the 5' and 3' end. **B.** Electrophoresis of PCR amplification of different dCas13b-ADAR2$_{DD}$ genes for use in the reaction in A. **C.** Electrophoresis of digestion of AAV plasmid (pX601-AAV-SaCas9) to remove the insert (small band) and isolate the backbone fragment (large band, arrow) containing the AAV plasmid backbone with ITRs for excision, purification and use for cloning as shown in (A). **D.** The AAV-gRNA plasmid was generated by digestion of an AAV-CAG-GFP-WPRE vector with KpnI shown in the electrophoresis. A synthetic fragment encoding the hU6 promoter and PspCas13b gRNA direct repeat (DR) scaffold with dual BveI sites for golden gate assembly gRNA cloning was inserted at this KpnI site. Final assembled plasmid maps are shown in Figure 6-17 and Figure 6-19

Plasmid Name	Cloning Details
All-in-one EFS-PspCas13-gRNA Vectors AAV-EFS-dPspCas13b-ADAR2$_{DD}$(E488Q)-sNRP1-U6-gRNA AAV-EFS-dPspCas13b-ADAR2$_{DD}$(E488Q/T375G)-sNRP1-U6-gRNA	The dPspCas13bdel-ADAR2$_{DD}$ genes (excluding the stop codon) were amplified from plasmids pc0053 and pc0055 via PCR with Phusion DNA Polymerase (NEB) with 5' extensions on the forward primers to generate complementary overhangs. The fragment encoding the EFS promoter and appropriate overhang was synthesised as a double stranded DNA GBlocks (IDT). The fragment encoding the 1×FLAG-stop codon-sRNP1polyA-U6-PspCas13 gRNA direct repeat was similarly synthesised.
Dual Vector EFS-PspCas13 Vectors AAV-EFS-dPspCas13bdel-ADAR2$_{DD}$(E488Q)-sNRP1 AAV-EFS-dPspCas13bdel-ADAR2$_{DD}$(E488Q/T375G)-sNRP1	U6-gRNA was excised from the all-in-one EFS plasmids using SpeI and XbaI restriction enzymes flanking the U6-gRNA and re-ligated.
Dual Vector RK-PspCas13 Vectors AAV-RK-dPspCas13bdel-ADAR2$_{DD}$(E488Q)-sNRP1	The dPspCas13bdel-ADAR2$_{DD}$(E488Q)-sNRP1 fragment was PCR amplified from the all-in-one EFS vector. The RK promoter was synthesised with appropriate overhangs (IDT GBlock) and assembled with multi-fragment assembly with the pX601 backbone.
Dual Vector PspCas13 gRNA Vectors AAV-U6-gRNA-CAG-GFP-WPRE-bGH	A fragment was synthesised to encode the U6 promoter with a downstream PspCas13 gRNA scaffold and an intervening dual BveI golden gate cloning site of gRNA insertion. This was cloned into the KpnI site of the AAV-CAG-GFP-WPRE-bGH plasmid (gift from Maria Patricio).
All-in-one RK-Cas13bt3-gRNA Vectors AAV-RK-dCas13bt3-ADAR2$_{DD}$(E488Q)-SV40-U6-gRNA	dCas13bt3-ADAR2$_{DD}$(E488Q) was amplified from the CMV-IE-HIVNES-dCas13bt3-ADAR2DD(E488Q)-bGH plasmid. GBlocks encoding the 3×FLAG-SV40pA-U6-gRNA and the RK promoter were synthesised (IDT), and all fragments assembled with the Px601 backbone.

Table 6-2 Cloning of AAV plasmids with multi-fragment assembly
Cloning details for each AAV plasmid, assembled with NEBuilder HiFi DNA assembly (primers for insert amplification to generated overhangs detailed in appendix)

6.2.3 Detection of RNA editing with RT-PCR Sequencing

RNA was extracted from cells harvested 48 hours following transfection using the RNeasy Plus Mini kit (Qiagen). Both gDNA eliminator columns and on-column DNA-se digestion were used to remove genomic DNA and plasmid contamination. Following OligoDT(20) primed cDNA synthesis with SuperScript III (Thermo Fisher Scientific), samples were PCR purified and regions of interest were amplified with high fidelity KOD Hotstart Mastermix (Merck, UK) using 5 μL of cDNA template. For amplification of the target cassette, a universal primer set was used (pSGDLucF2/pSGDLucR1) at an annealing temperature of 57°C with an extension time of 10 sec for a 472 bp product. Successful amplification of the product was confirmed by gel electrophoresis and then Sanger sequenced with pSGDLucF2. Chromatograms were inspected for quality prior to analysis and manually trimmed as required. Only trimmed chromatograms with >80% high-quality base calls (defined as Phred Quality>40, >99.99% base call accuracy) were included for analysis.

RNA editing rates were quantified using MultiEditR.[438] This software quantifies proportion of bases present at each position in a sequence from decomposition of base peaks in chromatogram data generated from Sanger sequencing.[439,440] A chromatogram from cells transfected with the target plasmid only was used as the reference sequence. The following settings were used for analysis of A>G editing sites: motif of interest (A), WT Base (A), Edited Base (G), Phred Cutoff (0.001, equivalent to Phred Quality of 30), p-value cutoff (0.0001), multiple comparison correction (yes). A custom Python script was used to extract the percent base height of G nucleotides at significant A>G editing sites relative to the reference sequence. Non-significant editing sites were set to zero.

6.2.4 Western blot

Western blots were performed as described in the general methods. Specifically, 40ug of denatured protein lysate in RIPA buffer from HEK293T cells was loaded into 10% Tris-Glycine

gels (Criterion TGX, Bio-Rad Laboratories) and run in Tris-Glycine SDS-PAGE running buffer (National Diagnostics, USA). Following transfer, PVDF membranes were blocked in Odyssey TBS Blocking Buffer (LI-COR Biosciences) and incubated in a primary antibody solution containing 10% blocking buffer with mouse anti-FLAG M2 1:1000 (F1804, Sigma-Aldrich) and rabbit anti-actin 1:2500 (Ab8227, Abcam).

6.2.5 Immunocytochemistry

ICC was performed as described in the general methods. Primary antibodies used were mouse anti-FLAG M2 1:1000 (F1804, Sigma-Aldrich) and donkey anti-mouse 1:500 AlexaFluor 488 (Thermo Fisher Scientific).

6.3 Results

6.3.1 Development of a Luciferase assay to report RNA editing

6.3.1.1 Validation of luciferase reporter plasmids

Dose-response experiments were performed using the dual luciferase plasmids transfected into HEK293T cells (see section 6.2.1.1 for design and cloning). Renilla luciferase was expressed stably and similarly at all doses tested across each plasmid (Figure 6-5) acting as an appropriate normalisation control. In cells transfected with the positive control plasmid (in-frame firefly), firefly expression increased with dose as expected, with expression levels at 1.5×10^6 RLU at 100 ng. In contrast, in the negative control plasmid (out-frame firefly) and experimental plasmids (premature termination codon), firefly expression plateaued between 5×10^3 and 1×10^4 RLU. When normalised for renilla expression, the firefly:renilla ratio was stable between 50 ng and 100 ng of positive control plasmid at 14.3 ± 3.5 and 15.2 ± 2.4. At this dose range, the firefly:renilla ratio of the experimental and negative control plasmids had a mean of 0.11 (range 0.06 – 0.27), demonstrating that the termination codon in the experimental plasmids effectively suppresses firefly expression to a background level with minimal readthrough at a similar rate to the negative control with the firefly coding sequence out of the reading frame. This provided a large dynamic range in the firefly:renilla ratio between the positive control and the experimental plasmids, across which restoration of firefly expression could be detected. For all further experiments, 50 ng of dual luciferase vector was used to minimise luciferase overexpression minimise the total mass of transfected plasmids for future triple transfection RNA editing experiments.

To further validate the assay, the stability of the firefly:renilla ratio when triple transfected with the positive control, Cas13-ADAR and guide RNA was assessed (Table 6-3). Across multiple plates, the positive control firefly:renilla ratio was 14.26 ± 1.58 (mean $\pm$ SD) generating

an inter-assay coefficient of variation (CV) of 11.1%. This ratio was similar to that found from transfection of the luciferase plasmid alone.

	Firefly:Renilla Luminescence Ratio						
Plate	Replicate 1	Replicate 2	Replicate 3	Replicate 4	Mean	SD	Intra-CV (%)
1	17.38	13.92	12.68	14.55	14.63	1.99	17.38
2	11.47	14.54	11.36	10.52	11.97	1.76	11.47
3	12.65	13.98	13.46	14.40	13.62	0.75	12.65
4	18.48	21.56	14.89	13.75	17.17	3.55	18.48
5	15.42	18.71	16.03	14.27	16.11	1.88	15.42
6	14.35	16.76	15.85	9.98	14.24	3.01	14.35
7	14.93	15.11	13.27	12.06	13.84	1.45	14.93
8	12.57	13.76	10.47	14.40	12.80	1.73	12.57
9	15.49	15.06	14.61	10.76	13.98	2.18	15.49
			Mean of means		14.26	1.58	14.10
			Inter-Assay CV (%)		11.10		

Table 6-3 Luciferase assay characteristics with triple transfection
Characteristics of the luciferase assay in HEK293T cells cultured in 96 well plates triple transfected with in-frame dual luciferase (50 ng), Cas13-ADAR and guide plasmids. All data is expressed as background subtracted luminescence of firefly expression normalised to renilla expression. SD = standard deviation, CV = coefficient of variation, RLU = relative luciferase units.

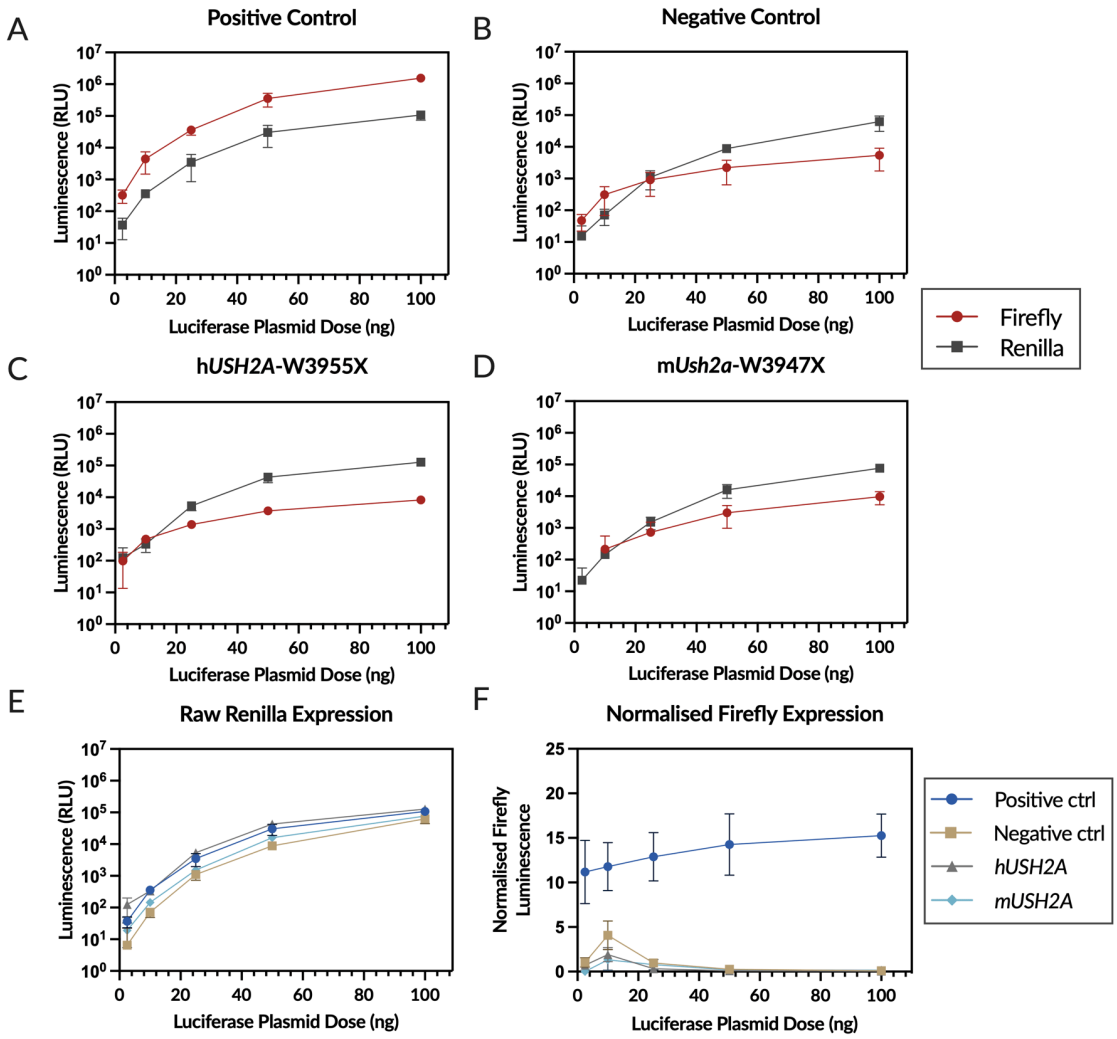


Figure 6-5 Dose response of luciferase plasmids in HEK293T cells

Across all plasmids (**A-D**), the expression of renilla luciferase increases with increased dose of transfected plasmid. Increased firefly expression increases with dose when the firefly gene is in frame (**A**). In plasmids where firefly is out of frame or is preceded by a stop codon (**B-C**), firefly expression plateaus at a low background level. **E.** Raw background subtracted renilla expression summarised by plasmid across the dose range is similar across all plasmids. **F.** Renilla expression can be used to normalise firefly expression. Although the ratio between firefly:renilla is variable at low doses of plasmid with low absolute renilla and firefly luminescence, at higher doses (50-100 ng) the ratio is close to zero in both the premature stop and out of frame plasmids and gives the assay over a log unit of dynamic range between the positive control and experimental plasmids for detection of restoration of firefly signal. RLU = relative luciferase units. Mean ± SEM, n = 3.

6.3.1.2 Pilot of RNA editing detection with luciferase assay

Cox et al. developed a number of different RNA editing effectors (evaluated later in this chapter),[300] however the shorter coding sequence of the C-terminally truncated (dPspCas13b-del-984-1090) potentially permits packaging within AAV and thus was used for initial characterisation and optimisation. This was paired with the $ADAR2_{DD}$(E488Q) hyperactive deaminase to maximise editing rates for detection. A 50nt guide RNA with an A-C mismatch at 36nt from the scaffold sequence at the adenosine to be edited was designed to mediate repair of the *hUSH2A*-W3955X mutation (*hUSH2A*-50nt-36).

In this initial test, the luciferase vectors were transfected with and without dPspCas13b-ADAR, together with a targeting or non-targeting gRNA. Editing efficiency of the targeting and non-targeting guide was normalised to the positive and negative controls (see section 6.2.1.4). This demonstrated an encouraging mean (± SEM) editing efficiency of 23.4% ± 0.9 (Figure 6-6B). No restoration of firefly expression was seen in samples transfected with the dCas13-ADAR effector and a non-targeting guide, or in samples transfected with a targeting guide alone without dCas13-ADAR indicating no recruitment of any endogenously expressed ADAR (Figure 6-6). No toxicity differences were seen between cells transfected with or without the dPspCas13b. This supports the conclusion that the restoration of firefly expression observed in samples transfected with targeting RNA editing constructs is due to the targeted repair of the termination (TAG) codon preceding the firefly coding sequence to a tryptophan (TGG) codon, and not a spurious increase in firefly expression secondary to other mechanisms.

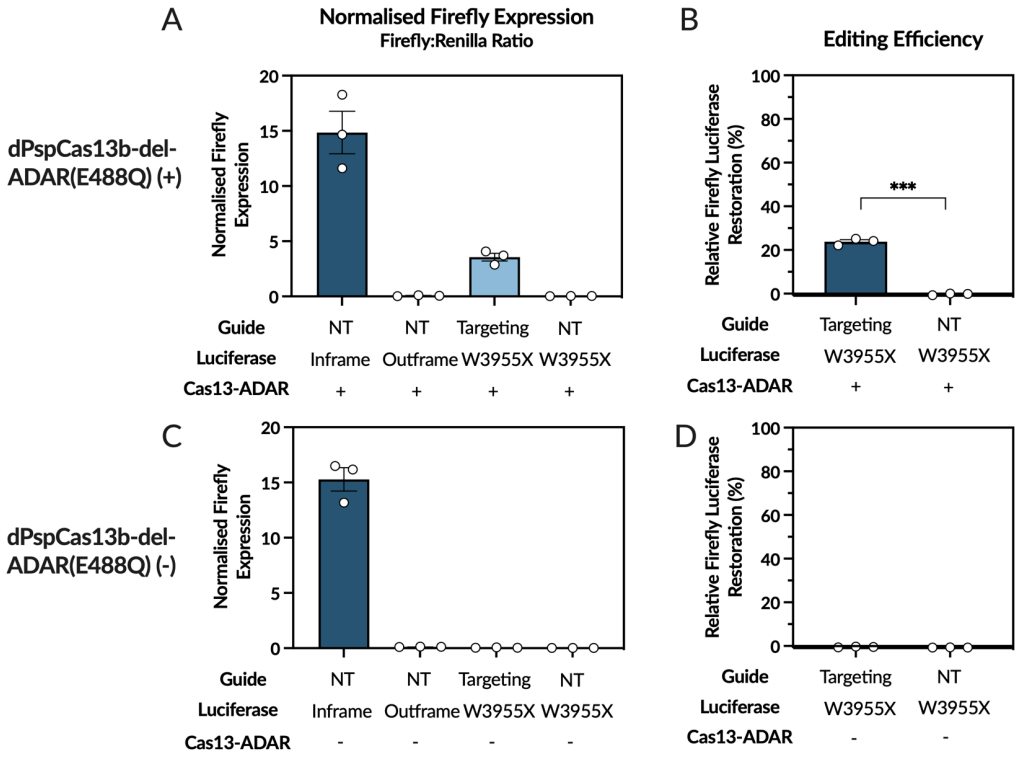


Figure 6-6 Calculation of RNA editing efficiency from luciferase assay

A. Normalised ratios from HEK293T cells transfected with 50 ng dPspCas13b-del-ADAR$_{DD}$(E488Q), 100 ng of guide RNA (*hUSH2A*-50nt-G3) and 50 ng of dual luciferase vector. No firefly expression is observed in cells transfected with an out-frame or W3955X luciferase plasmid, but restoration is seen when a targeting guide RNA is transfected targeting repair of the W3955X termination codon **B**. The relative restoration of repair between the positive control (in-frame) and negative control (out-frame) plasmids can be calculated as percentage, demonstrating the efficiency of the guide RNA for restoring firefly expression relative to a non-targeting guide ($p < 0.0001$, students t-test). **C-D.** RNA editing was not detectable in cells transfected with guide RNA alone (without the Cas13-ADAR construct), or in cells transfected with non-targeting (NT) guides. Mean ± SEM, n = 3.

6.3.2 Testing and optimisation of RNA editing constructs

To optimise the editing efficiency of the system a series of gRNAs were screened with the luciferase assay, followed by testing of a range of doses and types of RNA editing constructs.

6.3.2.1 Guide RNA screening

Guided by published data, an initial guide screen was performed to test guides against the *hUSH2A*-W3955X and *mUsh2a*-W3947X targets with mismatch distances between 32-36nt—the distance between the gRNA direct repeat and the mismatched cytosine in the gRNA to the target adenine (Figure 6-7).[300] Repair rates of *hUSH2A* up to 24% with guide 50nt-36 were observed, with the highest rates generated with a 36nt mismatch distance. Guides targeting *mUsh2a* performed poorly, with editing rates of up to 5%.

Given the different editing rates seen between the two targets, an extended guide screen with optimised doses of editing constructs was conducted to encompass a broader range of mismatch distances, and additionally screen for the activity of 30nt guides (Figure 6-8). Against the *hUSH2A* target, the previously identified *hUSH2A*-50nt-36 guide was most active, with an 38.0% ± 2.2 editing rate. This screen used a higher total plasmid dose of 75 ng of PspCas13-ADAR and 150 ng of gRNA plasmid, compared to the 50 ng and 100 ng respective doses used in the pilot screen. Against the *mUsh2a* target, the screen identified a significantly more efficient guide (*mUsh2a*-50nt-24) with an editing rate of 50%. The limited number of 30nt guides screened showed lower editing efficiency relative to the 50nt guides.

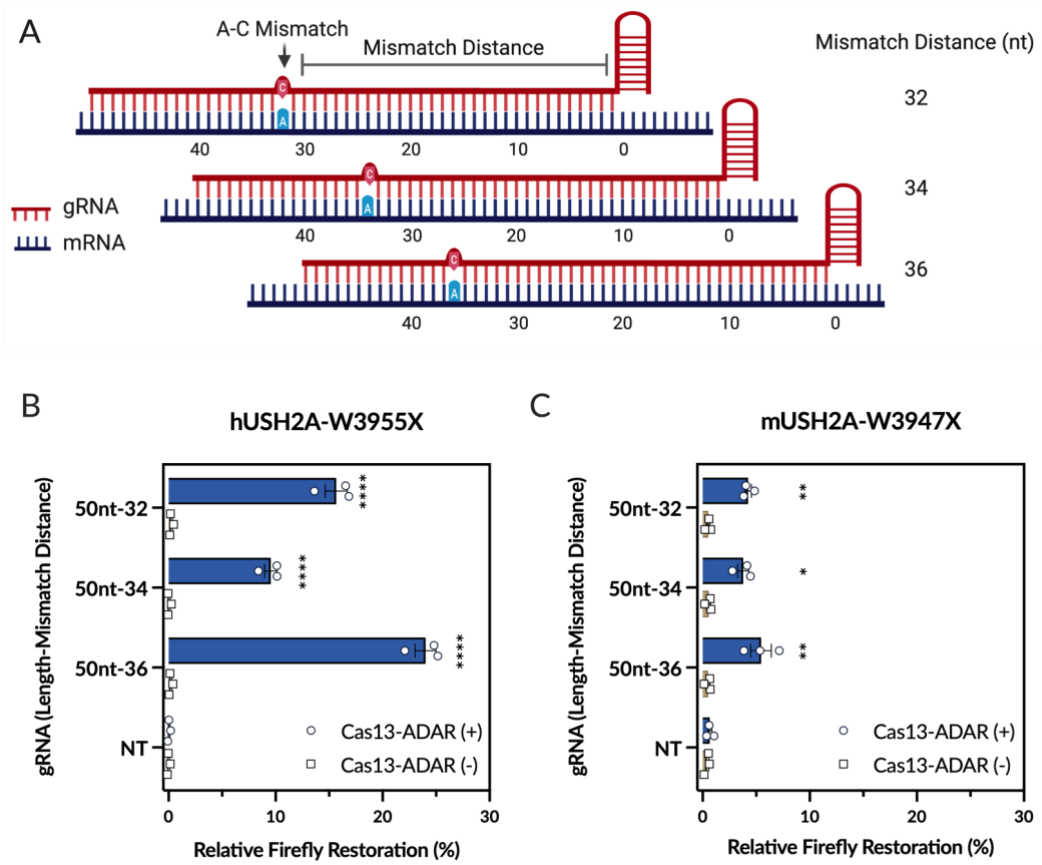


Figure 6-7 Initial guide RNA screening for *hUSH2A*-W3955X and *mUsh2a*-W3947X repair

A. Three 50 nt guides designed to tile the target sequence with mismatch differences of 32-36 nt measured from the gRNA-target nucleotide A-C mismatch to the gRNA direct repeat were selected for an initial screen. Guides were screened against the human (**A**) and mouse (**B**) USH2A target sequences using the luciferase assay. Robust repair of *hUSH2A*-W3955X and low levels of *mUsh2a*-W3947X repair was observed. RNA editing was not detectable above background levels in cells transfected with guide RNA alone (without the Cas13 construct), or in cells transfected with non-targeting guides. Guide nomenclature = Guide length-Mismatch Distance. All data mean ± SEM, n = 3, one-way ANOVA with Dunnet's test for multiple comparisons between guides and dPspCas13b-del-ADAR$_{dd}$(E488Q) (+) non-targeting control. Performed with doses of luciferase plasmid (50 ng), dPspCas13del-ADAR2(E488Q) plasmid (50 ng) and gRNA plasmid (100 ng). NT = non-targeting

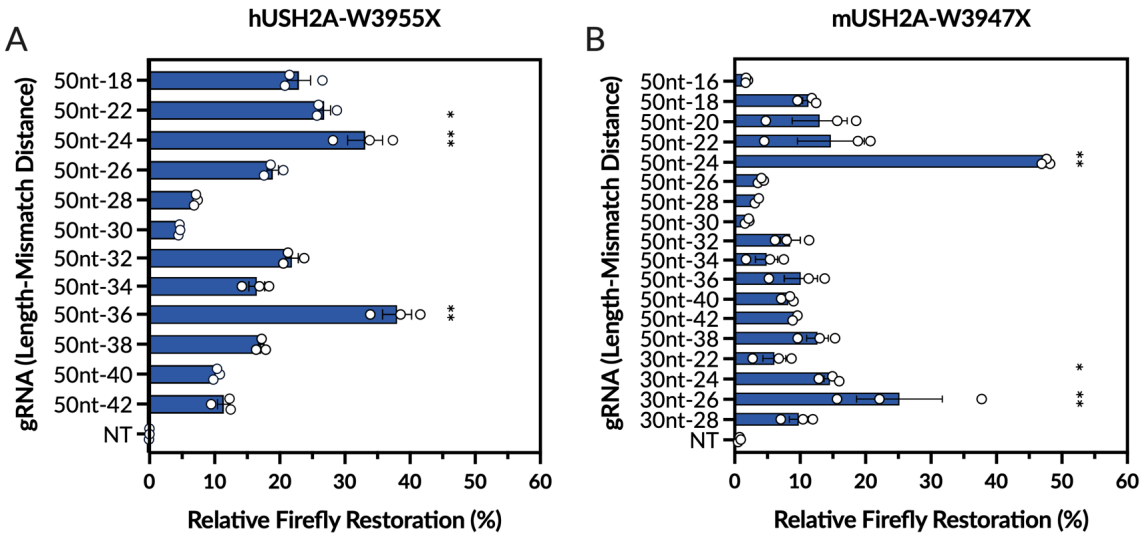


Figure 6-8 Extended gRNA screen for *hUSH2A*-W3955X and *mUsh2a*-W3947X repair
A. 50nt guides tiling mismatch positions 18-42 were screened against the *hUSH2A*-W3955X target. The most active guide was the previously identified 50nt-36 guide ($p = 0.0015$), with similar activity demonstrated by the 50nt-24 guide. **B.** 50nt guides tiling mismatch positions 16-42, and four 30nt guides tiling mismatch positions 22-28 were screened for the *mUsh2a*-W3947X mutations. The 50nt guide with the 24nt mismatch (50nt-24) demonstrated markedly higher activity than other guides ($p = 0.013$). Data shown as mean ± SEM, n = 3, Kruskal-Wallis Test with Dunn's multiple comparison testing. Performed with doses of luciferase plasmid (50 ng), dPspCas13del-ADAR2(E488Q) plasmid (75 ng) and gRNA plasmid (150 ng). NT = non-targeting

6.3.2.2 Dose optimisation of dPspCas13b-ADAR2$_{DD}$ and gRNA constructs

Given the differences in activity with the same guide against the *hUSH2A* target at different plasmid doses, the optimal dose of dCas13b-ADAR and gRNA vector and ratio between these constructs for maximum A>G editing efficiency was explored for transfection of HEK293T cells in a 96-well plate using the dual luciferase assay. The ratio of gRNA to dPspCas13bdel-ADAR2$_{DD}$ was varied from 1:4 to 4:1 across these doses. Similar rates of editing were observed between both the doses of dPspCas13 plasmid at all gRNA doses (Figure 6-9A), suggesting that 75 ng of del-dPspCas13 plasmid was sufficient for maximum editing. Editing rates increased with the dose of gRNA delivered, however at doses of 300 ng this led to higher variability in the editing efficiencies between replicates. At these doses, toxicity observed as patchy cell death

on microscopy was occasionally evident (Figure 6-9B), particularly at the highest overall dose which was 500 ng of total transfected plasmid including the reporter plasmid. As no significant increases in editing efficiency were seen beyond a dose of 150 ng:75 ng of dPspCas13b-ADAR:gRNA, this was chosen as the dose for future experiments.

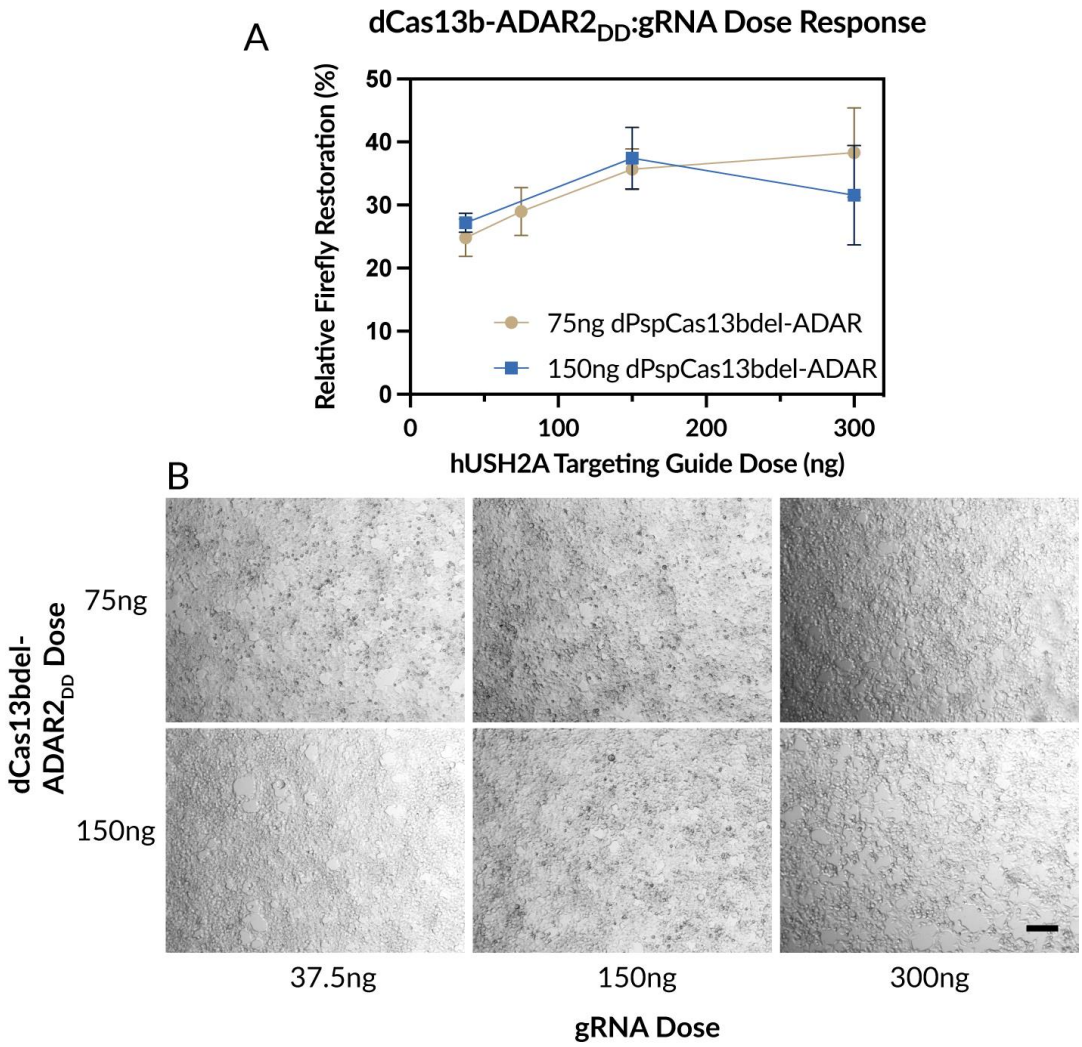


Figure 6-9 Dose response testing of dPspCas13b-ADAR2$_{DD}$ constructs
A. Repair efficiencies calculated using *hUSH2A*-W3955X dual luciferase construct. HEK293T cells were transfected with 50 ng of luciferase plasmid, two doses of the dPspCas13bdel-ADAR2$_{DD}$ construct (75 ng and 150 ng) and increasing doses of a *hUSH2A* targeting guide plasmid. **B.** Representative light microscope images (10× magnification) of HEK293T cells 48hrs post-transfection prior to lysis for luciferase assay. Toxicity is seen at the highest dose of plasmids (150 ng Cas13b, 300 ng guide RNA, 50 ng luciferase plasmid) with reduced confluency of cells likely due to cell death. Scale bar, 100 μm.

6.3.2.3 Comparison of RNA editing constructs

Having identified highly active gRNAs and optimal doses for transfection in HEK293T cells, four different Cas13-based RNA editing effector constructs were compared evaluating the full-length (dPspCas13b) and C-terminal truncated (dPspCas13b-del) Cas13s, and between hyperactive (E488Q) and specific (E488Q/T375G) $ADAR_{DD}$ variants (Figure 6-10, Table 6-1).

Using a *hUSH2A* targeting guide (*hUSH2A*-50nt-36), significant editing was achieved with each construct relative to the non-targeting guide (all $p<0.05$). Comparison between groups with two-way ANOVA revealed a significant effect for both the $ADAR_{DD}$ and the Cas13b construct, and interaction between these factors. *Post hoc* testing demonstrated significantly higher editing on-target editing efficiency with the E488Q compared to the E488Q/T375G $ADAR_{DD}$ variant for both the full length ($p=0.0006$) and truncated ($p<0.0001$) constructs as expected.

No loss of efficiency was observed in the C-terminally truncated Cas13b constructs compared to the full-length constructs. With the E488Q/T375G $ADAR_{DD}$ no significant differences were observed ($p=0.99$), while surprisingly in constructs with the E488Q variant, the C-terminally truncated construct had a mean absolute editing rate 8.3% ± 2.3 higher than the full-length construct ($p=0.027$).

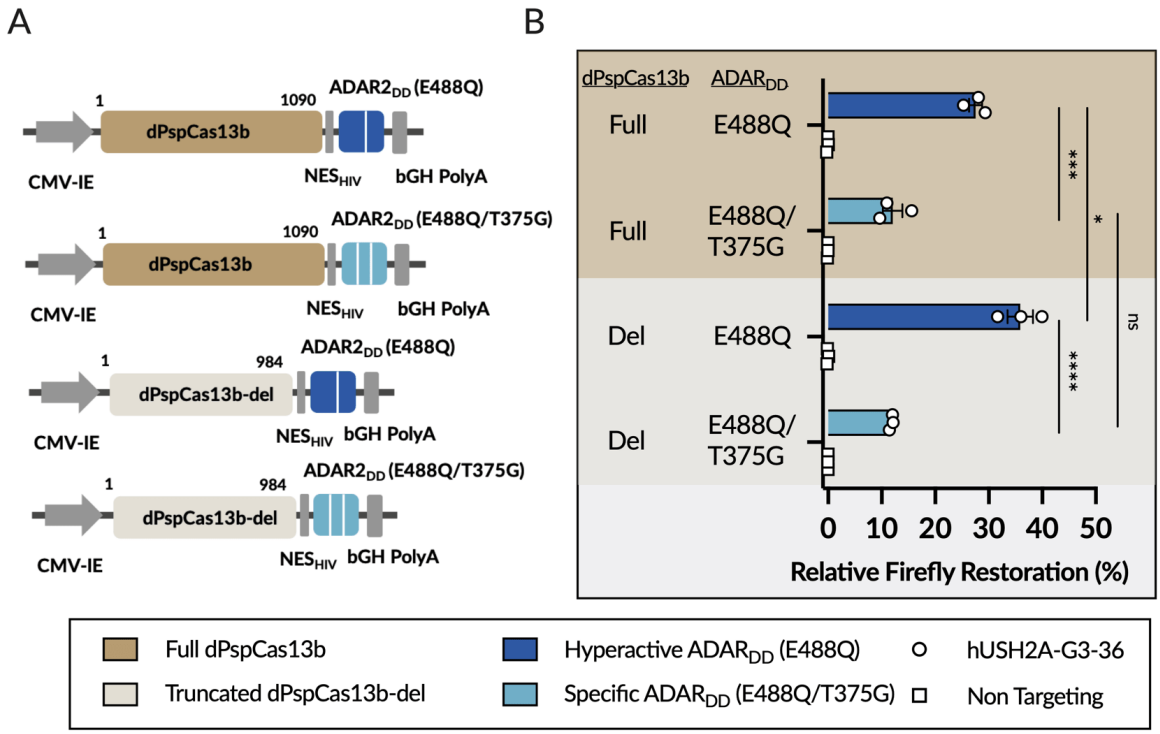


Figure 6-10 Comparison of dPspCas13b-ADAR2$_{DD}$ editing constructs

A. Schematic diagram of the four tested dPspCas13b-ADAR$_{DD}$ editing constructs. All plasmids have an identical construction, driven by the same ubiquitous CMV promoter, HIV-derived nuclear export signal and a bGH poly(A) tail. Two contain the full coding sequence for the dPspCas13b (1090 amino acids), while the dPspCas13b-del constructs contain C-terminal truncated CDS (984 amino acids). Two ADAR2 deaminase domain variants were tested, containing either the E488Q hyperactive editing mutation (single white line), or the more specific less active dual E488Q/T375G variants (double white lines). **B**. Editing efficiencies of each construct were compared using the *hUSH2A*-50nt-36 guide. The deaminase domain used significantly affected editing, with the E488Q mutation conferring higher editing efficiency than the E488Q/T375G variants for both construct lengths ($p < 0.001$). The C-terminal truncation did not affect the editing efficiency of the E488Q/T375G constructs ($p > 0.05$). The C-terminal truncated construct was more efficient than the full length dPspCas13b with the E488Q variant ($p = 0.027$). Mean ± SEM, n = 3, Two-way ANOVA of data from targeting guides with Cas13 length and ADAR type as factors with Tukey test for multiple comparisons: $F(1, 8) = 6.346$, $p = 0.036$ for effect of Cas13; $F(1, 8) = 149.2$, $p<0.0001$ for effect of ADAR; $F(1, 8) = 6.897$, $p = 0.030$ for interaction between factors.

6.3.2.4 Evaluation of minimal Cas13bt orthologues

Three recently identified minimal orthologues termed Cas13bt identified from mining of metagenomes were also screened for activity (Table 6-4, Figure 6-11).[282] As the optimal guide length and mismatch distance for these orthologues was unknown, 30nt and 50nt spacer sequences were cloned into the respective gRNA scaffolds for each orthologue, and a luciferase assay screen of tiled guides was performed against the *mUsh2a*-W3947X target (Figure 6-11). The 30nt guides all demonstrated editing rates of less than 10%, but editing rates of up to 21% were seen with the 50nt guides. Of note, a 17% ± 1.2 editing rate was achieved with guide 50nt-28 with the shortest orthologue, Cas13bt3. This orthologue is ~600nt shorter than the dPspCas13b(del) construct and allows for greater flexibility for AAV packaging, however, it is substantially less active.

Orthologue Name	Organism Derived From (NCBI Accession)	Protein Size (aa)	Cas13(NES)-$ADAR2_{DD}$ Size (nt)
dPspCas13b	Prevotella sp. P5-125, Prevotella Pectinovora. (JXQL00000000)	1090	4467
dPspCas13b(del)	As above, C-terminal truncated	984	4152
dCas13bt1	Atlantic deep subsurface marine sediment (SAMN13385563)	803	3625
dCas13bt3	Planctomycetes bacterium isolate B28_G16 (QNBS01000103.1)	774	3538
dCas13bt5	Hotspring sediment (SAMN06343857)	873	3853

Table 6-4 Characteristics of Cas13b orthologues used
Four Cas13 orthologues were used in this study. All plasmids encoding these genes were gifts from Feng Zhang, Broad Institute. dPspCas13 has been published for use in RNA editing, while the dCas13bt enzymes are purported Cas13 enzymes identified from metagenomes. National Centre for Biotechnology Information (NCBI) nucleotide sequence, genome sequence, or BioProject accession numbers are listed. The nucleotide size includes the coding sequence of the Cas13 together with the $ADAR2_{DD}$ and associated linkers and localisation sequences. aa = amino acid, nt = nucleotide.

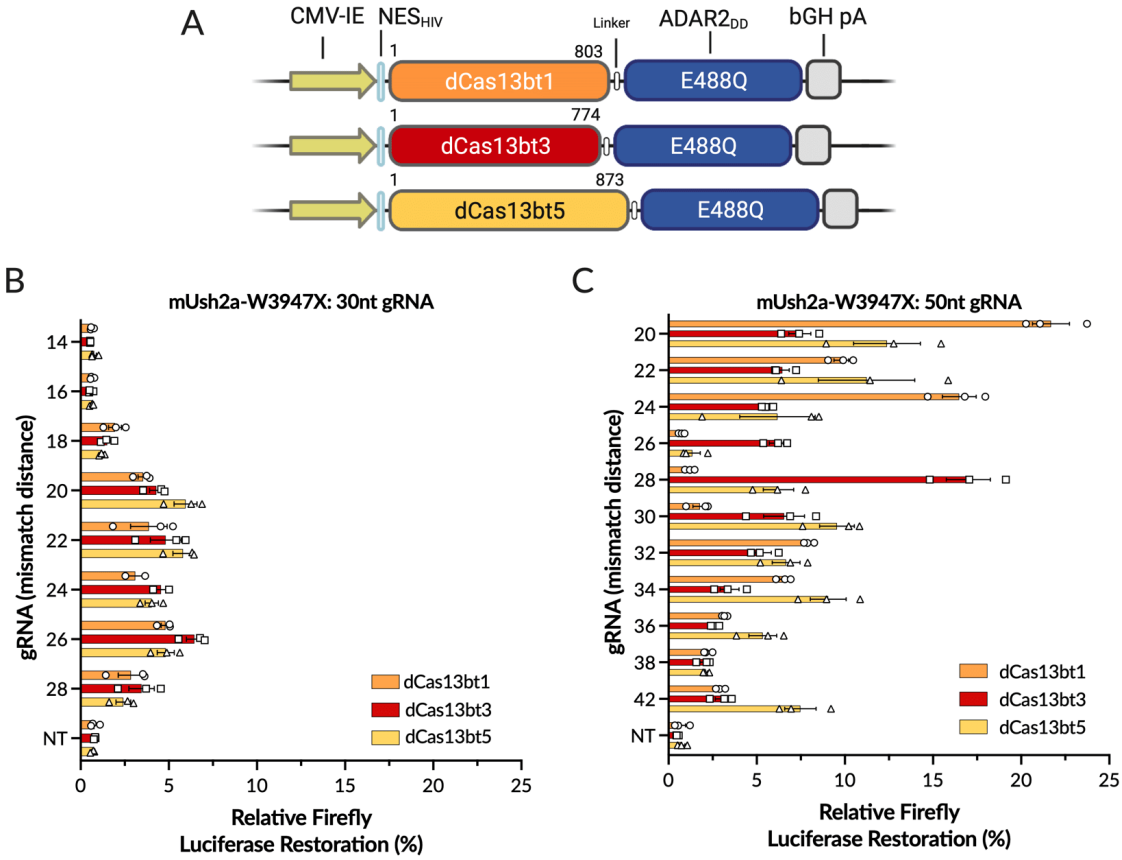


Figure 6-11 Guide screening and comparison of Cas13bt orthologues
A. Vector maps of the minimal Cas13bt constructs. Differences to the dPspCas13b constructs include the N-terminal placement of the nuclear export signal (NES) and the use of a GGS_2 linker rather than 2 GS linkers. **B.** 30nt guides tiling mismatch positions 14-28 were screened against the *mUsh2a*-W3947X target, yielding low editing rates of <10%. **C.** 50nt guides tiling mismatch positions 20-42 were screened against the *mUsh2a*-W3947X target, yielding improved editing rates, but still below those seen with dPspCas13. All data mean ± SEM.

6.3.3 Comparison of luciferase assay with Sanger sequencing

To confirm that the detected firefly restoration is a result of RNA editing correction of the upstream nonsense mutation, Sanger sequencing of amplicons generated from reverse transcribed RNA and the luciferase assay were conducted in parallel. As the luciferase assay requires cell lysis, precluding the extraction of RNA from that well, RNA was extracted from adjacent wells on the same plate transfected under identical conditions. Methods to reduce carryover of plasmid DNA were optimised, and all samples were purified with DNA eliminator

columns and treated with DNAse. Using RT-PCR sequencing, editing rates were derived from Sanger sequencing peak heights using trace decomposition.[438]

Samples transfected with the dPspCas13bdel-ADAR2$_{DD}$(E488Q) construct showed on-target editing rates of 77% ± 0.9 and 86% ± 1.2 for *hUSH2A* and *mUsh2a* respectively. The dPspCas13bdel-ADAR2$_{DD}$(E488Q/T375G) constructs edited at a lower on-target rate of 40% ± 3.0 and 45% ± 3.0 for each target (Figure 6-12). No on-target editing was detected in samples transfected with non-targeting guides, or in samples transfected with a targeting guide but no editing construct.

Editing rates of each replicate quantified by RT-PCR sequencing were strongly correlated with those quantified with the luciferase assay conducted in parallel (Pearson's $r = 0.88$) (Figure 6-13). Editing rates quantified by sequencing were higher than by the luciferase assay, and for the dPspCas13bdel-ADAR2$_{DD}$(E488Q) construct approach a ceiling of 100% editing.

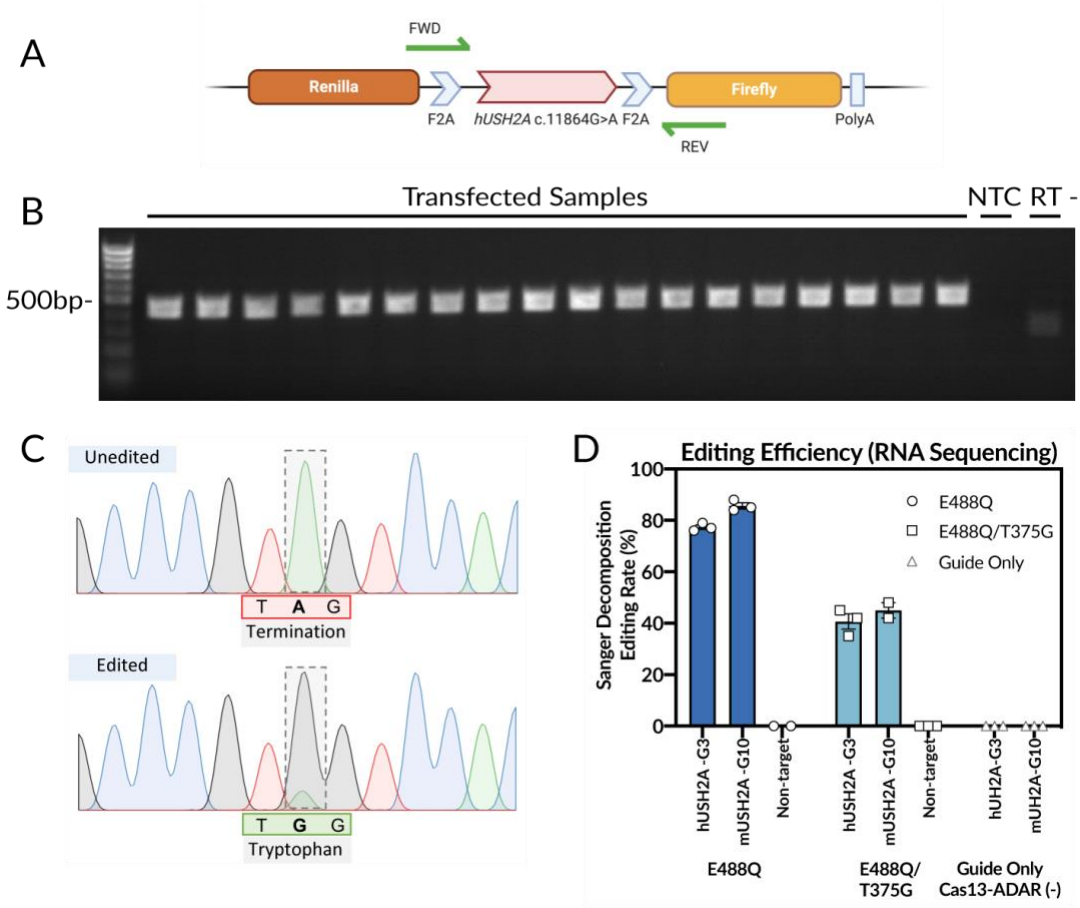


Figure 6-12 Editing efficiency from RNA sanger sequencing and decomposition
A. Universal primer pairs were designed to bind either side of the targeted region of the reverse transcribed RNA transcript. Diagram demonstrates a *hUSH2A* target cloned into the dual luciferase assay. **B.** Representative image of gel electrophoresis of RT-PCR products to confirm successful amplification and verify the correct amplicon length, predicted to be 427 bp. Amplification was not detected in non-transfected samples (NTC), or in the reverse transcription negative (RT-) controls. **C.** Representative trace from an unedited sample (transfected with the luciferase plasmid only) and an edited sample (transfected with luciferase plasmid and the editing constructs). Sanger sequencing chromatograms were aligned to a reference target. The editing rate at the target base was determined by calculating the relative proportions of amplicons containing adenine or guanosine using decomposition of the sanger sequencing peaks. This example demonstrates an 81% A to G editing rate. **D.** Editing rates as determined by RNA sequencing and decomposition using the dPspCas13b-Del-ADAR$_{DD}$ constructs. Both the *hUSH2A* and *mUsh2a* targeting guides produced robust on-target editing relative to non-targeting guides for both constructs (One-way ANOVA, all $p < 0.001$). Editing rates are higher with the ADAR$_{DD}$(E488Q) than the ADAR$_{DD}$(E488Q/T375G) deaminase domain. On-target editing was not detected using a non-targeting guide, or in samples transfected with guide only and no Cas13-ADAR$_{DD}$ construct. Data mean ± SEM.

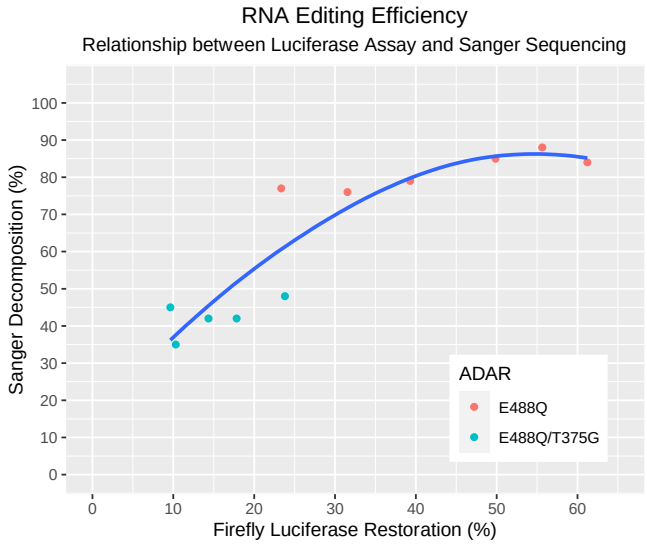


Figure 6-13 Correlation between RNA editing with dPspCas13b-ADAR2$_{DD}$ measured by luciferase assay and sanger sequencing
On-target editing rates as measured using the luciferase assay (x axis) decomposition of sanger sequencing (y axis) from adjacent samples transfected identically in the same plate are plotted. Results are from samples transfected with different guides and different editing constructs. A curve fitted with local regression (loess) is plotted with 95% confidence intervals. A positive relationship between editing rates detected by each method is observed (Pearson's r = 0.88). Editing rates are observed as higher by sanger sequencing for a given sample, compared to editing rate detected with the luciferase assay. Editing rates determined by Sanger sequencing appear to approach a ceiling of maximum editing.

6.3.4 Local off-target effects detected by Sanger sequencing

The propensity for each construct to edit local adenosines other than the target nucleotide was assessed across the 200nt target (Figure 6-14) edited with dPspCas13bdel-ADAR2$_{DD}$ constructs. In agreement with previous reports,[300] the E488Q construct demonstrated off-targets in both the *hUSH2A* (2 sites) and *mUsh2a* targets (8 sites). The one significant off-target adenosine in the *hUSH2A* sequence produces a silent change (Leu>Leu), however most of the off-target sites within the *mUsh2a* sequence produce missense mutations (Table 6-5).

Off-target editing of adenosines occurred within the gRNA binding region for both guides, while editing outside the gRNA-target duplex occurred in *mUsh2a* but not *hUSH2A*. Comparatively, the E488Q/T375G deaminase mutant was far more specific, editing at only the target adenosine in both targets, with no off-target editing in with non-targeting guides. Off-

targeting in the *mUsh2a* transcript outside the gRNA duplex region also occurred in corresponding positions with the non-targeting guide and no editing was detected in samples transfected with targeting guides only. This suggests that the off-target editing at these sites was not due to editing due to any endogenously expressed ADAR, but also that the off-target editing by the exogenous ADAR(E488Q) was independent of gRNA binding at the site.

Hypothesising that differences in RNA structure between the *hUSH2a* and *mUsh2a* targets may allow for the formation of dsRNA substrates for ADAR editing and account for the higher number of off-target sites within the *mUsh2a* sequence, the folded structures of the 200nt target sequences were predicted and plotted with a partition function to predict base-pairing probability (Figure 6-15). Comparatively, the *mUsh2a* structure forms a more extensive double stranded structure with bulges, whereas the *hUSH2A* sequence is predicted to form larger loops with short double stranded regions. The off-target locations in *mUsh2a* appeared to occur in or close to bulges in the predicted structure, rather than in regions with high binding probability.

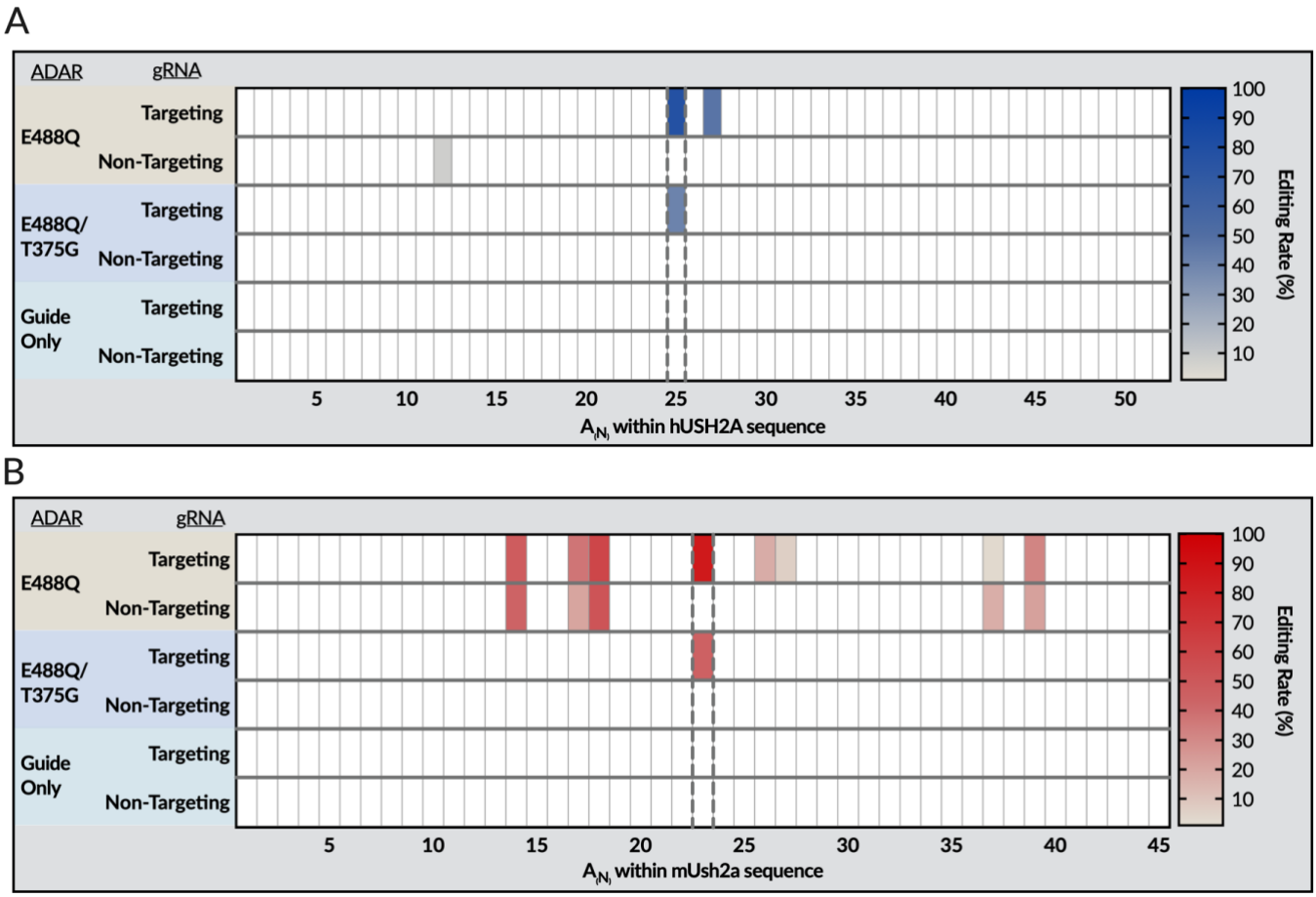


Figure 6-14 Local off-target analysis by sanger sequence decomposition
MultiEditR decomposition of the sanger sequencing reads was used to find sites of significant local A>G editing sites in the *hUSH2A* (**A**) and *mUsh2a* (**B**) amplicons in HEK293T cells transfected with the luciferase targeting construct and dPspCas13bdel-ADAR2$_{DD}$. Each cell along the x axis describes each sequential A within the reference sequence, with the target base outlined by a grey dotted line. Positions without detected significant editing are white, while the heatmap colours indicate the A>G conversion rate at that base position. Local off-target editing is more prevalent in samples transfected with the hyperactive E488Q ADARDD, including with a non-targeting guide. Off-target editing is not detectable in samples transfected with the specific E488Q/T375G or in cells transfected with guide RNAs only. Values are mean editing rate, n = 3.

Adenosine in sequence	Original Codon	Altered Codon	Original Amino Acid	Altered Amino acid	Mean editing rate (%)	
					E488Q	E488Q/ T375G
hUSH2A						
12	TAC	TGC	Tyr	Cys	0*	0
27	TTA	TTG	Leu	Leu	47	0
mUsh2a						
14	TAC	TGC	Tyr	Cys	47	0
17	AAC	GAC	Asn	Cys	37	0
18	AAC	AGC	Asn	Ser	60	0
17+18	AAC	GGC	Asn	Gly	22^	0
26	ATA	GTA	Ile	Val	18	0
27	ATA	ATG	Ile	Met	6	0
26+27	ATA	GTG	Ile	Val	1^	0
37	CAA	CAG	Gln	Gln	3	0
39	AGT	GGT	Ser	Gly	31	0

Table 6-5 Codon changes due to off-target editing

Off-target editing sites in samples transfected with a targeting guide in the *hUSH2A* and *mUsh2a* sequences and predicted codon changes. The one significant off-target edit in *hUSH2A* results in a synonymous change. The majority of edits within the *mUsh2a* sequence are predicted to result in missense changes. No off-targets are editing is seen in the E488Q/T375G transfected cells. ^where a codon contains two adenosines that are edited, the editing rate listed for that codon is estimated by multiplying the editing rates of these two sites together to predict the likelihood of this codon change. *editing at this site was detected in one non-targeting sample at 16%. Data = mean of targeting guide, n = 3.

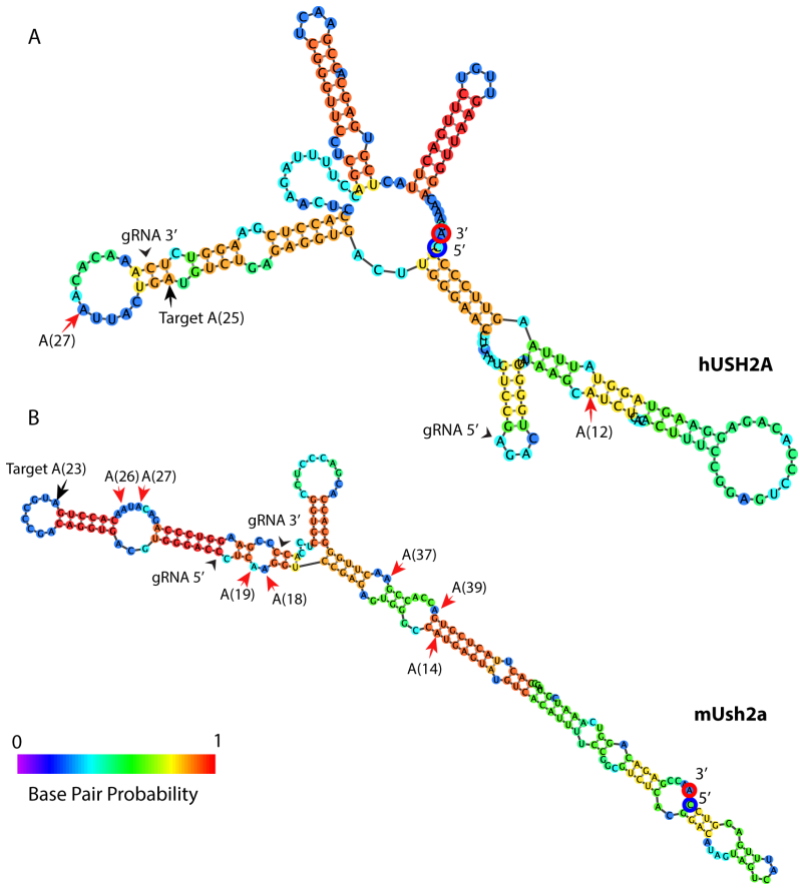


Figure 6-15 RNA structures of *USH2A* targets

RNA fold predictions of the 200 nt *hUSH2A* (**A**) and *mUsh2a* (**B**) targets from the luciferase assay. The target nucleotides for RNA editing (black arrows), the 5' and 3' boundaries of the gRNA binding region (black arrow heads) and the nucleotides with significant off-target editing sites (red arrows) from Figure 6-14 are demonstrated. The 5' and 3' ends are labelled and circled. Comparatively, the *mUsh2a* target is predicted to form a more extensively paired structure with a number of smaller internal loops and bulges, compared to the greater frequency of larger loops formed in the *hUSH2A* target. The off-target editing sites in *mUsh2a* that lie outside the gRNA binding site appear to form within or close to these predicted bulge sites. Structures and partition function generated with Vienna RNAfold[441] using the Turner (2004)[442] algorithm within Geneious software.

6.3.5 Evaluation of minimal regulatory elements to enable AAV packaging

6.3.5.1 Minimal RNA Pol II promoters

Constructs to this point used the strong CMV-IE (584 bp) promoter and bGH polyA (225 bp) sequences to drive Cas13-ADAR expression, however, they are too long for packaging of the C-terminal truncated dPspCas13bdel-ADAR$_{DD}$ construct (4.15 kb) within AAV. Short promoters and polyA sequences were screened in the luciferase assay to investigate if RNA editing activity could be maintained.

Minimal ubiquitous RNA polymerase II promoters were desired for expression of Cas13-ADAR, as these allow testing of the constructs in HEK293T cells and would allow potential use of the vectors across a wide range of tissues or cell lines. The human-derived human elongation factor-1α core (EFS, 212 bp) promoter has demonstrated activity for driving Cas9 mediated gene editing *in vitro*[443–445] and *in vivo*[443], and for driving ubiquitous expression in the retina.[446] The super core promoter 1 (SCP1, 80 bp) is a synthetic promoter composed of core promoter transcription factor binding sites[447] and is reported to drive efficient expression of SaCas9 for transcriptional modulation at comparable rates to the CMV-IE promoter.[448]

The EFS and SCP1 promoters were cloned in place of the CMV-IE promoter in the CMV-IE.dPspCas13b-del-ADAR$_{DD}$(E488Q) plasmid and RNA editing rates compared in the luciferase assay. Although weaker than CMV-IE promoter, editing rates obtained with the EFS promoter were equivalent to those with the CMV-IE promoter (Figure 6-16A). This was consistent using either a *mUsh2a* or *hUSH2A* targeting guide. Compared to CMV-IE, editing rates with the SCP1 promoter were reduced by a mean of 45%. A significant effect for the influence of the promoter was found with two-way ANOVA ($p=0.01$ for effect of promoter), however no significant differences between promoters were seen on multiplicity testing.

6.3.5.2 Minimal polyA sequence

The soluble neuropilin-1 (sNRP1) polyadenylation signal is a 17bp highly minimal sequence that efficiently polyadenylates mRNA at equivalent levels to the common SV40 polyA signal.[449] Functionally, it has been used for polyadenylation of SaCas9 for transcriptional modulation at levels equivalent to the longer bGH polyA,[448] and has been used for neuronal gene expression.[450] To ensure efficient polyadenylation, a repeated sNRP1 sequence (34 bp, referred to as sNRP1 henceforth) was cloned in place of the bGH polyA in the CMV-IE.dPspCas13bdel-ADAR$_{DD}$(E488Q).bGH plasmid.

Editing efficiency with constructs containing the sNRP1 compared to the bGH polyA signal was reduced by a mean of 25% for *mUsh2a* and *hUSH2A* (Figure 6-16), although this difference was not significant (p=0.23 for effect of polyA) (Figure 6-16B).

6.3.5.3 tRNA Promoter to drive gRNA expression

The human U6 (hU6, 249 bp) promoter is commonly used as an RNA Pol III promoter for the strong constitutive expression of CRISPR gRNAs as the defined transcriptional start site results in accurate gRNA transcription without additional nucleotides added to the 5' end.[196,451] tRNA promoters have also been used for gRNA expression, as precise processing by RNAase Z at the 3' end of the tRNA allows for gRNA definition.[452] Although tRNA-mediated gRNA expression is typically lower than that by hU6, many authors have found this to have minimal effects on editing rates with both Cas9 and Cas13,[286,452–456] and their shorter length allows for space saving in compact vectors.

The strong constitutive tRNA$_{GLN}$ (70 bp, tRNAscan-SE-ID: chr15.trna7) promoter[453,455] was chosen and cloned in place of the hU6 promoter. Editing with the tRNA promoter compared with the hU6 promoter of *hUSH2A* and *mUsh2a* was reduced by 76.8% ± 20.0 (p=0.009) and 45.8% ± 12.7 (p=0.014) respectively (Two-way ANOVA with promoter and gRNA as factors: $F(1, 8) = 27.64$, p=0.008 for effect of promoter) (Figure 6-16C).

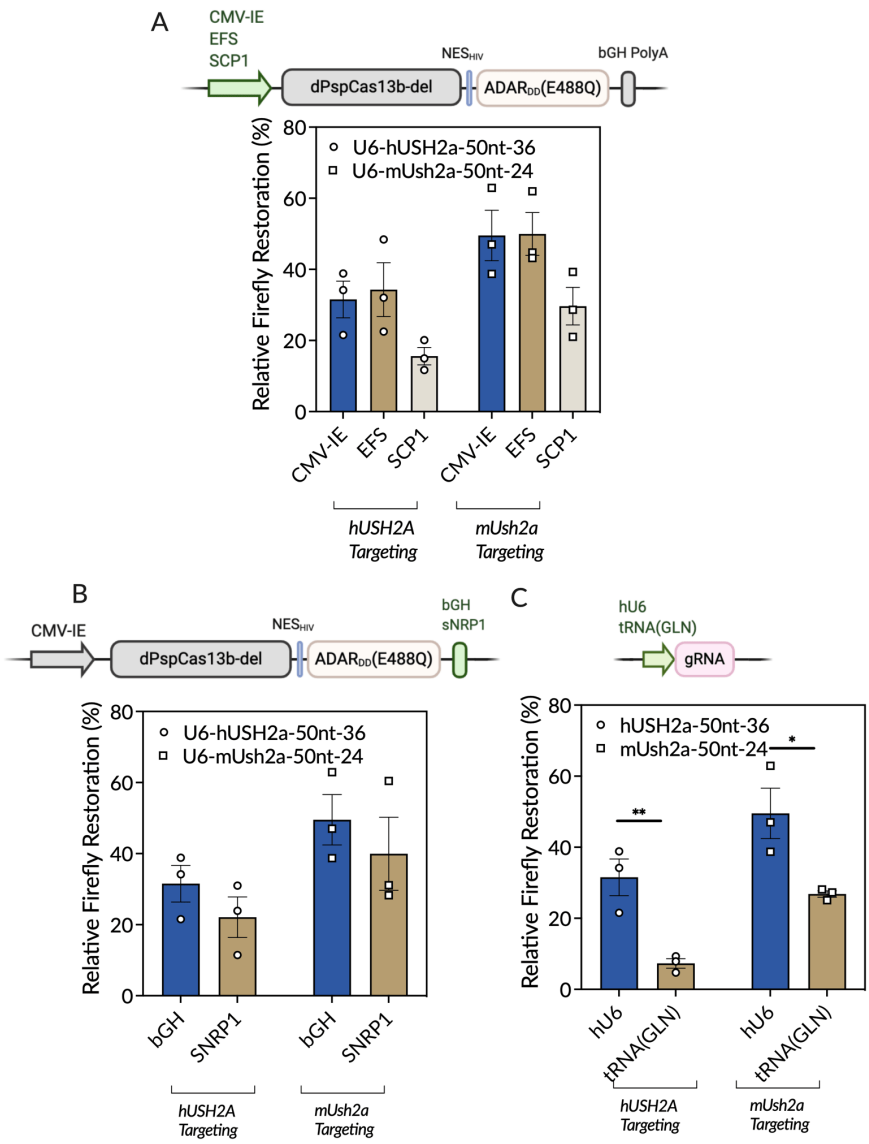


Figure 6-16 Minimal promoters and polyA signals for RNA editing

A. Comparison of RNA editing rates between three different RNA Pol II promoters. Two-way ANOVA with promoter and gRNA as factors: F(2, 12) = 6.89, p = 0.01 for effect of promoter; F (2, 12) = 0.058, p = 0.94 for interaction between guide and promoter. No significant difference on Tukey's multiple comparison testing. **B.** Comparison of RNA editing rates between two polyA signals demonstrates efficient editing with the sNRP1 polyA. Two-way ANOVA with polyA and gRNA as factors: F(1, 8) = 1.67, p = 0.23 for effect of polyA; F (1, 8) = 0.0001, p = 0.99 for interaction between guide and polyA. **C.** Comparison of RNA editing rates between RNA Pol III promoters driving gRNA demonstrates loss of editing efficiency with a tRNA promoter. Two-way ANOVA with promoter and gRNA as factors: F(1, 8) = 27.64, p = 0.008 for effect of promoter; F (1, 8) = 0.029, p = 0.87 for interaction between promoter and guide. **p = 0.009 and *p = 0.014, Tukey's multiple comparison test. All data shown as mean ± SEM, n = 3. Data from the CMV-IE.dPspCas13b-del-ADAR$_{DD}$(E488Q) with a hU6 driven gRNA construct (blue bars) used as a reference and displayed in A, B and C. Plasmid maps displayed over graph, with variable region in green.

6.3.6 Cloning and testing of AAV-Cas13-ADAR2$_{DD}$ Constructs

6.3.6.1 Testing of EFS driven RNA editing constructs

Following testing of a range of minimal vector elements, a series of plasmids cloned with a transgene flanked by AAV2 ITRs were generated for downstream AAV production.

As the EFS promoter and the sNRP1 polyA sequence individually both produced similar editing rates to the reference plasmid with the CMV promoter and the bGH polyA sequence, the EFS and sNRP1 sequences were cloned to drive expression of dPspCas13bdel-ADAR2$_{DD}$, reducing the overall construct size by ~560bp. The U6 promoter was retained due to the reduced efficiency seen with the tested tRNA promoter. This enabled the cloning of two types of ubiquitously expressed vectors (Figure 6-17).

Firstly, a dual vector approach where the dPspCas13bdel-ADAR2$_{DD}$ was encoded by one plasmid, and the U6-gRNA by a second plasmid. In this approach the Cas13b vector has a transgene size of 4.8kb including the ITR sequences and is within the AAV packaging capacity. The U6-gRNA was cloned upstream of a GFP sequence driven by a CAG promoter to enable assessment of transduction area following subretinal injection, and for potential selection of transduced cells. This dual vector approach was tested via transfection into HEK293T cells using the luciferase assay, benchmarked against the reference plasmids. Encouragingly, the use of the weaker promoter and polyA signal did not reduce editing efficiency at the tested doses for either guide (Two-way ANOVA with construct and gRNA as factors, $F(1,8)=0.18$, $p=0.68$ for effect of construct) (Figure 6-17B).

Secondly, an all-in-one plasmid was generated to express both the Cas13 and the guide. This resulted in a 5.13kb transgene including ITRs. Although this is larger than the ~4.7-4.9kb upper packaging capacity of AAV, some evidence suggests that AAV serotypes including AAV8 tolerate transgenes up to 5.2kb without truncation.[75,76] Experiments in Figure 6-9 demonstrated that a high ratio of gRNA to Cas13 plasmid resulted in higher editing rates, so it was unknown whether comparable editing rates could be achieved when copies of EFS-Cas13 and U6-gRNA

were introduced at equal molar ratios in an all-in-one plasmid. Dose-response experiments using the *mUsh2a*-targeting construct demonstrated increasing editing rates with dose as expected, and encouragingly 150 ng of all-in-one plasmid was sufficient to reach equivalent editing rates to the reference plasmids (75 ng Cas13/150 ng gRNA) ($p=0.73$) (Figure 6-17C).

Cloning of these AAV RNA editing constructs allowed for the introduction of a C-terminal FLAG tag to the dPspCas13b-ADAR2$_{DD}$ construct. This allowed for the detection of the protein product and overcome the lack of commercially available Cas13 antibodies (Figure 6-18). Immunocytochemistry of transfected HEK293T cells demonstrated the cytoplasmic expression of the dPspCas13b-ADAR2$_{DD}$ protein, as expected due to the fused HIV nuclear export signal. Western blot demonstrated the fusion protein at the appropriate predicted size (~160kDa).

Finally, transfection of the cells with the AAV-U6-gRNA-CAG-GFP-WPRE plasmids demonstrated robust GFP expression, confirming the activity of these plasmids (Figure 6-18).

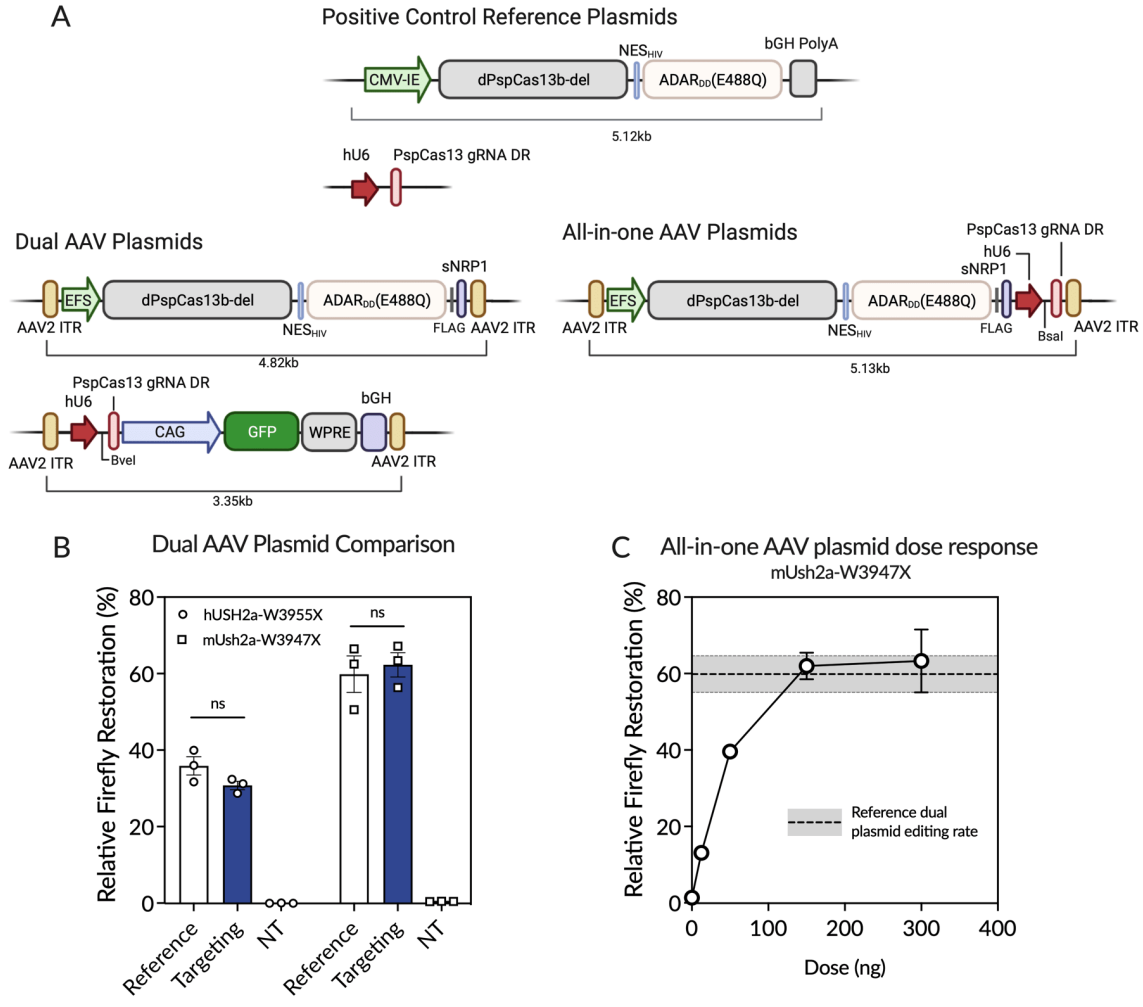

A
Positive Control Reference Plasmids
CMV-IE
dPspCas13b-del
NESHIV
ADARDD(E488Q)
bGH PolyA
5.12kb
hU6
PspCas13 gRNA DR
Dual AAV Plasmids
EFS
dPspCas13b-del
ADARDD(E488Q)
sNRP1
AAV2 ITR
NESHIV
FLAG
AAV2 ITR
4.82kb
PspCas13 gRNA DR
hU6
CAG
GFP
WPRE
bGH
AAV2 ITR
BveI
AAV2 ITR
3.35kb
All-in-one AAV Plasmids
PspCas13 gRNA DR
hU6
sNRP1
EFS
dPspCas13b-del
ADARDD(E488Q)
AAV2 ITR
NESHIV
FLAG
BsaI
AAV2 ITR
5.13kb
B
Dual AAV Plasmid Comparison
Relative Firefly Restoration (%)
hUSH2a-W3955X
mUsh2a-W3947X
ns
ns
Reference
Targeting
NT
Reference
Targeting
NT
C
All-in-one AAV plasmid dose response
mUsh2a-W3947X
Relative Firefly Restoration (%)
Reference dual plasmid editing rate
Dose (ng)

Figure 6-17 RNA editing activity of EFS-driven AAV plasmid constructs
A. Plasmid maps of the tested constructs. The reference plasmids used for initial testing driven by a CMV-IE promoter with a bGH polyA signal were used as positive controls. Plasmids designed for AAV packaging were cloned into plasmid backbone containing AAV2 ITRs. A dual AAV-construct approach was cloned driven by an EFS promoter with a dual sNRP1 polyA signal for the dPspCas13b-ADAR$_{DD}$. The second plasmid expresses the gRNA from the U6 promoter, cloned upstream of GFP driven by the ubiquitous CMV early enhancer/chicken β-actin (CAG) promoter with a woodchuck hepatitis virus post-transcriptional regulatory element (WPRE) and bGH polyA. An all-in-one AAV-construct was cloned to express both the dPspCas13b-ADAR$_{DD}$ and the gRNA from a single plasmid. **B.** Transfection of HEK293T cells with targeting and non-targeting (NT) dual AAV constructs, compared to the reference constructs (75 ng Cas13 plasmid/150 ng gRNA plasmid each). Equivalent editing rates were seen between constructs for both guides, without loss of editing efficiency from the weaker EFS promoter and sNRP1 terminator (Two-way ANOVA between targeting guides with construct and gRNA as factors, $F(1,8)=0.18$, $p=0.68$ for effect of construct). **C.** Transfection of HEK293T cells with dose response of all-in-one AAV construct targeting *mUsh2a*-W3947X. Despite differences in stochiometry of the gRNA and Cas13, 150 ng of all-in-one plasmid achieved equivalent levels of editing as the reference constructs (75 ng Cas13 plasmid/150 ng gRNA plasmid each) shown as dotted line with grey area representing the SEM (Unpaired t-test, $p = 0.73$). All data mean ± SEM, $n = 3$.

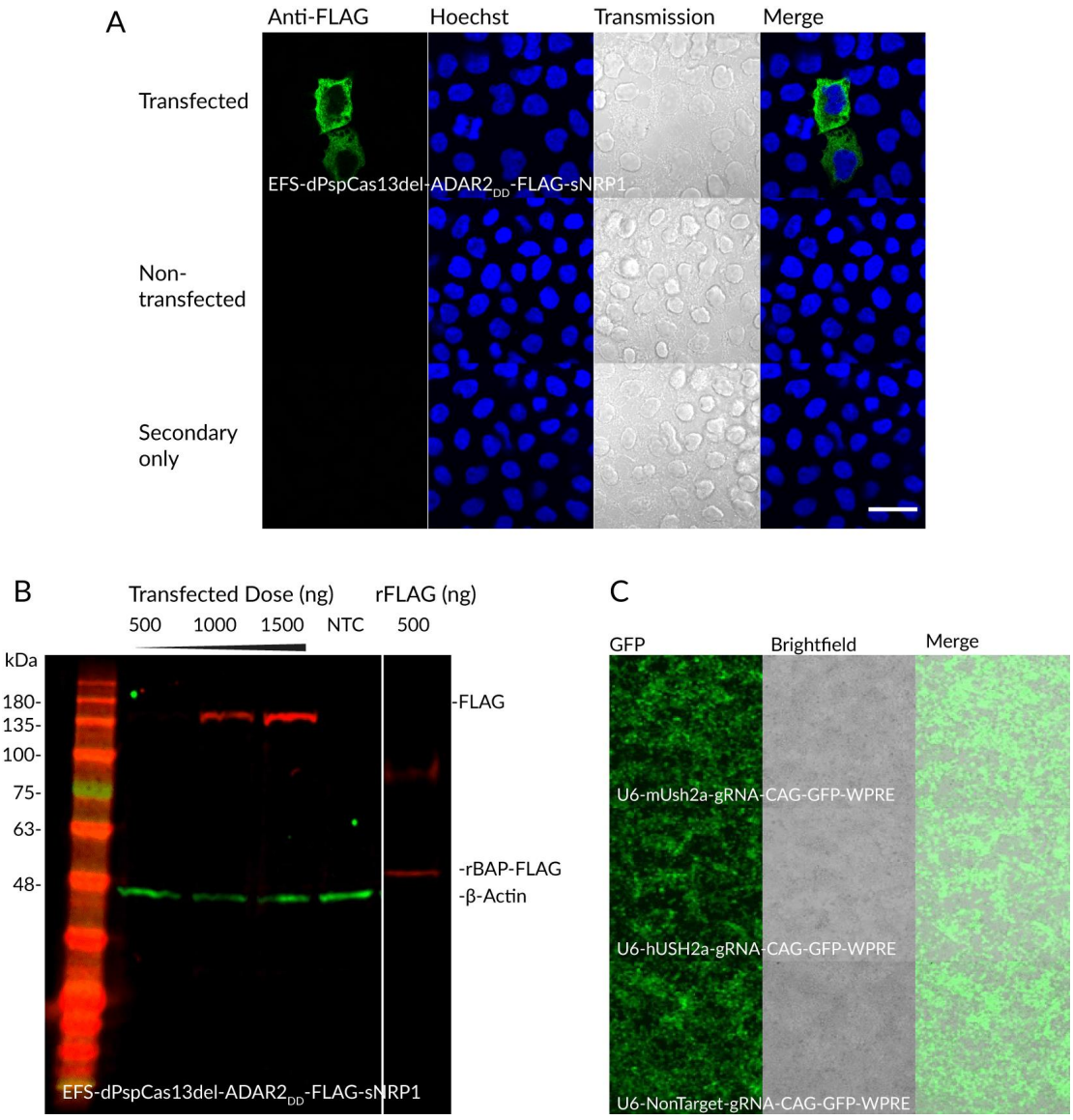


Figure 6-18 Protein expression from EFS-driven AAV plasmid constructs in HEK293T cells

A. Immunocytochemistry following transfection with the all-in-one AAV-EFS-dPspCas13bdel-ADAR2$_{dd}$-sNRP1 construct. dPspCas13bdel-ADAR2$_{DD}$ expression detected by anti-FLAG staining is observed in the cytoplasmic compartment, as expected due to the fused HIV-derived nuclear export signal. **B.** Western blot of protein lysates from cells in 12-well plates transfected with increasing doses of the all-in-one construct in A. dPspCas13bdel-ADAR2$_{DD}$ expression is detected with anti-FLAG staining with the appropriate predicted size (~160kDa, red) at doses greater than 500 ng. A c-terminal FLAG tagged recombinant bacterial alkaline phosphatase (rBAP) protein (~49kDa) was used as a positive control, with β-actin as a protein loading control (green). **C.** Transfection of the AAV-gRNA-GFP vector from the dual vector approach demonstrates robust GFP expression from the downstream CAG-GFP-bGH-WPRE from all guide constructs. CAG = CMV early enhancer/chicken β-actin promoter. WPRE = woodchuck hepatitis virus post-transcriptional regulatory element

6.3.6.2 Generation of RK Driven constructs

Having demonstrated in HEK293T cells that these AAV-RNA editor constructs can drive efficient RNA editing and express an appropriate protein product, further constructs were made using multi-fragment plasmid assembly techniques to replace the EFS promoter with the rhodopsin kinase (RK) promoter to create an additional set of constructs. The RK promoter is photoreceptor specific and drives strong expression in rods and cones,[457] where usherin is expressed. A number of versions of this promoter exist; for this experiment the 199bp -112/+87 described by Khani et al. was chosen as it is similar in size to the EFS promoter and is used in clinical trials for gene therapy for RPGR-related RP.[43,458] RK-driven plasmids were generated to express dPspCas13b-ADAR2$_{DD}$(E488Q) to be used in a dual vector approach with the previously cloned AAV-gRNA-GFP plasmids. Additionally, an all-in-one plasmid was cloned to express dCas13bt3-ADAR2$_{DD}$(E488Q). dCas13bt3 was chosen as it is the smallest of the tested orthologues, and demonstrated up to 17% editing efficiency with guide 50nt-28. Due to the minimal size of the Cas13bt3 orthologue, this enabled the inclusion of a 3× FLAG sequence (rather than a 1×FLAG sequence used in the previous vectors), a stronger SV40 polyA terminator, and the U6-gRNA, with the transgene remaining within the AAV packaging capacity (4.6kb). The plasmid maps of these are shown in Figure 6-19. As the RK promoter is not active within readily available and easily transfectable cell lines, RNA editing activity of these constructs was not testable with the luciferase assay.

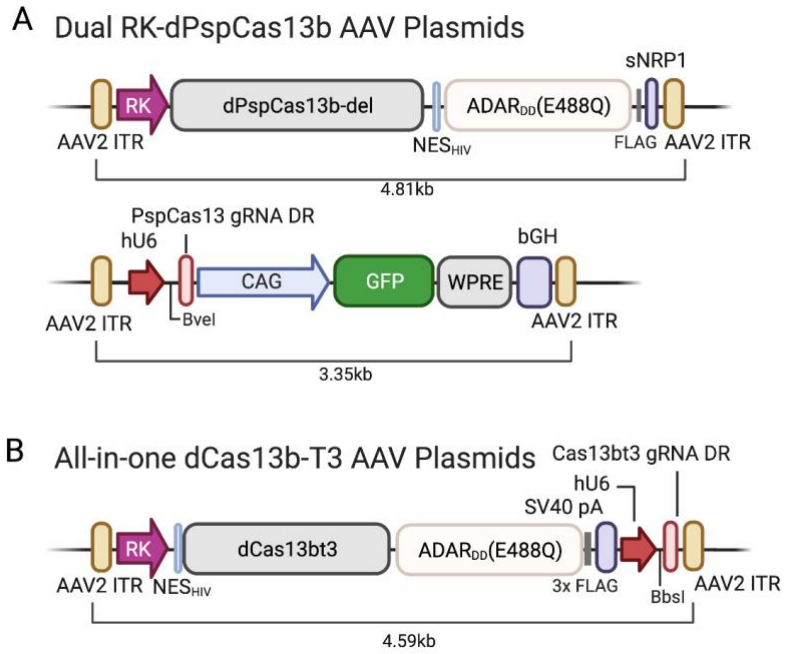


Figure 6-19 Vector maps of RK-driven AAV RNA editor constructs
A. Vectors expressing dPspCas13bdel-ADAR2$_{DD}$ under an RK promoter rather than an EFS promoter within AAV ITRs were generated, for use with the AAV-gRNA-GFP vectors. **B.** An all-in-one vector construct with dCas13bt3. A 3× FLAG tag and an SV40 polyA was included in this construct.

6.4 Discussion

RNA editing is an emerging base editing approach with potential for future clinical translation. As mRNA molecules are transient, editing RNA offers an inherent safety advantage over DNA base editing as the introduced changes are not permanent. This offers the possibility of reversing or stopping editing if required, and contrasts against the risk of DNA editing strategies introducing permanent and accumulating off-target mutations throughout the genome. Furthermore, as in gene therapy, RNA editing requires continuous, stable expression of the editing construct for ongoing mutation repair. This approach is therefore well-suited to AAV-mediated delivery, and the eye is an excellent candidate site to trial RNA editing as a therapeutic approach.

This chapter firstly developed an *in vitro* assay that allows for screening of RNA editing constructs and gRNAs against a target sequence containing a premature termination codon. Secondly, it used this assay to engineer and validate dCas13b-ADAR RNA editing plasmids with short regulatory sequences for future AAV delivery.

6.4.1 Luciferase assay development

Development of an RNA editing approach for *USH2A* was challenging, as the target transcript was not expressed in commonly cultured cell lines. The dual luciferase system used in this chapter was employed to overcome this to detect the correction of a premature termination codon to a tryptophan codon, and allows for the targeting of any sequence of interest containing a similar mutation. It would also be possible to use this for other base editing applications, such as the introduction of stop codons for transcript knockdown with a CRISPR-STOP strategy.[459]

Detection of luminescence emission does not require excitation light leading to a low background signal and a high signal to background ratio and high sensitivity.[460] This provided a high dynamic range for detection of editing, and the normalisation approach of the dual

luciferase system generated consistent results. This system allowed for screening in a 96-well format and could be readily adapted for high-throughput screening. Further adaptions could include the generation of a knock-in cell line containing the dual luciferase transgene to reduce the number of plasmids needed for transfection. The use of secreted luciferase proteins with short half-lives that do not require cell lysis would also allow for dynamic changes in luciferase activity to be monitored.[460,461]

6.4.2 Use of the luciferase assay for quantifying RNA editing

Editing rates calculated by restoration of firefly luminescence correlated well with editing rates calculated from Sanger sequencing, although consistently reported lower editing rates than those quantified by sequencing. The accuracy of calculating A-I editing rates in RNA from Sanger sequencing peak heights from reverse transcribed cDNA has previously been validated,[462] and calculation of editing rates with base decomposition of Sanger chromatograms by MultiEditR software has shown equivalent precision to RNA-seq.[438] One explanation for the discrepancy is that nonsense decay of the unedited transcript leads to sequencing bias towards the corrected transcript. This is unlikely, however, as the transcript lacks a downstream intron and the splice junctions required for binding of exon-junction complexes for detection by nonsense decay mechanisms.[463,464] The maximum firefly luciferase expression (e.g. 100% restoration) was calculated by the expression of firefly luciferase from a plasmid with a short 20bp sequence that places firefly in-frame. This serves as a universal positive control, and allows for many different mutations of interest to be evaluated on the same plate. Alternatively, a specific positive control that contains the corrected sequence for each mutation could have been used. As this has not been tested it is unknown whether this may account for the under-reporting of the editing rate relative to sequencing. Further investigation into the lower limit of detection for this assay would be of interest to characterise its sensitivity. Finally, PCR bias

towards the repaired transcript is another possible, but unlikely, explanation for this discrepancy.

A disadvantage of this system is that it was performed in an immortal cell line, using an overexpressed reporter construct with short RNA target that likely differs in features to the endogenously expressed full-length transcript (for instance expression level, localisation, folding, RNA-RNA/RNA-protein interactions, or methylation). Therefore, while this is useful for screening of constructs and gRNAs, it does not recapitulate the biological context. Further work could investigate the use of this system in different cell lines. Ideally, however, gRNAs identified in this system would be validated in a cell line endogenously expressing the transcript of interest. Recent data has demonstrated that *USH2A* is expressed in human fibroblast-derived iPSC cells.[167] For this project, RNA editing correction was attempted in collaboration with the Kalatzis lab (IMN Montpellier, France) in patient-derived iPSC cells carrying a W3955X mutation in compound heterozygosity. Despite extensive optimisation of transfection conditions and detection of the *USH2A* transcript, reliable quantification of RNA editing was not possible (data not shown). Differentiation of these iPSCs to retinal organoids will allow additional future assessment as another *in vitro* means of validating results obtained in the luciferase system. Finally, with the development of a mouse model (see next chapter), primary culture of photoreceptors will allow for an additional *in vitro* source of *Ush2a* expressing cells.

6.4.3 Insights from gRNA screening

The luciferase assay permitted the screening of ~20 guides for each target and Cas construct, tiling across the target mutation with increasing distance between the A-C mismatch and the DR scaffold. In the first description of Cas13-ADAR editors, Cox et al. suggested that a 32-36nt mismatch distance was optimal.[300] Although this was true for *hUSH2A*, this was not the case for *mUsh2a*, with the most efficient guides being located at a mismatch distance of 24 and 28nt for Pspcas13 and Cas13bt3 respectively. This emphasises the need for screening of

many gRNAs for each target. It is not yet clear what factors influence the activity of a gRNA, and to answer this question large-scale datasets and machine learning approaches may be required, such as used for Cas13d.[465]

No editing was observed when non-targeting guides were delivered with Cas13 constructs supporting that editing was gRNA-Cas13 mediated. Although not expected to be expressed in HEK293 cells,[466] endogenous ADAR was not mediating the editing as no editing was seen when gRNAs were delivered without Cas13 constructs. Interestingly, it has now been shown that low editing rates can be achieved using the dPspCas13b-ADAR2$_{DD}$(E488Q) with a 50 nucleotide guide without a direct repeat (DR) scaffold,[299,304] with recent papers demonstrating that while this is target dependent, may account for up to 20-60% of the observed editing rate when using the ADAR2$_{DD}$(E488Q/T375G).[284] Although editing rates are markedly improved by inclusion of the DR,[304] this suggests a portion of editing efficiency is attributable to ADAR editing at the spacer-mRNA duplex independent of dPspCas13b recruitment. Other orthologues such as dCas13X.1-ADAR, dRanCas13b-ADAR and dCasRx-ADAR systems appear to require the DR for editing.[284,303,304] As the potential magnitude of DR-independent editing has only recently come to light,[284] scaffold-deleted gRNA controls were not tested in these experiments so this cannot be assessed here, but would be important to include in future work.

6.4.4 Comparison of RNA editing constructs

Evaluation of the dPspCas13b-ADAR2$_{DD}$ plasmids confirmed previously published data demonstrating the robust on-target activity of the E488Q mutant ADAR and reduced on-target activity of the E488Q/T375G mutation.[300] Encouragingly, the preserved editing activity seen in dPspCas13bdel constructs with the C-terminal 984-1090 deletion confirms this truncated protein retains its function for on-target editing.[300]

The identification and engineering of further Cas13 orthologues and new deaminases for RNA editing is an exciting area of further research.[282,284,303,304,306,467,468] While the Cas13bt

constructs evaluated here have significant potential due to their minimal size, the activity of these orthologues was markedly reduced compared to PspCas13. In this study these were only tested against one target however (*mUsh2a*), and it would be of interest to use these in screens against other targets to characterise their activity more fully.

Some of the many other non-CRISPR based RNA editing systems discussed in the general introduction were not tested here,[288] but this rapidly developing field is offering many RNA editing tools that could be further compared with this *in vitro* assay.

6.4.5 Off-target editing

Previous evaluations have characterised the off-targets profile of the PspCas13 editing systems in HEK293 cells, documenting widespread deamination with ADAR2$_{DD}$(E488Q) mutation, and more limited deamination with the ADAR2$_{DD}$(E488Q /T375G).[300,303] In this context, only local bystander off-targets in the target transcript were evaluated, with the results in this limited region consistent with previous studies. Notably with ADAR2$_{DD}$(E488Q), editing of off-target adenosines was seen both within the gRNA binding region, and outside the gRNA binding region in the case of the *mUsh2a* target. Furthermore, these off-targets also occurred in the presence of a non-targeting guide. This suggests that while on-target editing and off-target editing within the gRNA duplex region is promoted by the binding of the gRNA (as seen in the *hUSH2A* target), off-target editing can also occur at significant rates independent of gRNA binding.

ADAR$_{DD}$ editing requires dsRNA structures, and these can be as short as 15nt duplexes.[469,470] RNAs with more extensive regions of perfect dsRNA binding or with small bulges are associated with higher rates of promiscuous deamination relative to those with secondary structures containing larger internal loops ≥6 nt which decrease the number of available double stranded binding sites.[466,471] Given that these gRNA independent off-targets occurred more extensively in the *mUsh2a* target, it may be hypothesised that the greater off-

targeting is due to more extensive folding and base pairing across the *mUsh2a* target, facilitating the formation of necessary double stranded structures edited by ADAR(E488Q). Within the limitations of predictive software for generating accurate structures of RNA folding, the predicted more extensive folding of the *mUsh2a* target support this hypothesis (Figure 6-15). Counter-intuitively however, the off-target locations in *mUsh2a* appeared to occur in or close to bulges in the predicted structure, rather than in regions with high binding probability or internal loops. Given that this prediction only includes local folding (200 nt), and that long range interactions (>1000 nt) frequently form dsRNA structures that are subject to ADAR editing,[466] there are limitations to the interpretation of these base-pairing predictions. Furthermore, the fusion of the Cas13 to the $ADAR_{DD}$ may alter the binding kinetics of the $ADAR_{DD}$ to these double stranded sites.

Further work is required to understand whether the C-terminal truncation in PspCas13del affects specificity as this has not yet been well characterised. Furthermore, no assessment of the off-target effects of the Cas13bt constructs has been published. Finally, it should be noted that deconvolution of Sanger sequencing using MultiEditR has limited sensitivity for edits <5%,[438] and more sensitive detection with NGS approaches with adequate sequencing depth will be required for more thorough off-target analysis. This would be appropriate for analysis of off-targets within the target cell of interest (i.e., photoreceptors).

6.4.6 Optimisation of RNA editing constructs for AAV packaging

Following validation of vector regulatory elements, four AAV vector arrangements were generated: an all-in-one EFS-driven PspCas13b vector, a dual EFS-driven PspCas13b vector, a dual RK-driven PspCas13b vector, and an all-in-one RK-driven Cas13bt3 vector. The EFS-driven vectors should provide ubiquitous expression while the RK-driven vectors should provide robust expression within photoreceptors, and limit activity to those cells. A dual vector system is less desirable than an all-in-one system, as it requires the dual transduction of the

target cell for editing, potentially reducing efficiency. The oversized transgene of an all-in-one PspCas13b vector may result in reduced titres or truncated transgenes in AAV production, however. While the all-in-one Cas13bt3 vector overcomes this large transgene size, the editing efficiency with this orthologue is markedly reduced. With these limitations in mind, these vectors can be used for AAV production in the following chapter. Overall, it remains encouraging that robust editing levels and Cas13b expression can still be achieved *in vitro* when using minimal promoter and polyA elements.

Ideally, the promoters would have been tested for activity in photoreceptors or photoreceptor-like cells. This also would have enabled testing of the RK-driven plasmids. Prior experience in the lab using retinoblastoma derived cell lines such as WERI, and Y79 or the immortalised cone photoreceptor line 661W have all demonstrated that these cells do not transfect reliably. Nevertheless, these cell lines might be used for testing of these constructs in future experiments. In place of this, direct testing *in vivo* with sub-retinal injection of AAV vectors is an alternative.

6.4.7 Conclusion

Collectively, this chapter has investigated and engineered plasmid systems for *in vitro* RNA editing that can be packaged into AAV, with the next step to evaluate these systems *in vivo* for the editing of endogenous transcripts.

7

DEVELOPMENT AND CORRECTION OF A MOUSE MODEL OF USHER SYNDROME

7.1 Introduction

As established in the preceding chapters, mutations in *USH2A* are a common cause of inherited retinal degeneration not amenable to AAV-gene supplementation.[472] The pathogenic c.11864G>A (W3955X) *USH2A* mutation is a common premature termination variant in that is ideal for correction with base editing, and could be used to demonstrate proof of concept that base editing may be able to treat other pathogenic SNVs in *USH2A*. *In vitro* data suggests that RNA editing can correct this mutation with high efficiency.

Accumulating evidence suggests that precision correction of disease mutations with DNA and RNA base editing is a possible *in vivo*.[255,412,413,473] To determine whether base editors can effectively and safely edit genes in diseased photoreceptors, appropriate animal models are required that harbour pathogenic single nucleotide variants amenable to base editing. Mouse models are invaluable for assessing the safety and efficacy of new therapeutic strategies and are widely used to develop pre-clinical data for gene therapy translation. Most mouse models available however, have been generated using techniques that introduce large insertions, deletions, or multi-nucleotide changes such as with transgenic or chemical mutagenesis technologies.[474] As demonstrated in Table 7-1 there are very few available models with single G>A transitions in relevant models of common IRDs editable with current RNA editors. Gene

editing techniques now permit the facile insertion of precise genomic edits in mouse embryos,[475] enabling the generation of bespoke models containing SNVs of interest, that can be used for testing base editing approaches.

The human *USH2A* (Chr 1q41)[115] gene and its mouse orthologue *Ush2a* (Chr 1 H6 92.29 cM)[476] are both located on chromosome 1. The long *USH2A* isoform is predominantly expressed in the retina and cochlea in humans (isoform B, 15,609bp, 72 exons, 5,202aa, ~590kDa),[117] while in mice, a long *Ush2a* isoform (15,582bp, 71 exons, 5,192aa, ~590kDa) is the predominant transcript in the murine retina and cochlea.[128,140] As described in the introduction, the only available mouse model of *USH2A* demonstrated that *Ush2a*-null mice mimic the human phenotype with a slow progressive retinal degeneration and congenital non-progressive hearing deficits. This model has a complete deletion of exon 5 that is not amenable to base editing.[128]

This chapter describes the generation and characterisation of a novel *Ush2a*-W3947X mouse model containing a premature termination codon (c.11840G>A) at a homologous position to the common *USH2A*-W3955X mutation. This TGG>TAG mutation is editable with both RNA and DNA base editors to restore the wildtype tryptophan codon. This model is then used to test the safety and efficacy of AAV-delivered dCas13-ADAR2$_{DD}$ RNA editing constructs in a series of pilot experiments.

7.1.1 Aims

This chapter aims to:

1. Characterise the molecular phenotype of the retina and cochlea of the *Ush2a*-W3947X mouse model designed and generated in collaboration with MRC Harwell
2. Initiate a long-term natural history study of the *Ush2a*-W3947X mouse model to characterise the structural and functional phenotype of the retina and cochlea over time
3. Generate AAV vectors expressing dPspCas13b-del-ADAR2$_{DD}$ and dCas13bt3-ADAR2$_{DD}$ RNA editing constructs described and cloned in Chapter 6
4. Evaluate the expression and efficacy of AAV-delivered Cas13 RNA editors for the repair of the *Ush2a*-W3947X mutation in RNA transcripts and restoration of usherin expression
5. Characterise aspects of the safety of AAV-delivered Cas13 RNA editors including assessing effects on retinal structure and off-target effects in the target transcript

Table 7-1 Current mouse models of IRD with G>A transitions

Table on following page. Table summarising the current mouse models listed in the Mouse Genome Informatics (MGI) database.[477] Data sourced from Collin et al. to collate retinal phenotypes of models and assess degeneration speed and ERG abnormality.[474] Prevalence of families affected in the UK sourced from Pontikos et al.[31] CRD = cone-rod dystrophy, LCA = Leber's congenital amurosis, RP = retinitis pigmentosa, ACHM = achromatopsia.

Mouse Gene	Human Gene	Human Phenoytpe	Allele Name	cDNA Change	Protein Change	Zygosity	Degeneration Speed	ERG Abnormality	Families Affected (%)
Aipl1	*AIPL1*	*LCA, RP, CRD*	tvrm119	c.276+5G>A	p.Val33_Ile92del	hom	Fast	Yes	0.34
Rpgrip1	*RPGRIP1*	*LCA, CRD*	tvrm111	c.813+1G>A	Splice	hom	Fast	Yes	0.23
Ush1c	*USH1C*	*USH1C, RP*	tm1Bkts	c.216G>A	Splice	hom	Slow	Yes	0.34
Cngb3	*CNGB3*	*ACHM*	cpfl10	c.692G>A	p.Arg231His	hom	Medium	Yes	1.53
Gnat2	*GNAT2*	*ACHM*	cpfl3	c.598G>A	p.Asp200Asn	hom	Slow	Yes	0.04
Pde6a	*PDE6A*	*RP*	nmf282	G>A	p.Val685Met	hom	Fast	Yes	0.38
Pde6b	*PDE6B*	*RP*	atrd2	G>A	Splice	hom	Fast	Not tested	0.73
Rho	*RHO*	*RP*	Noerg1	c.329G>A	p.Cys110Tyr	het	Fast	Yes	2.83
Rho	*RHO*	*RP*	tm1.1Eye	c.568G>A	p.Asp190Asn	het	Slow	Yes	2.83
Rho	*RHO*	*RP*	tm2.1Kpal	c.448G>A	p.Glu150Lys	het / hom	Het (Fast) Hom (Fast)	Yes	2.83
Nmnat1	*NMNAT1*	*LCA*	imh	c.25G>A	p.Val9Met	hom	Fast	Yes	0
Pex1	*PEX1*	*Zellweger syndrome*	tm1.1Sjms	c.2531G>A	p.Gly844Asp	hom	N/A	Yes	0
Mitf	*MITF*	*RP*	Mi-b	c.731G>A	p.Gly244Glu	hom	Fast	Not tested	0
Mitf	*MITF*	*RP*	Mi-vit	c.664G>A	p.Asp222Asn	hom	Medium	Not tested	0

Table 7-1 Current mouse models of IRD with G>A transitions
Table legend on preceding page

7.2 Methods

7.2.1 Animal models and procedures

USH2A-W3947X-EM1-CDH23-B6 mice (henceforth *Ush2a*-W3947X mice) were generated by the Mary Lyon Centre (MRC Harwell, Harwell, UK) as described in section 7.3.2.1 following previously described procedures.[475] To generate cohorts used for characterisation of the molecular phenotype and for natural history experiments, heterozygous *Ush2a*-W3947X breeders were maintained at MRC Harwell to produce homozygous offspring with wildtype littermate controls. Mixed mutant and wildtype cages were maintained to eliminate cage effects and ensure investigator blinding during procedures. To generate cohorts used for experiments injected with AAV, first generation homozygous *Ush2a*-W3947X or wildtype breeders derived from heterozygous parents were intercrossed at the University of Oxford to produce homozygous *Ush2a*-W3947X or wildtype offspring for mutation repair and construct expression experiments respectively.

Subretinal injections were performed as described in the general methods using a single 1.5 μL injection delivered to the superior retina. Electroretinography, CSLO and OCT imaging was performed as described in general methods. Measurement and analysis were performed blind to genotype.

7.2.1.1 Genotyping

Genotyping was performed by MRC Harwell using a multiplexed qPCR-based allelic discrimination assay using primers common to both alleles and fluorescence-conjugated probes specific to either the wildtype (FAM-labelled) or mutant (TET-labelled) allele. DNA was extracted from ear clips using Applied Biosystems TaqMan Sample-to-SNP Kit (Thermo Fisher Scientific). qPCR was performed with an Applied Biosystems 7500 thermocycler in reactions as specified in Table 7-2. Results were analysed with 7500 software v2.0.6 (Thermo Fisher Scientific).

Component	Volume (10uL total)
ABI GTX TaqMan Mastermix	5 μL
Probe-Primer Assay *WT and mutant Probes 5 μM each.* *Forward and Reverse Primers 15 μM each*	2 μL
ddH_2O	0.5 μL
DNA *1:10 dilution of ABI Sample to SNP preparation*	2.5 μL

Table 7-2 Allelic Discrimination Assay Mastermix
Components of mastermix for qPCR allelic discrimination assay for genotyping of the *Ush2a*-W3947X mouse. Primer and probe sequences are listed in the appendix.

7.2.1.2 ddPCR copy counting assay

Digital droplet PCR (ddPCR) copy counting assays were performed by MRC Harwell as previously described.[475] Dot1l was used as the normalisation control, a gene present in two copies on chromosome 10.[475] A duplex reaction with a VIC-labelled probe to Dot1l and a FAM-labelled universal probe to *Ush2a* binding to both the wildtype and mutant alleles, or a mutant specific FAM-labelled probe binding to the W3947X mutation. Assays were performed with a QX200 ddPCR system (Bio-Rad Laboratories). with 20 μL reactions of 2 μL crude DNA lysate, 1× ddPCR Supermix for probes (Bio-Rad Laboratories), 225nM of each primer (two primers per assay) and 50 nM of each probe. Droplets were generated in plate format using a QX200 AutoDG (Bio-Rad Laboratories). Samples were amplified in 96 well-plates on a C1000 Touch thermocycler (Bio-Rad Laboratories) and subsequently loaded into the QX200 Droplet Reader. Results were analysed using Quantasoft software.

7.2.1.3 Auditory brainstem responses

Auditory brainstem response (ABR) tests were performed in collaboration with Chris Breen at the Andrew King Lab, University of Oxford (Figure 7-1). Anaesthetised mice were placed in anechoic chamber on a heated pad and monitored remotely via video feed. Sound stimuli were presented using a free-field speaker (VISATON FR10) located 8 cm in front of the animal and connected to an amplifier (RA15, Alesis, USA). Auditory stimuli were generated

using an RP2.1 Enhanced Real-time processor (Tucker Davis Technologies (TDT), Alachua, FL, USA) with a sampling frequency of 100kHz connected to a TDT PA5 programmable attenuator. The speaker was calibrated using SigCalRP TDT calibration software to generate compensation filters ensuring stable intensity levels for a frequency range from 250 to 30000Hz. Click stimuli were presented at a rate of 17/sec at intensities from 90 to 30dB and pure tones at increasing frequencies were presented at a rate of 21/sec at intensities from 90 to 20dB, attenuating in 10dB steps. Signals were recorded from two active subcutaneous electrodes, placed close to the left and right auditory bullae, respectively, and referenced to an electrode placed at the vertex of the skull. A ground electrode was placed on the back of the animal. The signal was routed to a preamplifier (Medusa TDT RA16PA) via a low impedance headstage (TDT RA4LI) and recorded by an RZ2 Bioamp Processor controlled by BioSigRP software (TDT). Average responses from 1024 stimuli were recorded with BioSigRZ software (TDT) with a recording time of 10ms with a gain of 20 and a 0.3-3000kHz bandpass filter. Waveforms were analysed by a blinded assessor with thresholds determined as the minimum sound pressure level (SPL) that wave 1 of the ABR, derived from the auditory nerve, could be observed.[478,479]

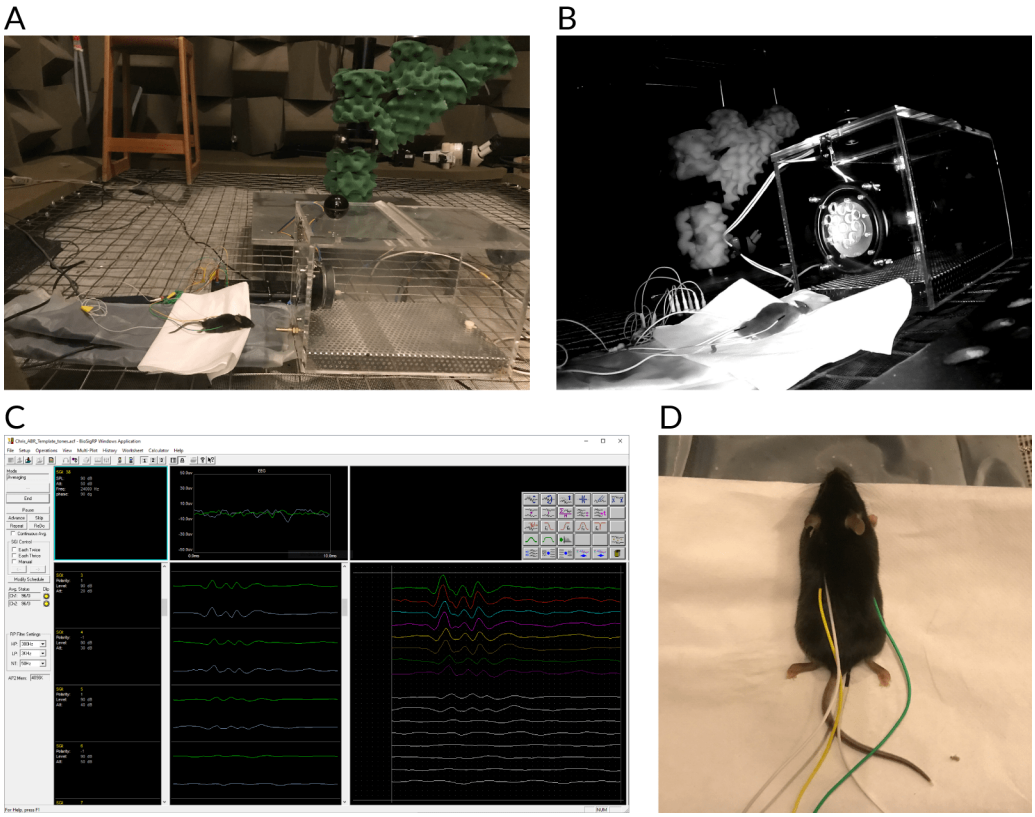


Figure 7-1 Auditory Brainstem Response Recording Setup
A. Photo of mouse within anechoic chamber on heating pad placed 8cm from speaker. **B.** Mice were monitored during recording via remote camera. **C.** Screenshot from recording software during ABR measurement. **D.** Placement of subcutaneous electrodes for recording. Laterally at the ventral edge of each pinna and adjacent to the bulla in both ears (yellow and green, positive electrodes), in the vertex at the midline (white, negative electrode), and a ground electrode placed dorsal to the lumbar spine in the midline (yellow).

7.2.2 Western blot

Western blots for Cas13-ADAR were performed as described earlier. Successful blotting of the large usherin protein required the following modifications to protocols described in the general methods. Following preparation of retinal lysates as described in the general methods, 60-80µg of protein was loaded into NuPAGE 3 -8%, Tris-Acetate gels in Tris-Acetate SDS Running Buffer and run with a HiMarker ladder (all Thermo Fisher Scientific). Proteins were transferred overnight at 4 °C in 1× Towbin Buffer (Table 7-3) with 10% methanol and 0.05% SDS to low fluorescence PVDF membranes using the Criterion system (Bio-Rad Laboratories) set to a current of 70mA. Membranes were blocked in 10% skim milk for two hours, before

overnight incubation at 4 °C with primary antibodies to USH2A and Vinculin as a loading control (Table 7-4).

Component	Amount
TRIS Base	30.3g
Glycine	144.1g
MilliQ Water	700 mL to dissolve, then 300 mL to a final volume of 1L

Table 7-3 Towbin Buffer (10×)
Recipe for Towbin Buffer. The final pH should be 8.2-8.5 and should not be adjusted

Antibody	Dilution	Host	Application	Source
USH2A (C-terminal)[134,142]	1:4000*	Rabbit	WB IHC	Gift from Dr. Jun Yang, University of Utah
USH2A (N-terminal)	1:200	Rabbit	WB	Abcam (ab42131)
USH2A (C-terminal)	1:200	Rabbit	WB	Abcam (ab82714)
USH2A (N-terminal)	1:100	Mouse	WB	SantaCruz, USA (sc-515555)
Vinculin	1:200	Mouse	WB	Sigma-Aldrich (V9131)
RED1 ($ADAR_{DD}$)	1:500	Rabbit	WB	Abcam (ab64830)
FLAG M2	1:1000	Mouse	WB, IHC	Sigma-Aldrich (F1804)
Rootletin	1:400	Chicken	IHC	MerckMillipore (ABN1686)
Phalloidin (Alexa Fluor 488)	1:40	Amanita phalloides	IHC	Thermo Fisher Scientific (A12379)

Table 7-4 Primary antibodies used for western blot and immunohistochemistry
USH2A antibodies raised against mouse epitopes. Anti-RED1 antibody raised against amino acids 370-737 of human ADAR (Uniprot #P78563) (Personal communication with Abcam). *Used at 1:2000 for cochlea wholemounts

7.2.3 Immunohistochemistry

7.2.3.1 Retinal Sections

It has been described elsewhere that for detection of usherin expression, 10 μm sections of unfixed tissue frozen in OCT is required.[128, 131,134] Testing of the standard protocol with fixation of eye cups in 4% PFA at 4 °C for 20 minutes and subsequent sectioning at 16 μm was also successful for labelling of usherin. Sections were blocked in 5% BSA/5% NGS/0.3%

Triton X-100, and primary (overnight, 4 °C, Table 7-4) and appropriate secondary (2 hours, RT) antibody staining performed in blocking solution.

7.2.3.2 Cochlea wholemounts

Cochlea were dissected and processed from P4 mice following published protocols.[480,481] Following sagittal hemi-section of the cranium and blunt dissection of the brain and meninges, the temporal bone was identified adjacent to the stapedial artery at the lateral base of skull. The overlying cartilaginous temporal bone was removed to expose the cochlea, and then the cochlea was bluntly dissected and removed. The otic capsule was gently removed to expose the organ of Corti, and then the spiral ligament carefully dissected away. The cochlea was then divided into apical, middle, and basal portions. The tectorial membrane was then removed from each portion.

Immunolabelling of wholemounts was performed in a 48-well plate. Following fixation in 4% PFA on ice for 30 minutes, cochleas were washed and then permeabilised in 0.5% Triton X-100 for 15 minutes, and incubated in blocking solution (8% NGS/5% BSA/0.5% Triton X-100) for 1hr at RT. Cochleas were incubated in primary antibody solution at 4 °C overnight (anti-USH2A in 5% NGS/0.1% Triton X-100), then washed and labelled with a secondary solution (5% NGS/0.1% Triton X-100) containing Alexa Fluor 488-conjugated phalloidin and goat anti-rabbit Alexa Fluor 568 for 90 minutes at RT. Washes were performed three times in PBS, and all solutions diluted in PBS. Antibodies are listed in Table 7-4.

7.2.4 Editing efficiency quantification

7.2.4.1 Target amplification

Whole retinal RNA was isolated, and reverse transcribed with $OligoDT_{20}$ as described in the general methods. *Ush2a* exon 60 was PCR amplified from cDNA with Phusion High Fidelity polymerase using exon-junction spanning primers with partial Illumina adapters (see appendix).

Products were visualised on an agarose gel to confirm the amplification of a single product and column purified (Qiagen).

7.2.4.2 Sanger sequencing

Amplicons were subject to bi-directional Sanger sequencing. On-target editing was quantified as the mean on-target editing rate detected in the target region (5'-ACAGCCCGTAGTCCACAATA-3') in forward and reverse chromatogram traces analysed EditR software[439] with a significance cut-off of $p<0.01$.

7.2.4.3 Targeted Deep Sequencing

Amplicon purity was analysed with spectrophotometry and concentrations were measured with a Qubit high sensitivity dsDNA kit (both Thermo Fisher Scientific). Amplicons were sent for library preparation and Illumina sequencing at GENEWIZ through the AmpliconEZ service. Sequencing was performed with a 2 × 250 bp paired-end configuration, with adapter trimmed Raw Fastq data provided for analysis. Fastq files were aligned, filtered, and analysed with CRISPResso2 (v2.1.3) to calculate editing efficiency from counts of A and G nucleotides across all adenosines in the amplicon.[387] Reads were filtered with a minimum average read quality >30 and minimum single base quality >20, with 15000-30000 aligned reads analysed per sample post-filtering. Fisher's exact test (two-tailed) was performed (fisher.test function) with multiple comparison testing using a false discovery rate (FDR) controlled at 5% with the Benjamini-Hochberg method (p.adjust function) using base R (v4.0.0), comparing experimental to PBS injected eyes on pooled count data from all replicates for each condition, with editing sites with an adjusted $p<0.01$ deemed significant.[320]

7.3 Results

7.3.1 Comparison of *USH2A* species homology

The humans (*USH2A)* and mice (*Ush2a)* usherin homologues were compared using the basic local alignment search tool (BLAST).[482] The coding sequences of *USH2A* isoform B and *Ush2a* are highly conserved, with a 78% nucleotide identity, and a 71% amino acid identity. Both human and mouse usherin display a similar domain architecture (Figure 7-2).[121]

The human W3955X mutation occurs within exon 61. In the mouse, the equivalent position lies in exon 60. Alignment of exon 60 and 61 demonstrated an equivalent tryptophan residue at position 3947 in the mouse protein, with similar nucleotide (77%) and amino acid (71%) identities within the exons. Reasoning that a nonsense mutation in a similar position in the human sequence results in a null-phenotype, we hypothesised that the installation of a c.11840G>A (p.W3947X) mutation in the *Ush2a* gene should lead to a truncated protein product and also nonsense mediated decay of the transcript, leading to knockout of the *Ush2a* gene.

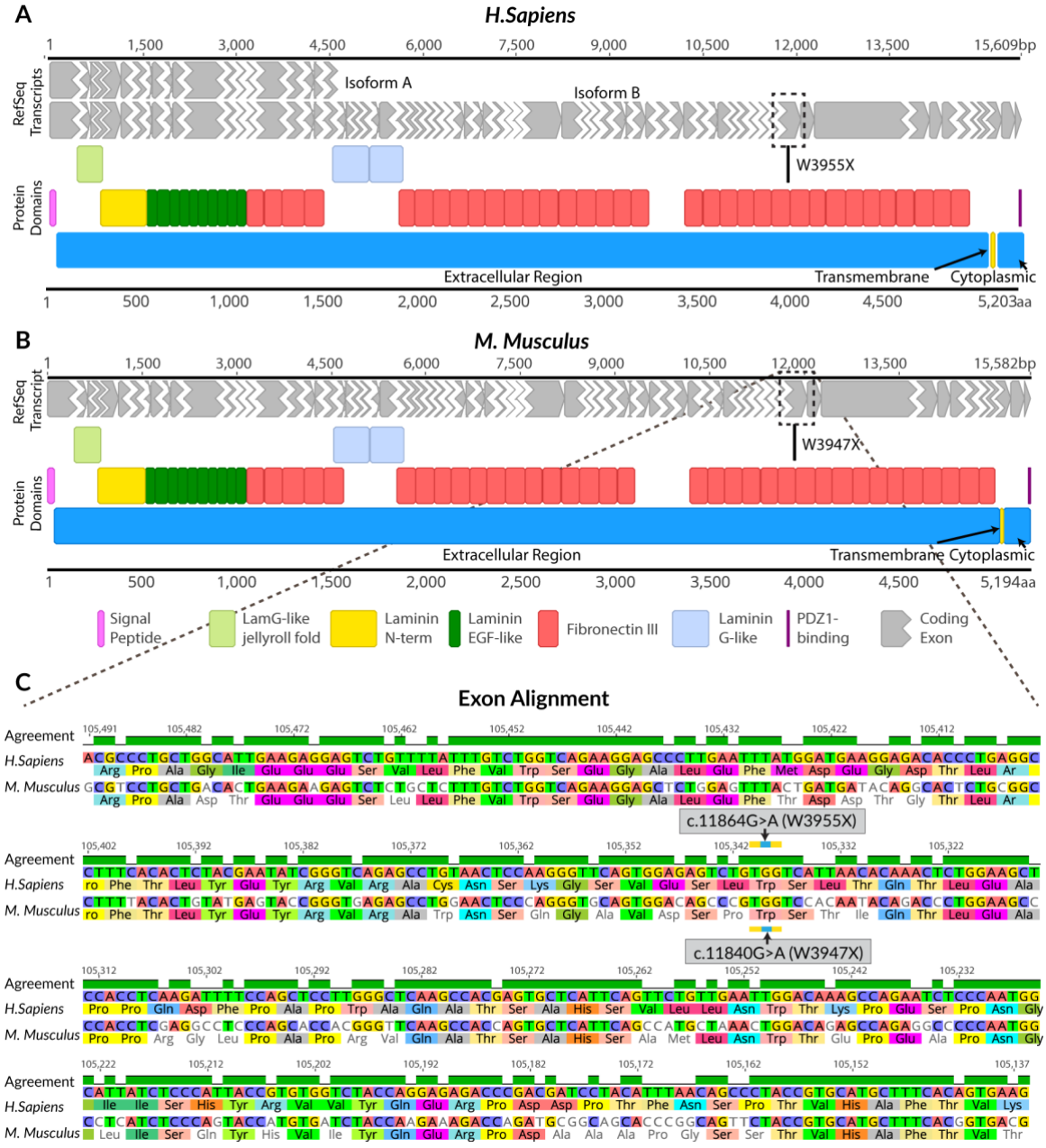


Figure 7-2 Comparison of human and murine usherin coding and protein sequences
Schematic diagrams of the coding sequences and protein domains of usherin in (**A**) humans (h*USH2A)* and (**B**) the mouse (m*Ush2a)*. The Refseq[483] transcripts demonstrate the coding exons of each gene. Short (isoform A) and long (isoform B) alternatively spliced isoforms of *USH2A* are demonstrated, with isoform B predominating in the retina and cochlea. Only the longer isoform of *Ush2a* is annotated in the Refseq database. The protein domain diagrams derived from the UniProt[484] database demonstrate a similar array of protein domains. Usherin is has a large extra-cellular region with a short transmembrane and cytosolic portion. The p.W3955X and p.W3947X mutations in exon 61 and 60 of *hUSH2A* and *mUsh2a* are shown respectively. **C.** Alignment of exon 61 (*hUsh2a)* and exon 60 (*mUsh2a*) nucleotide sequences (dashed boxes) with identity agreement shown in green. The location of the c.11864G>A (p.W3955X) and c.11840G>A (p.W3947X) in each sequence is shown.

7.3.2 Characterisation of the *Ush2a*-W3947X mouse

7.3.2.1 Design, generation & genotyping

To generate a mouse model containing an *Ush2a* c.11840G>A (p.W3947X) mutation amenable to repair by ADAR-based RNA editors and adenine DNA base editors, a collaboration with the Mary Lyon Centre, MRC Harwell was initiated. The C57BL/6J and N strains carry a fixed hypomorphic Cadherin-23 allele (*Cdh23*$^{ahl(753G>A)}$) that results in high frequency age-related hearing loss.[485] Therefore, to generate a model that allows for the effect of the *Ush2a*-W3947X mutation on hearing to be investigated, mice were generated on a C57BL/6J background with a repaired *Cdh23* allele (*Cdh23*$^{753A>G}$).[486]

MRC Harwell designed and generated mice using an HDR knock-in strategy. Briefly, a single stranded oligonucleotide DNA (ssDNA) template containing the c.11840G>A mutation was designed with flanking homology arms (Figure 7-3A). A gRNA for SpCas9 was designed to target the TGG PAM site at the target tryptophan codon. Successful insertion of the TAG codon at this locus abolished the PAM site to prevent re-cleavage of the successfully inserted donor sequence. Following pro-nuclear injection of zygotes with SpCas9 mRNA, sgRNA and donor template, embryos were implanted in pseudo-pregnant CD1 females. F_0 offspring were mated with wildtype animals to produce founder heterozygote animals. Successful transmission of the mutant allele to the F_1 generation was detected by Sanger sequencing (Figure 7-3B). The F_1 generation was screened for single insertion of the donor template using a ddPCR copy counting assay with no evidence of off-target donor insertion (Figure 7-3C). The line was established with back-crossing to wildtype to produce an F_2 generation for mating. Heterozygous inter-crosses of the F_2 generation produced homozygous W3947X and wildtype offspring. All mice were healthy, fertile and no welfare issues were observed. Genotyping was performed by MRC Harwell using a qPCR-based allelic discrimination assay (Figure 7-3D) and confirmed where appropriate with Sanger sequencing of amplicons of the target exon (Figure 7-3E).

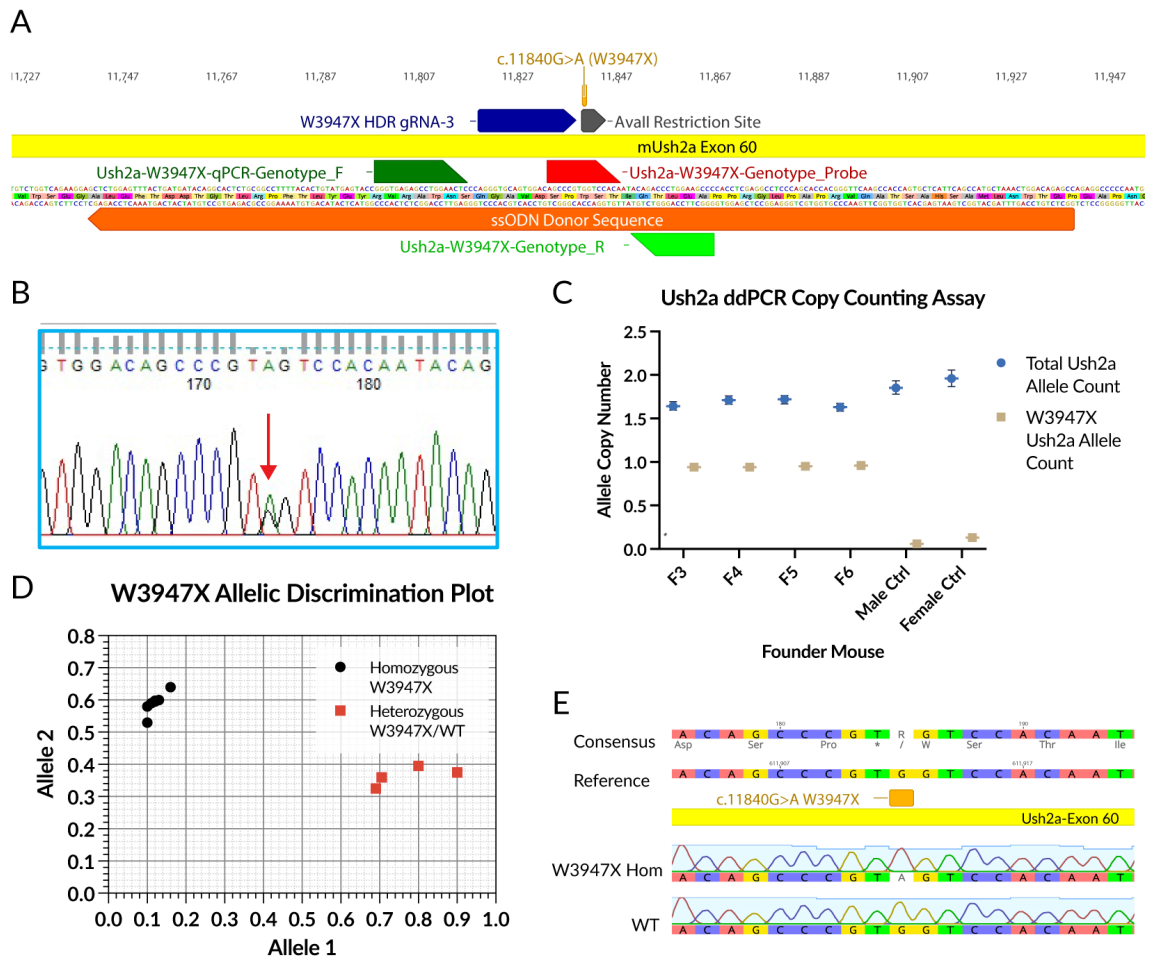


Figure 7-3 Generation and genotyping of *Ush2a*-W3947X mouse

A. Locus map of *Ush2a* exon 60. The gRNA sequence (blue) designed to generate a double stranded break for subsequent homology directed repair from the single stranded donor nucleotide template sequence containing the c.118640G>A (p.W3947X) mutation is annotated. This mutation abolishes an AvaII restriction site in the WT sequence. Primers and probes for allelic discrimination genotyping assay are annotated. **B**. Sanger sequencing of founder F_1 heterozgyote performed by MRC Harwell. **C.** ddPCR copy counting assay of founder mice (F3-F6) performed by MRC Harwell. **D.** Example allelic discrimination assay performed by MRC Harwell, showing differentiation between homozygous and heterozygous offspring. **E.** Sanger sequencing chromatogram traces of gDNA of offspring of F2 heterozygous intercrosses to generate homozygous and wildtype offspring.

7.3.2.2 Molecular analysis of *Ush2a*-W3947X retinas

To examine the effect of the W3947X mutation on usherin expression in the retina, immunostaining of retinal sections and western blot of retinal protein lysates was performed. In wildtype mice, usherin immunoreactivity was localised correctly between the inner and outer photoreceptor segments (Figure 7-4).[128] Usherin expression was not detected in W3947X homozygous retinal sections. Western blot with an antibody to the C-terminus of the 590kDa isoform demonstrated a protein band of expected size in wildtype retinae, with no band detected in W3947X retinae (Figure 7-4D). Protein lysates derived from either wildtype or W3947X eye cups did not demonstrate an usherin band, consistent with the specific photoreceptor expression of usherin.

Next, RT-qPCR was performed on retinal RNA using assays spanning exon 12-13 and exons 63-64 (Figure 7-5). Unexpectedly, qPCR demonstrated equivalent levels of *Ush2a* transcripts between the wildtype and the W3947X for both the exon 12-13 (RQ = 1.23, 95% CI [1.01, 1.49], p = 0.14) and exon 63-64 (RQ = 1.03, 95% CI [0.76, 1.40], p = 0.84) assays. These results are inconsistent with nonsense-mediated decay of the transcript predicted by the premature termination codon.

These results indicate an absence of full-length protein expression detectable with the C-terminal antibody used. Experiments to probe for the presence of truncated protein product with all available commercially available N-terminal antibodies did not detect usherin in wildtype tissues in western blot (Figure 7-6) or immunohistochemistry (not shown) and so were not tested on mutant tissues.

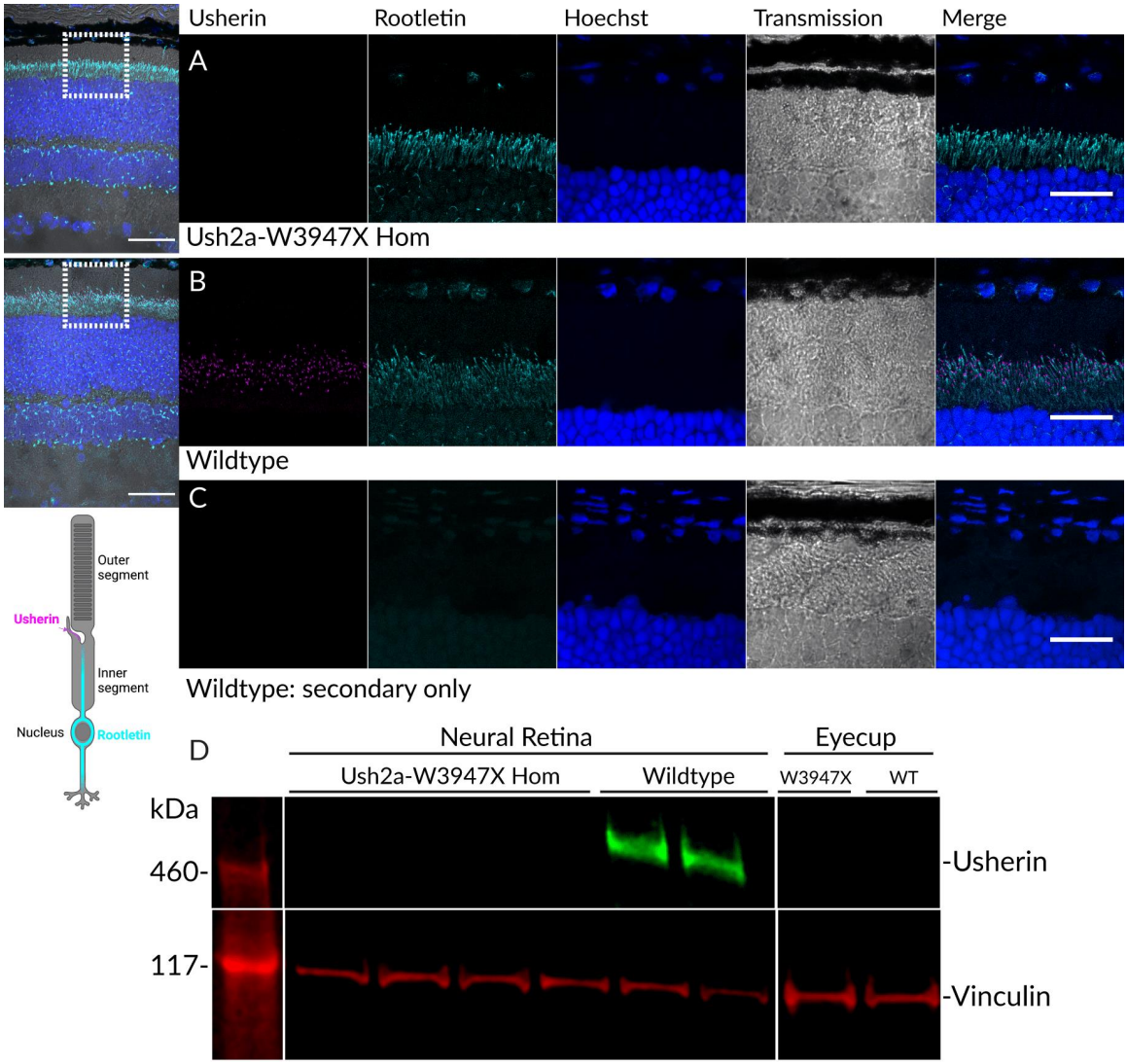


Figure 7-4 Usherin expression in retina of *Ush2a*-W3947X mouse

Immunofluorescence images of retinal sections from 11wk old animals using a 40× overview (scale = 50 μm) of the full thickness of the retina and a 63× image (scale = 30 μm) of the outer retina (inset). A schematic demonstrates the cellular localisation usherin at the connecting cilium at the tips of rootletin staining demarcating the inner segment. **A.** No usherin expression is seen in the *Ush2a*-W3947X homozygous mouse. **B.** Punctate usherin staining is observed in the wildtype mouse. **C.** Secondary only control image of the same eye in B. **D.** Western blot of protein lysates from the neural retina and eye cup (comprising RPE, sclera and choroid), each lane representing an eye of one animal. No usherin expression is seen in *Ush2a*-W3947X homozygotes, with appropriately sized bands (predicted ~590kDa) in wildtype animals. As expected, expression is specific to the neural retina. Vinculin was used as a loading control. Immunofluorescence images representative images of n = 3.

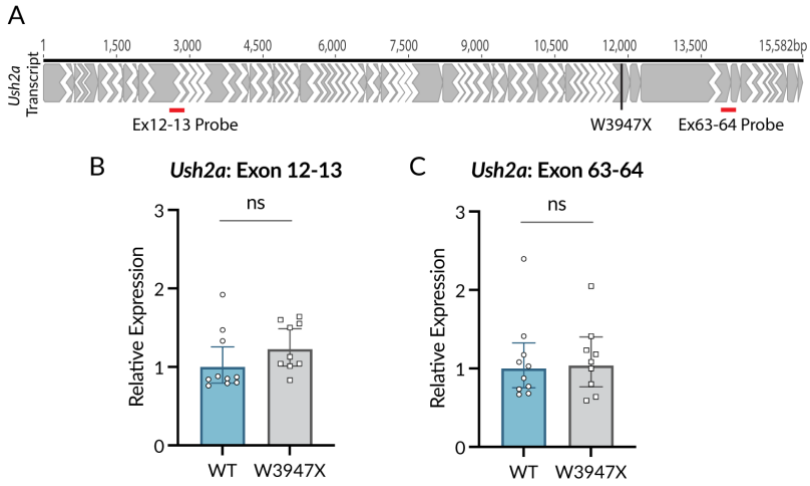


Figure 7-5 *Ush2a* mRNA expression in retina of *Ush2a*-W3947X mouse
A. Schematic of *Ush2a* transcript with exons represented by grey arrow boxes. Exon-exon boundary locations of the primer-probe binding sites of the assays used for qPCR are labelled. **B-C.** No significant difference in retinal expression of *Ush2a* assess by RT-qPCR is seen between wildtype (WT, n = 10) and W3947X (n = 9) mice assessed using assays for either exon 12-13 (p = 0.84) or exon 63-64 (p = 0.14). Expression normalised to *Actb* and *Gapdh* with relative expression normalised to WT. Data expressed as geometric mean of relative quantity [95% CI]. Statistics = unpaired student t-test of dCT values.

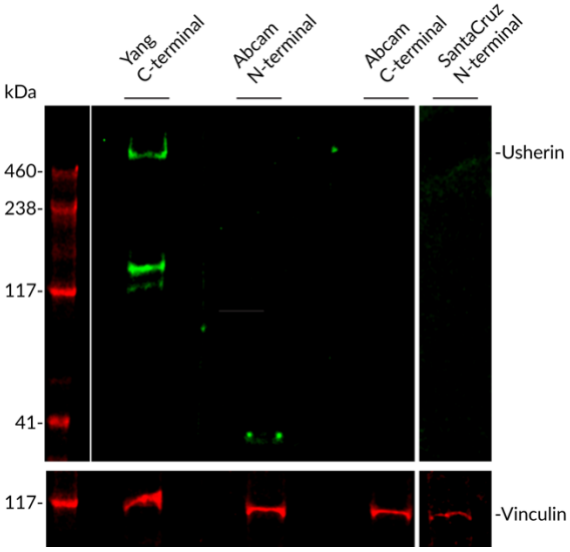


Figure 7-6 USH2A antibody testing
Western blot of wildtype retinal tissue to test currently commercially available anti-usherin antibodies, with the Yang C-terminal antibody as a positive control. Non-specific labelling observed in the Yang antibodies at ~150kDa. No clear bands were detected using any commercial antibody.

7.3.2.3 Natural history of the retinal phenotype of the *Ush2a*-W3947X mouse

The retinal phenotype was examined over time in a cohort of *Ush2a*-W3947X mice with littermate controls at 3- and 6-months of age. Confocal scanning laser ophthalmoscopy (CSLO) imaging with modalities including infrared reflectance, blue autofluorescence and infrared autofluorescence did not reveal any abnormalities in the W3947X mice such as vessel thinning or hyperfluorescent dots that might represent debris, macrophage infiltration or lipid accumulation from degenerating photoreceptors (Figure 7-7).[342,487]

Cross-sectional SD-OCT imaging did not reveal any retinal thinning of the photoreceptor layer or of the entire retinal thickness by 6-months (Figure 7-8). The integrity of the ellipsoid zone, thought to represent the photoreceptor inner-segment or the border of the inner- and outer-segments[488] of the photoreceptors, remained intact.

Full-field dark- and light-adapted ERG was performed to examine rod and cone function with both flash and flicker stimuli. Dark-adapted irradiance response curves demonstrated no difference in a- or b-wave amplitudes at 3-months. At 6-months there were no differences in a-wave amplitudes, but unexpectedly greater b-wave amplitudes were seen in the W3947X mice compared to the wildtype littermate controls (Two way ANOVA for effect of genotype, $F(1,162=24.53)$, $p<0.0001$). Multiple comparison testing revealed significant differences in b-wave amplitudes were seen in the mesopic range at intensities of 1.0 and 1.4 photopic log cd.s/m^2

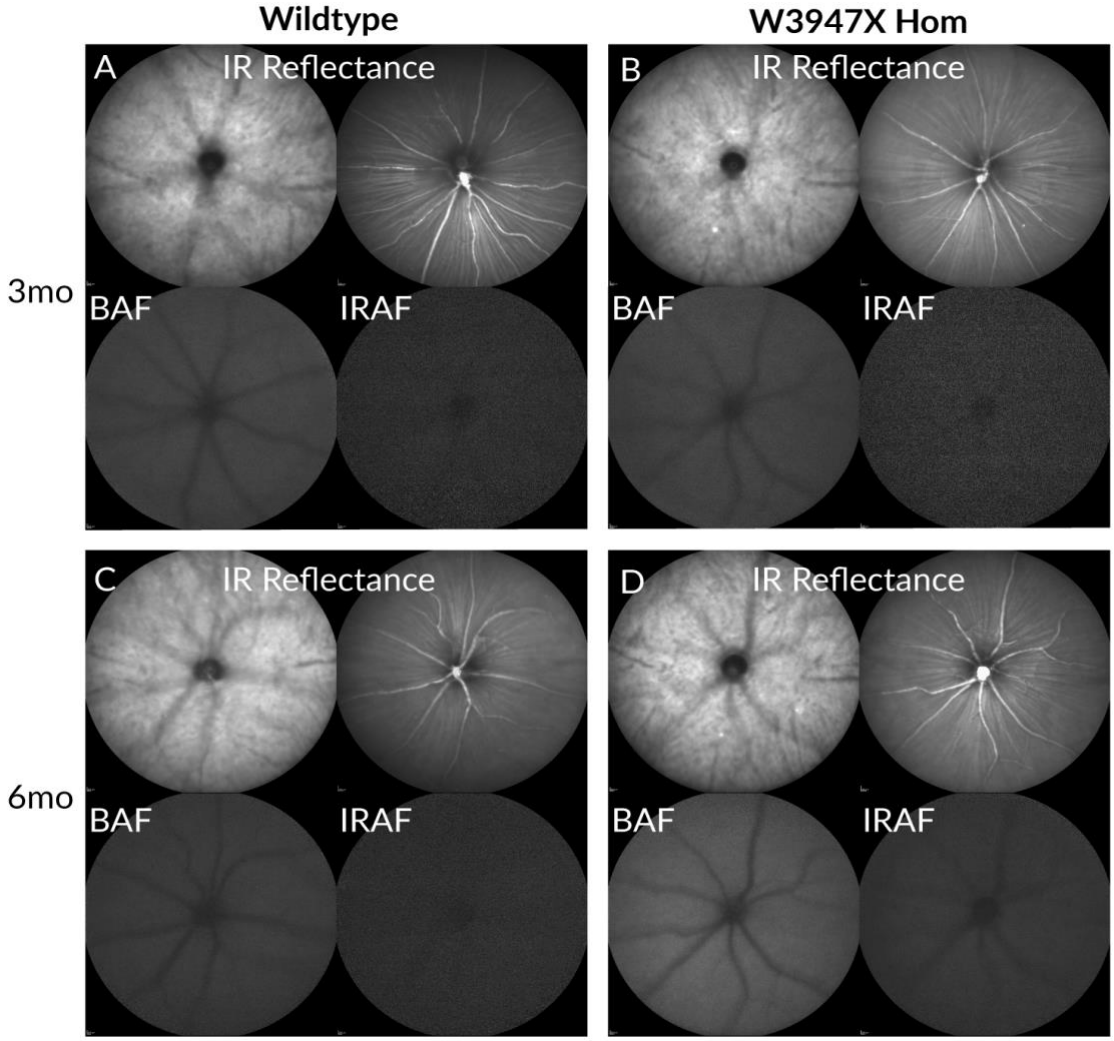


Figure 7-7 Natural history of CSLO retinal imaging of *Ush2a*-W3947X mouse
Representative *en face* confocal scanning laser ophthalmoscopy (CSLO) images of fundus of *Ush2a*-W3947X homozygous mice and wildtype littermate controls at 3- (**A, B)** and 6-months-old (**C, D**) using infrared (IR) reflectance focused on the outer and inner retina, and blue autofluorescence (BAF) and infrared autofluorescence (IRAF) focused on the outer retina. No obvious differences were observed.

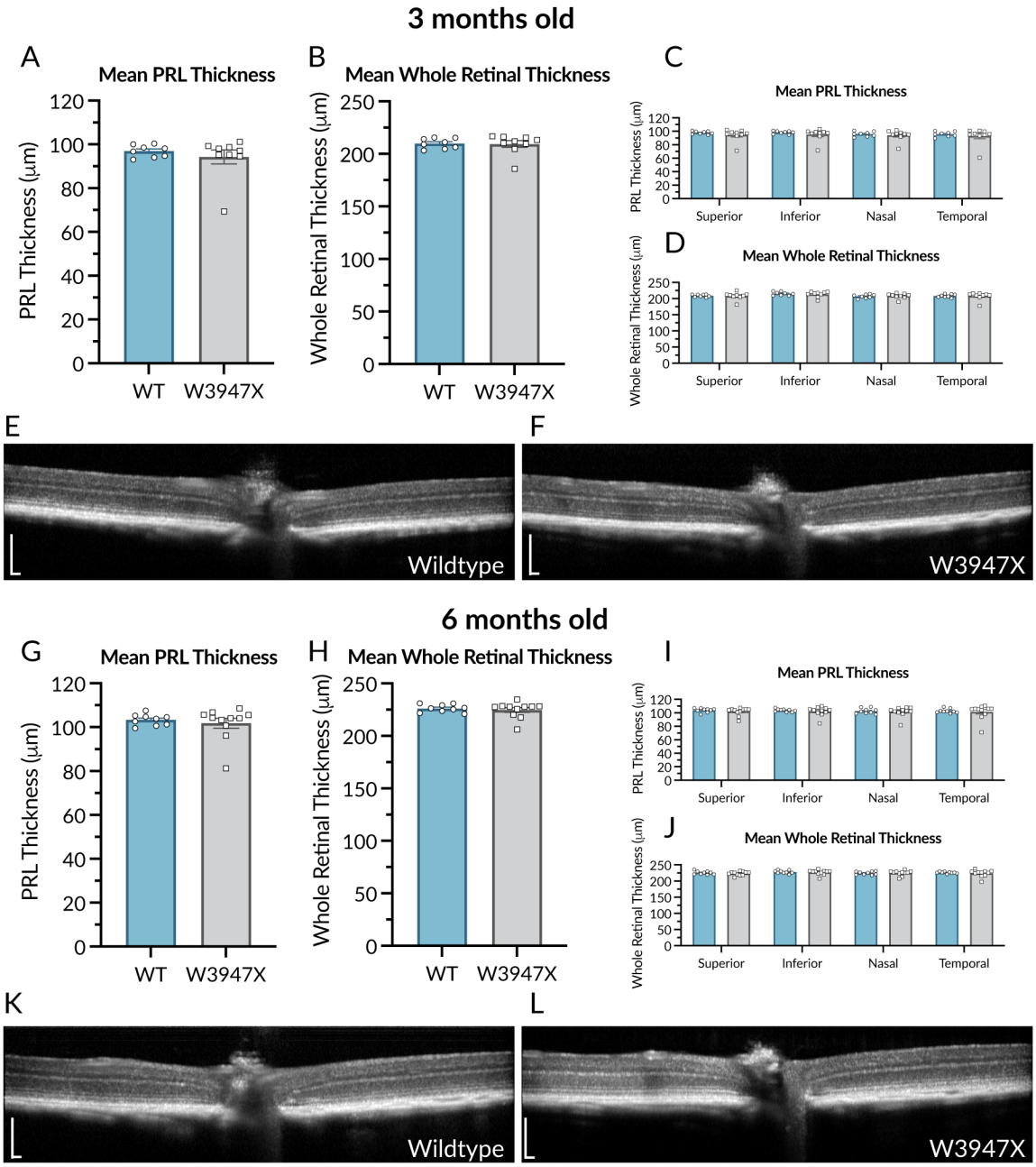


Figure 7-8 Natural history of OCT imaging of *Ush2a*-W3947X mouse

Mean thickness measurements from OCT b-scans of both eyes between *Ush2a*-W3947X homozygous mice and littermate wildtype controls. In 3-month-old animals, there was no difference in (**A**) photoreceptor layer (PRL) thickness ($p > 0.99$) or (**B**) whole retinal thickness ($p = 0.54$). No differences were seen by anatomical location (**C, D**). Representative OCT scans are shown from both wildtype (**E**) and W3947X animals (**F**). In 6-month-old animals, there was no difference in (**G**) PRL thickness ($p = 0.75$) or (**H**) whole retinal thickness ($p = 0.98$). No differences were seen by anatomical location (**I,J**). Representative OCT scans are shown from both wildtype (**K**) and W3947X (**L**) animals. OCT b-scans from inferior (left) to superior (right) centred on the optic nerve. Scale bars = 200 µm. Data = mean ± SEM, pairwise comparisons with Mann-Whitney test.

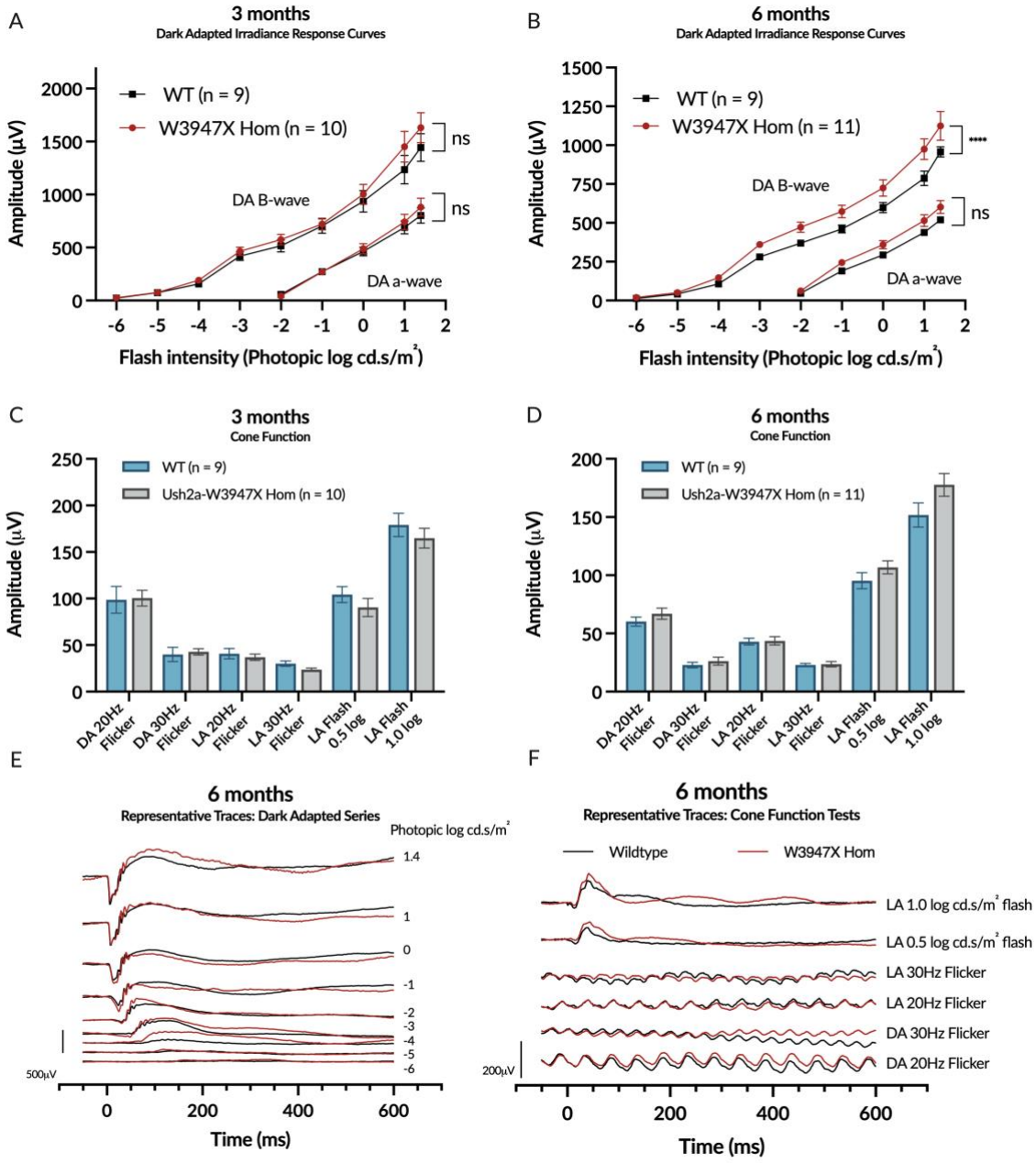


Figure 7-9 Natural history of ERG function of *Ush2a*-W3947X mouse

Retinal function measured by ERG in *Ush2a*-W3947X homozygous mice and littermate wildtype controls. The mean response from both eyes was recorded. (**A & B**) Full field dark-adapted a- and b-wave amplitudes plotted as irradiance response curves from mice at 3- and 6-months of age. Two-way ANOVA for effect of genotype, ****$p<0.0001$. (**C & D**) Measures of cone function including dark-adapted (DA) and light-adapted (LA) flicker, and LA flash responses. No significant differences are seen on any measure ($p > 0.05$, multiple unpaired t-tests with Holm-Sidak adjustment for multiple comparisons) (**E & F**) Representative traces from the dark-adapted series and cone function tests from mice aged 6 months. Data presented as mean ± SD.

7.3.2.4 Characterisation of the cochlea phenotype

As *Ush2a* is also expressed in hair cells of the developing cochlea, immunostaining of cochleas from P4 mice were performed. A complete absence of usherin staining was observed at the bases of the stereociliary bundle in mutant mice, with strong signal in wildtypes (Figure 7-10A).

To examine the functional effect on hearing, auditory brainstem response (ABR) thresholds to a range of tone frequencies were measured. Like the *Ush2a*$^{-/-}$ mouse,[142] ABR thresholds in the *Ush2a*-W3947X mouse were significantly elevated ($p<0.0001$, two-way ANOVA), with the effect predominantly observed at higher frequencies (8-24Hz, $p<0.05$, Sidak's multiple comparisons). This indicates a deficit in auditory nerve response consistent with hearing impairment (Figure 7-10B).

As no vestibular phenotype was expected, extensive testing of vestibular function was not performed. Observation of the mice did not reveal any head-bobbing, shaker-waltzer behaviour, or abnormalities in trunk-curl responses or self-righting.[478]

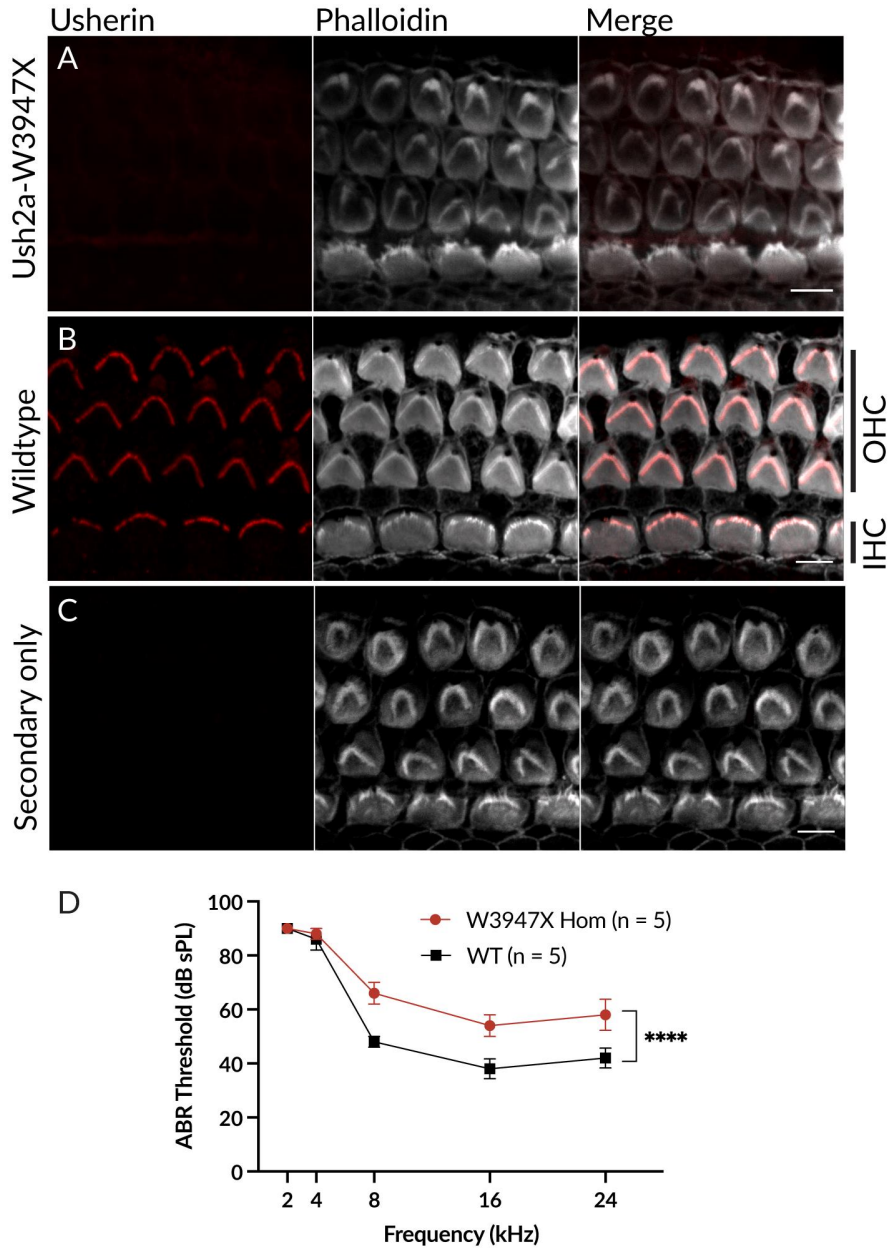


Figure 7-10 Cochlea phenotype of *Ush2a*-W3947X mouse

A-C. Immunofluorescence microscopy of wholemount cochlea middle turn dissected from P4 *Ush2a*-W3947X homozygous mice (**A**) and wildtype controls (**B, C**). Usherin immunoreactivity (red) is seen at the base of the stereociliary bundle in the inner hair cell layer (IHC) and in the three outer hair cell layers (OHC) in wildtype mice but is absent in *Ush2a*-W3947X mice. Phalloidin staining of actin filaments is in grey. Scale bars = 5 μm. **D.** Auditory brainstem responses (ABR) from 9-week-old *Ush2a*-W3947X homozygous mice and wildtype littermate controls. ABR thresholds are significantly elevated in W3947X mice ((Two-way ANOVA for effect of genotype, $F(1,40)=22.92$, $p<0.0001$) at 8, 16 and 24Hz frequencies ($p < 0.05$, Sidak's multiple comparison test). ABR measurements performed in collaboration with Chris Breen (Andrew King Lab, University of Oxford). Data mean ± SEM.

7.3.3 Pilot study of EFS-driven AAV vectors for *Ush2a*-W3947X repair

7.3.3.1 AAV Vector production

As an initial pilot study, EFS-driven dPspCas13b AAV vectors were generated using plasmids cloned in the previous chapter comprising both a dual vector and a single, all-in-one, oversized approach with the m*Ush2a*-50nt-24 targeting and 50nt non-targeting guides. These were produced in AAV8-Y733F capsids. AAV8-Y733F vectors have been previously described to retain the photoreceptor tropism of AAV8 capsids, while the single point mutation of the surface exposed capsid tyrosines significantly improves transduction strength and area of retina transduced through enhancement of escape from proteasome-mediated degradation.[489,490]

Six recombinant AAV vectors were produced to express the different combinations of ADAR mutants and gRNAs (Figure 7-11A). The oversized all-in-one vectors were found to have lower titres (4-5E+11gc/mL) than the those of the dual vector dPspCas13 (1-2E+12 gc/mL) and gRNA (1-2E+13 gc/mL) preparations by qPCR. To investigate the possibility of truncation of the oversize transgene, the all-in-one vector was probed further with qPCR primers designed to amplify the 5', central and 3' ends with equal efficiency.[75] Although truncation typically occurs at the 5' end due the 3'-5' packaging direction of AAV vectors,[76,77] as the positive and negative strands of the ssDNA genome package approximately at a 50:50 ratio,[491] truncation would expect to result in a relative reduction in copies of the 5' and 3' amplicons to the central amplicon. The all-in-one vectors demonstrated approximately equivalent copies of each amplicon, with a suggestion of a greater quantity of amplicons from the 3' end than the central or 5' end (Figure 7-11C). This was inconsistent with truncation of the genome, although AAV genome sequencing or southern blot analyses were not performed to validate this further.[492,493] Denatured concentrated AAV samples were analysed by SDS-PAGE electrophoresis and total protein staining, which demonstrated three distinct bands

representing the AAV capsid subunits (Figure 7-11D). Endotoxin testing showed all AAV samples to contain <1EU/mL.

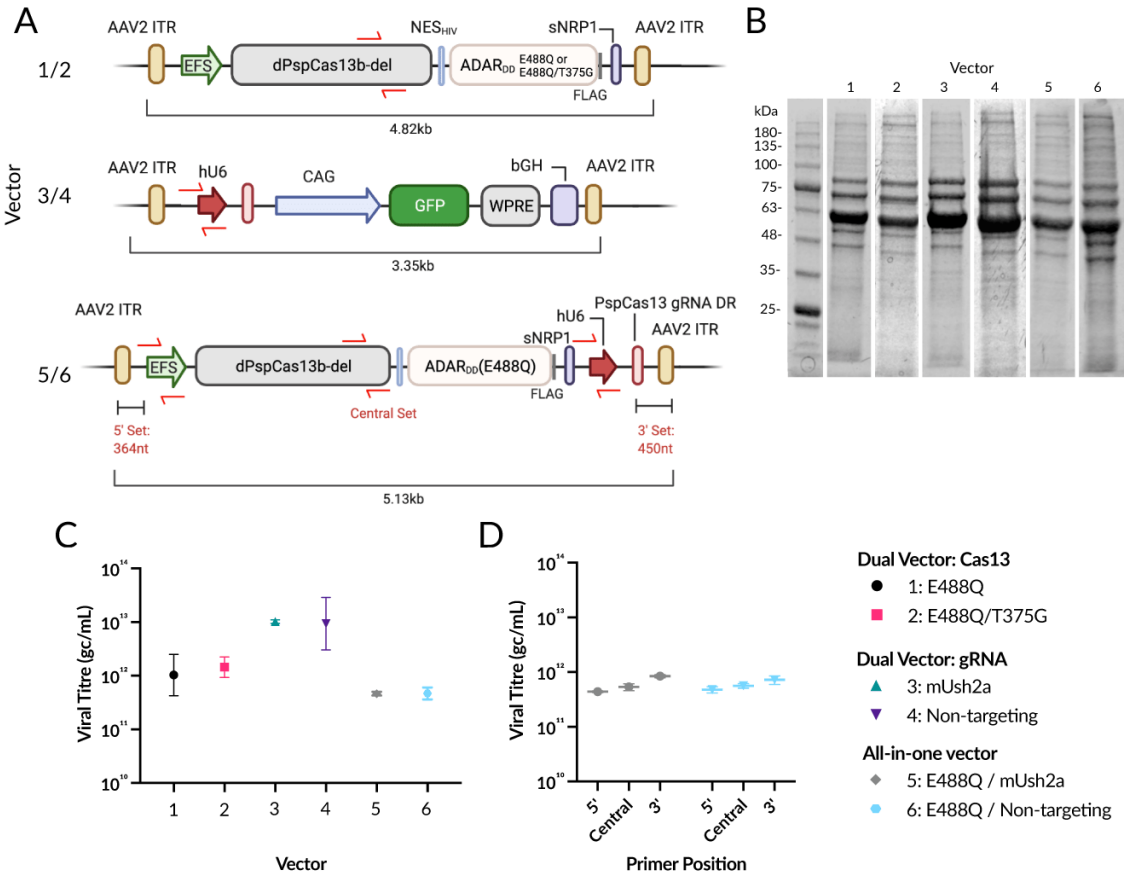


Figure 7-11 Analysis of EFS-driven AAV Vectors

A. Vector maps of analysed AAV. Vectors 1 & 2 comprise the EFS-Cas13-ADAR vectors with either the E488Q or the E488Q/T375G mutations for the dual vector approach. Vectors 3 & 4 are the gRNA vectors with either mouse *Ush2a* (m*Ush2a*) targeting and non-targeting guides for use with the dual vector strategy. Vector 5 & 6 are the all-in-one vectors with the Cas13-ADAR(E488Q), with either a m*Ush2a* targeting or non-targeting gRNA. Vector sizes including ITRs, and locations of qPCR binding pairs for determining titre are annotated. **B.** SDS-PAGE electrophoresis of denatured pure AAV with total protein staining. VP1 (87kDa), VP2 (72kDa), and VP3 (62kDa) capsid proteins are present at the approximate ratio of 1:1:10. Band intensity increases with vector titre. Additional bands of uncharacterised origin are present at low levels. **C.** Vector titres of each AAV (n = 2-3 replicates). Titres for the all-in-one and dual Cas13 vectors determined with the same central primer pair binding to Cas13. Data geometric mean ± geometric SD. **D.** Analysis of vector truncation of all-in-one vector by qPCR with primers binding to the 5', 3' and central regions of the vector (n = 2). No obvious reduction of titre at either the 3' or 5' end is observed.

7.3.3.2 On-target m*Ush2a* editing with dual vector EFS-dPspCas13b-del-ADAR(E488Q) strategy

A pilot study of the dual AAV EFS-driven strategy was undertaken as these vectors demonstrated the highest titres, and the hyperactive E488Q $ADAR_{DD}$ mutant was tested first as this was predicted to give the highest editing rate. A cohort of *Ush2a*-W3947X mice received bilateral injections of a mixture of 1E+9 gc/eye of AAV-EFS-dPspCas13b-del-ADAR(E488Q) and 1E+9 gc/eye of either a targeting or non-targeting AAV-U6-gRNA-CAG-GFP.WPRE vectors for a total dose of 2E+9 gc/eye. At 4-weeks post-injection, retinal imaging was performed, and eyes were harvested.

Sanger sequencing of amplicons from retinal cDNA did not detect any on-target editing in eyes injected with targeting AAVs (Figure 7-12B). Subsequent deep sequencing demonstrated a mean 0.93% ± 0.57 editing rate in eyes injected with the target vector, however editing was only observed in 2 of 5 eyes. No on-target editing was detected by deep sequencing of non-target or PBS injected eyes, although the availability of samples (n=2 each) was limited by experimental factors. Immunohistochemistry of retinal sections detected robust usherin expression in uninjected wildtype animals, but no usherin restoration in treated *Ush2a*-W3947X mice (Figure 7-12C). Furthermore, while robust GFP expression was observed in the photoreceptor layer at the injection site for all AAV-injected samples, no anti-FLAG immunolabelling of the FLAG-tagged Cas13-ADAR transgene was seen.

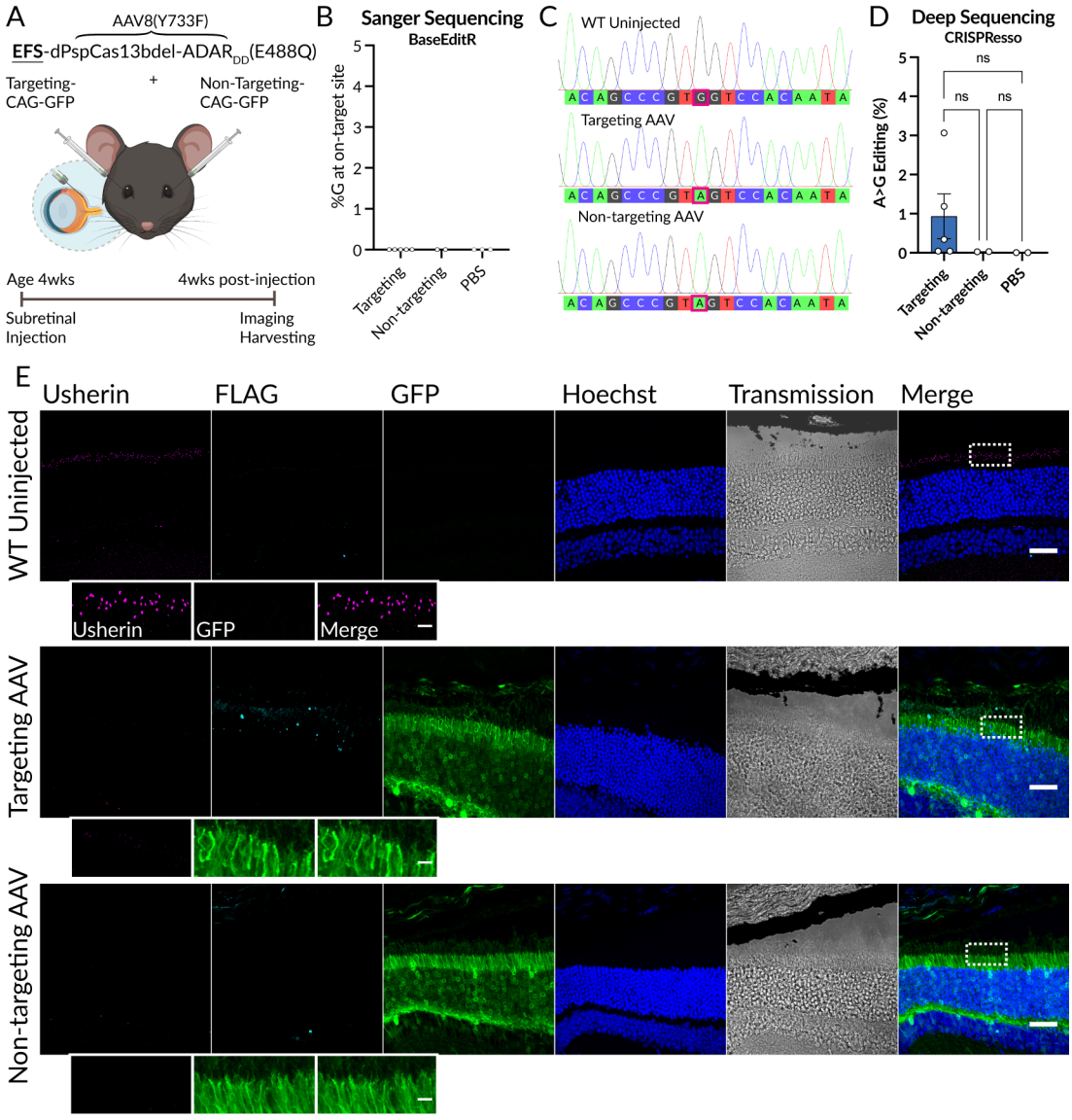


Figure 7-12 EFS-driven dPspCas13b-del-ADAR(E488Q) on-target editing

A. *Ush2a*-W3947X homozygous mice received bilateral subretinal injections containing a mixture of the AAV8(Y733F) capsid EFS-dPspCas13b-ADAR(E488Q) vector (1E+9 gc/eye) plus a targeting (n = 5) or non-targeting (n = 2) U6-gRNA-CAG-GFP.WPRE vector (1E+9 gc/eye) or PBS buffer alone (n = 3) at 4 weeks of age and tissue was harvested at four weeks post injection. **B.** On-target editing rate determined by Sanger sequence decomposition from amplicons generated from retinal cDNA. No editing was detected in the transduced retinas. **C.** Representative chromatogram traces, with the target base highlighted in magenta. **D.** On-target editing rate at the target base determined by deep amplicon sequencing. One-way ANOVA ($F(2,6)=0.86$, $p = 0.46$). **E.** Representative retinal immunofluorescence images at 40× (scale = 30 μm) with inset 63× images focused on the distal inner segment (scale = 5 μm). Endogenous GFP fluorescence from the gRNA-GFP vector is seen at the injection site in treated animals. Clear usherin labelling is observed in the wildtype control but not in the AAV injected animals. FLAG staining to detect the FLAG-tagged Cas13-ADAR transgene is not appreciable beyond punctate background staining in the injected animals. Data mean ± SEM.

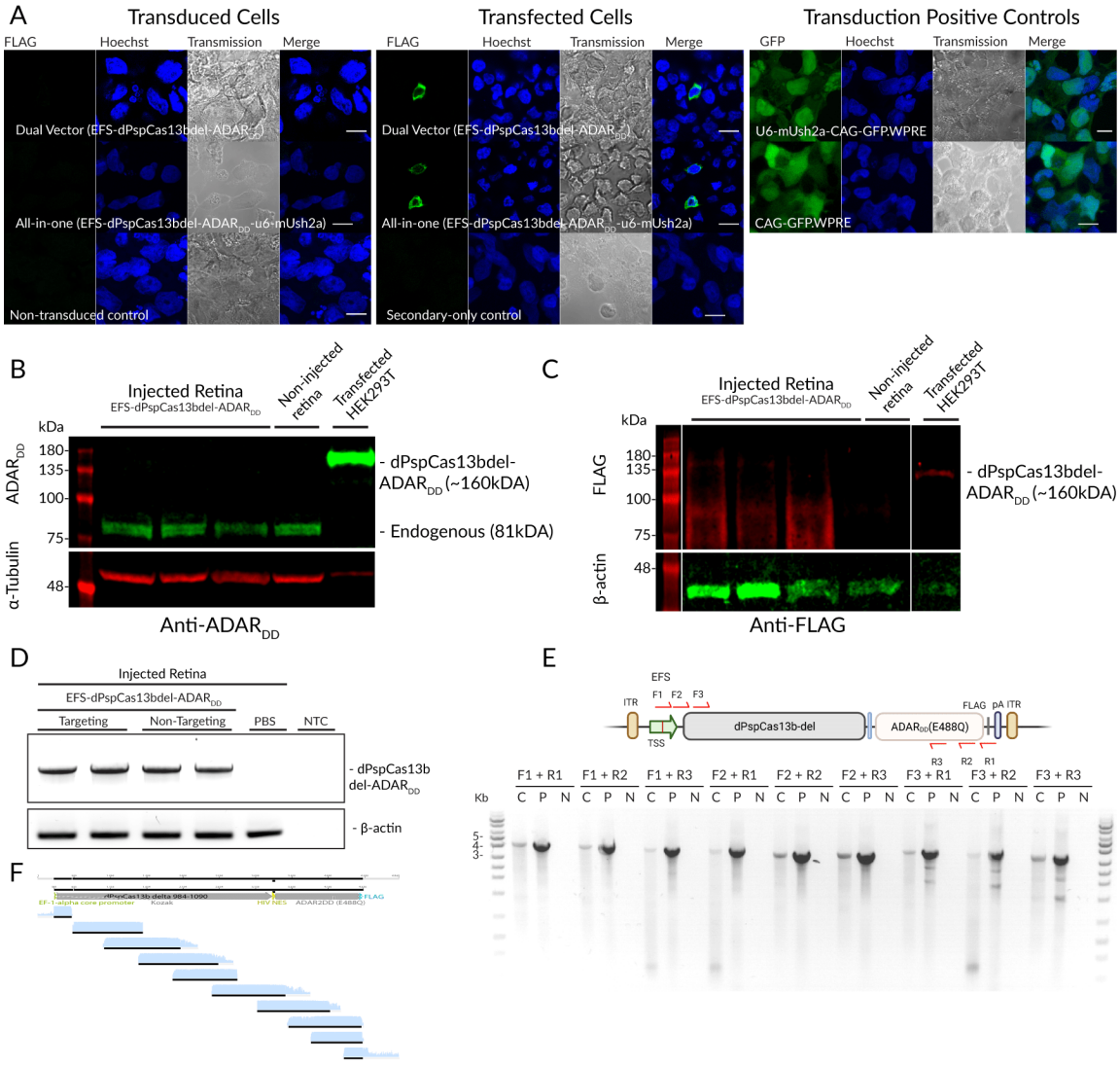

A
Transduced Cells
Transfected Cells
Transduction Positive Controls
FLAG
Hoechst
Transmission
Merge
GFP
Dual Vector (EFS-dPspCas13bdel-ADAR)
All-in-one (EFS-dPspCas13bdel-ADARDD-u6-mUsh2a)
Non-transduced control
Secondary-only control
U6-mUsh2a-CAG-GFP.WPRE
CAG-GFP.WPRE
B
Injected Retina
EFS-dPspCas13bdel-ADARDD
Non-injected retina
Transfected HEK293T
kDa
ADARDD
α-Tubulin
180
135
100
75
48
- dPspCas13bdel-ADARDD (~160kDA)
- Endogenous (81kDA)
Anti-ADARDD
C
FLAG
β-actin
Anti-FLAG
D
Targeting
Non-Targeting
PBS
NTC
- dPspCas13b del-ADARDD
- β-actin
E
EFS
ITR
F1
F2
F3
TSS
dPspCas13b-del
ADARDD(E488Q)
FLAG
pA
R3
R2
R1
F1 + R1
F1 + R2
F1 + R3
F2 + R1
F2 + R2
F2 + R3
F3 + R1
F3 + R2
F3 + R3
C
P
N
Kb
5
4
3
F

Figure 7-13 Analysis of EFS-driven transgene expression
A. Immunocytochemistry of HEK293T cells 96hrs post transduction with AAV or transfected with the equivalent plasmid transgene. Both the 'dual vector' EFS-dPspCas13b-ADAR(E488Q) construct (without a gRNA) and the 'all-in-one vector' (with a m*Ush2a* targeting gRNA) were tested. Transfected cells show anti-FLAG immunolabelling of the Cas13b-ADAR construct, appropriately localised to the cytoplasm due to the nuclear export signal. No immunolabelling is seen in cells transduced with AAV. Transduction positive control cells with CAG-GFP constructs showed early and robust GFP expression after 36hrs of transduction. B. Western blot with an antibody to the $ADAR_{DD}$ against retinal lysates 4 weeks following injection with 1E9 gc/eye of the 'dual vector' Cas13-ADAR construct. An appropriate size band is seen in lysates from HEK293T cells transfected with a plasmid containing the AAV transgene. Cas13-ADAR expression is not seen in retinal lysates. Endogenous $ADAR_{DD}$ is observed as the smaller band. C. Western blot with the anti-FLAG antibody used in A, against lysates with the same conditions as B. This antibody shows poorer labelling with higher background due to mouse origin of the primary antibody, but similarly Cas13-ADAR expression is not seen in retinal lysates. **D.** Gel electrophoresis of RT-PCR products from RNA extracted from transduced retinas. Transcripts from the viral transgene are detected in injected eyes. **E**. Further analysis using RT-PCR with primer pairs targeting the transcriptional start site (TSS) of the EFS promoter and the beginning of the polyA tail, with further pairs walked in along the transgene. No deletions were observed in products amplified from cDNA (C) compared to plasmid DNA (P). Amplification was not observed in the no-template control (NTC, N). **F.** Sanger sequencing of the F1 + R1 RT-PCR product with full coverage and no errors detected.

7.3.3.3 Analysis of expression from EFS-driven vectors

Considering the low editing rates and FLAG immunolabelling from the EFS-driven vector, further experiments were undertaken to investigate whether the EFS promoter was driving Cas13-ADAR expression at a sufficient level. Immunocytochemistry of HEK293T cells transfected with the AAV transgene plasmid, or transduced with the AAV with doxorubicin pre-treatment to augment transduction[494] showed successful transduction in cells treated with AAVs with GFP driven by a CAG promoter. Expression of Cas13-ADAR was detected via anti-FLAG immunolabelling in the cytoplasm of transfected cells but not in transduced cells (Figure 7-13A). Western blot of whole retinal lysates from mice injected with AAV was unable to detect transgene expression using antibodies to the $ADAR_{DD}$ and to the FLAG-tag of the Cas13-$ADAR_{DD}$ (Figure 7-13B,C).

Although these modalities did not detect protein expression, Cas13-ADAR transcripts were detected with RT-PCR (Figure 7-13D) from transduced retinas. To detect any deletions or changes to the transgene, sequential primer pairs were used to amplify the transgene from retinal cDNA and from the plasmid used to create the AAV. No truncation of the transgene was detected, and the correct full-length transgene from the transcriptional start site to the polyA sequence was Sanger sequenced with full coverage (Figure 7-13E-F).

Finally, a wildtype mouse received a subretinal injection with an AAV5-EFS-GFP.WPRE vector available in the lab (a gift from M. McClements) to investigate the expression profile of the EFS promoter in the retina. Although this was a different capsid to the AAV8-Y733F used, AAV5 demonstrates excellent tropism for photoreceptors and allows for the photoreceptor activity of EFS to be assessed.[495] At three-weeks post-injection, low levels of GFP expression could be detected on BAF CSLO imaging (Figure 7-14). Immunohistochemistry revealed barely detectable endogenous GFP expression, with anti-GFP immunolabelling revealing expression predominantly within horizontal cells. Occasional photoreceptor nuclei and inner segments were GFP positive.

Collectively, these analyses indicated that the AAV transgene produced a full-length Cas13-ADAR transcript however protein levels could not be detected. Minimal on-target editing of *Ush2a* could be detected, and this may be associated with the weak translation of the Cas13-ADAR protein, and the minimal activity of the EFS promoter in photoreceptors. Given these findings, the E488Q/T375G $ADAR_{DD}$ mutant and the all-in-one EFS vectors were not tested *in vivo*.

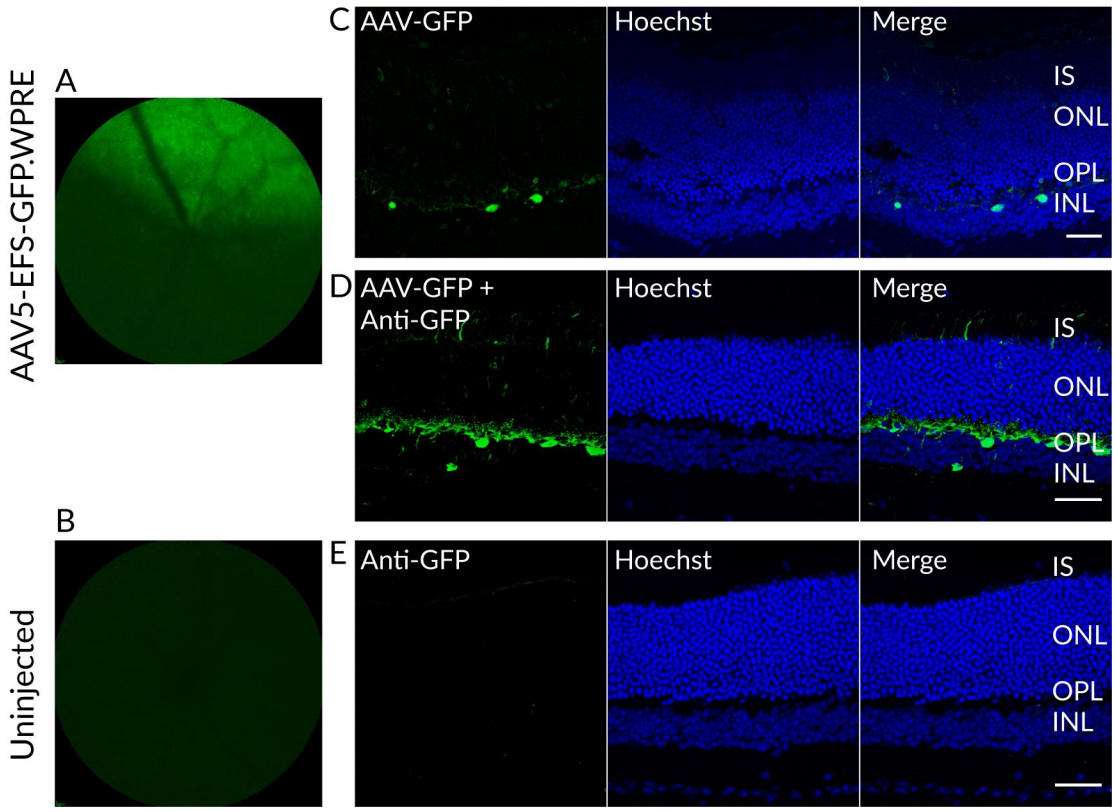


Figure 7-14 Expression GFP under an EFS promoter following subretinal injection
A-B. *In vivo* CSLO imaging with blue autofluorescence (BAF) demonstrating superior retinal transduction at 3 weeks post-injection with an AAV5-EFS-GFP.WPRE vector (1E+9 gc/eye). **C**. Microscopy of retinal section counterstained with Hoechst. High exposure settings were required to visualise AAV expressed GFP without secondary immunolabelling for signal amplification. **D**. Immunolabelling with anti-GFP antibodies demonstrates GFP expression predominantly in the outer plexiform layer (OPL) with a pattern consistent with expression in horizontal cells. Occasional GFP positive photoreceptor nuclei in the outer nuclear layer (ONL) and inner segments (IS) are seen. **E**. GFP expression is not observed in the un-injected eye. BAF images acquired at 100 detector sensitivity.

7.3.3.4 Analysis of retinal structure in EFS-dual vector strategy pilot

Retinal imaging was performed on mice prior to harvesting at 4-weeks post injection. Consistent with the histological analyses, BAF imaging revealed robust GFP expression throughout the retina from the gRNA-GFP vector (Figure 7-15). However, dual vector transduction with both the targeting (29% ± 8, difference of means ± SE) and non-targeting (20% ± 8) vectors caused loss of photoreceptor layer thickness in the injected superior retina relative to the inferior retina on OCT. This was greater than the surgery-related loss seen in PBS injected eyes (10% ± 12%).

To investigate the cause of this retinal thinning, a further cohort was injected with the EFS-Cas13 vector alone and the gRNA-GFP vector alone (Figure 7-15). The Cas13 vector alone (1E+9 gc/eye) was associated with a 17% ± 9 loss, however this was driven by one significant outlier. The gRNA vector at 1E+9 gc/eye caused a 41% ± 8 loss with two eyes with almost absent photoreceptor layers in the superior retina. At 5E+8 gc/eye, this was reduced to a 16% ± 9 loss. As a preliminary study this indicated a dose-dependent toxicity primarily driven by the gRNA vector. This may be associated with overall AAV dose or cellular toxicity of GFP overexpression as observed by others,[391,496] although further studies to characterise this further were not undertaken.

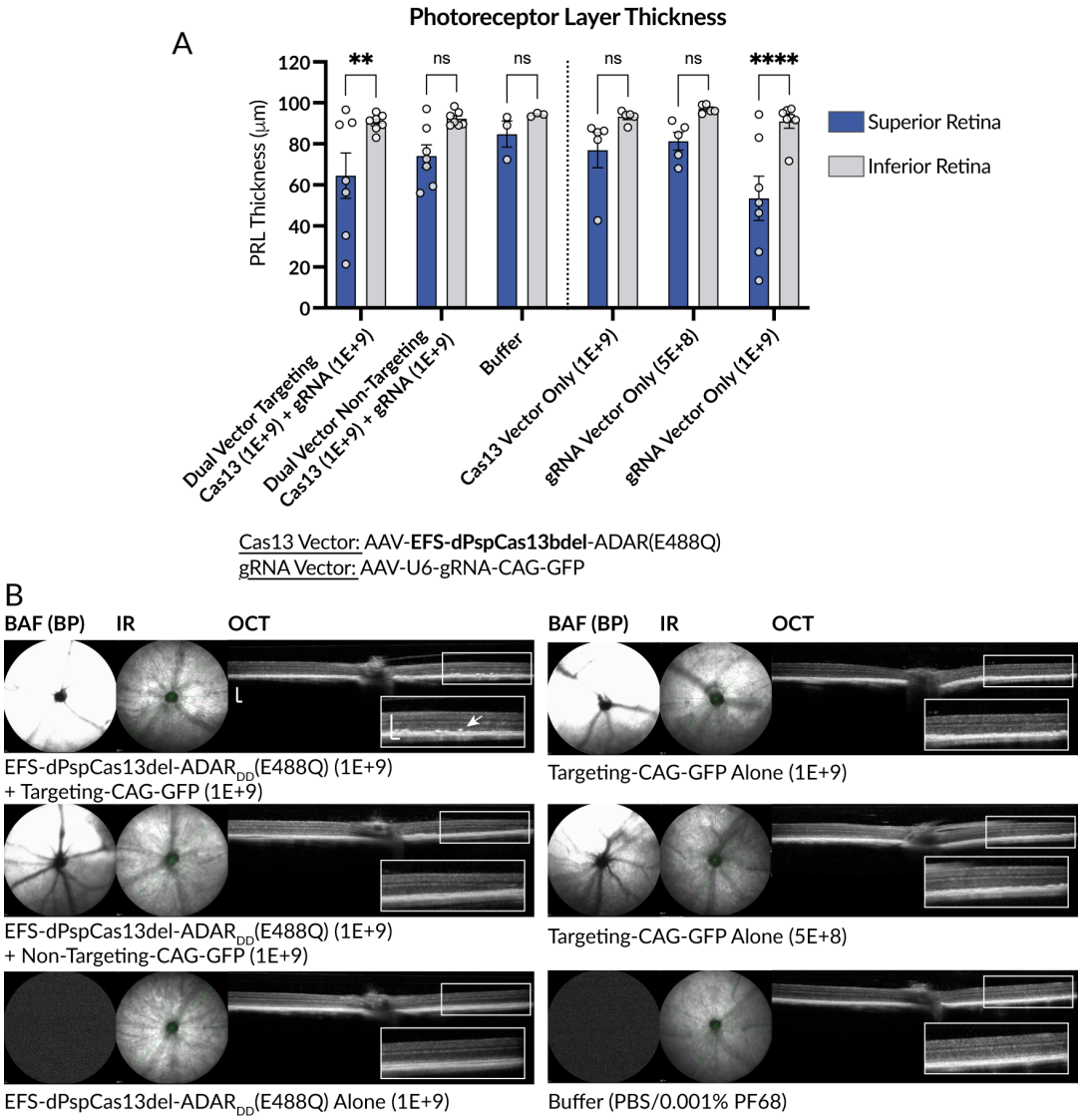


Figure 7-15 Retinal structure following subretinal injection of EFS-driven AAVs

A. Photoreceptor layer thickness at 4-weeks post-subretinal injection with AAV8-Y733F vectors in the superior retina (at the injection site) and inferior retina (away from the injection site). Superior retinal thinning was seen with a dual vector approach of EFS-dPspCas13b-del-ADARDD(E488Q) (1E+9 gc/eye) with targeting and non-targeting U6-gRNA-CAG-GFP vectors (1E+9 gc/eye). When constructs were injected individually retinal thinning was seen with all vectors but was most apparent with a 1E+9 gc/eye dose of the gRNA vector. Halving the dose to 5E+8 gc/eye reduced the retinal thinning to the level seen in buffer injected eyes. Dotted line indicates second cohort. Paired two way ANOVA for effect of retinal location ($F(1, 28)=36.51$, $P<0.0001$) with Sidak's multiple comparison testing. Mean ± SEM. **B**. CSLO images acquired with blue autofluorescence (BAF) imaging with a bandpass filter (BP), infrared reflectance (IR) and OCT for each condition. BAF imaging shows robust GFP expression in the superior retina from GFP constructs. In eyes with retinal thinning, this was seen principally in the outer retina, and associated with loss of the hyper-reflective ellipsoid zone and external limiting membrane bands. In some eyes, subretinal hyper-reflective foci were observed at the injection site (arrow). BAF images acquired at 90 detector sensitivity. Scale bars = 200 µm.

7.3.4 Pilot study of RK-driven AAV vectors for *Ush2a*-W3947X repair

7.3.4.1 AAV Production

As minimal expression of the Cas13 was detected from the EFS-driven vectors, a further four AAVs were generated driven by the photoreceptor specific rhodopsin kinase (RK) promoter (cloning described in the previous chapter), previously used to drive strong expression for retinal gene therapy.[43,458] These included two dPspCas13bdel-ADAR vectors with either the E488Q or E488Q/T375G mutant $ADAR_{DD}$, to be used with the previously generated gRNA vectors in a dual vector approach. Additionally, two vectors with the minimal dCas13bt3 effector were generated to also encode a targeting or non-targeting gRNA in an all-in-one approach. A 50nt guide with a 28nt mismatch distance (gRNA 50nt-28) was cloned in as the best performing guide from the luciferase screen (Figure 6-11). Titres of 5E+12 to 1E+13 gc/mL were achieved with all vectors—a half to full log unit greater than achieved with the EFS vectors—possibly due to the lack of transgene expression during AAV production in HEK cells from the RK promoter (Figure 7-16). Denatured concentrated AAV samples were analysed by SDS-PAGE electrophoresis and total protein staining subunits. Endotoxin testing showed all AAV samples to contain <1EU/mL.

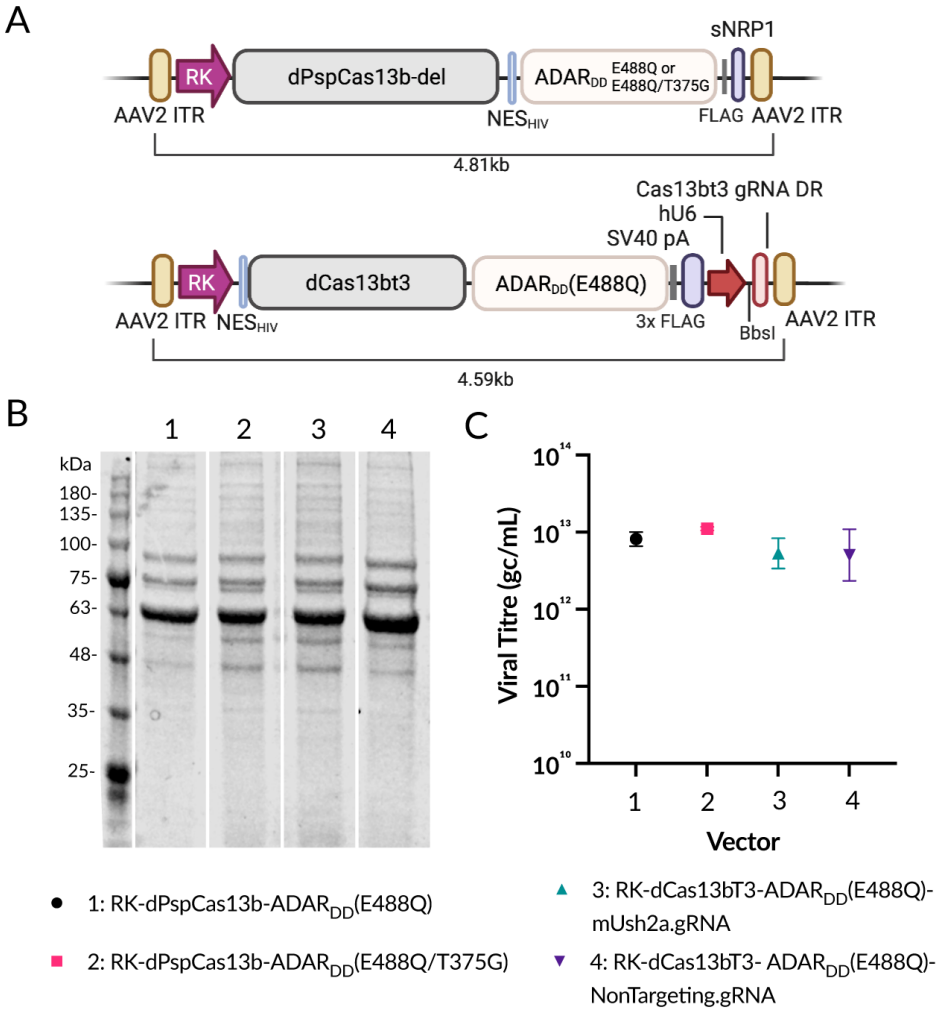


Figure 7-16 Analysis of RK-driven AAV Vectors

A. Vector maps of analysed AAV. Vectors 1 & 2 comprise the RK-dPspCas13bdel-ADAR vectors with either the E488Q or the E488Q/T375G mutations for the dual vector approach. Vector 5 & 6 are the all-in-one RK-dCas13bt3-ADAR(E488Q) vectors with a downstream m*Ush2a* targeting or non-targeting gRNA driven by a U6 promoter. Vector sizes including ITRs are annotated. **B**. SDS-PAGE electrophoresis of denatured pure AAV with total protein staining. VP1 (87kDa), VP2 (72kDa), and VP3 (62kDa) capsid proteins are present at the approximate ratio of 1:1:10. **C**. Vector titres of each AAV (n = 2-3 replicates). Data geometric mean ± geometric SD.

7.3.4.2 RK-dPspCas13b-del-ADAR(E488Q) dual vector strategy

7.3.4.2.1 On-target editing with RK-dPspCas13b-del-ADAR(E488Q)

In this pilot study, a dual vector approach using the RK-driven dPspCas13b-del-ADAR(E488Q) construct was tested. A cohort of *Ush2a*-W3947X mice received bilateral injections of a mixture of 1E+9 gc/eye of AAV-RK-dPspCas13b-del-ADAR(E488Q) and a lower dose of 5E+8 gc/eye of either a targeting or non-targeting AAV-U6-gRNA-CAG-GFP.WPRE vectors for a total dose of 1.5E+9 gc/eye. At 4-weeks post-injection, retinal imaging was performed, and eyes were harvested for RNA.

Decomposition of Sanger chromatograms of retinal cDNA amplicons showed a low level of background in the traces, but eyes injected with targeting AAVs appeared to have a higher rate of G nucleotides detected at the target base above background suggesting an editing rate of ~2% ($p<0.03$) (Figure 7-17B). When subject to deep sequencing, eyes injected with the targeting gRNA vector demonstrated a 2.04% ± 0.16 G>A editing rate, significantly higher than the non-detectable editing (<0.04%) in the non-targeting and PBS-injected retinas ($p<0.0001$).

To explore whether the low level of correction of the premature stop codon could restore usherin expression, immunohistochemistry and western blot was performed on retinas from injected animals (Figure 7-18). Immunohistochemistry revealed a low level of usherin restoration in the EGFP positive injected area observed as punctate labelling at the distal inner segment, which was not present in non-targeting or PBS injected animals. Western blot did not however detect any restoration of usherin expression in whole retinal lysates.

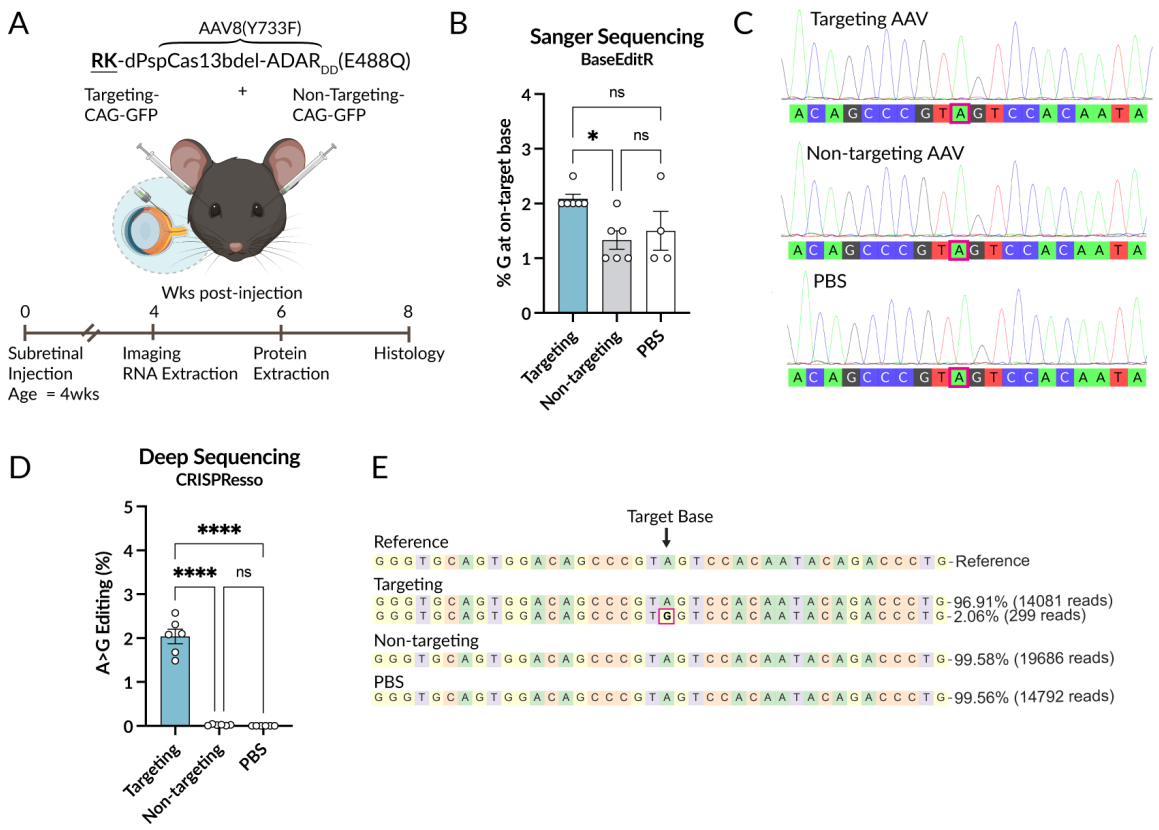


Figure 7-17 RK-driven dPspCas13b-del-ADAR(E488Q) on-target editing of *Ush2a*-W3947X

A. *Ush2a*-W3947X homozygous mice received bilateral subretinal injections containing a mixture of the AAV8(Y733F) capsid RK-dPspCas13b-ADAR(E488Q) vector (1E+9 gc/eye) plus a targeting (n = 6) or non-targeting (n = 6) U6-gRNA-CAG-GFP.WPRE vector (5E+8 gc/eye) at 4 weeks of age. A separate group received a PBS control injection (n = 6). Following retinal imaging at four weeks post injection, retinas were harvested for further processing as shown. **B.** On-target editing rate determined by EditR analysis of Sanger sequencing chromatograms from amplicons generated from retinal cDNA (mean rate from forward and reverse sequencing traces). A marginal difference is seen between the targeting and non-targeting groups ($p = 0.03$) however this was barely detectable above trace background. **C.** Representative chromatogram traces, with the target base highlighted in magenta. **D.** On-target editing rate at the target base determined by NGS deep amplicon sequencing analysed with CRISPResso2. Significant on-target editing is seen in the edited retinas relative to the non-targeting ($p < 0.0001$) or PBS injected retinas ($p < 0.0001$). No editing was detected in the control samples. **E.** Example CRISPResso2 analysis showing alleles present in population. Data = mean ± SEM, analysed with one-way ANOVA, Tukey's multiple comparisons.

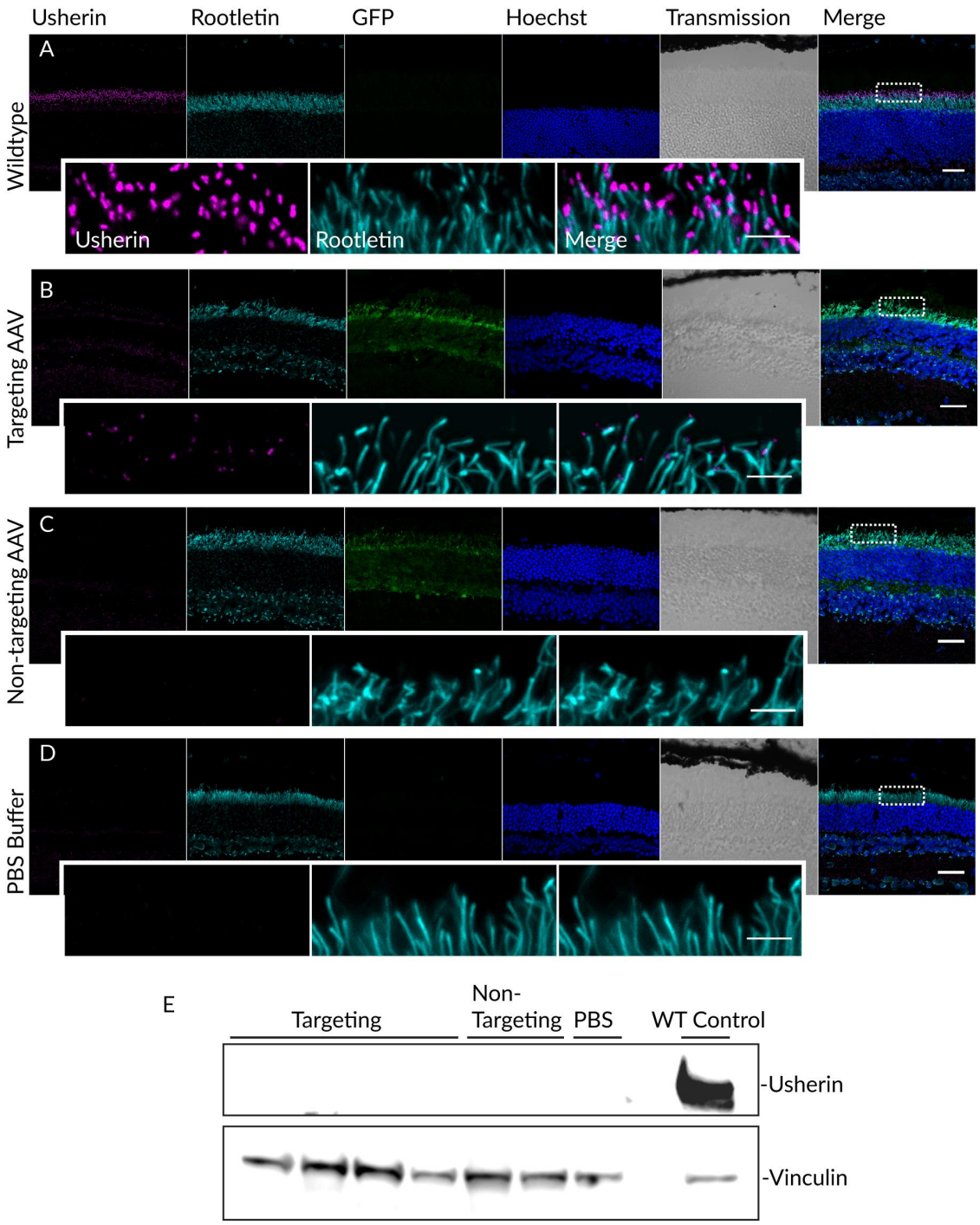


Figure 7-18 Usherin expression following RK-dPspCas13bdel-ADAR(E488Q) repair of *Ush2a*-W3947X mutation

A-D. Representative retinal immunofluorescence images at 40× (scale = 30 μm) with inset 63× images focused on the distal inner segment labelled by rootletin (scale = 5 μm). Endogenous GFP fluorescence from the gRNA-GFP vector is seen at the injection site in treated animals. Clear usherin labelling is observed in the wildtype control. Low levels of signal that localises to the tips of the inner segment are observed in the animals injected with targeting vector but not the non-targeting or PBS injected eyes. **E.** Western blot to detect usherin expression with vinculin as a loading control in whole retinal lysates. No usherin restoration is detected by western blot.

7.3.4.2.2 Analysis of RK-driven dPspCas13b-del-ADAR(E488Q) expression

A similar expression analysis to that performed in section 7.3.3.3 for the EFS vectors was performed for the RK-vectors (Figure 7-19). Likewise, RT-PCR demonstrated the presence of full-length transcripts of the dPspCas13b-del-ADAR transgene, that were sequenced with Sanger sequencing without errors. Immunohistochemistry demonstrated weak anti-FLAG immunoreactivity in the inner segments and outer nuclear layer, consistent with the localisation expected from the RK promoter, although at lower levels than expected. Western blot did not demonstrate detectable protein expression from whole retinal lysates using either an anti-FLAG or anti-$ADAR_{DD}$ antibody.

7.3.4.2.3 Analysis of retinal structure in the AAV-RK-dPspCas13b-del-ADAR(E488Q) pilot

Retinal imaging was performed on mice prior to harvesting at 4-weeks post injection. Robust GFP expression was seen from the gRNA-GFP vector (Figure 7-15). Although this vector combination was tolerated in some eyes, toxicity observed as retinal thinning was seen in others. Like the EFS approach, dual vector transduction with both the RK-driven targeting (24% ± 6, mean difference ± SEM) and non-targeting (26% ± 6) vectors caused loss of photoreceptor layer thickness in the injected superior retina relative to the inferior retina on OCT. This was greater than the surgery-related loss seen in PBS injected eyes (7% ± 11).

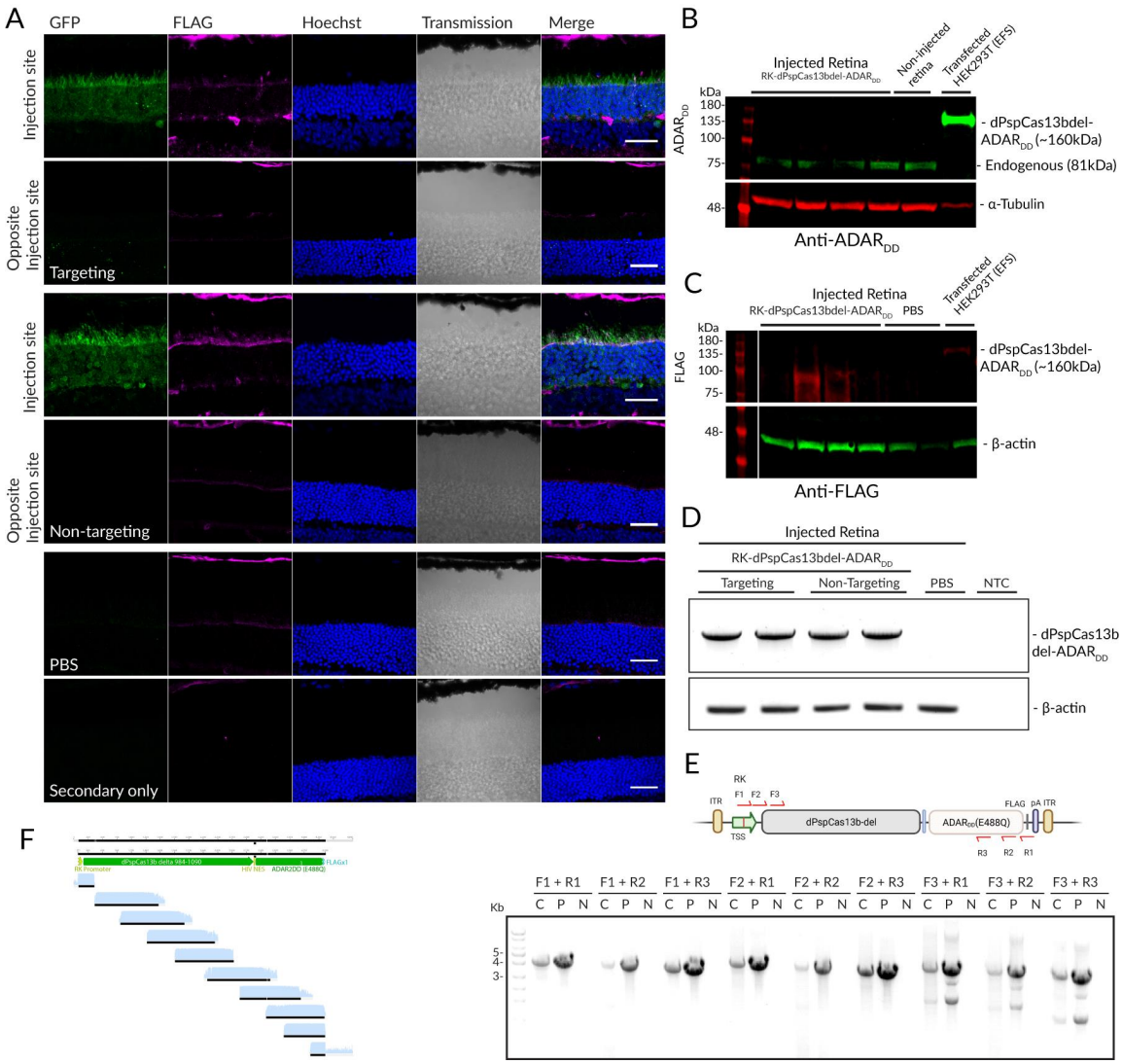


Figure 7-19 Analysis of RK-driven dPspCas13b-del-ADAR(E488Q) expression

A. Immunohistochemistry of retinal sections from eyes injected with either dual AAV-RK-dPspCas13b-del-ADAR(E488Q) vector plus a targeting or non-targeting vector. Sections from the superior retina at the injection site demonstrate GFP expression, not present in sections from the same eye opposite the injection site. Anti-flag staining demonstrates signal in photoreceptor inner segments, and weakly in the ONL, which is not present in the un-transduced retina or in PBS injected eyes. Mouse-on-mouse background immunoreactivity is seen in the RPE of all sections, and in vascular/immune cells at the border of the ONL in injected eyes. **B.** Western blot with an antibody to the $ADAR_{DD}$ against retinal lysates 6 weeks following injection with 1E9 gc/eye of the 'dual vector' Cas13-ADAR construct. An appropriate size band is seen in lysates from HEK293T cells transfected with a plasmid containing the AAV transgene. Cas13-ADAR expression is not seen in retinal lysates. Endogenous $ADAR_{DD}$ is observed as the smaller band. **C**. Western blot with the anti-FLAG antibody used in A, against lysates with the same conditions as B. This antibody shows poorer labelling with higher background due to mouse origin of the primary antibody, but similarly Cas13-ADAR expression is not seen in retinal lysates. *Figure legend continued on the following page*

Figure 7-19 Analysis of RK-driven dPspCas13b-del-ADAR(E488Q) expression

Figure on preceding page **D.** Gel electrophoresis of RT-PCR products from RNA extracted from transduced retinas. Transcripts from the viral transgene are detected in injected eyes. **E**. Further analysis using RT-PCR with primer pairs targeting the transcriptional start site (TSS) of the RK promoter and the beginning of the polyA tail, with further pairs walked in along the transgene. No deletions were observed in products amplified from cDNA (C) compared to plasmid DNA (P). Amplification was not observed in the no-template control (NTC, N). **F.** Sanger sequencing of the F1 + R1 RT-PCR product with full coverage and no errors detected.

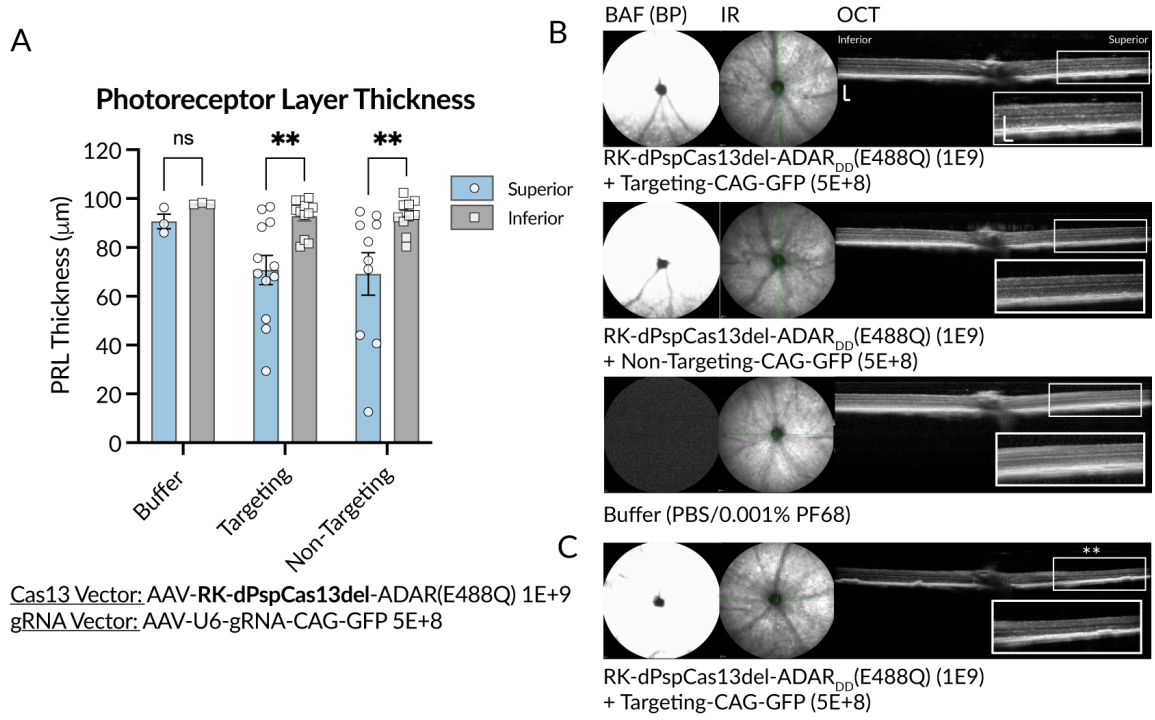


Figure 7-20 Retinal structure following subretinal injection of RK-dPspCas13bdel-ADAR(E488Q) AAV vectors

A. Photoreceptor layer thickness at 4-weeks post-subretinal injection with AAV8-Y733F vectors in the superior retina (at the injection site) and inferior retina (away from the injection site). Superior retinal thinning was seen with a dual vector approach of RK-dPspCas13b-del-ADARDD(E488Q) (1E+9 gc/eye) with targeting and non-targeting U6-gRNA-CAG-GFP vectors (5E+8 gc/eye). Paired two way ANOVA for effect of retinal location ($F(1, 22)=16.45$, $P=0.0005$) with Sidak's multiple comparison testing. Mean ± SEM. **B**. CSLO images acquired with blue autofluorescence (BAF) imaging with a bandpass filter (BP), infrared reflectance (IR) and OCT for each condition. BAF imaging shows robust GFP expression in the superior retina from GFP constructs. **C.** An example of superior retinal thinning (asterisk) associated with loss of the hyper-reflective ellipsoid zone and external limiting membrane bands is shown in the second image. Retinal thinning of varying severity was seen in approximately 50-70% of AAV injected eyes. Scale bars = 200 µm. BAF images acquired at 90 detector sensitivity.

7.3.4.3 All-in-one AAV-RK-Cas13bt3-ADAR(E488Q)-U6-gRNA pilot

7.3.4.3.1 On-target editing with all-in-one Cas13bt3 vector

Ideally, an RNA editing therapeutic would be delivered in an all-in-one vector, and the minimal size of the Cas13bt3 effector allowed the inclusion of the gRNA within the AAV. This also created space for a more potent and well-characterised SV40 polyA terminator[370] in place of the relatively unknown minimal sNRP1 terminator to potentially improve vector expression. Furthermore, to increase sensitivity of detection of expression on western blot and immunohistochemistry, a 3×-FLAG sequence was included in place of a 1×-FLAG sequence.[497] Furthermore, hypothesising that the toxicity observed with the gRNA/GFP vector may be causing death of successfully transduced cells due to GFP overexpression,[391] GFP was not co-delivered.

In this pilot a similar protocol was followed: a cohort of *Ush2a*-W3947X mice received bilateral injections 1E+9 gc/eye of AAV-RK-dCas13bt3l-ADAR(E488Q) containing either a targeting or non-targeting gRNA, or a buffer-only injection. At 4-weeks post-injection, retinal imaging was performed, and eyes were harvested for RNA.

Decomposition of Sanger chromatograms of amplicons from retinal cDNA did not detect any editing above background in the targeting injected eyes (Figure 7-21B). When subject to deep sequencing, eyes injected with the targeting gRNA vector demonstrated a low 0.32% ± 0.06 on-target editing rate G>A editing rate, however significantly greater than seen in the non-targeting eyes (0.02% ± 0.01, p=0.0007) (Figure 7-21C). Immunohistochemistry of retinas harvested at 8 weeks post-injection did not reveal any restoration of usherin expression (Figure 7-21D).

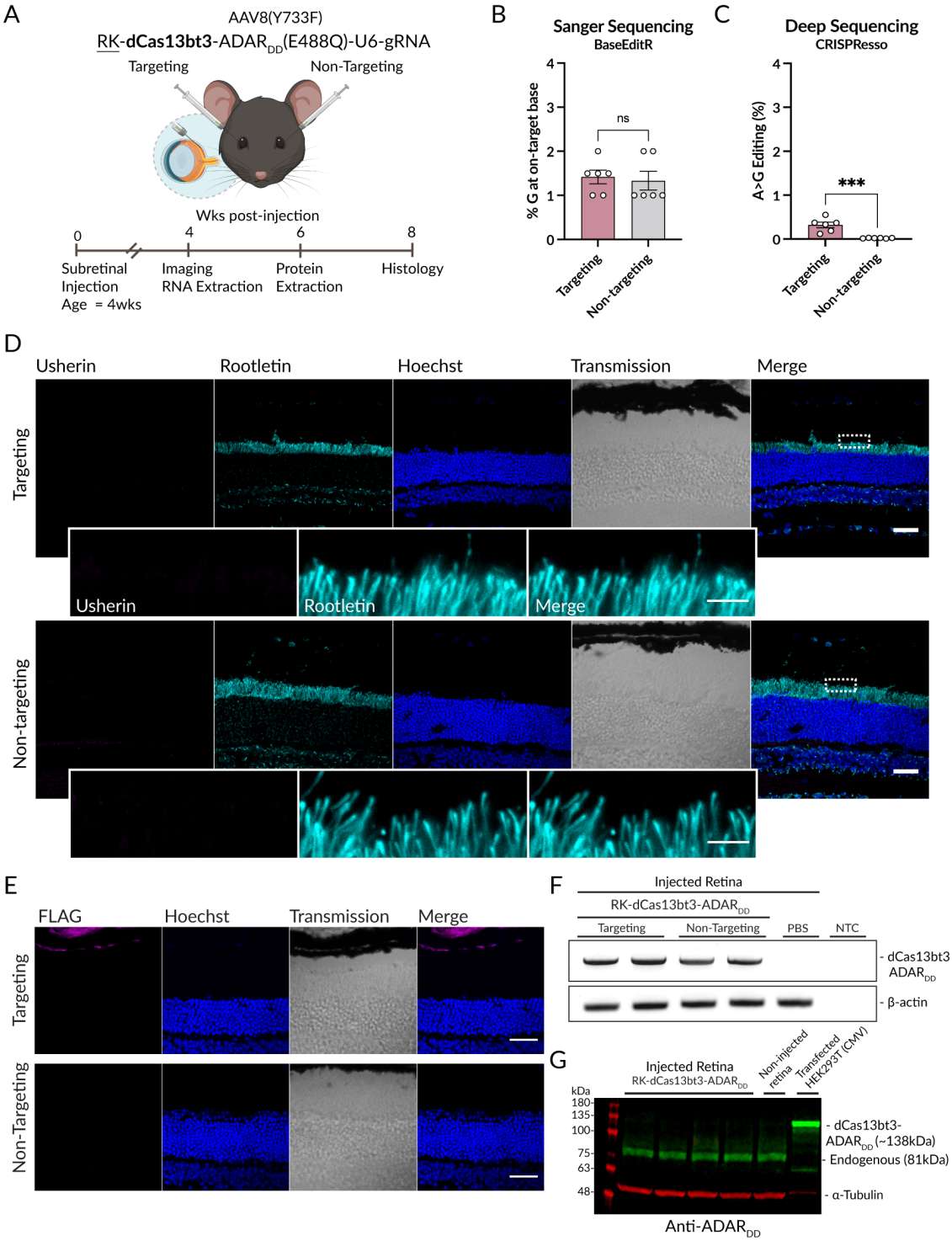

A
AAV8(Y733F)
RK-dCas13bt3-ADAR$_{DD}$(E488Q)-U6-gRNA
Targeting
Non-Targeting
Wks post-injection
0
4
6
8
Subretinal Injection Age = 4wks
Imaging RNA Extraction
Protein Extraction
Histology
B
Sanger Sequencing
BaseEditR
% G at on-target base
ns
Targeting
Non-targeting
C
Deep Sequencing
CRISPResso
A>G Editing (%)
***
Targeting
Non-targeting
D
Usherin
Rootletin
Hoechst
Transmission
Merge
Targeting
Non-targeting
E
FLAG
Hoechst
Transmission
Merge
Targeting
Non-Targeting
F
Injected Retina
RK-dCas13bt3-ADAR$_{DD}$
Targeting
Non-Targeting
PBS
NTC
- dCas13bt3 ADAR$_{DD}$
- β-actin
G
Injected Retina
RK-dCas13bt3-ADAR$_{DD}$
Non-injected retina
Transfected HEK293T (CMV)
kDa
180
135
100
75
63
48
- dCas13bt3-ADAR$_{DD}$ (~138kDa)
- Endogenous (81kDa)
- α-Tubulin
Anti-ADAR$_{DD}$

Figure 7-21 *Ush2a* RNA editing with all-in-one Cas13bt3 vectors
A. *Ush2a*-W3947X homozygous mice received bilateral subretinal injections of the AAV8(Y733F)-RK-dCas13bt3-ADAR(E488Q)-U6-gRNA all-in-one vector (1E+9 gc/eye) containing either a targeting (n = 6) or non-targeting (n = 6) gRNA at 4 weeks of age. Following retinal imaging at four weeks post injection, retinas were harvested for further processing as shown. **B.** On-target editing rate from Sanger chromatogram decomposition analysis of amplicons from retinal cDNA (mean rate from forward and reverse sequencing traces). No difference is seen between groups above background (p=0.76). **C.** On-target editing determined by NGS deep amplicon sequencing. Significant on-target editing is seen in the targeting relative to the non-targeting (p =0.0007) injected eyes. **D**. Immunohistochemistry of retinal sections from injected eyes, with high magnification images of outlined areas of the rootletin tips at the expected region of usherin localisation inset. No usherin immunolabelling is seen in either condition. **E.** No FLAG immunolabelling is detected in retinas injected with the 3×-FLAG c-terminally tagged Cas13bt3 constructs. Signal in the RPE/choroid from non-specific mouse-on-mouse labelling also seen in PBS injected eyes. **F.** Gel electrophoresis of RT-PCR products from RNA extracted from transduced retinas. Transcripts from the viral transgene are detected in injected eyes. **G.** Western blot with an antibody to the $ADAR_{DD}$ against retinal lysates 6 weeks following injection. An appropriate size band is seen in lysates from HEK293T cells transfected with a plasmid with a CMV promoter driving Cas13bt3-$ADAR_{DD}$ expression. Cas13-ADAR expression is not seen in retinal lysates. Endogenous $ADAR_{DD}$ is observed as the smaller band. Data = mean ± SEM, analysed with unpaired t test.

7.3.4.3.2 Transgene expression from the all-in-one Cas13bt3 vector

Assessment of RNA and protein expression from the transgene was undertaken (Figure 7-21). RT-PCR demonstrated the presence of dCas13bt3-ADAR transcripts from injected eyes, however this did not correlate with detectable protein. Immunohistochemistry did not reveal FLAG immunoreactivity in the retina, despite the inclusion of a 3×FLAG sequence. Western blot did not demonstrate detectable protein expression from whole retinal lysates.

7.3.4.3.3 Retinal Structure

Retinal imaging was performed on mice prior to harvesting at 4-weeks post injection. Relative to the un-injected inferior retina as an internal control, the PBS eyes demonstrated non-significant superior thinning as expected following subretinal injection (5% ± 3% mean difference ± SEM). The vector injected eyes showed a 12% ± 2% and 14% ± 2% superior thinning in the targeting and non-targeting eyes respectively (both $p<0.0001$). Injection with

the non-targeting vector resulted in a greater number of highly degenerated retinas with a photoreceptor layer thickness of <70 μm.

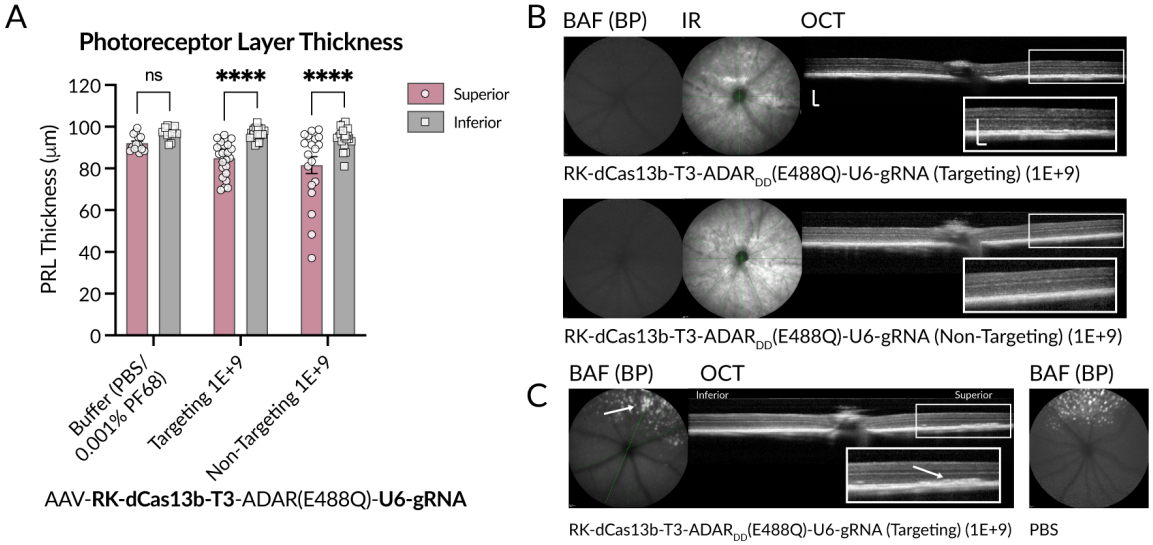


Figure 7-22 Retinal structure following subretinal injection of all-in-one dCas13bt3-ADAR(E488Q)-U6-gRNA AAV vectors

A. Photoreceptor layer thickness at 4-weeks post-subretinal injection with AAV8-Y733F vectors in the superior retina (at the injection site) and inferior retina (away from the injection site). Minimal retinal thinning was seen with a single vector approach (1E+9 gc/eye) with targeting vectors, although some eyes in the non-targeting group showed significant thinning. Paired two way ANOVA for effect of retinal location ($F(1, 54)=55.64$, $P<0.0001$) with Sidak's multiple comparison testing. Mean ± SEM. **B**. CSLO images acquired with blue autofluorescence (BAF) imaging with a bandpass filter (BP), infrared reflectance (IR) and OCT. **C.** An example of BAF signal at the injection site (arrow). This was frequently associated with subretinal deposits or RPE thickening (arrow). This was also observed in some PBS injected eyes, although more commonly occurred in those injected with AAV. Scale bars = 200 μm. BAF images acquired at 100 detector sensitivity.

7.3.5 Local off-target editing *in vivo*

To explore local off-target effects in the *Ush2a* transcript, the rates of A>G conversion of bystander adenosines were explored in the deep sequencing data analysed with CRISPResso2 (Figure 7-23). Off-target sites were determined by adenosines with A>G conversion at a significant rate above that detected in PBS injected eyes (see methods).

In eyes injected with the dPspCas13b and the targeting gRNA, off-target sites were predominantly bystander adenosines clustered within the dsRNA region created by gRNA

binding, with a mean (± SEM) editing rate of 0.05% ± 0.01 and 0.10% ± 0.03 for the EFS and RK driven vectors respectively. The highest edited sites in dPspCas13 injected eyes were positions A_{35} and A_{36}, which showed editing rates up to 0.36% in the RK-driven vector. These common sites, as well as A_{23} were also identified in the *in vitro* analysis (labelled there as sites A_{14} A_{26} and A_{27}), and all produce missense changes in the protein. The higher on-target editing rate achieved with the RK-driven vectors also correlated with a higher overall number and greater rate of editing at off-target sites compared to the EFS vectors. Off-target editing at sites distant to the gRNA binding site was seen across both constructs, and additionally, at two sites in eyes injected with the non-targeting RK-dPspCas13b vector.

Off-target editing rates in the Cas13bt3-injected eyes were lower, but across a greater and more sporadic number of sites outside the gRNA binding region, observed in both the targeting and non-targeting constructs.

Mapping of the deep-sequencing reads enabled an analysis of the number of transcripts that contained the desired TAG > TGG edit only, without potentially deleterious off-target deamination events, an estimate of the precision of the editing (Figure 7-23C). Therefore, although an on-target rate of 2.04% was seen in RK-dPspCas13b eyes, 1.45% of transcripts were corrected to the precise wildtype sequence. This was similarly seen with EFS-dPspCas13b (0.93% on-target, 0.68% precision correction), and to a lesser extent the RK-dCas13bt3 (0.32% on-target, 0.27% precision correction) vectors.

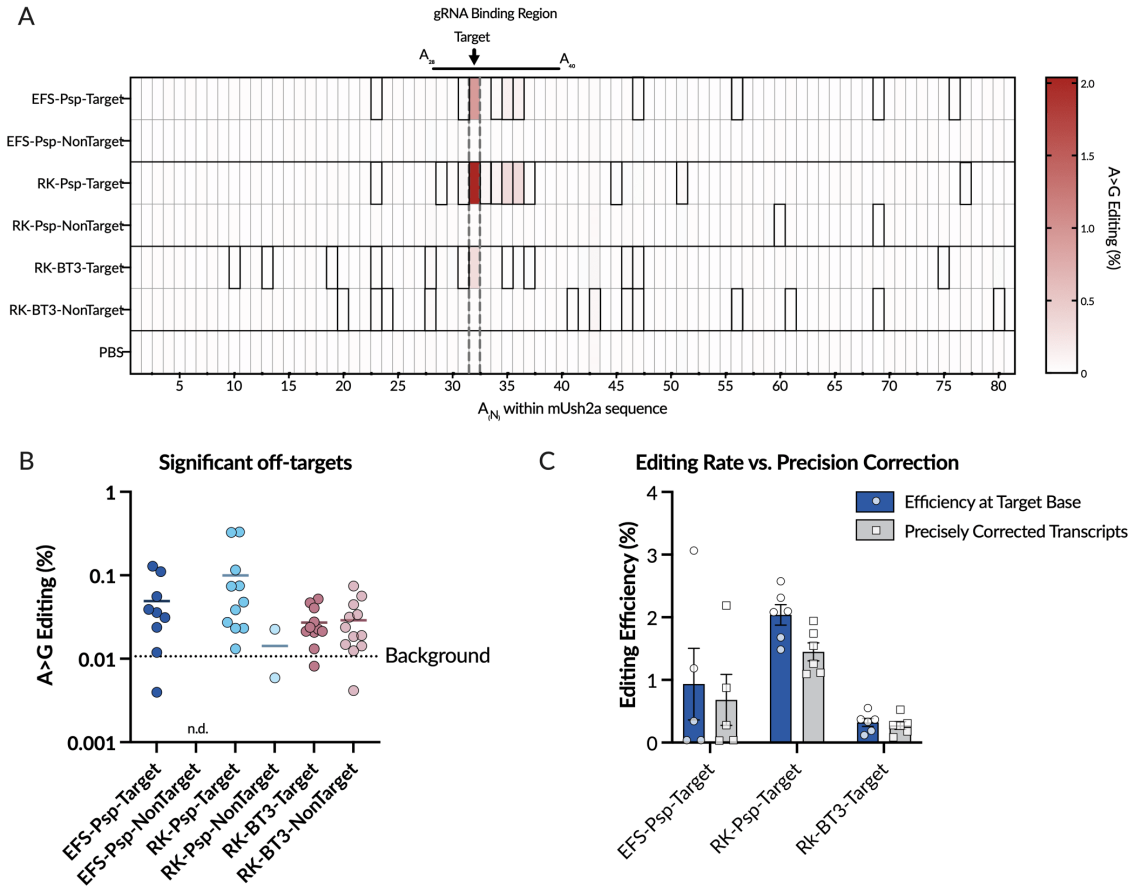


Figure 7-23 Local off-target editing with RK-dPspCas13b-del-ADAR(E488Q)

A. Off-target analysis by deep sequencing, demonstrating A>G editing rate at every local adenosine in the *Ush2a* exon 60 amplicon for each vector (n = 6 retinas per vector, PBS n = 8). Significant editing sites outlined in black (adjusted $p<0.01$, PBS injected eyes as controls). **B.** Significant off-target sites with editing rates plotted on a log-scale. Background rate of detected A>G in PBS injected eyes shown in dotted line, demonstrating most discovered off-target sites with editing rates above the expected sequencing error rate. **C.** Comparison of editing rates at the target base, and 'precision' editing rates. Precisely corrected transcripts were defined as amplicon reads containing only on-target editing and no off-target editing sites. n.d. = not detected. Mean ± SEM.

7.4 Discussion

The purpose of this chapter was to develop a novel mouse model of Usher syndrome amenable to base editing and then use this to develop and compare a range of AAV-delivered Cas13-based RNA editing approaches *in vivo*.

7.4.1 Ush2a-W3947X mouse

The design of this mouse was conceptualised following a review of available mouse models to test the *in vivo* use of RNA and adenine DNA base editors for IRDs, which demonstrated a lack of models of common autosomal recessive conditions. A model of *USH2A* was selected given the high prevalence of *USH2A*-related retinopathy, and the identification of the common W3955X premature termination variant in humans. Using an Cas9-HDR knock-in strategy, MRC Harwell successfully generated a viable *Ush2a-W3947X* line on an age-related hearing loss corrected (*Cdh23*$^{753A>G}$) background, a novel *USH2A* model for investigating disease mechanisms in vision and hearing loss, and for evaluation of potential therapeutics.

7.4.1.1 Molecular Characterisation

Molecular characterisation of the model suggests that the homozygous W3947X mutation results in absence of full-length usherin protein expression in the retina and cochlea. This is an ideal model for testing of therapeutics as repair of the mutation at a sufficient rate should be detectable by restoration of usherin expression.

Interestingly, the absence of usherin expression in the retina does not appear to be due to nonsense-mediated decay of the transcript, with no reduction in *Ush2a* expression seen in homozygous mutant mice. Similar findings have been shown in other CRISPR-generated mouse models containing PTCs.[498] There are several potential explanations for this. Rates of NMD can be highly variable between transcripts and tissues,[499] however it is surprising that no reduction in expression was observed as the mutation occurs 202nt upstream of an exon-exon junction, satisfying the dogma that NMD occurs if a PTC is located >50-55nt upstream of an

exon-exon junction.[500] It is possible that this mutation produces a truncated protein product not detectable by the C-terminal antibody available for usherin detection in this work. Unfortunately, the available N-terminal antibodies did not work in wildtype tissue. Analysis of the downstream sequence with polyA prediction tools does not reveal the existence of any consensus cryptic polyA sites (AATAAA or ATTAAA) in the *Ush2a* open reading frame.[501–503] One non-canonical sequence (Figure 7-24) identified lies 3,325nt downstream of the PTC, which would generate a very long 3' UTR unlikely to be utilised by the truncated transcript to avoid NMD. Finally, any out-of-frame ribosomal skipping of the W3947X PTC would lead to the ribosomal encountering further PTCs before the end of the ORF. A C-terminally truncated product would be predicted to be non-functional, as it would lack the necessary C-terminal transmembrane domain for correct localisation and the PDZ-binding domain for interaction with the Usher-interactome at the connecting cilium. The predicted lack of usherin function in this model is supported by the early hearing loss phenotype.

Further investigation into this continues, with plans to repeat the expression studies and obtain working antibodies to N-terminal and mid-protein epitopes. Future studies will also investigate changes to other interacting proteins such as ADGVR1 and SANS, localisation of proteins trafficked through the connecting cilia such as opsins, and markers of retinal remodelling such as GFAP.[128, 133, 142,174] Additionally, ongoing development of retinal organoids from patient derived iPSCs containing the human W3955X mutation may shed further light on this (personal communication, V. Kalatzis, IMN Montpellier, France).

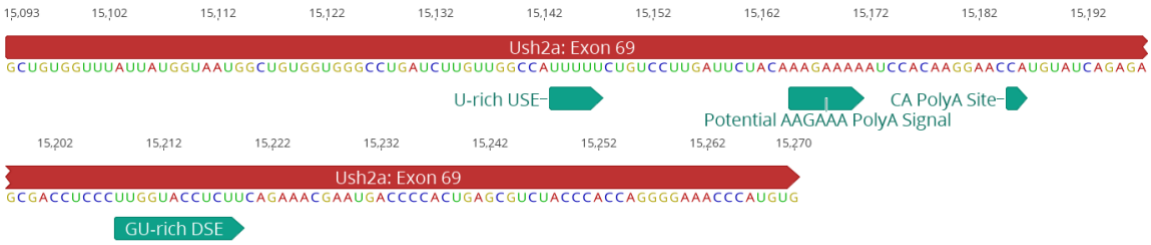


Figure 7-24 Potential alternative *Ush2a* polyA site
A potential non-canonical polyA signal (AAGAAA) lies in exon 69 at position c.15165 together with putative associated polyA sequence elements including a U-rich upstream element (USE), CA polyA site and GU-rich downstream element (DSE). Located 3,325nt downstream of the c.11840G>A PTC, this would generate a far larger than expected 3' UTR for a truncated transcript.

7.4.1.2 Natural History

This work initiated a natural history study of the *Ush2a*-W3947X mouse with a limited cohort of available mice. It is highly encouraging that a hearing loss phenotype was demonstrated, suggesting the lack of cochlear usherin expression has a functional effect, albeit with a smaller effect size in this data (ABR threshold 1.5× that of wildtype at 16kHz) compared to the *Ush2a*$^{-/-}$ mouse (ABR threshold 4× that of wildtype at 16kHz) in published data.[142]

Larger cohorts have now been bred and will be followed over time to establish the retinal phenotype. Published data from the *Ush2a*$^{-/-}$ model suggests retinal thinning on OCT and reductions in ERG amplitudes should be detectable beyond 12-months of age. Data obtained to 6-months of age indicates there is little early difference between the wildtype and W3947X homozygous mouse. While the 6-month ERG data indicated that the wildtype mouse has smaller dark-adapted b-wave amplitudes relative to the mutant, further replication experiments on a second cohort and at a later 12-month time point will establish whether this is a true (and unexpected) result or an artefact of experimental variability. Finally, retinal tissue has been taken at 3-monthly timepoints from 3- to 12-month animals and is awaiting histological analysis of retinal thickness over time.

7.4.2 AAV-dCas13-ADAR2$_{DD}$ RNA editors for repair of *Ush2a*

7.4.2.1 RNA editors are capable of *in vivo* repair in photoreceptors

Data from this chapter is the first demonstration of RNA editing using Cas13-based RNA editors *in vivo,* and the first demonstration of RNA editing in the retina. Through an iterative approach, a range of AAV-dCas13-ADAR constructs were tested, demonstrating up to 2% correction of the W3947X mutation in *Ush2a* using a photoreceptor-specific RK promoter to drive dPspCas13b-ADAR expression. Notably, this also correlated with a weak restoration of usherin expression in photoreceptors in injected eyes.

Comparing the approaches used generates several notable findings. Firstly, restoration of usherin expression was only seen in the RK-dPspCas13b injected eyes, where a mean correction of 2% was observed, and not with the other vectors with <1% correction, suggesting a minimum threshold of editing is required to detect expression. This level of restoration was still below the limit of detection of western blot, however this is not unexpected given whole retinal lysates were used for analysis. Usherin detection might be possible with mass spectrometry analysis for increased sensitivity. Secondly, the *in vivo* activity of the dPspCas13b and dCas13bt3 reflected the *in vitro* activity. This is promising for the development of new RNA editors, as it indicates that comparative *in vitro* screening remains of use. Thirdly, it is encouraging that RNA editing can be achieved with a photoreceptor-specific promoter, limiting the activity of the editor to the target cell of interest.

This study adds to a rapidly emerging literature demonstrating the potential of a suite of RNA editing technologies for correction of clinically-relevant mutations.[288] In primary cells site-directed RNA editing has been used for the correction of mutations in the Rett syndrome associated gene *Mecp2* in primary neurons using a BoxB-λN-ADAR system,[310] in *STAT1* in RPE cells and *IDUA* in patient-derived fibroblasts derived using endogenous systems for ADAR recruitment.[319,320] Finally, *in vivo* AAV-mediated delivery of MS2-MCP-ADAR and GluR2-ADAR tools to correct mutations in the muscular dystrophy gene *Dmd* and the ornithine

transcarbamylase deficiency gene *Otc*, resulted in low level RNA correction and protein restoration, similar to that seen in this study.[312]

7.4.2.2 Off-target effects and toxicity

In vitro data suggested that the ADAR2$_{DD}$(E488Q) is associated with widespread off-target events in the context of plasmid over-expression, however the off-target profile was unknown *in vivo*. The limited local off-target analysis conducted on the *Ush2a* amplicon here suggests a similar off-target pattern. Deamination events were concentrated in the dsRNA region formed by the gRNA, but also occurred sporadically across the transcript. Sporadic off-target events were more common in the dPspCas13b targeting compared to the non-targeting conditions suggesting that these were increased by ADAR recruitment, however they were also seen in the non-targeting conditions. Comparatively, the dCas13bt3 generated sporadic off-targets throughout the transcript in both the targeting and non-targeting conditions, suggesting a promiscuous editing profile and low target affinity.

Transcriptome-wide off-target analyses were not performed in this study—expensive analyses that would be considered if higher on-target editing could be achieved. Extrapolating from the local off-target events based on other published data,[299,300,304] it can be hypothesised that transcriptome wide off-target editing is occurring with the ADAR2$_{DD}$(E488Q) variant, and that these sites may increase with any increases in transgene expression.

Transgene toxicity was also investigated by *in vivo* OCT imaging. Evidence of toxicity was demonstrated by reductions in photoreceptor layer thickness in injected areas, and in some eyes, subretinal intrusions or deposits. A proportion of the photoreceptor/RPE toxicity may be attributed to the gRNA-GFP vector. GFP is very helpful as a marker or transduction and was included to potentially conduct cell sorting experiments. GFP overexpression is likely toxic to photoreceptors, however. Similar toxicity has been demonstrated following subretinal injection of AAV vectors expressing GFP under ubiquitous promoters at doses above 1e+9 gc/eye.[391]

The AAV8(Y733F)-U6-gRNA-CAG-GFP-WPRE was associated with greater retinal thinning at 1e+9 gc/eye than at 5e+8 gc/eye in this study. Reducing the dose to 5e+8 gc/eye reduced the toxicity observed in the dual vector RK-dPspCas13b pilot compared to the EFS-dPspCas13b pilot. This is consistent with recent findings that demonstrated a 1e+9 gc/eye dose of a AAV8(Y733F)-CAG-GFP-WPRE induces a greater retinal inflammatory response than an identical dose of a AAV8-CAG-hREP1-WPRE vector.[504]

A proportion of the toxicity is also likely due to dCas13b and/or $ADAR2_{DD}$(E488Q). Less toxicity was seen in the dCas13bt3 injected retinas, suggesting that this may be more attributable to the dCas13b used, however dCas13bt3-ADAR expression may be less than dPspCas13b-ADAR as it was not detected on immunohistochemistry. Katrekar et al. detected toxicity in animals systemically injected with AAV-delivered $ADAR_{DD}$(E488Q), hypothesising the hyperactive editor was associated with deleterious effects. In its active form PspCas13b is known to have collateral RNA cleavage and cause cell death *in vivo*, however this is not typically observed in the deactivated enzyme. The immunogenicity of expressing these bacterial-derived proteins in the retina is still to be investigated.

Finally, AAV-related toxicity is also a potential contributing factor. The tyrosine mutant AAV8-Y733F vector has been successfully used for widespread transduction for gene therapy rescue of IRD models at log-unit higher doses,[490,505] however the capsid also likely contributes to the retinal inflammatory response following subretinal injection.[504] Vectors were free from endotoxin.

Taken together, it is not possible from this data to determine the relative contributions of each component to the observed toxicity and off-target effects. These results indicate however, that substantial efforts need to be devoted to improving the safety of these editors for translation. Encouraging developments in this area have been the engineering of more specific $ADAR2_{DD}$ mutants such as E488Q/T375G[300] used in the previous chapter, as well as E620G and Q696L.[282] The more specific but less active E488Q/T375G mutant was not tested *in vivo*

as the on-target efficiency of the E488Q variant was not sufficient. Other innovations such as in-laid deaminase domains have also been shown to reduce off-target effects.[256,304] Other authors have used alternative Cas13 orthologues such as Cas13Rx which unlike Cas13b is more active in the nucleus,[285,300] and thus may have fewer off-target effects. Local off-targets might also be abrogated by introducing G-A mismatches within the spacer region at bystander adenosines subject to high off-target editing.[319] Systematic engineering to improve RNA binding affinities should enable deaminase expression to be reduced while retaining on-target efficiency, and reduce global off-targeting.

7.4.2.3 AAV-mediated expression of dCas13b-ADAR

Despite high *in vitro* editing rates, *in vivo* rates were much lower. Analysis of transgene expression indicates that this is likely due to low translation of the dCas13-ADAR transgene when delivered via AAV vectors. Attempts to address this iteratively through vector design were only moderately successful. It was surprising that despite driving strong transgene expression in plasmid overexpression, that the EFS vector did not drive strong expression in AAV transduction despite a high MOI (10,000) in HEK293T cells. Exchanging the EFS for the RK promoter did result in detectable low transgene expression by immunohistochemistry, and more specific expression in photoreceptors rather than horizontal cells. However, Cas13bt expression was not detected with an RK promoter even with a more sensitive 3×-FLAG tag and a more potent SV40 polyA signal in place of an sNRP1 polyA. Difficulties with obtaining high Cas13bt-ADAR expression and editing with an AAV2-EFS-Cas13bt1-ADAR vector have been noted by other authors.[282] Use of the FLAG tag for detection was also complicated by significant background staining particularly in the RPE, as noted by others,[506] and use of other tags such as the HA tag used in Chapter 4 may be more appropriate in future vectors.

While undoubtedly plasmid transfection produces massive overexpression, it is unclear why expression from AAV is so low. RT-PCR analyses clearly demonstrated the production of

full-length transcripts and preliminary qPCR analyses (not shown) indicated the transgene expression from EFS and RK promoters of the dPspCas13b constructs to have Ct values similar to those of *Gapdh*. It is therefore possible that there is an issue with the translation of dCas13-ADAR constructs, however this requires further investigation. Optimisation of codon usage, UTR sequences, RNA secondary structure and promoter elements may lead to translation efficiency improvements.

7.4.3 Translational considerations

This data has demonstrated a molecular correction of the *Ush2a*-W3947X mouse, however given the slow degeneration of this model it is obviously difficult to demonstrate a functional or structural rescue of the degeneration required for successful translation. Notably, the toxic effects of the vectors will need to be overcome before any rescue can been demonstrated.

Although low editing rates were achieved, high levels of correction may not be required for the treatment of IRDs. While the level of correction required for functional levels of usherin protein expression remains unknown, given the large size and stability of the usherin protein in the photoreceptor cilium, speculatively only a small amount of protein is required to improve or slow down degeneration. In two choroideremia patients, the presence of only approximately 5% of wildtype *REP1* transcripts due to a non-canonical splice site mutation was associated with a markedly slower degenerative phenotype, demonstrating high levels of wildtype transcript are not necessarily required to ameliorate the disease course.[507]

Finally, while the *Ush2a*-W3947X mouse is an excellent model for the evaluation of genetic therapeutics, it should be noted that while there is sequence and amino acid homology between the human and mouse sequences, the differences in the sequence surrounding the W3947X mutation to the W3955X human mutation mean that therapeutics developed in the *Ush2a*-W3947X mouse may not be immediately translatable. For instance, different gRNA sequences are required to target the human and mouse mutations. The implication of this sequence

difference can be further appreciated by the different off-target profiles of the human and mouse sequences in the *in vitro* data from the prior chapter. Therefore, following demonstration of *in vivo* efficacy, future therapeutics will need testing in other models such as retinal organoids.

7.4.4 Conclusions

This chapter has firstly presented a novel mouse model of USH2A-related retinopathy. While intended for characterisation of genetic therapeutics such as RNA and DNA base editing, further characterisation may also yield insights into novel disease mechanisms. Secondly, Correction of this model with AAV-delivered RNA editors demonstrated the therapeutic potential of these technologies, while also highlighting several key areas for further investigation, notably improving transgene expression, and reducing off-target editing and toxicity.

8

GENERAL DISCUSSION

The overall objective of this thesis was to investigate the use of gene editing therapeutic strategies for inherited retinal disease. This discussion describes the five aims successfully addressed in this thesis, and then considers these contributions in the context of the future development of genetic therapeutics for retinal disease.

8.1 Summary of thesis aims and outcomes

1. To investigate the effect of promoter orientation within an AAV-CRISPR vector

Using an all-in-one AAV-SaCas9-U6-gRNA vector, it was found that in transduced HEK293 cells, the reverse orientated U6-gRNA complex significantly reduced editing rates. This was associated with a reduction in *SaCas9* and gRNA transcript expression, as well as a reduction in SaCas9 protein expression. This work did not explore all possible orientations of guide to Cas9, the use of different promoters, whether this effects changes across different cell types, or explore this effect across different Cas orthologues. It does, however, highlight to the field the importance of vector optimisation, specifically the need to evaluate vectors when expressed as AAV, and not just as transfected plasmids. Given the conflicting reports in this area, it is likely promoter orientation may have differing effects within differing systems and should be tested for each application.

2. To characterise a novel class II Cas nuclease for in vivo editing of photoreceptors

An engineered CRISPR orthologue, CasX, was developed and packaged into an all-in-one AAV vector by Scribe Therapeutics. This was used to target EGFP expressed only in photoreceptors in an *Nrl.EGFP* mouse model to explore efficacy and toxicity of the molecule *in vivo*. Subretinal injection of the AAV.CasX produced robust dose-dependent editing and inactivation of EGFP in mature photoreceptors at both low (1E+9 gc/eye) and high (1E+10 gc/eye) doses measured by molecular, histological, and *in vivo* imaging techniques. Structural and functional assessments established 1E+9gc/eye as a non-toxic dose, with moderate retinal toxicity observed at the high dose. These data have been used to inform ongoing studies targeting disease-relevant genes for therapeutic gene editing. Future work in human-derived retinal organoids will further establish the genotoxicity of prospective therapeutic strategies.

3. To analyse 'base-editable' pathogenic variants causing IRD

Using data sets of pathogenic variants in IRD genes, a focused investigation was performed to identify frequent transition variants in large, common recessive genes that are not suited for gene augmentation but are potential candidates for therapeutic base editing. This established the landscape of editable mutations to direct approaches to retinal base editing with established base editors capable of correcting transition variants. This work also identified the W3955X *USH2A* mutation that was used to conceptualise the final two aims. As base editor engineering expands in scope to address all SNVs, further analyses can be conducted to explore non-transition variants in future.

4. To develop a CRISPR-based RNA editing to correct a common mutation in USH2A

Using dPspCas13b and dCas13bt orthologues fused to engineered variants of the human $ADAR2_{DD}$, these CRISPR-based RNA editing systems were evaluated and compared *in vitro* for editing of premature termination variants in *USH2A* and *Ush2a*. Due to the photoreceptor-specific expression of *USH2A*, a luciferase assay in HEK293T cells was successfully developed

to enable guide and construct screening for editing of the target sequence. Using these systems, highly active gRNA and Cas13 constructs were developed and then minimised to enable delivery within dual- and single-AAV vector approaches. Overall, the dPspCas13b system outperformed the dCas13bt approach using 50nt spacers. The hyperactive $ADAR_{DD}$(E488Q) mutant had the highest on-target editing, although had a higher off-target effects. Although the $ADAR_{DD}$(E488Q/T375G) mutant offered greater specificity, this resulted in a significant loss of on-target performance, in agreement with other studies.[300,304]

5. To develop a novel mouse model of USH2A amenable to base editing and test AAV-delivered RNA editing systems in this model

In collaboration with The Mary Lyon Centre (MRC Harwell Institute, UK), the *Ush2a*-W3947X mouse was successfully generated. Molecular characterisation established that the desired mutation resulted in the knockout of the full-length usherin protein in the retina and cochlea, and functional studies found this results in a hearing loss phenotype. A natural history study of the slow retinal degeneration predicted in this model is ongoing.

Three pilot studies were undertaken to evaluate AAV-dCas13-$ADAR2_{DD}$ vectors: dPspCas13b-del-$ADAR2_{DD}$(E488Q) with either an EFS or an RK promoter in a dual vector approach with the gRNA delivered on a separate vector, and dCas13bt3-$ADAR2_{DD}$(E488Q) in an all-in-one approach with the gRNA included in the same vector. Collectively these all demonstrated detectable on-target editing at the *Ush2a*-W3947X locus in homozygous mice following subretinal injection, the first *in vivo* use of dCas13-$ADAR2_{DD}$ RNA editors at time of writing. The best performing RK-dPspCas13b-del-$ADAR2_{DD}$(E488Q) dual vector approach edited the target base at approximately 2%, with low but detectable restoration of usherin expression. These studies demonstrated promise for RNA base editing. They highlighted the need to improve on-target editing rates and expression of the transgene from the vector, while also addressing concerns with off-target effects and toxicity in future studies.

8.2 Delivery of CRISPR-Cas with AAV Vectors for inherited retinal disease

AAV vectors remain the delivery method of choice for retinal gene therapy, due to strong photoreceptor and RPE transduction, and established clinical safety profile.[63] They are a leading option for the delivery of CRISPR-Cas transgenes for therapeutic gene editing for inherited retinal disease, and accordingly they have been used in the majority of *in vivo* pre-clinical studies, and the only clinical trial, of retinal gene editing to date.[433]

For a clinical AAV-approach, an all-in-one vector containing the entire genetic therapy system is ideal. Single vector approaches consistently demonstrate increased efficiency compared to a variety of dual vector systems.[508] They also reduce the likelihood of the creation of unwanted truncated protein by-products potentially generated by approaches that use techniques such as AAV genome recombination, or inteins to reconstitute protein fragments into a full-length product.[79, 254,508,509]

A primary focus of this thesis was therefore on developing all-in-one approaches to CRISPR gene therapy. When experimental work for this thesis began, SaCas9 was the main minimal orthologue capable of effective editing *in vivo*. This was used to make interesting observations on how to arrange vector elements for maximising AAV-mediated editing. Since then, the discovery of new orthologues has rapidly developed to now include a raft of minimal DNA targeting effectors such as CjCas9,[199] Nme2Cas9,[200] CasΦ,[203] and a variety of Cas12f nucleases,[204–206] with many more to be characterised. The work presented here with the minimal effector is CasX[207,385] has demonstrated the future potential for all-in-one therapies with these new orthologues. They provide more space in the vector to enable potent, stable and rapid transgene expression through use of more efficient regulatory elements. One of these all-in-one approaches using SaCas9 has moved into clinical trials for the treatment of CEP290-associated LCA;[224] the multitude of academic and commercial groups collaborating at speed on these new approaches promises more clinical trials for a broader range of targets soon.

For pre-clinical development, dual vector strategies do still offer some advantages. Notwithstanding the limitations discussed above, dual AAV approaches have demonstrated clinically useful on-target editing rates through separate delivery of the gRNA and Cas,[218] or the use of trans-splicing inteins to reconstitute large base editing constructs.[253,254,412] In the case of the RNA editing strategies presented here, the use of a separate vector with the gRNA and GFP was useful as a positive control for transduction, and to precisely identify injected areas on histology to examine for transgene expression and restoration of usherin expression.

8.2.1 Alternative perspectives on AAV delivery

One alternative that encoding the Cas effector without the guide in an AAV vector may enable, is the separate delivery of the gRNA using an alternative delivery method. Modified ASOs have demonstrated stability following intravitreal injection, and produced sustained restoration of visual function in select patients with CEP290-associated LCA.[91,426] If the gRNA could be similarly modified to enable stability with minimal immunogenicity and maintain interaction with the Cas and target, it may be possible to deliver the guide separately via intravitreal injection. If delivered with an AAV-encoded DNA editor, this would enable a one-time 'hit-and-run' approach to prevent ongoing editing after the therapeutic edit is installed. If delivered with the ongoing expression of an AAV-encoded RNA editor, this might enable titratable and reversible editing that could be dosed as required with repeated administration of the gRNA.

AAV vectors are only one armament in the delivery arsenal however and do have limitations. The safety of the sustained expression of a bacterial-derived nuclease in the retina remains unknown, although NHP pre-clinical and clinical trials have started to contribute answers to the questions around the immunogenicity and genotoxicity of these vectors.[224,225,266] One solution to this might be to use inactivating or inducible vectors that allow the transgene to be turned off following desired editing.[262, 265,510–515]

Non-viral approaches allow transient expression of much larger transgenes, again enabling a 'hit and run' gene editing suitable for clinical applications. As demonstrated in the widespread success of the lipid nanoparticle-based mRNA vaccines to generate immunogenic proteins to develop immunity to SARS-CoV-2 infection,[516] non-viral vectors can be a highly effective means of gene transfer. A successful example of this is the lipid-nanoparticle delivered mRNA Cas9 construct used to edit the *TTR* locus in hepatocytes of patients with transthyretin amyloidosis.[329] Direct delivery of Cas9 as a ribonucleoprotein pre-complexed with a gRNA is another possible strategy, and *in vivo* studies in the inner ear and brain using chemical transfection reagents and cell-penetrating peptide motifs to enable the RNP to cross the cell- and nuclear- membranes have demonstrated potential.[517,518] Pilot studies of subretinal injections of SpCas9 RNP[518] with and without transfection reagents conducted alongside this thesis found substantial retinal toxicity (unpublished).

The unique anatomical considerations of photoreceptors may prove challenging relative to other more readily transduced tissues such as the liver. Delivery to the nucleus requires traversing the multi-layered retina following intravitreal delivery, or the lipid-laden outer segment discs and the connecting cilium following subretinal delivery, all without causing toxicity from the delivery vehicle.[88]

8.3 Next generation gene editing therapeutics for inherited retinal disease

8.3.1 Protein discovery and engineering

Rapid developments in the field during this research have emphasised the importance of straddling the nexus between molecular biology and clinical application. This has been driven by the ever-expanding understanding of the CRISPR-Cas adaptive immune system, and how it might be harnessed as a molecular tool.[197,519] This has been accelerated by synthetic biology approaches that have generated innovative protein fusions such as base and prime-editing[245],

chimeric proteins such as the CasX used in this thesis and evolved mutants proteins such as more efficient and specific deaminases or Cas effectors.[381] Synthetic CRISPR systems consisting only of human derived protein domains have also been developed, pointing to one avenue for overcoming immunogenicity concerns.[318] Data driven approaches such as using machine learning techniques will enable better understanding of protein and RNA functions, interactions, and design, as well as for greater insights from large scale screening experiments.[520–522]

The collaboration with Scribe Therapeutics in this thesis was a productive demonstration of moving synthetic biology advances towards the clinic for IRDs. It is likely that protein discovery and engineering will be critical to addressing some of the safety and efficacy concerns raised in this data.

8.3.2 DNA editing without double stranded breaks

The first half of this thesis considered DNA editors that generate DSBs, which are likely to be particularly useful for diseases where robust gene inactivation is desired and the generation of complex mixed products of indels is acceptable. One example of this might be dominant RHO mutations treated with an allele-specific editing strategy.[218] DSBs are associated with a unwanted outcomes however, including large deletions and translocations,[408] insertions of AAV genomes,[324] and activation of p53.[523,524] Given this, in some cases of dominant IRDs, highly efficient epigenetic repression strategies may be preferable.[243,525] In recessive IRDs, as highlighted in Chapter 5, many pathogenic variants are small insertions, deletions and substitutions for which precision correction may be more appropriate.

At the outset of this work the first base editors had just been published. Recently, Beam Therapeutics (MA, USA) has demonstrated pre-clinical data for proof of principle therapies for *ex vivo* treatment haemotopoetic stem and progenitor cells for the treatment of sickle cell disease,[526] while Verve Therapeutics (MA, USA) has shown convincing reductions of PCSK9

levels in NHP models to reduce low-density lipoprotein levels to reduce the risk of atherosclerotic cardiovascular disease.[527] Both plan to move toward clinical trials which should soon provide more safety data on these approaches. Base editors have now demonstrated activity in the RPE,[255] have been delivered in dual AAV vectors with trans-splicing inteins to the retina,[254] and in a mouse model of progeria with remarkable results.[253] With construct engineering and minimisation, these would be a promising tool for inherited retinal disease to address some of the common variants identified in this thesis.

Although more recently developed, prime editing tools may also offer a therapeutic approach to mutations not amenable to base editing such as small indels.[257] One prominent example of this would be the two most common pathogenic variants in *USH2A* (c.2299delG; p.(Glu767fs), c.2276G>T; p.(Cys759Phe)) which account for approximately 35% of cases.[149,150,152] Given their proximity, a single prime editing approach that could treat both mutations could be developed. *In vivo* retinal prime editing has recently been demonstrated with low on-target editing;[271] further developments in this space are expected.

8.3.3 RNA Base editing

RNA base editing is the newest addition to a range of RNA targeting tools that include RNA interference, ASO therapies and CRISPR-mediated knockdown and splice modulation.[89, 272,285] Currently, RNA editing systems use $ADAR_{DD}$-mediated deamination to effect A>G edits which have broad applicability for the correction of point mutations, premature termination codons and modulation of splicing. The generation of further deaminases that can effect C>U edits has recently expanded this scope.[303,306]

This thesis has explored and compared Cas13 mediated RNA editing tools. These are one of several exogenous ADAR over-expression systems.[288] It remains to be seen which of these tools performs with better on- and off-target profiles, with benchmarking studies demonstrating conflicting results depending on the experimental setup and tools compared.[299,300,304]

Characterisation of new RNA-targeting orthologues, such as the recently published Cas13X, Cas13Y or Cas7-11 systems,[284,467] will likely yield more specific and compact effectors with higher binding affinity, to improve the efficacy of Cas13-mediated RNA editing.

Approaches using endogenous ADAR recruitment have been limited by approaches that need gRNA chemical modification, or very low editing rates due to low endogenous ADAR and the inability to use engineered ADAR mutants.[312,319] Recent work to engineer stabilised gRNAs delivered via AAV to recruit endogenous ADAR in the liver has demonstrated high *in vivo* editing rates,[528] and is now being commercialised by Shape Therapeutics (CA, USA). As ADAR appears to be only strongly expressed in RGCs in the retina,[529] this approach may require supplementation of exogenous ADAR in the AAV construct for photoreceptor editing, but this should be packageable in an AAV.

The clinical appeal of targeting the transcriptome is that unlike the genome, edits are not permanent. This is pertinent considering our increasing understanding of off-target effects. Due to the transience of RNA transcripts, any off-target effects are theoretically reversible if the system can be turned off. That said, even transient deleterious RNA edits in oncogenic genes may still pose a risk.[304] It can be argued that the strength of editing transient transcripts can also be considered a limitation: persistent editing requires persistent RNA editor expression much like in gene augmentation, and there are strong arguments for a one-and-done DNA edit.

Given AAV vectors generate persistent and safe expression of transgenes in the retina, it would seem appropriate to use AAV to persistently express an RNA rather than a DNA editor. In the event of DNA editors that could be transiently expressed with high specificity, these may be preferable. All options require further study.

Finally, ADAR deaminases are widely expressed throughout the human body and implicated in a range of physiological functions and alterations to ADAR function and expression are implicated in a range of pathologies.[530] Any strategy using ADAR overexpression will require careful assessment of the implications of this.

8.4 Models and therapeutics for Usher syndrome

The *Ush2a*-W3947X mouse adds an additional model for understanding of the pathogenesis and treatment of Usher syndrome and *USH2A*-related retinopathy. This model is now available for evaluating a range of further RNA and adenine base editor constructs, as well as PTC skipping therapies. It adds to the recently and preliminarily described *Ush2a*-ΔEx12 model designed for understanding the effect of in-frame exon 12 (mouse) or 13 (human) skipping therapeutics on usherin function,[163] and the more well described *Ush2a*$^{-/-}$ model[128] that has informed understanding of Usher syndrome pathophysiology to date. Together these advance the field towards therapeutics for patients, providing complementary means of evaluating a broad range of therapeutic approaches.

Ongoing evaluation of the *Ush2a*-W3947X model will determine whether the phenotype will recapitulate the *Ush2a*$^{-/-}$ mouse with age.[128] Regardless, any differences in phenotype between these models will be of interest to explore and generate further research questions that may shed light on unknown aspects of pathophysiology.

Ideally, a disease model would develop an early structural or functional phenotype to quickly evaluate therapeutics to correct it, but as with the *Ush2a*$^{-/-}$, this is not the case for the *Ush2a*-W3947X. Nevertheless, future gene editing therapeutic efficiency can be rapidly assessed through molecular methods, and then the best candidates tested over time once the natural history is known.

8.5 Progress in genetic therapeutics for inherited retinal disease

Immense progress has been made in genetic therapeutics for IRD since the first rescue of a retinal degeneration mouse model was shown in 1996 following subretinal injection of an adenoviral vector expressing PDE6β in the *rd* mouse.[531] The intervening 25 years have seen many incremental and monumental milestones, that are now culminating in patient treatments

—the first approval for a retinal gene therapy product, voretigene neparvovec (Luxturna) for patients with *RPE65* mutations, occurred while completing this degree.[40] A notable contribution of gene therapy trials beyond treatment of the specific IRD has been establishing the surgical techniques and clinical safety for subretinal AAV gene therapy, including for the fovea,[532] and new tools and knowledge to inform clinical end-points.[38]

Building on knowledge from years of gene therapy research, this thesis has considered new approaches, leveraging recent leaps in gene editing technologies. These have the potential to fill therapeutic gaps not easily filled by gene supplementation, such as for editing of large genes and in dominantly inherited disease. Questions have also recently been raised about durability and efficacy of gene therapy following translation to patients.[63] Voretigene neparvovec was eventually approved with a multi-luminance mobility test as a primary endpoint,[40] however results from two of three clinical trials for the product showed decline in visual improvements over time,[533,534] raising questions about whether the underlying degeneration could be halted. Recent pivotal results from trials for *CHM*[535] and *RPGR*[536] have also failed to meet their primary endpoints despite promising initial results.[41,43] These results may reflect the complexities in trial design, such as determining outcome measures and appropriate intervention periods. They nevertheless raise questions as to whether alternative approaches to gene supplantation may be more efficacious.[537] Perhaps gene editing of the endogenous locus or correction of the mutant transcript may provide a more physiologically relevant approach.

USH2A is an excellent target for these next generation therapeutics. It affects a substantial number of patients, the disease process provides a wide window for intervention (especially if identified via childhood hearing testing), and it predominantly affects rods in the peripheral retina to allow time to prevent the secondary cone degeneration and central visual loss which arguably has the greatest impact on patient's livelihoods.[103,114] Pre-clinical data from models such as the *Us2ha*-W3947X mouse should provide a strong base from which to translate these therapeutics. Ongoing studies to characterise the natural history of the disease,[110,538,539] and

results from clinical trials of the ASO QR-421a for mutations in exon 13 Gene (ProQR Therapeutics)[183] will assist in the design of future trials.

While monogenic retinal disease is an obvious first application for gene editing, treatment of diseases with more complex or multifactorial pathogenesis such as glaucoma and age-related macular degeneration (AMD) are further avenues to explore. Targeting of angiogenesis pathways with anti-vascular endothelial growth factor (VEGF) antibodies has been hugely clinically successful in neovascular AMD and proliferative diabetic retinopathy,[540] and numerous pre-clinical gene editing studies have attempted to generate a clinically relevant permanent manipulation of angiogenesis pathways to reduce the need for repeated intravitreal injections.[541] More recently a gene therapy cocktail of transcription factors was used to remarkably restore DNA methylation patterns and reverse optic nerve degeneration and vision loss in a mouse model of glaucoma.[542] These select examples of molecular therapies point towards conditions where genetic therapeutics might be used beyond rare diseases in the eye.

8.6 Societal considerations of gene editing

As gene editing progresses towards the clinic, an important consideration is how to use this technology responsibly and with social licence. Research into somatic gene editing for the treatment of disease, as discussed in this thesis, appears to have broad social and scientific support[543,544] and there is confidence in existing frameworks to regulate these technologies legally, democratically and with policy.[545–547] From a policy perspective, additional thought will now need to be given to how best to identify patients, conduct trials and implement therapies within a healthcare system,[548] and how to ensure these are accessible to patients given their predicted high costs.[549]

Heritable genome editing of the human germline generates a broader range of opinions,[543,544,550,551] a more complex ethical discussion beyond the remit of this thesis, and has been subject to several global summits and reports.[552–554] Consideration of safety and efficacy,

ethical principles, governance frameworks, public education and democratic engagement should be key aspects in future decisions around what situations, if any, the use of genome engineering in human reproduction should be considered.[555,556]

8.7 Conclusions

In summary, the five presented aims of this thesis were achieved. AAV-mediated genome editing strategies using DNA and RNA editors were explored *in vitro* and *in vivo*, a new mouse model of Usher syndrome was generated, and a computational analysis of IRD variants amenable to base editing correction was performed. Valuable insights into the successes and limitations of each technique were highlighted and have generated pilot data from which to base further research.

Results from this work have formed the basis for the contribution to peer reviewed publications, including three review articles,[243, 288,537] a book chapter,[433] two original research articles from data presented within this thesis[472,557] and a further two original research articles on data not able to be included in this thesis.[507,558] Further manuscripts are in preparation.

This thesis was undertaken in a rapidly evolving era of gene editing to which these data contribute. Returning now to clinical medicine, the experience and knowledge gained from this research will enhance my ability to care for future patients receiving gene editing treatments for inherited retinal diseases that I expect are just over the horizon.

References

1. Sung CH, Chuang JZ. The cell biology of vision. *J Cell Biol*. 2010;190:953–63. DOI: 10.1083/jcb.201006020.
2. Gross AK, Wensel TG. Biochemical Cascade of Phototransduction. In: Levin LA, ed. Adler's Physiol. eye. 11th ed.Edinburgh: Saunders/Elsevier; 2011;394–410.
3. Staurenghi G, Sadda S, Chakravarthy U, et al. Proposed lexicon for anatomic landmarks in normal posterior segment spectral-domain optical coherence tomography: The IN•OCT consensus. *Ophthalmology*. 2014;121:1572–8. DOI: 10.1016/j.ophtha.2014.02.023.
4. Nachury M V., Seeley ES, Jin H. Trafficking to the Ciliary Membrane: How to Get Across the Periciliary Diffusion Barrier? *Annu Rev Cell Dev Biol*. 2010;26:59–87. DOI: 10.1146/annurev.cellbio.042308.113337.
5. May-Simera H, Nagel-Wolfrum K, Wolfrum U. Cilia - The sensory antennae in the eye. *Prog Retin Eye Res*. 2017;60:144–80. DOI: 10.1016/j.preteyeres.2017.05.001.
6. Pearring JN, Salinas RY, Baker SA, et al. Protein sorting, targeting and trafficking in photoreceptor cells. *Prog Retin Eye Res*. 2013;36:24–51. DOI: 10.1016/j.preteyeres.2013.03.002.
7. Yang J, Liu X, Yue G, et al. Rootletin, a novel coiled-coil protein, is a structural component of the ciliary rootlet. *J Cell Biol*. 2002;159:431–40. DOI: 10.1083/jcb.200207153.
8. Curcio CA, Sloan KR, Kalina RE, et al. Human photoreceptor topography. *J Comp Neurol*. 1990;292:497–523. DOI: 10.1002/cne.902920402.
9. Peichl L. Diversity of mammalian photoreceptor properties: Adaptations to habitat and lifestyle? *Anat Rec Part A Discov Mol Cell Evol Biol*. 2005;287A:1001–12. DOI: 10.1002/ar.a.20262.
10. Volland S, Esteve-Rudd J, Hoo J, et al. A Comparison of Some Organizational Characteristics of the Mouse Central Retina and the Human Macula. *PLoS One*. 2015;10:e0125631. DOI: 10.1371/journal.pone.0125631.
11. Ortín-Martínez A, Nadal-Nicolás FM, Jiménez-López M, et al. Number and Distribution of Mouse Retinal Cone Photoreceptors: Differences between an Albino (Swiss) and a Pigmented (C57/BL6) Strain. *PLoS One*. 2014;9:e102392. DOI: 10.1371/journal.pone.0102392.

12. Nadal-Nicolás FM, Kunze VP, Ball JM, et al. True S-cones are concentrated in the ventral mouse retina and wired for color detection in the upper visual field. *Elife*. 2020;9:196. DOI: 10.7554/eLife.56840.
13. Broadgate S, Yu J, Downes SM, et al. Unravelling the genetics of inherited retinal dystrophies: Past, present and future. *Prog Retin Eye Res*. 2017;59:53–96. DOI: 10.1016/j.preteyeres.2017.03.003.
14. Sahel JA, Marazova K, Audo I. Clinical characteristics and current therapies for inherited retinal degenerations. *Cold Spring Harb Perspect Med*. 2015;5:1–26. DOI: 10.1101/cshperspect.a017111.
15. Berger W, Kloeckener-Gruissem B, Neidhardt J. The molecular basis of human retinal and vitreoretinal diseases. *Prog Retin Eye Res*. 2010;29:335–75. DOI: 10.1016/j.preteyeres.2010.03.004.
16. Liew G, Michaelides M, Bunce C. A comparison of the causes of blindness certifications in England and Wales in working age adults (16–64 years), 1999–2000 with 2009–2010. *BMJ Open*. 2014;4:e004015. DOI: 10.1136/bmjopen-2013-004015.
17. Heath Jeffery RC, Mukhtar SA, McAllister IL, et al. Inherited retinal diseases are the most common cause of blindness in the working-age population in Australia. *Ophthalmic Genet*. 2021;42:431–9. DOI: 10.1080/13816810.2021.1913610.
18. Rahman F, Zekite A, Bunce C, et al. Recent trends in vision impairment certifications in England and Wales. *Eye*. 2020;34:1271–8. DOI: 10.1038/s41433-020-0864-6.
19. Campochiaro PA, Mir TA. The mechanism of cone cell death in Retinitis Pigmentosa. *Prog Retin Eye Res*. 2018;62:24–37. DOI: 10.1016/j.preteyeres.2017.08.004.
20. Hartong DT, Berson EL, Dryja TP. Retinitis pigmentosa. *Lancet*. 2006;368:1795–809.
21. Gill JS, Georgiou M, Kalitzeos A, et al. Progressive cone and cone-rod dystrophies: clinical features, molecular genetics and prospects for therapy. *Br J Ophthalmol*. 2019;103:711–20. DOI: 10.1136/bjophthalmol-2018-313278.
22. Daiger SP, Bowne SJ, Sullivan LS. Perspective on genes and mutations causing retinitis pigmentosa. *Arch Ophthalmol*. 2007;125:151–8. DOI: 10.1001/archopht.125.2.151.
23. Tatour Y, Ben-Yosef T. Syndromic inherited retinal diseases: genetic, clinical and diagnostic aspects. *Diagnostics*. 2020;10. DOI: 10.3390/diagnostics10100779.
24. Thiadens AAHJ, Roosing S, Collin RWJ, et al. Comprehensive Analysis of the Achromatopsia Genes CNGA3 and CNGB3 in Progressive Cone Dystrophy. *Ophthalmology*. 2010;117:825-830.e1. DOI: 10.1016/j.ophtha.2009.09.008.
25. Boon CJF, Klevering BJ, Leroy BP, et al. The spectrum of ocular phenotypes caused

by mutations in the BEST1 gene. *Prog Retin Eye Res*. 2009;28:187–205. DOI: 10.1016/j.preteyeres.2009.04.002.

26. Yang J, Wang L, Song H, et al. Current understanding of usher syndrome type II. *Front Biosci*. 2012;17:1165. DOI: 10.2741/3979.
27. Lee K, Berg JS, Milko L, et al. High Diagnostic Yield of Whole Exome Sequencing in Participants With Retinal Dystrophies in a Clinical Ophthalmology Setting. *Am J Ophthalmol*. 2015;160:354-363.e9. DOI: 10.1016/j.ajo.2015.04.026.
28. Ellingford JM, Barton S, Bhaskar S, et al. Molecular findings from 537 individuals with inherited retinal disease. *J Med Genet*. 2016;53:761–7. DOI: 10.1136/jmedgenet-2016-103837.
29. Shah M, Shanks M, Packham E, et al. Next generation sequencing using phenotype-based panels for genetic testing in inherited retinal diseases. *Ophthalmic Genet*. 2020;41:331–7. DOI: 10.1080/13816810.2020.1778736.
30. Weisschuh N, Mayer AK, Strom TM, et al. Mutation Detection in Patients with Retinal Dystrophies Using Targeted Next Generation Sequencing. *PLoS One*. 2016;11:e0145951. DOI: 10.1371/journal.pone.0145951.
31. Pontikos N, Arno G, Jurkute N, et al. Genetic basis of inherited retinal disease in a molecularly characterised cohort of over 3000 families from the United Kingdom. *Ophthalmology*. 2020. DOI: 10.1016/j.ophtha.2020.04.008.
32. Paskowitz DM. Light and inherited retinal degeneration. *Br J Ophthalmol*. 2006;90:1060–6. DOI: 10.1136/bjo.2006.097436.
33. Pardue MT, Allen RS. Neuroprotective strategies for retinal disease. *Prog Retin Eye Res*. 2018;65:50–76. DOI: 10.1016/j.preteyeres.2018.02.002.
34. West EL, Ribeiro J, Ali RR. Development of stem cell therapies for retinal degeneration. *Cold Spring Harb Perspect Biol*. 2020;12:1–23. DOI: 10.1101/cshperspect.a035683.
35. Wang Y, Tang Z, Gu P. Stem/progenitor cell-based transplantation for retinal degeneration: a review of clinical trials. *Cell Death Dis*. 2020;11. DOI: 10.1038/s41419-020-02955-3.
36. Mills JO, Jalil A, Stanga PE. Electronic retinal implants and artificial vision: Journey and present. *Eye*. 2017;31:1383–98. DOI: 10.1038/eye.2017.65.
37. Lee JH, Wang J-H, Chen J, et al. Gene therapy for visual loss: Opportunities and concerns. *Prog Retin Eye Res*. 2018. DOI: 10.1016/j.preteyeres.2018.08.003.
38. Jolly JK, Bridge H, MacLaren RE. Outcome measures used in ocular gene therapy

trials: A scoping review of current practice. *Front Pharmacol*. 2019;10:1–7. DOI: 10.3389/fphar.2019.01076.

39. Ramlogan-Steel CA, Murali A, Andrzejewski S, et al. Gene therapy and the adeno associated virus in the treatment of genetic and acquired ophthalmic diseases in humans: trials, future directions and safety considerations. *Clin Experiment Ophthalmol*. 2018. DOI: 10.1111/ceo.13416.
40. Russell S, Bennett J, Wellman JA, et al. Efficacy and safety of voretigene neparvovec (AAV2-hRPE65v2) in patients with RPE65 -mediated inherited retinal dystrophy: a randomised, controlled, open-label, phase 3 trial. *Lancet*. 2017;390:849–60. DOI: 10.1016/S0140-6736(17)31868-8.
41. Xue K, Jolly JK, Barnard AR, et al. Beneficial effects on vision in patients undergoing retinal gene therapy for choroideremia. *Nat Med*. 2018;24:1507–12. DOI: 10.1038/s41591-018-0185-5.
42. Spark Therapeutics. Identifier NCT02341807: Safety and Dose Escalation Study of AAV2-hCHM in Subjects With CHM (Choroideremia) Gene Mutations. *ClinicalTrialsGov*. 2015. https://clinicaltrials.gov/ct2/show/NCT02341807 (accessed May 22, 2021).
43. Cehajic-Kapetanovic J, Xue K, Martinez-Fernandez de la Camara C, et al. Initial results from a first-in-human gene therapy trial on X-linked retinitis pigmentosa caused by mutations in RPGR. *Nat Med*. 2020. DOI: 10.1038/s41591-020-0763-1.
44. Applied Genetic Technologies Corp. Identifier NCT03316560: Safety and Efficacy of rAAV2tYF-GRK1-RPGR in Subjects With X-linked Retinitis Pigmentosa Caused by RPGR Mutations. *ClinicalTrialsGov*. 2017. https://clinicaltrials.gov/ct2/show/NCT03316560 (accessed May 22, 2021).
45. Meira GTx UK II Ltd. Identifier NCT03252847: Gene Therapy for X-linked Retinitis Pigmentosa (XLRP) Retinitis Pigmentosa GTPase Regulator (RPGR). *ClinicalTrialsGov*. 2017. https://clinicaltrials.gov/ct2/show/NCT03252847 (accessed May 22, 2021).
46. 4D Molecular Therapeutics. Identifier NCT04517149: 4D-125 in Patients With X-Linked Retinitis Pigmentosa (XLRP). *ClinicalTrialsGov*. 2020.
47. Ghazi NG, Abboud EB, Nowilaty SR, et al. Treatment of retinitis pigmentosa due to MERTK mutations by ocular subretinal injection of adeno-associated virus gene vector: results of a phase I trial. *Hum Genet*. 2016;135:327–43. DOI: 10.1007/s00439-016-1637-y.
48. STZ eyetrial. Identifier NCT04611503: PDE6A Gene Therapy for Retinitis

Pigmentosa (Pigment). *ClinicalTrialsGov*. 2020. https://clinicaltrials.gov/ct2/show/NCT04611503 (accessed May 22, 2021).

49. Horama S.A. Identifier NCT03328130: Safety and Efficacy Study in Patients With Retinitis Pigmentosa Due to Mutations in PDE6B Gene. *ClinicalTrialsGov*. 2017. https://clinicaltrials.gov/ct2/show/NCT03328130 (accessed May 22, 2021).
50. Novartis Pharmaceuticals. Identifier NCT03374657: A First-in-human, Proof of Concept Study of CPK850 in Patients With RLBP1 Retinitis Pigmentosa. *ClinicalTrialsGov*. 2017. https://clinicaltrials.gov/ct2/show/NCT03374657 (accessed May 22, 2021).
51. Cukras C, Wiley HE, Jeffrey BG, et al. Retinal AAV8-RS1 Gene Therapy for X-Linked Retinoschisis: Initial Findings from a Phase I/IIa Trial by Intravitreal Delivery. *Mol Ther*. 2018;26:2282–94. DOI: 10.1016/j.ymthe.2018.05.025.
52. Applied Genetic Technologies Corp. Identifier NCT02416622: Safety and Efficacy of rAAV-hRS1 in Patients With X-linked Retinoschisis (XLRS). *ClinicalTrialsGov*. 2015. https://clinicaltrials.gov/ct2/show/NCT02416622 (accessed May 22, 2021).
53. Beijing Tongren Hospital. Identifier NCT04722107: The Gene Replacement Therapy by rAAV2/8-hCYP4V2. *ClinicalTrialsGov*. 2021. https://clinicaltrials.gov/show/NCT04722107 (accessed May 22, 2021).
54. Applied Genetic Technologies Corp. Identifier NCT02935517: Safety and Efficacy Trial of AAV Gene Therapy in Patients With CNGA3 Achromatopsia. *ClinicalTrialsGov*. 2016. https://clinicaltrials.gov/ct2/show/NCT02935517 (accessed May 22, 2021).
55. Fischer MD, Michalakis S, Wilhelm B, et al. Safety and Vision Outcomes of Subretinal Gene Therapy Targeting Cone Photoreceptors in Achromatopsia. *JAMA Ophthalmol*. 2020;138:643. DOI: 10.1001/jamaophthalmol.2020.1032.
56. Meira GTx UK II Ltd. Identifier NCT03001310: Gene Therapy for Achromatopsia (CNGB3) (CNGB3). *ClinicalTrialsGov*. 2016. https://clinicaltrials.gov/ct2/show/NCT03001310 (accessed May 22, 2021).
57. Applied Genetic Technologies Corp. Identifier NCT02599922: Safety and Efficacy Trial of AAV Gene Therapy in Patients With CNGB3 Achromatopsia. *ClinicalTrialsGov*. 2015. https://clinicaltrials.gov/ct2/show/NCT02599922 (accessed May 22, 2021).
58. Li C, Samulski RJ. Engineering adeno-associated virus vectors for gene therapy. *Nat Rev Genet*. 2020;21:255–72. DOI: 10.1038/s41576-019-0205-4.

59. Wilmott P, Lisowski L, Alexander IE, et al. A User's Guide to the Inverted Terminal Repeats of Adeno-Associated Virus. *Hum Gene Ther Methods*. 2019;30:206–13. DOI: 10.1089/hgtb.2019.276.

60. Trapani I, Puppo A, Auricchio A. Vector platforms for gene therapy of inherited retinopathies. *Prog Retin Eye Res*. 2014;43:108–28. DOI: 10.1016/j.preteyeres.2014.08.001.

61. Lee JH, Wang JH, Chen J, et al. Gene therapy for visual loss: Opportunities and concerns. *Prog Retin Eye Res*. 2019;68:31–53. DOI: 10.1016/j.preteyeres.2018.08.003.

62. Sonntag F, Kother K, Schmidt K, et al. The Assembly-Activating Protein Promotes Capsid Assembly of Different Adeno-Associated Virus Serotypes. *J Virol*. 2011;85:12686–97. DOI: 10.1128/jvi.05359-11.

63. Trapani I, Auricchio A. Seeing the Light after 25 Years of Retinal Gene Therapy. *Trends Mol Med*. 2018;24:669–81. DOI: 10.1016/j.molmed.2018.06.006.

64. Duan D, Sharma P, Yang J, et al. Circular intermediates of recombinant adeno-associated virus have defined structural characteristics responsible for long-term episomal persistence in muscle tissue. *J Virol*. 1998;72:8568–77. DOI: 10.1128/JVI.72.11.8568-8577.1998.

65. Wang D, Tai PWL, Gao G. Adeno-associated virus vector as a platform for gene therapy delivery. *Nat Rev Drug Discov*. 2019;18:358–78. DOI: 10.1038/s41573-019-0012-9.

66. Deyle DR, Russell DW. Adeno-associated virus vector integration. *Curr Opin Mol Ther*. 2009;11:442–7.

67. Suzuki M, Bertin TK, Rogers GL, et al. Differential Type I Interferon-dependent Transgene Silencing of Helper-dependent Adenoviral vs. Adeno-associated Viral Vectors In Vivo. *Mol Ther*. 2013;21:796–805. DOI: 10.1038/mt.2012.277.

68. Vandendriessche T, Thorrez L, Acosta-Sanchez A, et al. Efficacy and safety of adeno-associated viral vectors based on serotype 8 and 9 vs. lentiviral vectors for hemophilia B gene therapy. *J Thromb Haemost*. 2007;5:16–24. DOI: 10.1111/j.1538-7836.2006.02220.x.

69. Zaiss A-K, Liu Q, Bowen GP, et al. Differential Activation of Innate Immune Responses by Adenovirus and Adeno-Associated Virus Vectors. *J Virol*. 2002;76:4580–90. DOI: 10.1128/JVI.76.9.4580-4590.2002.

70. Chandler LC, Yusuf IH, McClements ME, et al. Immunomodulatory Effects of Hydroxychloroquine and Chloroquine in Viral Infections and Their Potential

Application in Retinal Gene Therapy. *Int J Mol Sci*. 2020;21. DOI: 10.3390/ijms21144972.

71. Chan YK, Dick AD, Hall SM, et al. Inflammation in Viral Vector-Mediated Ocular Gene Therapy: A Review and Report From a Workshop Hosted by the Foundation Fighting Blindness, 9/2020. *Transl Vis Sci Technol*. 2021;10:3. DOI: 10.1167/tvst.10.4.3.
72. Shirley JL, de Jong YP, Terhorst C, et al. Immune Responses to Viral Gene Therapy Vectors. *Mol Ther*. 2020;28:709–22. DOI: 10.1016/j.ymthe.2020.01.001.
73. Rabinowitz J, Chan YK, Samulski RJ. Adeno-associated Virus (AAV) versus immune response. *Viruses*. 2019;11:1–11. DOI: 10.3390/v11020102.
74. Dong B, Nakai H, Xiao W. Characterization of genome integrity for oversized recombinant AAV vector. *Mol Ther*. 2010;18:87–92. DOI: 10.1038/mt.2009.258.
75. Krooss SA, Dai Z, Schmidt F, et al. Ex Vivo/In vivo Gene Editing in Hepatocytes Using "All-in-One" CRISPR-Adeno-Associated Virus Vectors with a Self-Linearizing Repair Template. *IScience*. 2020;23. DOI: 10.1016/j.isci.2019.100764.
76. Wu Z, Yang H, Colosi P. Effect of genome size on AAV vector packaging. *Mol Ther*. 2010;18:80–6. DOI: 10.1038/mt.2009.255.
77. King JA, Dubielzig R, Grimm D, et al. DNA helicase-mediated packaging of adeno-associated virus type 2 genomes into preformed capsids. *EMBO J*. 2001;20:3282–91. DOI: 10.1093/emboj/20.12.3282.
78. McClements ME, Barnard AR, Singh MS, et al. An AAV Dual Vector Strategy Ameliorates the Stargardt Phenotype in Adult Abca4 −/− Mice. *Hum Gene Ther*. 2019;30:590–600. DOI: 10.1089/hum.2018.156.
79. McClements ME, Maclaren RE. Adeno-associated virus (AAV) dual vector strategies for gene therapy encoding large transgenes. *Yale J Biol Med*. 2017;90:611–23.
80. Cavalieri V, Baiamonte E, Iacono M Lo. Non-primate lentiviral vectors and their applications in gene therapy for ocular disorders. *Viruses*. 2018;10. DOI: 10.3390/v10060316.
81. Sanofi. Identifier NCT01367444: Phase I/IIA Study of SAR422459 in Participants With Stargardt's Macular Degeneration. *ClinicalTrialsGov*. 2011. https://clinicaltrials.gov/ct2/show/NCT01367444 (accessed June 9, 2021).
82. Sanofi. Identifier NCT02065011: A Study to Determine the Long-Term Safety, Tolerability and Biological Activity of SAR421869 in Patients With Usher Syndrome Type 1B. *ClinicalTrialsGov*. 2014. https://clinicaltrials.gov/ct2/show/NCT02065011 (accessed May 22, 2021).

83. Wilson DJ, Sahel JA, Weleber RG, et al. One Year Results of a Phase I/IIa Study of SAR422459 in Patients with Stargardt Macular Degeneration (SMD). *Invest Ophthalmol Vis Sci*. 2017;58:3385.

84. Puppo A, Cesi G, Marrocco E, et al. Retinal transduction profiles by high-capacity viral vectors. *Gene Ther*. 2014;21:855–65. DOI: 10.1038/gt.2014.57.

85. Nayak S, Herzog RW. Progress and prospects: Immune responses to viral vectors. *Gene Ther*. 2010;17:295–304. DOI: 10.1038/gt.2009.148.

86. Matet A, Kostic C, Bemelmans AP, et al. Evaluation of tolerance to lentiviral LV-RPE65 gene therapy vector after subretinal delivery in non-human primates. *Transl Res*. 2017;188:40-57.e4. DOI: 10.1016/j.trsl.2017.06.012.

87. Slivac I, Guay D, Mangion M, et al. Non-viral nucleic acid delivery methods. *Expert Opin Biol Ther*. 2017;17:105–18. DOI: 10.1080/14712598.2017.1248941.

88. Charbel Issa P, MacLaren RE. Non-viral retinal gene therapy: a review. *Clin Experiment Ophthalmol*. n.d.;40:39–47. DOI: 10.1111/j.1442-9071.2011.02649.x.

89. Xue K, MacLaren RE. Antisense oligonucleotide therapeutics in clinical trials for the treatment of inherited retinal diseases. *Expert Opin Investig Drugs*. 2020;00:1–8. DOI: 10.1080/13543784.2020.1804853.

90. Dulla K, Slijkerman R, van Diepen HC, et al. Antisense oligonucleotide-based treatment of retinitis pigmentosa caused by USH2A exon 13 mutations. *Mol Ther*. 2021:121398. DOI: 10.1016/j.ymthe.2021.04.024.

91. Cideciyan A V, Jacobson SG, Drack A V, et al. Effect of an intravitreal antisense oligonucleotide on vision in Leber congenital amaurosis due to a photoreceptor cilium defect. *Nat Med*. 2019;25:225–8. DOI: 10.1038/s41591-018-0295-0.

92. ProQR Therapeutics. Identifier NCT04123626: A Study to Evaluate the Safety and Tolerability of QR-1123 in Subjects With Autosomal Dominant Retinitis Pigmentosa Due to the P23H Mutation in the RHO Gene (AURORA). *ClinicalTrialsGov*. 2019. https://clinicaltrials.gov/ct2/show/NCT04123626 (accessed May 22, 2021).

93. Vázquez-Domínguez I, Garanto A, Collin RWJ. Molecular Therapies for Inherited Retinal Diseases—Current Standing, Opportunities and Challenges. *Genes (Basel)*. 2019;10:654. DOI: 10.3390/genes10090654.

94. Nagel-Wolfrum K, Möller F, Penner I, et al. Translational read-through as an alternative approach for ocular gene therapy of retinal dystrophies caused by in-frame nonsense mutations. *Vis Neurosci*. 2014;31:309–16. DOI: 10.1017/S0952523814000194.

95. Stone EM, Andorf JL, Whitmore SS, et al. Clinically Focused Molecular Investigation of 1000 Consecutive Families with Inherited Retinal Disease. *Ophthalmology*. 2017;124:1314–31. DOI: 10.1016/j.ophtha.2017.04.008.

96. Sharon D, Ben-Yosef T, Goldenberg-Cohen N, et al. A nationwide genetic analysis of inherited retinal diseases in Israel as assessed by the Israeli inherited retinal disease consortium (IIRDC). *Hum Mutat*. 2020;41:140–9. DOI: 10.1002/humu.23903.

97. Verbakel SK, van Huet RAC, Boon CJF, et al. Non-syndromic retinitis pigmentosa. *Prog Retin Eye Res*. 2018;66:157–86. DOI: 10.1016/j.preteyeres.2018.03.005.

98. Graefe V, A. Exceptionelles verrhalten des gesichtsfeldes bei pigmentenartung der netzhaut. *Von Graefe's Arch Ophtlalmol*. 1858;4:250–3.

99. Usher CH. On the inheritance of retinitis pigmentosa, with notes of cases. *R L Ophthalmol Hosp Rep*. 1914;19:130–236.

100. Boughman JA, Vernon M, Shaver KA. Usher syndrome: Definition and estimate of prevalence from two high-risk populations. *J Chronic Dis*. 1983;36:595–603. DOI: 10.1016/0021-9681(83)90147-9.

101. Kimberling WJ, Hildebrand MS, Shearer AE, et al. Frequency of Usher syndrome in two pediatric populations: Implications for genetic screening of deaf and hard of hearing children. *Genet Med*. 2010;12:512–6. DOI: 10.1097/GIM.0b013e3181e5afb8.

102. Stabej PLQ, Saihan Z, Rangesh N, et al. Comprehensive sequence analysis of nine Usher syndrome genes in the UK National Collaborative Usher study. *J Med Genet*. 2012;49:27–36. DOI: 10.1136/jmedgenet-2011-100468.

103. Toms M, Pagarkar W, Moosajee M. Usher syndrome: clinical features, molecular genetics and advancing therapeutics. *Ther Adv Ophthalmol*. 2020;12. DOI: 10.1177/2515841420952194.

104. Abadie C, Blanchet C, Baux D, et al. Audiological findings in 100 USH2 patients. *Clin Genet*. 2012;82:433–8. DOI: 10.1111/j.1399-0004.2011.01772.x.

105. Blanco-Kelly F, Jaijo T, Aller E, et al. Clinical aspects of usher syndrome and the USH2A gene in a cohort of 433 patients. *JAMA Ophthalmol*. 2015;133:157–64. DOI: 10.1001/jamaophthalmol.2014.4498.

106. Reisser CFV, Kimberling WJ, Otterstedde CR. Hearing loss in Usher syndrome type II is nonprogressive. *Ann Otol Rhinol Laryngol*. 2002;111:1108–11. DOI: 10.1177/000348940211101208.

107. Pakarinen L, Karjalainen S, Simola KOJ, et al. Usher's syndrome type 3 in Finland. *Laryngoscope*. 1995;105:613–7. DOI: 10.1288/00005537-199506000-00010.

108. Ness SL, Ben-Yosef T, Bar-Lev A, et al. Genetic homogeneity and phenotypic variability among Ashkenazi Jews with Usher syndrome type III. *J Med Genet*. 2003;40:767–72. DOI: 10.1136/jmg.40.10.767.

109. Mathur P, Yang J. Usher syndrome: Hearing loss, retinal degeneration and associated abnormalities. *Biochim Biophys Acta - Mol Basis Dis*. 2015;1852:406–20. DOI: 10.1016/j.bbadis.2014.11.020.

110. Birch DG, Cheng P, Duncan JL, et al. The RUSH2A Study: Best-Corrected Visual Acuity, Full-Field Electroretinography Amplitudes, and Full-Field Stimulus Thresholds at Baseline. *Transl Vis Sci Technol*. 2020;9:9. DOI: 10.1167/tvst.9.11.9.

111. Sandberg MA, Rosner B, Weigel-DiFranco C, et al. Disease course in patients with autosomal recessive retinitis pigmentosa due to the USH2A gene. *Investig Ophthalmol Vis Sci*. 2008;49:5532–9. DOI: 10.1167/iovs.08-2009.

112. Calzetti G, Levy RA, Cideciyan A V., et al. Efficacy Outcome Measures for Clinical Trials of USH2A Caused by the Common c.2299delG Mutation. *Am J Ophthalmol*. 2018;193:114–29. DOI: 10.1016/j.ajo.2018.06.017.

113. Lima LH, Cella W, Greenstein VC, et al. Structural assessment of hyperautofluorescent ring in patients with retinitis pigmentosa. *Retina*. 2009;29:1025–31. DOI: 10.1097/IAE.0b013e3181ac2418.

114. Toms M, Dubis AM, De Vrieze E, et al. Clinical and preclinical therapeutic outcome metrics for USH2A-related disease. *Hum Mol Genet*. 2020;29:1882–99. DOI: 10.1093/HMG/DDAA004.

115. Eudy JD, Yao S, Weston MD, et al. Isolation of a gene encoding a novel member of the nuclear receptor superfamily from the critical region of usher syndrome type IIa at 1q41. *Genomics*. 1998;50:382–4. DOI: 10.1006/geno.1998.5345.

116. Eudy JD, Weston MD, Yao SF, et al. Mutation of a gene encoding a protein with extracellular matrix motifs in Usher syndrome type IIa. *Science*. 1998;280:1753–7. DOI: 10.1126/science.280.5370.1753.

117. van Wijk E, Pennings RJE, te Brinke H, et al. Identification of 51 Novel Exons of the Usher Syndrome Type 2A (USH2A) Gene That Encode Multiple Conserved Functional Domains and That Are Mutated in Patients with Usher Syndrome Type II. *Am J Hum Genet*. 2004;74:738–44. DOI: 10.1086/383096.

118. Pearsall N, Bhattacharya G, Wisecarver J, et al. Usherin expression is highly conserved in mouse and human tissues. *Hear Res*. 2002;174:55–63. DOI: 10.1016/S0378-5955(02)00635-4.

119. Bhattacharya G, Miller C, Kimberling WJ, et al. Localization and expression of usherin: A novel basement membrane protein defective in people with Usher's syndrome type IIa. *Hear Res*. 2002;163:1–11. DOI: 10.1016/S0378-5955(01)00344-6.

120. Bhattacharya G, Kalluri R, Orten DJ, et al. A domain-specific usherin/collagen IV interaction may be required for stable integration into the basement membrane superstructure. *J Cell Sci*. 2004;117:233–42. DOI: 10.1242/jcs.00850.

121. Yu D, Zou J, Chen Q, et al. Structural modeling, mutation analysis, and in vitro expression of usherin, a major protein in inherited retinal degeneration and hearing loss. *Comput Struct Biotechnol J*. 2020;18:1363–82. DOI: 10.1016/j.csbj.2020.05.025.

122. Bhattacharya G, Cosgrove D. Evidence for Functional Importance of Usherin/Fibronectin Interactions in Retinal Basement Membranes. *Biochemistry*. 2005;44:11518–24. DOI: 10.1021/bi050245u.

123. Reiners J, Nagel-Wolfrum K, Jürgens K, et al. Molecular basis of human Usher syndrome: Deciphering the meshes of the Usher protein network provides insights into the pathomechanisms of the Usher disease. *Exp Eye Res*. 2006;83:97–119. DOI: 10.1016/j.exer.2005.11.010.

124. Slijkerman RW, Kremer H, van Wijk E. Molecular Genetics of Usher Syndrome: Current State of Understanding. *ELS*. 2017:1–12. DOI: 10.1002/9780470015902.a0021456.pub2.

125. Toualbi L, Toms M, Moosajee M. USH2A-retinopathy: From genetics to therapeutics. *Exp Eye Res*. 2020;17:108330. DOI: 10.1016/j.exer.2020.108330.

126. Cowan CS, Renner M, De Gennaro M, et al. Cell Types of the Human Retina and Its Organoids at Single-Cell Resolution. *Cell*. 2020;182:1623-1640.e34. DOI: 10.1016/j.cell.2020.08.013.

127. Dona M, Slijkerman R, Lerner K, et al. Usherin defects lead to early-onset retinal dysfunction in zebrafish. *Exp Eye Res*. 2018;173:148–59. DOI: 10.1016/j.exer.2018.05.015.

128. Liu X, Bulgakov O V., Darrow KN, et al. Usherin is required for maintenance of retinal photoreceptors and normal development of cochlear hair cells. *Proc Natl Acad Sci*. 2007;104:4413–8. DOI: 10.1073/pnas.0610950104.

129. Zou J, Li R, Wang Z, et al. Studies of the Periciliary Membrane Complex in the Syrian Hamster Photoreceptor. In: Bowes Rickman C, Grimm C, Anderson R, Ash J, LaVail M, Hollyfield J, eds. Retin. Degener. Dis. Adv. Exp. Med. Biol. Springer; 2019;543–7. DOI: 10.1007/978-3-030-27378-1_89.

130. Chen Q, Zou J, Shen Z, et al. Whirlin and PDZ domain-containing 7 (PDZD7) proteins are both required to form the quaternary protein complex associated with Usher syndrome type 2. *J Biol Chem*. 2014;289:36070–88. DOI: 10.1074/jbc.M114.610535.

131. van Wijk E, van der Zwaag B, Peters T, et al. The DFNB31 gene product whirlin connects to the Usher protein network in the cochlea and retina by direct association with USH2A and VLGR1. *Hum Mol Genet*. 2006;15:751–65. DOI: 10.1093/hmg/ddi490.

132. Maerker T, van Wijk E, Overlack N, et al. A novel Usher protein network at the periciliary reloading point between molecular transport machineries in vertebrate photoreceptor cells. *Hum Mol Genet*. 2008;17:71–86. DOI: 10.1093/hmg/ddm285.

133. Yang J, Liu X, Zhao Y, et al. Ablation of whirlin long isoform disrupts the USH2 protein complex and causes vision and hearing loss. *PLoS Genet*. 2010;6:9. DOI: 10.1371/journal.pgen.1000955.

134. Zou J, Luo L, Shen Z, et al. Whirlin replacement restores the formation of the USH2 protein complex in whirlin knockout photoreceptors. *Investig Ophthalmol Vis Sci*. 2011;52:2343–51. DOI: 10.1167/iovs.10-6141.

135. Sorusch N, Baub K, Plutniok J, et al. Characterization of the ternary Usher syndrome SANS/ush2a/whirlin protein complex. *Hum Mol Genet*. 2017;26:1157–72. DOI: 10.1093/hmg/ddx027.

136. Reiners J, van Wijk E, Märker T, et al. Scaffold protein harmonin (USH1C) provides molecular links between Usher syndrome type 1 and type 2. *Hum Mol Genet*. 2005;14:3933–43. DOI: 10.1093/hmg/ddi417.

137. Overlack N, Kilic D, Bauß K, et al. Direct interaction of the Usher syndrome 1G protein SANS and myomegalin in the retina. *Biochim Biophys Acta - Mol Cell Res*. 2011;1813:1883–92. DOI: 10.1016/j.bbamcr.2011.05.015.

138. Papal S, Cortese M, Legendre K, et al. The giant spectrin βV couples the molecular motors to phototransduction and Usher syndrome type I proteins along their trafficking route. *Hum Mol Genet*. 2013;22:3773–88. DOI: 10.1093/hmg/ddt228.

139. Michalski N, Michel V, Bahloul A, et al. Molecular characterization of the ankle-link complex in cochlear hair cells and its role in the hair bundle functioning. *J Neurosci*. 2007;27:6478–88. DOI: 10.1523/JNEUROSCI.0342-07.2007.

140. Adato A, Lefèvre G, Delprat B, et al. Usherin, the defective protein in Usher syndrome type IIA, is likely to be a component of interstereocilia ankle links in the inner ear

sensory cells. *Hum Mol Genet*. 2005;14:3921–32. DOI: 10.1093/hmg/ddi416.

141. Zou J, Zheng T, Ren C, et al. Deletion of PDZD7 disrupts the Usher syndrome type 2 protein complex in cochlear hair cells and causes hearing loss in mice. *Hum Mol Genet*. 2014;23:2374–90. DOI: 10.1093/hmg/ddt629.
142. Zou J, Mathur PD, Zheng T, et al. Individual USH2 proteins make distinct contributions to the ankle link complex during development of the mouse cochlear stereociliary bundle. *Hum Mol Genet*. 2015;24:6944–57. DOI: 10.1093/hmg/ddv398.
143. Schwaller F, Bégay V, García-García G, et al. USH2A is a Meissner's corpuscle protein necessary for normal vibration sensing in mice and humans. *Nat Neurosci*. 2021;24:74–81. DOI: 10.1038/s41593-020-00751-y.
144. Hunter DG, Fishman GA, Mehta RS, et al. Abnormal Sperm and Photoreceptor Axonemes in Usher's Syndrome. *Arch Ophthalmol*. 1986;104:385–9. DOI: 10.1001/archopht.1986.01050150085033.
145. Van Aarem A, Wagenaar M, Tonnaer E, et al. Semen analysis in the Usher syndrome type 2A. *Orl*. 1999;61:126–30. DOI: 10.1159/000027656.
146. Ribeiro JC, Oliveiros B, Pereira P, et al. Accelerated age-related olfactory decline among type 1 Usher patients. *Sci Rep*. 2016;6:28309. DOI: 10.1038/srep28309.
147. Ramos JN, Ribeiro JC, Pereira AC, et al. Evidence for impaired olfactory function and structural brain integrity in a disorder of ciliary function, Usher syndrome. *NeuroImage Clin*. 2019;22:101757. DOI: 10.1016/j.nicl.2019.101757.
148. Fokkema IFAC, Taschner PEM, Schaafsma GCP, et al. LOVD v.2.0: the next generation in gene variant databases. *Hum Mutat*. 2011;32:557–63. DOI: 10.1002/humu.21438.
149. Baux D, Blanchet C, Hamel C, et al. Enrichment of LOVD-USHbases with 152 USH2A Genotypes Defines an Extensive Mutational Spectrum and Highlights Missense Hotspots. *Hum Mutat*. 2014;35:1179–86. DOI: 10.1002/humu.22608.
150. Dreyer B, Tranebjærg L, Brox V, et al. A Common Ancestral Origin of the Frequent and Widespread 2299delG USH2A Mutation. *Am J Hum Genet*. 2001;69:228–34. DOI: 10.1086/321269.
151. Aller E, Larrieu L, Jaijo T, et al. The USH2A c.2299delG mutation: Dating its common origin in a Southern European population. *Eur J Hum Genet*. 2010;18:788–93. DOI: 10.1038/ejhg.2010.14.
152. Pérez-Carro R, Blanco-Kelly F, Galbis-Martínez L, et al. Unravelling the pathogenic role and genotype-phenotype correlation of the USH2A p.(Cys759Phe) variant among

Spanish families. *PLoS One*. 2018;13:1–18. DOI: 10.1371/journal.pone.0199048.

153. Bonnet C, Riahi Z, Chantot-Bastaraud S, et al. An innovative strategy for the molecular diagnosis of Usher syndrome identifies causal biallelic mutations in 93% of European patients. *Eur J Hum Genet*. 2016;24:1730–8. DOI: 10.1038/ejhg.2016.99.
154. Neuhaus C, Eisenberger T, Decker C, et al. Next-generation sequencing reveals the mutational landscape of clinically diagnosed Usher syndrome: copy number variations, phenocopies, a predominant target for translational read-through, and PEX26 mutated in Heimler syndrome. *Mol Genet Genomic Med*. 2017;5:531–52. DOI: 10.1002/mgg3.312.
155. Zupan A, Fakin A, Battelino S, et al. Clinical and Haplotypic Variability of Slovenian USH2A Patients Homozygous for the c. 11864G>A Nonsense Mutation. *Genes (Basel)*. 2019;10:1015. DOI: 10.3390/genes10121015.
156. Pierrache LHM, Hartel BP, Van Wijk E, et al. Visual Prognosis in USH2A-Associated Retinitis Pigmentosa Is Worse for Patients with Usher Syndrome Type IIa Than for Those with Nonsyndromic Retinitis Pigmentosa. *Ophthalmology*. 2016;123:1151–60. DOI: 10.1016/j.ophtha.2016.01.021.
157. Hartel BP, Löfgren M, Huygen PLM, et al. A combination of two truncating mutations in USH2A causes more severe and progressive hearing impairment in Usher syndrome type IIa. *Hear Res*. 2016;339:60–8. DOI: 10.1016/j.heares.2016.06.008.
158. Lenassi E, Vincent A, Li Z, et al. A detailed clinical and molecular survey of subjects with nonsyndromic USH2A retinopathy reveals an allelic hierarchy of disease-causing variants. *Eur J Hum Genet*. 2015;23:1318–27. DOI: 10.1038/ejhg.2014.283.
159. Lenassi E, Robson AG, Luxon LM, et al. Clinical heterogeneity in a family with mutations in USH2A. *JAMA Ophthalmol*. 2015;133:352–5. DOI: 10.1001/jamaophthalmol.2014.5163.
160. McFall RC, Sery TW, Makadon M. Characterization of a new continuous cell line derived from a human retinoblastoma. *Cancer Res*. 1977;37:1003–10.
161. Reid TW, Albert DM, Rabson AS, et al. Characteristics of an Established Cell Line of Retinoblastoma. *JNCI J Natl Cancer Inst*. 1974;53:347–60. DOI: 10.1093/jnci/53.2.347.
162. Kalinec F. Establishment and characterization of conditionally immortalized organ of corti cell lines. *Cell Biol Int*. 1999;23:175–84. DOI: 10.1006/cbir.1998.0339.
163. Pendse N, Lamas V, Maeder M, et al. Exon 13-skipped USH2A protein retains functional integrity in mice, suggesting an exo-skipping therapeutic approach to treat USH2A-associated disease. *BioRxiv*. 2020.
164. Orlans HO, Edwards TL, De Silva SR, et al. Human Retinal Explant Culture for Ex

Vivo Validation of AAV Gene Therapy. 2018;289–303. DOI: 10.1007/978-1-4939-7522-8_21.

165. Vaché C, Besnard T, Blanchet C, et al. Nasal epithelial cells are a reliable source to study splicing variants in Usher syndrome. *Hum Mutat*. 2010;31:734–41. DOI: 10.1002/humu.21255.

166. Slijkerman RW, Vaché C, Dona M, et al. Antisense Oligonucleotide-based Splice Correction for USH2A-associated Retinal Degeneration Caused by a Frequent Deep-intronic Mutation. *Mol Ther - Nucleic Acids*. 2016;5:e381. DOI: 10.1038/mtna.2016.89.

167. Sanjurjo-Soriano C, Erkilic N, Baux D, et al. Genome Editing in Patient iPSCs Corrects the Most Prevalent USH2A Mutations and Reveals Intriguing Mutant mRNA Expression Profiles. *Mol Ther - Methods Clin Dev*. 2020;17:156–73. DOI: 10.1016/j.omtm.2019.11.016.

168. Bell CM, Zack DJ, Berlinicke CA. Human Organoids for the Study of Retinal Development and Disease. *Annu Rev Vis Sci*. 2020;6:91–114. DOI: 10.1146/annurev-vision-121219-081855.

169. Tucker BA, Mullins RF, Streb LM, et al. Patient-specifc iPSC-derived photoreceptor precursor cells as a means to investigate retinitis pigmentosa. *Elife*. 2013;2013:1–18. DOI: 10.7554/eLife.00824.001.

170. Guo Y, Wang P, Ma JH, et al. Modeling Retinitis Pigmentosa: Retinal Organoids Generated From the iPSCs of a Patient With the USH2A Mutation Show Early Developmental Abnormalities. *Front Cell Neurosci*. 2019;13:1–17. DOI: 10.3389/fncel.2019.00361.

171. Parfitt DA, Lane A, Ramsden CM, et al. Identification and Correction of Mechanisms Underlying Inherited Blindness in Human iPSC-Derived Optic Cups. *Cell Stem Cell*. 2016;18:769–81. DOI: 10.1016/j.stem.2016.03.021.

172. Deng WL, Gao ML, Lei XL, et al. Gene Correction Reverses Ciliopathy and Photoreceptor Loss in iPSC-Derived Retinal Organoids from Retinitis Pigmentosa Patients. *Stem Cell Reports*. 2018;10:1267–81. DOI: 10.1016/j.stemcr.2018.02.003.

173. Lane A, Jovanovic K, Shortall C, et al. Modeling and Rescue of RP2 Retinitis Pigmentosa Using iPSC-Derived Retinal Organoids. *Stem Cell Reports*. 2020;15:1–13. DOI: 10.1016/j.stemcr.2020.05.007.

174. Lu B, Wang S, Francis PJ, et al. Cell transplantation to arrest early changes in an ush2a animal model. *Investig Ophthalmol Vis Sci*. 2010;51:2269–76. DOI: 10.1167/iovs.09-4526.

175. Perrino PA, Talbot L, Kirkland R, et al. Multi-level evidence of an allelic hierarchy of

USH2A variants in hearing, auditory processing and speech/language outcomes. *Commun Biol*. 2020;3:1–14. DOI: 10.1038/s42003-020-0885-5.

176. Perrino PA, Newbury DF, Fitch RH. Peripheral anomalies in USH2A cause central auditory anomalies in a mouse model of usher syndrome and CAPD. *Genes (Basel)*. 2021;12:1–12. DOI: 10.3390/genes12020151.
177. Pendse ND, Lamas V, Pawlyk BS, et al. In Vivo Assessment of Potential Therapeutic Approaches for USH2A-Associated Diseases. *Adv Exp Med Biol*. 2019;1185:91–6. DOI: 10.1007/978-3-030-27378-1_15.
178. Slijkerman RWN, Song F, Astuti GDN, et al. The pros and cons of vertebrate animal models for functional and therapeutic research on inherited retinal dystrophies. *Prog Retin Eye Res*. 2015;48:137–59. DOI: 10.1016/j.preteyeres.2015.04.004.
179. Han S, Liu X, Xie S, et al. Knockout of ush2a gene in zebrafish causes hearing impairment and late onset rod-cone dystrophy. *Hum Genet*. 2018;137:779–94. DOI: 10.1007/s00439-018-1936-6.
180. Sengillo JD, Cabral T, Schuerch K, et al. Electroretinography Reveals Difference in Cone Function between Syndromic and Nonsyndromic USH2A Patients. *Sci Rep*. 2017;7:1–11. DOI: 10.1038/s41598-017-11679-y.
181. Slijkerman R, Goloborodko A, Broekman S, et al. Poor Splice-Site Recognition in a Humanized Zebrafish Knockin Model for the Recurrent Deep-Intronic c.7595-2144A>G Mutation in USH2A. *Zebrafish*. 2018;15:597–609. DOI: 10.1089/zeb.2018.1613.
182. Sahly I, Dufour E, Schietroma C, et al. Localization of usher 1 proteins to the photoreceptor calyceal processes, which are absent from mice. *J Cell Biol*. 2012;199:381–99. DOI: 10.1083/jcb.201202012.
183. ProQR Therapeutics. Identifier NCT03780257: A First-in-Human Study to Evaluate the Safety and Tolerability of QR-421a in Subjects With Retinitis Pigmentosa (RP) Due to Mutations in Exon 13 of the USH2A Gene. *ClinicalTrialsGov*. 2019. https://clinicaltrials.gov/ct2/show/NCT03780257 (accessed May 5, 2020).
184. ProQR Therapeutics. QR-421a STELLAR Trial Results 2021. https://www.proqr.com/files/2021-03/ProQR_QR-421a-STELLAR-trial-results_March2021.pdf (accessed June 9, 2021).
185. Nagel-Wolfrum K, Möller F, Penner I, et al. Translational read-through as an alternative approach for ocular gene therapy of retinal dystrophies caused by in-frame nonsense mutations. *Vis Neurosci*. 2014;31:309–16. DOI:

10.1017/S0952523814000194.

186. Rouet P, Smih F, Jasin M. Introduction of double-strand breaks into the genome of mouse cells by expression of a rare-cutting endonuclease. *Mol Cell Biol*. 1994;14:8096–106. DOI: 10.1128/MCB.14.12.8096.

187. Bibikova M, Carroll D, Segal DJ, et al. Stimulation of Homologous Recombination through Targeted Cleavage by Chimeric Nucleases. *Mol Cell Biol*. 2001;21:289–97. DOI: 10.1128/MCB.21.1.289-297.2001.

188. Moscou MJ, Bogdanove AJ. A Simple Cipher Governs DNA Recognition by TAL Effectors. *Science*. 2009;326:1501–1501. DOI: 10.1126/science.1178817.

189. Boch J, Scholze H, Schornack S, et al. Breaking the Code of DNA Binding Specificity of TAL-Type III Effectors. *Science*. 2009;326:1509–12. DOI: 10.1126/science.1178811.

190. Urnov FD. Genome Editing B.C. (Before CRISPR): Lasting Lessons from the "Old Testament." *CRISPR J*. 2018;1:34–46. DOI: 10.1089/crispr.2018.29007.fyu.

191. Epstein BE, Schaffer D V. Combining Engineered Nucleases with Adeno-associated Viral Vectors for Therapeutic Gene Editing. 2017;29–42. DOI: 10.1007/978-3-319-63904-8_2.

192. Mojica FJM, Díez-Villaseñor C, García-Martínez J, et al. Intervening Sequences of Regularly Spaced Prokaryotic Repeats Derive from Foreign Genetic Elements. *J Mol Evol*. 2005;60:174–82. DOI: 10.1007/s00239-004-0046-3.

193. Nakata A, Amemura M, Makino K. Unusual nucleotide arrangement with repeated sequences in the Escherichia coli K-12 chromosome. *J Bacteriol*. 1989;171:3553–6. DOI: 10.1128/jb.171.6.3553-3556.1989.

194. Cong L, Ran FA, Cox D, et al. Multiplex genome engineering using CRISPR/Cas systems. *Science*. 2013;339:819–23. DOI: 10.1126/science.1231143.

195. Jinek M, Chylinski K, Fonfara I, et al. A Programmable Dual-RNA-Guided DNA Endonuclease in Adaptive Bacterial Immunity. *Science*. 2012;337:816–21. DOI: 10.1126/science.1225829.

196. Mali P, Yang L, Esvelt KM, et al. RNA-Guided Human Genome Engineering via Cas9. *Science*. 2013;339:823–6. DOI: 10.1126/science.1232033.

197. Makarova KS, Wolf YI, Iranzo J, et al. Evolutionary classification of CRISPR–Cas systems: a burst of class 2 and derived variants. *Nat Rev Microbiol*. 2020;18:67–83. DOI: 10.1038/s41579-019-0299-x.

198. Ran FA, Cong L, Yan WX, et al. In vivo genome editing using Staphylococcus aureus Cas9. *Nature*. 2015;520:186–91. DOI: 10.1038/nature14299.

199. Kim E, Koo T, Park SW, et al. In vivo genome editing with a small Cas9 orthologue derived from Campylobacter jejuni. *Nat Commun*. 2017;8:1–12. DOI: 10.1038/ncomms14500.

200. Edraki A, Mir A, Ibraheim R, et al. A Compact, High-Accuracy Cas9 with a Dinucleotide PAM for In Vivo Genome Editing. *Mol Cell*. 2018:1–13. DOI: 10.1016/j.molcel.2018.12.003.

201. Li F, Wing K, Wang JH, et al. Comparison of CRISPR/Cas Endonucleases for in vivo Retinal Gene Editing. *Front Cell Neurosci*. 2020;14:1–9. DOI: 10.3389/fncel.2020.570917.

202. Koo T, Park SW, Jo DH, et al. CRISPR-LbCpf1 prevents choroidal neovascularization in a mouse model of age-related macular degeneration. *Nat Commun*. 2018;9. DOI: 10.1038/s41467-018-04175-y.

203. Pausch P, Al-Shayeb B, Bisom-Rapp E, et al. CRISPR-CasΦ from huge phages is a hypercompact genome editor. *Science*. 2020;369:333–7. DOI: 10.1126/science.abb1400.

204. Xu X, Chemparathy A, Zeng L, et al. Engineered miniature CRISPR-Cas system for mammalian genome regulation and editing. *Mol Cell*. 2021:1–13. DOI: 10.1016/j.molcel.2021.08.008.

205. Wu Z, Zhang Y, Yu H, et al. Programmed genome editing by a miniature CRISPR-Cas12f nuclease. *Nat Chem Biol*. 2021. DOI: 10.1038/s41589-021-00868-6.

206. Kim DY, Lee JM, Moon S Bin, et al. Efficient CRISPR editing with a hypercompact Cas12f1 and engineered guide RNAs delivered by adeno-associated virus. *Nat Biotechnol*. 2021. DOI: 10.1038/s41587-021-01009-z.

207. Liu JJ, Orlova N, Oakes BL, et al. CasX enzymes comprise a distinct family of RNA-guided genome editors. *Nature*. 2019;566:218–23. DOI: 10.1038/s41586-019-0908-x.

208. Walton RT, Christie KA, Whittaker MN, et al. Unconstrained genome targeting with near-PAMless engineered CRISPR-Cas9 variants. *Science*. 2020;8853:eaba8853. DOI: 10.1126/science.aba8853.

209. Bakondi B, Lv W, Lu B, et al. In Vivo CRISPR/Cas9 Gene Editing Corrects Retinal Dystrophy in the S334ter-3 Rat Model of Autosomal Dominant Retinitis Pigmentosa. *Mol Ther*. 2016;24:556–63. DOI: 10.1038/mt.2015.220.

210. Hung SSC, Chrysostomou V, Li F, et al. AAV-Mediated CRISPR/Cas Gene Editing of Retinal Cells In Vivo. *Investig Opthalmology Vis Sci*. 2016;57:3470–6. DOI: 10.1167/iovs.16-19316.

211. Jiang F, Doudna JA. CRISPR–Cas9 Structures and Mechanisms. *Annu Rev Biophys*.

2017;46:505–29. DOI: 10.1146/annurev-biophys-062215-010822.

212. Ceccaldi R, Rondinelli B, D'Andrea AD. Repair Pathway Choices and Consequences at the Double-Strand Break. *Trends Cell Biol.* 2016;26:52–64. DOI: 10.1016/j.tcb.2015.07.009.

213. Kim K, Park SW, Kim JH, et al. Genome surgery using Cas9 ribonucleoproteins for the treatment of age-related macular degeneration. *Genome Res.* 2017;27:419–26. DOI: 10.1101/gr.219089.116.

214. Holmgaard A, Askou AL, Benckendorff JNE, et al. In Vivo Knockout of the Vegfa Gene by Lentiviral Delivery of CRISPR/Cas9 in Mouse Retinal Pigment Epithelium Cells. *Mol Ther - Nucleic Acids.* 2017;9:89–99. DOI: 10.1016/j.omtn.2017.08.016.

215. Holmgaard AB, Askou AL, Jensen EG, et al. Targeted Knockout of the Vegfa Gene in the Retina by Subretinal Injection of RNP Complexes Containing Cas9 Protein and Modified sgRNAs. *Mol Ther.* 2021;29:191–207. DOI: 10.1016/j.ymthe.2020.09.032.

216. Chung SH, Mollhoff IN, Nguyen U, et al. Factors Impacting Efficacy of AAV-Mediated CRISPR-Based Genome Editing for Treatment of Choroidal Neovascularization. *Mol Ther - Methods Clin Dev.* 2020;17:409–17. DOI: 10.1016/j.omtm.2020.01.006.

217. Ling S, Yang S, Hu X, et al. Lentiviral delivery of co-packaged Cas9 mRNA and a Vegfa-targeting guide RNA prevents wet age-related macular degeneration in mice. *Nat Biomed Eng.* 2021;5. DOI: 10.1038/s41551-020-00656-y.

218. Tsai YT, Wu WH, Lee TT, et al. Clustered Regularly Interspaced Short Palindromic Repeats-Based Genome Surgery for the Treatment of Autosomal Dominant Retinitis Pigmentosa. *Ophthalmology.* 2018;125:1421–30. DOI: 10.1016/j.ophtha.2018.04.001.

219. Li P, Kleinstiver BP, Leon MY, et al. Allele-Specific CRISPR-Cas9 Genome Editing of the Single-Base P23H Mutation for Rhodopsin-Associated Dominant Retinitis Pigmentosa. *CRISPR J.* 2018;1:55–64. DOI: 10.1089/crispr.2017.0009.

220. Giannelli SG, Luoni M, Castoldi V, et al. Cas9/sgRNA selective targeting of the P23H Rhodopsin mutant allele for treating retinitis pigmentosa by intravitreal AAV9.PHP.B-based delivery. *Hum Mol Genet.* 2018;27:761–79. DOI: 10.1093/hmg/ddx438.

221. Patrizi C, Llado M, Benati D, et al. Allele-specific editing ameliorates dominant retinitis pigmentosa in a transgenic mouse model. *Am J Hum Genet.* 2021;108:295–308. DOI: 10.1016/j.ajhg.2021.01.006.

222. Burnight ER, Giacalone JC, Cooke JA, et al. CRISPR-Cas9 genome engineering: Treating inherited retinal degeneration. *Prog Retin Eye Res.* 2018;65:28–49. DOI:

10.1016/j.preteyeres.2018.03.003.

223. Yu W, Mookherjee S, Chaitankar V, et al. Nrl knockdown by AAV-delivered CRISPR/Cas9 prevents retinal degeneration in mice. *Nat Commun*. 2017;8:14716. DOI: 10.1038/ncomms14716.

224. Editas Medicine. Identifier NCT03872479: Single Ascending Dose Study in Participants With LCA10. *ClinicalTrialsGov*. 2018. https://clinicaltrials.gov/ct2/show/record/NCT03872479 (accessed March 14, 2021).

225. Maeder ML, Stefanidakis M, Wilson CJ, et al. Development of a gene-editing approach to restore vision loss in Leber congenital amaurosis type 10. *Nat Med*. 2019;25:229–33. DOI: 10.1038/s41591-018-0327-9.

226. Jo DH, Song DW, Cho CS, et al. CRISPR-Cas9–mediated therapeutic editing of Rpe65 ameliorates the disease phenotypes in a mouse model of Leber congenital amaurosis. *Sci Adv*. 2019;5:1–10. DOI: 10.1126/sciadv.aax1210.

227. Matsuda T, Oinuma I. Optimized CRISPR/Cas9-mediated in vivo genome engineering applicable to monitoring dynamics of endogenous proteins in the mouse neural tissues. *Sci Rep*. 2019;9:11309. DOI: 10.1038/s41598-019-47721-4.

228. Vagni P, Perlini LE, Chenais NAL, et al. Gene Editing Preserves Visual Functions in a Mouse Model of Retinal Degeneration. *Front Neurosci*. 2019;13:1–18. DOI: 10.3389/fnins.2019.00945.

229. Hu S, Du J, Chen N, et al. In Vivo CRISPR/Cas9-Mediated Genome Editing Mitigates Photoreceptor Degeneration in a Mouse Model of X-Linked Retinitis Pigmentosa. *Investig Opthalmology Vis Sci*. 2020;61:31. DOI: 10.1167/iovs.61.4.31.

230. Cai Y, Cheng T, Yao Y, et al. In vivo genome editing rescues photoreceptor degeneration via a Cas9/RecA-mediated homology-directed repair pathway. *Sci Adv*. 2019;5:eaav3335. DOI: 10.1126/sciadv.aav3335.

231. Burnight ER, Gupta M, Wiley LA, et al. Using CRISPR-Cas9 to Generate Gene-Corrected Autologous iPSCs for the Treatment of Inherited Retinal Degeneration. *Mol Ther*. 2017;25:1999–2013. DOI: 10.1016/j.ymthe.2017.05.015.

232. Burnight ER, Bohrer LR, Giacalone JC, et al. CRISPR-Cas9-Mediated Correction of the 1.02 kb Common Deletion in CLN3 in Induced Pluripotent Stem Cells from Patients with Batten Disease. *CRISPR J*. 2018;1:75–87. DOI: 10.1089/crispr.2017.0015.

233. Bassuk AG, Zheng A, Li Y, et al. Precision Medicine: Genetic Repair of Retinitis Pigmentosa in Patient-Derived Stem Cells. *Sci Rep*. 2016;6:1–6. DOI:

10.1038/srep19969.

234. Bohrer LR, Wiley LA, Burnight ER, et al. Correction of NR2E3 Associated enhanced S-cone Syndrome Patient-specific IPSCS using CRISPR-Cas9. *Genes (Basel)*. 2019;10. DOI: 10.3390/genes10040278.

235. Fuster-García C, García-García G, González-Romero E, et al. USH2A Gene Editing Using the CRISPR System. *Mol Ther - Nucleic Acids*. 2017;8:529–41. DOI: 10.1016/j.omtn.2017.08.003.

236. Liu X, Lillywhite J, Zhu W, et al. Generation and Genetic Correction of USH2A c.2299delG Mutation in Patient-Derived Induced Pluripotent Stem Cells. *Genes (Basel)*. 2021;12:805. DOI: 10.3390/genes12060805.

237. Sakuma T, Nakade S, Sakane Y, et al. MMEJ-assisted gene knock-in using TALENs and CRISPR-Cas9 with the PITCh systems. *Nat Protoc*. 2016;11:118–33. DOI: 10.1038/nprot.2015.140.

238. Suzuki K, Tsunekawa Y, Hernandez-Benitez R, et al. In vivo genome editing via CRISPR/Cas9 mediated homology-independent targeted integration. *Nature*. 2016;540:144–9. DOI: 10.1038/nature20565.

239. Nishiguchi KM, Fujita K, Miya F, et al. Single AAV-mediated mutation replacement genome editing in limited number of photoreceptors restores vision in mice. *Nat Commun*. 2020;11:1–9. DOI: 10.1038/s41467-019-14181-3.

240. Nakamura M, Gao Y, Dominguez AA, et al. CRISPR technologies for precise epigenome editing. *Nat Cell Biol*. 2021;23:11–22. DOI: 10.1038/s41556-020-00620-7.

241. Moreno AM, Fu X, Zhu J, et al. In Situ Gene Therapy via AAV-CRISPR-Cas9-Mediated Targeted Gene Regulation. *Mol Ther*. 2018;26:1818–27. DOI: 10.1016/j.ymthe.2018.04.017.

242. Böhm S, Splith V, Riedmayr LM, et al. A gene therapy for inherited blindness using dCas9-VPR–mediated transcriptional activation. *Sci Adv*. 2020;6:eaba5614. DOI: 10.1126/sciadv.aba5614.

243. Peddle CF, Fry LE, McClements ME, et al. CRISPR Interference–Potential Application in Retinal Disease. *Int J Mol Sci*. 2020;21:2329. DOI: 10.3390/ijms21072329.

244. Rees HA, Liu DR. Base editing: precision chemistry on the genome and transcriptome of living cells. *Nat Rev Genet*. 2018;19:770–88. DOI: 10.1038/s41576-018-0059-1.

245. Anzalone A V., Koblan LW, Liu DR. Genome editing with CRISPR–Cas nucleases, base editors, transposases and prime editors. *Nat Biotechnol*. 2020;38:824–44. DOI:

10.1038/s41587-020-0561-9.

246. Komor AC, Kim YB, Packer MS, et al. Programmable editing of a target base in genomic DNA without double-stranded DNA cleavage. *Nature*. 2016;533:420–4. DOI: 10.1038/nature17946.

247. Gaudelli NM, Komor AC, Rees HA, et al. Programmable base editing of A•T to G•C in genomic DNA without DNA cleavage. *Nature*. 2017;551:464–71. DOI: 10.1038/nature24644.

248. Anzalone A V, Koblan LW, Liu DR. Genome editing with CRISPR-Cas nucleases, base editors, transposases and prime editors. *Nat Biotechnol*. 2020. DOI: 10.1038/s41587-020-0561-9.

249. Koblan LW, Arbab M, Shen MW, et al. Efficient C•G-to-G•C base editors developed using CRISPRi screens, target-library analysis, and machine learning. *Nat Biotechnol*. 2021. DOI: 10.1038/s41587-021-00938-z.

250. Molla KA, Qi Y, Karmakar S, et al. Base Editing Landscape Extends to Perform Transversion Mutation. *Trends Genet*. 2020;36:899–901. DOI: 10.1016/j.tig.2020.09.001.

251. Mok BY, de Moraes MH, Zeng J, et al. A bacterial cytidine deaminase toxin enables CRISPR-free mitochondrial base editing. *Nature*. 2020;583:631–7. DOI: 10.1038/s41586-020-2477-4.

252. Gaudelli NM, Lam DK, Rees HA, et al. Directed evolution of adenine base editors with increased activity and therapeutic application. *Nat Biotechnol*. 2020. DOI: 10.1038/s41587-020-0491-6.

253. Koblan LW, Erdos MR, Wilson C, et al. In vivo base editing rescues Hutchinson–Gilford progeria syndrome in mice. *Nature*. 2021;589:608–14. DOI: 10.1038/s41586-020-03086-7.

254. Levy JM, Yeh W-H, Pendse N, et al. Cytosine and adenine base editing of the brain, liver, retina, heart and skeletal muscle of mice via adeno-associated viruses. *Nat Biomed Eng*. 2020;4:97–110. DOI: 10.1038/s41551-019-0501-5.

255. Suh S, Choi EH, Leinonen H, et al. Restoration of visual function in adult mice with an inherited retinal disease via adenine base editing. *Nat Biomed Eng*. 2020. DOI: 10.1038/s41551-020-00632-6.

256. Nguyen Tran MT, Mohd Khalid MKN, Wang Q, et al. Engineering domain-inlaid SaCas9 adenine base editors with reduced RNA off-targets and increased on-target DNA editing. *Nat Commun*. 2020;11. DOI: 10.1038/s41467-020-18715-y.

257. Anzalone A V., Randolph PB, Davis JR, et al. Search-and-replace genome editing

without double-strand breaks or donor DNA. *Nature*. 2019. DOI: 10.1038/s41586-019-1711-4.

258. Chemello F, Chai AC, Li H, et al. Precise correction of Duchenne muscular dystrophy exon deletion mutations by base and prime editing. *Sci Adv*. 2021;7. DOI: 10.1126/sciadv.abg4910.

259. Klompe SE, Vo PLH, Halpin-Healy TS, et al. Transposon-encoded CRISPR–Cas systems direct RNA-guided DNA integration. *Nature*. 2019;571:219–25. DOI: 10.1038/s41586-019-1323-z.

260. Latella MC, Di Salvo MT, Cocchiarella F, et al. In vivo Editing of the Human Mutant Rhodopsin Gene by Electroporation of Plasmid-based CRISPR/Cas9 in the Mouse Retina. *Mol Ther - Nucleic Acids*. 2016;5:e389. DOI: 10.1038/mtna.2016.92.

261. Zhu J, Ming C, Fu X, et al. Gene and mutation independent therapy via CRISPR-Cas9 mediated cellular reprogramming in rod photoreceptors. *Cell Res*. 2017;27:830–3. DOI: 10.1038/cr.2017.57.

262. Ruan G-X, Barry E, Yu D, et al. CRISPR/Cas9-Mediated Genome Editing as a Therapeutic Approach for Leber Congenital Amaurosis 10. *Mol Ther*. 2017;25:331–41. DOI: 10.1016/j.ymthe.2016.12.006.

263. McCullough KT, Boye SL, Fajardo D, et al. Somatic gene editing of GUCY2D by AAV-CRISPR/Cas9 alters retinal structure and function in mouse and macaque. *Hum Gene Ther*. 2018:hum.2018.193. DOI: 10.1089/hum.2018.193.

264. Lin Q, Lv JN, Wu KC, et al. Generation of Nonhuman Primate Model of Cone Dysfunction through In Situ AAV-Mediated CNGB3 Ablation. *Mol Ther - Methods Clin Dev*. 2020;18:869–79. DOI: 10.1016/j.omtm.2020.08.007.

265. Li F, Hung SSC, Mohd Khalid MKN, et al. Utility of self-destructing CRISPR/Cas constructs for targeted gene editing in the retina. *Hum Gene Ther*. 2019;30:1349–60. DOI: 10.1089/hum.2019.021.

266. Jo DH, Koo T, Cho CS, et al. Long-term effects of in vivo genome editing in the mouse retina using Campylobacter jejuni Cas9 expressed via adeno-associated virus. *Mol Ther*. 2018. DOI: 10.1016/j.ymthe.2018.10.009.

267. Wang Q, Zhuang P, Huang H, et al. Mouse gamma-Synuclein Promoter-Mediated Gene Expression and Editing in Mammalian Retinal Ganglion Cells. *J Neurosci*. 2020;40:3896–914. DOI: 10.1523/jneurosci.0102-20.2020.

268. Katayama S, Sato K, Nakazawa T. In vivo and in vitro knockout system labelled using fluorescent protein via microhomology-mediated end joining. *Life Sci Alliance*.

2020;3:1–8. DOI: 10.26508/lsa.201900528.

269. Xia C hong, Ferguson I, Li M, et al. Essential function of NHE8 in mouse retina demonstrated by AAV-mediated CRISPR/Cas9 knockdown. *Exp Eye Res*. 2018;176:29–39. DOI: 10.1016/j.exer.2018.06.026.

270. Jang H, Jo DH, Cho CS, et al. Application of prime editing to the correction of mutations and phenotypes in adult mice with liver and eye diseases. *Nat Biomed Eng*. 2021. DOI: 10.1038/s41551-021-00788-9.

271. Zhi S, Chen Y, Wu G, et al. Dual-AAV delivering split prime editor system for in vivo genome editing. *Mol Ther*. 2021:135907. DOI: 10.1016/j.ymthe.2021.07.011.

272. Zhou H, Su J, Hu X, et al. Glia-to-Neuron Conversion by CRISPR-CasRx Alleviates Symptoms of Neurological Disease in Mice. *Cell*. 2020:1–14. DOI: 10.1016/j.cell.2020.03.024.

273. Zhou C, Hu X, Tang C, et al. CasRx-mediated RNA targeting prevents choroidal neovascularization in a mouse model of age-related macular degeneration. *Natl Sci Rev*. 2020;7:835–7. DOI: 10.1093/nsr/nwaa033.

274. Vitravene Study Group. A randomized controlled clinical trial of intravitreous fomivirsen for treatment of newly diagnosed peripheral cytomegalovirus retinitis in patients with AIDS. *Am J Ophthalmol*. 2002;133:467–74. DOI: 10.1016/s0002-9394(02)01327-2.

275. Gupta A, Kafetzis KN, Tagalakis AD, et al. RNA therapeutics in ophthalmology - translation to clinical trials. *Exp Eye Res*. 2021;205:108482. DOI: 10.1016/j.exer.2021.108482.

276. O'Connell MR, Oakes BL, Sternberg SH, et al. Programmable RNA recognition and cleavage by CRISPR/Cas9. *Nature*. 2014;516:263–6. DOI: 10.1038/nature13769.

277. Batra R, Nelles DA, Pirie E, et al. Elimination of Toxic Microsatellite Repeat Expansion RNA by RNA-Targeting Cas9. *Cell*. 2017;170:899-912.e10. DOI: 10.1016/j.cell.2017.07.010.

278. Liu Y, Chen Z, He A, et al. Targeting cellular mRNAs translation by CRISPR-Cas9. *Sci Rep*. 2016;6:2–10. DOI: 10.1038/srep29652.

279. East-Seletsky A, O'Connell MR, Knight SC, et al. Two distinct RNase activities of CRISPR-C2c2 enable guide-RNA processing and RNA detection. *Nature*. 2016;538:270–3. DOI: 10.1038/nature19802.

280. Abudayyeh OO, Gootenberg JS, Konermann S, et al. C2c2 is a single-component programmable RNA-guided RNA-targeting CRISPR effector. *Science*. 2016;353. DOI:

10.1126/science.aaf5573.

281. Smargon AA, Cox DBT, Pyzocha NK, et al. Cas13b Is a Type VI-B CRISPR-Associated RNA-Guided RNase Differentially Regulated by Accessory Proteins Csx27 and Csx28. *Mol Cell*. 2017;65:618-630.e7. DOI: 10.1016/j.molcel.2016.12.023.

282. Kannan S, Altae-Tran H, Jin X, et al. Compact RNA editors with small Cas13 proteins. *Nat Biotechnol*. 2021. DOI: 10.1038/s41587-021-01030-2.

283. Zhang C, Konermann S, Brideau NJ, et al. Structural Basis for the RNA-Guided Ribonuclease Activity of CRISPR-Cas13d. *Cell*. 2018;175:212-223.e17. DOI: 10.1016/j.cell.2018.09.001.

284. Xu C, Zhou Y, Xiao Q, et al. Programmable RNA editing with compact CRISPR–Cas13 systems from uncultivated microbes. *Nat Methods*. 2021;18:499–506. DOI: 10.1038/s41592-021-01124-4.

285. Konermann S, Lotfy P, Brideau NJ, et al. Transcriptome Engineering with RNA-Targeting Type VI-D CRISPR Effectors. *Cell*. 2018;173:665--676.e14. DOI: 10.1016/j.cell.2018.02.033.

286. Abudayyeh OO, Gootenberg JS, Essletzbichler P, et al. RNA targeting with CRISPR-Cas13. *Nature*. 2017;550:280–4. DOI: 10.1038/nature24049.

287. Woolf TM, Chase JM, Stinchcomb DT. Toward the therapeutic editing of mutated RNA sequences. *Proc Natl Acad Sci U S A*. 1995;92:8298–302. DOI: 10.1073/pnas.92.18.8298.

288. Fry LE, Peddle CF, Barnard AR, et al. RNA editing as a therapeutic approach for retinal gene therapy requiring long coding sequences. *Int J Mol Sci*. 2020;21. DOI: 10.3390/ijms21030777.

289. Nishikura K, Yoo C, Kim U, et al. Substrate specificity of the dsRNA unwinding/modifying activity. *EMBO J*. 1991;10:3523–32. DOI: 10.1002/j.1460-2075.1991.tb04916.x.

290. Higuchi M, Single FN, Köhler M, et al. RNA editing of AMPA receptor subunit GluR-B: a base-paired intron-exon structure determines position and efficiency. *Cell*. 1993;75:1361–70. DOI: 10.1016/0092-8674(93)90622-w.

291. Bazak L, Haviv A, Barak M, et al. A-to-I RNA editing occurs at over a hundred million genomic sites, located in a majority of human genes. *Genome Res*. 2014;24:365–76. DOI: 10.1101/gr.164749.113.

292. Nishikura K. A-to-I editing of coding and non-coding RNAs by ADARs. *Nat Rev Mol Cell Biol*. 2016;17:83–96. DOI: 10.1038/nrm.2015.4.

293. Matthews MM, Thomas JM, Zheng Y, et al. Structures of human ADAR2 bound to dsRNA reveal base-flipping mechanism and basis for site selectivity. *Nat Struct Mol Biol.* 2016;23:426–33. DOI: 10.1038/nsmb.3203.

294. Wong SK, Sato S, Lazinski DW. Substrate recognition by ADAR1 and ADAR2. *Rna.* 2001;7:846–58. DOI: 10.1017/S135583820101007X.

295. Kim U, Wang Y, Sanford T, et al. Molecular cloning of cDNA for double-stranded RNA adenosine deaminase, a candidate enzyme for nuclear RNA editing. *Proc Natl Acad Sci U S A.* 1994;91:11457–61. DOI: 10.1073/pnas.91.24.11457.

296. Desterro JMP, Keegan LP, Lafarga M, et al. Dynamic association of RNA-editing enzymes with the nucleolus. *J Cell Sci.* 2003;116:1805–18. DOI: 10.1242/jcs.00371.

297. Melcher T, Maas S, Herb A, et al. A mammalian RNA editing enzyme. *Nature.* 1996;379:460–4. DOI: 10.1038/379460a0.

298. Kuttan A, Bass BL. Mechanistic insights into editing-site specificity of ADARs. *Proc Natl Acad Sci.* 2012;109:E3295–304. DOI: 10.1073/pnas.1212548109.

299. Vogel P, Moschref M, Li Q, et al. Efficient and precise editing of endogenous transcripts with SNAP-tagged ADARs. *Nat Methods.* 2018;15:535–8. DOI: 10.1038/s41592-018-0017-z.

300. Cox DBT, Gootenberg JS, Abudayyeh OO, et al. RNA editing with CRISPR-Cas13. *Science.* 2017;358:1019–27. DOI: 10.1126/science.aaq0180.

301. Vallecillo-Viejo IC, Liscovitch-Brauer N, Montiel-Gonzalez MF, et al. Abundant off-target edits from site-directed RNA editing can be reduced by nuclear localization of the editing enzyme. *RNA Biol.* 2018;15:104–14. DOI: 10.1080/15476286.2017.1387711.

302. Wang Y, Havel J, Beal PA. A Phenotypic Screen for Functional Mutants of Human Adenosine Deaminase Acting on RNA 1. *ACS Chem Biol.* 2015;10:2512–9. DOI: 10.1021/acschembio.5b00711.

303. Abudayyeh OO, Gootenberg JS, Franklin B, et al. A cytosine deaminase for programmable single-base RNA editing. *Science.* 2019;538:382–6. DOI: 10.1126/science.aax7063.

304. Liu Y, Mao S, Huang S, et al. REPAIR x, a specific yet highly efficient programmable A > I RNA base editor. *EMBO J.* 2020:1–12. DOI: 10.15252/embj.2020104748.

305. Abudayyeh OO, Gootenberg JS, Franklin B, et al. A cytosine deaminase for programmable single-base RNA editing. *Science.* 2019;365:382–6. DOI: 10.1126/science.aax7063.

306. Huang XX, Lv J, Li Y, et al. Programmable C-to-U RNA editing using the human APOBEC 3A deaminase . *EMBO J*. 2020;39:1–12. DOI: 10.15252/embj.2020104741.

307. Baron-Benhamou J, Gehring NH, Kulozik AE, et al. Using the λN Peptide to Tether Proteins to RNAs. mRNA Process. Metab. New Jersey: Humana Press; n.d.;135–54. DOI: 10.1385/1-59259-750-5:135.

308. Montiel-Gonzalez MF, Vallecillo-Viejo I, Yudowski GA, et al. Correction of mutations within the cystic fibrosis transmembrane conductance regulator by site-directed RNA editing. *Proc Natl Acad Sci*. 2013;110:18285–90. DOI: 10.1073/pnas.1306243110.

309. Montiel-Gonźalez MF, Vallecillo-Viejo IC, Rosenthal JJC. An efficient system for selectively altering genetic information within mRNAs. *Nucleic Acids Res*. 2016;44:1–12. DOI: 10.1093/nar/gkw738.

310. Sinnamon JR, Kim SY, Corson GM, et al. Site-directed RNA repair of endogenous Mecp2 RNA in neurons. *Proc Natl Acad Sci*. 2017:201715320. DOI: 10.1073/pnas.1715320114.

311. Sinnamon JR, Kim SY, Fisk JR, et al. In vivo repair of a protein underlying a neurological disorder by programmable RNA editing. *BioArxiv*. 2020. DOI: https://doi.org/10.1101/2020.02.26.966820.

312. Katrekar D, Chen G, Meluzzi D, et al. In vivo RNA editing of point mutations via RNA-guided adenosine deaminases. *Nat Methods*. 2019;16:239–42. DOI: 10.1038/s41592-019-0323-0.

313. Azad TA, Qulsum U, Tsukahara T. Comparative Activity of Adenosine Deaminase Acting on RNA (ADARs) Isoforms for Correction of Genetic Code in Gene Therapy. *Curr Gene Ther*. 2018;18:31–9. DOI: 10.2174/1566523218666181114122116.

314. Tohama T, Sakari M, Tsukahara T. Development of a single construct system for site-directed rna editing using MS2-ADAR. *Int J Mol Sci*. 2020;21:1–11. DOI: 10.3390/ijms21144943.

315. Wettengel J, Reautschnig P, Geisler S, et al. Harnessing human ADAR2 for RNA repair - Recoding a PINK1 mutation rescues mitophagy. *Nucleic Acids Res*. 2017;45:2797–808. DOI: 10.1093/nar/gkw911.

316. Stafforst T, Schneider MF. An RNA-deaminase conjugate selectively repairs point mutations. *Angew Chemie - Int Ed*. 2012;51:11166–9. DOI: 10.1002/anie.201206489.

317. Vogel P, Schneider MF, Wettengel J, et al. Improving site-directed RNA editing in vitro and in cell culture by chemical modification of the guideRNA. *Angew Chemie - Int Ed*. 2014;53:6267–71. DOI: 10.1002/anie.201402634.

318. Rauch S, He E, Srienc M, et al. Programmable RNA-Guided RNA Effector Proteins Built from Human Parts. *Cell*. 2019:1–13. DOI: 10.1016/j.cell.2019.05.049.

319. Qu L, Yi Z, Zhu S, et al. Programmable RNA editing by recruiting endogenous ADAR using engineered RNAs. *Nat Biotechnol*. 2019;37:1059–69. DOI: 10.1038/s41587-019-0178-z.

320. Merkle T, Merz S, Reautschnig P, et al. Precise RNA editing by recruiting endogenous ADARs with antisense oligonucleotides. *Nat Biotechnol*. 2019;37:133–8. DOI: 10.1038/s41587-019-0013-6.

321. Naeem M, Majeed S, Hoque MZ, et al. Latest Developed Strategies to Minimize the Off-Target Effects in CRISPR-Cas-Mediated Genome Editing. *Cells*. 2020;9:1–23. DOI: 10.3390/cells9071608.

322. Fu Y, Foden JA, Khayter C, et al. High-frequency off-target mutagenesis induced by CRISPR-Cas nucleases in human cells. *Nat Biotechnol*. 2013;31:822–6. DOI: 10.1038/nbt.2623.

323. Cullot G, Boutin J, Toutain J, et al. CRISPR-Cas9 genome editing induces megabase-scale chromosomal truncations. *Nat Commun*. 2019;10:1–14. DOI: 10.1038/s41467-019-09006-2.

324. Hanlon KS, Kleinstiver BP, Garcia SP, et al. High levels of AAV vector integration into CRISPR-induced DNA breaks. *Nat Commun*. 2019;10:1–11. DOI: 10.1038/s41467-019-12449-2.

325. Grünewald J, Zhou R, Garcia SP, et al. Transcriptome-wide off-target RNA editing induced by CRISPR-guided DNA base editors. *Nature*. 2019;569:433–7. DOI: 10.1038/s41586-019-1161-z.

326. Grünewald J, Zhou R, Iyer S, et al. CRISPR DNA base editors with reduced RNA off-target and self-editing activities. *Nat Biotechnol*. 2019;37:1041–8. DOI: 10.1038/s41587-019-0236-6.

327. Cheng Y, Tsai SQ. Illuminating the genome-wide activity of genome editors for safe and effective therapeutics. *Genome Biol*. 2018;19:1–7. DOI: 10.1186/s13059-018-1610-2.

328. Finn JD, Smith AR, Patel MC, et al. A Single Administration of CRISPR/Cas9 Lipid Nanoparticles Achieves Robust and Persistent In Vivo Genome Editing. *Cell Rep*. 2018;22:2455–68. DOI: 10.1016/j.celrep.2018.02.014.

329. Gillmore JD, Gane E, Taubel J, et al. CRISPR-Cas9 In Vivo Gene Editing for Transthyretin Amyloidosis. *N Engl J Med*. 2021:NEJMoa2107454. DOI: 10.1056/NEJMoa2107454.

330. Jo DH, Koo T, Cho CS, et al. Long-Term Effects of In Vivo Genome Editing in the Mouse Retina Using Campylobacter jejuni Cas9 Expressed via Adeno-Associated Virus. *Mol Ther*. 2018;27:130–6. DOI: 10.1016/j.ymthe.2018.10.009.

331. Platt RJ, Chen S, Zhou Y, et al. CRISPR-Cas9 knockin mice for genome editing and cancer modeling. *Cell*. 2014;159:440–55. DOI: 10.1016/j.cell.2014.09.014.

332. Charlesworth CT, Deshpande PS, Dever DP, et al. Identification of preexisting adaptive immunity to Cas9 proteins in humans. *Nat Med*. 2019;25:249–54. DOI: 10.1038/s41591-018-0326-x.

333. Evans MD. Usher syndrome: A phenomenological study of adults across the lifespan living in England. *Disabil Soc*. 2017;0:1–420. DOI: 10.1080/09687599.2021.1889981.

334. Wang J, Geisert EE, Struebing FL. RNA sequencing profiling of the retina in C57BL/6J and DBA/2J mice: Enhancing the retinal microarray data sets from GeneNetwork. *Mol Vis*. 2019;25:345–58.

335. Rocha-Martins M, Njaine B, Silveira MS. Avoiding pitfalls of internal controls: Validation of reference genes for analysis by qRT-PCR and western blot throughout rat retinal development. *PLoS One*. 2012;7. DOI: 10.1371/journal.pone.0043028.

336. Livak KJ, Schmittgen TD. Analysis of Relative Gene Expression Data Using Real-Time Quantitative PCR and the 2−ΔΔCT Method. *Methods*. 2001;25:402–8. DOI: 10.1006/meth.2001.1262.

337. Wright JF. Transient transfection methods for clinical adeno-associated viral vector production. *Hum Gene Ther*. 2009;20:698–706. DOI: 10.1089/hum.2009.064.

338. Grimm D, Kay MA, Kleinschmidt JA. Helper virus-free, optically controllable, and two-plasmid-based production of adeno-associated virus vectors of serotypes 1 to 6. *Mol Ther*. 2003;7:839–50. DOI: 10.1016/S1525-0016(03)00095-9.

339. Strobel B, Miller FD, Rist W, et al. Comparative Analysis of Cesium Chloride- and Iodixanol-Based Purification of Recombinant Adeno-Associated Viral Vectors for Preclinical Applications. *Hum Gene Ther Methods*. 2015;26:147–57. DOI: 10.1089/hgtb.2015.051.

340. Green MR, Sambrook J. Analysis of rAAV Purity Using Silver-Stained SDS-PAGE. Mol. cloning a Lab. Man. 4th ed.Cold Spring Harbor, N.Y.: Cold Spring Harbor Laboratory Press; 2012;1304–6.

341. Green MR, Sambrook J. Titration of rAAV Genome Copy Number Using Real-Time qPCR. Mol. cloning a Lab. Man. 4th ed.Cold Spring Harbor, N.Y.: Cold Spring Harbor Laboratory Press; 2012;1294–8.

342. Issa PC, Singh MS, Lipinski DM, et al. Optimization of in vivo confocal autofluorescence imaging of the ocular fundus in mice and its application to models of human retinal degeneration. *Investig Ophthalmol Vis Sci*. 2012;53:1066–75. DOI: 10.1167/iovs.11-8767.

343. Gramatikov BI. Modern technologies for retinal scanning and imaging: An introduction for the biomedical engineer. *Biomed Eng Online*. 2014;13:1–34. DOI: 10.1186/1475-925X-13-52.

344. Orlans HO, Barnard AR, MacLaren RE. Dynamic in vivo quantification of rod photoreceptor degeneration using fluorescent reporter mouse models of retinitis pigmentosa. *Exp Eye Res*. 2020;190:107895. DOI: 10.1016/j.exer.2019.107895.

345. Dietrich M, Hecker C, Hilla A, et al. Using optical coherence tomography and optokinetic response as structural and functional visual system readouts in mice and rats. *J Vis Exp*. 2019;2019:1–7. DOI: 10.3791/58571.

346. Sagdullaev BT, DeMarco PJ, McCall MA. Improved contact lens electrode for corneal ERG recordings in mice. *Doc Ophthalmol*. 2004;108:181–4. DOI: 10.1007/s10633-004-5734-1.

347. Kinoshita J, Peachey NS. Noninvasive Electroretinographic Procedures for the Study of the Mouse Retina. *Curr Protoc Mouse Biol*. 2018;8:1–16. DOI: 10.1002/cpmo.39.

348. Colella P, Ronzitti G, Mingozzi F. Emerging Issues in AAV-Mediated In Vivo Gene Therapy. *Mol Ther - Methods Clin Dev*. 2018;8:87–104. DOI: 10.1016/j.omtm.2017.11.007.

349. Lau CH, Suh Y. In vivo genome editing in animals using AAV-CRISPR system: Applications to translational research of human disease. *F1000Research*. 2017;6:1–21. DOI: 10.12688/f1000research.11243.1.

350. Carvalho LS, Turunen HT, Wassmer SJ, et al. Evaluating efficiencies of dual AAV approaches for retinal targeting. *Front Neurosci*. 2017;11:1–8. DOI: 10.3389/fnins.2017.00503.

351. Kleinstiver BP, Prew MS, Tsai SQ, et al. Broadening the targeting range of Staphylococcus aureus CRISPR-Cas9 by modifying PAM recognition. *Nat Biotechnol*. 2015;33:1293–8. DOI: 10.1038/nbt.3404.

352. Stone D, Long KR, Loprieno MA, et al. CRISPR-Cas9 gene editing of hepatitis B virus in chronically infected humanized mice. *Mol Ther - Methods Clin Dev*. 2021;20:258–75. DOI: 10.1016/j.omtm.2020.11.014.

353. Friedland AE, Baral R, Singhal P, et al. Characterization of Staphylococcus aureus

Cas9: a smaller Cas9 for all-in-one adeno-associated virus delivery and paired nickase applications. *Genome Biol.* 2015:1–10. DOI: 10.1186/s13059-015-0817-8.

354. Bengtsson NE, Hall JK, Odom GL, et al. Muscle-specific CRISPR/Cas9 dystrophin gene editing ameliorates pathophysiology in a mouse model for Duchenne muscular dystrophy. *Nat Commun*. 2017;8. DOI: 10.1038/ncomms14454.
355. Tabebordbar M, Zhu K, Cheng JKW, et al. In vivo gene editing in dystrophic mouse muscle and muscle stem cells. *Science.* 2016;351:407–11. DOI: 10.1126/science.aad5177.
356. Long C, Amoasii L, Mireault AA, et al. Postnatal genome editing partially restores dystrophin expression in a mouse model of muscular dystrophy. *Science.* 2016;351:400–3. DOI: 10.1126/science.aad5725.
357. Nelson CE, Hakim CH, Ousterout DG, et al. In vivo genome editing improves muscle function in a mouse model of Duchenne muscular dystrophy. *Science*. 2016;351:403–7. DOI: 10.1126/science.aad5143.
358. Curtin JA, Dane AP, Swanson A, et al. Bidirectional promoter interference between two widely used internal heterologous promoters in a late-generation lentiviral construct. *Gene Ther*. 2008;15:384–90. DOI: 10.1038/sj.gt.3303105.
359. Park SK, Hwang BJ, Kee Y. Promoter cross-talk affects the inducible expression of intronic shRNAs from the tetracycline response element. *Genes and Genomics*. 2019;0:0. DOI: 10.1007/s13258-019-00784-z.
360. Semple-Rowland SL, Coggin WE, Geesey M, et al. Expression characteristics of dual-promoter lentiviral vectors targeting retinal photoreceptors and Müller cells. *Mol Vis.* 2010;16:916–34.
361. Nie L, Thakur M Das, Wang Y, et al. Regulation of U6 Promoter Activity by Transcriptional Interference in Viral Vector-Based RNAi. *Genomics, Proteomics Bioinforma.* 2010;8:170–9. DOI: 10.1016/S1672-0229(10)60019-8.
362. Lambeth LS, Van Hateren NJ, Wilson SA, et al. A direct comparison of strategies for combinatorial RNA interference. *BMC Mol Biol.* 2010;11:77. DOI: 10.1186/1471-2199-11-77.
363. Kleinstiver BP, Prew MS, Tsai SQ, et al. Engineered CRISPR-Cas9 nucleases with altered PAM specificities. *Nature.* 2015;523:481–5. DOI: 10.1038/nature14592.
364. Brinkman EK, Chen T, Amendola M, et al. Easy quantitative assessment of genome editing by sequence trace decomposition. *Nucleic Acids Res.* 2014;42:e168–e168. DOI: 10.1093/nar/gku936.

365. Ellis BL, Hirsch ML, Barker JC, et al. A survey of ex vivo/in vitro transduction efficiency of mammalian primary cells and cell lines with Nine natural adeno-associated virus (AAV1-9) and one engineered adeno-associated virus serotype. *Virol J*. 2013;10:74. DOI: 10.1186/1743-422X-10-74.

366. Xiao X, Li J, Samulski RJ. Efficient long-term gene transfer into muscle tissue of immunocompetent mice by adeno-associated virus vector. *J Virol*. 1996;70:8098–108. DOI: 10.1128/JVI.70.11.8098-8108.1996.

367. Kessler PD, Podsakoff GM, Chen X, et al. Gene delivery to skeletal muscle results in sustained expression and systemic delivery of a therapeutic protein. *Proc Natl Acad Sci*. 1996;93:14082–7. DOI: 10.1073/pnas.93.24.14082.

368. Hastie E, Samulski RJ. Adeno-Associated Virus at 50: A Golden Anniversary of Discovery, Research, and Gene Therapy Success - A Personal Perspective. *Hum Gene Ther*. 2015;26:257–65. DOI: 10.1089/hum.2015.025.

369. Domenger C, Grimm D. Next-generation AAV vectors - don't judge a virus (only) by its cover. *Hum Mol Genet*. 2019:517–22. DOI: 10.1093/hmg/ddz148.

370. Buck TM, Wijnholds J. Recombinant adeno-associated viral vectors (RAAV)-vector elements in ocular gene therapy clinical trials and transgene expression and bioactivity assays. *Int J Mol Sci*. 2020;21:1–52. DOI: 10.3390/ijms21124197.

371. Choi J-H, Yu N-K, Baek G-C, et al. Optimization of AAV expression cassettes to improve packaging capacity and transgene expression in neurons. *Mol Brain*. 2014;7:17. DOI: 10.1186/1756-6606-7-17.

372. Yew NS, Wysokenski DM, Wang KX, et al. Optimization of Plasmid Vectors for High-Level Expression in Lung Epithelial Cells. *Hum Gene Ther*. 1997;8:575–84. DOI: 10.1089/hum.1997.8.5-575.

373. Xie J, Mao Q, Tai PWL, et al. Short DNA Hairpins Compromise Recombinant Adeno-Associated Virus Genome Homogeneity. *Mol Ther*. 2017;25:1363–74. DOI: 10.1016/j.ymthe.2017.03.028.

374. Yeung E, Dy AJ, Martin KB, et al. Biophysical Constraints Arising from Compositional Context in Synthetic Gene Networks. *Cell Syst*. 2017;5:11-24.e12. DOI: 10.1016/j.cels.2017.06.001.

375. Ma J, Bai L, Wang MD. Transcription under torsion. *Science*. 2013;340:1580–3. DOI: 10.1126/science.1235441.

376. Kouzine F, Liu J, Sanford S, et al. The dynamic response of upstream DNA to transcription-generated torsional stress. *Nat Struct Mol Biol*. 2004;11:1092–100. DOI:

10.1038/nsmb848.

377. Shearwin KE, Callen BP, Egan JB. Transcriptional interference - A crash course. *Trends Genet*. 2005;21:339–45. DOI: 10.1016/j.tig.2005.04.009.

378. Penaud-Budloo M, Le Guiner C, Nowrouzi A, et al. Adeno-Associated Virus Vector Genomes Persist as Episomal Chromatin in Primate Muscle. *J Virol*. 2008;82:7875–85. DOI: 10.1128/JVI.00649-08.

379. Nakai H, Yant SR, Storm TA, et al. Extrachromosomal Recombinant Adeno-Associated Virus Vector Genomes Are Primarily Responsible for Stable Liver Transduction In Vivo. *J Virol*. 2001;75:6969–76. DOI: 10.1128/jvi.75.15.6969-6976.2001.

380. Yan Z, Sun X, Feng Z, et al. Optimization of Recombinant Adeno-Associated Virus-Mediated Expression for Large Transgenes, Using a Synthetic Promoter and Tandem Array Enhancers. *Hum Gene Ther*. 2015;26:334–46. DOI: 10.1089/hum.2015.001.

381. Liu R, Liang L, Freed EF, et al. Directed Evolution of CRISPR/Cas Systems for Precise Gene Editing. *Trends Biotechnol*. 2021;39:262–73. DOI: 10.1016/j.tibtech.2020.07.005.

382. Yan WX, Hunnewell P, Alfonse LE, et al. Functionally diverse type V CRISPR-Cas systems. *Science*. 2019;363:88–91. DOI: 10.1126/science.aav7271.

383. Li SY, Cheng QX, Liu JK, et al. CRISPR-Cas12a has both cis- and trans-cleavage activities on single-stranded DNA. *Cell Res*. 2018;28:491–3. DOI: 10.1038/s41422-018-0022-x.

384. Chen JS, Ma E, Harrington LB, et al. CRISPR-Cas12a target binding unleashes indiscriminate single-stranded DNase activity. *Science*. 2018;360:436–9. DOI: 10.1126/science.aar6245.

385. Adil M, Baney K, Colin I, et al. Engineered CasX Systems - WO2020247882 2020. https://worldwide.espacenet.com/patent/search?q=pn%3DWO2020247882A1 (accessed June 25, 2021).

386. Akimoto M, Cheng H, Zhu D, et al. Targeting of GFP to newborn rods by Nrl promoter and temporal expression profiling of flow-sorted photoreceptors. *Proc Natl Acad Sci U S A*. 2006;103:3890–5. DOI: 10.1073/pnas.0508214103.

387. Clement K, Rees H, Canver MC, et al. CRISPResso2 provides accurate and rapid genome editing sequence analysis. *Nat Biotechnol*. 2019;37:224–6. DOI: 10.1038/s41587-019-0032-3.

388. Armstrong RA. Statistical guidelines for the analysis of data obtained from one or both

eyes. *Ophthalmic Physiol Opt.* 2013;33:7–14. DOI: 10.1111/opo.12009.

389. Allocca M, Mussolino C, Garcia-Hoyos M, et al. Novel Adeno-Associated Virus Serotypes Efficiently Transduce Murine Photoreceptors. *J Virol.* 2007;81:11372–80. DOI: 10.1128/jvi.01327-07.
390. Allocca M, Mussolino C, Garcia-Hoyos M, et al. Novel Adeno-Associated Virus Serotypes Efficiently Transduce Murine Photoreceptors. *J Virol.* 2007;81:11372–80. DOI: 10.1128/jvi.01327-07.
391. Xiong W, Wu DM, Xue Y, et al. AAV cis-regulatory sequences are correlated with ocular toxicity. *Proc Natl Acad Sci U S A.* 2019;116:5785–94. DOI: 10.1073/pnas.1821000116.
392. Khabou H, Cordeau C, Pacot L, et al. Dosage Thresholds and Influence of Transgene Cassette in Adeno-Associated Virus-Related Toxicity. *Hum Gene Ther.* 2018;29:1235–41. DOI: 10.1089/hum.2018.144.
393. Swaroop A, Kim D, Forrest D. Transcriptional regulation of photoreceptor development and homeostasis in the mammalian retina. *Nat Rev Neurosci.* 2010;11:563–76. DOI: 10.1038/nrn2880.
394. Petit L, Ma S, Cheng SY, et al. Rod Outer Segment Development Influences AAV-Mediated Photoreceptor Transduction after Subretinal Injection. *Hum Gene Ther.* 2017;28:464–81. DOI: 10.1089/hum.2017.020.
395. Daiger SP. RetNet 2020. https://sph.uth.edu/retnet/ (accessed April 10, 2020).
396. Motta FL, Martin RP, Filippelli-Silva R, et al. Relative frequency of inherited retinal dystrophies in Brazil. *Sci Rep.* 2018;8:1–9. DOI: 10.1038/s41598-018-34380-0.
397. Coppieters F, Lefever S, Leroy BP, et al. CEP290, a gene with many faces: Mutation overview and presentation of CEP290base. *Hum Mutat.* 2010;31:1097–108. DOI: 10.1002/humu.21337.
398. Messchaert M, Haer-Wigman L, Khan MI, et al. EYS mutation update: In silico assessment of 271 reported and 26 novel variants in patients with retinitis pigmentosa. *Hum Mutat.* 2018;39:177–86. DOI: 10.1002/humu.23371.
399. Cornelis SS, Bax NM, Zernant J, et al. In Silico Functional Meta-Analysis of 5,962 ABCA4 Variants in 3,928 Retinal Dystrophy Cases. *Hum Mutat.* 2017;38:400–8. DOI: 10.1002/humu.23165.
400. Landrum MJ, Lee JM, Benson M, et al. ClinVar: improving access to variant interpretations and supporting evidence. *Nucleic Acids Res.* 2018;46:D1062–7. DOI: 10.1093/nar/gkx1153.

401. Li H, Durbin R. Fast and accurate long-read alignment with Burrows–Wheeler transform. *Bioinformatics*. 2010;26:589–95. DOI: 10.1093/bioinformatics/btp698.

402. Rimmer A, Phan H, Mathieson I, et al. Integrating mapping-, assembly- and haplotype-based approaches for calling variants in clinical sequencing applications. *Nat Genet*. 2014;46:912–8. DOI: 10.1038/ng.3036.

403. Richards S, Aziz N, Bale S, et al. Standards and guidelines for the interpretation of sequence variants: a joint consensus recommendation of the American College of Medical Genetics and Genomics and the Association for Molecular Pathology. *Genet Med*. 2015;17:405–23. DOI: 10.1038/gim.2015.30.

404. Stoltzfus A, Norris RW. On the Causes of Evolutionary Transition:Transversion Bias. *Mol Biol Evol*. 2016;33:595–602. DOI: 10.1093/molbev/msv274.

405. Kreutzer DA, Essigmann JM. Oxidized, deaminated cytosines are a source of C → T transitions in vivo. *Proc Natl Acad Sci U S A*. 1998;95:3578–82. DOI: 10.1073/pnas.95.7.3578.

406. Lindahl T. Instability and decay of the primary structure of DNA. *Nature*. 1993;362:709–15. DOI: 10.1038/362709a0.

407. Shin HY, Wang C, Lee HK, et al. CRISPR/Cas9 targeting events cause complex deletions and insertions at 17 sites in the mouse genome. *Nat Commun*. 2017;8:15464. DOI: 10.1038/ncomms15464.

408. Kosicki M, Tomberg K, Bradley A. Repair of double-strand breaks induced by CRISPR–Cas9 leads to large deletions and complex rearrangements. *Nat Biotechnol*. 2018;36:765–71. DOI: 10.1038/nbt.4192.

409. Yang H, Ren S, Yu S, et al. Methods Favoring Homology-Directed Repair Choice in Response to CRISPR/Cas9 Induced-Double Strand Breaks. *Int J Mol Sci*. 2020;21:6461. DOI: 10.3390/ijms21186461.

410. Porto EM, Komor AC, Slaymaker IM, et al. Base editing: advances and therapeutic opportunities. *Nat Rev Drug Discov*. 2020. DOI: 10.1038/s41573-020-0084-6.

411. Komor AC, Zhao KT, Packer MS, et al. Improved base excision repair inhibition and bacteriophage Mu Gam protein yields C:G-to-T:A base editors with higher efficiency and product purity. *Sci Adv*. 2017;3:eaao4774. DOI: 10.1126/sciadv.aao4774.

412. Villiger L, Grisch-Chan HM, Lindsay H, et al. Treatment of a metabolic liver disease by in vivo genome base editing in adult mice. *Nat Med*. 2018;24:1519–25. DOI: 10.1038/s41591-018-0209-1.

413. Ryu SM, Koo T, Kim K, et al. Adenine base editing in mouse embryos and an adult

mouse model of Duchenne muscular dystrophy. *Nat Biotechnol.* 2018;36:536–9. DOI: 10.1038/nbt.4148.

414. Jiang T, Henderson JM, Coote K, et al. Chemical modifications of adenine base editor mRNA and guide RNA expand its application scope. *Nat Commun*. 2020;11:1979. DOI: 10.1038/s41467-020-15892-8.
415. Song C-Q, Jiang T, Richter M, et al. Adenine base editing in an adult mouse model of tyrosinaemia. *Nat Biomed Eng*. 2020;4:125–30. DOI: 10.1038/s41551-019-0357-8.
416. Yeh WH, Chiang H, Rees HA, et al. In vivo base editing of post-mitotic sensory cells. *Nat Commun*. 2018;9:1–10. DOI: 10.1038/s41467-018-04580-3.
417. Rees HA, Komor AC, Yeh WH, et al. Improving the DNA specificity and applicability of base editing through protein engineering and protein delivery. *Nat Commun*. 2017;8:1–10. DOI: 10.1038/ncomms15790.
418. Li X, Wang Y, Liu Y, et al. Base editing with a Cpf1-cytidine deaminase fusion. *Nat Biotechnol.* 2018;36:324–7. DOI: 10.1038/nbt.4102.
419. Hu JH, Miller SM, Geurts MH, et al. Evolved Cas9 variants with broad PAM compatibility and high DNA specificity. *Nature.* 2018;556:57–63. DOI: 10.1038/nature26155.
420. Cremers FPM, Lee W, Collin RWJ, et al. Clinical spectrum, genetic complexity and therapeutic approaches for retinal disease caused by ABCA4 mutations. *Prog Retin Eye Res.* 2020:100861. DOI: 10.1016/j.preteyeres.2020.100861.
421. Cella W, Greenstein VC, Zernant-Rajang J, et al. G1961E mutant allele in the Stargardt disease gene ABCA4 causes bull's eye maculopathy. *Exp Eye Res*. 2009;89:16–24. DOI: https://doi.org/10.1016/j.exer.2009.02.001.
422. Sangermano R, Bax NM, Bauwens M, et al. Photoreceptor Progenitor mRNA Analysis Reveals Exon Skipping Resulting from the ABCA4 c.5461-10T→C Mutation in Stargardt Disease. *Ophthalmology*. 2016;123:1375–85. DOI: https://doi.org/10.1016/j.ophtha.2016.01.053.
423. Gapinske M, Luu A, Winter J, et al. CRISPR-SKIP: Programmable gene splicing with single base editors. *Genome Biol*. 2018;19:1–11. DOI: 10.1186/s13059-018-1482-5.
424. Ivanova ME, Trubilin VN, Atarshchikov DS, et al. Genetic screening of Russian Usher syndrome patients toward selection for gene therapy. *Ophthalmic Genet*. 2018;39:706–13. DOI: 10.1080/13816810.2018.1532527.
425. Sheck L, Davies WIL, Moradi P, et al. Leber Congenital Amaurosis Associated with Mutations in CEP290, Clinical Phenotype, and Natural History in Preparation for

Trials of Novel Therapies. *Ophthalmology*. 2018;125:894–903. DOI: 10.1016/j.ophtha.2017.12.013.

426. Dulla K, Aguila M, Lane A, et al. Splice-Modulating Oligonucleotide QR-110 Restores CEP290 mRNA and Function in Human c.2991+1655A>G LCA10 Models. *Mol Ther - Nucleic Acids*. 2018;12:730–40. DOI: 10.1016/j.omtn.2018.07.010.
427. Jacobson SG, Cideciyan A V., Gibbs D, et al. Retinal disease course in Usher syndrome 1B due to MYO7A mutations. *Investig Ophthalmol Vis Sci*. 2011;52:7924–36. DOI: 10.1167/iovs.11-8313.
428. Astuto LM, Bork JM, Weston MD, et al. CDH23 mutation and phenotype heterogeneity: A profile of 107 diverse families with Usher syndrome and nonsyndromic deafness. *Am J Hum Genet*. 2002;71:262–75. DOI: 10.1086/341558.
429. Mizutari K, Mutai H, Namba K, et al. High prevalence of CDH23 mutations in patients with congenital high-frequency sporadic or recessively inherited hearing loss. *Orphanet J Rare Dis*. 2015;10. DOI: 10.1186/s13023-015-0276-z.
430. Bork JM, Peters LM, Riazuddin S, et al. Usher syndrome 1D and nonsyndromic autosomal recessive deafness DFNB12 are caused by allelic mutations of the novel cadherin-like gene CDH23. *Am J Hum Genet*. 2001;68:26–37. DOI: 10.1086/316954.
431. Valero R, De Castro-Miró M, Jiménez-Ochoa S, et al. Aberrant splicing events associated to CDH23 noncanonical splice site mutations in a proband with atypical usher syndrome 1. *Genes (Basel)*. 2019;10:1–12. DOI: 10.3390/genes10100732.
432. Quinn J, Musa A, Kantor A, et al. Genome editing strategies for treating human retinal degenerations. *Hum Gene Ther*. 2020. DOI: 10.1089/hum.2020.231.
433. Kantor A, McClements ME, Peddle CF, et al. CRISPR genome engineering for retinal diseases. Prog. Mol. Biol. Transl. Sci. 2021; DOI: 10.1016/bs.pmbts.2021.01.024.
434. Khan YA, Loughran G, Atkins JF. Contesting the evidence for -1 frameshifting in immune-functioning C-C chemokine receptor 5 (CCR5) – the HIV-1 co-receptor. *BioRxiv*. 2019. DOI: http://dx.doi.org/10.1101/513333.
435. Loughran G, Howard MT, Firth AE, et al. Avoidance of reporter assay distortions from fused dual reporters. *RNA*. 2017;23:1285–9. DOI: 10.1261/rna.061051.117.
436. Szymczak AL, Vignali DAA. Development of 2A peptide-based strategies in the design of multicistronic vectors. *Expert Opin Biol Ther*. 2005;5:627–38. DOI: 10.1517/14712598.5.5.627.
437. García-Nafría J, Watson JF, Greger IH. IVA cloning: A single-tube universal cloning system exploiting bacterial In Vivo Assembly. *Sci Rep*. 2016;6:27459. DOI:

10.1038/srep27459.

438. Kluesner M, Tasakis RN, Lerner T, et al. MultiEditR: The first tool for detection and quantification of multiple RNA editing sites from Sanger sequencing demonstrates comparable fidelity to RNA-seq. *Mol Ther - Nucleic Acids*. 2021. DOI: 10.1016/j.omtn.2021.07.008.
439. Kluesner MG, Nedveck DA, Lahr WS, et al. EditR: A Method to Quantify Base Editing from Sanger Sequencing. *CRISPR J*. 2018;1:239–50. DOI: 10.1089/crispr.2018.0014.
440. Brinkman EK, van Steensel B. Rapid Quantitative Evaluation of CRISPR Genome Editing by TIDE and TIDER. *Methods Mol Biol*. 2019;1961:29–44. DOI: 10.1007/978-1-4939-9170-9_3.
441. Lorenz R, Bernhart SH, Höner zu Siederdissen C, et al. ViennaRNA Package 2.0. *Algorithms Mol Biol*. 2011;6:26. DOI: 10.1186/1748-7188-6-26.
442. Mathews DH, Disney MD, Childs JL, et al. Incorporating chemical modification constraints into a dynamic programming algorithm for prediction of RNA secondary structure. *Proc Natl Acad Sci*. 2004;101:7287–92. DOI: 10.1073/pnas.0401799101.
443. Nishiyama J, Mikuni T, Yasuda R. Virus-Mediated Genome Editing via Homology-Directed Repair in Mitotic and Postmitotic Cells in Mammalian Brain. *Neuron*. 2017;96:755-768.e5. DOI: 10.1016/j.neuron.2017.10.004.
444. Kumar N, Stanford W, de Solis CA, et al. The development of an AAV based CRISPR SaCas9 genome editing system that can be delivered to neurons in vivo and regulated via Doxycycline and Cre-recombinase. *Front Mol Neurosci*. 2018;11:413. DOI: 10.3389/FNMOL.2018.00413.
445. Heckl D, Kowalczyk MS, Yudovich D, et al. Generation of mouse models of myeloid malignancy with combinatorial genetic lesions using CRISPR-Cas9 genome editing. *Nat Biotechnol*. 2014;32:941–6. DOI: 10.1038/nbt.2951.
446. Kostic C, Chiodini F, Salmon P, et al. Activity analysis of housekeeping promoters using self-inactivating lentiviral vector delivery into the mouse retina. *Gene Ther*. 2003;10:818–21. DOI: 10.1038/sj.gt.3301948.
447. Juven-Gershon T, Cheng S, Kadonaga JT. Rational design of a super core promoter that enhances gene expression. *Nat Methods*. 2006;3:917–22. DOI: 10.1038/nmeth937.
448. Vora S, Cheng J, Xiao R, et al. Rational design of a compact CRISPR-Cas9 activator for AAV- mediated delivery. *BioRxiv*. 2018;9:298620. DOI: 10.1101/298620.
449. McFarland TJ, Zhang Y, Atchaneeyaskul L ongsri, et al. Evaluation of a novel short

polyadenylation signal as an alternative to the SV40 polyadenylation signal. *Plasmid*. 2006;56:62–7. DOI: 10.1016/j.plasmid.2005.11.005.

450. Wheeler MA, Smith CJ, Ottolini M, et al. Genetically targeted magnetic control of the nervous system. *Nat Neurosci*. 2016;19:756–61. DOI: 10.1038/nn.4265.
451. Ma H, Wu Y, Dang Y, et al. Pol III Promoters to Express Small RNAs: Delineation of Transcription Initiation. *Mol Ther Nucleic Acids*. 2014;3:e161. DOI: 10.1038/mtna.2014.12.
452. Xie K, Minkenberg B, Yang Y. Boosting CRISPR/Cas9 multiplex editing capability with the endogenous tRNA-processing system. *Proc Natl Acad Sci U S A*. 2015;112:3570–5. DOI: 10.1073/pnas.1420294112.
453. Knapp DJHF, Michaels YS, Jamilly M, et al. Decoupling tRNA promoter and processing activities enables specific Pol-II Cas9 guide RNA expression. *Nat Commun*. 2019;10. DOI: 10.1038/s41467-019-09148-3.
454. Dong F, Xie K, Chen Y, et al. Polycistronic tRNA and CRISPR guide-RNA enables highly efficient multiplexed genome engineering in human cells. *Biochem Biophys Res Commun*. 2017;482:889–95. DOI: 10.1016/j.bbrc.2016.11.129.
455. Mefferd AL, Kornepati AVR, Bogerd HP, et al. Expression of CRISPR/Cas single guide RNAs using small tRNA promoters. *RNA*. 2015;21:1683–9. DOI: 10.1261/rna.051631.115.
456. Wei Y, Qiu Y, Chen Y, et al. CRISPR/Cas9 with single guide RNA expression driven by small tRNA promoters showed reduced editing efficiency compared to a U6 promoter. *RNA*. 2016;23:1–5. DOI: 10.1261/rna.057596.116.
457. Khani SC, Pawlyk BS, Bulgakov O V., et al. AAV-mediated expression targeting of rod and cone photoreceptors with a human rhodopsin kinase promoter. *Investig Ophthalmol Vis Sci*. 2007;48:3954–61. DOI: 10.1167/iovs.07-0257.
458. Fischer MD, McClements ME, Martinez-Fernandez de la Camara C, et al. Codon-Optimized RPGR Improves Stability and Efficacy of AAV8 Gene Therapy in Two Mouse Models of X-Linked Retinitis Pigmentosa. *Mol Ther*. 2017;25:1854–65. DOI: 10.1016/j.ymthe.2017.05.005.
459. Kuscu C, Parlak M, Tufan T, et al. CRISPR-STOP: Gene silencing through base-editing-induced nonsense mutations. *Nat Methods*. 2017;14:710–2. DOI: 10.1038/nmeth.4327.
460. Thorne N, Inglese J, Auld DS. Illuminating Insights into Firefly Luciferase and Other Bioluminescent Reporters Used in Chemical Biology. *Chem Biol*. 2010;17:646–57. DOI:

10.1016/j.chembiol.2010.05.012.

461. Hall MP, Unch J, Binkowski BF, et al. Engineered Luciferase Reporter from a Deep Sea Shrimp Utilizing a Novel Imidazopyrazinone Substrate. *ACS Chem Biol.* 2012;7:1848–57. DOI: 10.1021/cb3002478.

462. Eggington JM, Greene T, Bass BL. Predicting sites of ADAR editing in double-stranded RNA. *Nat Commun.* 2011;2:1–9. DOI: 10.1038/ncomms1324.

463. Maquat LE, Li X. Mammalian heat shock p70 and histone H4 transcripts, which derive from naturally intronless genes, are immune to nonsense-mediated decay. *RNA.* 2001;7:S1355838201002229. DOI: 10.1017/S1355838201002229.

464. Hug N, Longman D, Cáceres JF. Mechanism and regulation of the nonsense-mediated decay pathway. *Nucleic Acids Res.* 2015;44:1483–95. DOI: 10.1093/nar/gkw010.

465. Wessels H-H, Méndez-Mancilla A, Guo X, et al. Massively parallel Cas13 screens reveal principles for guide RNA design. *Nat Biotechnol.* 2020:1–6. DOI: 10.1038/s41587-020-0456-9.

466. Song Y, Yang W, Fu Q, et al. irCLASH reveals RNA substrates recognized by human ADARs. *Nat Struct Mol Biol.* 2020. DOI: 10.1038/s41594-020-0398-4.

467. Özcan A, Krajeski R, Ioannidi E, et al. Programmable RNA targeting with the single-protein CRISPR effector Cas7-11. *Nature.* 2021. DOI: 10.1038/s41586-021-03886-5.

468. Tang G, Xie B, Hong X, et al. Creating RNA Specific C-to-U Editase from APOBEC3A by Separation of Its Activities on DNA and RNA Substrates. *ACS Synth Biol.* 2021;10:1106–15. DOI: 10.1021/acssynbio.0c00627.

469. Phelps KJ, Tran K, Eifler T, et al. Recognition of duplex RNA by the deaminase domain of the RNA editing enzyme ADAR2. *Nucleic Acids Res.* 2015;43:1123–32. DOI: 10.1093/nar/gku1345.

470. Thomas JM, Beal PA. How do ADARs bind RNA? New protein-RNA structures illuminate substrate recognition by the RNA editing ADARs. *BioEssays.* 2017;39:1–8. DOI: 10.1002/bies.201600187.

471. Lehmann KA, Bass BL. The importance of internal loops within RNA substrates of ADAR1. *J Mol Biol.* 1999;291:1–13. DOI: 10.1006/jmbi.1999.2914.

472. Fry LE, McClements ME, MacLaren RE. Analysis of Pathogenic Variants Correctable With CRISPR Base Editing Among Patients With Recessive Inherited Retinal Degeneration. *JAMA Ophthalmol.* 2021;139:319. DOI: 10.1001/jamaophthalmol.2020.6418.

473. Koblan LW, Doman JL, Wilson C, et al. Improving cytidine and adenine base editors

by expression optimization and ancestral reconstruction. *Nat Biotechnol.* 2018;36:843–8. DOI: 10.1038/nbt.4172.

474. Collin GB, Gogna N, Chang B, et al. Mouse Models of Inherited Retinal Degeneration with Photoreceptor Cell Loss. *Cells.* 2020;9:1–67. DOI: 10.3390/cells9040931.
475. Mianné J, Codner GF, Caulder A, et al. Analysing the outcome of CRISPR-aided genome editing in embryos: Screening, genotyping and quality control. *Methods.* 2017;121–122:68–76. DOI: 10.1016/j.ymeth.2017.03.016.
476. Huang D, Eudy JD, Uzvolgyi E, et al. Identification of the mouse and rat orthologs of the gene mutated in Usher syndrome type IIA and the cellular source of USH2A mRNA in retina, a target tissue of the disease. *Genomics.* 2002;80:195–203. DOI: 10.1006/geno.2002.6823.
477. Bult CJ, Blake JA, Smith CL, et al. Mouse Genome Database (MGD) 2019. *Nucleic Acids Res.* 2019;47:D801–6. DOI: 10.1093/nar/gky1056.
478. Hardisty-Hughes RE, Parker A, Brown SDM. A hearing and vestibular phenotyping pipeline to identify mouse mutants with hearing impairment. *Nat Protoc.* 2010;5:177–90. DOI: 10.1038/nprot.2009.204.
479. Willott JF. Measurement of the Auditory Brainstem Response (ABR) to Study Auditory Sensitivity in Mice. *Curr Protoc Neurosci.* 2006;34:1–738. DOI: 10.1002/0471142301.ns0821bs34.
480. Landegger LD, Dilwali S, Stankovic KM. Neonatal murine cochlear explant technique as an in vitro screening tool in hearing research. *J Vis Exp.* 2017;2017:1–8. DOI: 10.3791/55704.
481. Parker M, Brugeaud A, Edge ASB. Primary culture and plasmid electroporation of the murine organ of corti. *J Vis Exp.* 2010:1–6. DOI: 10.3791/1685.
482. Altschul SF, Gish W, Miller W, et al. Basic local alignment search tool. *J Mol Biol.* 1990;215:403–10. DOI: 10.1016/S0022-2836(05)80360-2.
483. O'Leary NA, Wright MW, Brister JR, et al. Reference sequence (RefSeq) database at NCBI: current status, taxonomic expansion, and functional annotation. *Nucleic Acids Res.* 2016;44:D733–45. DOI: 10.1093/nar/gkv1189.
484. Bateman A, Martin M-J, Orchard S, et al. UniProt: the universal protein knowledgebase in 2021. *Nucleic Acids Res.* 2021;49:D480–9. DOI: 10.1093/nar/gkaa1100.
485. Kane KL, Longo-Guess CM, Gagnon LH, et al. Genetic background effects on age-related hearing loss associated with Cdh23 variants in mice. *Hear Res.* 2012;283:80–8.

DOI: 10.1016/j.heares.2011.11.007.

486. Mianné J, Chessum L, Kumar S, et al. Correction of the auditory phenotype in C57BL/6N mice via CRISPR/Cas9-mediated homology directed repair. *Genome Med.* 2016;8:16. DOI: 10.1186/s13073-016-0273-4.

487. Huber G, Beck SC, Grimm C, et al. Spectral domain optical coherence tomography in mouse models of retinal degeneration. *Investig Ophthalmol Vis Sci.* 2009;50:5888–95. DOI: 10.1167/iovs.09-3724.

488. Tao LW, Wu Z, Guymer RH, et al. Ellipsoid zone on optical coherence tomography: a review. *Clin Exp Ophthalmol.* 2016;44:422–30. DOI: 10.1111/ceo.12685.

489. Petrs-Silva H, Dinculescu A, Li Q, et al. High-efficiency transduction of the mouse retina by tyrosine-mutant AAV serotype vectors. *Mol Ther.* 2009;17:463–71. DOI: 10.1038/mt.2008.269.

490. Deng WT, Dinculescu A, Li Q, et al. Tyrosine-mutant AAV8 delivery of human MERTK provides long-term retinal preservation in RCS rats. *Invest Ophthalmol Vis Sci.* 2012;53:1895–904. DOI: 10.1167/iovs.11-8831.

491. Mayor HD, Torikai K, Melnick JL, et al. Plus and minus single-stranded DNA separately encapsidated in adeno-associated satellite virions. *Science.* 1969;166:1280–2. DOI: 10.1126/science.166.3910.1280.

492. Lecomte E, Leger A, Penaud-Budloo M, et al. Single-stranded DNA virus sequencing (SSV-Seq) for characterization of residual DNA and AAV vector genomes. *Methods Mol Biol.* 2019;1950:85–106. DOI: 10.1007/978-1-4939-9139-6_5.

493. Tran NT, Heiner C, Weber K, et al. AAV-Genome Population Sequencing of Vectors Packaging CRISPR Components Reveals Design-Influenced Heterogeneity. *Mol Ther - Methods Clin Dev.* 2020;18:639–51. DOI: 10.1016/j.omtm.2020.07.007.

494. Yan Z, Zak R, Zhang Y, et al. Distinct Classes of Proteasome-Modulating Agents Cooperatively Augment Recombinant Adeno-Associated Virus Type 2 and Type 5-Mediated Transduction from the Apical Surfaces of Human Airway Epithelia. *J Virol.* 2004;78:2863–74. DOI: 10.1128/JVI.78.6.2863-2874.2004.

495. Wiley LA, Burnight ER, Kaalberg EE, et al. Assessment of Adeno-Associated Virus Serotype Tropism in Human Retinal Explants. *Hum Gene Ther.* 2018;29:424–36. DOI: 10.1089/hum.2017.179.

496. Khabou H, Cordeau C, Pacot L, et al. Dosage Thresholds and Influence of Transgene Cassette in Adeno-Associated Virus-Related Toxicity. *Hum Gene Ther.* 2018;29:1235–41. DOI: 10.1089/hum.2018.144.

497. Lacava J, Molloy KR, Taylor MS, et al. Affinity proteomics to study endogenous protein complexes: Pointers, pitfalls, preferences and perspectives. *Biotechniques*. 2015;58:103–19. DOI: 10.2144/000114262.

498. Lyu QR, Yao P, Miano JM. Generating a CRISPR knockout mouse through a strong premature termination codon: a cautionary tale. *J Biomed Res*. 2021;35:174. DOI: 10.7555/JBR.34.20200106.

499. Zetoune AB, Fontanière S, Magnin D, et al. Comparison of nonsense-mediated mRNA decay efficiency in various murine tissues. *BMC Genet*. 2008;9:83. DOI: 10.1186/1471-2156-9-83.

500. Kurosaki T, Popp MW, Maquat LE. Quality and quantity control of gene expression by nonsense-mediated mRNA decay. *Nat Rev Mol Cell Biol*. 2019;20:406–20. DOI: 10.1038/s41580-019-0126-2.

501. Liu H, Han H, Li J, et al. An in-silico method for prediction of polyadenylation signals in human sequences. *Genome Inform*. 2003;14:84–93.

502. Proudfoot NJ. Ending the message: Poly(A) signals then and now. *Genes Dev*. 2011;25:1770–82. DOI: 10.1101/gad.17268411.

503. Kalkatawi M, Rangkuti F, Schramm M, et al. Dragon PolyA Spotter: predictor of poly(A) motifs within human genomic DNA sequences. *Bioinformatics*. 2012;28:127–9. DOI: 10.1093/bioinformatics/btr602.

504. Chandler LC, McClements ME, Yusuf IH, et al. Characterizing the cellular immune response to subretinal AAV gene therapy in the murine retina. *Mol Ther - Methods Clin Dev*. 2021;22:52–65. DOI: 10.1016/j.omtm.2021.05.011.

505. Pang JJ, Dai X, Boye SE, et al. Long-term retinal function and structure rescue using capsid mutant AAV8 vector in the rd10 mouse, a model of recessive retinitis pigmentosa. *Mol Ther*. 2011;19:234–42. DOI: 10.1038/mt.2010.273.

506. Ferrando RE, Newton K, Chu F, et al. Immunohistochemical Detection of FLAG-Tagged Endogenous Proteins in Knock-In Mice. *J Histochem Cytochem*. 2015;63:244–55. DOI: 10.1369/0022155414568101.

507. Fry LE, Patrício MI, Williams J, et al. Association of Messenger RNA Level with Phenotype in Patients with Choroideremia: Potential Implications for Gene Therapy Dose. *JAMA Ophthalmol*. 2020;138:128–35. DOI: 10.1001/jamaophthalmol.2019.5071.

508. Tornabene P, Trapani I, Minopoli R, et al. Intein-mediated protein trans-splicing expands adeno-associated virus transfer capacity in the retina. *Sci Transl Med*. 2019;11:1–14. DOI: 10.1126/scitranslmed.aav4523.

509. Trapani I. Adeno-Associated Viral Vectors as a Tool for Large Gene Delivery to the Retina. *Genes (Basel)*. 2019;10:287. DOI: 10.3390/genes10040287.

510. Pfeifer A, Brandon EP, Kootstra N, et al. Delivery of the Cre recombinase by a self-deleting lentiviral vector: Efficient gene targeting in vivo. *Proc Natl Acad Sci*. 2001;98:11450–5. DOI: 10.1073/pnas.201415498.

511. Datta S, Renwick M, Chau VQ, et al. A Destabilizing Domain Allows for Fast, Noninvasive, Conditional Control of Protein Abundance in the Mouse Eye – Implications for Ocular Gene Therapy. *Investig Ophthalmol Vis Sci*. 2018:4909–20. DOI: 10.1167/iovs.18-24987.

512. Ferry QRV, Lyutova R, Fulga TA. Rational design of inducible CRISPR guide RNAs for de novo assembly of transcriptional programs. *Nat Commun*. 2017;8:1–10. DOI: 10.1038/ncomms14633.

513. Davis KM, Pattanayak V, Thompson DB, et al. Small molecule-triggered Cas9 protein with improved genome-editing specificity. *Nat Chem Biol*. 2015;11:316–8. DOI: 10.1038/nchembio.1793.

514. Kumar N, Stanford W, de Solis C, et al. The Development of an AAV-Based CRISPR SaCas9 Genome Editing System That Can Be Delivered to Neurons in vivo and Regulated via Doxycycline and Cre-Recombinase. *Front Mol Neurosci*. 2018;11. DOI: 10.3389/fnmol.2018.00413.

515. Polstein LR, Gersbach CA. A light-inducible CRISPR-Cas9 system for control of endogenous gene activation. *Nat Chem Biol*. 2015;11:198–200. DOI: 10.1038/nchembio.1753.

516. Polack FP, Thomas SJ, Kitchin N, et al. Safety and Efficacy of the BNT162b2 mRNA Covid-19 Vaccine. *N Engl J Med*. 2020;383:2603–15. DOI: 10.1056/NEJMoa2034577.

517. Zuris JA, Thompson DB, Shu Y, et al. Cationic lipid-mediated delivery of proteins enables efficient protein-based genome editing in vitro and in vivo. *Nat Biotechnol*. 2015;33:73–80. DOI: 10.1038/nbt.3081.

518. Staahl BT, Benekareddy M, Coulon-Bainier C, et al. Efficient genome editing in the mouse brain by local delivery of engineered Cas9 ribonucleoprotein complexes. *Nat Biotechnol*. 2017;35:431–4. DOI: 10.1038/nbt.3806.

519. Wright A V., Nuñez JK, Doudna JA. Biology and Applications of CRISPR Systems: Harnessing Nature's Toolbox for Genome Engineering. *Cell*. 2016;164:29–44. DOI: 10.1016/j.cell.2015.12.035.

520. Jumper J, Evans R, Pritzel A, et al. Highly accurate protein structure prediction with

AlphaFold. *Nature*. 2021;596:583–9. DOI: 10.1038/s41586-021-03819-2.

521. Wang J, Zhang X, Cheng L, et al. An overview and metanalysis of machine and deep learning-based CRISPR gRNA design tools. *RNA Biol*. 2020;17:13–22. DOI: 10.1080/15476286.2019.1669406.
522. Xu Y, Verma D, Sheridan RP, et al. Deep Dive into Machine Learning Models for Protein Engineering. *J Chem Inf Model*. 2020;60:2773–90. DOI: 10.1021/acs.jcim.0c00073.
523. Ihry RJ, Worringer KA, Salick MR, et al. p53 inhibits CRISPR–Cas9 engineering in human pluripotent stem cells. *Nat Med*. 2018;24:939–46. DOI: 10.1038/s41591-018-0050-6.
524. Haapaniemi E, Botla S, Persson J, et al. CRISPR–Cas9 genome editing induces a p53-mediated DNA damage response. *Nat Med*. 2018;24:927–30. DOI: 10.1038/s41591-018-0049-z.
525. Orlans HO, McClements ME, Barnard AR, et al. Mirtron-mediated RNA knockdown/replacement therapy for the treatment of dominant retinitis pigmentosa. *Nat Commun*. 2021;12:1–13. DOI: 10.1038/s41467-021-25204-3.
526. Chu SH, Lam D, Packer MS, et al. Adenine Base Editing of the Sickle Allele in CD34 Hematopoietic Stem and Progenitor Cells Eliminates Hemoglobin S [Abstract]. Mol. Ther., vol. 28. 2020;1–592. DOI: 10.1016/j.ymthe.2020.04.019.
527. Musunuru K, Chadwick AC, Mizoguchi T, et al. In vivo CRISPR base editing of PCSK9 durably lowers cholesterol in primates. *Nature*. 2021;593:429–34. DOI: 10.1038/s41586-021-03534-y.
528. Katrekar D, Yen J, Xiang Y, et al. Robust RNA editing via recruitment of endogenous ADARs using circular guide RNAs. *BioRxiv*. 2021:2021.01.12.426286.
529. Wang AL, Carroll RC, Nawy S. Down-regulation of the RNA editing enzyme ADAR2 contributes to RGC death in a mouse model of glaucoma. *PLoS One*. 2014;9. DOI: 10.1371/journal.pone.0091288.
530. Gallo A, Vukic D, Michalík D, et al. ADAR RNA editing in human disease; more to it than meets the I. *Hum Genet*. 2017;136:1265–78. DOI: 10.1007/s00439-017-1837-0.
531. Bennett J, Tanabe T, Sun D, et al. Photoreceptor cell rescue in retinal degeneration (rd) mice by in vivo gene therapy. *Nat Med*. 1996;2:649–54. DOI: 10.1038/nm0696-649.
532. Davis JL, Gregori NZ, Maclaren RE, et al. Surgical Technique for Subretinal Gene Therapy in Humans with Inherited Retinal Degeneration. *Retina*. 2019;39:S2–8. DOI: 10.1097/IAE.0000000000002609.

533. Bainbridge JWB, Mehat MS, Sundaram V, et al. Long-Term Effect of Gene Therapy on Leber's Congenital Amaurosis. *N Engl J Med*. 2015;372:1887–97. DOI: 10.1056/nejmoa1414221.

534. Jacobson SG, Cideciyan A V., Roman AJ, et al. Improvement and Decline in Vision with Gene Therapy in Childhood Blindness. *N Engl J Med*. 2015;372:1920–6. DOI: 10.1056/nejmoa1412965.

535. Biogen. Identifier NCT03496012: Efficacy and Safety of BIIB111 for the Treatment of Choroideremia (STAR). *ClinicalTrialsGov*. 2020. https://clinicaltrials.gov/ct2/show/NCT03496012 (accessed September 16, 2021).

536. Biogen. Identifier NCT03116113: A Clinical Trial of Retinal Gene Therapy for X-linked Retinitis Pigmentosa Using BIIB112 (XIRIUS). *ClinicalTrialsGov*. 2021. https://clinicaltrials.gov/ct2/show/NCT03116113 (accessed September 16, 2021).

537. Han RC, Fry L, Kantor A, et al. Is subretinal AAV gene replacement still the only viable treatment option for choroideremia? *Expert Opin Orphan Drugs*. 2021. DOI: 10.1080/21678707.2021.1882300.

538. Jaeb Center for Health Research. Rate of Progression in USH2A-related Retinal Degeneration (RUSH2A). *ClinicalTrialsGov*. 2017. https://clinicaltrials.gov/ct2/show/NCT03146078 (accessed September 16, 2021).

539. Centre Hospitalier National d'Ophtalmologie des Quinze-Vingts. Identifier NCT04665726: Natural History Study of Usher Syndrome (Light4Deaf). *ClinicalTrialsGov*. 2020. https://clinicaltrials.gov/ct2/show/NCT04665726 (accessed September 16, 2021).

540. Finger RP, Daien V, Eldem BM, et al. Anti-vascular endothelial growth factor in neovascular age-related macular degeneration – a systematic review of the impact of anti-VEGF on patient outcomes and healthcare systems. *BMC Ophthalmol*. 2020;20:294. DOI: 10.1186/s12886-020-01554-2.

541. Chung SH, Sin T-N, Ngo T, et al. CRISPR Technology for Ocular Angiogenesis. *Front Genome Ed*. 2020;2:1–12. DOI: 10.3389/fgeed.2020.594984.

542. Lu Y, Brommer B, Tian X, et al. Reprogramming to recover youthful epigenetic information and restore vision. *Nature*. 2020;588:124–9. DOI: 10.1038/s41586-020-2975-4.

543. McCaughey T, Sanfilippo PG, Gooden GEC, et al. A global social media survey of attitudes to human genome editing. *Cell Stem Cell*. 2016;18:569–72. DOI: 10.1016/j.stem.2016.04.011.

544. Armsby AJ, Bombard Y, Garrison NA, et al. Attitudes of Members of Genetics Professional Societies Toward Human Gene Editing. *CRISPR J*. 2019;2:331–9. DOI: 10.1089/crispr.2019.0020.

545. Grant E. FDA regulation of clinical applications of CRISPR-CAS gene-editing technology. *Food Drug Law J*. 2016;71:608–33.

546. Sherkow JS. Controlling CRISPR Through Law: Legal Regimes as Precautionary Principles. *CRISPR J*. 2019;2:299–303. DOI: 10.1089/crispr.2019.0029.

547. National Academy of Sciences, National Academy of Medicine, National Academies of Sciences Engineering and Medicine. Human Genome Editing: Science, Ethics, and Governance. Washington, DC: The National Academies Press; 2017. DOI: 10.17226/24623.

548. Sergouniotis PI. Inherited Retinal Disorders: Using Evidence as a Driver for Implementation. *Ophthalmologica*. 2019;242:187–94. DOI: 10.1159/000500574.

549. Wilson RC, Carroll D. The Daunting Economics of Therapeutic Genome Editing. *CRISPR J*. 2019;2:280–4. DOI: 10.1089/crispr.2019.0052.

550. Halpern J, O'Hara SE, Doxzen KW, et al. Societal and Ethical Impacts of Germline Genome Editing: How Can We Secure Human Rights? *CRISPR J*. 2019;2:293–8. DOI: 10.1089/crispr.2019.0042.

551. Greely HT. Human Germline Genome Editing: An Assessment. *CRISPR J*. 2019;2:253–65. DOI: 10.1089/crispr.2019.0038.

552. National Academy of Sciences, Medicine NA of. Heritable Human Genome Editing. Washington, DC: The National Academies Press; 2020. DOI: 10.17226/25665.

553. WHO Expert Advisory Committee on Developing Global Standards for Governance and Oversight of Human Genome Editing. Human genome editing: position paper. Geneva: World Health Organization; 2021.

554. Nuffield Council on Bioethics. Genome Editing and Human Reproduction: social and ethical issues. London: Nuffield Council on Bioethics; 2018.

555. McCaughey T, Budden DM, Sanfilippo PG, et al. A Need for Better Understanding Is the Major Determinant for Public Perceptions of Human Gene Editing. *Hum Gene Ther*. 2019;30:36–43. DOI: 10.1089/hum.2018.033.

556. Jasanoff S, Hurlbut JB, Saha K. Democratic Governance of Human Germline Genome Editing. *CRISPR J*. 2019;2:266–71. DOI: 10.1089/crispr.2019.0047.

557. Fry LE, Peddle CF, Stevanovic M, et al. Promoter Orientation within an AAV-CRISPR Vector Affects Cas9 Expression and Gene Editing Efficiency. *CRISPR J*. 2020;3:276–

83. DOI: 10.1089/crispr.2020.0021.

558. Fry LE, Patrício MI, Jolly JK, et al. Expression of rab prenylation pathway genes and relation to disease progression in choroideremia. *Transl Vis Sci Technol*. 2021;10:1–12. DOI: 10.1167/tvst.10.8.12.

Appendix

A. Nucleotide sequences

Chapter 3

Name	Sequence 5'-3'
Subcloning primers used for PCR	
NotI-hu6-F1	*AT*GCGGCCGCTACCGAGGGCCTATTTCCCA
KpnI-gRNA-R1	*AT*GGTACCCCGCAAAAATCTCGCCAACA

Italicised sequences are stuffer nucleotides to enable restriction enzyme binding, underlined nucleotides are restriction enzyme sites.

gRNA Sequences	
VEGF	GGTGAGTGAGTGTGTGCGTG
RHO	TGCCATTACCTGGACCAGCCG
EGFP-13	CTGCCGTCCTCGATGTTGTG
EGFP-15	CTTGTACAGCTCGTCCATGCC
RT-PCR and sequencing primers for TIDE Analysis	
hRHO+2097F	CTTAGGCAGTGGGGTCTGTG
hRHO+2699R	GAGTGGGACCCAGTTCCAAG
VEGFA_F1	GGCTCCAACAGGTCCTCTTC
VEGFA_R1	CACCAAGGTTCACAGCCTGA
EGFP_F1	CGAGGAGCTGTTCACCGG
EGFP_R1	GTCCATGCCGAGAGTGATCC
EGFP_R3	GCAGCGTATCCACATAGCGT
qPCR Primers	
AAV Titration	
bGH AAV titre-FWD	CCAGCCATCTGTTGTTTGCC
bGH AAV titre-REV	GAAAGGACAGTGGGAGTGGC
Custom TaqMan Assays	
sgRNA.Scaffold-FWD	GTTTTAGTACTCTGGAAACAGAATCTACT
sgRNA.Scaffold-REV	GCCAACAAGTTGACGAGATAAACAC

sgRNA.Scaffold-Probe (FAM-labelled)	AAACAAGGCAAAATGC
SaCas9.FWD	GCAAAGAGAACGCCAAGTACCT
SaCas9.REV	CACTTGCCTTCCTGCATGTC
SaCas9.Probe (FAM-labelled)	ATCGAGAAGATCAAGCTGC
Reverse Transcription Gene Specific Primers	
SaCas9-gRNA-RT	ATCTCGCCAACAAGTTGACG

Chapter 4

Name	Sequence 5'-3'
Primers for EGFP Amplification	
2F (GFP)	*ACACTCTTTCCCTACACGACGCTCTTCCGATCT*NNNNNNNNNNNNNNNNGACGTAAACGGCCACAAGTTCAGC
2R (GFP)	*GTGACTGGAGTTCAGACGTGTGCTCTTCCGATCT*CGTTCTTCTGCTTGTCGGCCATGA

Italicised sequences are Illumina Adapter sequences, underlined nucleotides are random 16nt sequences acting as unique molecular identifiers for multiplexed NGS. Grey highlight indicates target binding region.

gRNA Sequences	
CasX-EGFP-Spacer	TGTGGTCGGGGTAGCGGCTG

Chapter 6

Name	Sequence 5'-3'
Subcloning primers used for PCR	
CMV-IE.BglII.FW	*ACTCAG*AGATCTCTCGAGGCGTTGACATTGAT
CMV-IE.NheI.RV	*ACTCAG*GCTAGCACCGGTAGTTAGCCAGAGAG
EFS.BglII.FW	*ACTCAG*AGATCTTGAAAGGAGTGGGAATTGGC
EFS.NheI.FW	*ACTCAG*GCTAGCACCGGTCCTGTGTTCTGG
PspCas13-NEB-EFS-FW	**TTTGCCGCCAGAACACAGGA**GGCTAGCGTTTAAACTTAAGC
PspCas13-NEB-EFS-RV	CGTGAGTGAGAACTGGTC
PspCas13-NEB-RK-FW	GTTTAAACTTAAGCTTGCCAC

PspCas13-NEB-RK-RV	GGCCAACTCCATCACTAG
Cas13bt3-NEB-RK-FW	GTTTAAACTTAAGCTTGCCAC
Cas13bt3-NEB-RK-FW	CGTGAGTGAGAACTGGTC

Italicised sequences are stuffer nucleotides to enable restriction enzyme binding, underlined nucleotides are restriction enzyme sites. Bold is overhang regions for multifragment assembly.

In Vivo Assembly primers

tRNA-Clone-FW1	**TGGACTCTGAATCCAGCGAT**CCGAGTTCAAATCTCGGTGG AACCTATGTCTTCCTGGGACGAAGACAAGTTGTGG
tRNA-Clone-RV1	**ATCGCTGGATTCAGAGTCCA**GAGTGCTAACCATTACACCAT GGAACCCTCTGGCGTAATCATGGTCATAGCTG

Bold sequences are the central homology region. Underlined sequences are the 3' primer binding region

Single stranded oligonucleotides annealed for cloning

PspXI-SGDLuc-in-frame-F	TCGACAGGACTGTCCTTACGAA
BGlII-SGDLuc-in-frame-R	GATCTTCGTAAGGACAGTCCTG
minCMV.INR.FW	GAT CTC TCG AG GGTA GGC GTG TAC GGT GGG AGG CCT ATA TAA GCA GAG CTC GTT TAG TGA ACC GTC AGA TC
minCMV.INR.RV	CTA GCA CCG GT GATC TGA CGG TTC ACT AAA CGA GCT CTG CTT ATA TAG GCC TCC CAC CGT ACA CGC CTA CC
minCMV.SCP3.FW	GAT CTC TCG AG GGTA GGC GTG TAC GGT GGG AGG CCT ATA TAA GCA GAG CTC GTT TAG TGA ACC GTC AGT CCG CCT GGA TAC ATC GAG CCG AGT GGT CGT GCC TCC ATA GAA
minCMV.SCP3.RV	CTA GCA CCG GT TTCT ATG GAG GCA CGA CCA CTC GGC TCG ATG TAT CCA GGC GGA CTG ACG GTT CAC TAA ACG AGC TCT GCT TAT ATA GGC CTC CCA CCG TAC ACG CCT ACC

Underlined nucleotides are restriction enzyme overhangs. Grey highlight indicates the promoter sequence.

Double-stranded DNA fragments

hUSH2A-W3955X *Luciferase assay target cassette*	*GATCGAT* ACTCGAGC GCC CTT GAA TTT ATG GAT GAA GGA GAC ACC CTG AGG CCT TTC ACA CTC TAC GAA TAT CGG GTC AGA GCC TGT AAC TCC AAG GGT TCA GTG GAG AGT CTG TAG TCA TTA ACA CAA ACT CTG GAA GCT CCA CCT CAA GAT TTT CCA GCT CCT TGG GCT CAA GCC ACG AGT GCT CAT TCA GTT CTG TTG AAT TGG ACA AAG AGATCT *GATCGAT*

mUsh2a-W3947X
Luciferase assay target cassette

GATCGAT ACTCGAGC CTG GAG TTT ACT GAT GAT ACA GGC ACT CTG CGG CCT TTT ACA CTG TAT GAG TAC CGG GTG AGA GCC TGG AAC TCC CAG GGT GCA GTG GAC AGC CCG T**A**G TCC ACA ATA CAG ACC CTG GAA GCC CCA CCT CG***T***GGC CTC CCA GCA CCA CGG GTT CAA GCC ACC AGT GCT CAT TCA GCC ATG CTA AAC TGG ACA GAG CCA AGATCT *GATCGAT*

SCP1 Promoter
(PsiCheck2 Cloning)

TCA GTC AGA TCT GTC GAC ACT AGT GTA CTT ATA TAA GGG GGT GGG GGC GCG TTC GTC CTC AGT CGC GAT CGA ACA CTC GAG CCG AGC AGA CGT GCC TAC GGA CCG GTC TCG TAC CTA GAG GTA CCG ACC GGT AAG CTT GCT AGC *ACT GAT*

EFS Promoter
(PsiCheck2 Cloning)

TCA GTC AGA TCT GTC GAC ACT AGT GGG CAG AGC GCA CAT CGC CCA CAG TCC CCG AGA AGT TGG GGG GAG GGG TCG GCA ATT GAT CCG GTG CCT AGA GAA GGT GGC GCG GGG TAA ACT GGG AAA GTG ATG TCG TGT ACT GGC TCC GCC TTT TTC CCG AGG GTG GGG GAG AAC CGT ATA TAA GTG CAG TAG TCG CCG TGA ACG TTC TTT TTC GCA ACG GGT TTG CCG CCA GAA CACA GGGTCT CG TAC CTA GAG GTA CCG ACC GGT AAG CTT GCT AGC *ACT GAT*

sNRP1 polyA for insertion into the pU6 backbone
Also includes upstream CMV enhancer nucleotides for cloning

*ACTGACG*TCGACATTTAAATGGTTGACATTGATTATTGACT AGTTCAGGCTCGAGGTAAGAGACCTGCTCGTGCTCTTCAAA ATAAAATACGAAATGAAATAAAATACGAAATGTGAAGAGCT CGGTTCCATGGTGTAATGGTTAGCACTCTGGACTCTGAATC CAGCGATCCGAGTTCAAATCTCGGTGGAACCTATGTCTTCC TGGGACGAAGACAAGTTGTGGAAGGTCCAGTTTTGAGGG GCTATTACAACTTTTTTTGGATCCATTTAAATTCTAGA*ACTGA C*

FLAG-sNRP1-U6-PspCas13b gRNA
Assembly for all-in-one EFS vector

AGGACCAGTTCTCACTCACGGATTACAAGGATGACGACGAT AAGTAAGAATTCCTAGAGCTCGCTGATCGCTCTTCGAAATA AAATACGAAATGAAATAAAATACGAAATGGAAGAGCACTA GTGAGGGCCTATTTCCCATGATTCCTTCATATTTGCATATAC GATACAAGGCTGTTAGAGAGATAATTGGAATTAATTTGACT GTAAACACAAAGATATTAGTACAAAATACGTGACGTAGAAA GTAATAATTTCTTGGGTAGTTTGCAGTTTTAAAATTATGTTT TAAAATGGACTATCATATGCTTACCGTAACTTGAAAGTATTT CGATTTCTTGGCTTTATATATCTTGTGGAAAGGACGAAACA CCAGAGACCTGTCGACCAGGTCTCA**GTTGTGGAAGGTCCA GTTTTGAGGGGCTATTACAAC**TTTTTTTCTAGA*GCAGGAACC CCTAGTGATGG*

U6-PspCas13b gRNA
Insertion into AAV-U6-gRNA-CAG-GFP-WPRE-bGH vector

*ACGCCA*GGTACCTCTCGAGGAGGGCCTATTTCCCATGATTC CTTCATATTTGCATATACGATACAAGGCTGTTAGAGAGATA ATTGGAATTAATTTGACTGTAAACACAAAGATATTAGTACA AAATACGTGACGTAGAAAGTAATAATTTCTTGGGTAGTTTG CAGTTTTAAAATTATGTTTTAAAATGGACTATCATATGCTTA CCGTAACTTGAAAGTATTTCGATTTCTTGGCTTTATATATCT TGTGGAAAGGACGAAACACCGATTGCAGGTGAACCTGCAC CG**GTTGTGGAAGGTCCAGTTTTGAGGGGCTATTACAAC**TT TTTTTGGACCAATTGCTCGATTCACTGGCCGTCGAACGTCGT GACTGGGAAAACCCTACTAGTGGTACC*CTGAGT*

RK -112/+87 Fragment *For multifragment assembly of RK driven plasmids*	*CCATCACTAGGGGTTCCT*GCGGCCTCTAGAGGGCCCCAGAA GCCTGGTGGTTGTTTGTCCTTCTCAGGGGAAAAGTGAGGC GGCCCCTTGGAGGAAGGGGCCGGGCAGAATGATCTAATCG GATTCCAAGCAGCTCAGGGGATTGTCTTTTTCTAGCACCTT CTTGCCACTCCTAAGCGTCCTCCGTGACCCCGGCTGGGATT TAGCCTGGTGCTGTGTCAGCCCCGGG*GTTTAAACTTAAGCT TGCCACCATG*
3×FLAG-SV40-U6-Cas13bt3 gRNA *Assembly for all-in-one Cas13bt3 vector*	*CGAGCAGGACCAGTTCTCACTCACG*GACTACAAAGACCATG ACGGTGATTATAAAGATCATGACATCGATTACAAGGATGAC GATGACAAGTAAGAATTCCTAGAGCTCGCTGATCAGCCTCG ATAAGATACATTGATGAGTTTGGACAAACCACAACTAGAAT GCAGTGAAAAAAATGCTTTATTTGTGAAATTTGTGATGCTA TTGCTTTATTTGTAACCATTATAAGCTGCAATAAACAAGTTA CTAGTGAGGGCCTATTTCCCATGATTCCTTCATATTTGCATA TACGATACAAGGCTGTTAGAGAGATAATTGGAATTAATTTG ACTGTAAACACAAAGATATTAGTACAAAATACGTGACGTAG AAAGTAATAATTTCTTGGGTAGTTTGCAGTTTTAAAATTAT GTTTTAAAATGGACTATCATATGCTTACCGTAACTTGAAAGT ATTTCGATTTCTTGGCTTTATATATCTTGTGGAAAGGACGA AACACCATGTCTTCCGTCGACGAAGACAA**GCTGGAGCAGCC CCCGATTTGTGGGGTGATTACAGC**TTTTTGCTAGC*GCAGG AACCCCTAGTGATGGAGTTG*

Italicised sequences are stuffer nucleotides to enable restriction enzyme binding or overlap sequences for multifragment assembly, underlined nucleotides are restriction enzyme sites. Grey highlight indicates the promoter or polyA sequence. The target mutation is highlight in bold red. A silent A>T mutation was introduced into the mUsh2a-W3947X sequence to abolish a PspXi site for cloning (italicised, underlined). Bold sequences indicated gRNA direct repeats.

gRNA Sequences

PspCas13b guides

5' overhangs, U6 promoter	FW: CACC RV: CAAC
5' overhangs, tRNA(GLN) promoter	FW: ACCT RV: CAAC
mUsh2a-G1-32 5'G added	GAGGGTCTGTATTGTGGAC**C**ACGGGCTGTCCACTGCACC CTGGGAGTTCCA
mUsh2a-G2-34	GGTCTGTATTGTGGAC**C**ACGGGCTGTCCACTGCACCCTGG GAGTTCCAGG
mUsh2a-G3-36 5'G added	GTCTGTATTGTGGAC**C**ACGGGCTGTCCACTGCACCCTGGGA GTTCCAGGCT
mUsh2a-G4-26	GCTTCCAGGGTCTGTATTGTGGAC**C**ACGGGCTGTCCACTGC ACCCTGGGA
mUsh2a-G5-42 5'G added	GTTGTGGAC**C**ACGGGCTGTCCACTGCACCCTGGGAGTTCCA GGCTCTCACC
mUsh2a-G6-16 5'G added	GACGAGGTGGGGCTTCCAGGGTCTGTATTGTGGAC**C**ACGG GCTGTCCACTG

mUsh2a-G7-18 5'G added	GGAGGTGGGGCTTCCAGGGTCTGTATTGTGGAC**C**ACGGGC TGTCCACTGCA
mUsh2a-G8-20	GGTGGGGCTTCCAGGGTCTGTATTGTGGAC**C**ACGGGCTGT CCACTGCACC
mUsh2a-G9-22 5'G added	GTGGGGCTTCCAGGGTCTGTATTGTGGAC**C**ACGGGCTGTC CACTGCACCCT
mUsh2a-G10-24	GGGCTTCCAGGGTCTGTATTGTGGAC**C**ACGGGCTGTCCAC TGCACCCTGG
mUsh2a-G11-28 5'G added	GTTCCAGGGTCTGTATTGTGGAC**C**ACGGGCTGTCCACTGCA CCCTGGGAGT
mUsh2a-G12-30 5'G added	GCCAGGGTCTGTATTGTGGAC**C**ACGGGCTGTCCACTGCACC CTGGGAGTTC
mUsh2a-G13-38 5'G added	GTGTATTGTGGAC**C**ACGGGCTGTCCACTGCACCCTGGGAG TTCCAGGCTCT
mUsh2a-G14-40 5'G added	GTATTGTGGAC**C**ACGGGCTGTCCACTGCACCCTGGGAGTTC CAGGCTCTCA
mUsh2a-G15-30nt-22 5'G added	GTTGTGGAC**C**ACGGGCTGTCCACTGCACCCT
mUsh2a-G16-30nt-24 5'G added	GGTGGAC**C**ACGGGCTGTCCACTGCACCCTGG
mUsh2a-G17-30nt-26	GGAC**C**ACGGGCTGTCCACTGCACCCTGGGA
mUsh2a-G18-30nt-28 5'G added	GAC**C**ACGGGCTGTCCACTGCACCCTGGGAGT
hUSH2A-G1-32 5'G added	GAGAGTTTGTGTTAATGAC**C**ACAGACTCTCCACTGAACCCT TGGAGTTACA
hUSH2A-G2-34 5'G added	GAGTTTGTGTTAATGAC**C**ACAGACTCTCCACTGAACCCTTG GAGTTACAGG
hUSH2A-G3-36 5'G added	GTTTGTGTTAATGAC**C**ACAGACTCTCCACTGAACCCTTGGA GTTACAGGCT
hUSH2A-G4-18	GAGGTGGAGCTTCCAGAGTTTGTGTTAATGAC**C**ACAGACTC TCCACTGAA
hUSH2A-G5-20	GGTGGAGCTTCCAGAGTTTGTGTTAATGAC**C**ACAGACTCTC CACTGAACC
hUSH2A-G6-22	GTGGAGCTTCCAGAGTTTGTGTTAATGAC**C**ACAGACTCTCC ACTGAACCCT
hUSH2A-G7-24	GAGCTTCCAGAGTTTGTGTTAATGAC**C**ACAGACTCTCCACT GAACCCTTG
hUSH2A-G8-26	GCTTCCAGAGTTTGTGTTAATGAC**C**ACAGACTCTCCACTGA ACCCTTGGA
hUSH2A-G9-28	GTTCCAGAGTTTGTGTTAATGAC**C**ACAGACTCTCCACTGAA CCCTTGGAGT
hUSH2A-G10-30	GCCAGAGTTTGTGTTAATGAC**C**ACAGACTCTCCACTGAACC CTTGGAGTTA
hUSH2A-G11-38	GTGTGTTAATGAC**C**ACAGACTCTCCACTGAACCCTTGGAGT TACAGGCTCT

hUSH2A-G12-40	GTGTTAATGAC**C**ACAGACTCTCCACTGAACCCTTGGAGTTACAGGCTCTGA
hUSH2A-G13-42	GTTAATGAC**C**ACAGACTCTCCACTGAACCCTTGGAGTTACAGGCTCTGACC
Non-targeting-50nt	GTAATGCCTGGCTTGTCGACGCATAGTCTGGTAATGCCTGGCTTGTCGAC
Non-targeting-30nt	GTAATGCCTGGCTTGTCGACGCATAGTCTG

Cas13bt Guides

5' overhangs, U6 promoter	FW: CACC RV: CAGC
bt-mUsh2a-30nt-14	GGTCTGTATTGTGGAC**C**ACGGGCTGTCCAC
bt-mUsh2a-30nt-16	GTCTGTATTGTGGAC**C**ACGGGCTGTCCACTG
bt-mUsh2a-30nt-18	GTGTATTGTGGAC**C**ACGGGCTGTCCACTGCA
bt-mUsh2a-30nt-20	GTATTGTGGAC**C**ACGGGCTGTCCACTGCACC
bt-mUsh2a-30nt-22	GTTGTGGAC**C**ACGGGCTGTCCACTGCACCCT
bt-mUsh2a-30nt-24	GTGGAC**C**ACGGGCTGTCCACTGCACCCTGG
bt-mUsh2a-30nt-26	GGAC**C**ACGGGCTGTCCACTGCACCCTGGGA
bt-mUsh2a-30nt-28	GAC**C**ACGGGCTGTCCACTGCACCCTGGGAGT
Bt-Non-target-30nt	GTAATGCCTGGCTTGTCGACGCATAGTCTG
bt-mUsh2a-50nt-18 5'G added	GGAGGTGGGGCTTCCAGGGTCTGTATTGTGGAC**C**ACGGGCTGTCCACTGCA
bt-mUsh2a-50nt-20	GGTGGGGCTTCCAGGGTCTGTATTGTGGAC**C**ACGGGCTGTCCACTGCACC
bt-mUsh2a-50nt-22 5'G added	GTGGGGCTTCCAGGGTCTGTATTGTGGAC**C**ACGGGCTGTCCACTGCACCCT
bt-mUsh2a-50nt-24	GGGCTTCCAGGGTCTGTATTGTGGAC**C**ACGGGCTGTCCACTGCACCCTGG
bt-mUsh2a-50nt-26	GCTTCCAGGGTCTGTATTGTGGAC**C**ACGGGCTGTCCACTGCACCCTGGGA
bt-mUsh2a-50nt-28 5'G added	GTTCCAGGGTCTGTATTGTGGAC**C**ACGGGCTGTCCACTGCACCCTGGGAGT
bt-mUsh2a-50nt-30 5'G added	GCCAGGGTCTGTATTGTGGAC**C**ACGGGCTGTCCACTGCACCCTGGGAGTTC
bt-mUsh2a-50nt-32	GAGGGTCTGTATTGTGGAC**C**ACGGGCTGTCCACTGCACCCTGGGAGTTCCA
bt-mUsh2a-50nt-34	GGTCTGTATTGTGGAC**C**ACGGGCTGTCCACTGCACCCTGGGAGTTCCAGG
bt-mUsh2a-50nt-36	GTCTGTATTGTGGAC**C**ACGGGCTGTCCACTGCACCCTGGGAGTTCCAGGCT
bt-mUsh2a-50nt-38 5'G added	GTGTATTGTGGAC**C**ACGGGCTGTCCACTGCACCCTGGGAGTTCCAGGCTCT

bt-mUsh2a-50nt-40	GTTGTGGAC**C**ACGGGCTGTCCACTGCACCCTGGGAGTTCCA GGCTCTCACC
Bt-Non-target-50nt	GTAATGCCTGGCTTGTCGACGCATAGTCTGGTAATGCCTGG CTTGTCGAC

All guides were synthesised as single stranded oligonucleotides and annealed to a synthesised complementary sequence for cloning. Appropriate restriction overhangs were added depending on the golden gate cloning destination specified above. A-C mismatch specifying the target nucleotide for editing is bold and underlined, with the mismatch distance specified in the gRNA sequence name. 5' G added to guide for U6 expression if not present.

RT-PCR and sequencing primers for editing detection

Base decomposition, luciferase plasmid

pSGDLuc F2	TTGACCTTCTTAAGCTGGCG
pSGDLuc R1	CTTCGAGTGGGTAGAATGGC

Sequences of Key Plasmid Elements

tRNA(GLN) Promoter	GGTTCCATGGTGTAATGGTTAGCACTCTGGACTCTGAATCC AGCGATCCGAGTTCAAATCTCGGTGGAACCT
SCP1 Promoter	GTA CTT ATA TAA GGG GGT GGG GGC GCG TTC GTC CTC AGT CGC GAT CGA ACA CTC GAG CCG AGC AGA CGT GCC TAC GGA CC
EFS Promoter	GGG CAG AGC GCA CAT CGC CCA CAG TCC CCG AGA AGT TGG GGG GAG GGG TCG GCA ATT GAT CCG GTG CCT AGA GAA GGT GGC GCG GGG TAA ACT GGG AAA GTG ATG TCG TGT ACT GGC TCC GCC TTT TTC CCG AGG GTG GGG GAG AAC CGT ATA TAA GTG CAG TAG TCG CCG TGA ACG TTC TTT TTC GCA ACG GGT TTG CCG CCA GAA CACA
MinCMV.Inr Promoter	GGTAGGCGTGTACGGTGGGAGGCCTATATAAGCAGAGCTC GTTTAGTGAACCGTCAGATC
minCMV.SCP3 Promoter	GGTAGGCGTGTACGGTGGGAGGCCTATATAAGCAGAGCTC GTTTAGTGAACCGTCAGTCCGCCTGGATACATCGAGCCGAG TGGTCGTGCCTCCATAGAA
CMV-IE Promoter	GACATTGATTATTGACTAGTTATTAATAGTAATCAATTACGG GGTCATTAGTTCATAGCCCATATATGGAGTTCCGCGTTACA TAACTTACGGTAAATGGCCCGCCTGGCTGACCGCCCAACGA CCCCCGCCCATTGACGTCAATAATGACGTATGTTCCCATAGT AACGCCAATAGGGACTTTCCATTGACGTCAATGGGTGGAGT ATTTACGGTAAACTGCCCACTTGGCAGTACATCAAGTGTAT CATATGCCAAGTACGCCCCCTATTGACGTCAATGACGGTAA ATGGCCCGCCTGGCATTATGCCCAGTACATGACCTTATGGG ACTTTCCTACTTGGCAGTACATCTACGTATTAGTCATCGCTA TTACCATGGTGATGCGGTTTTGGCAGTACATCAATGGGCGT GGATAGCGGTTTGACTCACGGGGATTTCCAAGTCTCCACCC CATTGACGTCAATGGGAGTTTGTTTTGGCACCAAAATCAAC GGGACTTTCCAAAATGTCGTAACAACTCCGCCCCATTGACG CAAATGGGCGGTAGGCGTGTACGGTGGGAGGTCTATATAA GCAGAGCTCTCTGGCTAACTACCGGTGCCACCATGG

CMV Promoter (no enhancer)	GTGATGCGGTTTTGGCAGTACATCAATGGGCGTGGATAGC GGTTTGACTCACGGGGATTTCCAAGTCTCCACCCCATTGAC GTCAATGGGAGTTTGTTTTGGCACCAAAATCAACGGGACTT TCCAAAATGTCGTAACAACTCCGCCCCATTGACGCAAATGG GCGGTAGGCGTGTACGGTGGGAGGTCTATATAAGCAGAGC TCTCTGGCTAACTA
RK -112/+87 promoter	GGGCCCCAGAAGCCTGGTGGTTGTTTGTCCTTCTCAGGGG AAAAGTGAGGCGGCCCCTTGGAGGAAGGGGCCGGGCAGA ATGATCTAATCGGATTCCAAGCAGCTCAGGGGATTGTCTTT TTCTAGCACCTTCTTGCCACTCCTAAGCGTCCTCCGTGACCC CGGCTGGGATTTAGCCTGGTGCTGTGTCAGCCCCGGG
hU6 Promoter	GAGGGCCTATTTCCCATGATTCCTTCATATTTGCATATACGA TACAAGGCTGTTAGAGAGATAATTGGAATTAATTTGACTGT AAACACAAAGATATTAGTACAAAATACGTGACGTAGAAAGT AATAATTTCTTGGGTAGTTTGCAGTTTTAAAATTATGTTTTA AAATGGACTATCATATGCTTACCGTAACTTGAAAGTATTTCG ATTTCTTGGCTTTATATATCTTGTGGAAAGGAC
bGH PolyA	CTGTGCCTTCTAGTTGCCAGCCATCTGTTGTTTGCCCCTCCC CCGTGCCTTCCTTGACCCTGGAAGGTGCCACTCCCACTGTCC TTTCCTAATAAAATGAGGAAATTGCATCGCATTGTCTGAGT AGGTGTCATTCTATTCTGGGGGGTGGGGTGGGGCAGGAC AGCAAGGGGGAGGATTGGGAAGACAATAGCAGGCATGCT GGGGATGCGGTGGGCTCTATGG
SV40 PolyA	TAAGATACATTGATGAGTTTGGACAAACCACAACTAGAATG CAGTGAAAAAAATGCTTTATTTGTGAAATTTGTGATGCTAT TGCTTTATTTGTAACCATTATAAGCTGCAATAAACAAGTT
sNRP1 PolyA (Dual)	AAAATAAAATACGAAATGAAATAAAATACGAAATG

Chapter 7

Name	Sequence 5'-3'
Mouse Generation	
gRNA W3947X-HDR-g3	AGGGTGCAGTGGACAGCCCG
ssDNA: W3947X HDR	GGCTCTGTCCAGTTTAGCATGGCTGAATGAGCACTGGTGG CTTGAACCCGTGGTGCTGGGAGGCCTCGAGGTGGGGCTTC CAGGGTCTGTATTGTGGACCACGGGCTGTCCACTGCACCCT GGGAGTTCCAGGCTCTCACCCGGTACTCATACAGTGTAAAA GGCCGCAGAGTGCCTGTATCATCAGTAAACTCCAGAGC
Mouse Genotyping	
Allelic Discrimination Assay	
Ush2a-W3947X_F *Common FW Primer*	GGGTGAGAGCCTGGAACTC
Ush2a-W3947X _WT_PROBE	5'-FAM-AGCCCGTGGTCCACA-BHQplus-3'

Ush2a-W3947X _Mutant_PROBE	5'-TET-AGCCCGTAGTCCACA-BHQplus-3'
Ush2a-W3947X _R	GGGCTTCCAGGGTCTGT
Common RV Primer	

ddPCR Assay

Universal Ush2a Assay	
FW Primer	GCTCTGGAGTTTACTGATGATACA
RV Primer	CAATACAGACCCTGGAAGCC
Probe	5'-FAM-TGTATGAGTACCGGGTGAGAGCCT
Ush2a-W3947X Assay	
FW Primer	GCAGTGGACAGCCCGTA
RV Primer	TGCTCATTCAGCCATGCTAAAC
Probe	5'-FAM-CCACAATACAGACCCTGGAAGCCC
Dot1l Reference Assay	
FW Primer	GCCCCAGCACGACCATT
RV Primer	TAGTTGGCATCCTTATGCTTCATC
Probe	5'-FAM-CCCAACAGGCCTGGATTCTCAATGC

AAV Titre Primers

PspCas13 AAVs

AAVtitre-Cas13-F4	AGAACAGAGCGGTACAGAAAG
AAVtitre-Cas13-R4	CCAGGATTGTCTCGATCTCTTC

Cas13bt3 AAVs and gRNA-GFP AAVs

AAVtitre-U6-F5	CGATACAAGGCTGTTAGAGAGATA
AAVtitre-U6-R5	AAACTGCAAACTACCCAAGAAA

On-target editing amplification and sequencing

Sanger Sequencing: Amplification and sequencing

mUsh2a-ex60-F1	TATGTCGTTCACAGGCGTCC
mUsh2a-ex60-R1	TTCCCGTCACCGTGAAAGC

PCR primers, targeted deep sequencing – partial illumine adapters underlined

mUsh2a-ex60-F1-NGS	ACACTCTTTCCCTACACGACGCTCTTCCGATCTTATGTCGTTCACAGGCGTCC
mUsh2a-ex60-R1-NGS	GACTGGAGTTCAGACGTGTGCTCTTCCGATCTTTCCCGTCACCGTGAAAGC

Transgene Amplification

EFS-PspCas13b Forward Primers

F1-EFS	TTTGCCGCCAGAACACAG
RK-PspCas13b Forward Primers	
F1-RK	CCTTCTTGCCACTCCTAAGC
RK-Cas13bt3 Forward Primers	
F1-bt3*	GCGACAGAATTACAACAG
Universal PspCas13b Forward Primers	
F2*	CTTAAGCTTGCCACCATGAAC
F3	GATGAGCCACCTGTACAACG
Universal ADAR2$_{DD}$ Reverse primers	
R1	ATCAGCGAGCTCTAGGAATTC
R2	GTACTCCTTTGCCGCCAG
R3*	TGCTCGAGAAGTAAATGGGC

* Used for amplification for detection and sequencing

B. Key Resources List

REAGENT or RESOURCE	SOURCE	IDENTIFIER
Antibodies		
Primary Antibodies		
Rabbit anti-SaCas9	Abcam	ab203933
Mouse anti-alpha-Tubulin	Abcam	ab7291
Mouse anti-HA	Abcam	ab18181
Rabbit anti-β actin	Abcam	Ab8227
Mouse anti-FLAG M2	Sigma-Aldrich	F1804
Mouse anti-GAPDH	Sigma-Aldrich	G8795
Rabbit anti-GFP (N-term)	Sigma-Aldrich	G1544
Rabbit anti-HA	Sigma-Aldrich	H9658
Rabbit anti-RED1 (ADAR)	Abcam	ab63840
Phalloidin (Alexa Fluor 488)	Thermo Fisher Scientific	A12379
Chicken Anti-rootletin	MerckMillipore	ABN1686
Rabbit anti-Ush2a (C-terminal)	Gift from Dr. Jun Yang, University of Utah	-
Rabbit anti-Ush2a (N-terminal)	Abcam	ab42131
Rabbit anti-Ush2a (C-terminal)	Abcam	ab82714
Mouse anti-Ush2a (N-terminal)	SantaCruz, USA	sc-515555
Vinculin	Sigma-Aldrich	V9131
Secondary Antibodies		
Donkey anti-rabbit 800W	LI-COR Biosciences	926-32213
Donkey anti-mouse 680RD	LI-COR Biosciences	926-68072
Goat anti-rabbit IgG, HRP-conjugate	Sigma-Aldrich	12-34812
Goat anti-mouse IgG (Fab Specific)-peroxidase conjugate	Sigma-Aldrich	A9917
AlexaFluor goat anti-mouse 488	Thermo Fisher Scientific	A32723
AlexaFluor goat anti-mouse 568	Thermo Fisher Scientific	A-11004
AlexaFluor goat anti-mouse 647	Thermo Fisher Scientific	A32728
AlexaFluor donkey anti-mouse 488	Thermo Fisher Scientific	A32766

AlexaFluor donkey anti-mouse 647	Thermo Fisher Scientific	A32787
AlexaFluor goat anti-chicken 488	Thermo Fisher Scientific	A-11039
AlexaFluor goat anti-chicken 647	Thermo Fisher Scientific	A32933
AlexaFluor goat anti-rabbit 488	Thermo Fisher Scientific	A32731
AlexaFluor goat anti-rabbit 568	Thermo Fisher Scientific	A-11011

Bacterial and Virus Strains

XL10-Gold Ultracompetent *E. Coli* Cells	Agilent Technologies	200315
NEB Stable Competent *E. Coli*	NEB	C3040I
NEB 5-alpha *E. Coli*	NEB	C2987I

Cell culture and AAV production

Amicon Ultra 100K filter	Sigma-Aldrich	UFC910024
0.4% Trypan Blue Solution	Thermo Fisher Scientific	15250061
Adherent Tissue Culture Plates (various sizes) - 6 Well - 12 Well - 24 Well - 96 Well	Sarstedt	Various
Adherent Vented Culture Flasks - T25 - T75 - T175	Sarstedt	Various
Corning CellBIND Surface HYPERflask	Sigma-Aldrich	10024
Corning white-walled 96 well adherent plates	Sigma-Aldrich	CLS3610
Dulbecco's Modified Eagle Medium (DMEM) without phenol red	Thermo Fisher Scientific	31053044
Heat-inactivated fetal bovine serum	Thermo Fisher Scientific	10500-064
L-glutamine	Sigma-Aldrich	G7513
Non-essential amino acids	Sigma-Aldrich	M7145
OptiMEM reduced serum media	Thermo Fisher Scientific	31985062
OptiSeal ultracentrifuge tube	Beckman-Coulter	361625
OptiPrep Density Gradient Medium	Merck Millipore	D1556
Poly-D-Lysine	Sigma-Aldrich	P6407

Polyethylenimine (PEI) transfection reagent	Polysciences	23966-2
Penicillin-streptomycin	Sigma-Aldrich	P4333
Phosphate Buffered Saline (PBS, 1X)	Thermo Fisher Scientific	10010023
Sodium pyruvate	Thermo Fisher Scientific	11360070
TransIT-LT1 transfection reagent	Mirus Bio	MIR2300
TrypLE Express dissociation reagent	Thermo Fisher Scientific	12604013

Cell Lines

HEK293-EGFP	GenTarget Inc, USA	SC001
HEK293T	PHE Culture Collections, UK	12022001

Equipment

CFX Connect Optics Module Thermal Cycler	Bio-Rad Laboratories	1855201
Cell Culture Incubator	ThermoElectron	-
Excella E24 Incubator-shaker	New Brunswick Scientific	M1352-0002
FiveEasy plus, pH meter	Mettler Toledo	01-911-302
Heat block	Techni	FBD02DD
iMark plate reader	Bio-Rad Laboratories	1681135
Megafuge Heraeus 16R	Thermo Fisher Scientific	41508322
Microstar 17 Bench top micro-centrifuge	VWR	521-1646
Multigene PCR thermocycler	Labnet International Inc	T100
NanoDrop One spectrophotometer	Thermo Fisher Scientific	840-329700
Non-toothed forceps	Surgitrac	SC71
Odyssey Fc imaging system	LI-COR Biosciences	2800
Operating microscope	Zeiss	OpMi-1
Optima XE-90, Ultracentrifuge	Beckman Coulter	CXE13016
Pipetboy	PBS Integra	939939
Pipette 1000 μL	Gilson	P1000
Pipette 200 μL	Gilson	P200
Pipette 20 μL	Gilson	P20
Pipette 2 μL	Gilson	P2N

PowerPac basic powerpack	Bio-Rad Laboratories	041BR69803
PowerPac HC High-Current Power Supply	Bio-Rad Laboratories	1645052
Qubit 3 Fluorometer	Thermo Fisher Scientific	Q33216
SimpliAmp PCR thermocycler	Thermo Fisher Scientific	A24811
Spectralis™ HRA+OCT	Heidelberg Engineering	-
Subretinal syringe	World Precision Instruments	Nanofil
TC20 automated cell counter	Bio-Rad Laboratories	1450102
Toothed forceps	Surgitrac	SC49
Touchclave Autoclave	LTE Scientific	0086 & 0037
Trans-Blot Turbo transfer system	Bio-Rad Laboratories	690BR013715
Type 70Ti, Ultracentrifuge rotor	Beckman Coulter	13E 1007
UV transilluminator (U:Genious)	Syngene, UK	SYUG/1343
Vannas scissors	Surgitrac	SC81
Waterbath	Fisherbrand	FB60305
Colordome Electroretinography machine	Diagnosys LLC	-
Cryotome LSE	Thermo Scientific	-
Nanofil 34G Bevelled subretinal needle	World Precision Instruments	NF34BV
Nanofil 10 µl syringe	World Precision Instruments	NANOFIL
Heated mouse recovery box	Mediheat	-
DTL Plus Electrodes	Diagnosys LLC	E300 (D141)
Experimental Models: Organisms/Strains		
B6.Cg-Tg(*Nrl-EGFP*)1Asw/J	Gift from Anand Swaroop	-
C57BL/6J	Charles River, UK	632C57BL/6J
USH2A-W3947X-EM1-CDH23-B6	MRC Harwell, UK	-
Glass and Plasticware		
Coverslips, Rectangular, #1 thickness 22 mm x 60 mm	VWR	10118-793
Coverslips, Round, #0 thickness, 6mm	SLS, UK	
Coverslips, Round, #1 thickness, 13mm	SLS, UK	

Falcon Tubes - 15 mL - 50 mL	Sarstedt	

Molecular reagents, chemicals and kits

100bp PCRRanger DNA Ladder	Norgen, USA	11300
1kb UltraRanger DNA Ladder	Norgen, USA	12100
2-Propanol	VWR	20842.300
5× reducing sample buffer	National Diagnostics, USA	EC-887
Agar	Thermo Fisher Scientific	30391049
Agarose	GeneFlow, UK	A4-0700
Ampicillin	Sigma-Aldrich	A9518-25G
Antisedan (Atipamezole)	Zoetis, UK	134787-2
B-Mercaptoethanol	Sigma-Aldrich	M3148-25ML
Betaine 5M	Sigma-Aldrich	B0300
BLUeye Protein size ladder	GeneFlow, UK	S6-0024
Bovine Serum Albumin	Fisher Scientific, UK	BP9703-100
Chloramphenicol eye drops (0.5%)	Bausch & Lomb	76836
Clarity Western ECL Substrate	Bio-Rad Laboratories	705061
cOmplete mini protease inhibitor	Sigma-Aldrich	4693159001
Criterion TGX gels	Bio-Rad Laboratories	5671033
DNAse digestion kit	Qiagen	79254
DNAse I	NEB	
EndoFree Plasmid Maxi Kit	Qiagen	FD1703
Ethanol (100%)	VWR	20821.321
FastDigest DpnI	ThermoFisher Scientific	FD1703
Formaldehyde (PFA) 16% w/v	Thermo-Fisher	28906
Gel Extraction Kit	Qiagen	28704
Gel loading dye 6×	NEB	B7024S
GenElute Plasmid Miniprep Kit	Sigma-Aldrich	PLN350-1KT
Hoechst 33342 10mg/mL	Thermo Fisher Scientific	H3570
Hypromellose 0.3%	Martindale Pharma	D01673
iTaq SYBR green mix	Bio-Rad Laboratories	172-5120
KOD Hotstart Mastermix	Merck	71842-3

Luria Broth	Thermo Fisher Scientific	12795-027
Methanol	VWR	20847.307
miRNeasy Mini kit	Qiagen	217084
Milk powder, Fat Free	Tesco, UK	-
NEBuilder Hifi DNA Assembly Kit	NEB	E5520S
Normal Goat Serum	Sigma-Aldrich	G9023
Normal Donkey Serum	Sigma-Aldrich	D9663
O.C.T compound	VWR	361603E
Odyssey TBS Blocking Buffer	LI-COR Biosciences	927-50000
OligoDT(20) reverse transcription primers	Thermo Fisher Scientific	18418020
OptiPrep density gradient medium	Sigma	D1556-250ML
Phosphate Buffered Solution tablets	Gibco	18912-014
Phusion DNA Polymerase	NEB	M0530S
Pierce BCA protein assay kit	Thermo Fisher Scientific	23225
Pierce 660nm Protein Assay	Thermo Fisher Scientific	22660
Pierce LAL Chromogenic Endotoxin Quantitation Kit	Thermo Fisher Scientific	88282
ProLong Diamond Antifade Mountant	Life technologies	P36961
Protein ladder	Geneflow	15H24
Proteinase K (Cat# 1045166)	Qiagen	1045166
Proxymetacaine HCl minims	Bausch & Lomb, UK	236-8017
PureLink HiPure Plasmid Midiprep Kit	Thermo Fisher Scientific	K2100-22
PVDF membranes, Low Fluorescence	Bio-Rad Laboratories	1704275
QIAamp DNA mini kit	Qiagen	51304
QiaQuick PCR purification kit	Qiagen	28106
Quick Calf Intestinal Phosphatase	NEB	M0525S
QuickChange II XL kit	Agilent, USA	200521
Qubit 1 dsDNA HS Assay Kit	Thermo Fisher Scientific	Q33231
Restriction enzymes, various	NEB	Various
RIPA Buffer	Sigma-Aldrich	20-188
RNEasy Mini Plus Kit	Qiagen	74136
Shrimp Alkaline Phosphatase	NEB	M0371S
SOC medium	Thermo Fisher Scientific	15544-03

Sodium Chloride, reagent grade	Sigma	S9625
SuperScript III reverse transcription kit	Thermo Fisher Scientific	18080-051
T4 DNA ligase	NEB	B0202S
T4 polynucleotide kinase (PNK)	Thermo Fisher Scientific	EK0031
TAE Buffer	Severn Biotech Ltd	20-6001-50
TaqMan Fast Universal Mastermix	Thermo Fisher Scientific	4352042
Trans-Blot Turbo 5× Transfer Buffer	Bio-Rad	36-22-42
Tris-Buffered Saline	Bio-Rad Laboratories	1706435
Tris-Buffered Saline (TBS) 10× buffer	Bio-Rad	170-6435
Tris/Glycine/SDS 10× running buffer	Nat Diagnostics	EC-870
Triton X-100	Sigma	9002-93-1
Tropicamide eye drops (1%)	Bausch & Lomb	76852
Tween 20	Sigma-Aldrich	P1373-500ML
Virkon 1%	VWR	330003
Viscotears	Alcon	44011T
Zyppy Plasmid Miniprep Kit	Zymo Research	D4036

Plasmids

pX601-AAV-CMV-IE-SaCas9.FWD-U6-gRNA	Addgene	61591
pX601-AAV-CMV-IE-SaCas9.REV-U6-gRNA	This study	
pC0048-CMV-IE-dPspCas13b-longlinker-ADAR2DD(E488Q)	Addgene	103864
pC0053-CMV-IE-dPspCas13b-GS-ADAR2DD(E488Q)-delta-984-1090	Addgene	103869
pC0054-CMV-IE-dPspCas13b-longlinker-ADAR2DD(E488Q/T375G)	Addgene	103870
pC0055-CMV-IE-dPspCas13b-GS-ADAR2DD(E488Q/T375G)-delta-984-1090	Addgene	103871
pC0043-U6-PspCas13b crRNA backbone	Addgene	103854
pSGDlucV3.0 (Out-frame)	Addgene	119760
pSGDlucV3.0 (In-frame)	This study	
pSGDlucV3.0 (hUSH2a-W3955X)	This study	
pSGDlucV3.0 (mUsh2a-W3947X)	This study	
AAV-EFS-SaCas9-U6-gRNA	Gift from A. Kantor	
psiCheck-2	Promega	C8021
MinCMV.Inr-psiCheck2	This study	

MinCMV.SCP3- psiCheck2	This study	
CMV-psiCheck2	Gift from M McClements	
CMV-IE-psiCheck2	This study	
EFS-psiCheck2	This study	
SCP1-psiCheck2	This study	
SCP1-dPspCas13b-GS-ADAR2DD(E488Q)-delta-984-1090	This study	
EFS-dPspCas13b-GS-ADAR2DD(E488Q)-delta-984-1090	This study	
CMV-dPspCas13b-GS-ADAR2DD(E488Q)-delta-984-1090-sNRP1	This study	
tRNA(GLN)-PspCas13b crRNA backbone	This study	
pU6-Cj-sgRNA	Addgene	89753
pU6-sNRP1 cloning backbone	This study	
AAV-CAG-GFP-WPRE-bGH	Gift from M Patricio	
AAV-CAG-dsRed	Gift from C. Peddle	
AAV-EFS-dPspCas13b-ADAR2$_{DD}$(E488Q)-sNRP1-U6-gRNA	This study	
AAV-EFS-dPspCas13b-ADAR2$_{DD}$(E488Q/T375G)-sNRP1-U6-gRNA	This study	
AAV-EFS-dPspCas13bdel-ADAR2$_{DD}$(E488Q)-sNRP1	This study	
AAV-EFS-dPspCas13bdel-ADAR2$_{DD}$(E488Q/T375G)-sNRP1	This study	
AAV-RK-dPspCas13bdel-ADAR2$_{DD}$(E488Q)-sNRP1	This study	
AAV-RK-dPspCas13bdel-ADAR2$_{DD}$(E488Q/T375G)-sNRP1	This study	
CMV-IE-HIVNES-dCas13b-T1-ADAR2DD(E488Q)-bGH	Gift from F. Zhang	
CMV-IE-HIVNES-dCas13b-T3-ADAR2DD(E488Q)-bGH	Gift from F. Zhang	
CMV-IE-HIVNES-dCas13b-T5-ADAR2DD(E488Q)-bGH	Gift from F. Zhang	
Bt1-cRNA	Gift from F. Zhang	
Bt3-cRNA	Gift from F. Zhang	
Bt5-cRNA	Gift from F. Zhang	
AAV-RK-dCas13b-T3-ADAR2$_{DD}$(E488Q)-SV40-U6-gRNA	This study	
pAdDeltaF6 (AAV Helper Plasmid)	Gift from M McClements	

pAAV2/8 Y733F (AAV capsid)	Gift from M McClements	
pDG plasmid (AAV2 Rep/Cap/Helper)	PlasmidFactory, Germany	PF421

Software and Algorithms

Benchling lab notebook	Benchling, USA	Http://www.benchling.com
CFX Maestro Software	Bio-Rad Laboratories	3.1
FIJI	NIH, USA	v.2.10
Geneious	Biomatters, New Zealand	R11
Prism 9	GraphPad, USA	v.9.2.0
HEYEX	Heidelberg, Germany	
Image Studio Lite software	LI-COR Biosciences	v5.2.5
MARS Data Analysis software	BMG Labtech, Germany	
Microsoft Excel (Mac)	Microsoft, USA	16.37
NEBuilder Assembly Tool	NEB	http://nebuilder.neb.com/
Omega Reader Control Software	BMG Labtech, Germany	
Python	https://www.python.org/	v.3.8.1
QuikChange primer design	Agilent Technologies	https://www.agilent.com/store/primerDesignProgram.jsp;
RStudio	RStudio, USA	v.1.2.5042
R Statistical Software	R Core Team, Austria	v.4.0.0
Tidyverse R Package	Hadley Wickham, USA	v.1.3.0

Other

Sanger sequencing service	Eurofins Genomics	
Sanger sequencing service	Source Bioscience	
Sanger sequencing service	Genewiz	
Next generation sequencing service, Amplicon-EZ	Genewiz	

TaqMan Assays

All ThermoFisher Scientific, USA		
GAPDH		Hs9999905_m1

ACTB	Hs01060665_g1
EGFP	Mr04329676_mr
Gapdh	Mm99999915_g1
Ush2a- Ex12/13	Mm00498761_m1
Ush2a-Exon 63/64	Mm01323936_m1

C. Code and Macros

Retinal Mean Grey Value Measurement

Spectralis_MGV Macro_v1.0.ijm
Written for ImageJ / FIJI macro 'Run' mode for quantification of mean grey value of blue autofluorescence images as described in Chapter 4

```
// Macro to measure the mean grey value of retina and export to
excel
//Lewis Fry Nov 21 2020
//This works with Spectralis HRA images saved as .tif
//Standard size = 16x17.04 inch (1536x1636px, 96px/inch) images
(longer than tall as there is an image info bar at bottom

//Dependencies: Install "Read to Excel Plugin" Before starting
//Processes a folder full of images - all images for analysis
should be placed in this folder.
//Saves to an excel file on desktop - rename and remove this
file before analysing another batch

//All images process with gaussian blur to smooth pixels


//#### DEFINE FUNCTIONS ####
//Each measurement consists of two functions - one to check the
folder and only process .tif, and one to measure the MGV

//--SUPERIOR MGV MEASUREMENT--
//make ellipse offset from centre to avoid nerve
//- Positioned 100px from top and 100x from side. Width = Total
width (1536px) - Border width (200px total)
//- Height set to avoid nerve. 1536px height - 250px for nerve
- 200px for borders

function processFolder_supMGV(input) {
list = getFileList(input);
      for (i = 0; i <list.length; i++) {
            if(endsWith(list[i], ".tif"))
                  processFile_supMGV(input, list[i]);
                  }
}

function processFile_supMGV(input, file) {

            print("Measuring Superior MGV: " + input + file);

            open(input+list[i]);

            run("Gaussian Blur...", "sigma=3");

            //Selection of superior half circle
            run("Specify...", "width=1336 height=1080 x=100
y=100 oval"); {
                        if (selectionType!=1)
```

```
                                exit("Elliptical selection
required");
                            getBoundingRect(x, y, width, height);
                            midy = y + height/2;
                            getSelectionCoordinates(sx, sy);
                            for (i=0; i<sy.length; i++) {
                                if (sy[i]>midy) sy[i] = midy;
                            }
                            makeSelection(3, sx, sy);
                        }
                run("Measure");
                close();

                    }

//--INFERIOR MGV MEASUREMENT--
//as above, but positioned into bottom. y set to offset from
bottom by 100 px

function processFolder_infMGV(input) {
list = getFileList(input);
      for (i = 0; i <list.length; i++) {
            if(endsWith(list[i], ".tif"))
                  processFile_infMGV(input, list[i]);
                  }
}

function processFile_infMGV(input, file) {

                print("Measuring Inferior MGV: " + input + file);

                open(input+list[i]);

                run("Gaussian Blur...", "sigma=3");

                run("Specify...", "width=1336 height=1080 x=100
y=356 oval");
                    {
                            if (selectionType!=1)
                                exit("Elliptical selection
required");
                            getBoundingRect(x, y, width, height);
                            midy = y + height/2;
                            getSelectionCoordinates(sx, sy);
                            for (i=0; i<sy.length; i++) {
                                if (sy[i]<midy) sy[i] = midy;
                            }
                            makeSelection(3, sx, sy);
                        }
                run("Measure");

                close();

                    }

//--360 BAND --
// Measures a donut shape around the optic nerve 600x600pixels
size with a band of 250pixels
```

```
function processFolder_bandMGV(input) {
list = getFileList(input);
      for (i = 0; i <list.length; i++) {
            if(endsWith(list[i], ".tif"))
                  processFile_bandMGV(input, list[i]);
                  }
}

function processFile_bandMGV(input, file) {

            print("Measuring Band MGV: " + input + file);

            open(input+list[i]);

            run("Gaussian Blur...", "sigma=3");

            run("Specify...", "width=600 height=600 x=468 y=468
oval constrain");
            run("Make Band...", "band=2.65");
            run("Measure");

            close();

                  }


//#### CODE ####
//run each of the above functions. Folder is done iteratively
e.g. measures superior for all images then exports to excel.
Then reads inferior and adds to same excel doc.
//results are populated with all images for each measurement
before export

setBatchMode(true); //This hides the images during processing

run("Clear Results");

//Set Measurements
run("Set Measurements...", "mean min display redirect=None
decimal=3");

//Ask user for directory. All images for analysis should be in
here.
input = getDirectory("Choose Directory");

//Superior MGV Measurement
processFolder_supMGV(input);
run("Read and Write Excel", "dataset_label=[Superior Mean Grey
Value]");
run("Clear Results");

//Inferior MGV Measurement
processFolder_infMGV(input);
run("Read and Write Excel", "dataset_label=[Inferior Mean Grey
Value]");
run("Clear Results");
```

```
//Band MGV Measurement
processFolder_bandMGV(input);
run("Read and Write Excel", "dataset_label=[Band Mean Grey
Value]");
run("Clear Results");
```

Retinal Imaging Thermal Heatmap

MGV Thermal.ijm
Written for ImageJ / FIJI macro visualisation blue autofluorescence images as thermal heatmaps, described in Chapter 4

```
// Macro to convert BAF images acquired from the Heidelberg
Spectralis into thermal heatmap profiles
// Run this through batch mode (Process > Batch > Macro)

run("8-bit");
run("Gaussian Blur...", "sigma=75");
run("Thermal");
run("RGB Color")
setBackgroundColor(0, 0, 0);
run("Specify...", "width=1536 height=1536 x=768 y=768 oval
constrain centered");
run("Crop")
run("Clear Outside");
run("Size...", "width=300 height=300 depth=1 constrain average
interpolation=Bilinear");
```

D. Publications, Presentations, Reviews, Grants, Awards & Prizes

Arising from or related to work completed during this thesis.

Published Manuscripts

Review article & Book Chapters

Fry LE, Peddle CF, Barnard AR, et al. RNA editing as a therapeutic approach for retinal gene therapy requiring long coding sequences. *Int J Mol Sci.* 2020;21. DOI: 10.3390/ijms21030777.

Elements of text, table and figures included and inform introduction and discussion. Re-use permission granted under Creative Commons Attributions Licence

Kantor A, McClements ME, Peddle CF, **Fry LE** et al. CRISPR genome engineering for retinal diseases. Prog. Mol. Biol. Transl. Sci. 2021; DOI: 10.1016/bs.pmbts.2021.01.024.

Han RC, **Fry L**, Kantor A, et al. Is subretinal AAV gene replacement still the only viable treatment option for choroideremia? *Expert Opin Orphan Drugs.* 2021. DOI: 10.1080/21678707.2021.1882300.

Peddle CF, **Fry LE**, McClements ME, et al. CRISPR Interference–Potential Application in Retinal Disease. *Int J Mol Sci.* 2020;21:2329. DOI: 10.3390/ijms21072329.

Original Articles

Fry LE, Peddle CF, Stevanovic M, et al. Promoter Orientation within an AAV-CRISPR Vector Affects Cas9 Expression and Gene Editing Efficiency. *CRISPR J.* 2020;3:276–83. DOI: 10.1089/crispr.2020.0021.

Elements of text, and figures used in Chapter 3. Re-use permission granted by Karen Ballen, Manager, Reprints, Permissions, and Liebert Open Access, Mary Ann Liebert, Inc publishers, New Rochelle, NY

Fry LE, McClements ME, MacLaren RE. Analysis of Pathogenic Variants Correctable With CRISPR Base Editing Among Patients With Recessive Inherited Retinal Degeneration. *JAMA Ophthalmol.* 2021;139:319. DOI: 10.1001/jamaophthalmol.2020.6418.

Elements of text, figures and tables used in Chapter 4. Re-use permission granted under American Medical Association licence number 5118980298753, Jul 30 2021

Fry LE, Patrício MI, Williams J, et al. Association of Messenger RNA Level with Phenotype in Patients with Choroideremia: Potential Implications for Gene Therapy Dose. *JAMA Ophthalmol*. 2020;138:128–35. DOI: 10.1001/jamaophthalmol.2019.5071.

Fry LE, Patrício MI, Jolly JK, et al. Expression of rab prenylation pathway genes and relation to disease progression in choroideremia. *Transl Vis Sci Technol*. 2021;10:1–12. DOI: 10.1167/tvst.10.8.12.

Presentations

AAV delivery of Cas13-ADAR for *in vivo* retinal RNA editing. Genome Engineering: Frontiers of CRISPR-Cas. Cold Spring Harbour Laboratory New York (Virtual Meeting) 2021. Poster presentation.

RNA editing for Usher Syndrome II, an inherited retinal degeneration. Genome Engineering Oxford (Virtual). Seminar held by the University of Oxford, Oxford, UK. December 2020. (Co-organiser and chair)

RNA Editing For Usher Syndrome Using CRISPR-Cas13. American Society for Cell and Gene Therapy (Virtual Meeting) 2020. Poster Presentation.

Guide RNA orientation influences Cas9 expression in a single vector approach to CRISPR editing in a model system. Genome Engineering: Frontiers of CRISPR-Cas. Cold Spring Harbour Laboratory New York 2019. Poster presentation.

Guide RNA orientation influences Cas9 expression in a single vector approach to CRISPR editing in a model system. Oxford Ophthalmological Congress 2019. Poster presentation.

Genome Engineering for Inherited Retinal Disease. OxVis Meeting. Seminar held by the University of Oxford, Oxford, UK. March 2019

Guide RNA orientation influences Cas9 expression in a single vector approach to CRISPR editing in a model system. ARVO 2019, Vancouver. Poster presentation.

Pathological donor splice site mutations beyond the dinucleotide canonical sequence in choroideremia. Oxford Ophthalmological Congress 2018. Poster presentation.

Pathological donor splice site mutations beyond the dinucleotide canonical sequence in choroideremia. ARVO 2018, Hawaii. Oral presentation.

Peer Review Activity

Experimental Eye Research. 2021. Journal peer review.

Genes. 2020. Journal peer review

AFM Telethon Scientific Council. 2020. Grant Round.

Ophthalmic Research Institute of Australia. 2019. Grant Round. Royal Australian and New Zealand College of Ophthalmologists. Prize for best review

Grants

MRC Harwell Genome Editing Mice for Medicine Programme 2019. Funding for the generation of a novel mouse model of Usher syndrome. Co-applicant.

Awards & Prizes

Thomas Willis Prize Nuffield Department of Clinical Neuroscience. Best three-minute thesis presentation, fourth year student (joint). 2021

Masters Medal Worshipful Company of Spectacle Makers. Best first published paper by a vision science PhD student in the UK. 2020

Alain Locke Studentship Hertford College. Research fellowship for final year of PhD. 2020

Merton Prize Scholarship Merton College. 2020

Rhodes Scholarship New Zealand & Merton. In conjunction with the Oxford-Mossouris-Merton Graduate Scholarship 2017

Supreme AIMES Award North Harbour Club, New Zealand. Scholarship recognising young leaders. 2017